P-1

THE INTERNATIONAL HYDROGRAPHIC REVIEW

VOL. 30 · Nº 2
NOVEMBER 2024

IHO International Hydrographic Organization



P-1

THE INTERNATIONAL HYDROGRAPHIC REVIEW

VOL. 30 · Nº 2
NOVEMBER 2024

IHO
International Hydrographic Organization

International Hydrographic Organization
Vol. 30 · Nº 2 — November 2024

© Copyright International Hydrographic Organization [2024]

This work is copyright. Apart from any use permitted in accordance with the Berne Convention for the Protection of Literary and Artistic Works (1886), and except in the circumstances described below, no part may be translated, reproduced by any process, adapted, communicated or commercially exploited without prior written permission from the Secretariat of the International Hydrographic Organization (IHO). Copyright in some of the material in this publication may be owned by another party and permission for the translation and/or reproduction of that material must be obtained from the owner.

This document or partial material from this document may be translated, reproduced or distributed for general information, on no more than a cost recovery basis. Copies may not be sold or distributed for profit or gain without prior written agreement of the IHO Secretariat and any other copyright holders.

In the event that this document or partial material from this document is reproduced, translated or distributed under the terms described above, the following statements are to be included:

"Material from IHO publication [reference to extract: Title, Edition] is reproduced with the permission of the IHO Secretariat (Permission No ……/…) acting for the International Hydrographic Organization (IHO), which does not accept responsibility for the correctness of the material as reproduced: in case of doubt, the IHO's authentic text shall prevail. The incorporation of material sourced from IHO shall not be construed as constituting an endorsement by IHO of this product." "This [document/publication] is a translation of IHO [document/publication] [name]. The IHO has not checked this translation and therefore takes no responsibility for its accuracy. In case of doubt the source version of [name] in [language] should be consulted."

The IHO Logo or other identifiers shall not be used in any derived product without prior written permission from the IHO Secretariat.

Cover image

The cover image shows a historic map of Easter Island (rapanui Rapa Nui) from 1888. In his article, Hugo Gorziglia presents the preparation of this chart as a historical document chronicling the 150-year history of the Hydrographic and Oceanographic Service of the Chilean Navy (pp. 146–157).

Open Access Policy

This journal provides immediate open access to its content on the principle that making research freely available to the public supports a greater global exchange of knowledge.

About the Journal

The International Hydrographic Review (IHR) is an international scientific journal publishing peer-reviewed papers on all aspects of hydrography and associated subjects, ranging from the latest technical developments and significant events to book reviews and historical recollections. The IHR was first published in 1923 and since then has been published regularly.

Editorial



Patrick Westfeld

Welcome to the second issue of the 30th volume of The International Hydrographic Review (IHR).

The current issue comprises a comprehensive and diverse range of topics related to the field of hydrography and associated disciplines. We will begin with the latest developments in key hydrographic topics, including data acquisition and processing, before moving on to present advanced work from navigation, oceanography, geology and, followed by community and social relevance topics such as a project through the International Hydrographic Organization (IHO) Capacity Building Programme and the Mapping the Plastic in the Sea initiative of the International Federation of Surveyors (FIG).

The first four of the eight scientific peer-reviewed articles in this issue address the provision of bathymetric information of the seabed from disparate perspectives: Peter Grabbert et al. have developed an innovative approach for extracting spatiotemporal-resolved bathymetry from satellite imagery using *AI-based optical hydrography*, offering a powerful tool *for the adaptive planning of hydrographic resources* (pp. 12–29). In their research, Mona Reithmeier et al. present a fully automatic, scalable, and globally applicable workflow for the provision of *coastal bathymetry from ocean surface wave kinematics* derived from satellite data. (pp. 30–43). Patrick Debroisse & Brian Miles introduce an *open-source software tool* designed *to assess the quality of volunteered bathymetric data*, which could serve as a crucial element in the process of incorporating such data into nautical charts, bathymetric models, survey planning, and decision-making tools (pp. 44–55). The latest version of a *digital bathymetric model for Danish waters*, offering a grid resolution of 50 metres, integrates hundreds of survey datasets, including both modern and historical sources, as well as bathymetric data derived from satellite imagery and crowdsourced sources (Giuseppe Masetti et al., pp. 56–69).

The following two scientific peer-reviewed articles address significant issues in the field of marine geodesy: Gilad Even-Tzur et al. enhance and refine the *Israeli geoid undulation model in the coastal zone* through the utilisation of nautical and shipborne GNSS observations (pp. 70–80). The potential for satellite navigation interference by jamming or spoofing the GNSS signal is investigated by Thiago Azevedo de Vasconcelos et al. in the Baltic and North Seas (pp. 82–97).

In one of the last two scientific peer-reviewed articles, Jan Rhomberg-Kauert et al. employ photogrammetric methods and techniques of high-dimensional data analysis to investigate submerged ecosystems, with a particular focus on the *detection of macrophytes using bathymetric LiDAR* (pp. 98–115). Finally, Yerinelys Santos Barrera et al. present a new approach to the structural and morphological model on the continental margin of the Colombian Caribbean using recent hydrographic data and bathymetric analysis techniques (pp. 116–126).

An eight-part series of notes / technical reports presents a synthesis of recent insights drawn from a variety of disciplinary perspectives: The *analysis of sedimentation* through the utilisation of hydrographic surveys (Harold Rojas Macías et al., pp. 128–135); the potential of neural networks in understanding the complex *hydrodynamic processes in the Black Sea* (Emre Gülher, pp. 134–145); a concise, chronological account of the *150-year history of the Hydrographic and Oceanographic Service of the Chilean Navy* (Hugo Gorziglia, pp. 148–159); an overview of the IHO-Nippon Foundation *Geospatial Marine Analysis and Cartography project* (Masan-

ISSN print: 0020-6946
DOI prefix: 10.58440
URL: https://ihr.iho.int/

Publisher:
International Hydrographic Organisation
4b Quai Albert 1er
98011 Monaco

Editorial Board:
https://ihr.iho.int/editorial-team/

ao Sumiyoshi et al., pp. 160–168); the necessity of *environmental and hydrospatial monitoring systems* exemplified by the UK Hydrographic Office Marine Environmental Monitoring Stations Framework (Becky Conway, pp. 170–173); the provision of community support by *mapping the plastic debris in coastal margins* from drones (Simon Ironside et al., pp. 174–181); the utilisation of *crowd-sourced bathymetry for* the purposes of *post-disaster analysis* (Shaul Solomon et al., pp. 182–189); the investigations on the increase in the number of *marine accidents* (BK Ramprasad, pp. 190–197).

The continued success of a peer-reviewed journal is contingent upon the willingness of reviewers to dedicate their time and provide constructive feedback to enhance the quality of submitted manuscripts. These endeavours are undertaken behind the scenes and are frequently not acknowledged. While ultimate responsibility for decision-making resides with the editorial team, the input of reviewers, who possess a wealth of technical expertise and scientific insights, an understanding of the social, environmental and economic implications of the material under consideration, as well as a keen passion for their subject matter, is of significant benefit to the editorial process. In recognition of the contributions made by our peer reviewers, we, the IHO Secretariat and the IHR Editorial Board, would like to express our profound gratitude and publicly acknowledge our peer reviewers. Henceforth, the names of these individuals will be published annually in the November issue of the IHR (pp. 198–199).

This issue includes a review of the recently published book *Legal and regulatory aspects of telecommunication submarine cables* by Andrés Fígoli Pacheco (Aldo Monaca & Gioia Alessia Chiara Grazia Indelicato, (pp. 200–202). The book addresses a number of legal and regulatory issues pertaining to submarine cables, encompassing a diverse array of legal topics related to the ownership, installation, operation, and maintenance of submarine telecommunications cables.

The current issue concludes with an obituary for Jean-Nicolas Pasquay (Gilles Bessero, pp. 204–205).

On behalf of the Editorial Board, I hope that you will enjoy reading this new issue of the IHR!



Dr Patrick Westfeld
Chief Editor, IHR

https://doi.org/10.58440/ihr-30-2-e03

Content

Peer-reviewed articles

12 **Spatiotemporal analysis of satellite imagery using AI-based optical hydrography for adaptive planning of hydrographic resources**
Peter Grabbert, Mirko Bothe and Patrick Westfeld

30 **Improving global coastal bathymetry from waves – Introducing scalable processing and post-processing workflows for 100 m resolution grids**
Mona Reithmeier, Ingo Laut, Matthijs Gawehn, Christoph Kleih, Jens Schneider von Deimling and Knut Hartmann

44 **Toward automated volunteer and authoritative bathymetry discovery and comparison**
Patrick Debroisse and Brian Miles

56 **Denmark's Depth Model version 2.0 – Improved compilation of bathymetric data within the Danish waters**
Giuseppe Masetti, Philip Sigaard Granding, Kasper Langdahl, Lasse Mondberg Schwenger and Kristian Villadsen Kristmar

70 **Expanding and improving the Israeli geoid undulation model in the coastal area using nautical and shipborne GNSS measurements**
Gilad Even-Tzur, Jareer Khalilieh and Barry Grinker

82 **Satellite navigation interference monitoring in the Baltic and North Seas**
Thiago Azevedo de Vasconcelos, Lothar Kurz, Andriy Konovaltsev, Tobias Ehlers and Michael Meurer

98 **Macrophyte detection with bathymetric LiDAR – Applications of high-dimensional data analysis for submerged ecosystems**
Jan Rhomberg-Kauert, Lucas Dammert, Michael Grömer, Martin Pfennigbauer and Gottfried Mandlburger

116 **Aguja Canyon – New approach added to the structural and morphological model in the continental margin of the Colombian Caribbean**
Yerinelys Santos Barrera, María Fernanda Calderón Grande, Eliana Gutiérrez Rincón and Johanna P. Vargas Morales

Notes / Technical reports

128 **Sedimentation analysis at the mouth of the Dique Channel to the Cartagena Bay through hydrographic surveys**
Harold Rojas Macías, Octavio Martinez Martinez and Marjohnny Monterroza Pantoja

136 **Investigation of tempo-spatial variability of the Black Sea hydrodynamics by means of neural networks**
Emre Gülher

148 **The establishment of the Hydrographic and Oceanographic Service of the Chilean Navy (SHOA) – A succinct chronological account of its 150 years**
Hugo Gorziglia

160 **Overview of the IHO–Nippon Foundation GEOMAC project and its evolution over 15 years**
Masanao Sumiyoshi, Kazufumi Matsumoto, Leonel Manteigas and Lucy Fieldhouse

170 **Importance of environmental and hydrospatial monitoring systems – The UK Hydrographic Office Marine Environmental Monitoring Stations Framework**
Becky Conway

174 **Mapping the plastic – Helping communities address the global plastic waste crisis**
Simon Ironside, Gordana Jakovljevic and Naa Dedei Tagoe

182 **Utilizing crowd-sourced bathymetry for post disaster analysis – A case study**
Shaul Solomon, Uri Yoselevich and Ariel Tunik

190 **Marine accidents ascribe to man or machine?**
BK Ramprasad

General information

198 **Acknowledgement to peer-reviewers**

Book review

200 **Legal and regulatory aspects of telecommunication submarine cables**
Aldo Monaca and Gioia Alessia Chiara Grazia Indelicato

Obituary

204 **In Memoriam: Jean-Nicolas Pasquay (1932–2024)**
Douglas Paul Brunt

PEER-REVIEWD ARTICLE

Spatiotemporal analysis of satellite imagery using AI-based optical hydrography for adaptive planning of hydrographic resources

Authors

Peter Grabbert[1], Mirko Bothe[1] and Patrick Westfeld[1]

Abstract

Demand-driven and resource-efficient hydrographic surveying requires prior knowledge of the variability of the seabed. This paper presents an approach to obtain this prior knowledge of changes in seabed topography by means of bathymetric data derived from less accurate but high frequency multispectral satellite imagery and a change analysis based on it. This approach is designed to be implemented as a fully automated operational service at the German Federal Maritime and Hydrographic Agency to provide decision support for the operational planning of hydrographic surveying. Spectrally-derived bathymetry is conducted using a convolutional neural network, with a median absolute error of 0.47 m and a RMSE of 0.86 m. Various change detection techniques such as principle component analysis, change vector analysis, least squares tracking and robust median difference are used for change analysis. The results are weighted together with additional current and wave information and summarised into a single change value. Finally, the data is spatially aggregated and converted into an intuitive traffic light scheme that provides a recommended course of action and enables a more targeted hydrographic surveying.

Keywords

optical hydrography · Sentinel-2 · spectrally-derived bathymetry · satellite-derived-bathymetry · SDB · change detection · seabed monitoring · hydrographic survey planning

Resumé

Les levés hydrographiques axés sur la demande et l'utilisation efficace des ressources nécessitent une connaissance préalable de la variabilité des fonds marins. Cet article présente une approche permettant d'obtenir cette connaissance préalable des changements dans la topographie des fonds marins au moyen de données bathymétriques dérivées d'images satellites multispectrales moins précises mais à haute fréquence, ainsi qu'une analyse des changements basée sur ces données. Cette approche est conçue pour être mise en œuvre en tant que service opérationnel entièrement automatisé à l'Agence fédérale maritime et hydrographique allemande afin de fournir une aide à la décision pour la planification opérationnelle des levés hydrographiques. La bathymétrie dérivée de la spectrométrie est réalisée à l'aide d'un réseau neuronal convolutif, avec une erreur absolue médiane de 0,47 m et un RMSE de 0,86 m. Diverses techniques de détection des changements, telles que l'analyse des composantes principales, l'analyse des vecteurs de changement, le suivi des moindres carrés et la différence médiane robuste, sont utilisées pour l'analyse des changements. Les résultats sont pondérés avec des informations supplémentaires sur les courants et les vagues et résumés en une seule valeur de changement. Enfin, les données sont agrégées dans l'espace et converties en un schéma intuitif de feux de circulation qui fournit un plan d'action recommandé et permet un levé hydrographique plus ciblé.

✉ Peter Grabbert · peter.grabbert@bsh.de

[1] German Federal Maritime and Hydrographic Agency, Nautical Hydrography, 18057 Rostock, Germany

https://doi.org/10.58440/ihr-30-2-a15

Resumen

Los levantamientos hidrográficos dirigidos por la demanda y eficientes en el uso de los recursos requieren un conocimiento previo de la variabilidad del fondo marino. Este artículo presenta un enfoque para obtener este conocimiento previo de los cambios en la topografía del fondo marino mediante datos batimétricos derivados de imágenes multiespectrales por satélite menos precisas pero de alta frecuencia, y un análisis de cambios basado en él. Este enfoque está diseñado para implementarlo como un servicio operativo totalmente automatizado en la Agencia Federal Marítima e Hidrográfica de Alemania para proporcionar apoyo a la toma de decisiones para la planificación operativa de levantamientos hidrográficos. La batimetría derivada espectralmente se realiza mediante una red neuronal convolucional, con un error de mediana absoluta de 0,47 m y un RMSE (error cuadrático medio) de 0,86 m. Para el análisis de los cambios se utilizan diversas técnicas de detección de cambios, como el análisis de componentes principales, el análisis de vectores de cambio, el seguimiento por mínimos cuadrados y la diferencia mediana robusta. Los resultados se ponderan junto con información adicional de corrientes y olas, y se resumen en un único valor de cambio. Finalmente, los datos se agregan espacialmente y se convierten en un esquema de semáforo intuitivo que proporciona un curso de acción recomendado y permite un levantamiento hidrográfica más dirigido.

1 Introduction

The German Federal Maritime and Hydrographic Agency (BSH) is responsible for monitoring the current state of Germany's coastal waters, including the Exclusive Economic Zones (EEZ) of the North Sea and the Baltic Sea, to ensure sustainable economic use while protecting the marine environment. Accurate and up-to-date information on water depths, tides, currents and weather conditions is essential for safe and sustainable maritime navigation. This requires the continuous acquisition, processing, analysis and provision of up-to-date geospatial data of the seabed. In recent years, user requirements for BSH products, particularly information on water depths, have increased significantly in terms of timeliness, accuracy and reliability. However, the underwater topography of the North Sea and Baltic Sea is constantly changing, especially in shallow coastal areas. As a result, more frequent hydrographic surveys are needed to provide the most up-to-date information on the topography of the seabed. Currently, survey planning at BSH is set according to a rigid schedule based on water depth and traffic volume, regardless of actual changes in seabed topography. This approach leads to poor resource allocation and only partially meets user needs. Improved knowledge of seabed changes would allow more efficient prioritisation of survey platform deployments and better planning of survey operations. A semi-automated service based on satellite imagery providing up-to-date information about temporal seabed variability would therefore be beneficial.

To date, a considerable body of literature has emerged on the use of multispectral satellite imagery for deriving water depths. This literature encompasses a range of approaches, including physical modelling, empirical regression techniques, and AI-based methods (Mandelburger, 2022; IHO, 2024). The spectrally-derived bathymetry (SDB) approaches that have been published to date are primarily research studies that necessitate at least some level of interactive input and derive bathymetry within a circumscribed research area, frequently in a clear water environment (e.g. the Caribbean or the Mediterranean Sea). One exception is the SDB-online tool developed by EOMAP (Hartmann et al., 2022). The objective of these SDB-algorithms is to estimate the bathymetric data on a one-off basis rather than a time series. This approach enables the selection of satellite images that are optimally aligned with the prevailing environmental conditions. The presented approaches are designed to analyse the optimal satellite image(s) with respect to cloud cover, atmospheric conditions, ocean waves, and turbidity levels in order to ascertain the least disturbed water column. In order to obtain a continuous time series, it is necessary to examine satellite imagery that is less suitable and which depicts more challenging environmental conditions. However, there is currently a lack of profound solutions to this problem. Additionally, there are only a few studies that use spectrally-derived water depths to estimate seabed change (Hermann et al., 2022; Erena et al., 2020). These studies employ a relatively simple and optimisable band-ratio approach for bathymetric calculation and simple differences for change analysis. The studies were conducted as academic research rather than as a fully automated service, and are thus not suitable as a ready-to-use solution for optimising decision-making in the planning of hydrographic surveys.

The main contribution of this work is the robust estimation of a water depth time series with SDB and their use for subsequent change analysis. Furthermore, the method is fully automated, allowing it to be deployed as a permanent service on a large scale to support the planning of hydrographic surveys. The paper proposes a prototype service as a means of achieving the aforementioned improvement in the BSH's survey planning strategy. Firstly, the service utilises freely available Sentinel-2 (ESA, 2024) multispectral data to derive underwater topography for large shallow-water areas, for which the service employs a SDB methodology. Although the SDB outcomes are less precise and reliable than those based on hydroacoustic surveys (Leder et al., 2023), they are available at an exceptionally high temporal resolution with minimal survey effort.

The derived bathymetric time series is employed to identify dynamic areas through the utilisation of change detection techniques, including principal component analysis, change vector analysis, robust median difference and 2.5D least squares tracking (LST). The derived change detection parameters are weighted, summed and clustered, resulting in a set of area-specific metrics and decision parameters, which are presented in an intuitive traffic light system. This is supported by recommendations for action to facilitate the operational planning of the hydrographic survey service.

2 Literature review

SDB is an optical hydrographic method that employs multispectral imaging (MSI) and is typically conducted from space-based or airborne platforms (Mandelburger, 2022; Laporte et al., 2023; IHO, 2024). SDB makes use of the established physical relationship between the radiometric values of the spectral bands and water depth, as first demonstrated by Poicyn et al. (1970). The process is intricate and contingent upon a multitude of variables, including water depth, atmospheric characteristics, water quality factors such as turbidity and algae, bottom reflectance, wave activity and the sun elevation angle. Furthermore, the wavelength λ of the light in question enables the water depth to be calculated using MSI (Lyzenga, 1978). SDB is constrained to the optically shallow water area, whereby the bottom of the water body must be visible; thus, it is limited to approximately one Secchi depth (Jégat et al., 2016). However, greater depths of up to approximately two times Secchi depth are possible (Leder et al., 2019). The accuracy is typically depth-dependent and decreases with increasing water depth, due to the reduction in light penetration and subsequent reduction in the signal-to-noise ratio (Stumpf et al., 2003; Chénier et al., 2018, 2023).

The implementation of SDB typically entails the integration of both intrinsic physical relationships and empirically derived parameters. However, the extent of physics-based modelling employed in the beam path can vary considerably, from comprehensive, physics-based models to purely regression-based machine learning models (Mandlburger, 2022). In theory, the physical approach requires no reference data and has no empirical component, provided that the substrate and the water conditions are considered to be homogeneous (Mandlburger, 2022). This is not the case in practice, and thus some parameters are usually determined empirically with at least some reference data (still referred to in the literature as the physics-based approach, e.g. Geyman & Maloof, 2019; Najar, 2022). The initial regression-based approaches employed straightforward physical relationships with the ratio of spectral bands, with a primary emphasis on empirical derivation from reference data (Stumpf et al., 2003). Contemporary machine learning models occasionally lack pre-programmed physical principles and instead establish the relationship between input variables and the output variable (water depth) through training (Chu et al., 2023; IHO, 2024).

Stumpf et al. (2003) established the traditional empirical bathymetry using the ratio of the natural logarithms of the reflectance R in the blue and green spectral channels to calculate the pseudo depth $PD_{\text{BlueGreen}}$:

$$PD_{BlueGreen} = \frac{\ln(R_{Blue})}{\ln(R_{Green})} \quad (1)$$

This pseudo depth exhibits a linear correlation with the undisturbed water depth, as determined by a linear regression with a minimal number of required reference depths. In an extension of this approach, Geyman & Maloof (2019) employed a greater number of similar logarithmic band ratios, derived from the blue/green, blue/red, green/red, blue/near-infrared (NIR) and green/NIR combinations. Subsequently, these variables are employed in a multiple linear regression with reference data to ascertain the correlation with water depth. Utilising this methodology, the study area exhibited an average absolute error of 25 cm at depths reaching 6 m near Andros Island (Bahamas).

Susa (2022) compared traditional band ratio algorithms with two machine learning methods, namely random forest and extreme gradient boosting (XGBoost). The performance of these algorithms was evaluated using multispectral Sentinel-2 imagery of a study area situated in the vicinity of Puerto Rico. The results demonstrated that the machine learning models yielded comparable outcomes that were significantly superior to those of the traditional band-ratio approaches. However, the machine learning models required much more training data. In addition, environmental factors such as near-shore waves, light penetration depth into the water body, water turbidity and surface glint or foam limit all the approaches tested. The best result was obtained with a random forest model, which could infer the water depth with a median absolute error (MedAE) of 0.71 m and a root mean square error (RMSE) of 1.81 m in the tested area. Another machine learning method is used in the study by Mandlburger et al. (2021), who used a convolutional neural network (CNN) in a U-net structure to analyse the depth of freshwater lakes in southern Germany. The images were captured by an unmanned aerial vehicle (UAV) with a resolution of approximately 5 cm × 5 cm and containing RGB and a coastal blue channel (~ 400–460 nm). To make efficient use of the computing power, the scenes were cut into 480 px × 480 px sub-scenes, and further augmented training images were generated by rotation and mirroring. A systematic deviation of about 12 cm and a standard deviation of about 40 cm could be achieved for an artificial lake used as a test site. An extended approach was developed by Xie et al. (2024), who implemented a physics-informed CNN in a U-net structure by including data based on radiative transfer. The training data set comprised bathymetric data extracted from

https://doi.org/10.58440/ihr-30-2-a15

ICESat-2 (Ice, Cloud and Land Elevation Satellite), resulting in bathymetric depths with an RMSE of 1.39–1.69 m down to a depth of 40 m for two test areas in the Caribbean with Sentinel-2 data.

The studies reviewed were preliminary pilot studies rather than long-term operational services, which are critical for an effective change detection based on an image sequence analysis. However, there is currently one fully automated approach provided by the commercial SDB-Online tool presented by Hartmann et al. (2022). The tool is based on the physical approach where the total backscatter received by the satellite sensor is split into its signal components from the seabed, the water surface, the atmosphere and the water column, allowing the contribution from the water depth to be derived (Legleiter et al., 2009). However, the service is not open source and remains a kind of black box, making it challenging to adapt the algorithms. Furthermore, the area of interest and configuration parameters must be shared with the server, which may be contrary to security interests. Additionally, the service is rather costly and therefore not well suited to widespread and frequent use.

Change analysis and the associated monitoring of bathymetric movements can be understood as image sequence analysis, where the images contain depth and spectral information. This allows the use of image sequence analysis methods, which are popular in photogrammetry and computer vision applications. Change detection usually proceeds according to the following scheme: The database of two or more images is pre-processed (e.g. for geometric registration, radiometric correction, denoising), then change detection algorithms such as image subtraction, change vector analysis (CVA), principal component analysis (PCA), statistical tests and tracking algorithms are used to quantify the variability of the image space and then segmented into variable and static areas (Asokan, 2018).

Deng et al (2008) employed MSI from SPOT-5 (10 m × 10 m) and Landsat-7 (30 m × 30 m) to analyse land use change in urban areas using PCA. As a consequence of the loss of information resulting from the transfer to the eigenvector space and back, variable areas are highlighted. These differences are significantly greater for the variable areas than for the unchanged areas, and thus may be more pronounced. A classification accuracy of 89 % of the area was obtained using reference data for comparison derived from government information. In contrast, Xu et al. (2019) employed a CVA to investigate ecological changes utilising multispectral data from MODIS (Moderate-resolution Imaging Spectroradiometer). An image sequence from 2002 to 2017 was used as a database, for each ecological index (RSEI), which describes the characteristics of moisture, greenness, dryness and heat points. A CVA combined with thresholds dynamically adapted to the respective standard deviation was used to detect changes. The process is automated, but the interpretation of the data is not.

A 3D time-of-flight camera image sequence was examined by Westfeld et al. (2013). A 2.5D LST (Westfeld, 2012) was employed, which is capable of utilising both the grey-scale intensity and range information of the camera simultaneously in an adapted least squares matching. This allows for the pixel-wise tracking of surface elements along an image sequence, thereby enabling the continuous estimation of body posture and motion vectors of individual human body parts.

To date, the authors are aware of two published studies that have conducted a change analysis or monitoring of bathymetry data extracted from remote sensing. Hermann et al. (2022) compared two epochs, 2019 and 2021, using one Sentinel-2 image and one ICESat-2 track per time point in a coastal area in the Gulf of Mexico. The bathymetric depth was calculated in accordance with the band ratio approach outlined by Stumpf et al. (2003), utilising the ICESat-2 data as a reference for the linear regression from pseudo to real depths. A simple difference formation is employed to perform the temporal comparison, which is then followed by a median filter for the purpose of data smoothing. The accuracy achieved is estimated using airborne LiDAR (light detection and ranging) data as a reference, and is reported as a standard deviation of 1.29 m and an RMSE of 2.11 m. Erena et al. (2020) processed a sequence of high-resolution images with a resolution of 50 cm to 2 m from Pléiades satellite sensors, comprising 22 time points from 2012 to 2019 of the Mediterranean Sea in south-eastern Spain. The SDB was calculated using the band ratio approach proposed by Stumpf et al. (2003). However, additional data sources were integrated from airborne LiDAR, an echosounder mounted on an unmanned surface vehicle (USV), and Global Navigation Satellite System (GNSS), in order to develop a digital terrain model (DTM) of the lagoon. The change analysis was conducted by calculating the water mask using the normalised difference water index (NDWI) for each time point and deriving the water level and storage volume from the DTM. However, it should be noted that the change analysis is not directly based on the SDB.

The works reviewed are primarily field studies, rather than ready-to-use solutions for an automated service. Furthermore, change analysis based on SDB results is still a rare and insufficiently performed endeavour. In light of this, the service presented in this paper attempts to address this gap in the existing literature.

3 Processing chain and data requirements of the SDB-based seabed monitoring service

The presented service (Fig. 1) employs a time series of MSI data and supplementary input information (Section 3.1; Appendix A), to initially ascertain the water depths within a specified region. To achieve this, the MSIs are subjected to a pre-processing and pre-sorting operation, after which the bathymetry is

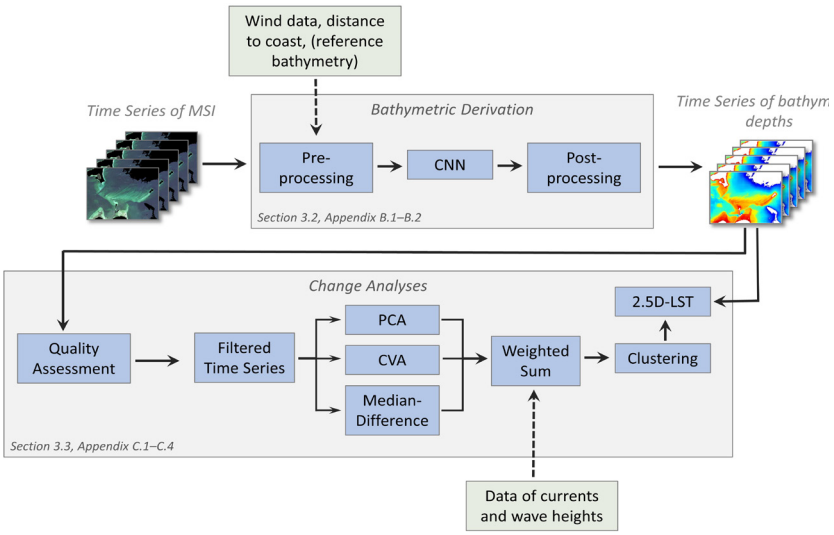


Fig. 1 Processing chain of the developed service.

computed using a CNN and subsequently undergoes a post-processing phase (Section 3.2; Appendix B). The change analysis (Section 3.3; Appendix C) is performed by first selecting the appropriate MSIs using a quality analysis. Subsequently, the changes are quantified through the utilisation of assorted change detection techniques, the outcomes are merged and clustered in accordance with the traffic light-inspired scheme.

3.1 Used data

Satellite imagery. The proposed service is based on Sentinel-2 data (ESA, 2024) due to its high spatial resolution of up to 10 m × 10 m and the availability of the data at no costs. The Sentinel-2 mission is operated by the European Space Agency (ESA) and currently compromises three satellites (launched in 2015, 2017 and 2024) with a revisit time of ten days for each satellite. The images captured by the satellites possess 13 spectral bands B, five of which, spanning from coastal blue (B_1) to very NIR (B_5), are capable of at least partial penetration into the water body. However, the other bands in the spectrum of NIR and short-wave infrared (SWIR) support the deviation of additional features such as algae, clouds and the land-water-mask (Section 3.2). Images with atmospheric correction and bottom-of-atmosphere (BOA) reflections, generated by the Sen2Cor processor as specified by Louis (2021), are employed for the service.

Bathymetric reference. To generate the CNN for the bathymetric deviation, a data-driven machine learning approach requires reference data on water depth. The data are obtained from multibeam and single-beam echosounder measurements from BSH hydrographic surveys. A 10 m × 10 m raster dataset has been generated from the latest available data, but there is still a time lag between the reference data and the satellite images. Therefore, especially in dynamic areas, they may be outdated and thus incorrect 'reference' data. Nevertheless, the aforementioned areas are of a relatively limited extent in comparison to the appropriate areas, thus allowing for the continued utilisation of the data for the training of the CNN.

Additional data. The service employs supplementary data, including wind information, to evaluate the appropriateness of satellite imagery and the distance from the coast to facilitate bathymetric derivation. Additionally, wave height and current ancillary data are integrated, as they are important environmental factors driving seabed variability. Further details regarding the utilised datasets can be found in Appendix A.

3.2 Bathymetric processing workflow

This section covers the steps from the provision of satellite imagery to the bathymetric time series that serve as the basis for the subsequent change analysis (Fig. 1).

In order to ensure the accuracy and reliability of bathymetric calculations derived from satellite imagery, it is of paramount importance to select images that are optimally suited to the prevailing environmental conditions. Factors such as clouds, cloud shadows, atmospheric conditions, turbidity, swell, sun glint, turbidity, foam, algae and ice must be considered to guarantee the precision of the resulting bathymetric data. These challenges are offset by a number of compensatory measures. At the level of the 100 km × 100 km Sentinel-2 images, the sorting process employs cloud masks and wind strength (correlated with turbidity, waves and foam ridges). Moreover, the satellite images are divided into sub-scenes of approximately 20 km × 20 km, with the cloud coverage calculated for each of these sub-scenes. The sub-scenes are then processed to remove any areas designated as land, ice, and foreign territory, after which they are evaluated for suitability (Appendix B.1). In the event that a sub-scene is to be calculated, then turbidity parameters and logarithmic band combinations, as proposed by Geyman & Maloof (2019), are calculated. Due to the computational limitations of the CNN, the sub-scenes are reduced to a smaller size of 256 px × 256 px. Further details on the pre-processing can be found in Appendix B.1.

The subsequent phase is the actual estimation of the bathymetry, which is conducted through the utilisation of CNN regression. CNNs constitute a subset of artificial neural networks (ANN), which are particularly well suited to image analysis due to the presence of built-in spatial filters (LeCun et al., 1998). The CNN is a wholly empirical approach, whereby the relationship between input variables and output bathymetry is learned from reference data without any physical background knowledge. Nevertheless, some physical principles are integrated through the inclusion of input parameters such as the turbidity parameters and the logarithmic band combinations. This work employs the CNN architecture developed by Żak (2020) and utilises a U-net structure (Appendix B.2). The latest model was trained for 80 epochs using 10,000 pre-processed images, as previously described, with 80 % allocated for training and 20 % for validation. The final result of the training process is a bathymetric

https://doi.org/10.58440/ihr-30-2-a15

model with a particular focus on the German Baltic Sea. During the prediction process, the trained model can be employed to derive the water depth from similarly pre-processed small images of new satellite MSI.

The bathymetric result of the CNN has a shape of 256 px × 256 px, which can be reasonable reassembled into a larger and more convenient size of sub-scenes covering an area of approximately 20 km × 20 km. This approach offers a suitable compromise between a comprehensive coverage and the avoidance of unnecessary expansion of the dataset with irrelevant areas such as land and deep waters. The boundary regions of the predicted scenes frequently exhibit considerable deviations due to the limited padding possibilities of the CNNs. Consequently, the prediction is performed with a substantial overlap (~ 80 % has proven useful). For reassembly, the border regions are trimmed and the inner regions are arithmetically averaged.

3.3 Change analysis workflow

The second step in the development of the service is the robust and reliable detection of seabed changes (Fig. 1). This involves the identification and quantification of changes in spatially delimited areas. The input is based on the previously derived time series of bathymetric data.

A qualitative analysis of the derived time series is initially conducted to evaluate the suitability of each time point. Parameters such as cloud cover, wind speed, mean turbidity and the mean difference of the bathymetry from the mean bathymetry are considered to derive an overall score that allows for the adaptive filtering of the time series. Further information may be found in Appendix C.1.

Secondly, a set of change detection techniques are applied to this filtered time series, with each pixel quantified according to its variability over the image series. Thus, a PCA, a CVA and a robust median difference are performed, with each producing one or more parameters describing change. Additionally, another change-describing value is calculated using the wave and current data in the time period under consideration. Further information may be found in Appendix C.2.

The change values are normalised, weighted and summed up to a total change value per pixel. This is then clustered using a k-means algorithm and transferred into four classes, ranging from 0 (no change) to 3 (very strong change). This is followed by morphological filtering to reduce noise. Further details can be found in Appendix C.3.

2.5D LST, an integrated matching technique developed by Westfeld (2012), estimates pixel-wise 3D motion vectors with subpixel accuracy between surface elements of a consecutive image sequence. It employs depth and intensity values in order to fully exploit the potential of the measurement signal, thereby providing a more accurate and reliable solution, particularly in instances where the contrast ratio within one of the two channels is challenging. 2.5D LST is applied to each pixel (and its surrounding 31 px × 31 px neighbourhood, corresponding to 620 m × 620 m on the seabed's surface) of areas previously identified as being subjected to significant change. Further information can be found in Appendix C.4.

4. Case studies

4.1 Study areas

The case studies employ two distinct areas to evaluate SDB and to examine the change analysis. The SDB evaluation is optimally conducted in a static setting while the change analysis necessitates a dynamic environment. The study area for the bathymetric processing workflow (Section 3.2) is located in the eastern German Baltic Sea in the Bay of Greifswald (German: Greifswalder Bodden; Fig. 2). It is characterised by large areas of shallow water with some deeper shipping lanes in between. Most of the seabed is covered with light-coloured sand and gravel, but there are also areas covered with vegetation that appear dark in the satellite images.

The study area for testing the developed seabed change analysis (Section 3.3) is located north of the Fischland-Darß-Zingst peninsula in the German Baltic Sea (Fig. 3), at a location subjected to very dynamic coastal erosion processes known as "Darßer Ort". The seabed is dominated by light sandy sediments, with some vegetation to the east, which appears as dark areas in the satellite image. There is an emergency harbour in the eastern part of the peninsula and its access routes are regularly dredged.

4.2 Spectrally-derived bathymetry results and accuracy analysis

The reference data needed to evaluate the bathymetric results were obtained from ship-based single and multibeam echosounder surveys conducted in the study area between 2013 and 2020. The echosounder data were used to generate a

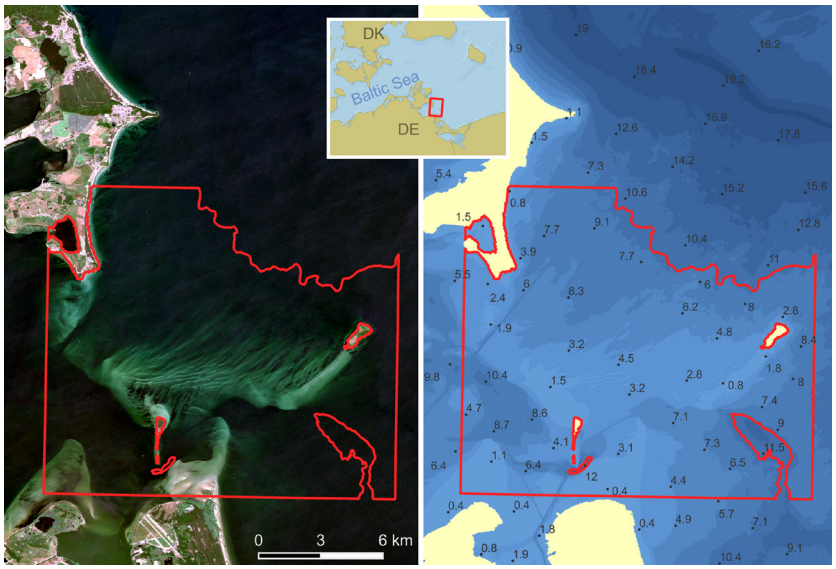


Fig. 2 Sentinel-2 RGB image showing the study area outlined in red down to 10 m depth in the Bay of Greifswald (Baltic Sea, Germany) used for the bathymetric processing workflow.

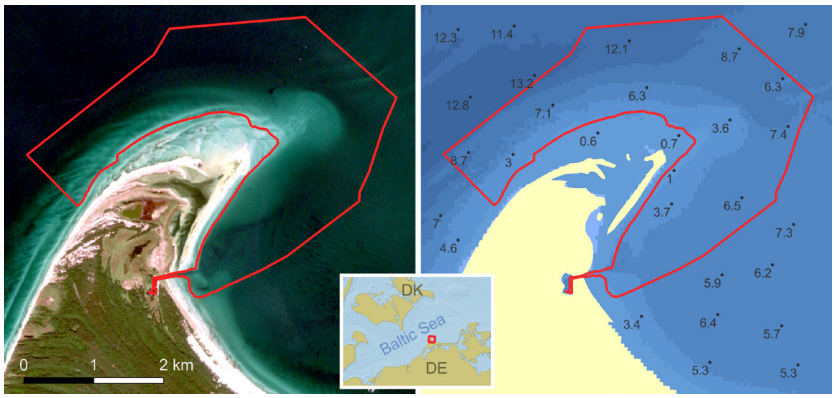


Fig. 3 Sentinel-2 RGB image of the study area outlined in red for the evaluation of the results of the developed seabed change analysis, located north of the Fischland-Darß-Zingst peninsula in the German Baltic Sea.

raster dataset with a resolution of 10 m × 10 m. The accuracy of the reference water depth data is a few centimetres, but within the interpolated area the deviations may be greater.

For the study case, the developed workflow described in Section 3.2 is tested and the results and accuracies achieved are evaluated. As input information, a bathymetric image is generated from the Sentinel-2 satellite image of 23 June 2019. During post-processing, depths less than 0.25 m were not considered for accuracy analysis, as these very shallow areas are not adequately represented in the reference data used for training, and SDB from very shallow areas is highly susceptible to errors caused by wave breaking. Data from areas deeper than 10 m were also not considered for the accuracy analysis, as the visibility conditions in the Baltic Sea generally do not allow analysis at greater depths (Section 2.1). The bathymetric results obtained are shown in Fig. 4. The characteristics of the seabed are well represented by the estimated bathymetry: Shipping lanes, sandbanks and the ripples on the sandbanks are clearly visible. However, particularly in deeper areas such as shipping lanes, there are systematic errors due to underestimation of water depth (Fig. 4). In addition, the use of 256 px × 256 px images for the CNN induces small raster biases of ~30 cm difference that cannot be adequately addressed by post-processing when merging the small images to the ~ 20 km sub-images (Section 3.2). The magnitude of these raster effects increases with increasing depth of penetration into the water body, due to the depth-related increase in uncertainty associated with the estimation of bathymetry (Section 2.1). The histogram of Fig. 5 illustrates the distribution of the deviation between the reference data and the SDB results, demonstrating a slight systematic underestimation of the bathymetric results with a median deviation of 26 cm (Table 1). Additionally, the results were obtained with a median absolute error (MedAE) of 47 cm, a RMSE of 86 cm, and a 95th percentile of 1.74 m.

The stated parameters describe the degree of accuracy with which the depth of the German Baltic Sea can be determined from Sentinel-2 MSI at any given time. As a consequence of the constraints imposed by the trained CNN model (Section 3.2), it is not possible to extend the quality metrics to other regions and/or other imaging sensors. The accuracy levels attained are inadequate to fulfil the requirements of Order 1b or better of the IHO S-44 hydrographic survey standard (IHO, 2022), and thus cannot be considered a direct replacement for high-accuracy hydrographic surveying. However, they are available in high temporal resolution and thus constitute an appropriate basis for change analysis, as intended for use in the operational service. Moreover, some systematic deviations are minimised due to the inherent differencing during change analyses (Section 3.3).

4.3 Change analysis

4.3.1 Seabed change monitoring results and accuracy analysis

In order to evaluate the results of the change analysis, single-beam echosounder surveys were conducted at Darßer Ort in the spring of 2018 and 2022. The two measurement campaigns were conducted to a minimum depth of 1.5 m. The datasets were processed using the standard workflow employed by the BSH survey division, which consisted of sound

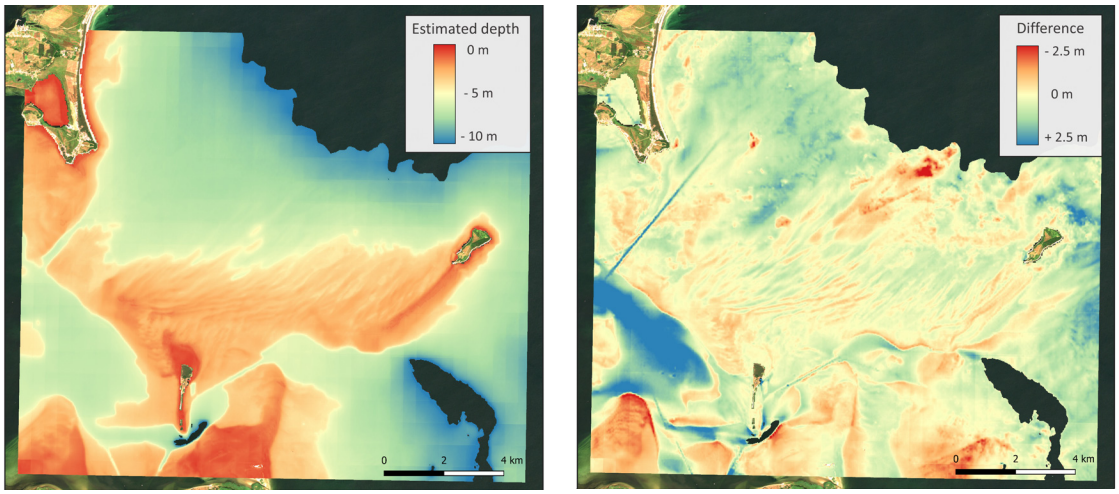


Fig. 4 Derived bathymetry of the SDB workflow (left) and the difference between the reference depth data and SDB results (right).

https://doi.org/10.58440/ihr-30-2-a15

speed correction, outlier removal, flagging vegetation, a Delaunay triangulation between the profile tracks and gridding. Two DTMs of the seabed with a resolution of 10 m × 10 m were ultimately produced. The difference between the two DTMs was calculated to determine a reference for seabed variations, as shown in Fig. 6.

The analysis is based on 43 Sentinel-2 MSI of the study area, acquired between 2018 and 2022. The bathymetry was calculated for these 43 epochs (Section 3.2). In the subsequent quality assessment, 26 epochs were excluded from the analysis (due to the presence of clouds and turbidity, among other factors). The remaining 17 epochs were used as the basis for change analysis. However, the resulting estimate of change is currently expressed as a unitless metric. In order to facilitate comparison with the reference change, both the reference data and the estimated change data have been normalised to a unitless scale between 0 (no change) and 1 (maximum change) using min-max normalisation with the 2.5th percentile as the minimum and the 97.5th percentile as the maximum. This approach was employed to reduce the influence of outliers. The results are normalised change intensity values presented in Fig. 7, which demonstrates that the estimated changes exhibit considerable variation in the coastal areas to the north-west and north-east of the peninsula and on the harbour access route in the south-east of the scene. The reference change also displays some corresponding areas of high change, although the areas are subtly different and the change is more clearly delineated, with less background noise.

Subsequently, the normalised change values were classified into two categories: change and no change. This differs from the clustering workflow described in Section 3.3, as the clustering algorithm cannot be applied similarly to the reference data. Further, a morphological filter was employed to reduce the influence of small filigree structures and the result is shown in Fig. 8. Afterwards, the discrepancy between the two representations was determined (Fig. 9), allowing the differences between the reference and the calculated seabed variation to be quantified. The majority of 85.0 % of the area shows no deviation between the reference and the estimated data, thereby providing substantiation for the appropriate classification. The occurrence of false positive misclassifications, whereby a change is identified when none exists, is 10.5 %. Conversely, false negative errors, where no change is detected despite the presence of one in the reference data, occur at a frequency of 4.5 %. The accumulation of false positive classifications is evident in areas of the south-east peninsula. Such occurrences are attributed to pronounced variations in reflectance, which are presumed to be the result of transient vegetative accumulations, with a high probability of being seaweed.

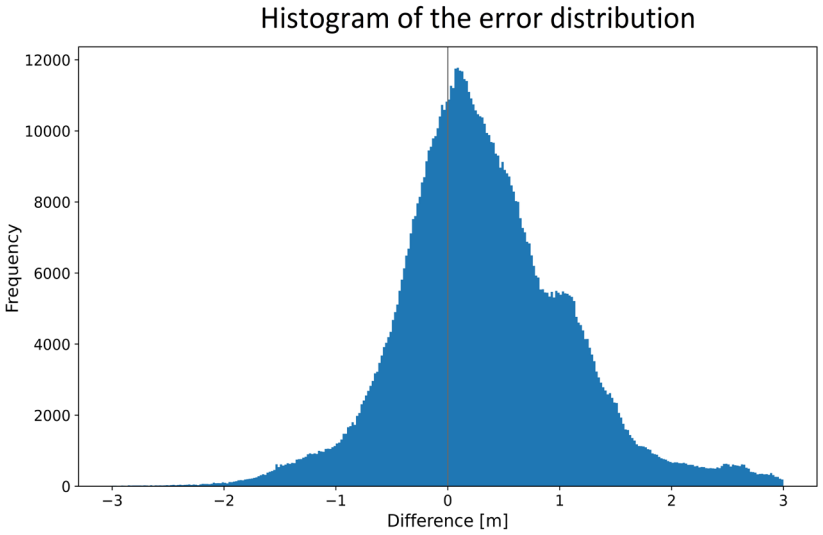


Fig. 5 Histogram of the difference between reference depth and SDB results.

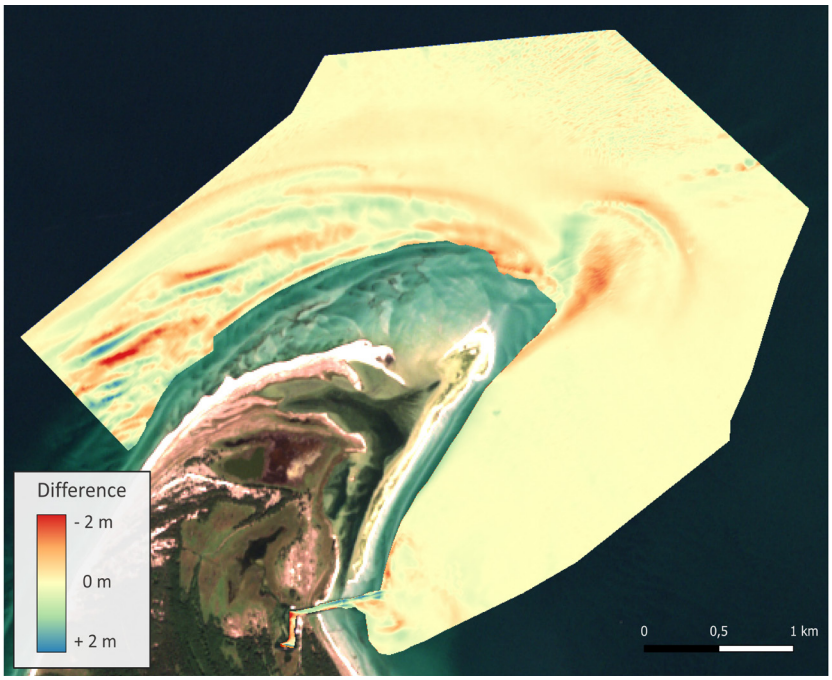


Fig. 6 Seabed changes at Darßer Ort from 2018 to 2022. The data is based on shipborne hydroacoustic single-beam echo sounding.

Table 1 Statistical parameters of the (signed) error (E) and absolute error (AE).

Median (E)	0.26 m
Standard deviation (E)	0.79 m
RMSE (AE)	0.86 m
MedAE (AE)	0.47 m
90th percentile (AE)	1.37 m
95th percentile (AE)	1.74 m

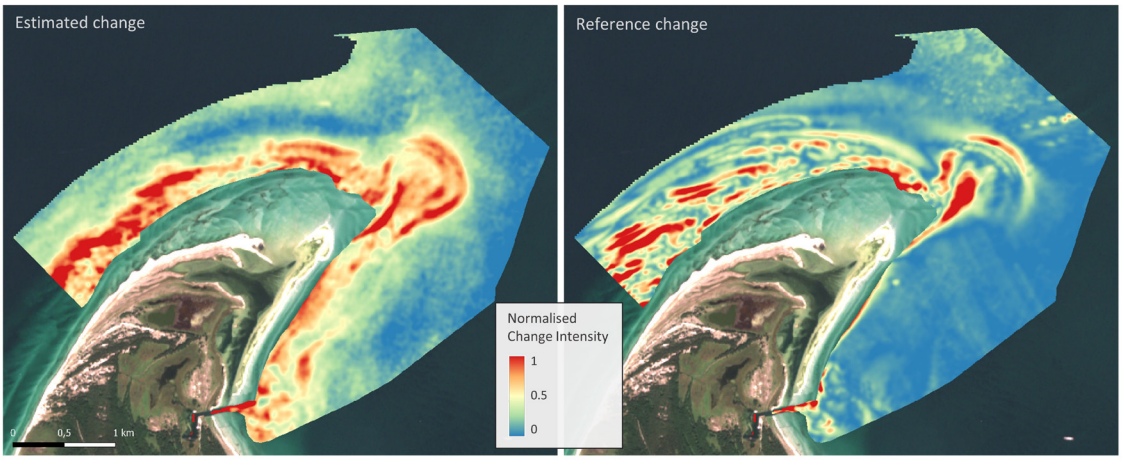


Fig. 7 Representation of the normalised absolute change intensity of the change analysis workflow results (left) and the reference change (right).

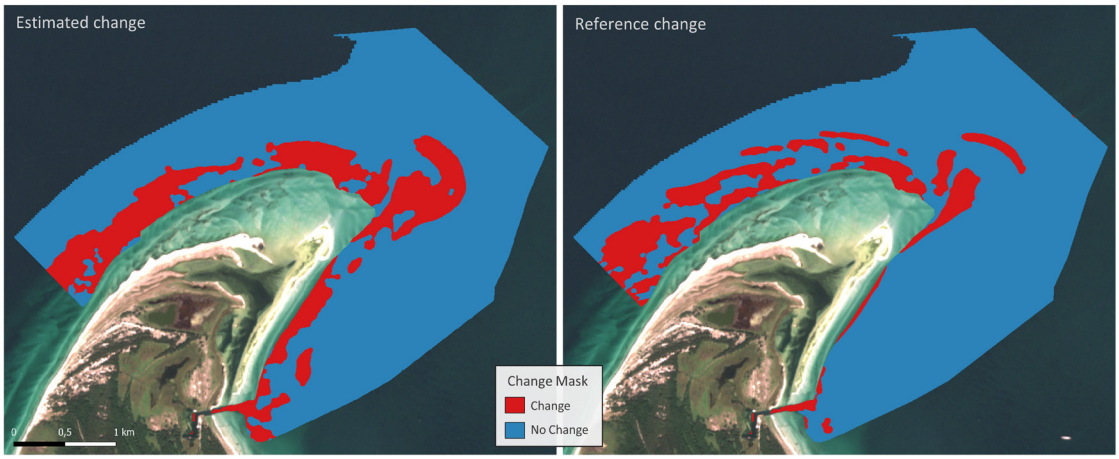


Fig. 8 Binary classified change metric of the change analysis workflow results (left) and the reference change (right).

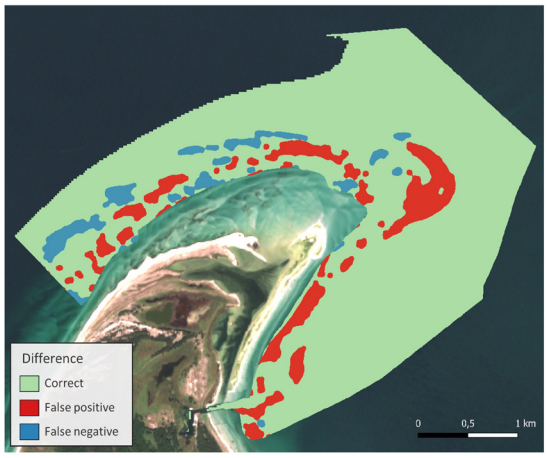


Fig. 9 Differences of the classified change metrics of Fig. 8.

The aforementioned vegetation deposits have resulted in erroneous entries in the SDB, leading to the misrecognition of changes. Furthermore, instances of distributed misclassifications are more prevalent in the north-western region of the peninsula. This is due to the fact that the entire area is characterised by considerable variability, which gives rise to the detection of such changes, although the spatial extent of specific changes differs in some areas. This discrepancy may be attributed to the fact that the satellite imagery encompasses the entire time span, thereby rendering the continuous changes less discernible than they would be if only two epochs were considered, as for the reference data. Another potential cause is the challenging and highly variable environmental conditions, which range from extremely turbid and foamy waters to those that are remarkably clear and undisturbed. These conditions render the SDB estimate variable, thus increasing the likelihood of error in the change analysis.

4.3.2 Seabed tracking results and evaluation

Fig. 10 shows the motion vector field estimated by 2.5D LST (Section 3.3) for areas that have been previously identified as undergoing change. The length of the derived motion vectors exhibited a range of 1.5 m to 466 m. The mean standard deviation for all lateral vector components estimated (thus ranging from a few metres up to half a kilometre) can be stated with sub-pixel accuracy, with a value of 0.29 px, which corresponds to 5.9 m on the seabed surface. The mean standard deviation for the estimation of the depth component of the motion vectors is 0.15 m. Median averaged over the entire motion vector range, the 3D motion vectors were estimated with a precision of approximately ⅒ of its lengths.

https://doi.org/10.58440/ihr-30-2-a15

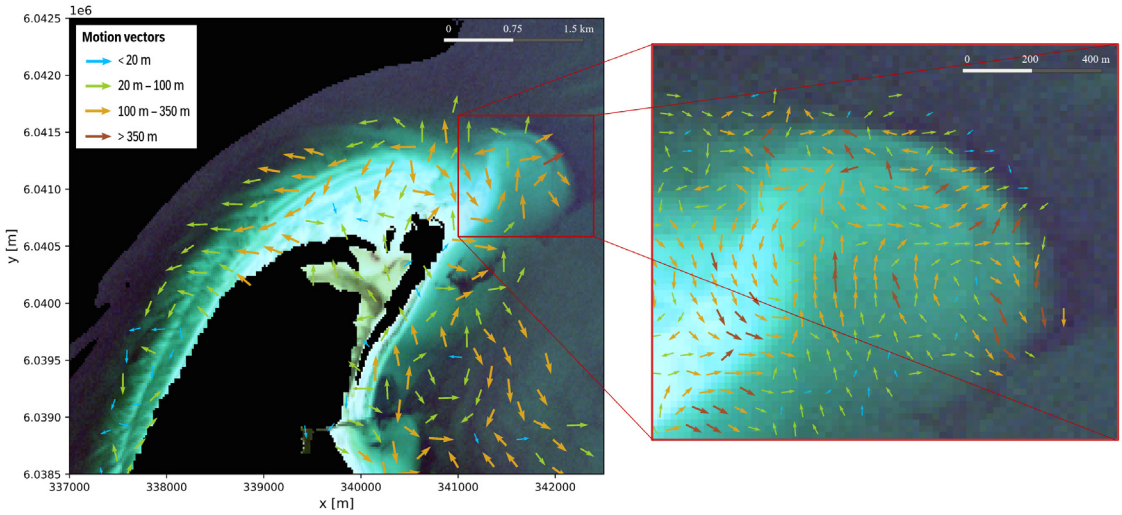


Fig. 10 2.5D LST motion vector field: The lateral displacements are shown for the whole study area in a generalised representation (left) and in a detailed representation in the north-east of the peninsula. In the background is an RGB visualisation of a Sentinel-2 image from 26th July 2019.

The reported accuracy values are encouraging when considered in the context of a ground sampling distance (GSD), defined as the distance between pixel centres measured on the seabed's surface, of 20 m (Section 3.2), and an accuracy of 0.86 m for depth value extraction from optical imagery (Section 4.2). It should be noted, however, that these are relative accuracy metrics, as an absolute accuracy analysis cannot be performed due to the lack of reference motion data.

Furthermore, a plausibility check was conducted using time-lapse image sequences of the satellite MSI. The majority of the derived motion patterns were adjudged to be reasonable. The area west of the peninsula is characterised by a uniform motion vector field oriented towards the south-west (Fig. 10, left). This phenomenon can be attributed to the influence of strong currents in easterly winds, which exert a less pronounced effect on the area in the presence of westerly winds. The magnified extract (Fig. 10, right) depicts the peninsula's tip and shows a motion vector field that is subjected to rotational effects caused by interactions between strong easterly currents and prevailing westerly winds. However, there are also areas with seemingly turbulent motion vectors, dominant especially in the south-east of the peninsula. This phenomenon can be attributed to the distinctive characteristics of the seabed in this region, which is characterised by the presence of marine vegetation. Consequently, in addition to tracking seabed motions, the monitoring also encompassed the tracking of organic material.

5 Towards a fully automated operational service

The objective is to implement a fully automated service that will necessitate the implementation of extensive automation and control of the individual processes. It is imperative that the system is able to accommodate a diverse range of scenarios, encompassing the routine execution of the SDB and change analysis workflow (Sections 3.2 and 3.3) for the entirety of the area under the purview of BSH, as well as manually initiated sub-processes for specific areas and timeframes.

Accordingly, a modular and extensible approach was adopted, with each component of the workflow encapsulated in a separate module class that implements a self-designed interface for configuration and execution. The interface stipulates that each module must provide a dictionary of named parameters that can be employed for configuration purposes, accompanied by the relevant default values. Subsequently, these values may be modified as required and transmitted to the module prior to the initiation of processing. Moreover, this allows the scheduling component to override parameters in a predefined workflow for the execution of a specific task.

The aforementioned modules can be employed either as standalone entities or in conjunction with other modules for the development of workflows. This involves chaining of module executions, whereby the output of one module is used as input for the next. This facilitates the straightforward replacement of specific workflow components with alternative algorithms and data sources in the future.

It is imperative to ensure that the MSI input data is preserved in standardised and predefined formats. Consequently, all satellite images, irrespective of their original format, are transformed into an open, platform-independent GeoPackage format (GeoPackage, 2024) with predefined names for the band layers and the file itself, as well as predefined metadata. This ensures the compatibility of the developed service with imagery from other satellite missions, necessitating only minor modifications to the algorithms implemented. The supplementary data, which includes reference depths, distances to the shore, currents and wave heights, is provided in the form of a Network Common Data Form (NetCDF4,

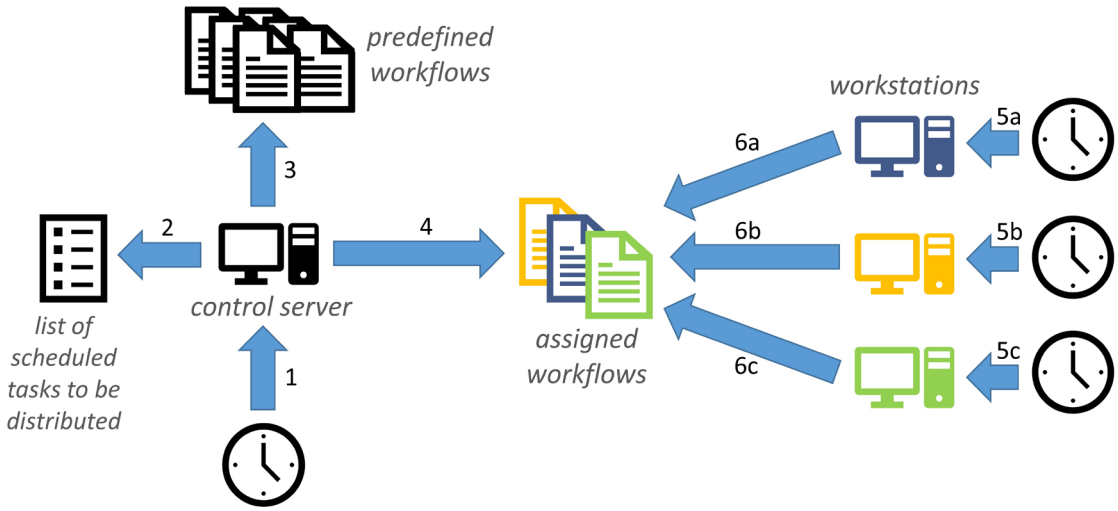


Fig.11 Schematic representation of the automated, time-controlled distribution of tasks or workflows.

2024). This is also employed for the resulting output data. Additional data, such as wind data or current data, are downloaded, pre-processed and stored as predefined comma-separated values (CSV) by an external process on a daily basis.

The scheduling process and an overview of the task assignment functionality are illustrated in Fig. 11. Based on a timer (1), the control server is executed on a daily basis and works through the list of scheduled tasks (2), for example, the daily execution of the entire SDB and change analysis. Consequently, the control server retrieves the pertinent workflows (3) and deposits the scripts of a workflow at a known location (4). The designated computers have access to the same data pool on a network drive and are programmed to perform a daily check (5a–5c) for any new tasks assigned to them, by searching for assigned workflows (6a–6c). The workstations responsible for executing the required tasks are standard staff computers, which typically perform these operations at night to minimise interference. The entire workflow is written in Python; however, the activation scripts are shell or batch scripts that are called via cron jobs (Linux) or the Task Scheduler (Windows).

6 Discussion

In light of the significant financial implications associated with the deployment of advanced hydrographic surveying techniques, such as shipborne hydroacoustic or airborne LiDAR technology, the imperative for event-driven resurveying remains. The present study demonstrates that the detection of varying regions of the seabed is feasible through the analysis of MSI sequences using SDB. The developed service is currently operational as a prototype in the German Baltic Sea, monitoring changes in the seabed down to a water depth of 10 metres, which represents approximately 25 % of the BSH's area of responsibility in the Baltic Sea. This has the potential to result in significant savings in the future, as shallow water areas are typically both highly dynamic and costly to survey due to the necessity for smaller multibeam echosounder line spacings.

The calculation of SDB water depth is of paramount importance. The accuracy of the bathymetric results is influenced by a number of environmental factors, including cloud cover, turbidity and algae, foam crests, seabed habitat and the sun elevation angle. These are discussed in Section 2.1, while Section 3.2 outlines the countermeasures taken by the service to address these issues. However, the impact of these disturbances on reflectance is not fully compensable, resulting in erroneous outcomes. Nonetheless, the accuracy of the SDB in the case study presented in Section 4.2 was achieved with a median absolute error (MedAE) of 0.47 m and a root mean square error (RMSE) of 0.86 m, which is comparable with state-of-the-art SDB methods (Section 2.1). Furthermore, the change analysis eliminates permanent systematic errors in the SDB by considering the differences over time. Consequently, a limited systematic underestimation of large water depths (e.g. in the shipping lanes in Fig. 4) is less problematic, assuming that this underestimation is consistent over time. However, errors that occur only in individual images and vary over time, usually due to the environmental influences mentioned above, present a challenge for the subsequent change analysis.

The findings of the study, as detailed in Section 4.3.1, indicate that the service, which is still in the prototype phase, is capable of accurately classifying a significant portion of the area (approximately 85 %) in accordance with the specified change. This represents a promising initial outcome. However, the service exhibits a tendency to erroneously classify a considerable proportion of areas as bathymetric seabed changes. This is evidenced by the aforementioned study, which identified approximately 10 % of false positives and 5 % of false negatives, and is further corroborated by empirical testing conducted during the development phase. This is primarily due to significant alterations in reflectance that are not accompanied by corresponding

https://doi.org/10.58440/ihr-30-2-a15

changes in water depth, which the SDB workflow is currently unable to capture. Consequently, these "undesirable" changes are identified by the change detection algorithms and can only be partially distinguished from the desired variations in seabed topography. The most challenging aspect is a long-term change in reflectance (without bathymetric change), which is typically caused by changes in the seabed habitat. These changes may include the growth or dieback of seagrass fields, deposition or washing of seaweed, and other factors. In order to compensate for this, it is necessary to identify the location of (or, ideally, to correct) the affected area prior to undertaking a change analysis, as it is not possible to make a compensation during the change analysis itself. Furthermore, recurring or periodic radiometric differences resulting from seasonal vegetation cycles, such as seagrass, kelp forests or algal blooms in bays with minimal water exchange, represent a significant challenge. In order to achieve full compensation of the periodic variations, a dense time series covering the total period, which is usually annual, is required. However, this is not currently feasible, as the most suitable images are generally available only in the summer months, and there are significant data gaps during winter. Additionally, the periods in question are not strictly annual, as growth patterns are influenced by weather conditions, resulting in fluctuations. An alternative approach to addressing this issue is to limit the use of images to those captured during the same time of year. However, this significantly reduces the number of available image sequences. Furthermore, areas that are subject to significant and persistent fluctuations in reflectance present a challenge. This encompasses the coastal surf zone, where turbidity, foam ridges, vegetation deposits, and potential bathymetric changes can all contribute to challenges in data interpretation. The restricted availability of undisturbed satellite images in these regions gives rise to a considerable degree of variability over a given period. Consequently, the change analysis frequently identifies these regions as exhibiting significant variations. This limitation can be addressed by selecting images on days with minimal wind activity. However, the majority of the observed spectral variability in most areas is characterised by one-off (or infrequent) short-term changes caused by factors such as turbidity, atmospheric conditions, waves, sun glint and ship traffic. These effects are largely accounted for by the use of time series information in the change analyses, which incorporates the inherent averaging and median formation, as well as the deliberate image selection during the quality assessment (Section 3.3). These measures also serve to mitigate, at least in part, the effects induced by the periodic and very frequent changes described above.

In order for a change to be reliably identified by the presented service, it must satisfy a number of prerequisites. In the first instance, the change in question must exceed a specific size threshold. The currently employed resolution of 20 m and the settings for morphological filtering during clustering (with the currently used kernel size of 3 px × 3 px) are the determining factors, resulting in a required minimum affected area size of 60 m × 60 m. Furthermore, the change must be discernible for a certain period of time. Nevertheless, it is not feasible to make a universal assertion in this regard, as the accessibility and quality of the satellite images exert a considerable influence. The current parameter configuration necessitates the capture of the change in two to five satellite images, contingent on the magnitude of the change. While this figure could be reduced, this would result in a greater number of areas being incorrectly identified as having undergone change. This is because it is not possible to exclude short-term false values (due to atmospheric conditions, ships, turbidity, etc.). Ultimately, a certain degree of seabed change is necessary, contingent on the precision of the SDB in the region. It is not possible to make a blanket assertion, given that systematic errors in the SDB are partially offset by differencing. However, a change of at least a few dm was typically required during developmental testing.

The fully automatic detection of bathymetric changes, which requires the workflow to be extremely robust, remains a challenge. However, it has been demonstrated that the service is capable of detecting variable areas (Section 4.3) and therefore represents a valuable additional asset in hydrographic survey planning. This is due to the fact that the service is provided free of charge and is fully automated, resulting in negligible financial and personal costs.

7 Summary and outlook

The objective of this research was to develop a prototype service capable of identifying changes in seabed topography based on the spectral data obtained from the Sentinel-2 MSI satellite. The implemented service is fully automated and comprises two distinct phases. The initial phase comprises the estimation of bathymetry through the utilisation of SDB, encompassing the selection of MSI in consideration of cloud cover and wind conditions, a preliminary processing stage (including normalisation, cropping, the calculation of turbidity and pseudo depth parameters, supplementary image selection), the derivation of actual depth through a CNN in a U-Net structure, and a post-processing phase. The CNN model was trained using Sentinel-2 images from the German Baltic Sea region and data from the BSH's echo sounder-based hydrographic surveying. In a case study, a MedAE of 0.47 m and RMSE of 0.86 m were achieved, thereby demonstrating the accuracy of the SDB. The second phase is the change analysis, which can be conducted once the water depth has been estimated at multiple time points. Firstly, a quality assessment of the available images is conducted, enabling the targeted selection of images. Subsequently, a series of change detection techniques (PCA, CVA and robust

difference) are applied to the image sequence with the objective of determining parameters that characterise the dynamics of an area. These parameters are then combined into a weighted sum, clustered and converted into an intuitive traffic light scheme with a recommendation for action. In a field study, 85 % correct classification between areas exhibiting change and those exhibiting no change was achieved. The service provides an estimate of the variability of shallow water areas in advance of a survey. This enables an event-based planning of the resource-intensive hydrographic survey, thereby avoiding the unnecessary repetition of surveys of static areas. Consequently, the allocation of survey resources can be re-prioritised at this juncture, with greater focus placed on dynamic areas to enhance the timeliness of hydrographic survey data. The service, therefore, represents an added value, particularly for hydrographic offices, which can be operated fully automatically and at minimal cost. Furthermore, the service provides comprehensive time series of bathymetric data and change information, which can be employed in environmental monitoring and analogous applications.

At the time of writing, the service is still in a prototype state, and the paper describes the current state of development. In general, the entire workflow is fully operational and produces the results presented. The bathymetry workflow is complete, with the exception of the training of alternative CNN models with modified parameter settings. The change analysis workflow is still undergoing development, revision and optimisation. The fundamental structure of the system remains unchanged; however, the incorporation of additional weights, parameter settings, and algorithms (for change detection or clustering) is still underway. The proposed improvements entail the incorporation of a situational weighting component into the existing static weighting methodology during weighted summation. This component would be calculated on-the-fly with respect to the noise of a summand, measured by the standard deviation of the neighbouring patch or similar parameters. Furthermore, the intention is to integrate the results of the 2.5D LST into the weighted sum, namely the normalised change indicator values. For this purpose, the vector results are to be averaged by magnitude with respect to their direction and converted into rasterised, normalised change information. Furthermore, the integration of current and wave data is intended to be employed for periods exceeding two years through a comparative analysis of the accumulated change activity. This does not permit a general assertion regarding the change; rather, it allows for a comparative assertion within the area under consideration. Furthermore, the integration of additional multi-spectral satellite missions with enhanced spatial resolution is anticipated. Furthermore, enhancing the SDB through the utilisation of local point-shaped data of greater precision, such as crowdsourced bathymetric data or space-borne LiDAR data (e.g. ICESat-2), can prove especially advantageous. The aforementioned data sources are not optimally suited for an area-wide survey, as only a limited number of tracks are measured within a given survey area. However, the data can be employed to ascertain systematic deviations in the SDB, thereby validating the SDB results or even correcting them by an offset, thus performing a local adjustment. This approach would likely enhance the results and increase confidence in the SDB results, thereby indirectly improving the change analysis results.

The accessibility of cost-free remote sensing data has propelled the advancement of satellite-based monitoring programmes and has been progressively acknowledged in the hydrographic community. The advantages of satellite-based monitoring programmes are global coverage, short revisit time and cost-effective data acquisition and analysis. New methods, such as CNNs, optimise the achievable depth accuracies, as demonstrated in this paper. Nevertheless, CNNs are still in the process of being developed, and new modifications, such as physically informed CNNs or multimodal CNNs, which allow the combination of satellite imagery with other data sources, will provide further improvements in achievable depth accuracies. Furthermore, the trend is towards higher resolution satellite imagery and greater computing power, which will further enhance the capabilities of SDB and an SDB-based monitoring programme, as presented in this paper.

Acknowledgements

We gratefully acknowledge financial support of the project *Satellitengestützte operationelle Einsatzplanung in der Seevermessung durch integrierte Verarbeitung multispektraler Sentinel-2-Satellitenbildsequenzen (S·O·S)* by German Aerospace Center (DLR) with funds from the German Federal Ministry for Digital and Transport (BMDV) under grant no. 50EW2204.

References

Abe, T. (1955). A Study on the Foaming of Sea Water A Tentative Analysis of Wind Wave Data in View of the Foaming of Sea Water. *Papers in Meteorology and Geophysics, 6*(2), pp. 164–171.

Afaq, Y. and Manocha, A. (2021). Analysis on change detection techniques for remote sensing applications: A review. *Ecological Informatics, 63*, 101310.

Ahmed, M., Seraj, R. and Islam, S. M. S. (2020). The k-means algorithm: *A comprehensive survey and performance evaluation. Electronics, 9*(8), 1295.

 https://doi.org/10.58440/ihr-30-2-a15

Asokan, A. and Anitha, J. J. E. S. I. (2019). Change detection techniques for remote sensing applications: A survey. *Earth Science Informatics, 12*, pp. 143–160.

BSWH (2024). *Baltic Sea Wave Hindcast*. E.U. Copernicus Marine Service Information (CMEMS). https://doi.org/10.48670/moi-00014

BSWAF (2024). *Baltic Sea Wave Analysis and Forecast*. E.U. Copernicus Marine Service Information (CMEMS). https://doi.org/10.48670/moi-00011

Braaten, J., Cohen, W. B. and Yang, Z. (2015). Automated cloud and cloud shadow identification in Landsat MSS imagery for temperate ecosystems. *Remote Sensing of Environment, 169*, pp. 128–138.

Brüning, T., Li, X., Schwichtenberg, F. and Lorkowski, I. (2021). An operational, assimilative model system for hydrodynamic and biogeochemical applications for German coastal waters. *Hydrographische Nachrichten – Journal of Applied Hydrography, 118*, pp. 6–15. https://doi.org/10.23784/HN118-01

Çelik, O. İ., Büyüksalih, G. and Gazioğlu, C. (2023). Improving the Accuracy of Satellite-Derived Bathymetry Using Multi-Layer Perceptron and Random Forest Regression Methods: A Case Study of Tavşan Island. *Journal of Marine Science and Engineering, 11*(11), 2090.

Chénier, R., Faucher, M. A. and Ahola, R. (2018). Satellite-derived bathymetry for improving Canadian Hydrographic Service charts. *ISPRS International Journal of Geo-Information, 7*(8), 306.

Chu, S., Cheng, L., Cheng, J., Zhang, X. and Liu, J. (2023). Comparison of Six Empirical Methods for Multispectral Satellite-derived Bathymetry. *Marine Geodesy, 46*(2), pp. 149–174.

CODE-DE (2024). *Copernicus data and cloud processing for German authorities: CODE-DE*. German Aerospace Center (DLR). https://code-de.org (accessed 15 August 2024).

Copernicus Marine Service (2024). *Access data*. E.U. Copernicus Marine Service Information (CMEMS). https://marine.copernicus.eu/access-data (accessed 9 August 2024).

Deng, J. S., Wang, K., Deng, Y. H. and Qi, G. J. (2008). PCA-based land-use change detection and analysis using multitemporal and multisensor satellite data. *International Journal of Remote Sensing, 29*(16), pp. 4823–4838.

Leder, T. D., Leder, N. and Peroš, J., 2019, Satellite Derived Bathymetry survey method – Example of Hramina Bay. *Transactions on Maritime Science, 8*(1), pp. 99–108. https://doi.org/10.7225/toms.v08.n01.010

Leder, T. D., Baučić, M., Leder, N. and Gilić, F. (2023). Optical satellite-derived bathymetry: An overview and wos and scopus bibliometric analysis. *Remote Sensing, 15*(5), 1294.

DWD (2024). *Dataset Description*. Deutscher Wetterdienst. https://opendata.dwd.de/climate_environment/CDC/observations_germany/climate/hourly/wind/DESCRIPTION_obsgermany_climate_hourly_wind_en.pdf (accessed 2 September 2024).

ESA (2024). *Overview of Sentinel-2 Mission*. SentiWiki. https://sentiwiki.copernicus.eu/web/s2-mission (accessed 4 September 2024).

Gower, J., King, S., Borstad, G. and Brown, L. (2005). Detection of intense plankton blooms using the 709 nm band of the MERIS imaging spectrometer. *International Journal of Remote Sensing, 26*(9), pp. 2005–2012.

Geofabrik GmbH (2024). *Download OpenStreetMap data for this region: Germany*. Geofabrik. https://download.geofabrik.de/europe/germany.html (accessed 14 August 2024).

GeoPackage (2024). *An Open Format for Geospatial Information*. Open Geospatial Consortium. http://www.geopackage.org/ (accessed 20 August 2024).

Geyman, E. C. and Maloof, A. C. (2019). A simple method for extracting water depth from multispectral satellite imagery in regions of variable bottom type. *Earth and Space Science, 6*(3), pp. 527–537.

Haklay, M. and Weber, P. (2008). Openstreetmap: User-generated street maps. *IEEE Pervasive computing, 7*(4), pp. 12–18.

Hartmann, K., Reithmeier, M., Knauer, K., Wenzel, J., Kleih, C. and Heege, T. (2022). Satellite-derived bathymetry online. *The International Hydrographic Review, 28*, pp. 53–75. https://doi.org/10.58440/ihr-28-a14

IHO (2022). *Standards for Hydrographic Surveys* (ed. 6.1). IHO Special Publication S-44, International Hydrographic Organization, Monaco. https://iho.int/uploads/user/pubs/standards/s-44/S-44_Edition_6.1.0.pdf (accessed 29 July 2024).

IHO (2024). *Guidance to Satellite-derived Bathymetry* (1st ed.). IHO Publication B-13, International Hydrographic Organization, Monaco. https://iho.int/uploads/user/pubs/bathy/B_13_Ed100_032024.pdf (accessed 29 July 2024).

Jégat, V., Pe'eri, S., Freire, R., Klemm, A. and Nyberg, J. (2016). Satellite-derived bathymetry: Performance and production. In *Proceedings of the Canadian Hydrographic Conference, Halifax, NS, Canada*, pp. 16–19.

Lacaux, J. P., Tourre, Y. M., Vignolles, C., Ndione, J. A. and Lafaye, M. (2007). Classification of ponds from high-spatial resolution remote sensing: Application to Rift Valley Fever epidemics in Senegal. *Remote sensing of environment, 106*(1), pp. 66–74.

Laporte, J., Dolou, H., Avis, J. and Arino, O. (2023). Thirty years of Satellite Derived Bathymetry: The charting tool that Hydrographers can no longer ignore. *The International Hydrographic Review, 29*(1), pp. 170–184. https://doi.org/10.58440/ihr-29-a20

Legleiter, C. J., Roberts, D. A. and Lawrence, R. L. (2009). Spectrally based remote sensing of river bathymetry. *Earth Surface Processes and Landforms, 34*(8), pp. 1039–1059.

Louis, J., Devignot, O. and Pessiot, L. (2021). *S-2 MPC – Level-2A Algorithm Theoretical Basis Document*. Tech. Rep. S2-PDGS-MPC-ATBD-L2A - 2.10, European Space Agency (ESA), Keplerlaan 1, 2201 AZ Noordwijk, The Netherlands, 2021. https://step.esa.int/thirdparties/sen2cor/2.10.0/docs/S2-PDGS-MPC-L2A-ATBD-V2.10.0.pdf (accessed 22 October 2024).

Lyzenga, D. R. (1978). Passive remote sensing techniques for mapping water depth and bottom features. *Applied Optics, 17*(3), pp. 379–383.

Mandlburger, G. (2022). A review of active and passive optical methods in hydrography. *The International Hydrographic Review, 28*, pp. 8–52. https://doi.org/10.58440/ihr-28-a15

Najar, M. A., Benshila, R., Bennioui, Y. E., Thoumyre, G., Almar, R., Bergsma, E. W. J., Delvit, J.-M. and Wilson, D. G. (2022). Coastal bathymetry estimation from Sentinel-2 satellite imagery: Comparing deep learning and physics-based approaches. *Remote Sensing, 14*(5), 1196. https://doi.org/10.3390/rs14051196

NetCDF4 (2024). *Network Common Data Form (NetCDF)*. NSF Unidata. https://www.unidata.ucar.edu/software/netcdf/ (accessed 20 August 2024).

Poicyn, F. C., Brown, W. and Sattinger, I. J. (1970). *The measurement of water depth by remote sensing techniques*. Technical Report 8973-26-F, Willow Run Laboratory, The University of Michigan.

Ronneberger, O., Fischer, P. and Brox, T. (2015). U-net: Convolutional networks for biomedical image segmentation. In *Medical image computing and computer-assisted intervention–MICCAI 2015: 18th international conference, Munich, Germany, October 5-9, 2015, proceedings, part III 18*, pp. 234–241. Springer International Publishing.

Stumpf, R. P., Holderied, K. and Sinclair, M. (2003). Determination of water depth with high-resolution satellite imagery over variable bottom types. *Limnology and Oceanography, 48*(1part2), 547–556.

Susa, T. (2022). Satellite derived bathymetry with Sentinel-2 imagery: Comparing traditional techniques with advanced methods and machine learning ensemble models. *Marine Geodesy, 45*(5), 435–461.

Westfeld, P. (2012). *Geometrische und stochastische Modelle zur Verarbeitung von 3D-Kameradaten am Beispiel menschlicher Bewegungsanalysen*. Verlag der Bayerischen Akademie der Wissenschaften in Kommission beim Verlag C. H. Beck, München, 281 p., ISBN 978-3-7696-5099-0.

Westfeld, P., Maas, H. G., Bringmann, O., Gröllich, D. and Schmauder, M. (2013). Automatic techniques for 3D reconstruction of critical workplace body postures from range imaging data. *ISPRS journal of photogrammetry and remote sensing, 85*, pp. 56–65. https://doi.org/10.1016/j.isprsjprs.2013.08.004

Wold, S., Esbensen, K. and Geladi, P. (1987). Principal component analysis. *Chemometrics and intelligent laboratory systems, 2*(1-3), pp. 37–52.

Xie, C., Chen, P., Zhang, S. and Huang, H. (2024). Nearshore Bathymetry from ICESat-2 LiDAR and Sentinel-2 Imagery Datasets Using Physics-Informed CNN. *Remote Sensing, 16*(3), p. 511.

Xu, H., Wang, Y., Guan, H., Shi, T. and Hu, X. (2019). Detecting ecological changes with a remote sensing based ecological index (RSEI) produced time series and change vector analysis. *Remote Sensing, 11*(20), 2345.

Żak, K. (2020). *keras-unet*. GitHub. https://github.com/karolzak/keras-unet?tab=readme-ov-file (accessed 9 July 2023).

Appendix A: Additional data

Wind data. The presented service employs wind data from a curated set of DWD weather stations situated within or in the immediate vicinity of the German Baltic Sea. These are employed to evaluate the MSI, given that the suitability of satellite images is impaired by strong winds, which result in the formation of waves, foam, and increased turbidity due to sediment swirls. The weather stations directly measure wind speed and direction, and the data are provided on an hourly to a 6-hours basis (DWD, 2024). In order to be included in the service, the daily average wind speed from the nearest weather station to the centre of the respective satellite image is used (Section 3.2).

Distance to coast data. In order to assist the CNN in determining the approximate location of an image (Section 3.2), a dataset comprising the distance from the shore is provided. The dataset has been derived from OpenStreetMap (Haklay & Weber, 2008) shoreline data provided by Geofabrik GmbH (2024). The dataset for the distance to the coast was calculated at a resolution of 10 m × 10 m using the QGIS tool "Proximity (Raster Distance)".

Wave height information. The Copernicus Marine Service (2024) data on wave height are employed as an independent information source for change analysis. The data set designated "Baltic Sea Wave Hindcast" (BSWH, 2024) and the data set designated "Baltic Sea Wave Analysis and Forecast" (BSWAF, 2024) are employed to obtain the "Sea Surface Wave Significant Height (SWH)", which is provided on an hourly basis with a resolution of 2 km × 2 km. In order to facilitate the utilisation of the data set within the developed service, the wave heights are aggregated on a daily basis, employing the 85th percentile. Furthermore, the resolution of the wave data is linearly interpolated in order to align with that of the change analysis. Finally, the ratio of the wave height to the water depth is calculated utilising the reference data outlined in Section 3.1, which provides information regarding the water depth information.

Current data. The current data derived from the BSH current forecast is included to serve as an external information source for change analysis (Brüning et al, 2021). The dataset has a spatial resolution of 0.5 nautical miles × 0.5 nautical miles and maps the current velocity in latitude, longitude and depth direction, resulting in a total of 25 depth layers every 15 minutes. The velocity is processed by means of a Euclidean sum across all three directions, an arithmetic average along the depth layers and a reduction in time to the 85th percentile of the day. The spatial resolution is then linearly interpolated to match that of the change analysis.

Appendix B: Processing workflow of the bathymetric deviation

B.1 Pre-processing

To reduce errors related to atmospheric conditions and clouds, a satellite image is only downloaded and processed if the percentage of clouds used by CODE-DE (2024) is below a threshold of 5 %. The objective of this rather strict limit is to mitigate the issues associated with the emergence of thin and barely perceptible veil clouds, which are especially prevalent in images characterised by elevated cloud cover. These clouds give rise to systematic errors in the bathymetric derivation. Furthermore, this reduces errors caused by cloud shadows. Images captured on days with high wind speeds are also

https://doi.org/10.58440/ihr-30-2-a15

sorted according to the weather station in the area. This is due to the fact that periods of high wind speed cause significant seabed visibility problems, namely swell, wave whitecaps and increased turbidity due to sediment turbulence. These factors are therefore excluded from the analysis. The threshold for this exclusion is set at four Beaufort, as this is the wind speed at which widespread foaming begins (Abe, 1955).

When the MSI data is downloaded, it is merged with the reference depth and shoreline distance supplements. It is then downsampled to a spatial resolution of 20 m × 20 m, which empirical studies have shown to be a good compromise between noise reduction and spatial resolution. After this, the original 100 km × 100 km Sentinel-2 images are sliced into smaller sub-images of ~ 20 km with an overlap of ~ 0.5 km. This helps to speed up the calculation process by excluding some sub-scenes because they are mainly on land, in optically deep-water areas or not in waters under the responsibility of BSH. Therefore, a mask is created that marks these non-relevant pixels and excludes them from the evaluation by setting the values to blank value (*NaN*). During prediction, the ratio of the relevant shallow water pixels to non-relevant pixels should be at least 0.25 %, rejecting only scenes made up of mostly irrelevant pixels. In contrast, the threshold is set at 5 % during the training phase to avoid bloating the number of training images with images showing mostly outmasked areas. Another exclusion of these ~ 20 km sub-scenes is caused by the cloud cover. Here, we use the cloud detector of Braaten et al. (2015) and an exclusion threshold of 10 %, which was found in empirical studies and is active during the training and prediction phase.

For the remaining sub-scenes in the un-masked area, we calculate various parameters describing water turbidity and algae such as the Normalised Difference Turbidity Index (NDTI; Lacaux et al., 2007), the Maximum Chlorophyll Index (MCI; Gower et al., 2005), the Green Normalised Difference Vegetation Index (GNDVI; Buschmannm & Nagel, 1993) and the hue angle. These parameters help to mitigate the influence of water quality through the CNN. Furthermore, we derive several logarithmic band combinations, inspired by Geyman & Maloof (2019), such as the band combinations between blue-green, blue-red, blue-NIR, green-red, green-NIR and red-NIR to support the link between spectral information and water depth. For the calculations in this paper, the scenes were reduced to a size of 256 px × 256 px containing 16 bands with the reference depth, the spectral bands B1–B5, the logarithmic band combinations, the turbidity parameters and the shoreline distance.

B.2 Bathymetric regression with CNN

The CNN architecture employed was developed by Żak (2020) and adopts a U-net structure, characterised by a contracting path (encoder) and an expanding path (decoder), as introduced by Ronneberger et al. (2015). The U-Net comprises multiple depth layers, formed by progressively downsampling the input image in the encoder path, extracting increasingly abstract features, and then upsampling in the decoder path to produce a full-resolution result. Each depth layer of the encoder compromises of a batch normalisation, followed by a 2D convolution, a 2D max-pooling, another batch normalisation, a 2D convolution, a batch normalisation, and a final 2D convolution with spatial resolution reduction. In contrast, a depth layer of the decoder is constituted by a concatenation operation with the corresponding encoder level, a batch normalisation, a 2D convolution, a batch normalisation, a 2D convolution, a batch normalisation and a transposed 2D convolution, which serves to restore the spatial dimensions. This architectural configuration enables the network to capture both local and global context. Training a CNN for SDB requires a sufficient amount of different training data that represent the expected variability in, among other factors, the atmosphere, turbidity, subsurface conditions, wave action and solar radiation. The estimation of water depth from new satellite imagery can only be reliable for those areas that have been included in the training data. For the results presented in this paper, the CNN was created using five depth layers, the "Rectified Linear Unit (ReLU)" as activation function, the "Adaptive Moment Estimation (Adam)" as optimiser, the "Mean Square Error (MSE)" as loss function and a batch size of 128.

Appendix C: Processing workflow of the change analysis

C.1 Quality assessment

The objective of the quality assessment is to select the images that exhibit the optimal environmental conditions, which are likely to result in the most precise bathymetric data, for change analysis. To this end, a series of quality parameters are compiled and analysed for each approximately 20 km sub-image. The parameters listed below are absolute values, with a calculated relative value that may not always be meaningful. For instance, the mean absolute turbidity value of a sub-image cannot be interpreted, but a temporal comparison in the same area can highlight points of lower turbidity. The following relative values are then used to generate scores to assess the suitability of the sub-images:

- $Score_{Clouds}$: The averaged relative cloud cover values for the full Sentinel-2 image, as found in the image attributes metadata, and for the sub-image, which was calculated using the cloud mask methodology proposed by Braaten et al. (2015).
- $Score_{Turb}$: The average of the relative values of the sub-image mean of the "turbidity" values NDTI and GNDVI.
- $Score_{Bathy}$: The relative value of the mean difference between the bathymetry of the sub-image and the

median bathymetry of the sub-image sequence.
- *ScoreOther*: The average of the relative wind and the relative land percentage.

The individual scores are aggregated to derive an overall score, with the following empirically determined weightings being applied:

$$Score = \frac{2 \cdot Score_{Clouds} + 2 \cdot Score_{Turb} + 3 \cdot Score_{Bathy} + 1 \cdot Score_{Other}}{8} \quad (1)$$

Ultimately, the most appropriate images are selected based on the aforementioned score value. Empirical studies have demonstrated that retaining approximately 40–60 % of images with the highest score value represents an appropriate selection of the image sequence for subsequent change analysis.

C.2 Change detection algorithms

Three change detection algorithms are executed in parallel in order to quantify the change in the time series and thus distinguish between static and dynamic areas using the filtered image sequence described in Appendix C.1.

One method is the PCA (Wold et al., 1987), which is a mathematical method used to reduce the dimensionality of large datasets by transforming a large set of variables into a smaller one that still contains most of the information in the original set. For the following PCA analysis, the time series of length t with two information channels (depth and intensity) are combined to an artificial image with 2 × *t* bands. These 2 × *t* bands are highly redundant due to the correlation between the depth and greyscale channels and, more importantly, because many areas have not changed and therefore all *t* images have the same content in these areas (Deng et al., 2008). The number of principle components (PC) is now determined until a certain percentage of the original information is contained. In previous analyses, a value of around 90–95 % has proved to be adequate. The original time series can now be reconstructed from these PCs, with static areas reproduced very well and dynamic areas much worse due to the loss of information of 5–10 %. To highlight the areas of change the median difference between the original and reconstructed time series is calculated.

The CVA is a widely used change detection technique in remote sensing that calculates the difference vector of the observed features (depth and greyscale) between two time points (Afaq, 2021). The difference vector consists of the magnitude and the direction, indicating the change. When analysing the time sequence, the difference vectors between the adjacent time points are calculated, resulting in *t*-1 vectors. Tests have shown that the median difference of these vectors is a robust indicator of variable areas.

A robust difference calculation is also performed. In addition to the pre-sorting by the quality assessment, a median image with as little noise as possible is calculated for the given start and end points. For this reason, a division into three parts over time has proved to be successful in tests. The images in the first and last third of the evaluation period are used to calculate the respective median image, while the images in the middle third are ignored. The difference between these two robust, almost noise-free images highlights variable areas.

Furthermore, change information is to be generated from the current and wave data by deriving activity indices for both current and wave data (or more precisely, the ratio of wave height to water depth). To do this, the current or wave activity for each day is assigned to a number from 0 to 10, depending on the current speed or the ratio of wave height to water depth respectively. These values are then summed up for the study period to a single value per pixel which indicates the probability of change due to currents or waves. The absolute value provides information on bathymetric changes in the area independent of the MSI data. However, it is only useful for limited time periods as the summed change value becomes very large in long-term observations due to multiple storm events in the meantime. Therefore, in the current workflow, these change values are only used for observation periods of less than 2 years (found in developmental studies).

C.3 Normalisation, weighted sum, post-processing and clustering

Before combining the results of the individual change detection techniques, the individual results must be normalised. Min-max normalisation is used with the 5th percentile as the minimum and the 95th percentile as the maximum to minimise the effect of outliers. Values that end up less than zero or greater than one are set to zero or one respectively. A weighted sum is calculated to combine these normalised change indicator values, where the weights are predefined with empirically determined values. The resulting summed up change value is then post-processed with respect to the estimated uncertainty of the resulting change value. For areas very close to the coast (< 200 m), a downward weighting is applied to compensate for the effects of strong disturbance of the water column, waves and foam. In addition, a downward weighting is applied with increasing water depth due to the generally decreasing accuracy of the SDB with increasing depth. The same change value is therefore much more reliable in shallow water than in deeper water. Finally, a single total change is derived for each pixel, which is used as input for the clustering and seabed tracking (Appendix C4).

Areas with similar change patterns are clustered and converted into a traffic light inspired scheme.

https://doi.org/10.58440/ihr-30-2-a15

A k-means clustering (Ahmed et al., 2020) is performed based on the total change values, followed by morphological filtering to reduce noise. The k-means model was generated by fitting the derived change values of the entire German Baltic Sea into 12 classes according to their change intensity. This model is now being used in the different sub-areas and time periods. For ease of interpretation, these 12 classes have been combined into four classes ranging from 0 (no change) to 3 (very strong change). As the classification is done pixelwise, there are many fine unrealistic structures with salt-and-pepper noise, which is minimised by morphological filtering.

C.4 Seabed tracking with 2.5D LST

A more detailed motion analysis is conducted using 2.5D LST, which is applied to the areas previously identified as changing. This algorithm enables the pixel-wise tracking of small elements of the surface of the seabed through a sequence of images, thereby inferring the magnitude and direction of seabed motions. 2.5D LST is formulated as an iterative least squares adjustment procedure. The algorithm maps small surface segments of consecutive depth and intensity image data sets on top of one another, with the objective of minimising the sum of the squares of the depth and intensity value differences. This is achieved by estimating eight geometric parameters for translation, rotation, scale, inclination and perspective-related deviation and two parameters for radiometric adjustments (Westfeld, 2013). The input images are selected based on the score value derived from the quality analysis, with a greater weight assigned to images captured at longer time intervals to ensure that the selected images represent the greatest possible temporal range. 2.5D LST provides fully 3D displacement vectors with subpixel accuracy, thus offering a comprehensive representation of seabed topography. This allows for a detailed insight into the dimensions and directions of changes in the seabed.

Authors' biographies

Since 2022, Peter Grabbert has been employed as a scientific assistant at BSH, the Federal Maritime and Hydrographic Agency of Germany. He holds a Master's degree in Geodesy from the Technische Universität Dresden, specialising in remote sensing and photogrammetry. During the Master's thesis and the project at the BSH, he developed an SDB-based change analysis to monitor seabed changes, which runs as an automatic service. He also utilises his expertise in AI applications in remote sensing to host the AI regulars' table at the BSH.



Peter Grabbert

Mirko Bothe pursued studies in the field of applied computer science, with a specialisation in geoinformatics, at the Georg-August-University in Göttingen. Upon completion of his Master's degree, he was employed at the University of Rostock as a GIS expert and subsequently as a developer of GIS software for agriculture and UAVs at a small company. In 2019, he was employed in a research and development role within the Hydrography and Geodesy division of the German Federal Maritime and Hydrographic Agency (BSH). His work involves the automation and optimisation of workflows for satellite-derived bathymetry.



Mirko Bothe

Dr.-Ing. Patrick Westfeld graduated as a geodesist from TU Dresden (Germany) in 2005. He conducted research in the fields of photogrammetry and laser scanning and completed his PhD in 2012 on geometric-stochastic modelling and motion analysis. Since 2017, Dr Westfeld has been Head of R&D in Hydrography and Geodesy at BSH, the German Federal Maritime and Hydrographic Agency. The activities of his division range from conceptual issues pertaining to hydroacoustic and imaging sensor technologies, sensor integration and modelling, algorithm development up to application-specific implementation and practical transfer into the production environment.



Patrick Westfeld

https://doi.org/10.58440/ihr-30-2-a15

PEER-REVIEWD ARTICLE

Improving global coastal bathymetry from waves – Introducing scalable processing and post-processing workflows for 100 m resolution grids

Authors

Mona Reithmeier[1], Ingo Laut[1], Matthijs Gawehn[2], Christoph Kleih[1], Jens Schneider von Deimling[3] and Knut Hartmann[1]

Abstract

Global bathymetry data is essential for coastal mapping, modeling, and management, especially in insufficiently mapped regions. Ocean surface Wave Kinematics Bathymetry from satellite data provides a solution independent of water clarity, seabed habitats, and seafloor brightness. This study presents a fully automatic, scalable, and globally applicable Wave Kinematics Bathymetry processing workflow at 100 m resolution. Validated across eleven sites, it introduces automatic post-processing that eliminates false positives by up to 80 %, reduces depth errors by an average of 4.6 m and enhances data reliability. Deployed on the AWS cloud platform, this scalable method advances efficient global coastal bathymetry mapping.

Keywords

Satellite-Derived Bathymetry · bathymetry from waves · wave kinematics · post-processing · hydrospatial · earth observation

Resumé

Les données bathymétriques mondiales sont essentielles pour la cartographie, la modélisation et la gestion des côtes, en particulier dans les régions insuffisamment cartographiées. La bathymétrie par cinématique des vagues à la surface de l'océan à partir de données satellitaires offre une solution indépendante de la clarté de l'eau, des habitats du fond marin et de la luminosité du fond marin. Cette étude présente un processus de traitement de la bathymétrie par cinématique des vagues entièrement automatique, ajustable et applicable à l'échelle mondiale à une résolution de 100 m. Validée sur onze sites, elle introduit un post-traitement automatique qui élimine les faux positifs jusqu'à 80 %, réduit les erreurs de profondeur de 4,6 m en moyenne et améliore la fiabilité des données. Déployée sur la plateforme cloud AWS, cette méthode ajustable permet d'améliorer l'efficacité de la cartographie de la bathymétrie côtière à l'échelle mondiale.

✉ Mona Reithmeier · reithmeier@eomap.de

[1] EOMAP GmbH & Co. KG, 82229 Seefeld, Germany

[2] Deltares, 2600 MH Delft, The Netherlands

[3] Christian-Albrechts-Universität zu Kiel, Marine Geophysics and Hydroacoustics, 24118 Kiel, Germany

https://doi.org/10.58440/ihr-30-2-a18

Resumen

Los datos batimétricos globales son esenciales para la cartografía, modelado y gestión costera, especialmente en regiones insuficientemente cartografiadas. La Batimetría Cinemática de Olas de la superficie oceánica a partir de datos de satélite proporciona una solución independiente de la claridad del agua, los hábitats del fondo marino y el brillo del fondo marino. Este estudio presenta un flujo de trabajo de procesamiento de Batimetría Cinemática de Olas totalmente automático, escalable y aplicable globalmente a escala mundial con una resolución de 100 metros. Validado en once emplazamientos, introduce un posprocesamiento automático que elimina los falsos positivos hasta en un 80 %, reduce los errores de profundidad en una media de 4,6 m y aumenta la fiabilidad de los datos. Implementado en la plataforma en la nube de AWS, este método escalable avanza en la eficiencia de la cartografía batimétrica costera global.

1 Introduction

Coastal zones host approximately 40 % of the global population and many essential infrastructure and ecosystems. These areas are vital for various economic sectors, such as maritime transport and tourism, and are prerequisite regions for deploying offshore renewable energy platforms. Moreover, coastal zones encompass unique habitats, and many major cities are situated along shorelines, making these regions critical for human settlement and development (Small and Nicholls, 2003). Coastal bathymetry is highly dynamic due to erosion, sediment transport and deposition mainly controlled by currents, wave activity, sea-level rise, storm events, and human activities. The ongoing population growth, human-induced changes such as land reclamation and dredging, subsidence issues of mega cities given overload, climate change, extreme weather events, and natural catastrophes are exerting significant pressures and altering the shape and structure of coasts and the bathymetry (Syvitski et al., 2005). Mapping, monitoring, and analyzing shallow water bathymetry and its dynamics are critical for modeling, predicting, and mitigating potential threats to coastal communities, economies, and ecosystems. Comprehensive and sustainable coastal management hinges on up-to-date and detailed bathymetric data availability. Despite its importance, vast global coastal zones remain unmapped, and survey data is often outdated or marred by significant gaps (Mayer et al., 2018). Traditional bathymetric onsite surveys using, e.g., ship-born acoustic measurements or Light Detection and Ranging (LiDAR) surveys face significant limitations in shallow nearshore areas, such as limited coverages, high costs, logistical challenges, and safe navigation access. Facing these challenges and considering the compelling need for area-wide high-resolution bathymetry data, Satellite-Derived Bathymetry (SDB) has become a cost-effective and efficient solution for mapping shallow waters, supporting stakeholders with their survey-planning and modeling activities, providing bathymetric maps in yet unmapped and inaccessible areas and enabling the constant monitoring of seabed dynamics (IHO, 2024).

In order to achieve high comprehensive spatial coverage, SDB methods with gridded results are of particular importance. According to the International Hydrographic Organization (IHO, 2024), these gridded SDB methods can be classified in the following five categories: (1) Empirical SDB methods require onsite bathymetric data and use mathematical models and spectral information from multi- or hyperspectral satellite images (Lyzenga et al., 2006; Stumpf et al., 2003). (2) Machine Learning (ML) models identify patterns in satellite images, correlating them with bathymetric depths based on initial training (Niederjasper, 2020). (3) Photogrammetric SDB utilizes matching points from high-resolution satellite images taken from varied angles to calculate depths through triangulation (Chénier et al., 2018). (4) Physics-based SDB methods invert radiative transfer equations and model the sunlight's pathway to determine depths without survey data based on multi- or hyperspectral imagery (Kisselev & Bulgarelli, 2004). (5) Bathymetry gathered from waves measures the shoaling effect of waves using radar or multispectral imagery (Pleskachevsky et al., 2011; Bergsma et al., 2019).

Bathymetry from waves has the great advantage that it can also be used in optically turbid waters and over seafloor with low reflectance, which makes it of particular importance regarding the achievement of a global coastal bathymetry coverage. Therefore, this paper focuses on the latter method (5), Wave Kinematics Bathymetry (WKB, e.g., Bergsma et al., 2019 and Almar et al., 2024), and its global applicability (Almar et al., 2021) to derive coastal bathymetry in 100 m spatial resolution. The WKB approach is based on the interconnection between bathymetry and surface wave speed and wavelength, which is also described by the dispersion relation equation (Holthuijsen, 2007). By measuring the wavelength and speed over a short time lag, this equation can be solved to determine water depth. Common analysis methods include the Fast Fourier Transform (Pleskachevsky et al., 2011) and Radon Transform (Bergsma et al., 2019) of image subsets to calculate average depths. Almar et al. (2021) applied the WKB approach in 500 m resolution on a global scale based on the freely available Copernicus Sentinel-2 satellite data. However, local and regional studies showed the potential to derive bathymetry in higher resolutions based on Sentinel-2 satellite data (Bergsma et al., 2019; Delay et al., 2022). Past studies completely

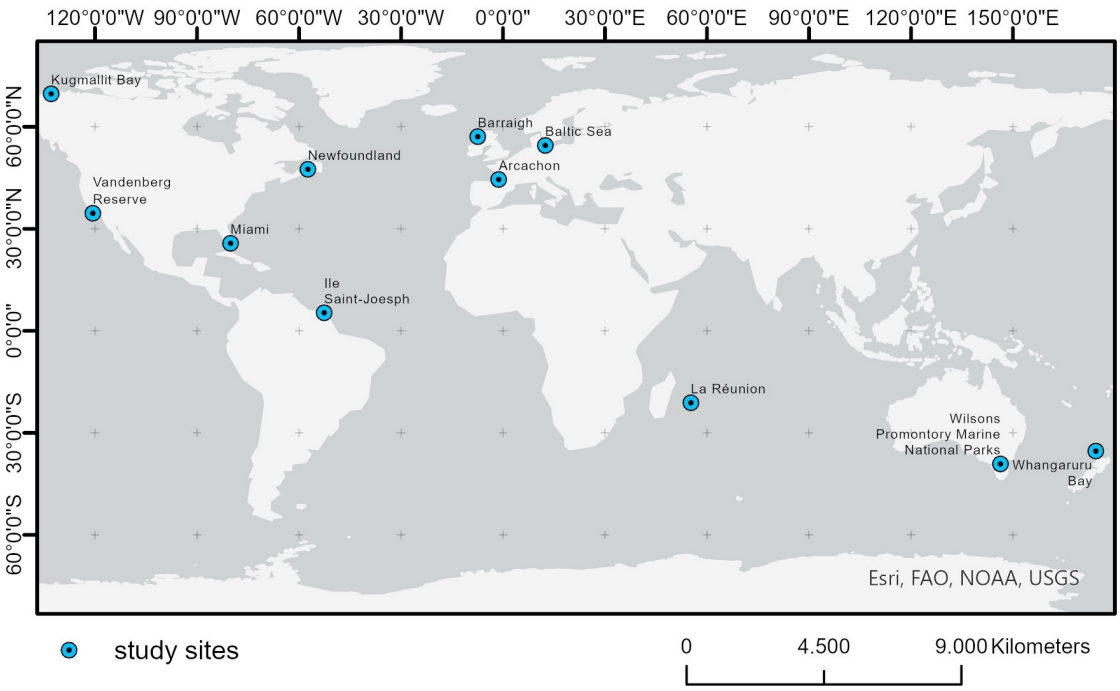


Fig. 1 Overview of the eleven globally distributed study sites, which represent diverse environmental conditions.

neglected post-processing, the systematic exclusion of unfeasible areas, and the elimination of false positives in the final dataset, leading to high error measurements (Almar et al., 2021; Almar et al., 2024).

This study elaborates on how the reliability and accuracy of satellite-derived WKB data can be improved while establishing a fully automatic, scalable, harmonized, and standardized processing framework. Verification and quantification strategies are explored, ensuring an effective process performance and improving the quality and reliability of the bathymetry. Methods are elaborated, increasing the data quality by developing systematic and automatic post-processing techniques to minimize false positives in the final dataset. Finally, a globally applicable WKB process in 100 m spatial resolution is set up.

2 Methodology

2.1 Study sites

All analyses are carried out on eleven globally distributed study sites shown in Fig. 1. The selected sites are Wilsons Promontory Marine National Parks, AUS, Kugmallit Bay, CAN, Newfoundland, CAN, Arcachon, FRA, Baltic Sea, GER, Ile Saint-Joseph, GF, Whangaruru Bay, NZ, La Réunion, RE, Barraigh, UK, Miami, USA and Vandenberg Reserve, USA. Table 1 summarizes the sites' most important characteristics and the information on the validation data used.

These study sites were chosen to test the methods in diverse environmental conditions and in a broad range of latitudes, from equatorial regions like Ile Saint-Joseph, GF, to polar regions like Kugmallit Bay, CAN. These sites exhibit a variety of wave and tide dynamics, ranging from the Baltic Sea, GER, with very low wave dynamics and wave heights (0.5 m) at minor tidal differences (0.2 m) to Barraigh, UK, with extremely high waves (2.2 m) and tide dynamics (4 m). Publicly accessible hydrographic shallow water survey data are available for each site, enabling a reliable validation of the final bathymetry results. The hydrographic survey data were transformed from their original coordinate system to the WGS84 geodetic reference system, resampled to 100 m spatial resolution, and referenced to the Lowest Astronomical Tide (LAT) accessing the tidal information from the respective tide gauges via Admiralty Total Tide. These processing steps ensure consistency with the spatial resolution and vertical reference of the WKB results.

The quality of the WKB results depends strongly on the presence of significant waves in the area (Almar et al., 2019). Accordingly, the WKB feasibility of an area can be assessed depending on globally available wave parameters like the temporally aggregated significant wave height (SWH; Copernicus, 2023b). In line with other WKB studies (Bell, 2008), preceding tests showed that areas with mean SWH smaller than 1 m are not feasible for calculating WKB. Following this, the study sites Kugmallit Bay, CAN, Baltic Sea, GER, and Miami, USA, are not considered feasible for WKB processing. However, they are included in the following analysis for proof of concept on a global scale and for assessing the feasibility prior to processing based on SWH values. Also, the test site at La Réunion is included to ensure a comprehensive analysis, even though it is unlikely to lead to meaningful WKB results. The site is dominated by a very short reef surrounding the island, dropping into deep waters at the reef crest. Despite a high average SWH of 1.8 m, waves mostly break at reef crests, where the elevation is exceptionally steep, and the terrain gets too deep for WKB processing. All other study sites show mean SWH values above 1 m and are categorized as feasible.

2.2 Wave kinematics bathymetry processing

The WKB method utilizes the interconnection between waves and bathymetry in intermediate to

https://doi.org/10.58440/ihr-30-2-a18

Table 1 Overview of study site characteristics. Including country and site name, latitude and longitude, tidal dynamics as difference between highest astronomical tide (HAT) and lowest astronomical tide (LAT), the closest tidal gauge, the temporarily and spatially aggregated Copernicus Secchi-Disc Depth (SDD; Copernicus, 2023a) and Significant Wave Height (SWH; Copernicus, 2023b), the wave activity, geographical and morphological site characteristics. Additionally, for each site the hydrographic survey data used for validation is listed by survey year, method, the data source of the survey and the maximum total vertical uncertainty (TVU) according to the International Hydrographic Organization (IHO, 2020) S-44 matrix.

Country, site name	LAT/ LON	HAT to LAT	Tidal station	Mean SDD	Mean SWH	Wave activity	Area characteristics	Survey year	Survey method	Source of survey data	TVU
AUS, Wilsons Promontory Marine N. P.	-39.13, 146.32	3.2 m	6068 Wara-tah Bay	19m	16m	moderate to high wave activity	Rocky coastline, soft sediment with single bigger rock formations	2013	Multibeam Sonar	Geo-science Australia	Not publicly available[1]
CAN, Kugmallit Bay	69.67, -132.91	0.8m	3378 Tuk-to-yaktuk	10m	0.4m	low wave activity	Muddy, low intertidal and low wave dynamics, extremely turbid	Survey Mosaic	Airborne Lidar Bathymetry	CHS, NONNA data	Bc7 and Bd5
CAN, New-foundland	47.49 -57.40	1.7m	3142 Con-noire Bay	17m	1.4m	moderate to high wave activity	Rocks, low intertidal dynamics	Survey Mosaic	Airborne Lidar Bathymetry	CHS, NONNA data	Bc6 and Bd3
FRA, Arcachon	44.50, -1.28	4.5m	1690 Cap Ferret	7m	1.8m	moderate to high wave activity	Sandy ground and inlet to Arcachon Bay	2009	Multibeam Echo-sounder	SHOM	Bc7
GER, Baltic Sea	54.50, 12.43	0.2m	1390 Gedser	7m	0.5m	low wave activity	Sand banks, reefs, sandy ground, intertidal dynamics mainly induced through wind	2018	Multi-source	BSH	Not publicly available[1]
GF, Ile Saint-Joseph	5.29, -52.61	3.5m	2271 Iles Du Salut	4m	1.1m	low to moderate wave activity	Soft, muddy sediment	2013	Multibeam Echo-sounder	SHOM	Bc7
NZ, Whangaruru Bay	-35.35, 174.3707	2.1m	6391C Whanga-mumu Harbour	14m	1.1m	low to moderate wave activity	Rocks and cliffs, moderate intertidal dynamics	2009	Multibeam Echo-sounder	Land Information New Zealand (LINZ)	Bc10
RE, La Réunion	-21.14, 55.27	0.9m	3950 Port Reunion	35m	1.8m	high wave activity	Reef	2009-2010	Multibeam Echo-sounder, airborne lidar bathymetry	SHOM	Bc8
UK, Barraigh	57.09, -7.43	4m	T032H	9m	2.2m	high wave activity	Rocky coastline, soft sediment in intermediate depths	2012	Multibeam Echo-sounder	UKHO	Bc8 and Bd6
USA, Vandenberg Reserve	34.57 -120.65	2.8m	9336 Oil Platform Harvest	7m	1.7m	moderate to high wave activity	Rocky cliffs along the coastline, sandy bays	2008	Multibeam Echo-sounder	NOAA	Bc7
USA, Miami	25.72, -80.14	1m	2639A Virginia Key	12m	0.3m	low wave activity	Shielded bay small sand ridges, radial bottom formations, shoals, reef	2008	Multibeam Echo-sounder	NOAA	Bc8

shallow waters. When waves approach more shallow waters, they increasingly interact with the seabed; propagation is expressed by the dispersion relation for free surface waves:

$$\omega^2 = k\, g \tanh(k\, h) \quad (1)$$

Where ω is the wave frequency, k is the wave number, g is the gravitational constant, and h is the water depth (Holthuijsen, 2007). The dispersion relation function can be solved for the water depth by deriving wavelength and speed from comparing two satellite image bands recorded with a slight time lag (Bergsma et al., 2019). This principle is visualized in Fig. 2.

The WKB processing in this study is based on the method described by Bergsma et al. (2019) and is executed in 100 m resolution. The approach combines the Radon transform (RT) and the Fast-Fourier transform (FFT) method to detect waves within a moving window. The window size needs to cover 1–2 surface water wavelengths. As waves become shorter when approaching the shoreline, the window size varies respectively. Areas directly at the shore are calculated using a window of 500 m, increasing to 800 m towards the deep water.

[1] The data was conducted in one or multiple hydrographic surveys. Therefore, a quality of order 1a with a maximum TVU of Bc8 and Bd6 (S-44 matrix; IHO, 2020) is assumed.

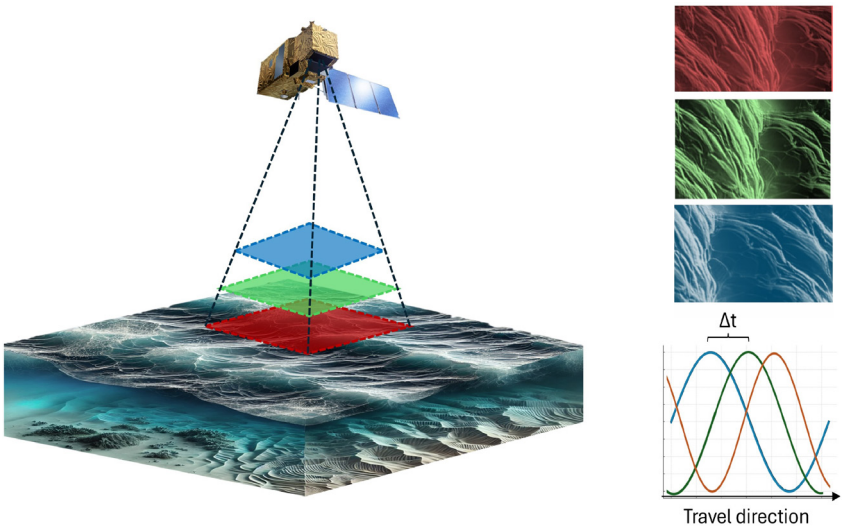


Fig. 2 Basic principle of WKB based on optical satellite data. The different image bands are captured with a slight time lag, enabling for observing the movement of waves and deriving wave parameters like speed and wavelength (image courtesy EOMAP with copyright material from European Space Agency 2024).

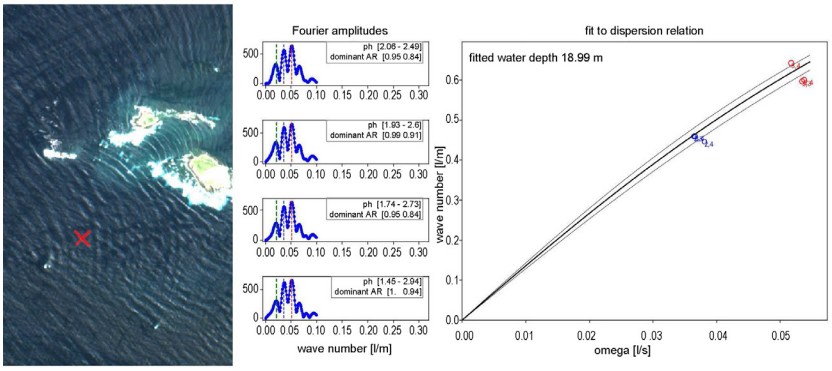


Fig. 3 Fourier analysis and fit to dispersion relation based on one sample point. Left, the red cross shows the location of the point. In the center, the FFT was performed for each Radon slice, showing multiple peaks. All peaks above a minimal wave number (shown as green hatched line) are considered with a weight that is proportional to the amplitude of the peak. On the right, for each valid band combination and for each Fourier peak, the wave frequency is calculated. The dispersion relation of water waves is fitted to the points and the best fit gives the water depth (in this example 19 meters).

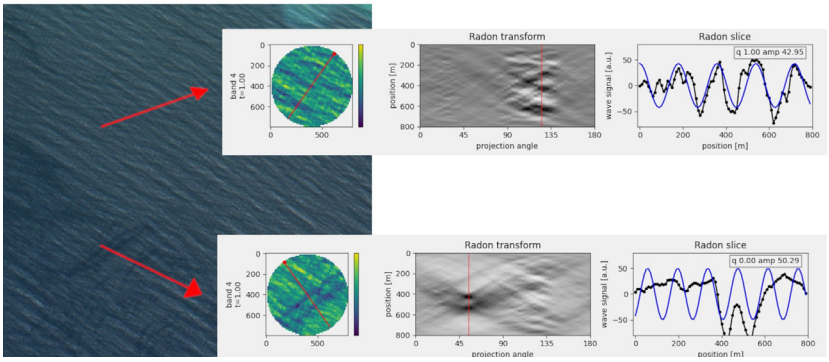


Fig. 4 Derivation of wave quality in the moving window. The RGB image shows well pronounced waves. The insets show on the left, the wave pattern from satellite band 4 of a moving window of size 800 m centered on the origin of the red arrows. In the center, the Radon transform of the wave pattern is depicted, including the dominant wave direction (red line). Along the dominant wave direction, the Radon slice is extracted (right, black line) and compared to a sinusoidal curve (blue line) with a wavelength corresponding to the dominant wavelength of the FFT. The wave quality *q* is calculated from a difference measure between the two curves.

First, an RT is applied to the window, detecting the wave direction (Bergsma et al., 2019). The slice of the RT at the dominant wave direction (the Radon slice) is extracted and shows a one-dimensional signal, which is then analyzed using an FFT that contains information on the wavelengths. Wave speed can be derived when relating multiple different subsets (e.g., from the different image bands) and the time lag of the captures. While past studies carried out the analysis only for one peak in the Fourier spectrum, this study involves analyzing multiple peaks, which enhances wave detection robustness. This methodology is depicted in Fig. 3, where multiple peaks are used to analyze the wave pattern.

Additionally, the algorithm now employs a versatile approach, fitting all speed-wavelength pairs to the wave dispersion relation. This approach, first introduced in the '80s for Xband radar-based studies by, e.g., Young et al. (1985) and later applied to satellite imagery by Gawehn et al. (2022), provides more robust results, especially in deeper waters. By considering all data points and identifying the best water depth, it overcomes the limitations of calculating effective water depth for each individual speed-wavelength pair, which can lead to invalid results or skewed depth estimates.

Past studies observed overestimation of depths in very shallow waters, resulting from the increasing non-linearity of waves moving toward the shore (Bell, 2001). On the other hand, errors increase with the water depth. The reason for these higher errors in deeper waters is that waves do not interconnect with the seafloor anymore at water depths much larger than the wavelength itself (Simarro et al., 2019).

To address these common errors, a wave quality estimation is calculated, which assesses the similarity of the wave pattern to an ideal sinusoidal pattern. Fig. 4 illustrates this approach based on an example image.

Two points are analyzed: the upper point reveals a well-defined wave pattern that the RT successfully detects, producing a quality estimate of q=1 compared to a sine wave. Conversely, the lower point, dominated by a strong sun glint pattern, shows a significant deviation from the sinusoidal curve, resulting in a quality score of q=0.

The full WKB processing workflow is installed on the AWS cloud environment.

2.3 Satellite data and scene selection

2.3.1 Sentinel-2 satellite data

The WKB processing is based on data from the European Space Agency's Sentinel-2 satellites. The two Sentinel-2 (2A and 2B) satellites capture the earth's surface every 3-5 days, depending on latitude, with publicly available data. Each Sentinel-2 satellite features four spectral bands in the visible and near-infrared regions with a spatial resolution of 10 meters, as well as nine additional bands in the visible to shortwave infrared with resolutions of 20 to 60 meters (ESA, 2024). The bands are recorded

https://doi.org/10.58440/ihr-30-2-a18

Table 2 Utilized Sentinel-2 satellite bands and the respective time lags Δt [s] compared to the blue band 02 (ESA, 2024).

Satellite band	Band 02	Band 03	Band 04	Band 05	Band 08	Band 09
Time lag Δt [s]	0	0.527	1.005	1.269	0.264	2.586

with a slight time lag, enabling wavelength and speed derivation and solving the linear dispersion function for water depth.

The bands used for this study are blue (band 02, ~490 nm), green (band 03, ~560 nm), red (band 04, ~665 nm), red edge (band 05, ~705 nm), and two more near-infrared bands (band 08, ~842 nm and band 09, ~945 nm). Table 2 lists the bands and the respective recording time lags.

2.3.2 Satellite scene selection workflow

Although waves may be present during satellite image acquisition, they might not exhibit a sufficiently clear optical signature to derive bathymetry (Danilo and Binet, 2013). Therefore, the scene selection must prioritize satellite images with visually detectable waves. The scene selection method utilizes the WKB processing methodology and includes the following steps:

1. Cloud filtering: Only Sentinel-2 images with less than 30 % cloud coverage above the processing area are considered for further analysis.
2. Wave detection: For the feasible imagery, point sampling is conducted. A window is created around each sample point. The RT, the extraction of the Radon slice, and the FFT are applied, to derive wavelength, speed, and amplitude.
3. Quality scoring: The quality score (described in chapter 2.2) is obtained for each sample point. The quality scores within one image are averaged, enabling a satellite scene ranking based on this quality score. The highest-ranked 10 scenes from the scene selection approach are processed and used as a basis for the multi-scene bathymetry grid creation.

All workflows are installed on an AWS cloud environment, enabling direct and fast access to the Sentinel-2 image archive and parallelizing the processing on 500 up to 1000 docker instances.

2.4 Data merging and post-processing

The merging of the single scene WKB results and post-processing of the data are pivotal steps as they reduce noise and artifacts and limit false positives, overall making the results more robust and reliable. In the context of SDB, fully automatic data cleaning presents significant challenges. Removing false positives by visual data analysis and comparisons with charts and other sources are effective on a smaller scale. However, this exclusion must be automated to develop a fully scalable approach. This study combines multiple statistical approaches to reduce invalid water depth values and refine the dataset systematically. The applied cleaning workflow consists of three significant steps:

1. Water level correction: All raw WKB single scene outputs are corrected from date and time of the satellite record to LAT using the FES2014 (Lyard et al., 2021) via a direct API access.
2. Leveraging multi-scene information on a pixel-basis: The first step involves an analysis on a pixel basis, considering all processed single scenes. A layer stack is created to facilitate this process. This includes:
   - Quality Filtering: In very shallow waters, the wavelengths shorten, leading to a lower quality index and higher noise. Pixels with an average quality index of less than 0.3 are removed from the dataset.
   - Removal of false positives: Single-scene false positives are removed on a pixel basis. Therefore, z-scores are calculated for each pixel's single scene values. Values with a z-score more than three are excluded.
   - Merging the single scenes: If a pixel contains less than 20 % of the original dataset's values, it lacks sufficient quality and is removed. The remaining valid water depth values are merged on a pixel basis, applying a weighted average utilizing their respective quality indices.
3. Spatial consistency: This step involves determining data noise within a moving window, by considering the standard deviation and the deviation of each pixel's value from the moving window average. Pixels with a higher absolute deviation from the window average than 2m+10 % water depth (set as TVU requirements Bc6 and Bd2 based on the S-44 matrix; IHO, 2020) and with a standard deviation higher than 2 m are considered noisy and are erased. While this step may create holes in the bathymetry grid, it enhances spatial consistency and removes false positives.
4. Smoothing the final dataset: The final dataset undergoes smoothing using a kernel filter to reduce residual noise and artifacts. Any remaining single pixels are deleted to achieve a cleaner and more coherent dataset. The result will show a smooth, spatially consistent bathymetry surface but still contain data holes where the WKB results were insufficient. In operational use, the kernel filter might be exchanged by a median filter or splines with tension interpolation (Wessel and Bercovici,1998), depending on the user requirements and application field of the bathymetry dataset.

2.5 Validation and quality assessment

The quality of the bathymetry results is assessed through visual interpretation and quantitative validation. Visual interpretation involves qualitative analysis

Table 3 Results of the satellite scene selection, listing for each study site the minimum scene quality, the maximum scene quality score, the average scene quality score of the highest ranked 10 scenes, the total number of scenes with a quality score above 0 and the average SWH.

Study site	Min. scene quality score	Max. scene quality score	Average scene quality score	Number of scenes > 0	Average SWH [m]
Wilsons Promontory Marine N. P.	0.5	0.8	0.6	9	1.6
Newfoundland	0.5	0.7	0.6	9	1.4
Arcachon	0.9	1.0	0.95	9	1.8
Ile Saint-Joseph	0.2	0.3	0.25	9	1.1
Whangaruru Bay	0.0	0.3	0.1	4	1.1
La Réunion	0.0	0.2	0.05	2	1.8
Barraigh	0.09	0.6	0.2	9	2.2
Vandenberg Reserve	0.8	1.0	0.9	9	1.7
Baltic Sea	0.0	0.0	0.0	0	0.5
Miami	0.0	0.0	0.0	0	0.6
Kugmallit Bay	0.0	0.0	0.0	0	0.4

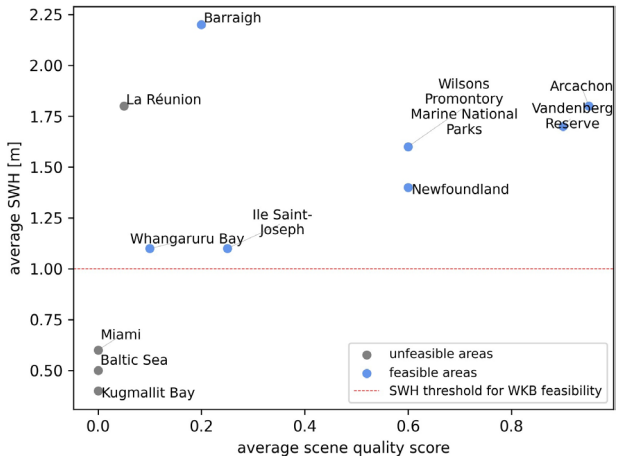


Fig. 5 Comparison between average SWH and the average scene quality score for each study site, with unfeasible areas visualized in grey and feasible areas visualized in blue. By applying an average SWH threshold of 1m (red hatched line) most unfeasible areas can be systematically excluded.

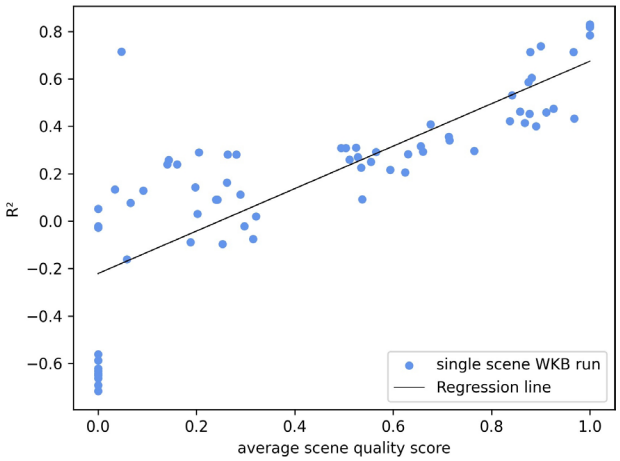


Fig. 6 Linear relationship between average scene quality score and the quality of the raw single scene WKB results. The quality is expressed as R^2 resulting from the validation of the WKB data against the hydrographic survey data.

of the dataset for anomalies or inconsistencies. The dataset is compared quantitatively against the respective hydrographic survey data. The results are analyzed for spatial correlation and standard error statistics, including correlation coefficient (*r*), Root Mean Square Error (RMSE), the coefficient of determination (R^2), and the slope of the linear regression function. Lower RMSE values, an r and R^2 close to 1, and a slope near 1 indicate high accuracy and strong spatial correlation.

3 Results

In this chapter, the results will be presented and interpreted.

3.1 Automatic scene selection

The scene selection approach proved to effectively detect the visible waves in the imagery. Table 3 summarizes the results of the scene selection approach for the different areas, including the minimum, maximum, and average scene quality score values.

The results initially deemed unfeasible also do not exhibit any distinctly detectable wave signals. Consequently, no satellite scenes with low cloud cover and sufficient wave signals were detected for Miami, US, Baltic Sea, GER, and Kugmallit Bay, CAN. La Réunion shows two scenes with very low scene quality scores. In the other areas, the average scene quality score ranges from very low scores of 0.1 (Whangaruru Bay, NZ) to high scores of 0.95 (Arcachon, FRA).

Fig. 5 illustrates the relation between each area's average scene quality score and its average SWH. It shows that by applying an average SWH threshold of 1 m, the unfeasible areas Miami, US, Baltic Sea, GER, and Kugmallit Bay, CAN, can be systematically excluded. The other areas show an increased average scene quality score with a higher average SWH. The Barraigh, UK area represents an outlier, which can be attributed to several factors: the region exhibits the highest seasonality

https://doi.org/10.58440/ihr-30-2-a18

Table 4 WKB validation results before post-processing and after post-processing.

Study site	before post-processing			after post-processing			
	r	RMSE	IHO S-44: Bc6, Bd2 (2m+10% depth)	*r*	RMSE	IHO S-44: Bc6, Bd2 (2m+10% depth)	Reduction of data points due to post-processing compared to the raw SDB output
Wilsons Promontory Marine National Park	0.43	17.5	8%	0.82	10.6	27%	-83%
Newfoundland	0.62	13.4	25%	0.62	10.2	26%	-76%
Arcachon	0.93	4.65	70%	0.97	2.46	85%	-15%
Ile Saint-Jospeh	0	6.0	48%	0.95	2.4	38%	-14%
Whangaruru Bay	0.4	13.5	19%	0.75	8.2	33%	-85%
Barraigh	-0.24	9.7	34%	0.85	2.5	68%	-46%
Vandenberg Reserve	0.8	9.8	27%	0.95	5.9	39%	-50%

of SWH (1.5 m in summer and 3.6 m in winter). In winter, when the SWH is highest, the sun elevation angle is too low to cause sun reflection on the water surface, making visual wave detection significantly more challenging. Additionally, the winter months in this region are the most precipitation-rich, leading to very high cloud cover and a reduction in the number of cloud-free scenes.

The extent to which the scene score affects the bathymetry results of individual scenes is illustrated in Fig. 6. Therefore, the raw (not post-processed) single-scene bathymetry results were validated against the hydrographic survey data. The resulting R^2 is compared to the respective scene quality score, showing a linear regression. Scene scores of 0 lead to a negative R^2 and contain no valid bathymetric information. Therefore, these must be discarded when processing the multi-scene image. Conversely, even scenes with low scores above 0 yield low but positive R^2 values. When combined to a multi-scene grid, these scenes can contribute to valid bathymetry information and are retained.

The image selection process, based on the automatic visual detection of waves using the average scene quality score proved to be effective to select suitable imagery for WKB processing. Thereby the impact of sun elevation angle and luminosity does not need to be quantified separately. Overall, the scene quality score represents a very good proxy for the WKB quality.

3.2 Wave Kinematics Bathymetry field results

The areas classified as non-feasible in Miami, USA, the Baltic Sea, GER, Kugmallit Bay, CAN, and La Réunion produced exclusively erroneous pixels during processing, which were subsequently automatically removed during post-processing. Consequently, none of these areas contains valid bathymetric information. These areas are excluded from further analysis. The WKB results for all other areas are presented in the following.

Table 4 presents the *r* values, RMSE, and the percentage of the WKB data meeting the IHO S-44 TVU requirement Bc6 and Bd2, for the raw multi-scene outputs and for the post-processed bathymetry, as well as the reduction of data points due to post-processing compared to the raw SDB output. The table indicates an average decrease of the RMSE of 4.6 m and a substantial increase of r, induced by the post-processing. Even if the IHO S-44 TVU requirements Bc6 and Bd2 were not achieved in any of the cases regarding the 95% confidence interval, an apparent increase in data points that fall into this category is evident for all areas. However, this quality improvement is accompanied by a considerable reduction of data points in the bathymetry result, shown

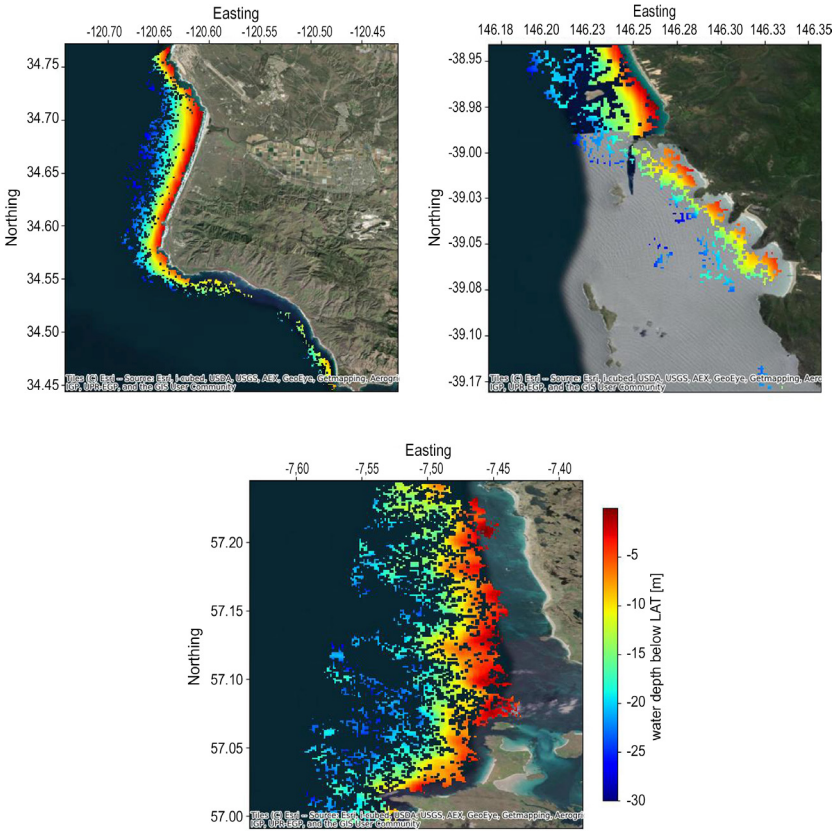


Fig. 7 Color-coded depths derived by WKB after post-processing for Vandenberg Reserve, USA (top left), Wilsons Promontory Marine National Park, AUS (top right) and Barraigh, UK (bottom center).

in the last column as a percentage change compared to the raw bathymetry output.

Fig. 7 showcases the results of the fully automated WKB, and post-processing based on the study sites Vandenberg Reserve, USA, Barraigh, UK, and Wilsons Promontory Marine National Park, AUS. The WKB surface is smoothly discernible in each of these areas, displaying visual consistency across varying environments. Areas characterized by lower SWH, such as Barraigh, UK, show larger data gaps due to the automated post-processing. This deliberate exclusion of potentially valid data points is a trade-off designed to enhance the overall dataset quality during post-processing.

Fig. 8 indicates the vertical error reduction achieved through the post-processing workflow for the three sites, by comparing the validation of the raw and post-processed results. Noise is significantly reduced in all three sites, resulting in point clouds that align more closely with the 1:1 regression line. This automated workflow represents a significant advancement in streamlining bathymetric data generation and ensuring more reliable outputs. Fig. 9 shows that despite these substantial improvements, there remains a tendency to underestimate deeper depths. The mean error increases with the water depth. The absolute Mean Error values differ significantly across the study sites, highlighting the necessity for an area-dependent deep-water cut-off threshold.

This maximum mapping depth was derived for the different study sites based on visual WKB interpretation by comparing chart data contour lines and the hydrographic survey data with the WKB results.

Fig. 10 shows the relationship between the visually derived maximum mapping depth and the average scene score quality. The area Ile Saint-Joseph, GF, is excluded, as it was not processed to the maximum mapping depth. This relationship allows for a further reduction of false positives in addition to the described post-processing steps. This integration of the automatically defined cut-off depth in the post-processing workflow, is crucial when scaling up the approach to the globe.

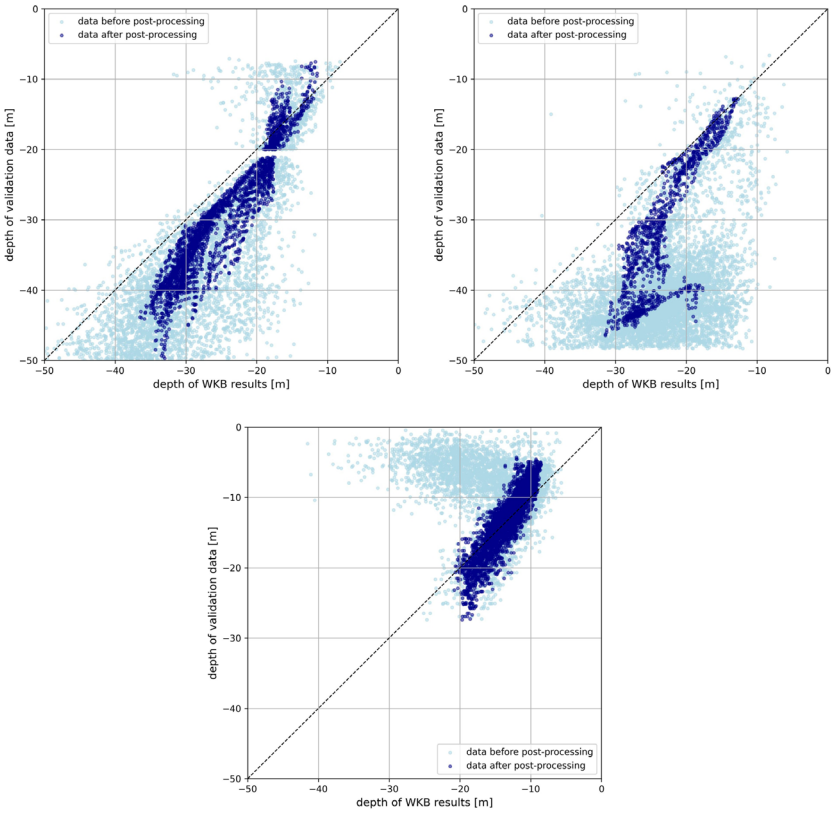


Fig. 8 Comparison of the validation of the raw WKB outputs (light blue scatters) with the post-processed WKB results (dark blue scatters), for the sites Vandenberg Reserve, USA (top left), Wilsons Promontory Marine National Park, AUS (top right) and Barraigh, UK (bottom center).

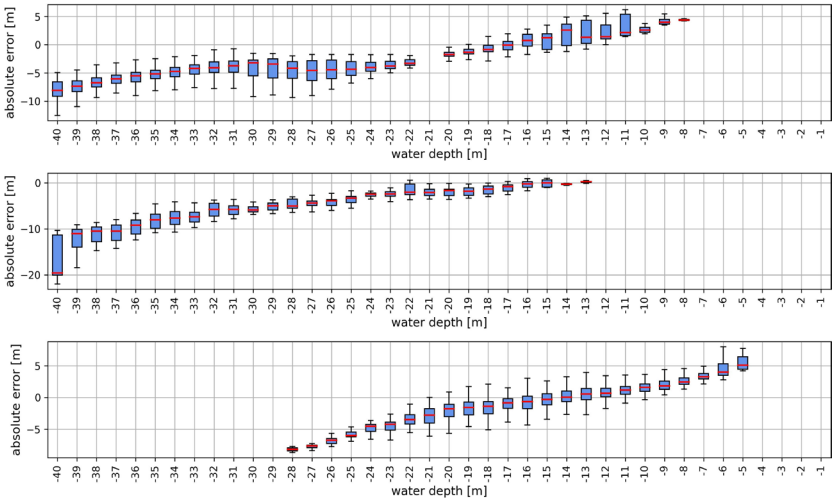


Fig. 9 Error distribution over water depths for the sites Vandenberg Reserve, USA (top), Wilsons Promontory Marine National Park, AUS (center) and Barraigh, UK (bottom), indicating the mean errors (red lines).

4 Discussion

In the following the results of this study and the potential of a global 100 m spatial resolution bathymetry derived from WKB methods are discussed and concluded.

4.1 Potential of 100 m WKB processing

This study demonstrates the improvements, results, performance, and accuracy of a fully automated and scalable WKB approach operating at a 100 m spatial resolution. The method leverages time lags between bands in multispectral Sentinel-2 satellite data, eliminating the need for locally adapted assumptions and calibration using pre-existing bathymetric data, which are often required in radar-based methods

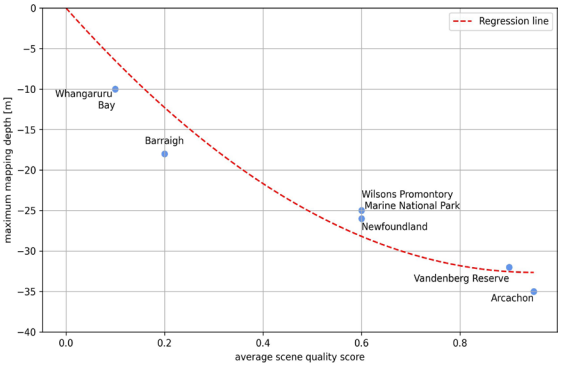


Fig. 10 Relationship between the site-specific maximum mapping depth [m] with the average scene quality score

https://doi.org/10.58440/ihr-30-2-a18

(Hennings, 1990; Wiehle et al., 2019). WKB is robust across various environmental conditions, including turbid waters and areas with extensive seafloor overprinting by flora and fauna, which typically change seafloor color and challenge optical SDB approaches (Hartmann et al. 2022). Introducing a sophisticated satellite scene quality score allows for systematically excluding unfeasible areas. This score provides a reliable proxy for the quality of the raw WKB results. Implementing the pixel-based quality score in a fully automatic post-processing routine significantly minimizes false positives, improving the results' reliability.

The designed workflow, running on the AWS cloud environment, is fully scalable and capable of global application. The bathymetry outputs offer substantial potential for a range of applications, particularly in unmapped, difficult-to-access, and turbid regions. This data can be instrumental in survey planning, bridging existing data gaps, and serving as a robust foundation for numerical coastal flooding and hazard modeling. Ultimately, this data resource supports more accurate coastal assessments and informed decision-making in marine and environmental management.

4.2 Horizontal and vertical accuracies

The bathymetry results have a raster resolution of 100 m. However, due to the moving window approach with window sizes of 500–800 m, only coastal features with a few hundred meters extent such as sand bars and coastal reefs become visible in such data. The WKB approach is most stable for intermediate to shallow water depths, ranging from -5 m to -35 m. Very shallow water depths (shallower than –5 m) are more sensitive to errors in the derivation of the single wave parameters due to the increasing non-linearity of the wave approaching the shore. The quality score depicts this non-linearity. Combined with the post-processing approach, false positives are eliminated in very shallow waters. Data gaps in the very shallow waters can be covered, e.g., by the fully scalable, optical physics-based SDB approach, described by Hartmann et al. (2022). Overall, with WKB, errors increase in deeper waters. The maximum mapping depth depends strongly on the site-specific morphology and waves and shows a relationship to the average scene quality score. This relationship can be applied to automatically derive a site-specific cut-off threshold and to eliminate false positives in deeper waters.

4.3 Limitations

The primary limitation of this methodology is the necessity of the presence of waves. Areas without sufficient wave dynamics can be precluded from processing using parameters such as the average SWH, with a threshold of 1 m (Bell, 2008). This limitation mainly affects bays, waters sheltered by morphology (e.g., fjords, or between islands) and shallow areas on reefs. By excluding these unfeasible areas prior to processing, the method ensures efficient and effective application of resources. Water depths can be calculated using WKB processing independent of water clarity, vegetation, or seafloor darkness. However, vertical uncertainties are typically higher in clear waters compared to optical approaches, especially the physics-based optical SDB method (Hartmann et al. 2022). Furthermore, this workflow does not cover very shallow areas. Therefore, a combination of WKB and physics-based optical SDB is considered to enhance overall accuracy and coverage.

4.4 Scalability and global applicability of WKB

By integrating all the methods described, a fully automated WKB workflow is achieved. The deployment on the AWS Cloud enables up to a 1,000-fold parallelization of computations, making the workflow fully scalable.

To showcase the degree of automation and scalability, the full scene selection, WKB processing and post-processing workflow were executed along

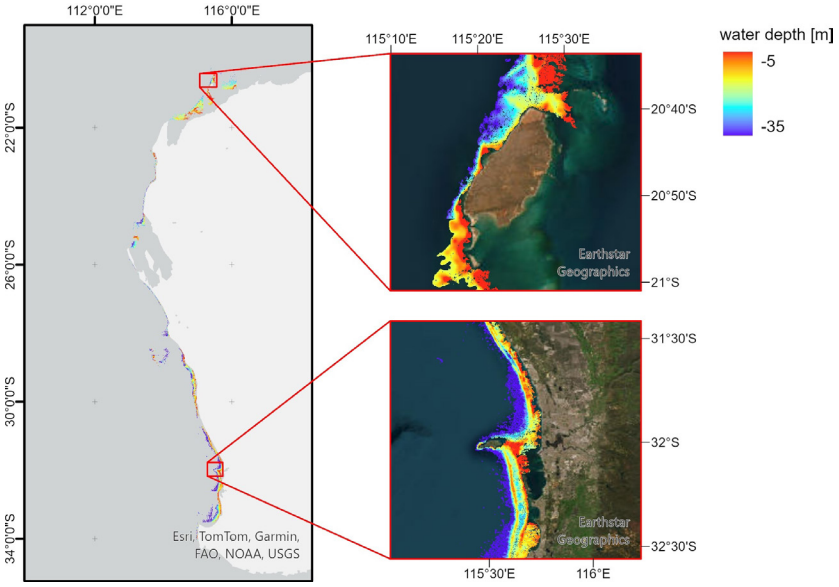


Fig. 11 WKB results for west Australia, showcasing the full processed bathymetry on left and two detailed views on the right.

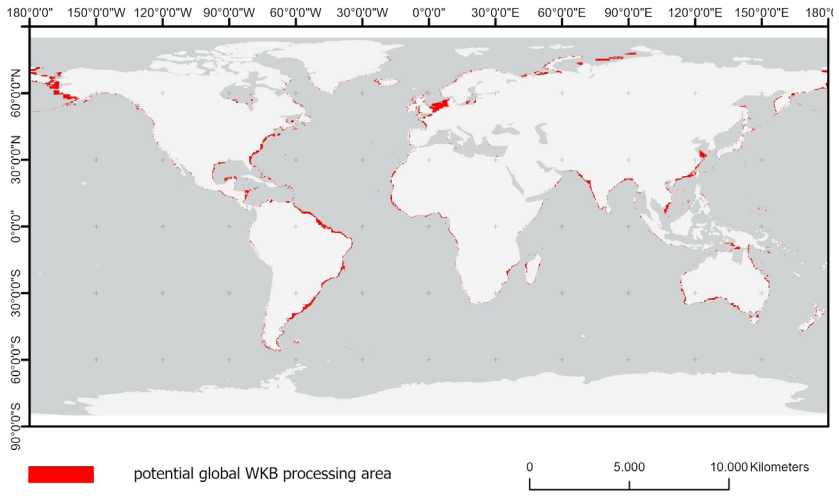


Fig. 12 Potential global WKB processing area, derived from the GEBCO -50 m contour line. Areas with an average SWH smaller 1m and major reefs and atolls were removed.

the entire west coast of Australia. This was completed within two hours (parallelized on 300 docker containers), without any manual data manipulation, demonstrating the method's robustness and efficiency. The result, depicted in Fig. 11, encompasses over 9,900 km² of data in a highly dynamic environment. The bathymetry was fully processed and post-processed within 90 min, further reinforcing the efficiency of the WKB process.

Given the full automation and scalability of this workflow, the 100 m WKB process holds substantial potential for achieving global coastal bathymetry coverage. This is particularly valuable for providing data for previously unmapped areas.

Fig. 12 illustrates the estimated global feasible WKB area based on the GEBCO 2024 bathymetry –50 m contour line, excluding reefs and atolls and regions with an average SWH of less than 1 m. Validation of a global data set can be carried out on a global scale or sample based. Validation against global data includes soundings of nautical charts (which need to be licensed) and the GEBCO bathymetry layer. Sample-based validation can be carried out for single sites, using the bathymetry points of the green active LiDAR IceSat-2 satellite in clear waters and the available hydrographic survey data in turbid waters. The processing of this global WKB dataset is already in progress and will support a wide range of applications, from survey planning to coastal hydrodynamic modeling (Gawehn et al., 2022).

4.5 Applications

The spatial resolution, depth coverage and uncertainties of the WKB model define its potential use for coastal applications. While the spatial resolution and uncertainties will forbid its use in nautical charting of safety of navigation it is of value for regional to global hydrodynamic models. This value is especially high when other bathymetric data do not exist, are not available or are interpolated. Its spatial resolution aligns with the Nippon Foundation-GEBCO Seabed 2030 Project, which aims to provide a global 100m bathymetry grid by 2030. It also supports the objective of Copernicus Marine to potentially include this dataset in the European Copernicus Marine Service. The latter funds this research and upscaling and the final datasets are aimed to be released in the data portal and contribute to Seabed2030 and the global GEBCO datasets.

5 Conclusion and outlook

This study successfully demonstrates the full automation and scalability of a standardized and harmonized WKB workflow, encompassing satellite scene selection, WKB processing, and post-processing at a 100 m spatial resolution. We identified a scene quality score as a reliable proxy for WKB result quality. This quality score is the basis of the new and effective satellite scene selection approach, enabling a feasibility analysis before processing. The WKB processing was improved by taking multiple peaks of the Fourier spectrum into account, making results more robust. Incorporating advanced fully automatic post-processing mechanisms significantly improved the accuracy of results, minimizing errors and false positives in very shallow and very deep waters. The degree of automation and scalability was showcased on a regional basis but enables the extension of this method globally, which is already ongoing. A comprehensive global WKB dataset will substantially enhance the utility of the SDB dataset for coastal applications like survey planning or hazard modeling. It will provide critical bathymetric insights in areas currently lacking data. WKB-derived data still falls short in accuracy when compared to optical physics-based SDB methods in shallow waters. Therefore, integrating WKB with optical physics-based techniques has the potential to harness the strengths of both methods, thereby minimizing their individual limitations and achieving the best possible global coverage and accuracy.

While this study focused on developing a fully automated and scalable WKB approach to derive one WKB dataset, it did not explore the applicability for monitoring areas characterized by high seabed dynamics. Investigating WKB's monitoring capabilities in such dynamic environments could significantly enhance our understanding of coastal processes and dynamics. This, in turn, would support more effective coastal management strategies, ultimately strengthening coastal resilience in the face of environmental changes.

Acknowledgements

This work has been carried out as part of a Copernicus Marine Service contract. Copernicus Marine Service is implemented by Mercator Ocean in the framework of a contribution agreement with the European Union.

References

Almar, R., Bergsma, E. W. J., Maisongrande, P. and Pedro Melo de Almeida, L. (2019). Wave-derived coastal bathymetry from satellite video imagery: A showcase with Pleiades persistent mode. *Remote Sensing of Environment, 231*, p. 111263.

Almar, R., Bergsma, E. W. J., Thoumyre, G., Solange, L. C., Loyer, S., Artigues, S., Salles, G., Garlan, T. and Lifermann, A. (2024). Satellite-derived bathymetry from correlation of Sentinel-2 spectral bands to derive wave kinematics: Qualification of Sentinel-2 S2Shores estimates with hydrographic standards. *Coastal Engineering, 189*, p. 104458.

Almar, R., Bergsma, E. W. J., Thoumyre, G., Baba, M. W., Cesbron, G., Daly, C., Garlan, T. and Lifermann, A. (2021). Global Satellite-Based Coastal Bathymetry from Waves. *Remote Sensing, 13*(22), p. 4628.

Bell, P. S. (2001). Determination of bathymetry using marine radar images of waves. *The Fourth International Symposium on*

https://doi.org/10.58440/ihr-30-2-a18

Ocean Wave Measurement and Analysis, pp. 241–257. San Francisco, USA.

Bell, P. S. (2008). Mapping shallow water coastal areas using a standard marine x-band radar. *Hydro8 Conference*. International Federation of Hydrographic Societies, Liverpool.

Bergsma, E. W. J., Almar, R. and Maisongrande, P. (2019). Radon-Augmented Sentinel-2 Satellite Imagery to Derive Wave-Patterns and Regional Bathymetry. *Remote Sensing, 11*(16), p. 1918.

Chénier, R., Faucher, M.-A., Ahola, R., Shelat, Y. and Sagram, M. (2018). Bathymetric Photogrammetry to Update CHS Charts: Comparing Conventional 3D Manual and Automatic Approaches. *International Journal of Geo-Information, 7*(10), p. 395.

Copernicus (2023a). *Global Ocean Colour* (Copernicus-GlobColour), Bio-Geo-Chemical, L3 (daily) from Satellite Observations (Near Real Time). Copernicus Marine Service, European Union. https://data.marine.copernicus.eu/product/OCEANCOLOUR_GLO_BGC_L3_NRT_009_101/description (accessed 15 August 2024).

Copernicus (2023b). *Global Ocean Waves Reanalysis*. Copernicus Marine Service, European Union. https://data.marine.copernicus.eu/product/GLOBAL_MULTIYEAR_WAV_001_032/description (accessed 15 August 2024).

Danilo, C. and Binet, R. (2013). Bathymetry estimation from wave motion with optical imagery: influence of acquisition parameters. *2013 MTS/IEEE OCEANS - Bergen, Bergen, Norway*, pp. 1–5. https://doi.org/10.1109/OCEANS-Bergen.2013.6608068

Delay, C., Baba, W., Bergsma, E., Thoumyre, G., Almar, R. and Garlan, T. (2022). The New Era of Regional Coastal Bathymetry from Space: A Showcase for West Africa using Sentinel-2 Imagery. *Remote Sensing of Environment, 278*, p. 113084.

ESA (2024). *S2 Mission - Overview of Sentinel-2 Mission*. SentiWiki, European Space Agency. https://sentiwiki.copernicus.eu/web/s2-mission (accessed 7 September 2024).

Gawehn, M., Almar, R., Bergsma, E. W. J. and De Vries, S. (2022). Depth Inversion from Wave Frequencies in Temporally Augmented Satellite Video. *Remote Sensing, 14*, p. 1847.

Hartmann, K., Reithmeier, M., Knauer, K., Wenzel, J., Kleih, C., Heege, T. (2022). Satellite-Derived Bathymetry Online. *The International Hydrographic Review, 30*(1), pp. 53–75. https://doi.org/10.58440/ihr-28-a14

Hennings, I. (1990). Radar Imaging of Submarine Sand Waves in Tidal Channels. *Journal of Geophysical Research, 95*(C6), pp. 9713–9721.

Holthuijsen, L. H. (2007). *Waves in Oceanic and Coastal Waters*. Camebridge University Press, Camebridge.

IHO (2022). *Standards for Hydrographic Surveys* (6th ed.). IHO Special Publication S-44, International Hydrographic Organization, Monaco. https://iho.int/uploads/user/pubs/standards/s-44/S-44_Edition_6.1.0.pdf (accessed 14 September 2024).

IHO (2024). *Satellite-Derived Bathymetry Best Practice Guide* (1st ed.). IHO Publication B-13, International Hydrographic Organization, Monaco. https://iho.int/uploads/user/pubs/bathy/B_13_Ed100_032024.pdf (accessed 6 September 2024).

Kisselev, V. and Bulgarelli, B. (2004). Reflection of light from a rough water surface in numerical methods for solving the radiative transfer equation. *Journal of Quantitative Spectroscopy and Radiative Transfer, 85*(3), pp. 419-435.

Lyard, F. H., Allain, D. J., Cancet, M., Carrère, L., and Picot, N. (2021). FES2014 global ocean tide atlas: design and performance. *Ocean Science, 17*(3), pp. 615–649.

Lyzenga, D. R., Malinas, N. P. and Tanis, F. J. (2006). Multispectral bathymetry using a simple physically based algorithm. *IEEE Transactions on Geoscience and Remote Sensing, 44*(8), pp. 2251–2259.

Mayer, L., Jakobsson, M., Allen, G., Dorschel, B., Falconer, R., Ferrini, V., Lamarche, G., Snaith, H. and Weatherall, P. (2018). The Nippon Foundation—GEBCO Seabed 2030 Project: The Quest to See the World's Oceans Completely Mapped by 2030. *Geosciences, 8*(2), p. 63.

Niederjasper, M. (2020). Satellite-derived bathymetry in practice. Hydrographische Nachrichten – *Journal of Applied Hydrography, 116*, pp. 40–47. https://doi.org/10.58440/10.23784/HN116-06

Pleskachevsky, A., Lehner, S., Heege, T. and Mott Claudius (2011). Synergy and fusion of optical and synthetic aperture radar satellite data for underwater topography estimation in coastal areas. *Ocean Dynamics, 61*, pp. 2099–2120.

Simarro, G., Calvete, D., Luque, P., Orfila, A., Ribas, F. (2019). UBathy: A New Approach for Bathymetric Inversion from Video Imagery. *Remote Sensing, 11*(23), 2722.

Small, C. and Nicholls, R. J. (2003). A Global Analysis of Human Settlement in Coastal Zones. *Journal of Coastal Research, 19*(3), pp. 584–599.

Stumpf, R. P., Holderied, K. and Sinclair, M. (2003). Determination of Water Depth with High-Resolution Satellite Imagery over Variable Bottom Types. *Limnology and Oceanography, 48*(1part2), pp. 547–556.

Syvitski, J. P., Harvey, N., Wolanski, E., Burnett, W. C., Perillo, G. M. E. and Gornitz, V. (2005). Dynamics of the Coastal Zone. In C. J. Crossland, H. H. Kremer, H. J. Lindeboom, J. I. Marshall Crossland and M. D. A. Le Tissier (Eds.), *Coastal Fluxes in the Anthropocene. Global Change — The IGBP Series*. Springer, Berlin, Heidelberg.

Wessel, P., Bercovici, D. (1998). Interpolation with Splines in Tension: A Green's Function Approach. *Mathematical Geology, 30*(1), pp. 77–93.

Wiehle, S., Pleskachevsky, A. and Gebhardt, C. (2019). Automatic bathymetry retrieval from SAR images. *CEAS Space Journal, 11*(5), pp. 105–114.

Young, I. R., Rosenthal, W. and Ziemer, F. (1985). A three-dimensional analysis of marine radar images for the determination of ocean wave directionality and surface currents. *Journal of Geophysical Research, 90*(C1), pp. 1049–1059.

Authors' biographies



Mona Reithmeier

Mona Reithmeier is a Remote Sensing expert with extensive experience in aquatic applications, data analysis, and product development. At EOMAP, she works as a project manager and EO data analyst for global mapping projects, specializing in Satellite-Derived Bathymetry (SDB) and Seafloor Classification (SFC). She also manages product development and go-to-market strategies for WebApps SDB-Online and COASTS, which support stakeholders in their decision-making for coastal projects. Mona holds an MSc in Physical Geography from the Ludwig-Maximilians University Munich and joined EOMAP in 2021.



Ingo Laut

Dr. Ingo Laut is senior researcher at the EOMAP R&D department. He holds a PhD and Msc. in physics from the University of Munich and worked at the German Aerospace Centre (DLR) and the Max Planck Society in the fields of data analytics, time series analysis and numerical simulations. Since 2022 Ingo works at EOMAP and is – amongst others – responsible for the analytical process to derive bathymetry from EO using wave kinematics approach.



Matthijs Gawehn

Matthijs Gawehn, MSc, PhD, earned his degrees in Hydraulic Engineering with a specialization in Coastal Engineering from Delft University of Technology. Since 2015, he has been with the Applied Morphodynamics department at Deltares, focusing on coastal hydrodynamics and morphodynamics data analysis. His publications cover topics such as very-low frequency wave analysis at coral reefs and coastal bathymetry estimation using various optical imagery sources, including XBand radars, drones, fixed cameras, and satellites.



Christoph Kleih

Christoph Kleih is a senior software developer and works at EOMAP's IT department since 2009 as software engineer. He has profound knowledge in Software development, geoinformatics and IT infrastructure. Between 2015 and 2020 he worked in projects for companies in the automotive and in the medical sector. At EOMAP he was involved in developing the core workflow systems for automated processing and transformed that to cloud-based web applications.



Jens Schneider von Deimling

Dr. Jens Schneider von Deimling is a senior scientist and lecturer at the Institute of Geosciences at Kiel University, Germany, in the department of Marine Geophysics and Hydroacoustics. His work bridges gaps between hydrography and habitat mapping and his research focuses on seafloor mapping combining optics and experimental hydroacoustic methods. Dr. Schneider von Deimling has spent more than 600 days at sea and led many cruises and research projects. In addition to intensive scientific collaboration, he works closely together with hydroacoustic system manufacturers, authorities and surveyors. Dr. Schneider von Deimling supports international and national hydrographic societies, e.g. via his former vice-presidency of the German Hydrographic Society (www.dhyg.de) and now as an active member of the international GEOHAB Backscatter Working Group (https://geohab.org/backscatter-working-group/).He was recently coordinating the multinational EU habitat mapping project ECOMAP (www.bonus-ecomap.eu).

https://doi.org/10.58440/ihr-30-2-a18

Dr. Knut Hartmann leads EOMAP's coastal team, where he is responsible for delivering geospatial data and IT solutions. He holds the position of Chief Operating Officer (COO). His technical expertise lies in business and technology development and remote sensing and geospatial innovations, with a special emphasis on coastal and aquatic environments. Knut has received academic awards for excellence, served as an expert advisor for Earth Observation in the International Law of the Sea (ITLOS) court case, chairs the Satellite-Derived Bathymetry Best Practice Project Team (SDBPT) – a supporting body of the International Hydrographic Office (IHO)'s Hydrographic Surveys Working Group (HSWG) –, and is a member of the UK and Ireland Hydrographic Society as well as the German Hydrographic Society.



Knut Hartmann

https://doi.org/10.58440/ihr-30-2-a18

PEER-REVIEWD ARTICLE

Toward automated volunteer and authoritative bathymetry discovery and comparison

Authors

Patrick Debroisse[1,2] and Brian Miles[2]

Abstract

Volunteered Bathymetric Information (VBI) (commonly called Crowdsourced Bathymetry, CSB) is a relatively untapped data source that could be used in many ways such as filling data gaps and informing future data collection expeditions. Determining the quality of VBI, has been difficult and time consuming leading to limited use in official nautical charts by national Hydrographic Offices. Despite this, the International Hydrographic Organization continues to collect and store CSB in its Data Centre for Digital Bathymetry (DCDB) in the hopes of widespread future use. Multiple methods of rapidly determining the quality of Volunteered Bathymetric Information are being developed, but data discovery, acquisition, management, and correlation with authoritative data remain cumbersome. In a world of limited staff and resources, automating this process will help to increase the speed with which VBI could be assessed for quality and incorporated into nautical charts, bathymetric models, survey planning, and decision-making tools. This article introduces an open-source program called *VBI Compare*, built to ease data discovery and management of VBI for quality calculations. *VBI Compare* automates interactions with the Data Centre for Digital Bathymetry and the NOAA National Bathymetric Source to locate, acquire, and manage the data required for quality calculations. As part of the data discovery process, *VBI Compare* ensures colocation of VBI and authoritative chart data and displays the data collected and processing status to the user. It also allows for data reputation calculations to be initiated. To demonstrate the significant efficiency of *VBI Compare* versus manual searching and downloading, an area near Galveston, Texas (US Gulf Coast) was used as a case study demonstrating the real-world utility of *VBI Compare* to a Hydrographic Office.

Keywords

volunteered bathymetric information · crowdsourced bathymetry · data discovery

✉ Patrick Debroisse · patrick.j.debroisse@noaa.gov

[1] National Oceanic and Atmospheric Administration (NOAA), Ship Ferdinand Hassler, U.S.A.

[2] University of New Hampshire, Center for Coastal and Ocean Mapping, Durham, NH, U.S.A.

https://doi.org/10.58440/ihr-30-2-a14

Resumé

L'information bathymétrique volontaire (VBI) (communément appelées « Bathymétrie participative », CSB) constituent une source de données relativement inexploitée qui pourrait être utilisée de nombreuses façons, notamment pour combler les lacunes en matière de données et informer les futures expéditions de collecte de données. La détermination de la qualité de la VBI a été difficile et a pris du temps, ce qui a conduit à une utilisation limitée dans les cartes marines officielles par les Services hydrographiques nationaux. Malgré cela, l'Organisation hydrographique internationale continue de collecter et de stocker les données de CSB dans son Centre de données pour la bathymétrie numérique (DCDB) dans l'espoir d'une utilisation future généralisée. De multiples méthodes permettant de déterminer rapidement la qualité de l'information bathymétrique volontaire sont en cours d'élaboration, mais la découverte, l'acquisition et la gestion des données, ainsi que leur corrélation avec des données faisant autorité, restent fastidieuses. Dans un monde où le personnel et les ressources sont limités, l'automatisation de ce processus permettra d'accélérer l'évaluation de la qualité de la VBI et son intégration dans les cartes marines, les modèles bathymétriques, la planification des levés et les outils d'aide à la décision. Cet article présente un programme open-source appelé VBI Compare, conçu pour faciliter la découverte de données et la gestion de la VBI pour les calculs de qualité. VBI Compare automatise les interactions avec le Centre de données pour la bathymétrie numérique et la National Bathymetric Source de la NOAA pour localiser, acquérir et gérer les données nécessaires aux calculs de qualité. Dans le cadre du processus de découverte des données, VBI Compare assure la colocalisation des données de VBI et des données cartographiques faisant autorité et affiche à l'utilisateur les données collectées et l'état d'avancement du traitement. Il permet également d'initier des calculs de fiabilité des données. Pour démontrer l'efficacité significative de VBI Compare par rapport à la recherche et au téléchargement manuels, une zone proche de Galveston, Texas (côte du Golfe des Etats-Unis) a été utilisée comme étude de cas démontrant l'utilité réelle de VBI Compare pour un Service hydrographique.

Resumen

La Información Batimétrica Voluntaria (VBI) (comúnmente llamada Batimetría Participativa, CSB) es una fuente de datos relativamente por explotar que podría utilizarse de muchas maneras, por ejemplo para cubrir carencias de datos e informar sobre futuras expediciones de recogida de datos. Determinar la calidad de la VBI ha sido difícil y ha llevado mucho tiempo, lo que ha limitado su uso en las cartas náuticas oficiales de los Servicios Hidrográficos nacionales. A pesar de ello, la Organización Hidrográfica Internacional sigue recogiendo y almacenando la CSB en su Centro de Datos para Batimetría Digital (DCDB) con la esperanza de generalizar su uso en el futuro. Se están desarrollando múltiples métodos para determinar rápidamente la calidad de la Información Batimétrica Voluntaria, pero el descubrimiento, adquisición, gestión y correlación de los datos con los datos oficiales siguen siendo complicados. En un mundo de personal y recursos limitados, automatizar este proceso ayudará a aumentar la velocidad con la que se puede evaluar la calidad de la VBI e incorporarla a las cartas náuticas, modelos batimétricos, planificación de levantamientos y herramientas de toma de decisiones. Este artículo presenta un programa de código abierto llamado VBI Compare, creado para facilitar el descubrimiento de datos y la gestión de la VBI para cálculos de calidad. VBI Compare automatiza las interacciones con el Centro de Datos para Batimetría Digital y la Fuente Batimétrica Nacional de NOAA para localizar, adquirir y gestionar los datos necesarios para los cálculos de calidad. Como parte del proceso de descubrimiento de datos, VBI Compare asegura la colocación de datos cartográficos VBI y oficiales, y muestra al usuario los datos recogidos y el estado del procesamiento. También permite iniciar cálculos de reputación de datos. Para demostrar la significativa eficiencia de VBI Compare frente a la búsqueda y descarga manual, se usó un área cercana a Galveston, Texas (Costa del Golfo de EE.UU.) como ejemplo de estudio demostrando la utilidad en el mundo real de VBI Compare para un Servicio Hidrográfico.

1 Introduction

According to the Nippon Foundation-GEBCO Seabed 2030 Project, approximately 74 % of the world's oceans remain unmapped (Seabed 2030 Project, 2024). With limited worldwide resources to fill these gaps, Hydrographic Offices (HOs), private industry, and educational institutions are trying to find novel ways to collect and process data to augment traditional mapping. One option is the use of Volunteered Bathymetric Information (VBI), commonly called Crowdsourced Bathymetry (CSB; Jencks & Chappell, 2018). VBI is data that is supplied to an HO from an outside source (Calder, 2021). The capabilities of these sources range from those with survey-grade equipment to data collected with standard navigational sonar systems. This disparity in capability necessitates rigorous data quality analysis to determine the viability of data from each contributor.

A large amount of VBI data is publicly available in the International Hydrographic Organization (IHO) Data Centre for Digital Bathymetry (DCDB; Jencks & Chappell, 2018). Data stored in the DCDB CSB database were collected by contributors using vessel navigational sonar and positioning equipment during normal maritime operations (IHO, 2022a). Determining the quality of this data is difficult and time consuming using traditional methods due to a general lack of metadata, limiting its current use. Many HOs agree that CSB has potential use in ocean mapping initiatives, but there is disagreement about its role because quality is so difficult to ascertain (Calder, 2021).

In 2021, a method of determining VBI contributor (and data) reputation by comparing it to authoritative data sources (vetted for charting or official use) was proposed (Calder, 2021). Additionally, a standardized processing method for CSB data has been developed for HOs (Klemm & Krabiel, 2023) by applying tide data and deriving sonar draft via authoritative data comparisons. Notably, both methods provide potential options for determining data quality through comparisons to authoritative data, but currently require manual discovery and data management, a time-consuming process prone to error. The advent of the IHO's S-100 suite of specifications (IHO, 2022b) and the growing desire for more precise navigational and modeling tools is putting stress on the prevailing data pipelines. This necessitates the need for more time-efficient processes to allow additional data sources to be ingested.

The source of authoritative data used for VBI data comparisons depends on the needs of the HO employing the tool and should be based upon where and how their trusted data is stored. It could be a HO's own database, or an external database containing data trusted to be the best available for the area it covers. In this case study, by way of example, data from the NOAA National Bathymetric Source (NBS; OCS, 2024) is used as it is the authoritative public data source for the United States Office of Coast Survey. Other authoritative data sources for different regions (e.g. NONNA in Canada (NONNA, 2022), EMODnet for the European Union (EMODnet, 2024), etc.) could equally be used with similar techniques.

In addition to requiring VBI data and coincident authoritative data, the Calder VBI reputation calculation requires a file management scheme that allows the necessary spatially coincident data to be stored and later retrieved for processing (Calder, 2021). Both local and cloud data storage and processing are possible for the execution of data quality calculations, however each has different input requirements. Additionally, file management is critical to ensure the intended data is used in calculations to ensure the greatest possible accuracy. Therefore, a successful file management tool must be flexible to allow for multiple processing options, be time-efficient and capable of evaluating the age and condition of selected files.

Similar to file management, different methods of reputation calculation are required depending upon whether the algorithm is deployed locally or in the cloud. A programmatic solution for file management and reputation calculation could make this workflow less cumbersome thus helping to promote VBI as a viable data source for HOs.

Presented here are semi-automated methods to discover and manage data necessary for VBI data comparisons from the DCDB and diverse authoritative databases. These methods are integrated into a program dubbed *VBI Compare*[1] . A case study is also described using NOAA's National Bathymetric Source authoritative data and the DCDB CSB database to show how this semi-automated program compares to manual data discovery and management methods while demonstrating how it may be adopted by HOs to handle VBI in their areas of responsibility.

2 Databases

To compare VBI data to authoritative sources, the minimum set of VBI data attributes required includes location, depth, and observation time. Additional metadata may help increase accuracy and uncertainty estimation including, e.g., vessel offsets or sound speed profiles. These data are often managed differently, each with its own data storage, metadata and access methods; an approach to abstracting away these differences is therefore required. This section demonstrates an approach for DCDB and NBS as an illustration of how this could be done generally.

2.1 IHO Data Centre for Digital Bathymetry Database

According to the DCDB, their CSB database houses

[1] *VBI Compare* is available at https://github.com/CCOMJHC/VBI-Compare/ (accessed 29 July 2024).

https://doi.org/10.58440/ihr-30-2-a14

over 2.3 million linear nautical miles and 1 billion individual soundings of VBI data from all over the world (as of July 2024). These data sets have been standardized for metadata and format by trusted nodes prior to submission to the database (IHO, 2022a).

The DCDB has multiple ways to access the VBI data it houses. The first is a web map interface or a MapServer ArcGIS REST Service Application Programming Interface (API), which allows the user to select desired files geographically or by selected attributes then submit an asynchronous request to extract the data from the archive (DCDB, 2022). The user receives an email containing a download link to access the requested data in GeoJSON (GeoJSON, 2016) and Comma Separated Value (CSV) (Safranovich, 2005) format along with a limited amount of metadata in JSON format. The second access method is an Amazon Web Service (AWS) Simple Storage Service (S3) bucket (Amazon, 2023), or cloud object storage container, hosted by the NOAA Open Data Dissemination Program (NODD). The CSV-format data files in this cloud-hosted resource are organized by year/month/day which makes it convenient to programmatically download data within a given date range but more challenging when searching for files by geographic area of interest or other attributes. The third access method is a new Pointstore API (Pointstore-API, 2024)[2]. This API, while still in testing, allows the user to query the archive of soundings as a seamless virtual collection of data, i.e. without concern for which files contain the data of interest. Filter criteria include geographic envelope, platform, date, etc. The API uses an asynchronous request model and REST-style HTTP queries to POST a new request and GET the status (and download URL) of an existing request. The user will also be notified via email when a download package is available but all interaction can be handled programmatically. Data are in CSV format and the user can optionally request a gridded output of the data as well.

Regardless of which service is used, the files delivered contain depths, time, and location along with other metadata, satisfying the requirements of the VBI Comparison algorithm. The Web MapServer does not allow for direct download of the files it contains. When using this service, the user must supply an email address to receive a message containing a File Transfer Protocol (FTP) URL for local file downloads, making it difficult to automate. On the other hand, the S3 bucket does allow for file downloads or collection of URLs pointing directly to the data in the bucket itself. Currently, however there is no direct way to query the S3 bucket with geographic parameters or other attributes to determine the required data. A solution using the MapServer REST API to identify files and the S3 bucket to download them is outlined in Section 3.1.

2.2 National Bathymetric Source Database

The NBS S3 Bucket houses authoritative data in GeoTIFF format (OGC, 2019). The bucket contains a folder for each NBS tile area which contains the GeoTIFF and an associated XML file.

A difficulty in using NBS is that it uses its own tile tessellation convention, separate from that of the NOAA Marine Chart Division (MCD) electronic chart tiles used in navigation equipment. MCD uses a tile set at specific dimensions and resolutions that correspond to the areas, name, and characteristics of their Electronic Navigation Charts (ENCs). The tile scheme NBS uses has a different naming scheme and a wider range of resolution options. While many of the NBS tiles do line up with chart tiles geographically, they may be at a different, often finer, resolution. This disparity in naming conventions makes searching for specific NBS tiles based on a navigational chart name difficult. A mechanism for resolving this disparity is given in Section 3.1.

3 Programmatic data discovery methods

As described in Section 2, the schema and query methods of the databases required for VBI data comparison differ greatly which makes acquisition, visualization, and comparison of colocated datasets from each difficult and time consuming. Programmatic data discovery methods have been created to address each of these concerns allowing for semi-automated data processing.

3.1 Database selection and query

The DCDB S3 bucket contains the desired VBI data and access to it is relatively easy through downloading files from the bucket or direct access via S3 URL, making it the preferred database for obtaining VBI. Using the S3 bucket also allows for deployment of the reputation algorithm to the cloud, which could avoid data egress or copying charges if deployed in the same AWS region. To ease data querying, the REST API is used to enable programmatic search. The file names in the GeoJSON server and the S3 bucket are similar, so it is possible to use the API to determine the desired files and translate those file names to the S3 bucket naming convention to access them.

Similarly, easy access to NBS data stored in cloud object storage (i.e., AWS S3 bucket) makes it the preferred database for authoritative data. To overcome the aforementioned naming convention incompatibilities between ENC and NBS tiles, geographic area queries, based on the extent of the VBI for which authoritative data are needed, are executed against an index stored as a GeoPackage file (OGC, 2021) housed at the top level of the NBS S3 bucket. This file can be accessed directly in the S3 bucket and

[2] The DCDB Pointstore API was released in the spring of 2023 after the initial research and development phase of *VBI Compare* was completed and was therefore not considered for use.

queried to yield the desired file names and URLs to the data stored in the bucket. The area used is obtained from the ENC charts of interest using a programmatic API query of the MCD ENC Rescheme Status database (OCS, 2022b). Alternatively, the GeoPackage file can be queried using a user defined area then subsequently searching for colocated VBI. While the NBS database only covers areas where NOAA has charting authority, using it for this case study shows how an authoritative database controlled by an HO can be used to compare DCDB CSB data to determine reputation and uncertainty.

3.2 Query visualization

The data held in the DCDB can be visualized online using a web map display[3] designed by the National Centers for Environmental Information (NCEI). This web map also allows for geographic area or point queries. However, the map display cannot be reliably used to programmatically download data and is not connected to the DCDB S3 bucket, making it a less useful option for visualizing all required data streams.

NBS data tiles can be visualized in NOAA's nowCOAST suite (OCS, 2023), but nowCOAST does not have the capability to query the NBS tile set by a user-defined area, nor can it access the data in the S3 bucket. An alternative option is the GeoPackage file in the NBS S3 bucket. As described previously, this file can be used to query the NBS database, but it requires a separate geographic information system (GIS) software to open for visualization purposes.

Therefore, although both data sets have visualization methods, neither of them allows for the visualization of both datasets simultaneously. This inability is consequently addressed using a GIS monitoring window built into *VBI Compare*. The map display is the primary data visualization tool showing how many files were collected and their geographic location, allowing the user to confirm that the data extracted covers the area of interest and that the datasets are colocated.

3.3 Data integration

Collection of each individual data type from its respective database is possible programmatically. To execute a reputation calculation, both data sets are required. Further, for a calculation to be completed both data sets must be colocated. This necessitates a query of one database using the results of the other. While these databases and files are diverse as described previously, they both use the World Geodetic System of 1984 (WGS 84; NGA, 2022) geographic coordinate reference system both within the data files themselves and the query interfaces, making geographic queries possible across databases. In *VBI Compare*, regardless of how the first database is searched, whether by specific chart or vessel or by geographic area, the second database is queried using the geographic extent of the first.

3.4 Executing VBI comparisons

Comparison between VBI and authoritative data is conducted in a batch computation using an index file of local storage locations or URLs for the affected files. The outputs are saved to a local directory tree structure and a Fig. showing reputation score as a function of transit time is created. Access to the discovered files requires a local download or internet connectivity for cloud data. A programmatically constructed directory tree structure ensures the desired files are supplied to the calculation algorithm each time it is executed.

Two directory structures were considered in developing *VBI Compare*. The first was to collect all the files discovered by each query into one central directory built per run of *VBI Compare*. The second option was to construct a directory tree that houses the files corresponding to a specific tile or vessel in a separate directory for each along with index files detailing their locations. The second method provides a local cache, thereby minimizing local storage and maximizing reuse, improving performance thus making it the preferred directory structure.

In the cloud, for efficiency, processing is done through accessing the data directly in the database where it resides. This method is faster and may lead to cost savings because data egress fees are reduced over local downloads. Access via S3 URLs is more efficient for the VBI comparison algorithm as only segments of the GeoTIFF authoritative data that are coincident with VBI need to be downloaded rather than entire files and is therefore preferred in this example.

4 Implementation architecture

The DCDB/ NBS implementation of *VBI Compare* (Fig. 1) consists of five major steps. The code builds a directory tree structure for data handling [1], then determines which authoritative or VBI data the user is looking for [2], cross references those results with the files available in the S3 bucket for the respective data type [3], and either downloads or indexes the URLs for the required files [4] in a plain text file depending on user needs. The reputation algorithm is then executed [5] if certain constraints are met.

VBI Compare was developed as a desktop application in Python for compatibility with existing tools such as The Center for Coastal and Ocean Mapping (CCOM) / NOAA Hydroffice (HydrOffice, 2022) or the NOAA/ CCOM Pydro suite (OCS, 2022a). This application is open source, allowing for modification to suit the local environment (e.g. with different databases)

[3] https://www.ncei.noaa.gov/maps/iho_dcdb/ (accessed 29 July 2024).

https://doi.org/10.58440/ihr-30-2-a14

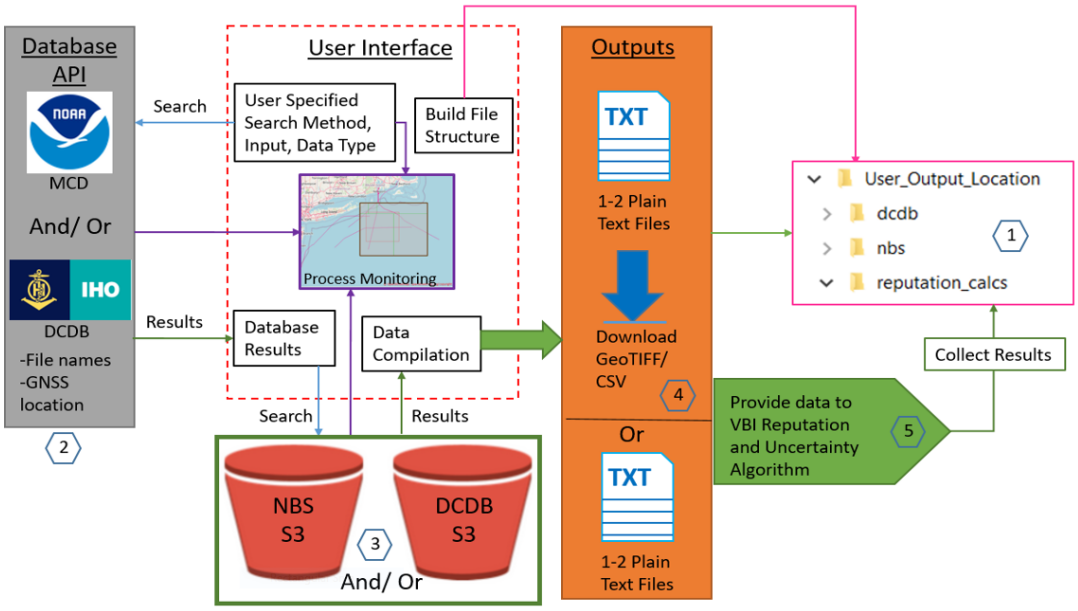


Fig. 1 Implementation architecture for the DCDB / NBS version of VBI Compare, illustrating the general workflow for S3 and API queries for the two databases.

without licensing.

The *VBI Compare* GUI provides for search parameter specification and can be customized to launch the reputation calculation for the area, vessel, or chart of interest. A monitoring subwindow allows for visualization of the data discovery processing status and the data collected. On the monitoring window, the map display is the primary data visualization tool showing how many files were collected and their geographic location. Additionally, text outputs and progress bars allow the user to monitor and confirm progress.

5 Case study

A case study was completed using the Galveston Ship Channel (US Gulf Coast). For comparison, the same data discovery was attempted both manually and programmatically using *VBI Compare*.

The use case for this study was to first search the DCDB CSB S3 bucket based on a user defined geographic area. Then the NBS bucket was searched using the resulting track-line geometry of the VBI data returned from DCDB. This use case was selected because it could be commonly used by HOs, and it exercises *VBI Compare* to its maximum extent. *VBI Compare* was instructed to collect S3 URLs for cloud-based processing. The manual data discovery and management attempt followed this same workflow. The settings used for the query can be seen in Appendix 1.

5.1 Case study using manual methods

The DCDB CSB ArcGIS REST API was used to determine the CSB files that are available for the area of interest. The query resulted in one thousand file names. This output does not provide data or links to data, so the user was required to copy the JSON text to a Microsoft Excel file, and then parse the result to yield the file names; Excel string manipulation formulae were used for transformation to URLs. The DCDB portion of the workflow was complete when the user copied these URLs to a plain text index file. Excel was used instead of, e.g., Python to reflect notional use experience in the field, i.e., Excel experience is more common than Python. This simulates the methods a user would need to employ without prior training, specialized programs, or skills yielding a better estimation for level of effort.

The DCDB trackline geometry was used to determine the intersecting NBS tiles. During manual testing, it was found that collecting and managing this track line geometry was difficult without writing a script. It became too cumbersome to attempt, so the user opted to query the NBS GeoPackage using the original user supplied area rather than track line geometry; this resulted in only the NBS tiles that were strictly necessary for the area.

The user opened the NBS GeoPackage in the desktop QGIS application. After importing the GeoPackage, a Shapefile layer was created encompassing the user supplied search area. An intersection analysis was completed between the two files yielding a list of the resultant file names and links to two NBS GeoTIFF tiles in the NBS S3 bucket (Fig. 2). The user then copied the GeoTIFF links to an index file, completing data discovery. The total time to complete manual data discovery took about 29 minutes, 17 minutes for the DCDB steps and 12 minutes for the NBS steps.

5.2 Case study using *VBI Compare*

The bounding box in Fig. 3 used for automated data discovery using *VBI Compare* was the same as that used above in the manual workflow.

The workflow of *VBI Compare* is given in Fig. 4. The *VBI Compare* run of the case study resulted in

the same one thousand DCDB track lines as were collected manually. However, this portion of the workflow completed in about 30 seconds (compared to 17 minutes). Additionally, the track line geometry could be automatically collected and managed by the program. Since track line geometry was extracted, 141 S3 URLs for NBS tiles were collected covering the entire length of each track line, compared to the 2 NBS tile URLs collected manually. This step was completed in approximately ninety seconds (compared to 12 minutes for this portion of the manual workflow). Execution of the workflow in *VBI Compare* resulted in the creation of two plain-text index files in the constructed directory tree as well as a download of the most up to date NBS GeoPackage file. Finally, the program took 13 seconds to determine that 122 MCD charts could be affected by the reputation calculations using the data sets collected. It also provided the user with a list of those chart numbers. In total, it took *VBI Compare* 180 seconds to collect, package, store, and display all this data (Fig. 5). This test was repeated several times with varying loads on the internet bandwidth. These tests all fell within a total runtime range of 120–210 seconds. This range of results showed some dependence on internet bandwidth but was still much faster (approximately 700–1,000 %) than the manual workflow, regardless of the load.

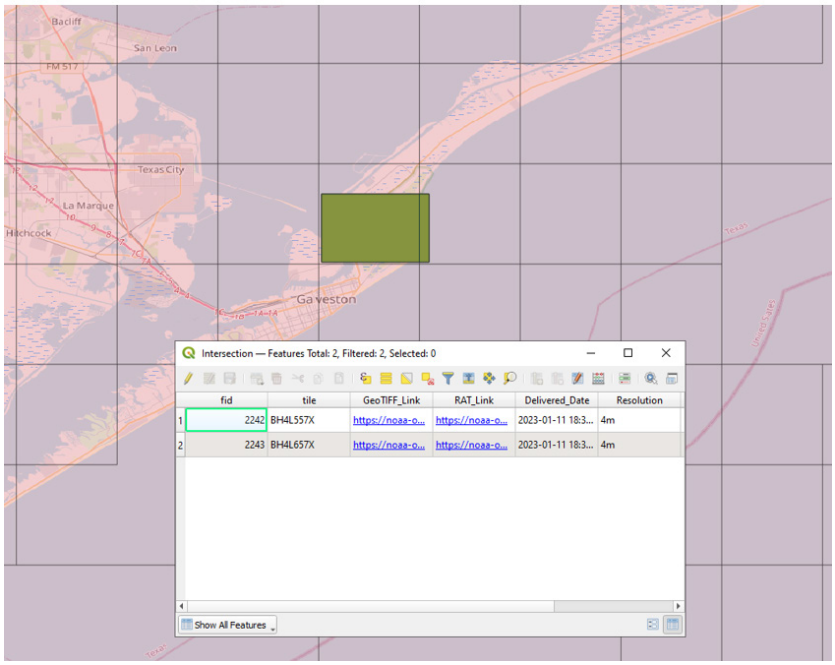


Fig. 2 Manual NBS query results displayed in QGIS.

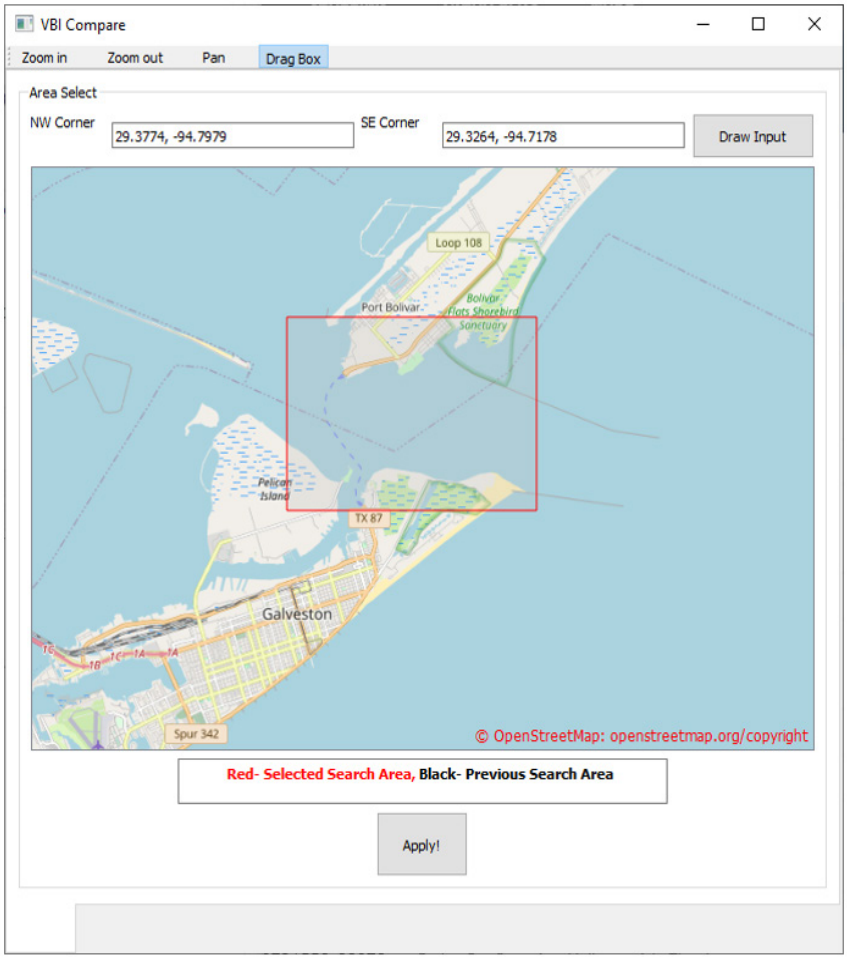


Fig. 3 Case study area selection.

6 Discussion

Several limitations became apparent while testing the manual data discovery workflow, shedding light on its limitations. The first was that the DCDB API query does not return data or links to data, but rather a simple list of file names. The need to translate the results from the query into URLs was a tedious and time-consuming process. While significant time might be saved with an experienced Excel user, the process is still error-prone. Secondly, the complexity of track-line geometry management made it impractical to do for manual processing. While the results are still valid collecting colocated data over only the original area of interest, the manual process collects far fewer NBS tiles, lacking additional context. Although the manual method collects all VBI data that exists for the area of interest, collecting all VBI data for track lines that intersect the area of interest (as *VBI Compare* can do) enables the user to discover more data points for the reputation algorithm to compare leading to more accurate reputation scores. The QGIS intersection analysis required by the manual workflow did not take much time, but still required basic knowledge of the QGIS platform or GIS systems. Additionally, manually creating the two index files (one for VBI and one for authoritative data) was not particularly taxing, but it is error-prone. Further, in the case where local downloads of the files is desired, the manual download process may be too difficult or time consuming to perform for large search areas. The 29-minutes it took to complete the manual method did not include the time to click each link and save each file in a manually constructed directory tree that would be required for local processing. While not fully evaluated, it was clear that the time added for local downloads and file management would be significant.

https://doi.org/10.58440/ihr-30-2-a14

With the manual method, determining the MCD charts that could be affected by a reputation calculation with the discovered datasets would require the collection of the track line geometry and an API search against that geometry using the MCD Rescheme Status API. There are six ENC resolution bands. Band one is excluded because of the small scales it uses, so each NBS tile would have to be cross referenced to each of the five remaining bands to determine the charts of interest. For one thousand track lines, this would result in five thousand manual API queries. Clearly this would be impractical. While not a strict requirement of the project, *VBI Compare* is able to determine the MCD nautical charts that might be affected by a reputation calculation. This could be used in the future to inform users about the reputation of data used to build a given chart.

The uptake of VBI as a data source by hydrographic offices has met resistance due to the time expense of determining data quality or constructing a final usable product. It has been shown here that *VBI Compare* in conjunction with a data comparison algorithm could unlock VBI as a viable data source by significantly reducing the workload of determining data quality. While *VBI Compare* has significant potential, additional updates to the DCDB and the NBS could further these contributions. Still, there are some potential limitations to *VBI Compare*.

As shown, the DCDB S3 bucket is not directly searchable, necessitating the use of its API and a translation of file names from the DCDB API to the S3 bucket naming convention. This could be alleviated by either making the file naming conventions of both databases the same, or alternatively using a GeoPackage type file within the S3 bucket similar to that of the NBS. Further, vessel metadata stored in DCDB VBI GeoJSON files (which are only accessible via the ArcGIS REST API) are not available in the CSV file encoding of the same data stored in the S3 bucket. If the DCDB were to store a dictionary file, mapping the vessel metadata attributes to vessel unique identifier, in the S3 bucket, *VBI Compare* would be able to collect this data as part of its data discovery process.

Until the DCDB S3 bucket becomes directly searchable, it will still be necessary to translate filenames returned by the ArcGIS REST API to the naming convention used in the S3 bucket, making the data discovery mechanism used by *VBI Compare* brittle to future changes in either the REST API or S3 file naming convention. In such cases, *VBI Compare* would no longer function until the code is updated. Aligning the naming conventions between these databases and updating *VBI Compare* would alleviate this issue going forward. The new Pointstore API may alleviate this concern because it can be interacted with programmatically and allows for a direct search with criteria such as geographic envelope, platform, date, and more.

The naming convention of the data tiles in the NBS differs from that of ENC, making a comparison between the tessellations necessary to determine which ENC charts may be affected by a data quality calculation. This disparity in conventions also makes searching by a specific ENC chart more difficult. The GeoPackage file used by NBS could also serve as a cross reference file for ENC charts. If a mapping between ENC charts and NBS tiles existed in the

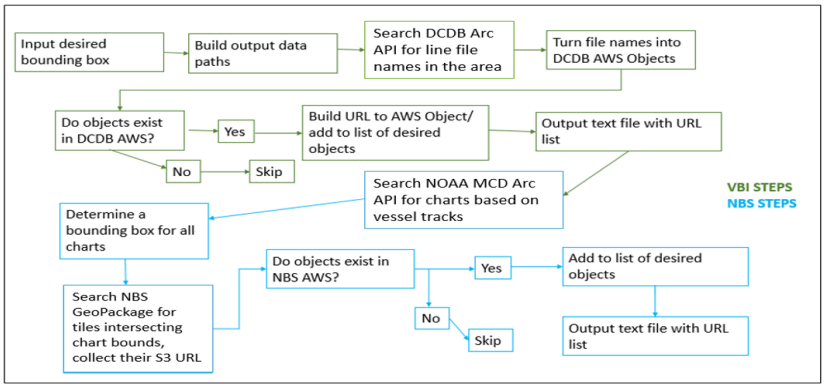


Fig. 4 Illustration of the *VBI Compare* process for the area in Fig. 3.

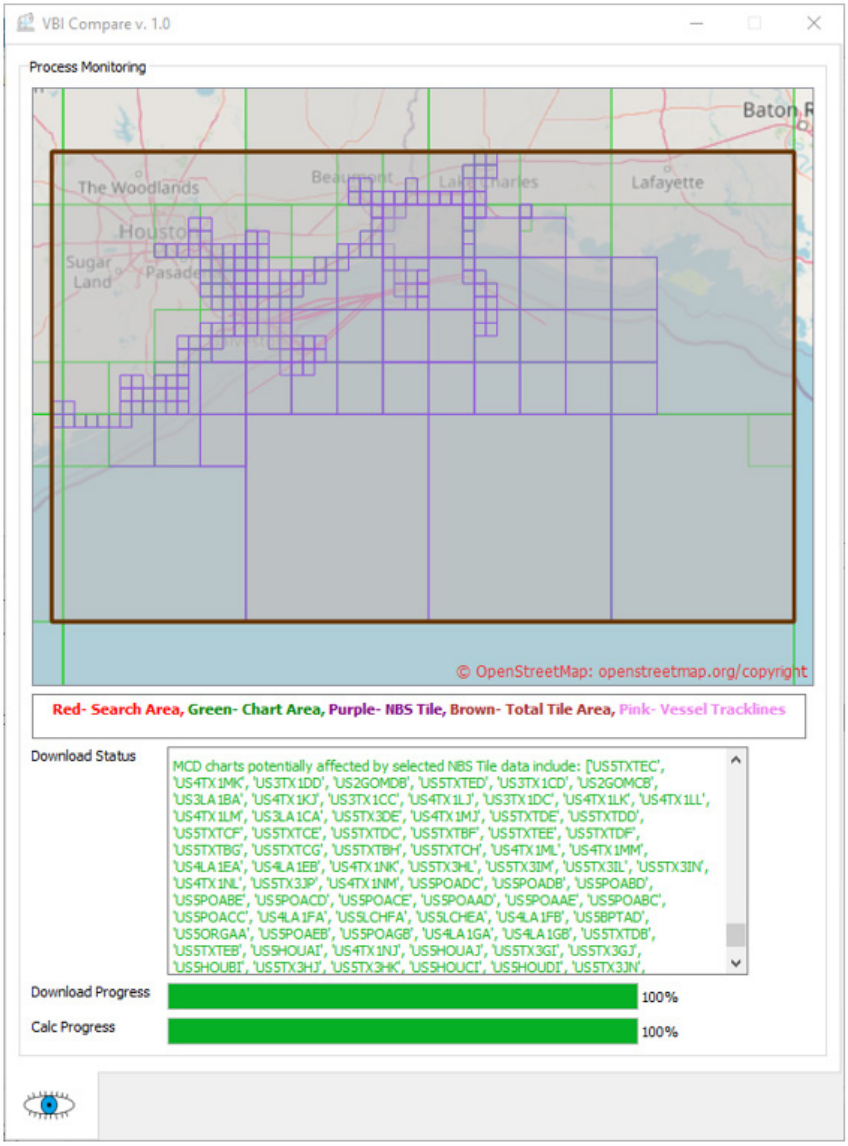


Fig. 5 Case study *VBI Compare* results.

GeoPackage file, then an intersection analysis could be executed on the GeoPackage by both geometry and chart number removing the need to use the MCD ENC Rescheme API.

7 Conclusion

VBI Compare makes significant contributions toward expanding the use of VBI by HOs for authoritative or monitoring purposes. This case study showed that rapid discovery of colocated authoritative and VBI data sets is possible using a semi-automated programmatic method. Not only can data sets be discovered in any geographic area where authoritative and VBI data sets exist, but they can be collected and managed rapidly. Additionally, by being open- source, *VBI Compare* can be adapted to the needs of the user allowing for different data sources or search criteria in the future. Furthermore, its design as a desktop application allows it to be integrated into existing hydrographic tool suites for ease of dissemination.

It was shown in this case study that consistent results given the same input were achieved, ensuring that *VBI Compare* could be used in further testing and development of VBI reputation and data uncertainty calculation algorithms. Its robust operation, simple interface, and transportability make *VBI Compare*, in conjunction with the VBI reputation and uncertainty calculation algorithm (Calder, 2021), a viable alternative to manually discovering, acquiring, and managing VBI data and calculating VBI reputation and uncertainty.

Acknowledgements

This research was supported by NOAA grant NA20NOS4000196, and significantly benefited from the comments of the peer reviewers. The support of the Center for Coastal and Ocean Mapping, Office of Coast Survey, NOAA National Bathymetric Source Team, and Data Centre for Digital Bathymetry is also gratefully acknowledged.

References

Amazon (2023). *Amazon S3 – Object storage built to retrieve any amount of data from anywhere*. Amazon Web Services, Inc. https://aws.amazon.com/s3/ (accessed 29 March 2023).

Calder, B. (2021). Estimating Observer and Data Reputation in Mariner Volunteered Bathymetry. *The International Hydrographic Review, 25*, pp. 77–96.

EMODnet (2024). *European Marine Observation and Data Network (EMODnet)*. European Commission, European Union. https://emodnet.ec.europa.eu/en (accessed 20 July 2024).

GeoJSON (2016). *The GeoJSON Format*. GeoJSON Working Group, Internet Engineering Task Force (IETF). https://datatracker.ietf.org/doc/html/rfc7946 (accessed 12 October2024).

HydrOffice (2022). HydrOffice – A Research Framework for Ocean Mapping. HydrOffice team. https://www.hydroffice.org/ (accessed 16 December 2022).

DCDB (2022). *csb (MapServer)*. IHO Data Centre for Digital Bathymetry. National Centers for Environmental Information, National Oceanic and Atmospheric Administration, USA. https://gis.ngdc.noaa.gov/arcgis/rest/services/csb/MapServer (accessed 19 December 2022).

IHO (2022a). *Guidance to crowdsourced bathymetry* (3rd ed.). IHO Publication B-12, International Hydrographic Organization, Monaco. https://iho.int/uploads/user/pubs/bathy/B_12_CSB-Guidance_Document-Edition_3.0.0_Final.pdf (accessed 16 December 2022).

IHO (2022b). *Universal Hydrographic Data Model* (5th ed.). International Hydrographic Organization, Monaco. https://iho.int/uploads/user/pubs/standards/s-100/S-100_5.0.0_Final_Clean_Web.pdf (accessed 16 December 2022).

Jencks, J. and Chappell, A. (2018). Working Together to Map the Gaps. *Hydro International, September*, p. 11.

Klemm, A. R. and Krabiel, T. (2023). *From Crowd to Chart: Methods and Applications of Crowdsourced Bathymetry in Support of Safe Navigation*. https://github.com/anthonyklemm/Crowdsourced_Bathy_Processing/blob/main/Klemm_CSB_USHYDRO23.pdf (accessed 6 April 2023).

NGA (2022). *World Geodetic System 1984* (WGS 84). Office of Geomatics, National Geospatial-Intelligence Agency, USA. https://earth-info.nga.mil/index.php?dir=wgs84&action=wgs84 (accessed 16 December 2022).

NONNA (2022). *Canadian Hydrographic Service Non-Navigational (NONNA) Bathymetric Data*. Canadian Hydrographic Service, Canada. https://open.canada.ca/data/en/dataset/d3881c4c-650d-4070-bf9b-1e00aabf0a1d (accessed 5 April 2023).

OCS (2022a). *Introduction to Pydro*. National Oceanic and Atmospheric Administration, USA. https://svn.pydro.noaa.gov/Docs/html/Pydro/universe_overview.html (accessed 16 December 2022).

OCS (2022b). *MarineChart_Services/Status_New_NOAA_ENCs (MapServer)*. National Oceanic and Atmospheric Administration, USA. https://gis.charttools.noaa.gov/arcgis/rest/services/MarineChart_Services/Status_New_NOAA_ENCs/MapServer (accessed 19 December 2022).

OCS (2023). *nowCoast*. National Oceanic and Atmospheric Administration, USA. https://nowcoast.noaa.gov/ (accessed 8 May 2023).

OCS (2024). *National Bathymetric Source*. National Oceanic and Atmospheric Administration, USA. https://www.nauticalcharts.noaa.gov/learn/nbs.html (accessed 20 July 2024).

OGC (2019). *OGC GeoTIFF standard*. Open Geospatial Consortium. http://docs.opengeospatial.org/is/19-008r4/19-008r4.html (acessed 16 December 2022).

OGC (2021). *OGC GeoPackage Encoding Standard*. Open Geospatial Consortium. https://www.geopackage.org/spec130/ (accessed 16 December 2022).

Pointstore-API (2024). *Crowdsourced Bathymetry Pointstore API*. National Centers for Environmental Information, National Oceanic and Atmospheric Administration, USA. https://github.com/CI-CMG/pointstore-api-docs/blob/main/pointstore_api.md (accessed 19 July 2024).

Safranovich, Y. (2005). *Common Format and MIME for CSV Files*. The Internet Society, Seabed 2030 Project, 2024, Seabed 2030 announces latest progress on World Hydrography Day. https://seabed2030.org/2024/06/21/seabed-2030-announces-latest-progress-on-world-hydrography-day/ (accessed 20 July 2024).

https://doi.org/10.58440/ihr-30-2-a14

Appendix 1: Query settings

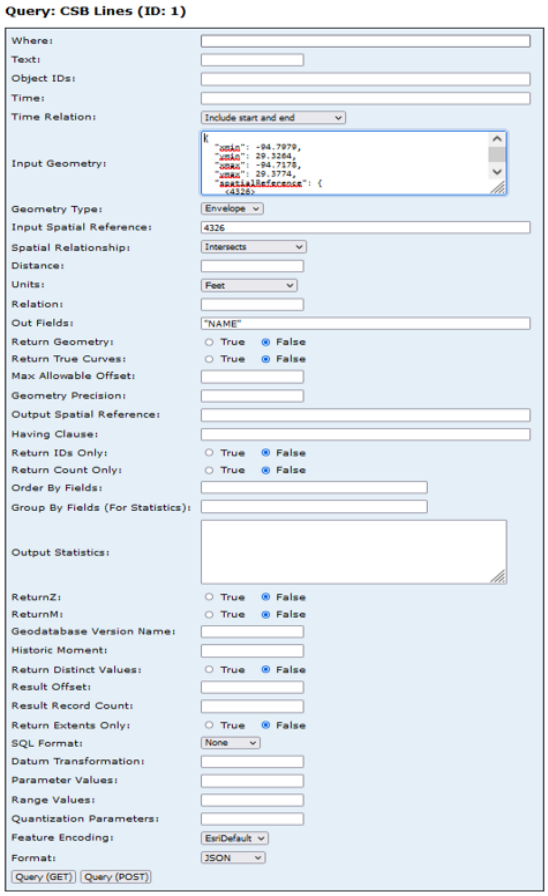


Fig. 6 Case study *VBI Compare* results.

Table 1 Case study CSB ArcQGIS API query settings.

Setting	User Input
Time Relation	Include start and end
Input Geometry	{ “xmin”: -94.7979, “ymin”: 29.3264, “xmax”: -94.7178, “ymax”: 29.3774, “spatialReference”: { <4326> } }
Geometry Type	Envelope
Input Spatial Reference	4326
Spatial Relationship	Intersects
Units	Feet
Out Fields	"NAME"
Return Geometry	False
Return True Curves	False
Return IDs Only	False
Return Count Only	False
ReturnZ	False
Return Count Only	False
Return Distinct Values	False
SQL Format	None
Feature Encoding	EsriDefault
Format	JSON

Fig. 7 Case study *VBI Compare* parameters.

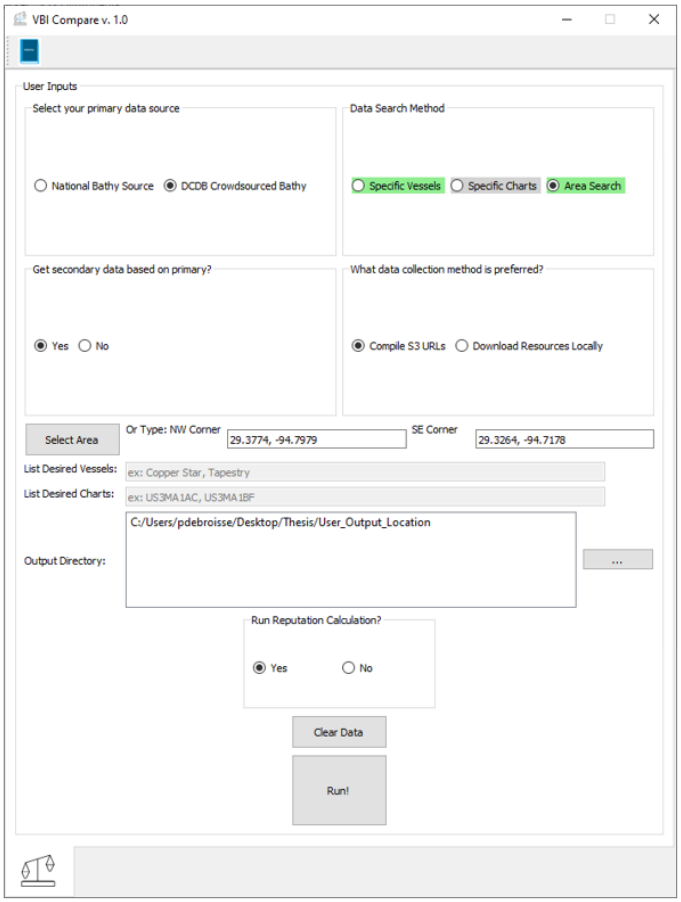


Table 2 Case study *VBI Compare* parameters.

Setting	User Input
Primary Data Source	DCDB Crowdsourced Bathy
Data Search Method	Area Search
Get Secondary Data Based on Primary?	Yes
Data Collection Method	Compile S3 URLs
NW Corner	29.3774, -94.7979
SE Corner	29.3264, -94.7178
Output Directory	C:/Users/***
Run Reputation Calculation	Yes

https://doi.org/10.58440/ihr-30-2-a14

Authors' biographies

LCDR Patrick Debroisse, CMH(A) has served in the NOAA Commissioned Officer Corps since 2014 and is currently the Operations Officer of the NOAA Ship Ferdinand R. Hassler. He earned his M.S. in Ocean Engineering: Ocean Mapping from the University of New Hampshire completing his thesis supporting programmatic solutions for Volunteered Bathymetric Information quality assessment in 2023. He also earned the FIG/ IHO Category A certification and became a THSOA/ NSPS Certified Master Hydrographer while studying at the University. In addition, he holds a degree in Mechanical Engineering from Norwich University (Vermont, USA).



Patrick Debroisse

Dr. Miles is trained as a software engineer and physical geographer. His research has focused on ecohydrology modeling in urbanized and forested watersheds; this work included developing tools to support reproducible ingest and transformation geospatial data, as well as model calibration and uncertainty estimation using HPC resources. He has current and prior experience in software engineering, Internet of Things, environmental monitoring, and geospatial data storage and analysis. Dr. Miles is currently focused on translating research codes and algorithms into deployable software artifacts supported by robust documentation, automated testing, continuous integration, observability, fault tolerance, and scalability.



Brian Miles

https://doi.org/10.58440/ihr-30-2-a14

PEER-REVIEWD ARTICLE

Denmark's Depth Model version 2.0 – Improved compilation of bathymetric data within the Danish waters

Authors

Giuseppe Masetti[1,2], Philip Sigaard Granding[1], Kasper Langdahl[1], Lasse Mondberg Schwenger[1] and Kristian Villadsen Kristmar[1]

Abstract

Denmark's Depth Model version 2.0 (DDM v2.0) is the latest iteration of a Digital Bathymetric Model (DBM) for Danish waters, offering a grid resolution of 50 meters. The compilation integrates hundreds of survey datasets, including both modern and historical sources, as well as satellite-derived and crowdsourced bathymetric data. The model is referenced to Mean Sea Level (MSL) datum and – due to the adopted compilation process – is not designed for safety of navigation. DDM v2.0 is accessible through the Danish Geodata Agency's website and constitutes a significant contribution to the European Marine Observation and Data Network (EMODnet) Bathymetry initiative.

Keywords

digital bathymetric model · ocean mapping · open geospatial data

Resumé

Le modèle de profondeur du Danemark version 2.0 (DDM v2.0) est la dernière itération d'un modèle bathymétrique numérique (DBM) pour les eaux danoises, offrant une résolution de grille de 50 mètres. La compilation intègre des centaines de lots de données de levés, y compris des sources modernes et historiques, ainsi que des données bathymétriques dérivées par satellite et des données de bathymétrie participative. Le modèle est référencé au niveau moyen de la mer (MSL) et - en raison du processus de compilation adopté - n'est pas conçu pour la sécurité de la navigation. Le DDM v2.0 est accessible sur le site web de l'Agence danoise des géodonnées et constitue une contribution significative à l'initiative Bathymétrie du Réseau européen d'observation et de données du milieu marin (EMODnet).

✉ Giuseppe Masetti · gimas@gst.dk

[1] Danish Geodata Agency, Danish Hydrographic Office, 9400 Nørresundby, Denmark

[2] University of New Hampshire, Center for Coastal and Ocean Mapping and NOAA-UNH Joint Hydrographic Center, Durham, NH 03824, U.S.A.

https://doi.org/10.58440/ihr-30-2-a17

Resumen

El Modelo de Profundidad de Dinamarca versión 2.0 (DDM v2.0) es la última iteración de un Modelo Batimétrico Digital (DBM) para aguas danesas, que ofrece una resolución de cuadrícula de 50 metros. La compilación integra cientos de conjuntos de datos de levantamientos, tanto de fuentes modernas como históricas, así como datos batimétricos obtenidos por satélite y por batimetría participativa. El modelo está referenciado al Nivel Medio del Mar (MSL) y - debido al proceso de compilación adoptado - no está diseñado para la seguridad de la navegación. Se puede acceder al DDM v2.0 de la página web de la Agencia Danesa de Geodatos, y constituye una contribución significativa a la iniciativa de batimetría de la Red Europea de Observación y Datos Marinos (EMODnet).

1 Introduction

Ocean bathymetry, the study and mapping of the seafloor topography, is a fundamental aspect of marine science, underpinning a wide range of scientific, environmental, and navigational applications (Brown et al., 2012; Jakobsson & Mayer, 2022; Lecours et al., 2016). Ocean bathymetry is typically represented using a specialized form of a Digital Terrain Model (DTM), known as a Digital Bathymetric Model (DBM). The DBM is commonly structured as a regular grid, where each grid cell is assigned a specific depth value corresponding to the seafloor elevation or depth below sea level (Jakobsson et al., 2019). This grid-based representation allows for the systematic analysis and visualization of underwater features, facilitating accurate mapping and modeling of marine environments (Erikstad et al., 2013; Lubczonek & Zaniewicz, 2023; Sowers et al., 2024).

The analysis of the available global and regional DBMs reveals significant gaps and uncertainties, challenging the notion that the ocean floor is fully understood (Mayer et al., 2018; Ware et al., 2023). The General Bathymetric Chart of the Oceans (GEBCO) is a widely recognized global DBM with a nominal resolution of 15 arc seconds, which translates to approximately 500 meters at the equator (GEBCO Bathymetric Compilation Group, 2024). However, it is important to note that GEBCO lacks direct depth measurements for approximately 75 % of its global coverage (McMichael-Phillips et al., 2024). This issue of incomplete data is not unique to GEBCO; similar challenges are observed in other global bathymetric compilations such as the Global Multi-Resolution Topography (GMRT; Drennon et al., 2023). Additionally, regional DBMs, including the International Bathymetric Chart of the Arctic Ocean (IBCAO; Jakobsson et al., 2020) and the European Marine Observation and Data Network (EMODnet) Bathymetry, which covers all European sea regions (Schaap & Schmitt, 2020), also face analogous limitations regarding data coverage and resolution. Regional and global DBMs predominantly depend on interpolation techniques and altimetry-derived datasets (Weatherall et al., 2015). Although altimetry-derived bathymetry is widely employed in global and regional bathymetric compilations, its utility is limited to providing only approximate representations of the seafloor. This limitation is primarily due to the challenges associated with upward continuation in deep-water regions and the inherent variability in sediment thickness and crustal structures along shallow continental margins (Andersen et al., 2010; Legeais et al., 2018; Sandwell et al., 2003). Consequently, the depth estimates derived from altimetry suffer from significant inaccuracies, often on the order of several hundred meters or more, and the spatial resolution is insufficient for resolving seafloor features smaller than a few kilometers in scale (Mayer et al., 2021).

Ocean mapping is inherently challenging due to the high attenuation of electromagnetic waves in water, limiting the effectiveness of sensors commonly used for land topography, such as those using multispectral images, lidar, and radar (De Giosa et al., 2019; Dierssen & Theberge, 2020; Parrish et al., 2019; Westfeld et al., 2017). Instead, ocean mapping relies heavily on acoustical remote sensing methods like Single-Beam Echo Sounders (SBES) and Multi-Beam Echo Sounders (MBES) (Mayer et al., 2018). Historical depth measurements, often derived from lead-lines, are sparse and cover minimal seafloor areas, while SBES provides denser measurements over larger area. MBES offers the highest density and resolution, providing a more accurate seafloor representation (Lebrec et al., 2021; Lurton, 2010). However, MBES is expensive and cumbersome, especially in deep waters, and is therefore less commonly used (Hughes Clarke, 2018a, 2018b). Mapping shallow waters also presents difficulties due to the coastal environment's complexity (Kjeldsen et al., 2017; Lucieer et al., 2018; Masetti et al., 2018a). Recent technological advancements, particularly in the development of uncrewed surface vessels (USVs), present a promising avenue to mitigate these limitations by potentially reducing operational costs and enhancing the efficiency of ocean mapping and exploration (Mayer, 2023). However, the significant costs, extensive time requirements, and inherent challenges in acquiring high-resolution bathymetric data have led to much of the ocean remaining inadequately mapped or even unexplored, despite extensive efforts over the years.

Bathymetric data provides critical insights into the

https://doi.org/10.58440/ihr-30-2-a17

structure and dynamics of ocean basins, continental margins, and the broader underwater landscape, playing a pivotal role in understanding geological processes, ocean circulation, and marine ecosystems (Mayer, 2022; Morrow et al., 2023; O'Toole et al., 2022; Sowers et al., 2020). DBMs are extensively utilized to precisely delineate critical boundary conditions essential for geophysical, biological, and oceanographic systems (Bogumil et al., 2024; Haigh et al., 2023; Weatherall et al., 2015). Moreover, DBM-based analyses are integral to a variety of environmental and geological studies, including geohazard assessments and the geological characterization of seafloor morphologies (Koop et al., 2021; Masetti et al., 2018b; Palmiotto & Loreto, 2019; Sowers et al., 2020). Detailed DBMs are crucial for delineating coastlines, which are vital for understanding storm surges and sea level changes (Dierssen & Theberge, 2020), as well as for mapping the seafloor's morphology, which plays a key role in controlling and constraining bottom currents and, consequently, global and regional heat transport (Ribergaard et al., 2004; Jakobsson & Mayer, 2022). Similarly, various aspects of marine geosciences, including seafloor characterization, sedimentary studies, and offshore engineering, rely on high-quality DBMs with comprehensive and meaningful associated metadata (Fonseca et al., 2021; Lebrec et al., 2022; Moses & Vallius, 2021). These applications increasingly demand higher resolution data to improve the accuracy and reliability of the models, as well as metadata and documentation – describing the main characteristics and limitations associated with a released DBM – that facilitate researchers in discovering the bathymetry best fitting their specific purposes (Jakobsson & Mayer, 2022; Vrdoljak, 2021).

Since early 2020, the Danish Geodata Agency has made significant efforts to organize available bathymetric datasets from Danish and Greenlandic waters into a modern geospatial data management system known as DYBDB (The term DYBDB comes from combining "dybde" – Danish for "depth" – and "DB" (short for "database"), meaning a "depth database"). This initiative includes the development of methodologies for compiling these diverse data sources into DBMs and other valuable products, such as hydrographic survey overviews (Danish Geodata Agency, 2021). This paper focuses specifically on Denmark's Depth Model version 2.0 (DDM v2.0) which represents the most recent advancement in Digital Bathymetric Modeling (DBM) for Danish territorial waters, providing a high-resolution grid with a spatial resolution of 50 meters (Masetti et al., 2022a).

One of the primary motivations for the creation of the Denmark's Depth Model (DDM) has been to enhance the bathymetric coverage within the Danish Exclusive Economic Zone (EEZ) as currently provided by the EMODnet Bathymetry (Masetti et al., 2022a). By improving the accuracy and resolution of bathymetric data in this region, the DDM aims to significantly support a wide range of environmental studies and research efforts in the North Sea and the Baltic Sea. These improvements are expected to facilitate more precise environmental monitoring, better understanding of marine ecosystems, and more effective management of marine resources. Additionally, enhanced bathymetric data will contribute to studies on coastal erosion, sediment transport, and sea level rise, providing critical insights for both scientific research and policy-making. The DDM is also poised to aid in the planning and execution of offshore engineering projects, such as wind farms and underwater pipelines, by offering more reliable seafloor characterizations, which are essential for ensuring the safety and sustainability of such developments.

This paper begins by detailing the management of the data sources, including the key components of DYBDB, before outlining the methodological and technical steps involved in the creation of DDM v2.0. A specific focus is reserved to Satellite-Derived Bathymetry (SDB) harmonization. Finally, the paper presents the content of the publicly available DBM layers and services, with the overarching goal of encouraging adoption of DDM v2.0 by researchers and other practitioners.

2 Materials and methods

2.1 Management of data sources

DYBDB is a modern hydrographic data management system developed and implemented by the Danish Hydrographic Office, part of the Danish Geodata Agency (Danish Geodata Agency, 2021). The DYBDB system integrates several automated procedures, predominantly scripted in Python, alongside task management mechanisms powered by Atlassian's Jira™ issue tracking product[1].

DYBDB incorporates three distinct types of geospatial databases, each serving a specific purpose (Fig. 1):

- Smart DB: The Survey Metadata And Raw data Tracker (Smart) geospatial database manages an extensive collection of survey metadata (e.g., collection time, used sensors and platforms, quality assessment) and tracks the integrity of the original submission, with a focus on the acquired raw data. Upon loading a dataset, the database links to the point cloud of cleaned soundings gathered during the survey.
- Grid DB: Tailored for handling dense datasets, such as those obtained from modern MBES, the

[1] https://www.atlassian.com/software/jira/ (accessed 31 August 2024).

https://doi.org/10.58440/ihr-30-2-a17

Grid database contains a subset of the cleaned soundings. These soundings are organized at a spatial resolution (5 meters as default resolution) specifically designed for nautical chart production.

- Model DB: This database stores intermediate products and final DBMs, serving as the repository for completed models ready for use in various applications.

The databases within DYBDB utilize the free and open-source PostgreSQL relational database management system (RDBMS)[2] as their backend infrastructure. PostgreSQL was chosen for its robustness, scalability, and support for complex queries, making it well-suited to handle the extensive and intricate datasets involved in hydrographic data management. To ensure the security and preservation of critical data, snapshots of the essential content within DYBDB are regularly generated using the GeoPackage format[3]. The management of all databases within DYBDB is facilitated by Teledyne CARIS' Bathy DataBASE Server™ software, a specialized tool designed to handle the storage, processing, and management of bathymetric data[4]. The Teledyne CARIS' BASE Editor™ serves as the primary Geographic Information System (GIS) client for accessing and interacting with the content stored in DYBDB. The use of these industry-standard tools aligns DYBDB with best practices in hydrographic data management, ensuring compatibility and integration with other hydrographic systems.

Since DYBDB became operational in early 2020, the Smart DB and the Grid DB have been populated with approximately 1,900 bathymetric datasets. These datasets were primarily sourced from hydrographic surveys conducted by the Danish Navy, public agencies, industry stakeholders, and academic institutions. The majority of these datasets were acquired using SBES and MBES, with the sounders typically mounted on the hull of the survey vessel or installed on a removable pole. The horizontal positioning of the soundings was predominantly achieved using Global Navigation Satellite Systems (GNSS), often enhanced with differential corrections or Real-Time Kinematic (RTK) positioning to improve accuracy. For MBES surveys, an attitude sensor was also employed to capture the dynamic movements of the survey platform, including roll, pitch, heave, and yaw. This information is crucial for accurately spatially orienting the acoustic swaths produced by the MBES, ensuring that the bathymetric data accurately represents the seafloor topography (Hughes Clarke, 2018b; Lurton, 2010). The integration of these technologies and methodologies reflects the high standards of data quality and precision required for modern hydrographic surveys, facilitating the production of reliable and detailed DBMs.

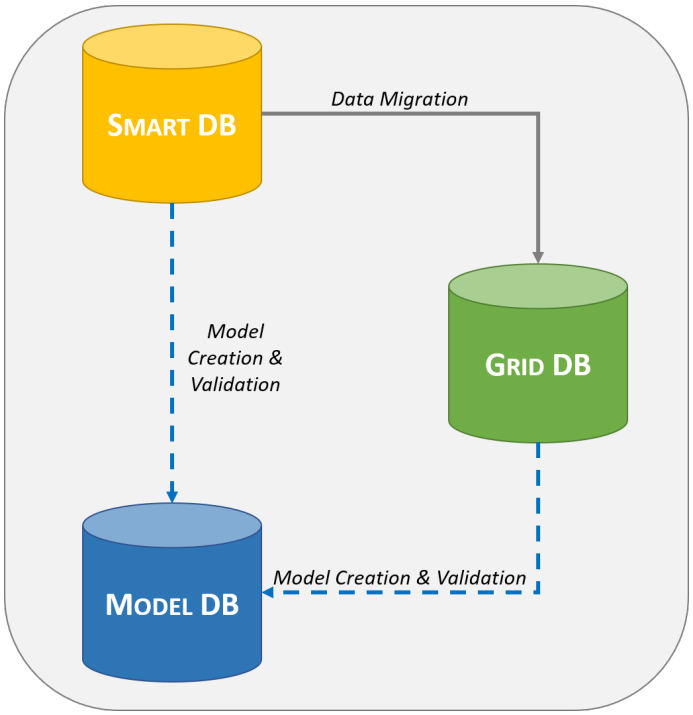


Fig. 1 The three types of DYBDB databases (Smart DB, Grid DB, and Model DB) and their interactions during key processes. The 'Data Migration' process (connectors shown in full grey) uploads depths to Grid DB based on the information stored in the Smart DB. The 'Model Creation & Validation' process (in dashed blue) combines soundings stored in Grid DB by retrieving the metadata information from the Smart DB. Once created, a semi-automated validation process is initiated which may require access to the point cloud of soundings at full resolution.

2.2 Compilation Approach

The latest EMODnet Bathymetry, released in November 2022, features a grid resolution of 1/16 arc minute, equivalent to approximately 115 meters (EMODnet Bathymetry Consortium, 2020). To enhance the resolution of publicly available bathymetric data within Danish waters, the Denmark's Depth Model (DDM) was designed with a target grid resolution of 50 meters. This 50-meter resolution was determined to be an optimal balance, offering a reasonable tradeoff between areas with extensive high-resolution surveys, such as those in the Kattegat region, and regions where only sparse historical soundings are available, such as large portions of the North Sea (Masetti et al., 2022a). The selected resolution ensures that the DDM can provide more detailed and accurate representations of the seafloor while still accommodating the variability in data density across different regions. This approach enhances the utility of the DDM for a range of applications, from detailed coastal studies to broader regional analyses.

During the model creation and validation processes, DYBDB facilitates access to relevant

[2] https://www.postgresql.org/ (accessed 31 August 2024).

[3] https://www.geopackage.org/ (accessed 31 August 2024).

[4] https://www.teledynecaris.com/en/products/bathy-database/ (accessed 31 August 2024).

datasets and associated metadata, particularly from the Smart DB and Grid DB. Additionally, the Model database provides storage for intermediate products and the finalized Digital Bathymetric Models (DBMs). This system ensures a seamless workflow from data access to the final model output (Fig. 1).

The overall compilation process consists of the following key steps (Fig. 2):

- Creation/update of the model tiles. The source datasets are retrieved from the Grid DB and related metadata from the Smart DB. The sources are gridded adopting a grid resolution of 50 meters and a tiling scheme with tile area of 1° of latitude by 1° of longitude (Masetti et al., 2022a). The tiles covered by at least one dataset are generated and stored in the Model DB. The bathymetric values are calculated as *representative average depth*, that is an average of all water depths allocated from the relevant input source to a given grid cell. When multiple datasets overlap, the relevant input source is selected based on the dataset coverage polygon and using a priority index based on time of data collection, assessed data quality and dataset type. Specifically, MBES and ALB gets higher priority than DIGI, SBES, CSB and Historical. This step is periodically executed to update the tiles in case of new datasets.
- Combine all the model tiles. All the populated DDM tiles stored in Model DB are combined into a continuous preliminary DBM.
- Merge with SDB and historical data. The DBM calculated in the previous step is extended by combining it with SDB – stored as grids – as well as historical soundings available on published nautical products.
- Create TIN and interpolate using the 'Natural Neighbors' algorithm. To fill areas with sparse soundings, an interpolated DBM is generated by first creating a Triangulated Irregular Network (TIN) from the extended DBM generated in the previous step, then using the TIN to interpolate based on the 'Natural Neighbors' (NN) algorithm (Lee, 1991; Watson, 1999).
- Extract coverage from coastline to EEZ. The interpolated DBM is updated to limit its coverage from the coastline (generalized at 1:100,000 scale) to EEZ. The resulting DBM is uploaded to the Model DB.
- Quality control on the resulting model. The quality of the DBM resulting from the previous steps is extensively assessed by a team of reviewers. During this iterative process, the reviewers have access to all the direct and indirect DBM sources through Smart DB, Grid DB, and historical data. In case of issues, adjustments to the model may require the (partial or total) re-execution of the previous steps. Only when the outcomes of the quality control are satisfactory, the DBM is finalized.

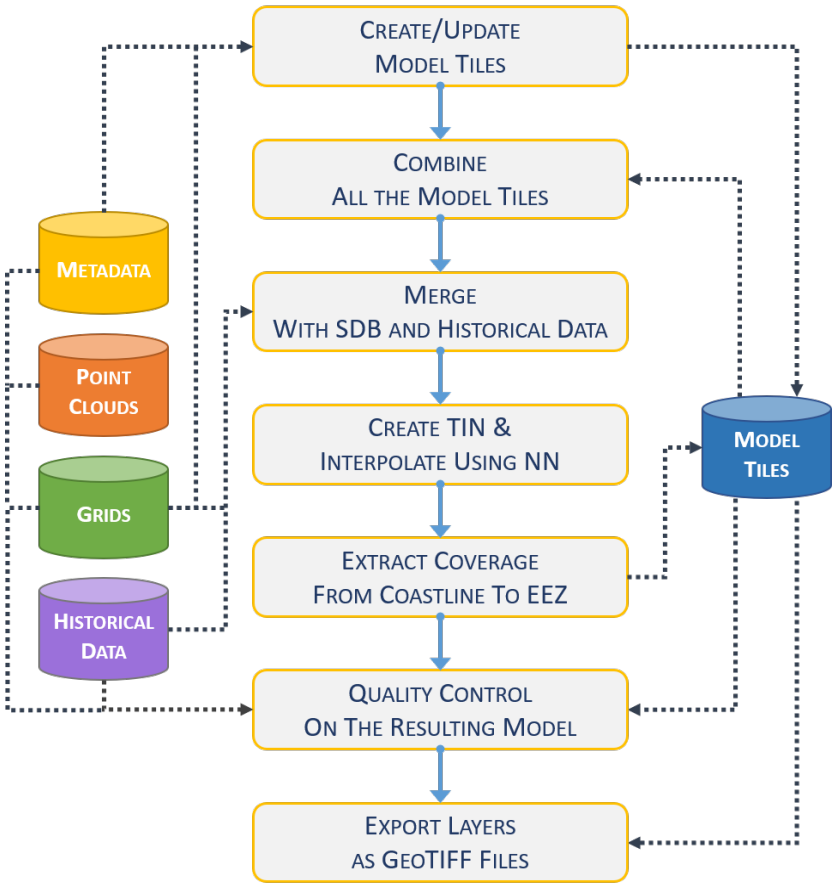


Fig. 2 Workflow showing the main steps of the compilation approach (connected using black arrows). The access to DYBDB databases and the retrieval of SDB and historical data are shown using dotted connectors. Point clouds, available through Smart DB, are used for low density datasets (e.g., SBES) and quality control of the resulting model. Historical data are currently stored outside DYBDB. Acronyms used in the workflow: EEZ for Exclusive Economic Zone, NN for the Natural Neighbor algorithm, SDB for Satellite-Derived Bathymetry and TIN for Triangulated Irregular Network.

2.3 SDB harmonization

The incorporation of Satellite-Derived Bathymetry (SDB) represents a significant enhancement in the development of DDM v2.0. The SDB dataset was generated by EOMAP GmbH & Co. KG (hereon referred to as EOMAP), a specialized remote sensing company[5], utilizing multispectral imagery acquired from the ESA Sentinel-2 A & B satellites. The entire dataset comprises 226 Sentinel-2 images, meticulously covering the coastal and shallow waters surrounding Denmark. For efficient processing, the dataset was divided into 17 tiles, each corresponding to the Sentinel-2 grid that spans Denmark (ESA, 2015). EOMAP employed the Radiative Transfer Equation (RTE) inversion method, also referred to as the physics-based method (Hartmann et al., 2022), to derive bathymetric data from the multispectral imagery.

Integrating SDB into DDM v2.0 necessitated the

[5] https://www.eomap.com/ (accessed 31 August 2024).

https://doi.org/10.58440/ihr-30-2-a17

development of a harmonization algorithm designed to minimize the introduction of depth artifacts, which could arise from inconsistencies between SDB and other established bathymetric data sources. As an initial step in this integration process, the SDB data was gridded into an SDB Digital Bathymetric Model (SDB DBM) with a spatial resolution of 50 meters, matching the resolution and extent of the final harmonized DBM. Depth values exceeding 6 meters were excluded from this dataset, a threshold empirically determined based on expert analysis. For each populated cell within the SDB DBM, the corresponding SDB depth value (d_{SDB}) was subjected to a rigorous evaluation process to determine its inclusion in the harmonized DBM. This evaluation was specifically applied in cases where no co-located "primary" depth data (d_{PRI}) – obtained from sources such as MBES, SBES, and Airborne Lidar Bathymetry (ALB) – was available. By selectively incorporating SDB data in the absence of higher-priority depth sources, the harmonization algorithm ensured the integrity and accuracy of the final depth model.

The inclusion of the d_{SDB} into the harmonized DBM is contingent upon passing two rigorous validation checks:

1. Area Kernel Check: This check assesses the consistency of d_{SDB} with d_{PRI} within a larger spatial context. Specifically, it evaluates d_{PRI} cells within an 8-node radius surrounding the d_{SDB} under consideration. The minimum $d_{\mathrm{PRI}}^{\min}$ and maximum $d_{\mathrm{PRI}}^{\max}$ depths within this area are identified. For the d_{SDB} to pass the Area Kernel Check, it must satisfy the following condition:

$$0.95 \times d_{\mathrm{PRI}}^{\min} \leq d_{\mathrm{SDB}} \leq 1.05 \times d_{\mathrm{PRI}}^{\max} \quad (1)$$

   This criterion ensures that the d_{SDB} value is within an acceptable range of variation relative to the primary depth data, thereby minimizing the risk of introducing significant depth discrepancies.
2. Neighbor Kernel Check: This check evaluates the immediate surroundings of d_{SDB}, specifically within a 2-node radius, to determine whether neighboring d_{PRI} cells are populated with primary depth data. The d_{SDB} passes the Neighbor Kernel Check only if all the evaluated d_{PRI} cells within this radius are unpopulated. This ensures that the d_{SDB} is utilized exclusively in areas where primary depth data is unavailable.

These two checks together provide a robust framework for integrating SDB data into the harmonized DBM, ensuring that SDB is incorporated only when it is consistent with or supplements existing primary depth data, thus maintaining the accuracy and reliability of the final model.

2.4 Reduction to a common vertical reference

One of the significant advancements in DDM v2.0 is the reduction of all depth values to a common vertical reference, specifically Mean Sea Level (MSL). This transformation process involved converting datasets originally referenced to various vertical datums, including the Dansk Normal Nul (DNN), Dansk Vertikal Reference 1990 (DVR90), Lowest Astronomical Tide (LAT), and Mean Low Water Springs (MLWS). The Danish Agency for Climate Data (KDS) has published models for DVR90, LAT and MSL, which were utilized as accurate realizations of these respective datums. For the DNN and MLWS datums, which lacked direct transformation models, *ad-hoc* methodologies were developed.

The DNN is a discontinued vertical datum that was originally established on land using specific reference points. To approximate the transformation of DNN to MSL, an assumption was made that the original surveys were conducted relative to the nearest available reference points. This approximation was informed by the *Vejledning om højdesystemet*, an official publication that provides average differences between DNN and DVR90 across various municipalities in Denmark (Jarmbæk, 2005). This information, combined with the existing transformation model from DVR90 to MSL, enabled the creation of a Voronoi-based approximation model for the DNN to MSL transformation. A similar methodological approach was employed to derive a transformation from MLWS to MSL. This involved utilizing tide gauge data provided by the Danish Meteorological Institute (DMI) to create a model that accurately reflects the relationship between MLWS and MSL.

These transformation processes ensured that all depth data within DDM v2.0 are consistently referenced to MSL, thereby improving the interoperability and accuracy of the depth model across different datasets and geographical regions.

2.5 Model products

Once the creation and validation processes are completed (following the steps described in the *Compilation Approach* section and summarized in Fig. 2), the layers listed in Table 1 are exported from the finalized DBM for public release.

The two auxiliary layers, *ddm_50m.kilde* and *ddm_50m.aar*, are utilized to detail the type and collection date of the source datasets used in estimating the DDM depths. DDM v2.0 layers listed in Table 1 are also made available as Open Geospatial Consortium (OGC) services (i.e., Web Map Service; Web Coverage Service). The original source datasets themselves are not distributed with the DDM. This approach aligns with the methodology adopted by EMODnet Bathymetry, which also does not distribute the original source data but instead provides metadata services when available (Thierry et al., 2019).

The horizontal datum of the model is a Lambert Conformal Conic (LCC) projection on the ETRS89 ellipsoid (EPSG:3034). The vertical datum is Mean Sea Level (MSL) as defined by KDS' DKMSL(2022) (EPSG:10547). The output format for the exported layers is GeoTIFF (Ritter & Ruth, 1997). A *readme* document (in PDF format) with a succinct description

Table 1 Layers extracted from the finalized DBM for public release.

Layer name (in Danish)	Description
ddm_50m.dybde	The primary layer containing the depth values (in meters; Fig. 3).
ddm_50m.kilde	An auxiliary layer providing the source of the depth data for each grid cell (Fig. 7). The layer uses the following convention: • *DIGI*: The source is a digitized survey fairsheet. • *SB*: The source depths were collected using a SBES. • *MB*: The source depths were collected using a MBES. • *ALB*: The source depths were collected using airborne lidar bathymetry (ALB) • *SDB*: The source depths were collected using satellite derived bathymetry (SDB) • *CSB*: The source depths were collected using crowdsourced bathymetry (CSB) • *Historical*: Historical depth values (e.g., leadline). • *Interpolated*: Depth interpolation was applied.
ddm_50m.aar	An auxiliary layer providing the year at which the data collection has ended (except for SDB, *Historical* and *Interpolated* dataset types).

on DDM v2.0 (i.e., how the model was generated and how to interpret the provided layers) is part of the compressed archive containing the DDM release. A contributors document (also in PDF format) listing data contributors is also made available.

3 Results

The official release of DDM v2.0 occurred on 28th of August, 2024. The compressed archive, which contains all materials detailed in the *Model Products* section, along with information for accessing the OGC (Open Geospatial Consortium) services, is available through the Danish Geodata Agency's website[6]. This release marks a significant update, providing enhanced resources for geospatial analysis and ensuring broader accessibility to the DDM's data and services.

The bathymetric layer (depicted in Fig. 3) encompasses a surveyed area of 98,045 square kilometers. The largest majority (~97.2 %) of the depth values are under 100 meters; they present a skewed bimodal distribution (peaks at 15–20 meters and 40–45 meters) with a median value of ~32.4 meter (Fig. 4).

DDM v2.0 comprises a DBM in which over 29 % of the depth cells are derived directly from measured depth values, with the remaining cells interpolated from these measurements to estimate depth values in areas lacking direct data (Fig. 5, pane b). The interpolated regions of DDM v2.0 can be derived by selecting the cells marked with the "Interpolated" value in the *ddm_50m.kilde* layer (Table 1). The primary source of these measured depth values is multibeam echosounder (MBES) surveys, as indicated by the *ddm_50m.kilde* auxiliary layer (Fig. 6, pane b). The panes a in Fig. 5 and Fig. 6 are shown for comparison with the data content of the first version of DDM.

Based on the *ddm_50m.aar* auxiliary layers, the first MBES-type contribution to the DDM occurred in 1993, with subsequent years showing a marked increase in the spatial coverage of MBES-derived bathymetry (Fig. 8). This temporal and spatial variability in data density, influenced by the varying types and years of data sources, has led to regions within the DDM where bathymetric detail is high due to dense MBES survey data (e.g., the Great Belt area). In contrast, other regions (e.g., the upmost western part of the North Sea) exhibit smoothed bathymetry as a result of interpolation processes applied to estimate depths in areas with sparse soundings.

4 Discussion

DDM v2.0 represents the second publicly released Digital Bathymetric Model (DBM) covering Danish waters, characterized by a grid resolution of 50 meters. This paper details the compilation process employed in the creation of the DDM v2.0 (Fig. 2), as well as the methods of its distribution through publicly accessible products. These aspects are particularly relevant for hydrographic offices and other national agencies that are committed to advancing research and modeling initiatives, considering the diverse range of applications for which DBMs are utilized. It is important to note that DDM v2.0 is generated using an averaging methodology, making it unsuitable for safety of navigation purposes. Nevertheless, several key steps within the described compilation workflow have been adapted for use in forthcoming projects aimed at developing high-resolution navigation surface and related S-100 products. The adoption of the navigation surface concept will facilitate the efficient production of nautical charts, as outlined by Smith (2003).

DDM v2.0 is constructed from hundreds of bathymetric survey datasets and historical sources within Denmark's Exclusive Economic Zone (EEZ). However, less than 23 % of the DDM's coverage is derived from surveys conducted using modern SBES and

[6] https://eng.gst.dk/danish-hydrographic-office/denmark-depth-model/ (accessed 31 August 2024).

https://doi.org/10.58440/ihr-30-2-a17

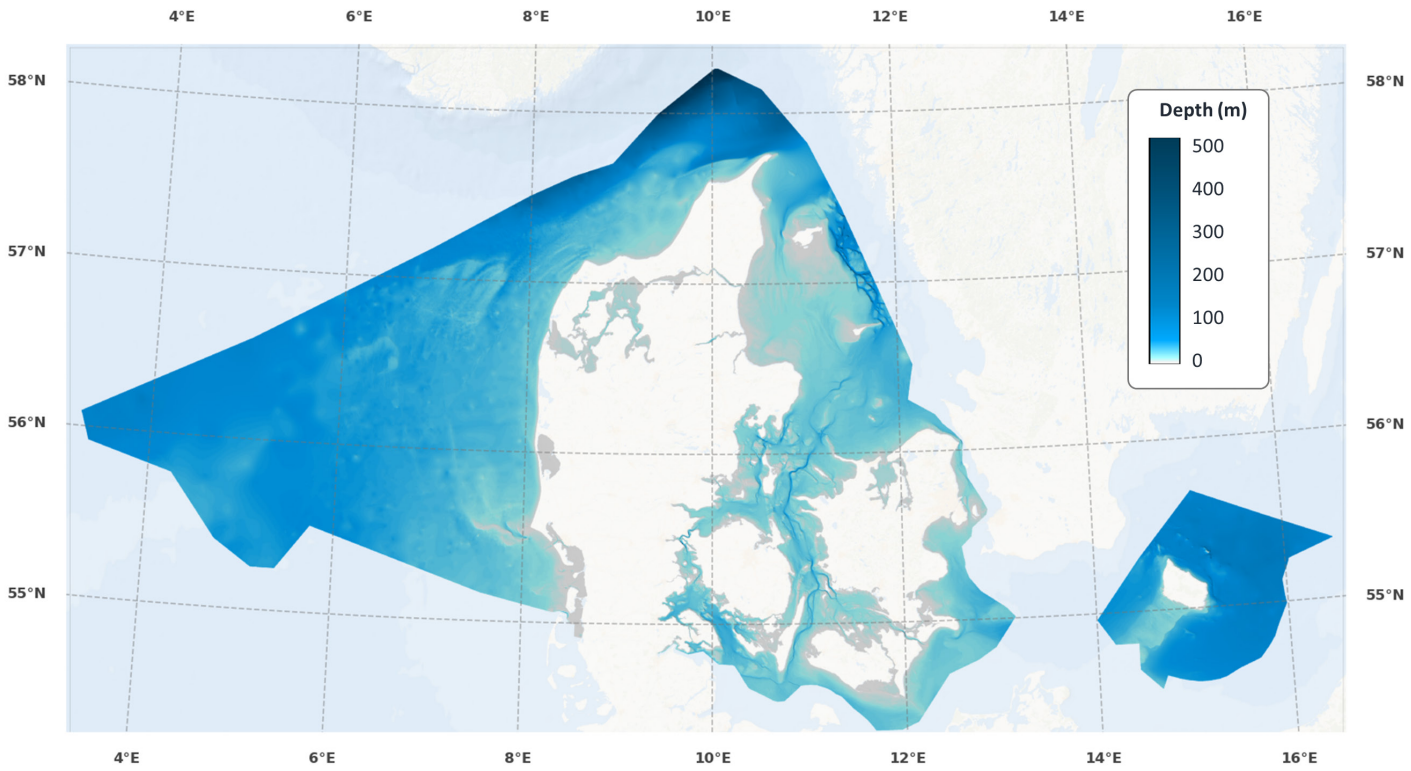


Fig. 3 The bathymetric layer (i.e., '*dybde*') of Denmark's Depth Model version 2.0. The depth values in the color legend are in meters. The ESRI Ocean Basemap is shown in the back-ground (Sources: ESRI, GEBCO, NOAA, National Geographic, DeLorme, HERE, Geonames.org, and other contributors).

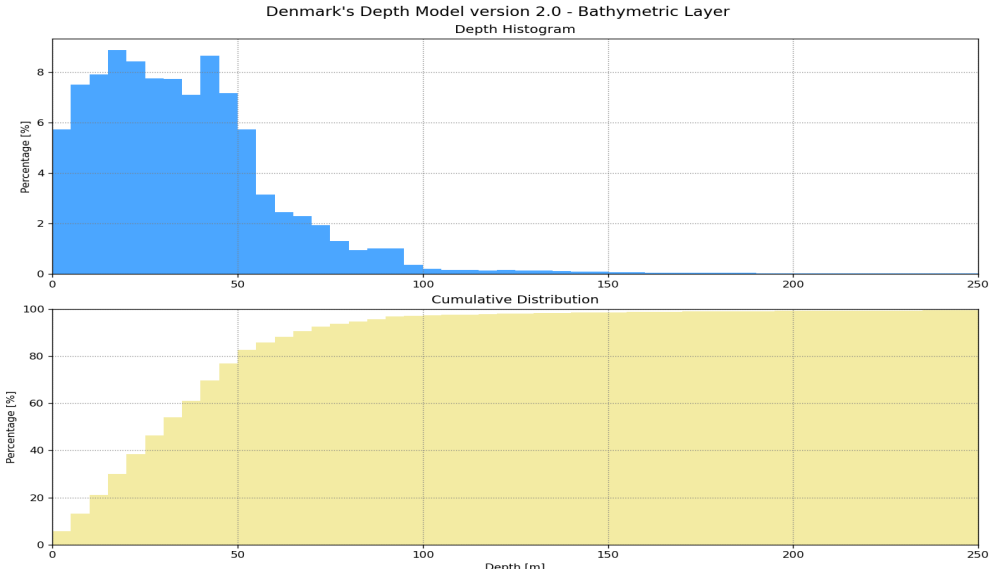


Fig. 4 Depth histogram (upper pane) and related cumulative distribution (lower pane) for the bathymetric layer of Denmark's Depth Model version 2.0. For better visualization, an upper limit of 250 meters has been applied to the axis of the depth values.

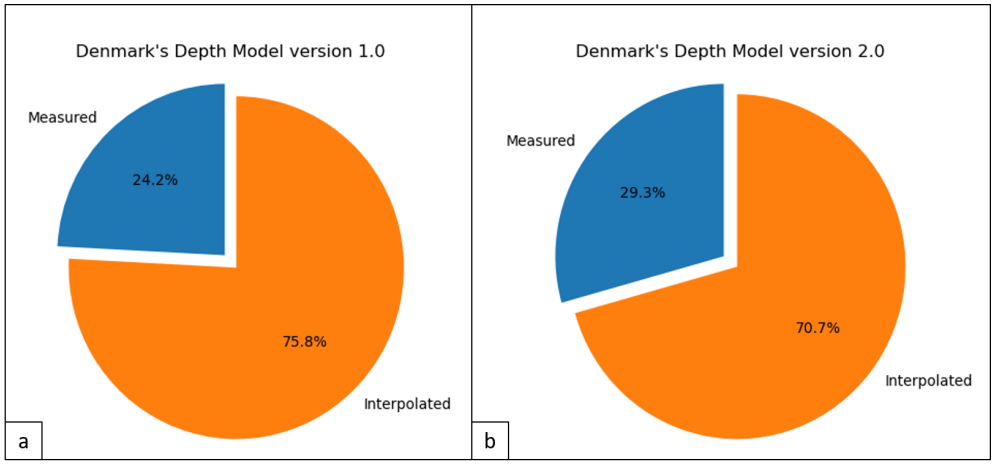


Fig. 5 The pie plots show the percentages of model cells derived from measured depth values (in blue) and interpolated (in orange) for Denmark's Depth Model versions 1.0 (pane a) and 2.0 (pane b).

https://doi.org/10.58440/ihr-30-2-a17

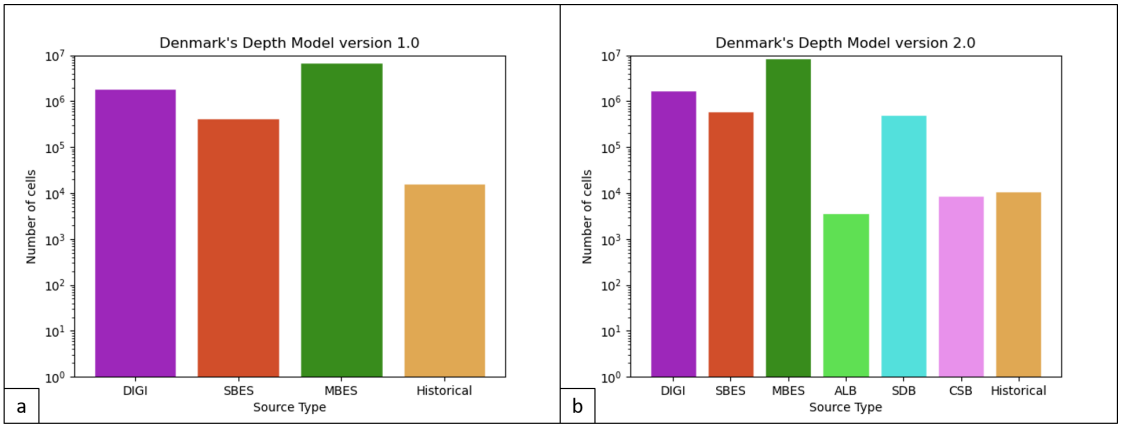


Fig. 6 The bar plots show the number of cells (on y axis, in logarithmic scale) for the different source types (on x axis) used in Denmark's Depth Model versions 1.0 (pane a) and 2.0 (pane b).

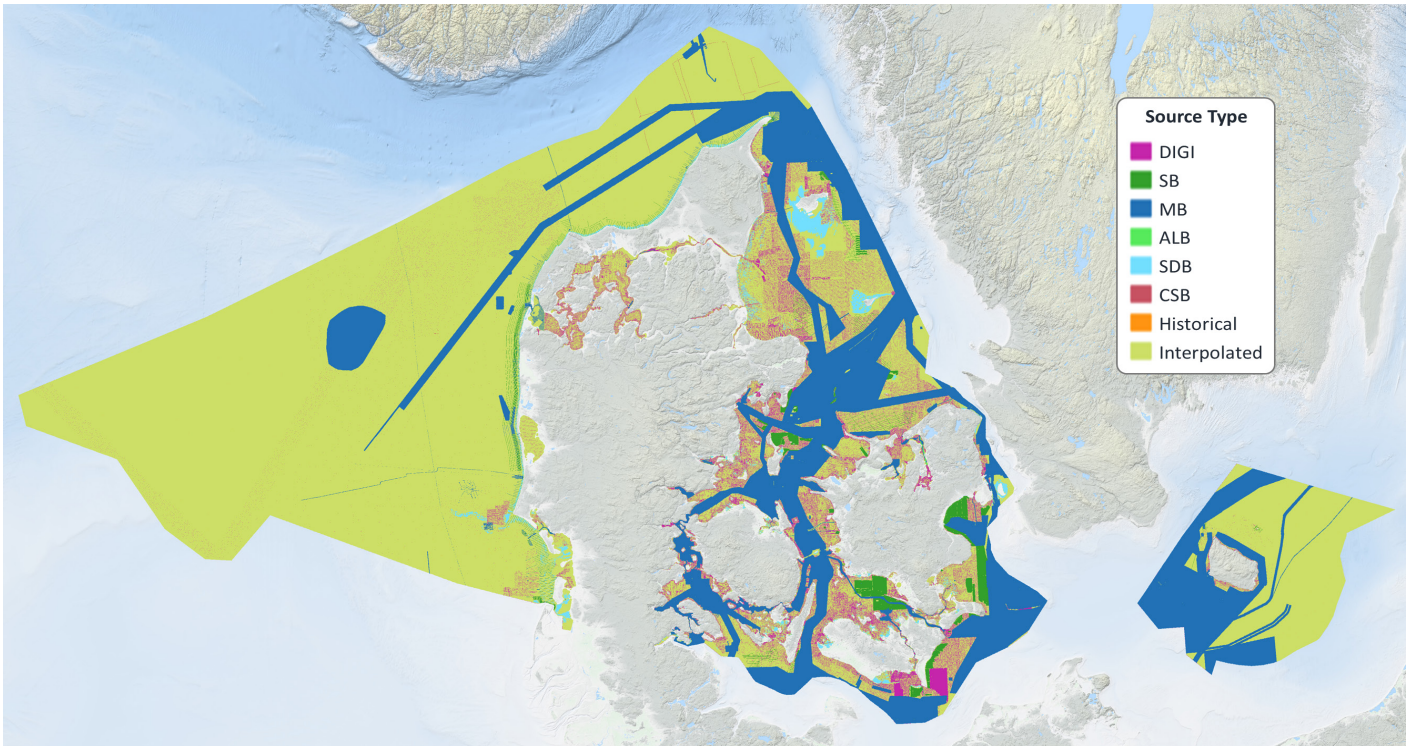
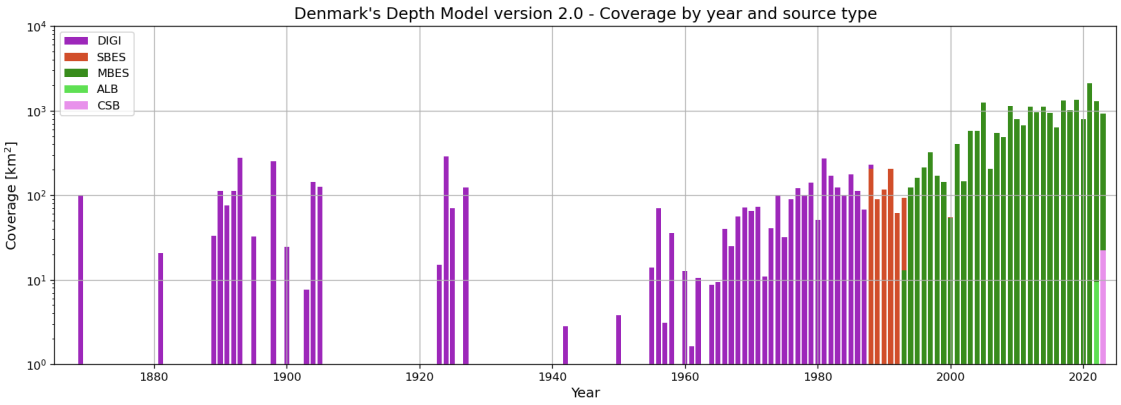


Fig. 7 The source type layer (i.e., '*kilde*') of Denmark's Depth Model version 2.0 retrieved using the publicly available WMS service (https://dataforsyningen.dk/data/4817). The EMODnet Digital Bathymetry (DTM 2022) with land coverage is shown in the back-ground (Sources: EMODnet Bathymetry Consortium, 2022).

Fig. 8 Coverage in km^2 (on the y axis, in logarithmic scale) by year (on the x axis) and source type (see color legend). The plot shows the transition to modern SBES surveys (in orange) in 1988, and the transition to MBES surveys (in green) – characterized by a higher density of soundings per cell – in 1993. It also highlights the use of other sources in the recent years (ALB in 2022, CSB in 2023).



on DDM v2.0 (i.e., how the model was generated and how to interpret the provided layers) is part of the compressed archive containing the DDM release. A contributors document (also in PDF format) listing data contributors is also made available.

3 Results

The official release of DDM v2.0 occurred on 28th of August, 2024. The compressed archive, which

https://doi.org/10.58440/ihr-30-2-a17

contains all materials detailed in the *Model Products* section, along with information for accessing the OGC (Open Geospatial Consortium) services, is available through the Danish Geodata Agency's website[6]. This release marks a significant update, providing enhanced resources for geospatial analysis and ensuring broader accessibility to the DDM's data and services.

The bathymetric layer (depicted in Fig. 3) encompasses a surveyed area of 98,045 square kilometers. The largest majority (~97.2 %) of the depth values are under 100 meters; they present a skewed bimodal distribution (peaks at 15–20 meters and 40–45 meters) with a median value of ~32.4 meter (Fig. 4).

DDM v2.0 comprises a DBM in which over 29 % of the depth cells are derived directly from measured depth values, with the remaining cells interpolated from these measurements to estimate depth values in areas lacking direct data (Fig. 5, pane b). The interpolated regions of DDM v2.0 can be derived by selecting the cells marked with the "Interpolated" value in the *ddm_50m.kilde* layer (Table 1). The primary source of these measured depth values is multibeam echosounder (MBES) surveys, as indicated by the *ddm_50m.kilde* auxiliary layer (Fig. 6, pane b). The panes a in Fig. 5 and Fig. 6 are shown for comparison with the data content of the first version of DDM.

Based on the *ddm_50m.aar* auxiliary layers, the first MBES-type contribution to the DDM occurred in 1993, with subsequent years showing a marked increase in the spatial coverage of MBES-derived bathymetry (Fig. 8). This temporal and spatial variability in data density, influenced by the varying types and years of data sources, has led to regions within the DDM where bathymetric detail is high due to dense MBES survey data (e.g., the Great Belt area). In contrast, other regions (e.g., the upmost western part of the North Sea) exhibit smoothed bathymetry as a result of interpolation processes applied to estimate depths in areas with sparse soundings.

4 Discussion

DDM v2.0 represents the second publicly released Digital Bathymetric Model (DBM) covering Danish waters, characterized by a grid resolution of 50 meters. This paper details the compilation process employed in the creation of the DDM v2.0 (Fig. 2), as well as the methods of its distribution through publicly accessible products. These aspects are particularly relevant for hydrographic offices and other national agencies that are committed to advancing research and modeling initiatives, considering the diverse range of applications for which DBMs are utilized. It is important to note that DDM v2.0 is generated using an averaging methodology, making it unsuitable for safety of navigation purposes. Nevertheless, several key steps within the described compilation workflow have been adapted for use in forthcoming projects aimed at developing high-resolution navigation surface and related S-100 products. The adoption of the navigation surface concept will facilitate the efficient production of nautical charts, as outlined by Smith (2003).

DDM v2.0 is constructed from hundreds of bathymetric survey datasets and historical sources within Denmark's Exclusive Economic Zone (EEZ). However, less than 23 % of the DDM's coverage is derived from surveys conducted using modern SBES and MBES (Fig. 8). Increasing this percentage significantly in the coming years presents substantial resource challenges, partly due to the limitations imposed by the relatively shallow depths surrounding Denmark (Fig. 3), which constrain the acoustic swath coverage of MBES. This constraint has prompted the exploration of alternative data sources, such as Airborne Lidar Bathymetry (ALB), Satellite-Derived Bathymetry (SDB), and Crowdsourced Bathymetry (CSB). While ALB and SDB are restricted to shallow coastal waters, CSB presents a significant potential to augment data coverage also in deeper waters. However, the effective adoption of CSB requires the development of practical solutions to address challenges such as data validation, quality assessment, and the variable reliability of data collectors (Masetti et al., 2020).

During the development of DDM v2.0, it became apparent that treating SDB datasets in the same manner as other data sources would introduce significant artifacts in regions where these datasets overlap. To address this issue, simply filling gaps in the existing data coverage with SDB data was deemed inappropriate. Therefore, a decision was made to prioritize the other data sources (listed in Table 1) over the SDB as well as implement a harmonization algorithm. The input SDB datasets originally covered approximately 5,000 km² within a depth range of 0 to 6 meters. However, due to the presence of bathymetric artifacts in early realizations of the model, a harmonization process was applied, resulting in about 1,274 km² – roughly one-quarter of the initial SDB coverage – being retained. The exclusion of the remaining SDB data was due to either redundancy, where it overlapped with higher-priority depth data, or filtering during the harmonization procedure. Future advancements, such as more precise differentiation between primary data sources, could enable a more sophisticated harmonization process. This improved process would potentially preserve a greater proportion of SDB data, thereby minimizing the need for interpolation and enhancing the overall accuracy and reliability of the final DBM.

DDM v2.0 substantially increases (more than 5 %) the percentages of model cells derived from measured depth values when compared with the first release of the DDM (Fig. 5). The major source of this increase is represented by the addition of more MBES datasets as well as the introduction of 3 new source types: ALB, SDB, and CSB (Fig. 6). In cases where modern datasets are unavailable for specific areas within DDM v2.0 coverage, historical data sources are utilized. When neither modern nor historical data are available, interpolation serves as a

last resort to estimate depth values. The interpolation method employed in these instances is the Natural Neighbor algorithm (Watson, 1999), which has demonstrated efficacy in preserving the fine details of regions with high-density MBES data. Additionally, this algorithm is effective in facilitating smooth transitions between areas of varying data density, thereby minimizing artifacts and maintaining the overall integrity of the bathymetric model.

The compilation mechanism employed for integrating the hundreds of sources from the Grid DB – specifically, the "Create/Update Model Tiles" process illustrated in Fig. 2 – optimizes computational efficiency by limiting updates to only those model tiles impacted by changes in source data. This targeted approach significantly reduces overall computation time. More broadly, the development of a robust workflow supports the seamless integration of new data sources into the DBM, while ensuring that the final product is presented consistently across iterations. Future research may focus on the development of automated procedures to enhance the efficiency and reliability of the quality control process for the finalized DBM, building on current methodologies (Lubczonek et al., 2021; Masetti et al., 2022b).

The comprehensive metadata and documentation associated with DDM v2.0 are designed to enhance its discoverability among researchers, ensuring that it can be readily identified and utilized for specific scientific purposes. The original datasets, which are not distributed with the DDM v2.0 model, are comprehensively described in the auxiliary layers to provide detailed information about the specific bathymetric sources utilized within the DBM. This approach aligns with the broader goals of facilitating access to marine data, a critical objective under the EU Marine Strategy Framework Directive and the EU Marine Knowledge 2020 agenda, including initiatives such as EMODnet (Schaap & Schmitt, 2020; Thierry et al., 2019). DDM v2.0 is also slated to serve as a data source for the upcoming new release of EMODnet Bathymetry and represents the base for future contributions. The EMODnet Bathymetry initiative supports the integration of 'composite grids' – gridded products derived from multiple sources – by employing the SeaDataNet Sextant catalogue service, which has been specifically extended to accommodate the detailed submission of such datasets (Thierry et al., 2019).

DDM v2.0 holds significant potential for a wide range of scientific applications, spanning geological studies, oceanography, and marine biology. High-quality DBMs such as DDM v2.0 are critical for various aspects of marine geosciences, including seafloor characterization, sedimentological analysis, and offshore engineering. Detailed information on how to access DDM v2.0 is available through the Danish Geodata Agency website: https://eng.gst.dk/danish-hydrographic-office/denmark-depth-model.

5 Conclusions

DDM v2.0 is the result of an extensive and rigorous compilation process that integrates a diverse array of bathymetric data sources. These sources encompass several hundred bathymetric surveys, including both contemporary and historical datasets, as well as SDB and CSB bathymetric information. By referencing all depth measurements to the LAT datum, DDM v2.0 ensures uniformity and compatibility with other regional and global bathymetric models.

The model's design and compilation methodology, which involves the synthesis of data with varying levels of precision and temporal relevance, precludes its use in applications for safety of navigation. Nevertheless, DDM v2.0 serves as an invaluable resource for a wide range of scientific, environmental, and marine spatial planning activities. The model supports coastal and marine researchers by providing detailed and reliable in-depth information essential for studies in areas such as marine geology, oceanography, and habitat mapping.

DDM v2.0 is made publicly accessible through the Danish Geodata Agency's official website, offering an important tool for both national and international stakeholders. Moreover, it represents a substantial contribution to the EMODnet Bathymetry initiative, thereby enhancing the collective understanding of seabed topography across European waters. The ongoing development and refinement of the DDM underscore Denmark's commitment to advancing marine science and supporting sustainable marine management.

Acknowledgements

Many past and present colleagues at the Danish Hydrographic Office and the Danish Navy's Hydrographic Service have contributed to this work by providing feedback, data, and endless source of inspiration. In particular, the authors would like to thank Yvonne Morville Petersen, Elizabeth Hagemann, Katrine Petersen, Torben Weinkouff Rasmussen, James Peter Harris, Jonas Madsen, Juho Salmia, Nicki Riber Andreasen, Niels Bo Nielsen, Ove Andersen, Sotirios Skarpalezos, Sara Despres Abecasis Cardigos, Ian Berg Sonne, Claudia Mirela Mikaelsen, Kasper Møllerup Schnedler, Marie Louise Agerbak Andersen and Claus Buus Jensen, for having actively supported the development and the publication of the model. Special thanks to the EMODnet Regional Coordinators – the Swedish Maritime Authority (SMA), Federal Maritime and Hydrographic Agency (BSH) of Germany and Kartverket of Norway for the provided support in harmonizing DDM v2.0 with neighboring national bathymetric models and available datasets.

https://doi.org/10.58440/ihr-30-2-a17

References

Andersen, O. B., Knudsen, P. and Berry, P. A. M. (2010). The DNSC08GRA global marine gravity field from double retracked satellite altimetry. *Journal of Geodesy, 84*(3), p. 191–199.

Bogumil, M., Mittal, T. and Lithgow-Bertelloni, C. (2024). The effects of bathymetry on the long-term carbon cycle and CCD. *Proceedings of the National Academy of Sciences, 121*(21), p. e2400232121.

Brown, C. J., Sameoto, J. A. and Smith, S. J. (2012). Multiple methods, maps and management applications: Purpose made seafloor maps in support of ocean management. *Journal of Sea Research, 72*, p. 1–13.

Danish Geodata Agency (2021). *National Report of Denmark*. IHO Baltic Sea Hydrographic Commission.

De Giosa, F., Scardino, G., Vacchi, M., Piscitelli, A., Milella, M., Ciccolella, A. and Mastronuzzi, G. (2019). Geomorphological Signature of Late Pleistocene Sea Level Oscillations in Torre Guaceto Marine Protected Area (Adriatic Sea, SE Italy). *Water, 11*(11), p. 2409.

Dierssen, H. M. and Theberge, A. E. (2020). Bathymetry: assessment. *Coastal and Marine Environments*: Boca Raton, FL, USA, CRC Press, p. 175–184.

Drennon, H., Ferrini, V. and Morton, J. J. (2023). Multibeam Data Curation and Access Through the Global Multi-Resolution Topography (GMRT) Synthesis. *Proceedings OCEANS 2023 - MTS/IEEE U.S. Gulf Coast* 25-28 Sept. 2023, p. 1–4.

EMODnet Bathymetry Consortium (2020). EMODnet Digital Bathymetry (DTM): Brussels, Belgium.

Erikstad, L., Bakkestuen, V., Bekkby, T. and Halvorsen, R. (2013). Impact of Scale and Quality of Digital Terrain Models on Predictability of Seabed Terrain Types. *Marine Geodesy, 36*(1), p. 2–21.

ESA (2015). *Sentinel-2 products specification document*. Thales Alenia Space, Rapport technique.

Fonseca, L., Lurton, X., Fezzani, R., Augustin, J.-M. and Berger, L. (2021). A statistical approach for analyzing and modeling multibeam echosounder backscatter, including the influence of high-amplitude scatterers. *The Journal of the Acoustical Society of America, 149*(1), p. 215–228.

GEBCO Bathymetric Compilation Group (2024). *GEBCO_2024 Grid*. NERC EDS British Oceanographic Data Centre NOC. https://doi.org/10.5285/1c44ce99-0a0d-5f4f-e063-7086abc0ea0f

Haigh, M., Holland, P. R. and Jenkins, A. (2023). The Influence of Bathymetry Over Heat Transport Onto the Amundsen Sea Continental Shelf. *Journal of Geophysical Research: Oceans, 128*(5), p. e2022JC019460.

Hartmann, K., Reithmeier, M., Knauer, K., Wenzel, J., Kleih, C. and Heege, T. (2022). Satellite-derived Bathymetry Online. *The International Hydrographic Review, 28*, p. 53–75.

Hughes Clarke, J. E. (2018a). The Impact of Acoustic Imaging Geometry on the Fidelity of Seabed Bathymetric Models. *Geosciences, 8*(4), p. 109.

Hughes Clarke, J. E. (2018b), Multibeam Echosounders. A. Micallef, S. Krastel and A. Savini (Eds.), *Submarine Geomorphology* (pp. 25–41). Springer International Publishing.

Ribergaard, M.H., Anker Pedersen, S., Ådlandsvik, B. and Kliem, N. (2004). Modelling the ocean circulation on the West Greenland shelf with special emphasis on northern shrimp recruitment. *Continental Shelf Research, 24*(13), p. 1505–1519.

Jakobsson, M. and Mayer, L. A. (2022). Polar Region Bathymetry: Critical Knowledge for the Prediction of Global Sea Level Rise. *Frontiers in Marine Science, 8*.

Jakobsson, M., Mayer, L. A., Bringensparr, C., Castro, C. F., Mohammad, R., Johnson, P., Ketter, T., Accettella, D., Amblas, D., An, L., Arndt, J. E., Canals, M., Casamor, J. L., Chauché, N., Coakley, B., Danielson, S., Demarte, M., Dickson, M.-L., Dorschel, B., Dowdeswell, J. A., Dreutter, S., Fremand, A. C., Gallant, D., Hall, J. K., Hehemann, L., Hodnesdal, H., Hong, J., Ivaldi, R., Kane, E., Klaucke, I., Krawczyk, D. W., Kristoffersen, Y., Kuipers, B. R., Millan, R., Masetti, G., Morlighem, M., Noormets, R., Prescott, M. M., Rebesco, M., Rignot, E., Semiletov, I., Tate, A. J., Travaglini, P., Velicogna, I., Weatherall, P., Weinrebe, W., Willis, J. K., Wood, M., Zarayskaya, Y., Zhang, T., Zimmermann, M. and Zinglersen, K. B. (2020). The International Bathymetric Chart of the Arctic Ocean Version 4.0, *Scientific Data, 7*(1), p. 176.

Jakobsson, M., Stranne, C., O'Regan, M., Greenwood, S. L., Gustafsson, B., Humborg, C. and Weidner, E. (2019). Bathymetric properties of the Baltic Sea. *Ocean Sci., 15*(4), p. 905–924.

Jarmbæk, J. (2005). *Vejledning om højdesystemet*. Kort og Matrikelstyrelsen.

Kjeldsen, K. K., Weinrebe, R. W., Bendtsen, J., Bjørk, A. A. and Kjær, K. H. (2017). Multibeam bathymetry and CTD measurements in two fjord systems in southeastern Greenland. *Earth Syst. Sci. Data, 9*(2), p. 589–600.

Koop, L., Snellen, M. and Simons, D. G. (2021). An Object-Based Image Analysis Approach Using Bathymetry and Bathymetric Derivatives to Classify the Seafloor. *Geosciences, 11*(2), p. 45.

Lebrec, U., Paumard, V., O'Leary, M. J. and Lang, S. C. (2021). Towards a regional high-resolution bathymetry of the North West Shelf of Australia based on Sentinel-2 satellite images, 3D seismic surveys and historical datasets. *Earth Syst. Sci. Data, 13*(11), p. 5191–5212.

Lebrec, U., Riera, R., Paumard, V., Leary, M. J. and Lang, S. C. (2022). Automatic Mapping and Characterisation of Linear Depositional Bedforms: Theory and Application Using Bathymetry from the North West Shelf of Australia. *Remote Sensing, 14*(2), p. 280.

Lecours, V., Dolan, M. F. J., Micallef, A. and Lucieer, V. L. (2016). A review of marine geomorphometry, the quantitative study of the seafloor. *Hydrol. Earth Syst. Sci., 20*(8), p. 3207–3244.

Lee, J. A. Y. (1991). Comparison of existing methods for building triangular irregular network, models of terrain from grid digital elevation models. *International Journal of Geographical Information Systems, 5*(3), p. 267–285.

Legeais, J. F., Ablain, M., Zawadzki, L., Zuo, H., Johannessen, J. A., Scharffenberg, M. G., Fenoglio-Marc, L., Fernandes, M. J. andersen, O. B., Rudenko, S., Cipollini, P., Quartly, G. D., Passaro, M., Cazenave, A. and Benveniste, J. (2018). An improved and homogeneous altimeter sea level record from the ESA Climate Change Initiative. *Earth Syst. Sci. Data, 10*(1), p. 281–301. ˇ

Lubczonek, J., Wlodarczyk-Sielicka, M., Lacka, M. and Zaniewicz, G. (2021). Methodology for Developing a Combined Bathymetric and Topographic Surface Model Using Interpolation and Geodata Reduction Techniques. *Remote Sensing, 13*(21), p. 4427.

Lubczonek, J. and Zaniewicz, G. (2023). Application of Filtering Techniques to Smooth a Surface of Hybrid Digital Bathymetric

Model. *Remote Sensing, 15*(19), p. 4737.

Lucieer, V., Lecours, V. and Dolan, M. F. J. (2018). Charting the Course for Future Developments in Marine Geomorphometry: An Introduction to the Special Issue. *Geosciences, 8*(12), p. 477.

Lurton, X. (2010). *An introduction to underwater acoustics: principles and applications*, Heidelberg, New York, Springer, published in association with Praxis Publishing, Chichester, UK.

Masetti, G., Andersen, O., Andreasen, N. R., Christiansen, P. S., Cole, M. A., Harris, J. P., Langdahl, K., Schwenger, L. M. and Sonne, I. B. (2022a). Denmark's Depth Model: Compilation of Bathymetric Data within the Danish Waters. *Geomatics, 2*(4), p. 486–498.

Masetti, G., Faulkes, T., Wilson, M. and Wallace, J. (2022b). Effective Automated Procedures for Hydrographic Data Review. *Geomatics, 2*(3), p. 338–354.

Masetti, G., Kelley, J. G. W., Johnson, P. and Beaudoin, J. (2018a). A Ray-Tracing Uncertainty Estimation Tool for Ocean Mapping. *IEEE Access, 6*, p. 2136–2144.

Masetti, G., Mayer, L. and Ward, L. (2018b). A Bathymetry- and Reflectivity-Based Approach for Seafloor Segmentation. *Geosciences, 8*(1), p. 14.

Masetti, G., Rondeau, M., Baron, B. J., Wills, P., Petersen, Y. M. and Salmia, J. (2020). *Trusted Crowd-Sourced Bathymetry: From the Trusted Crowd to the Chart*. Danish Geodata Agency & Canadian Hydrographic Service.

Mayer, L. (2023). Uncrewed surface systems facilitating a new era of global ocean exploration. *The International Hydrographic Review, 29*(1), pp. 42–55. https://doi.org/10.58440/ihr-29-a05.

Mayer, L., Jakobsson, M., Allen, G., Dorschel, B., Falconer, R., Ferrini, V., Lamarche, G., Snaith, H. and Weatherall, P. (2018). The Nippon Foundation—GEBCO Seabed 2030 Project: The Quest to See the World's Oceans Completely Mapped by 2030. *Geosciences, 8*(2), p. 63.

Mayer, L., Roach, J. A., Nordquist, M. H. and Long, R. (2021). Marine Biodiversity of Areas beyond National Jurisdiction. *The Quest to Completely Map the World's Oceans in Support of Understanding Marine Biodiversity and the Regulatory Barriers WE Have Created*: Leiden, Netherlands, Brill, p. 149–166.

Mayer, L. A. (2022). The Challenges of Mapping the Seafloor, *AGU Fall Meeting Abstracts*, Volume 2022: Chicago, IL, p. U56A-03.

McMichael-Phillips, J., Rovere, M., Snaith, H., Souri, P. and Weatherall, P. (2024). The pivotal role of bathymetry in safeguarding the future of the planet. *STATE OF THE OCEAN REPORT*, p. 75.

Morrow, R., Fu, L.-L., Rio, M.-H., Ray, R., Prandi, P., Le Traon, P.-Y. and Benveniste, J. (2023). Ocean Circulation from Space. *Surveys in Geophysics, 44*(5), p. 1243–1286.

Moses, C. A. and Vallius, H. (2021). Mapping the Geology and Topography of the European Seas (European Marine Observation and Data Network, EMODnet). *Quarterly Journal of Engineering Geology and Hydrogeology, 5*(1), p. qjegh2020–2131.

O'Toole, R., Judge, M., Sacchetti, F., Furey, T., Mac Craith, E., Sheehan, K., Kelly, S., Cullen, S., McGrath, F. and Monteys, X. (2022). Mapping Ireland's coastal, shelf and deep-water environments using illustrative case studies to highlight the impact of seabed mapping on the generation of blue knowledge. K. Asch, H. Kitazato and H. Vallius (Eds.). *From Continental Shelf to Slope: Mapping the Oceanic Realm*. Geological Society of London.

Palmiotto, C. and Loreto, M. F. (2019). Regional scale morphological pattern of the Tyrrhenian Sea: New insights from EMODnet bathymetry. *Geomorphology, 332*, p. 88–99.

Parrish, C. E., Magruder, L. A., Neuenschwander, A. L., Forfinski-Sarkozi, N., Alonzo, M. and Jasinski, M. (2019). Validation of ICESat-2 ATLAS Bathymetry and Analysis of ATLAS's Bathymetric Mapping Performance. *Remote Sensing, 11*(14), p. 1634.

Ritter, N. and Ruth, M. (1997). The GeoTiff data interchange standard for raster geographic images. *International Journal of Remote Sensing, 18*(7), p. 1637–1647.

Sandwell, D. T., Gille, S. T., Orcutt, J. and Smith, W. H. F. (2003). Bathymetry from space is now possible. *Eos, Transactions American Geophysical Union, 84*(5), p. 37–44.

Schaap, D. M. A. and Schmitt, T. (2020). EMODnet Bathymetry - further developing a high resolution digital bathymetry for European seas. p. 10296.

Smith, S. M. (2003). *The navigation surface: A multipurpose bathymetric database*. University of New Hampshire.

Sowers, D. C., Masetti, G., Mayer, L. A., Johnson, P., Gardner, J. V. and Armstrong, A. A. (2020). Standardized Geomorphic Classification of Seafloor Within the United States Atlantic Canyons and Continental Margin. *Frontiers in Marine Science, 7*.

Sowers, D. C., Mayer, L. A., Masetti, G., Cordes, E., Gasbarro, R., Lobecker, E., Cantwell, K., Candio, S., Hoy, S., Malik, M., White, M. and Dornback, M. (2024). Mapping and Geomorphic Characterization of the Vast Cold-Water Coral Mounds of the Blake Plateau. *Geomatics, 4*(1), p. 17–47.

Thierry, S., Dick, S., George, S., Benoit, L. and Cyrille, P. (2019), EMODnet Bathymetry a compilation of bathymetric data in the European waters. *Proceedings OCEANS 2019 - Marseille*17-20 June 2019, p. 1–7.

Vrdoljak, L. (2021). Comparison and analysis of publicly available bathymetry models in the East Adriatic Sea. *NAŠE MORE: znanstveni casopis za more i pomorstvo, 68*(2), p. 110–119.

Ware, C., Mayer, L. and Johnson, P. (2023). BathyGlobe GapFiller: A planning tool to help fill the gaps in world bathymetry. *The International Hydrographic Review, 29*(2), pp. 16–27. https://doi.org/10.58440/ihr-29-2-a19

Watson, D. (1999). The natural neighbor series manuals and source codes. *Computers & Geosciences, 25*(4), p. 463–466.

Weatherall, P., Marks, K. M., Jakobsson, M., Schmitt, T., Tani, S., Arndt, J. E., Rovere, M., Chayes, D., Ferrini, V. and Wigley, R. (2015). A new digital bathymetric model of the world's oceans. *Earth and Space Science, 2*(8), p. 331–345.

Westfeld, P., Maas, H.-G., Richter, K. and Weiß, R. (2017). Analysis and correction of ocean wave pattern induced systematic coordinate errors in airborne LiDAR bathymetry. *ISPRS Journal of Photogrammetry and Remote Sensing, 128*, p. 314–325. https://doi.org/10.1016/j.isprsjprs.2017.04.008

Authors' biographies

Lasse M. Schwenger earned a cand.polyt degree in Water & Environmental Engineering from Aalborg University in 2021. He then spent a year working in open-channel hydraulics, where he explored the use of sonar technology for river surveying to support flow modeling. Since august 2022 he has worked at the Danish Geodata Agency, engaging in remote sensing activities in both Denmark and Greenland.



Lasse M. Schwenger

Kristian V. Kristmar earned a cand.polyt in Geophysics and Space Engineering with a specialization in Mapping and Navigation at The Danish Technical University, where he graduated from in 2023. He has since worked as a geodesist for the Danish Geodata Agency.



Kristian V. Kristmar

Giuseppe Masetti holds a MSc in Ocean Engineering, a Master in Marine Geomatics and a PhD in System Monitoring and Environmental Risk Management. After having served as hydrographic officer with the Italian Navy, he was a Tyco PostDoc Fellow with the Center for Coastal and Ocean Mapping, where he is at present an adjunct research faculty. In 2019 he has joined the Danish Hydrographic Office, where he is currently focusing on streamlining hydrographic data workflows.



Giuseppe Masetti

Philip Sigaard Granding holds a MSc in Physics. He is specialized in the field of geophysics and has worked with different applications of remote sensing techniques such as airborne lidar- and satellite derived bathymetry. He joined the Danish Geodata Agency, Hydrographic Office, in 2017, and is currently focused on planning and leading development and innovation projects.



Philip Sigaard Granding

Kasper Langdahl, Cand.geom, Land surveyor. Specialized in database management. 5 years of experience in managing hydrographic data. Work tasks at the Danish Geodata Agency focus on quality control, refining and distributing bathymetry data.



Kasper Langdahl

https://doi.org/10.58440/ihr-30-2-a17

PEER-REVIEWD ARTICLE

Expanding and improving the Israeli geoid undulation model in the coastal area using nautical and shipborne GNSS measurements

Authors

Gilad Even-Tzur[1], Jareer Khalilieh[1] and Barry Grinker[1]

Abstract

The geoid, an equipotential surface of Earth's gravity field, corresponds to the global mean sea level, linking ellipsoidal and orthometric heights. As reliance on GNSS grows, accurate geoid models for coastal and marine areas are increasingly needed. We propose using a single shipborne GNSS receiver and nautical measurements as a cost-effective solution for coastal geoid modeling. Correcting GNSS data for vessel dynamics, tidal effects, atmospheric variations, and sea surface topography enables the creation of a local costal geoid model. Applied to Haifa Bay cruises (2019–2021), this method integrates into Israel's geoid, achieving sub-3 cm accuracy in coastal zones.

Keywords

marine geoid model · shipborne GNSS · geoid undulation · sea surface height

Resumé

Le géoïde, une surface équipotentielle du champ de pesanteur de la Terre, correspond au niveau moyen mondial de la mer, reliant les hauteurs ellipsoïdales et orthométriques. Avec l'utilisation croissante de GNSS, il est de plus en plus nécessaire de disposer de modèles précis du géoïde pour les zones côtières et maritimes. Nous proposons d'utiliser un seul récepteur GNSS embarqué et des mesures à la mer comme solution rentable pour la modélisation du géoïde côtier. La correction des données GNSS en fonction de la dynamique des navires, des effets de marée, des variations atmosphériques et de la topographie de la surface de la mer permet de créer un modèle local de géoïde côtier. Appliquée aux campagnes dans la baie de Haïfa (2019–2021), cette méthode s'intègre dans le géoïde israélien, atteignant une incertitude inférieure à 3 cm dans les zones côtières.

✉ Gilad Even-Tzur · eventzur@technion.ac.il

[1] Technion–Israel Institute of Technology, Division of Mapping and Geo-Information Engineering, Haifa, Israel

https://doi.org/10.58440/ihr-30-2-a10

Resumen

El geoide, superficie equipotencial del campo gravitatorio de la Tierra, se corresponde con el nivel medio global del mar, vinculando las alturas elipsoidales y ortométricas. Conforme aumenta la dependencia del GNSS, se hacen cada vez más necesarios modelos precisos del geoide para áreas costeras y marinas. Proponemos usar un único receptor GNSS a bordo y mediciones náuticas como solución efectiva en relación a su coste para el modelado del geoide costero. La corrección de datos GNSS según la dinámica de los buques, los efectos de las mareas, las variaciones atmosféricas, y la topografía de la superficie del mar permite crear un modelo local del geoide costero. Aplicado a las campañas en la Bahía de Haifa (2019–2021), este método se integra en el geoide de Israel, logrando una precisión inferior a 3 cm en las zonas costeras.

1 Introduction

A height system is a one-dimensional coordinate system employed to represent the vertical distance (height) of a point in relation to a chosen reference surface. There are two primary height systems used in geodetic positioning: Orthometric height and Ellipsoidal height. Orthometric height measures the vertical distance from a point on the Earth's surface to the geoid along the curved plumb line, while ellipsoidal height represents the vertical distance from a point on the Earth's surface to the reference ellipsoid along the ellipsoidal normal.

The geoid, closely associated with the undisturbed global mean sea level, is a fundamental equipotential surface of Earth's gravity field. Establishing the relationship between ellipsoidal height and orthometric height relies on geoid undulation modelling. This model is pivotal in geodetic infrastructure and continues to be a focal point in ongoing research. Its applications span geodesy and surveying, facilitating the conversion between ellipsoidal and orthometric heights. As reliance on Global Navigation Satellite Systems (GNSS) grows, the imperative for developing accurate and reliable geoid undulation models at centimeter-level precision across entire countries intensifies, requiring multiple resources (Wang et al., 2021).

On land, achieving a precise geoid model is possible through a combination of precise leveling, GNSS, and gravimetry. However, conducting leveling measurements in marine areas is impractical. Nonetheless, precise gravity data can be obtained through spaceborne, airborne, and shipborne gravimetry. However, processing challenges may arise due to the dynamic movements of the measurement platform, potentially leading to systematic errors.

The integration of airborne and shipborne gravity data into global and regional gravity models has been demonstrated to enhance their accuracy. A notable example of the successful integration of airborne gravity measurements into a local geoid model is evident in projects conducted around the island of Corsica (Duquenne et al., 2002) and the Greenland continental shelf (Forsberg et al., 2001), where improvements of several tens of centimeters were realized. Another instance is a study conducted in Japan, where the merge of shipborne gravity data and terrestrial gravity measurements with an altimetry-based gravity model led to an enhancement of several centimeters in the local geoid model (Kuroishi, 2009). Satellite altimetry is a valuable technology for monitoring sea level, primarily optimized for open ocean surfaces. Nevertheless, there have been numerous efforts to harness the potential of altimetry in the coastal zone. Enhancements in altimetry capabilities within coastal regions are discussed in Xu et al. (2019).

A fusion of shipboard gravimetry measurements with GNSS measurements is discussed in Lu et al. (2019). Their paper focuses on the data processing strategy for shipborne gravimetry, aiming to achieve high-accuracy and high-resolution gravimetry measurements in the Baltic Sea. The study investigates the use of GNSS-derived kinematic vertical accelerations to enhance the quality of gravity data.

In the absence of high-quality airborne and shipborne gravity measurements, geoid heights can be derived using shipborne GNSS measurements. These geoid heights derived from GNSS measurements can then be utilized for the expansion and enhancement of local geoid models. This method was applied to create a local geoid model in northern Germany, revealing that the standard deviation of the differences between the existing local model and the model adjusted using GNSS measurements is better than 2 cm (Lavrov et al., 2015). The method was also employed to extend the geoid undulation model in coastal areas along the Mediterranean Sea in Israel (Lavrov et al., 2017). The study's results demonstrated that geoid heights can be obtained with an accuracy of better than 2 cm and at a reduced cost compared to airborne and shipborne gravity measurements. A similar approach was employed by Varbla et al. (2020), which details the outcomes of a shipborne marine gravity and GNSS campaign designed to validate existing geoid models in the eastern part of the Baltic Sea. In an experiment conducted in the Gulf of Finland, GNSS measurements were utilized alongside gravity observations and sea level models to validate the existing geoid models in the region (Saari et al., 2021).

https://doi.org/10.58440/ihr-30-2-a10

The researchers successfully obtained geoid heights in the marine environment with an accuracy of a few centimeters. According to the research findings, the standard deviations of the differences between local geoid models and geoid heights derived from GNSS ranged from 1.4 to 6.3 centimeters.

In this study, we rely on a single shipborne GNSS receiver and nautical measurements to determine geoid undulation along the Haifa Bay coast in Israel, with the aim of expanding the official Israeli geoid undulation model to include the coastal area. We employed hydrographic surveys conducted across Haifa Bay to facilitate the development of the new HaMifratz port. The data were obtained from a dedicated survey vessel, and the resulting geoid model integrates multiple measurement profiles into a unified representation.

2 Methodology

The geoid, mean sea surface (MSS), and mean dynamic topography (MDT) are fundamental concepts in geodesy and oceanography, essential for understanding sea level variations and their practical implications. The MSS is the observed average sea level over a long period, influenced by factors like tides, ocean currents, and atmospheric pressure, and measured using satellite altimetry and tide gauges. The MSS is practical for representing sea level but is affected by forces causing deviations from the geoid. The MDT, representing the difference between the MSS and the geoid, reflects the ocean's dynamic response to currents, temperature, and salinity variations, showing sea level changes due to these processes. Sea surface topography (SST), also known as dynamic topography (DT), is the difference between the instantaneous sea surface height and the geoid. MDT is the time-averaged SST. The interrelationships between these concepts are crucial for understanding sea level variations. The unobservable nature of the geoid means that the MSS, influenced by dynamic factors, is used as a practical approximation. Consequently, SST provides valuable insights into the dynamic processes affecting sea level.

Expanding the geoid undulation model to the sea involves computation of geoid heights in coastal and sea areas and integrating them into the official Israeli geoid undulation model. In this study, such an expansion utilizes shipborne GNSS and nautical measurements. The ellipsoidal height of the phase center of the GNSS antenna mounted on the ship is measured. The critical aspect is that under certain conditions, the sea surface defines the "zero" orthometric height, effectively describing the geoid. Therefore, the challenge lies in reducing the ellipsoidal height of the antenna's phase center to sea level and calculating, for each measured epoch, the correction from the sea level to the geoid. To derive these geoid heights, the raw data must undergo several corrections, accounting for the vessel's dynamic motion, tidal effects, atmospheric variations, and sea surface topography.

Lavrov et al. (2015 and 2017) provide a detailed explanation of the essence of the corrections, their nature, and the way of realization. The method of performing the measurements, processing the data, and realizing the corrections for expanding the geoid undulation model in this study is outlined in the flow chart shown in Fig. 1 and described in more detail in the next chapter.

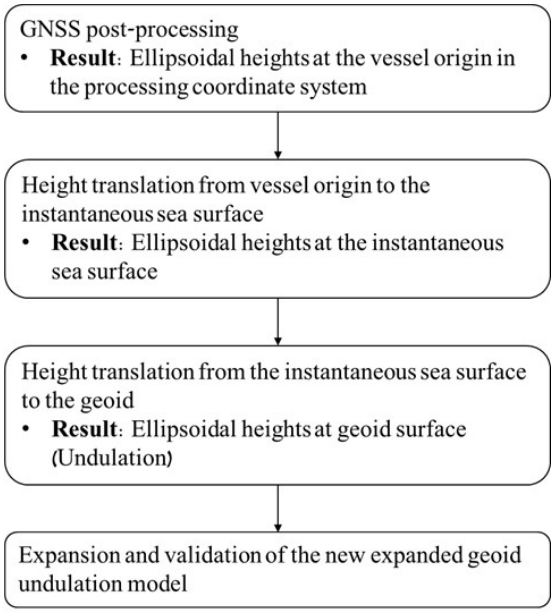


Fig. 1 Flowchart of the methodology steps.

3 Experiment set up, data collection and processing

To expand the official Israeli geoid undulation model to cover coastal areas along the coast of Haifa Bay in Israel three survey campaigns were carried out in the years 2019, 2020 and 2021. The survey vessel ADEL (Fig. 2) was used. The vessel was constructed by Armstrong Marine USA, a company specializing in manufacturing vessels tailored for hydrographic surveys, and its structure is specifically adapted to the demands of this task. Notably, the boat is designed to position the measuring system near the center of gravity, minimizing fluctuations. Additionally, it features a bottom with two pontoons, enhancing stability. Thus, this ship is optimized for conducting hydrographic surveys in coastal areas.

The vessel is equipped with the NORBIT iWBMS multibeam sonar system and the Motion Reference Unit (MRU) of the Applanix POS MV, WaveMaster II model. The MRU, housed within the sonar, is a comprehensive turnkey system, meticulously designed to provide precise attitude, heading, and heave data. Paired with a TRIMBLE GPS receiver, this sensor seamlessly integrates to deliver accurate position and velocity information for the vessel. The sensor is distinguished by its high precision, measuring roll and pitch angles with an accuracy of 0.02 degrees and measuring vertical elevation (Heave), with an absolute accuracy of up to 2 cm. The GPS antenna (Trimble

https://doi.org/10.58440/ihr-30-2-a10

540AP) is rigidly mounted to the ship's hull, significantly enhancing the quality of GPS measurements and it is positioned directly above the MRU.

As part of the research, a VALEPORT TideMaster radar tide gauge instrument was employed to continuously measure the combined effect of the tide and sea surface topography. It is located in the HaMifratz port close to the work and research area. The tide gauge operated as follows: it measured once per second for 30 seconds, paused for 30 seconds, then averaged the 30 measurements and displayed the average value every minute. Subsequently, the data was smoothed by averaging the data points from 45 minutes prior and 45 minutes ahead for each minute.

The position of the vessel's GPS antenna at each epoch was established using Real-Time Kinematic (RTK) relative to a nearby base station, which is part of the Continuously Operating Reference Stations (CORS) network in Israel. Using Post-Processing Kinematic (PPK) is also an option for calculating the ship's position. However, since there is a CORS station close to the work area within a distance not exceeding 10 km, we opted for RTK measurements. This choice offers immediate results, increased efficiency by eliminating the need for post-processing steps, and enhanced accuracy, especially in dynamic environments.

The GPS data-collection rate was 1 Hz and at a speed of 4 knots, translating to a measurement approximately every 2 meters. This configuration ensures a detailed and accurate representation of the surveyed area.

Instantaneous sea level is calculated every second, whereas sea surface topography values derived from the tide gauge are calculated every minute. Due to the discrepancy in measurement intervals, computing the geoid undulation every second is impractical. Therefore, the approach involves calculating the mean instantaneous sea level for each minute and integrating it with the sea surface topography to derive the geoid undulation values.



Fig. 2 The ADEL survey vessel. The GNSS antenna rigidly attached to the ship's hull is marked in red.

For data acquisition, the QPS Qinsy software was utilized to record the raw measurements. A designated software program was written to extract relevant parameters such as the position of the MRU in the Israel coordinate network, the ellipsoid height of the GPS antenna, pitch and roll angles, and vertical elevation from the raw data string. This software is employed for real-time hydrographic data acquisition in surveys, supporting a diverse range of industries, from straightforward multi-beam surveys to intricate offshore construction projects.

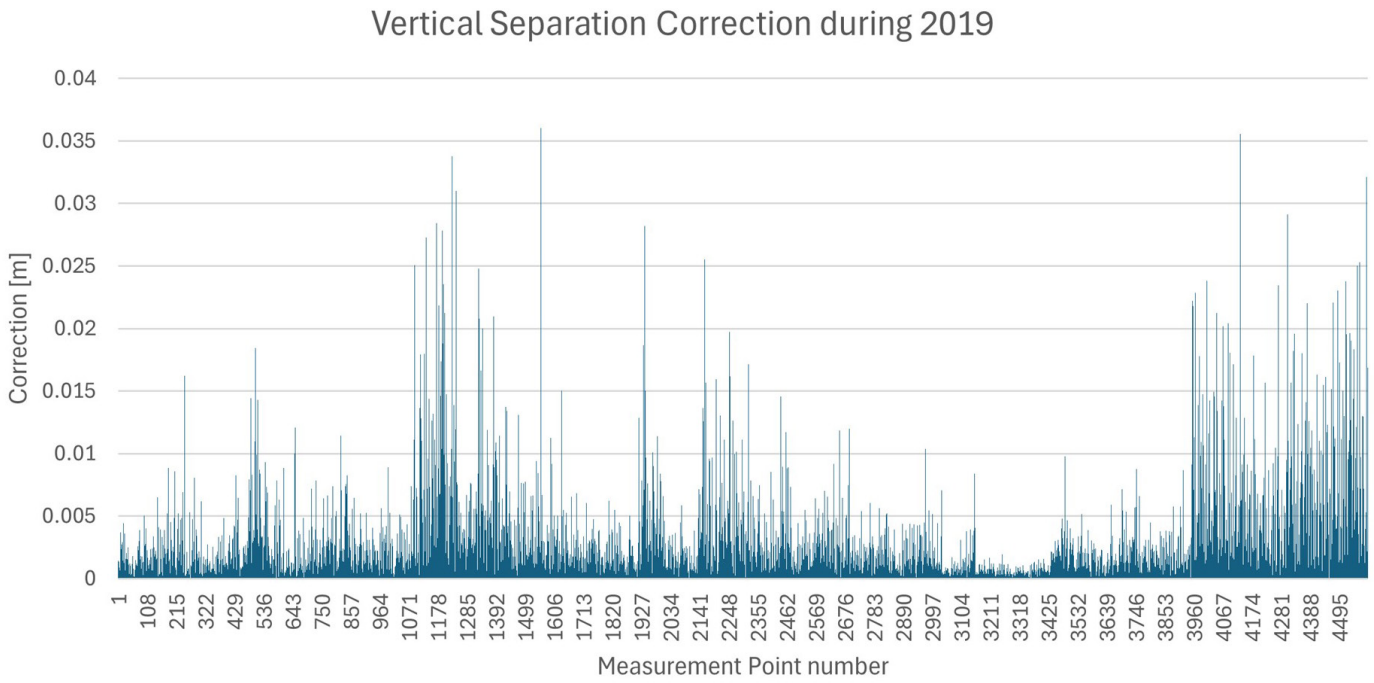


Fig. 3 Vertical separation correction values between the antenna and the MRU sensor during the surveys of 2019.

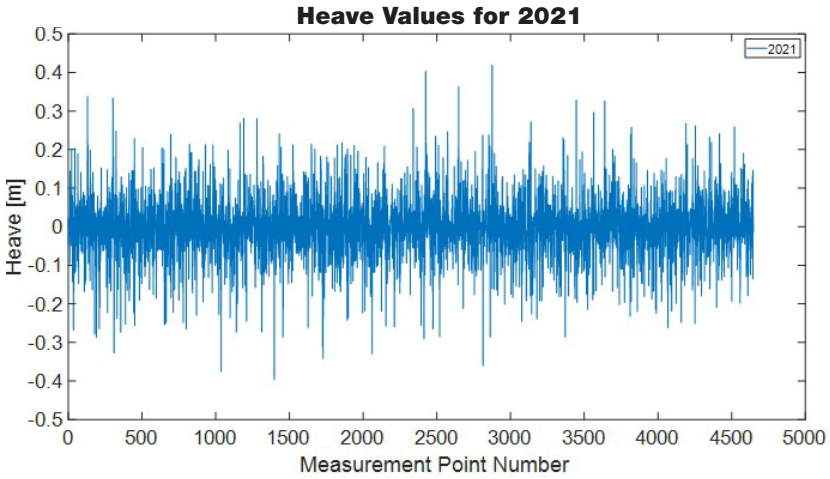


Fig. 4 The measured heave values during the surveys of 2021.

The fixed distance between a mark on the hull and the reference center of the MRU, along with the location of the GPS antenna phase center in the ship's reference frame relative to the MRU sensor was determined through total station measurements while the vessel was statically positioned on shore. Two sets of measurements were conducted, and based on the results, the accuracy of the MRU and antenna position in the ship's frame is within a few millimeters. The distance between the mark and the water surface can also be measured, allowing for the determination of the positions of the MRU and the antenna relative to the water surface.

Fig. 3 illustrates the correction values in the vertical separation between the GPS antenna phase center and the MRU sensor, as obtained for the 2019 survey. The results indicate that the maximum correction for the vertical separation between the phase center of the GPS antenna and the sensor, induced by the pitch and roll angles' fluctuations throughout all the surveys, does not exceed 4.5 cm.

In comparison to these small values primarily attributed to the GPS antenna's position relative to the sensor, the Heave values fluctuate between plus to minus half a meter over the three years of measurement. Fig. 4 illustrates the values obtained for the 2021 surveys.

The static draft of the vessel was measured using a tape measure with weights attached to its end. It was measured daily in the port before sailing and at the end of each measurement day. In most voyages, the average static draft value remained constant, indicating no significant changes in the ship's load over time. The dynamic draft of the ship can vary due to factors such as the squat effect (Härting et al., 2004), fuel consumption, and water density. Given that the survey vessel travels at a slow speed and doesn't push water forward when underway, the decision was made to neglect the squat effect, which does not induce changes in the ship's draft during voyages.

Furthermore, considering that the fuel consumption for a single working day may decrease the draft by a maximum of 1 cm, the survey was planned to last only a few hours to minimize the impact of fuel consumption on the dynamic draft. The process of calculating the ship's draft was conducted in the same area of the bay every survey day, mitigating expectations of changes in water density that could influence variations in the draft.

Atmospheric corrections aim to compensate for height variations caused by changes in atmospheric pressure and wind forces. In this study, the tide gauge and the vessel were affected by the same atmospheric changes due to their proximity to each other, thus canceling out those effects.

The mean dynamic topography (MDT) at the coast can be determined through both 'geodetic' and 'ocean' approaches (Woodworth et al., 2012; Huang, 2017). The oceanographic approach involves utilizing a hydrodynamic model that characterizes ocean flow, with the dynamic topography (DT) calculated as a temporal average over a specified period using the three-dimensional position of the vessel at the time of measurement. The geodetic approach includes employing ellipsoidal height of mean sea level or utilizing tidal observations from mean sea level (Andersen & Knudsen, 2009).

As there is no hydrodynamic model available in the Bay of Haifa, the decision was made to estimate the sea surface topography at a specific moment based on readings from the tide gauge near the study area. Given that the vessel's position is within 10 km of the tide gauge, this approach does not significantly affect the accuracy of the results. However, it is essential to note that extrapolating sea surface topography from sea level gauge readings towards the open sea may yield less accurate results at large distances.

To normalize elevations from the instantaneous water surface to the geoid surface, it is necessary to eliminate the influence of tides. This ensures obtaining a sea level height independent of the measurement time, along with the impact of sea surface topography derived from sea level measurements obtained with the tide gauge.

In summary, to determine the calculated geoid undulation (N) at each measurement epoch, we use the following equation:

$$N = h_{antenna} - L + dr - T \quad (1)$$

Where the ellipsoidal height of the GNSS antenna phase center is $h_{antenna}$, L is the vertical offset between the GNSS antenna and the MRU, dr is the dynamic draft, the vertical distance between the MRU and the still water level, and T is the combination of tide and sea surface topography, the still water level relative to the reference geoid as measured at the tide gauge.

It should be noted that L is the constant static offset corrected for the effects of Pitch and Roll, both measured by the MRU. In addition, dr, is calculated at each epoch incorporating Heave, Pitch and Roll.

https://doi.org/10.58440/ihr-30-2-a10

Between 2019 and 2021, three survey campaigns were conducted off the coast of Haifa, spanning almost 10 kilometers from the northernmost to the southernmost measurement points, with the distance from the coast reaching approximately 3 kilometers (Fig. 5).

Each campaign lasted approximately twenty days and involved roughly 60 hours of sailing. The spacing between sailing profiles depends on the depth of the sea: the deeper the sea, the wider the gap between profiles. This is because the sonar's coverage area is smaller in shallower waters, necessitating closer spacing between profiles. As a result, the distance between sailing profiles ranges from 10 to 80 meters.

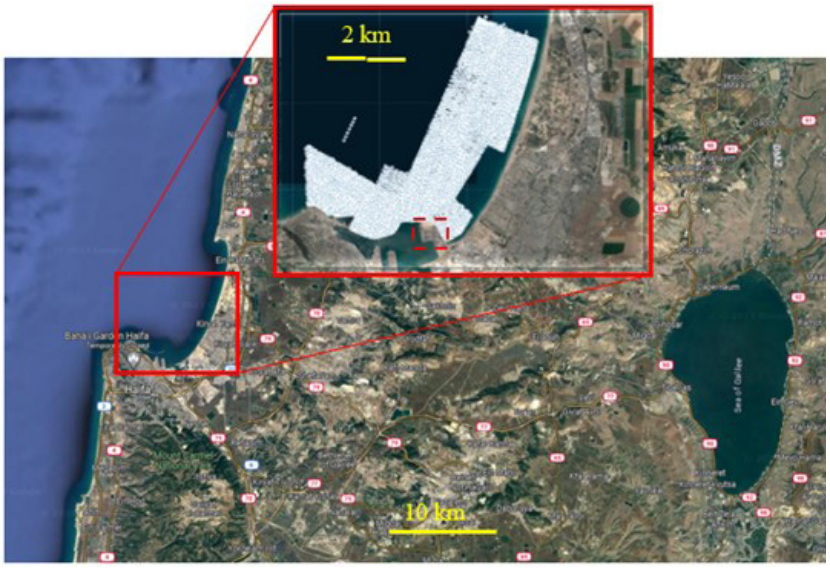


Fig. 5 Red square: study area in Haifa Bay, Northern Israel. Red box: measurement points of the various sailing profiles carried out along the Mediterranean coast. Dashed red rectangle: The region where nine points (1L to 9L) are situated along the HaMifratz port wharves, which were utilized to assess the accuracy of the extended geoid undulation model.

4 Adjustment of local linear geoid undulation model

Following the implementation of necessary corrections and the removal of temporal variations from the measurements, it becomes feasible to merge the various sailing profiles acquired over time. This option is grounded in the assumption that the average sea level has not undergone substantial changes during the time frame of this research; however, if any changes occurred, they are duly considered. The process of combining the diverse sailing profiles took place after identifying and rectifying gross errors in the measurements.

Robust methods were employed for the detection of gross errors, setting the a priori standard deviation of a measurement to 5 cm, corresponding to the error estimates of a measured undulation value. The results indicated that both Huber's method (Huber, 1981) and the Danish method (Krarup et al., 1980) outperformed others in terms of maximum absolute residual, average absolute residual, and the number of detected outliers. The Danish method particularly stood out, requiring the fewest iterations for solution convergence. A total of approximately 11,000 points were measured, with less than 10 % identified as gross errors. An examination of the distribution of these abnormal points revealed their concentration in specific work areas rather than being dispersed throughout the entire work area.

After eliminating all gross errors, we can fit a surface to the undulation values. This fitted surface will facilitate the examination of measurement quality and correction methods, as well as assessing the effectiveness of integrating sailing profiles measured over the years. Given the relatively small area, which can be presumed to lack extreme changes in undulation values, a linear surface of the following form can be fitted:

$$N = a \cdot \mathbf{e} + b \cdot \mathbf{n} + c \qquad (2)$$

where $\mathbf{e}$ and $\mathbf{n}$ are the coordinates of the measuring points in the Israeli coordinate system, N is the

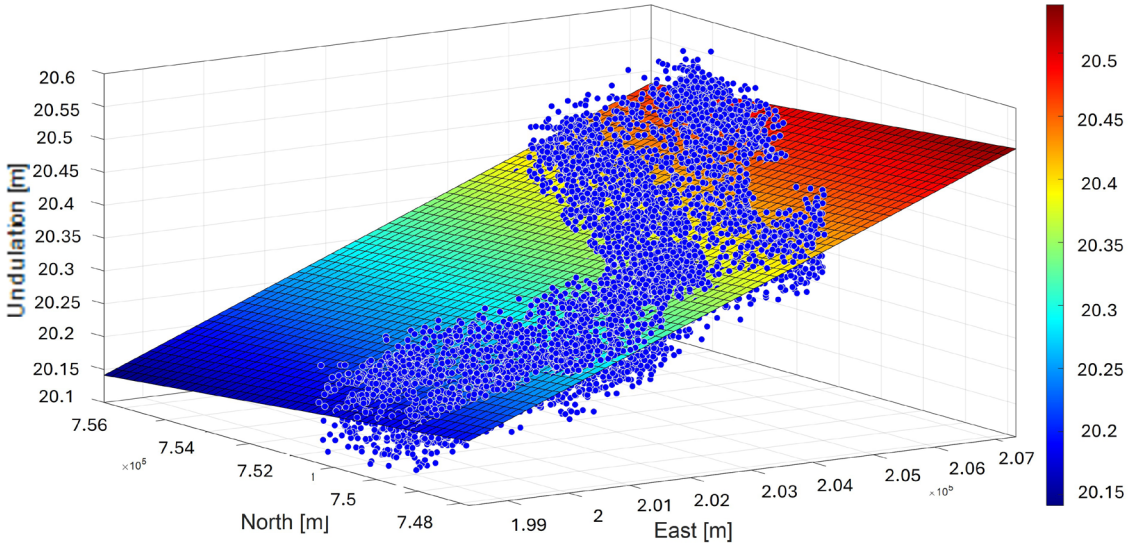


Fig. 6 Approximate geoid undulation surface based on all survey sailings over the three years, calculated using local linear regression. The undulation varies between 20.15 meters (dark blue) and 20.5 meters (red).

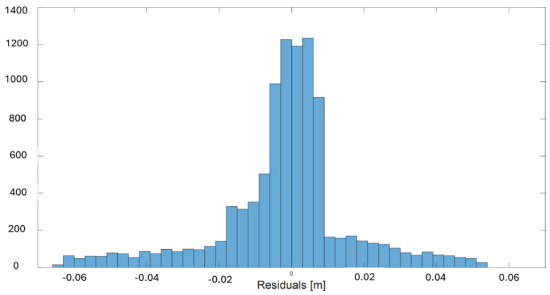


Fig. 7 Histogram of the residuals of the least-squares adjustment of the linear surface.

approximate geoid undulation, and *a*, *b*, and *c* are the surface parameters.

The fitted linear surface for all voyages conducted between 2019 and 2021 using least squares adjustment is illustrated in Fig. 6. The maximum absolute residual is 0.064 m, with an average of 0.014 m. The RMS error is 0.019 m. A histogram of the residuals is presented in Fig. 7.

The appropriateness of a parabolic second-order surface, characterized by six parameters, was also examined. However, it was concluded that the determination of the second-order coefficients does not significantly contribute to the solution. Therefore, it was deemed satisfactory to describe the measurements using a plane, which provides a good fit.

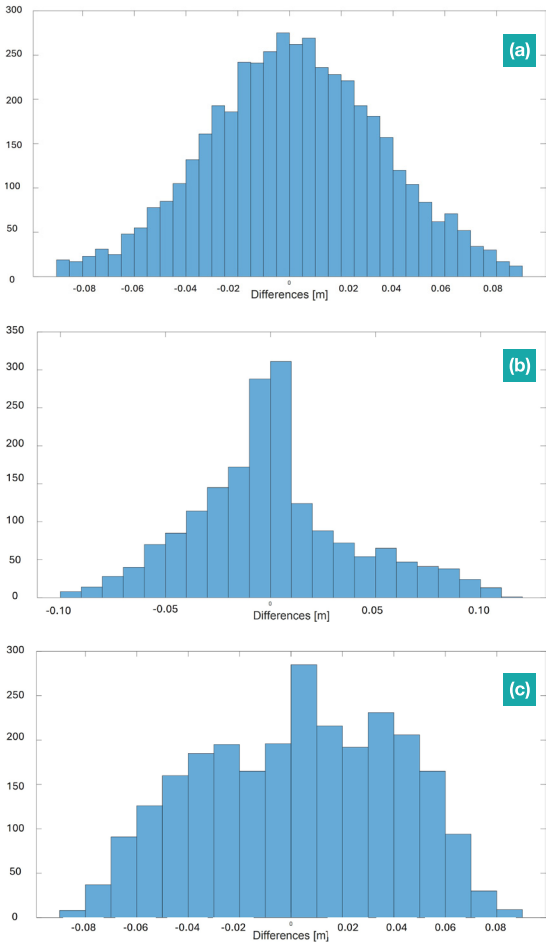


Fig. 8 Histograms displaying the differences between the adjusted undulation surface based on two voyages in relation to the measurements of the third voyage: (a) 2019 and 2020, and the measurements from the 2021 voyage. (b) 2019 and 2021, and the measurements from the 2020 voyage. (c) 2020 and 2021, and the measurements from the 2019 voyage.

Based on the results, it can be concluded that the accuracy of the adjusted surface, when compared to field measurements, is better than 2 cm. This precision indicates that the various sailing profiles conducted over the three years (2019–2021) were successfully integrated, and the linear surface aligns well with them.

Before proceeding, we would like to assess the quality of the modeling performed, and to achieve this, a cross-validation of the data was conducted. A linear surface was adjusted based on two voyages, and the resulting model was tested against the third voyage. In Fig. 8a, the histogram displays the differences between the geoid undulation surface adjusted using surveys from 2019 and 2020 and the measurements from the voyage conducted in 2021. The maximum difference is 0.090 m, the average absolute difference is 0.027 m, and the RMS is 0.034 m. Fig. 8b displays the histogram of the differences between the geoid undulation surface adjusted using surveys from 2019 and 2021 and the measurements from the voyage conducted in 2020. The maximum difference is 0.111 m, the average absolute difference is 0.029 m, and the RMS is 0.038 m. Fig. 8c displays the histogram of the differences between the geoid undulation surface adjusted using surveys from 2020 and 2021 and the measurements from the voyage conducted in 2019. The maximum difference is 0.088 m, the average absolute difference is 0.032 m, and the RMS is 0.037 m. The results of the cross-validation are summarized in Table 1. This also highlights the fact that the data collected in 2021 was significantly less comprehensive than that collected in 2019 and 2020. A comparative analysis was conducted to align the 2021 dataset with the values from the other two years, revealing that most errors or deviations originated from the 2021 data.

Yet, it is evident that the surface model, derived from only two voyages, aligns well with the results of the third voyage, indicating successful integration of the profiles. The accuracy of the surface is demonstrated to be better than 4.0 cm.

5 Expanding and improving the Israeli geoid undulation model

The estimated geoid undulation surface in the region covered by the experimental voyages can be incorporated with the existing official geoid model in Israel to construct an extended undulation model along the Haifa coast.

The official geoid model in Israel is called ILUM (IsraeL Undulation Model) and the current version is ILUM2.0 which is in use from 2007 (Even-Tzur & Steinberg, 2009). The model utilizes approximately 900 points with known orthometric and ellipsoidal heights, allowing for discrete estimations of the difference between the local Israel vertical datum and the

https://doi.org/10.58440/ihr-30-2-a10

Table 1 Cross-Validation summary: Linear surface adjustment based on two voyages tested against the third voyage.

Based on	Tested	Maximum difference [m]	Average absolute difference [m]	RMS [m]
2019 and 2020	2021	0.090	0.027	0.034
2019 and 2021	2020	0.111	0.029	0.038
2020 and 2021	2019	0.088	0.032	0.037

WGS84 ellipsoid. Kriging interpolation is used to compute the local Israeli geoid undulation model (Tuchin, 2006), and the accuracy of the official geoid model is better than 5 cm (Steinberg et al., 2021). The westernmost model points are located along the coastline of the Mediterranean Sea, with distances ranging from 1 to 3 km from the shoreline. As a result, the model does not cover the coastal region of Israel, requiring extrapolation for geoid heights in that area.

After computing a local geoid model derived from three years of surveying in the Haifa Bay, it can be seamlessly integrated into the official Israel model. The local geoid model was integrated with the official undulation model ILUM2.0 to create a new model that extends into Haifa Bay. The geostatistical kriging interpolation method is employed to construct the extended undulation surface, as the official undulation model relies on this interpolation technique. The newly developed model encompasses the southern region of the Bay of Haifa, facilitating the determination of geoid heights in that specific area. Directly comparing the undulation values obtained from the extended model with those from ILUM2.0 is not feasible due to the uncertainty surrounding the error introduced by the model in extrapolated areas. Consequently, to assess the accuracy of the new model, actual values of geoid heights were derived from supplementary measurements.

Nine points, numbered from 1L to 9L, were established on the wharves at the new HaMifratz port in collaboration with the Survey of Israel (refer to Fig. 5, dashed red rectangle). These points are situated 3 to 4 km away from the western and southern points utilized by the official geoid undulation model in the area. The points were measured using GNSS RTK in multiple sessions to determine their ellipsoidal heights. Their height accuracy is approximately 1 cm. Additionally, precise leveling was employed to measure the orthometric height differences between these points, achieving an accuracy of 5 mm/km. Since the leveling measurements were conducted within a small area, the measured height difference can be considered the orthometric height difference between the points. These measured height differences served as the ground truth for comparison. Subsequently, based on the ellipsoidal heights and geoid heights derived from each model, the orthometric height differences between the points were calculated and compared to the actual orthometric height differences.

The decision was made not to analyze the height differences between consecutive points; rather, the focus was on examining the height differences between each point and point 1L. The assumption was that if the official model introduces an error into the extrapolated values, it will escalate as we move away from the boundaries of the official model. Examining the height differences in this arrangement facilitates the easier identification of potential errors. Table 2 provides a summary of the comparison results between the actual height differences and those obtained using both models, combined with the ellipsoidal heights.

Based on the results presented in Table 2, it can be reasonably asserted that the expanded geoid model yields slightly superior outcomes compared to those provided by the official model. The improvement observed in the expanded model appears to be marginal. However, it is crucial to note that there are no significant geoid changes in this area. Consequently,

Table 2 Summary of height differences between the points and the differences between the uses of both undulation models.

	ΔH (Leveling)	ΔH (GPS + ILUM2.0)	ΔH (GPS + new model)	ΔH (Leveling) – ΔH (GPS + ILUM2.0)	ΔH (Leveling) – ΔH (GPS + new model)
	[m]	[m]	[m]	[m]	[m]
1L–2L	-0.019	-0.011	-0.013	-0.008	-0.006
1L–3L	-0.556	-0.545	-0.547	-0.011	-0.009
1L–4L	-1.349	-1.336	-1.339	-0.013	-0.010
1L–5L	-1.235	-1.221	-1.224	-0.014	-0.011
1L–6L	-1.069	-1.057	-1.059	-0.012	-0.010
1L–7L	-0.883	-0.872	-0.875	-0.011	-0.008
1L–8L	-0.227	-0.215	-0.218	-0.012	-0.009
1L–9L	-0.204	-0.193	-0.194	-0.011	-0.010
Absolute Average				0.012	0.009

it is feasible to obtain reasonably accurate geoid heights from the official model, regardless of the extrapolation. Nevertheless, one might assume that when comparing points situated farther away from the coast, the results from the official model could exhibit notably lower quality compared to those obtained from the expanded model.

6 Summary and conclusions

It has been demonstrated that a single shipborne GNSS receiver and nautical measurements enable the acquisition of high-quality geoid heights. The method presented facilitates obtaining local coastal geoid heights with good accuracy at a lower cost compared to airborne or shipborne gravity measurements. Data is readily available from any controlled hydrographic survey using state of the art calibrated equipment. The essential factor for obtaining valuable geoid heights lies in the rigorous processing of raw GNSS data, incorporating corrections for the vessel's dynamic movement, tidal influence, atmospheric changes, and sea surface topography.

Between 2019 and 2021, multiple cruises were conducted along Haifa's coast in Israel as part of an experimental study aimed at expanding the official Israeli geoid undulation model to its coastal region. The study delineates the essential steps for creating a comprehensive spatial representation of the geoid undulation model and compares the outcomes of the official Israeli geoid undulation model with the extended model, including an assessment of their respective accuracies.

Throughout the process of integrating profiles and generating a spatial image of the geoid undulation, the accuracy of the integration between different cruises was assessed, revealing an accuracy of better than 3.0 cm.

The approach of approximating the geoid with a linear surface is locally justified but may not scale to larger regions with significant MDT variations. Investigating MDT variations along the Israeli coast is necessary to determine the applicability and limitations of this method in larger areas.

As the official geoid model of Israel does not extend to its coastal area, the main goal of implementing this approach in our region was to improve the official geoid undulation model by integrating the measured marine geoid undulations and extending it to the maritime environment. After incorporating the measured values into the official model, its ability to provide accurate geoid undulation values in the new HaMifratz port was evaluated. The study results reveal a noteworthy enhancement in the performance of the new expanded model compared to the official model. The improvement was achieved despite the generally mild geoid slope in the shallow Haifa Bay area, supporting the use of a linear geoid undulation surface model for accurate representation. This emphasizes the importance and necessity of integrating the new approach with conventional measurements.

Geoid models in coastal areas still exhibit lower quality compared to terrestrial and open sea areas. In some cases, no model exists for coastal regions, as existing models only cover the country's land area. Therefore, enhancing geoid model capabilities by utilizing shipborne GNSS measurements can contribute to expanding the terrestrial geoid undulation model. Extracting the geoid in a coastal marine environment enables the extension of the national geoid undulation model into the maritime area of the State of Israel. Subsequently, this facilitates obtaining geoid undulation values up to the coastline and extending the geoid undulation model derived from altimetry satellites to the actual coastline.

The demonstrated method can be employed not only to generate a spatial representation of geoid undulations in coastal areas but also to accurately measure sea surface height in those regions. Continuous monitoring of coastal sea levels is essential due to fluctuations and the high concentration of the global population residing in such areas. However, conventional measurement methods, like tide gauges and satellite altimetry, have limitations, each with significant drawbacks. While tide gauges can precisely track sea level changes, they lack the capability to provide spatial information. Satellite altimetry, on the other hand, can offer spatial information, but its time and space resolution are limited, and its accuracy in coastal areas is subpar. The method presented in this research combines the benefits and strengths of existing measurement techniques. The measurements are spatially comprehensive, possess high resolution and accuracy. They maintain quality when applied in coastal areas, all while avoiding exorbitant costs especially when utilizing readily available data collected in hydrological surveys.

In essence, a geoid undulation model provides valuable information for comprehending and addressing the intricacies of coastal areas, playing a pivotal role in various applications such as coastal engineering, geospatial analysis, and environmental monitoring. Shipborne GNSS and nautical measurements stand as a valuable addition to geoid undulation modeling in coastal regions. When seamlessly integrated with other geodetic and gravimetric data sources, these measurements contribute significantly to enhancing the overall accuracy of the resultant model.

https://doi.org/10.58440/ihr-30-2-a10

References

Andersen, O. B. and Knudsen, P. (2009). DNSC08 mean sea surface and mean dynamic topography models. *Journal of Geophysical Research: Oceans, 114*(C11).

Duquenne, H., Olesen, A.V., Forsberg, R. and Gidskehaug, A. (2002). Improvement of the gravity field and geoid around Corsica by aerial gravimetry. *Gravity and Geoid*, pp. 167–172.

Even-Tzur, G. and Steinberg, G. (2009). Using an official undulation model for orthometric height acquisition by GNSS. *Survey Review, 41*(313), pp. 292–300.

Forsberg, R., Olesen, A.V., Keller, K., Møller, M., Gidskehaug, A. and Solheim, D. (2001). Airborne gravity and geoid surveys in the Arctic and Baltic seas. *Proceedings of international symposium on kinematic systems in geodesy, geomatics and navigation (KIS-2001)*, Banff, pp. 586–593.

Härting, A., Reinking, J. and Ellmer, W. (2004). Ship Squat in Hydrography – A study of the surveying vessel Deneb. *The International Hydrographic Review, 5*(3), pp. 41–47.

Huang, J. (2017). Determining coastal mean dynamic topography by geodetic methods. *Geophysical Research Letters, 44*(21), pp. 11–125.

Huber, P. J. (1981). *Robust Statistics*. Wiler. New York.

Krarup, T., Juhl, J. and Kubik, K. (1980). Götterdämmerung over least squares adjustment. *Proceedings of the 14th Congress of the International Society for Photogrammetry*, pp. 369–378, Hamburg, Germany.

Kuroishi, Y. (2009). Improved geoid model determination for Japan from GRACE and a regional gravity field model. *Earth, planets and space, 61*(7), pp. 807–813.

Lavrov, D., Even-Tzur, G. and Reinking, J. (2015). Extraction of geoid heights from shipborne GNSS measurements along the Weser River in northern Germany. *Journal of Geodetic Science, 5*(1).

Lavrov, D., Even-Tzur, G. and Reinking, J. (2017). Expansion and improvement of the Israeli geoid model by shipborne GNSS measurements. *Journal of Surveying Engineering, 143*(2), p. 04016022.

Lu, B., Barthelmes, F., Li, M., Förste, C., Ince, E.S., Petrovic, S., Flechtner, F., Schwabe, J., Luo, Z., Zhong, B. and He, K. (2019). Shipborne gravimetry in the Baltic Sea: Data processing strategies, crucial findings and preliminary geoid determination tests. *Journal of Geodesy, 93*, pp. 1059–1071.

Saari, T., Bilker-Koivula, M., Koivula, H., Nordman, M., Häkli, P. and Lahtinen, S. (2021). Validating geoid models with marine GNSS measurements, sea surface models, and additional gravity observations in the Gulf of Finland. *Marine Geodesy, 44*(3), pp. 196–214.

Steinberg, G., Even-Tzur, G., Ronen, H., Sarid, H. and Dalyot S. (2021). The Development of the Israeli Official Geoid Model. *FIG e-Working Week, virtually in the Nederland, 21-25 June 2021*.

Tuchin, Y. (2006). Development of a Geoid-Ellipsoid Separation Model in Israel. *Shaping the Change, XXIII FIG Congress*, Munich, Germany.

Varbla, S., Ellmann, A. and Delpeche-Ellmann, N. (2020). Validation of marine geoid models by utilizing hydrodynamic model and shipborne GNSS profiles. *Marine Geodesy, 43*(2), pp. 134–162.

Wang, Y. M., Sánchez, L., Ågren, J., Huang, J., Forsberg, R., Abd-Elmotaal, H.A., Ahlgren, K., Barzaghi, R., Bašić, T., Carrion, D. and Claessens, S. (2021). Colorado geoid computation experiment: overview and summary. *Journal of Geodesy, 95,* pp.1–21.

Woodworth, P. L., Hughes, C. W., Bingham, R. J. and Gruber, T. (2012). Towards worldwide height system unification using ocean information. *Journal of Geodetic Science, 2*(4), pp. 302–318.

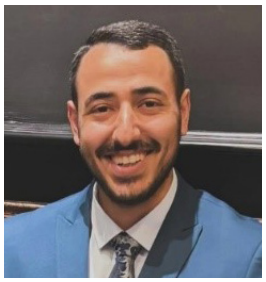
Xu, X. Y., Xu, K., Xu, Y. and Shi, L.W. (2019). Coastal altimetry: a promising technology for the coastal oceanography community. *Estuaries and Coastal Zones-Dynamics and Response to Environmental Changes*, pp. 1– 9. IntechOpen.

Authors' biographies



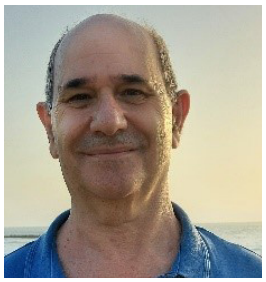
Gilad Even-Tzur

Gilad Even-Tzur is an Associate Professor with the Technion – Israel Institute of Technology, Faculty of Civil and Environmental Engineering. He serves as the head of the Division of Mapping and Geo-Information Engineering.



Jareer Khalilieh

Jareer Khalilieh earned his Master's degree with honors from the prestigious Technion Institute of Technology. Throughout his career as a mapping and geo-information engineer, he contributed to cutting-edge surveying projects, with a research focus on GNSS technology, geodetic network optimization, and high-precision measurement techniques. His expertise in hydrographic and cadastral surveying allowed him to tackle complex geospatial challenges with innovative solutions. In addition, Jareer embarked on developing a start-up, striving to revolutionize the field of geospatial technologies and push the boundaries of modern surveying.



Barry Grinker

Barry Grinker graduated from the US Naval Postgraduate School earning a MSc degree in Hydrographic Sciences in 1991. He served as Head of the Israel Navy Hydrographic Branch until retiring in 2005. Since 2001 Barry has been lecturing Marine Surveying at the Haifa Technion in the Mapping and Geo-information department in the Civil and Environmental Engineering faculty.

https://doi.org/10.58440/ihr-30-2-a10

PEER-REVIEWD ARTICLE

Satellite navigation interference monitoring in the Baltic and North Seas

Authors

Thiago Azevedo de Vasconcelos[1], Lothar Kurz[1], Andriy Konovaltsev[1], Tobias Ehlers[2] and Michael Meurer[1,3]

Abstract

The threats scenario of radio-frequency interference in maritime domain has been assessed through the results of measurement campaigns in the Baltic and North Seas. This work presents the monitoring equipment deployed for real-time interference detection and displaying capabilities, allowing live assessment of the interference impacts. The measurement system and the results of the post-campaign processing of the recorded data are described characterizing the observed interference signals and the impact on the satellite-based navigation of GPS L1/L5 and Galileo E1/E5a open services. The geographical distribution of the interference events and the severity of the situation is discussed.

Keywords

GNSS · radio-frequency interference · maritime · measurement campaign · signal processing

Resumé

Le scénario de menaces d'interférences radiofréquences dans le domaine maritime a été évalué grâce aux résultats des campagnes de mesure dans la mer Baltique et la mer du Nord. Ce travail présente l'équipement de surveillance déployé pour la détection des interférences en temps réel et les capacités d'affichage, permettant l'évaluation en direct des impacts des interférences. Le système de mesure et les résultats du traitement post-campagne des données enregistrées sont décrits pour caractériser les signaux de brouillage observés et l'impact sur la navigation par satellite des services ouverts GPS L1/L5 et Galileo E1/E5a. La distribution géographique des interférences et la gravité de la situation sont discutées.

Resumen

El escenario de amenazas de interferencias a las radiofrecuencias en el ámbito marítimo se ha evaluado a través de los resultados de campañas de medición en los Mares Báltico y del Norte. Este trabajo presenta el equipo de seguimiento desplegado con capacidad de detección y presentación de interferencias en tiempo real, permitiendo la evaluación en directo de los impactos de las interferencias. Describe el sistema de medición y los resultados del procesamiento posterior a la campaña de los datos registrados, caracterizando las señales de interferencia observadas y el impacto en la navegación por satélite de los servicios abiertos GPS L1/L5 y Galileo E1/E5a. Se debate la distribución geográfica de los eventos de interferencia y la gravedad de la situación.

✉ Thiago Azevedo de Vasconcelos · thiago.azevedodevasconcelos@dlr.de

[1] German Aerospace Center (DLR), Institute of Communications and Navigation, 82234 Wessling, Germany

[2] German Federal Maritime and Hydrographic Agency, Navigation and Communication, 20359 Hamburg, Germany

[3] RWTH Aachen University, Chair of Navigation, 52074 Aachen, Germany

https://doi.org/10.58440/ihr-30-2-a13

1 Introduction

Global navigation satellite systems (GNSS), such as the American GPS and the European Galileo, have very low-power received signals, sitting even bellow the noise level of a typical receiver, due to the long propagation paths between satellites and Earth receivers. For this reason, the system is considerably vulnerable to interference signals, which might come from varied sources, from TV stations to portable privacy devices (Dovis, 2015). Non-intentional GNSS interference might be caused by spurious transmissions generated by faults on electronic systems, by natural phenomena like solar bursts, and by other electronic systems sharing the spectrum, such as Aeronautical Radio-Navigation Services (ARNS) whose signals give support to the navigation of aircrafts. Intentional interference is caused by a malicious agent whose objective is to disrupt navigation by jamming or spoofing the signal. Jammers operate by emitting strong signals that saturate the GNSS receiver, and thus makes it blind to the satellites. Spoofers, as described in Günther (2014), intend to cause wrongful operation of the receiver, leading to integrity risks. Usually spoofing is achieved through the emission of fake GNSS signals carrying false positioning information. An overview of different types of GNSS interference and corresponding countermeasures can be found in Morales-Ferre et al. (2019).

Because of the ever-increasing reliance of the modern world on GNSS services (e.g. localization for transports, and time synchronization for banking systems), and the growing number of interference events, the attention on the threats posed by the GNSS interference has increased, bringing about efforts to closely monitor the situation and counteract accordingly. Because of good visibility of interference sources at the flight altitudes of airplanes even at long distances, the aviation community was probably one of the first alarmed and starting to search for efficient countermeasures (Duchet & Berz, 2018). The threat of GNSS jamming and spoofing was also recognized in the maritime domain leading to the inclusion of potential countermeasures in the e-Navigation plan issued by the International Maritime Organization (IMO, 2018). For supporting the identification of the suitable countermeasures, possible impact of GNSS jamming and spoofing on maritime navigation has been experimentally studied by several research groups (Grant et al., 2009; Medina et al., 2019; Bhatti & Humphreys, 2017; Appel et al., 2019). Although some large interference events got well known to the GNSS community, see for example a detailed analysis of so-called Black Sea spoofing event in C4ADS (2019), the actual interference situation experienced by the GNSS users in the maritime domain on the everyday basis is, however, not really well studied. While the interference threat scenarios for GNSS users in the aviation and ground-based navigation domains can be well assessed using information from multiple measurements campaigns (Dumville, 2018; Thombre et al., 2017; Gerrard et al., 2021; Sokolova et al., 2022) and existing monitoring capabilities (Jada, 2022; Raghuvanshi et al., 2024; Wiseman, 2022; Liu et al., 2023; SkAI-Data-Services, 2023) only few maritime-dedicated campaigns have been carried out in the past (Pérez-Marcos et al., 2018).

In this regard, the German Aerospace Center (DLR) in partnership with the German Federal Maritime and Hydrographic Agency (BSH) and the Maritime German Federal Police (BPol See) conducted measurement campaigns in the Baltic and North Seas to assess the current situation of the interference scenario in maritime. Three prototypes of an interference detection and monitoring system suitable for maritime applications have been developed on the basis of the DLR's GALANT receiver platform (Cuntz et al., 2008). Thanks to the measurement campaigns, a wealth of raw signal data and receiver observables could be gathered allowing for the characterization of the many interference events through signal processing. With these, the scenario of interference in maritime domain could be profiled with respect to the days and months, and to their location of occurrence.

In Section 2 the developed prototypes are presented with their antennas and electronic components. They provide extended monitoring capabilities thanks to the use of array antennas for signal reception, as has been proven in past in the maritime domain (Konovaltsev et al., 2017). The array provides spatial diversity for navigation and interference signals impinging from different directions resulting in the capacity of direction-of-arrival estimation, leading to the identification of interference sources in some situations. The prototypes allow also for real-time monitoring of the quality of the navigation signals and the signal spectra in two domains: GPS L1/Galileo E1 around 1575.42 MHz, and GPS L5/Galileo E5a around 1176.45 MHz.

Section 3 presents the interference detection strategies based on statistical and spatial signal processing, which also allowed for the identification and characterization of interference signals. Depending on the type of signal waveform, an interference event can be more or less destructive to the nominal GNSS signals reception. Further in Section 4, the perspective of the maritime interference scenario is presented with the geographical distributions of the relevant interference events in L1 and in L5. In Section 5, conclusions are drawn on the current threat level on the maritime domain.

2 Monitoring platform

Three prototypes of a system for detecting GNSS interference in the form of jamming and spoofing signals have been developed in order to allow the measurement campaigns and to prepare suitable monitoring solutions to be used by state authorities in the maritime domain such as BSH and BPol See. The interference detection was carried out for the civil signals of Galileo and GPS in E1/E5a and L1/L5 bands.

https://doi.org/10.58440/ihr-30-2-a13

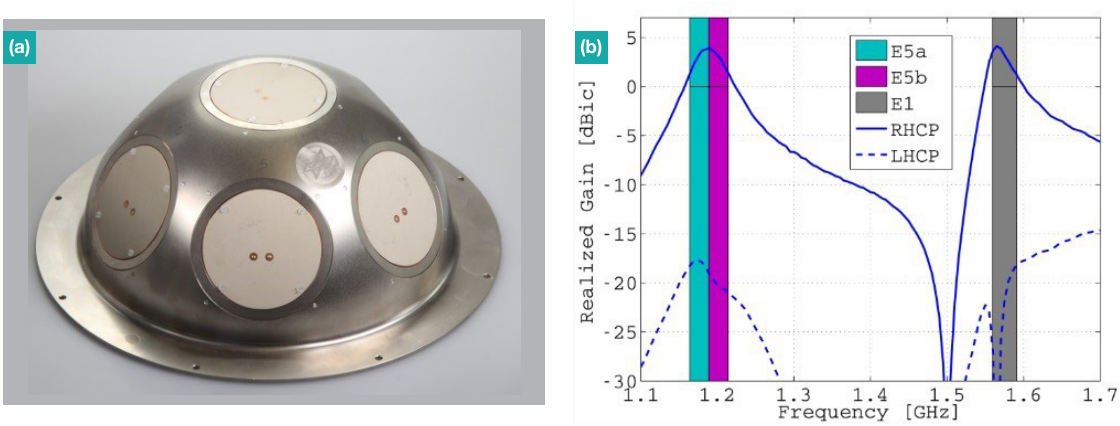


Fig. 1 L1/L5 antenna array used in first and third measurement campaigns. Side view (a), and frequency response of a single antenna (b).

In the last two prototypes, a suitable graphical user interface presenting information about the detected interference signals and status of GNSS-based navigation in an intuitive and concise form was one of the main design goals.

The prototype development was based on the GALANT flexible multi-antenna receiver platform that has being developed by the Institute of Communications and Navigation of DLR since 2008. The multi-antenna strategy adopted by the GALANT platform allows for exploring spatial diversity, i.e. discriminating received signals by their directions of arrival (DoA), and increasing the receiver's robustness to radio-frequency interference (RFI) (Heckler et al., 2011; Antreich et al., 2015).

In the first and third prototypes, a maritime version of the array consisting of seven antenna elements disposed in a hemispherical platform was used. In the array, six elements are arranged radially and the seventh is placed on the top as shown in Fig. 1. The patch antenna elements allow for dual-frequency reception in both L1/E1 and L5/E5a bands. The antenna array is connected to the radio-frequency (RF) front-ends capable of processing information from the seven antennas with two channels, L1 and L5, allocated for each antenna element. The front-end operates at the intermediate frequency of 75 MHz with a bandwidth of 20 MHz for L1 and 24 MHz for L5. The analog intermediate-frequency (IF) outputs of the frontends are connected to a Nutaq PicoDigitizer digital signal processing platform. For sampling, the platform uses a bank of 14-bits analog-to-digital (ADC) converters operating at 100 Msps sampling rate. The signal samples of all antennas at both frequency bands were recorded not continuously but in the form of snapshots, each of 30 ms long. The snapshot recording was triggered either on a regular basis for system monitoring purpose every 10 minutes or each time when GNSS interference is detected (Konovaltsev et al., 2017). Two ADCs are used for each array element because of the dual-band operation. The output power of the RF front-ends is fixed so that only 3–4 bits are used in nominal interference-free signal conditions and the most of the ADC dynamic range is preserved for strong interference signals. In this way, no automatic gain control is used and the increase of the received RF power due to RFI can be directly observed. The pictures of the hardware are reproduced on Fig. 2.

On the second measurement campaign, in 2022 on board of a ship of BPol See, a monitoring system prototype base on a miniaturized version of the GALANT platform, which was operated as an array GNSS receiver, was deployed. In order to enable the interference detection and monitoring, the array receiver was extended to produce several test metrics as described later. While this platform has a small form factor and reduced cost, only four antennas and single-band operation can be supported. Therefore, a four-elements array shaped in a two-by-two square grid was used in this case (Fig. 3). Each of the array elements operates on GPS L1/Galileo E1.

The digital hardware of the miniaturized GALANT is based on a PicoZed-type system-on-module (SoM) mounted on top of a commercial base-board. The SoM is equipped with a Xilinx system-on-chip formed by a field-programmable gate array (FPGA), which enables simultaneous parallel processing of the four antenna channels, and a central processing unit (CPU), which allows for fast data exchange between the FPGA and a generic processor (Fig. 4).

The prototype based on the miniaturized GALANT was deployed with a tablet running a graphical user interface (GUI) allowing the user to monitor in



Fig. 2 Hardware of prototypes of interference monitoring system used in first and third campaigns. Two multi-antenna RF front-ends below the Nutaq PicoDigitizer on top.

https://doi.org/10.58440/ihr-30-2-a13

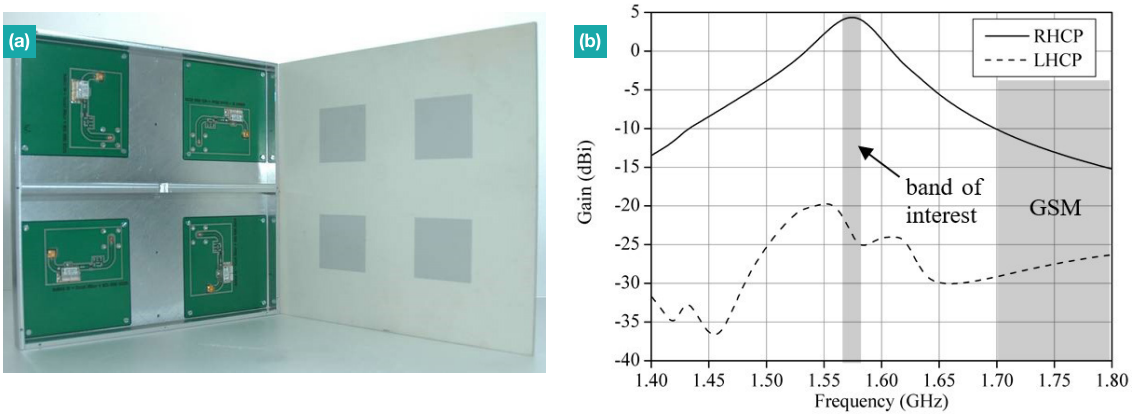


Fig. 3 L1 antenna array used with miniaturized version of interference monitoring system in second campaign. Square two-by-two antenna grid (a) and frequency response of a single antenna (b).

real-time the quality of the navigation signal and the directions of arrival of interference signals in form of an angular spectrum (Fig. 5). Among the signal quality metrics given by the GUI were: position information, the range accuracy, the quality of the satellites' signals represented by the ratio between the signal and noise power densities known as carrier-to-noise ratio (C/N0). In the angular spectrum, hotter colors depict stronger power impinging from the respective elevation and azimuth angles in the local Cartesian coordinates of the ship.

Following the GUI development from the second measurement campaign, on the third (and last) campaign, carried out again on board of the BSH ship, a graphical user interface was added to the monitoring system prototype as shown in Fig. 6. The user interface was displayed on a dedicated notebook. The GUI panels on the upper part show GNSS signal quality metrics such as the user position information, sky-plot of visible and used GNSS satellites as well as C/N0 bar plot. The lower half of the GUI screen presents several RF-level characteristics of the received antenna signal: angular spectrum allowing for identifying the angle of arrival of an interference signal as well as power spectrum density and spectrogram allowing for monitoring the behavior of an interference signal in time and frequency domains. Also, a commercial L1/L5 receiver, NEO-F10T of u-blox, was integrated in the monitoring system. The objective of that receiver was two-fold: to assess the actual interference effect on a typical commercial receiver, and to compare the interference detection available in the commercial receiver with the one provided by the system prototype. The use of commercial GNSS receivers for the RFI detection purposes is considered to be a practical option, especially in case of large area monitoring (Jada et al., 2022; Dimc et al., 2017).

3 Data analysis

3.1 Detection through signal and statistical processing

Due to the power of GNSS signals sitting below background noise level, the digital samples follow the Gaussian distribution characteristic of white noise samples. Moreover, GNSS signals are modulated with pseudo-random noise (PRN) codes at transmission, which allow them to be recovered even if the signal power is below that of noise. The latter, because of its properties similar to thermal noise, also causes the signal to have Gaussian distribution. For these two reasons, the shape of nominal signals (i.e. in interference-free scenarios) distributions is known to be approximately Gaussian.

Thus, increases in the received power caused by interference signals change the statistical distribution of the digital samples, and such changes can be

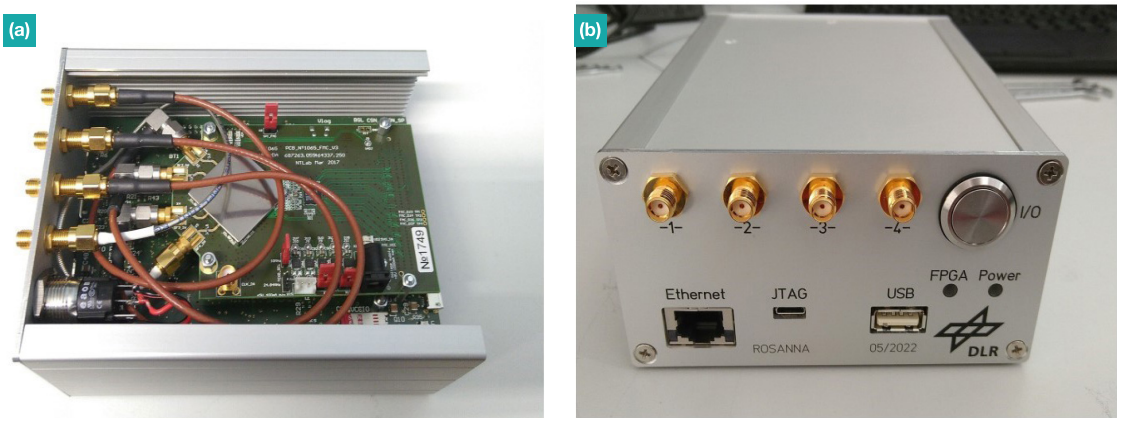


Fig. 4 Top- (a) and front-view (b) of the case with the four antenna channels containing the hardware of miniaturized version of interference monitoring system used in the second campaign.

detected via statistical methods that count the number of samples lying beyond pre-determined thresholds (Konovaltsev et al., 2009; Motella & Lo Presti, 2014). The thresholds are determined in laboratory to take into account the physical characteristics of the antennas and hardware when capturing signals in nominal conditions. A priori this threshold calibration can be made to implement the algorithm to any antenna and front-end designed to operate in GNSS frequencies. As depicted on Fig. 7, if power is increased due to interference too many samples lie beyond the thresholds, triggering the detection.

This type of power-based detection method is more suitable to detect interference signals with elevated power, i.e. usually jamming signals. However, as already shown in Akos (2012), even spoofing signals can be detected using power-based methods. Specifically, the publication monitors the Automatic Gain Control (AGC), which is implemented in the RF front-end and controls the gain of the incoming signal to adjust it to the ADC dynamic range and avoid receiver saturation. This gain serves as a metric for RFI detection. In GALANT, as already stated, there is no AGC but the very wide dynamic range of the ADCs allow for the observation and recording of RFI signals with good definition without saturation.

The signal power variations $\Delta P_{in,dB}$ due to interference have been profiled throughout the campaign as the increase of the average input power P_{in} of the n^{th} signal snapshot with respect to the nominal level – described by Eq. 1 and depicted on Fig. 8. The nominal level is represented by the expectation of the input power in nominal conditions $\mathbb{E}(P_{in,nom})$, and it was approximated by the mean of the average snapshot input power not flagged with interference in a selected time-window (e.g. a week of recordings). This metric was computed specifically for the top antenna of the array as it is representative of usual commercial receivers for possessing small low-elevation gains for being oriented upwards. With the power variations of interference events, they were classified in weak, medium and strong.

$$\Delta P_{in,dB}(n) = 10 \log \left(\frac{P_{in}(n)}{\mathbb{E}(P_{in,nom})} \right) \quad (1)$$

From the measurement campaigns, many different types of interference signals were recorded, and their waveforms could be identified from their time-frequency representation in their spectrograms (Fig. 9).

With these two information, the relevant interference events could be identified as caused by strong power signals with waveforms close to the GNSS center

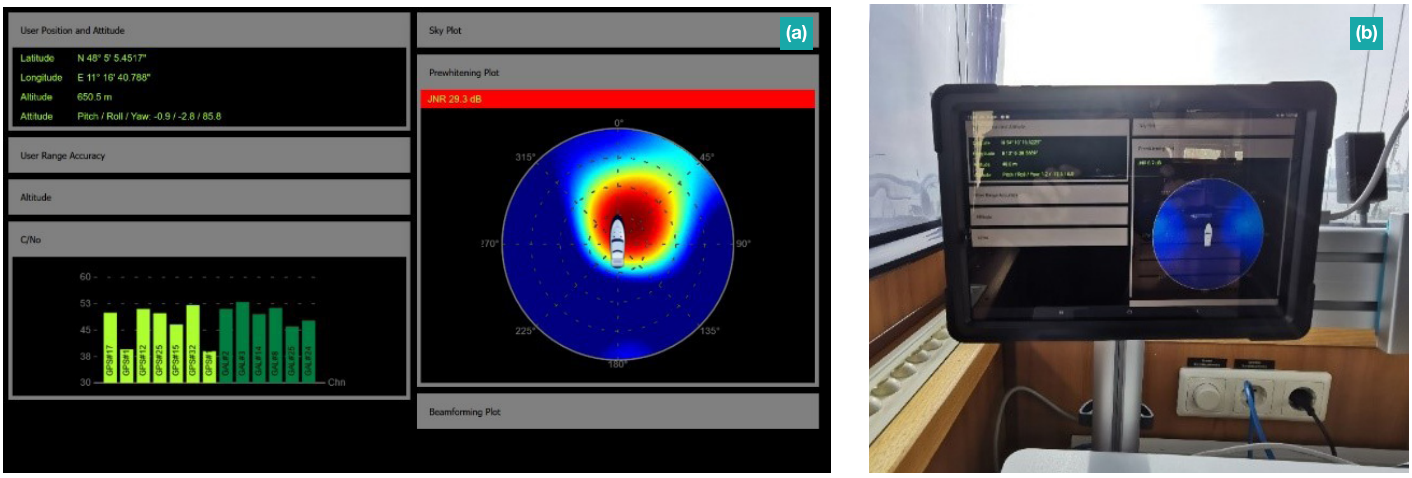


Fig. 5 GUI of miniaturized version of interference monitoring system. GUI information panels from laboratory test (a) and tablet running GUI on board of ship (b).

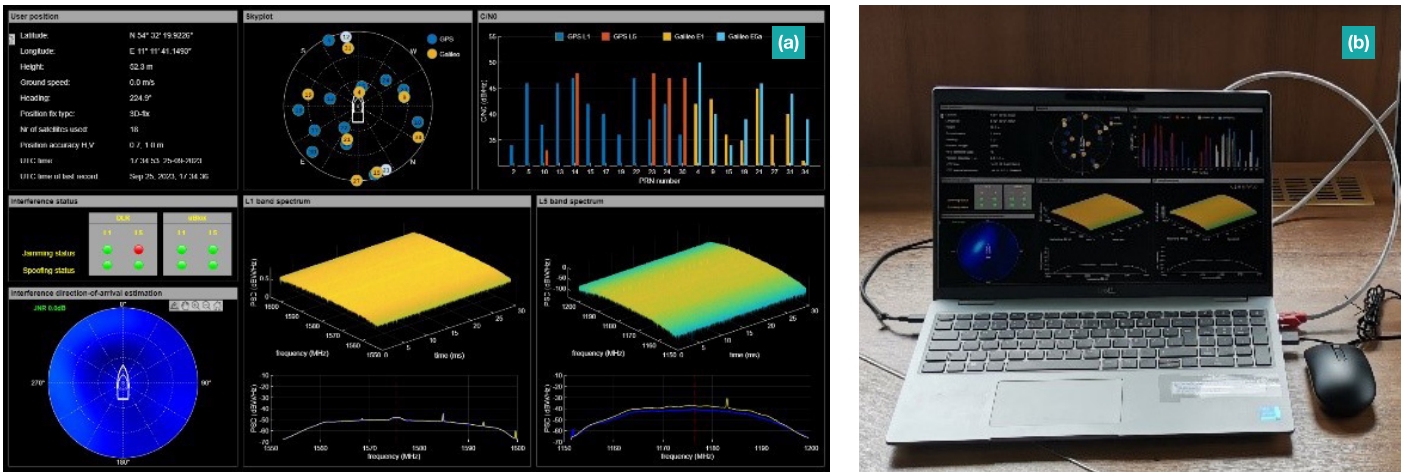


Fig. 6 GALANT Platform GUI in the third measurement campaign. Screenshot of the GUI in operation (a) and GUI continuously running on display laptop (b).

https://doi.org/10.58440/ihr-30-2-a13

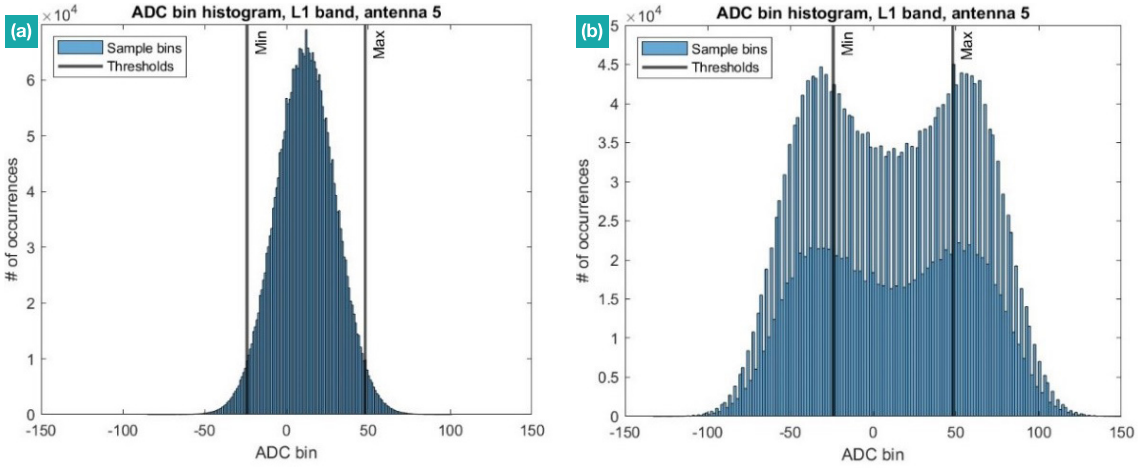


Fig. 7 Digital Samples of the Received Signal. Nominal case from June 26, 2021 at 10:21:43 MET (a) and RFI case from June 26, 2021 at 11:30:03 MET (b).

frequency of the respective system (e.g. the continuous-wave RFI close to the 1575.42 MHz carrier of GPS L1 in Fig. 9) or considerably overlapping the spectrum of the GNSS signal (see the wideband RFI in Fig. 9). It steered the data analysis, because these signals are the most efficient to cause degradation or the complete loss of navigation given their high power and their spectral match with the nominal signal.

Moreover, the analysis of the signal type made possible the identification of the source of the interference in some situations, as it was the case with signals emitted by ARNS base stations, which possess highly structured signals whose waveforms are known.

3.2 Detection through spatial processing

Another method used in the developed system prototypes to detect interference was based on spatial processing using the signals coming from the multiple antenna channels of the receiver. Given the geometries and the number of antennas, the system is capable of performing spatial processing for the estimation of the interference signals DoA, and consequently for the protection of the receiver by nulling the receiving power impinging from the estimated direction.

The capacity of interference detection relied primarily on the monitoring of a so-called pre-whitening screen which scans the environment around the receiver and shows the regions with increased power coming from the respective direction, as depicted on Fig. 10. If a specific area of the environment around the receiver has increased power, it means stronger signals are impinging from the respective direction, indicating the presence of interference signals.

This spatial processing and identification of the strong signals DoA was exploited in Pérez-Marcos et al. (2018) to detect also spoofing. There the authors worked with spatial processing to indicate if a large number of satellite signals was being emitted from the same direction, which is usually the case for sophisticated spoofers. Dangerous spoofing attacks often transmit not a few but a large number of fake satellite signals corresponding to different satellites. Thus, whereas authentic satellite signals come from different directions from the sky, signals of a spoofer attack come from the same direction, which can be detected by the technique of Pérez-Marcos et al. (2018).

3.3 Detection through signal quality monitoring

The last class of techniques adopted to detect interference is based on the monitoring of signal quality

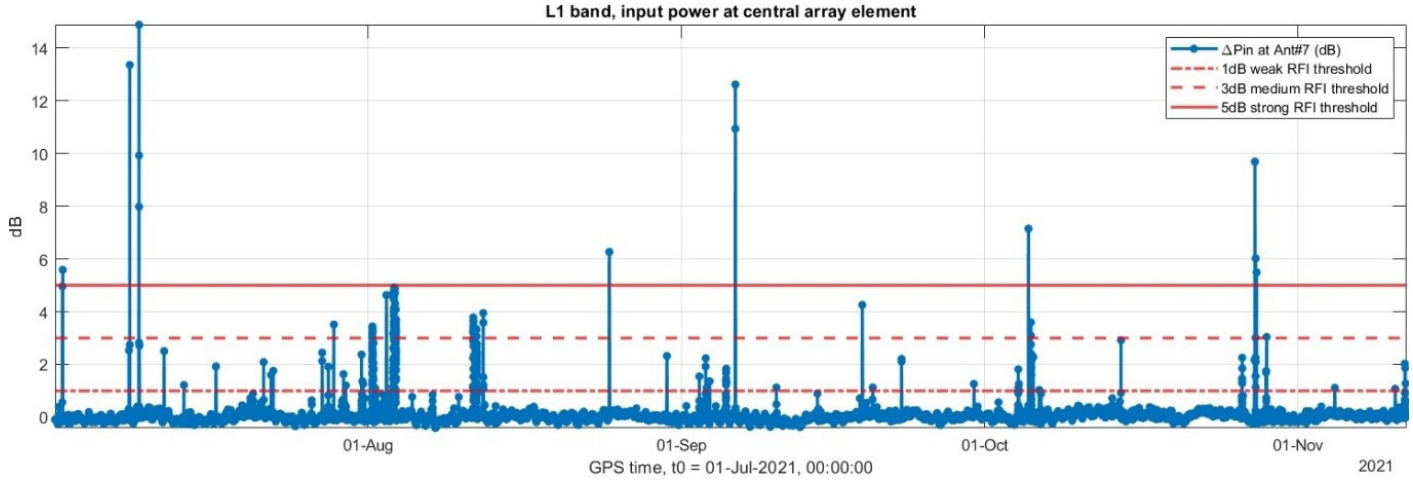


Fig. 8 Increase of the antenna array central element's input power due to RF interference in 2021.

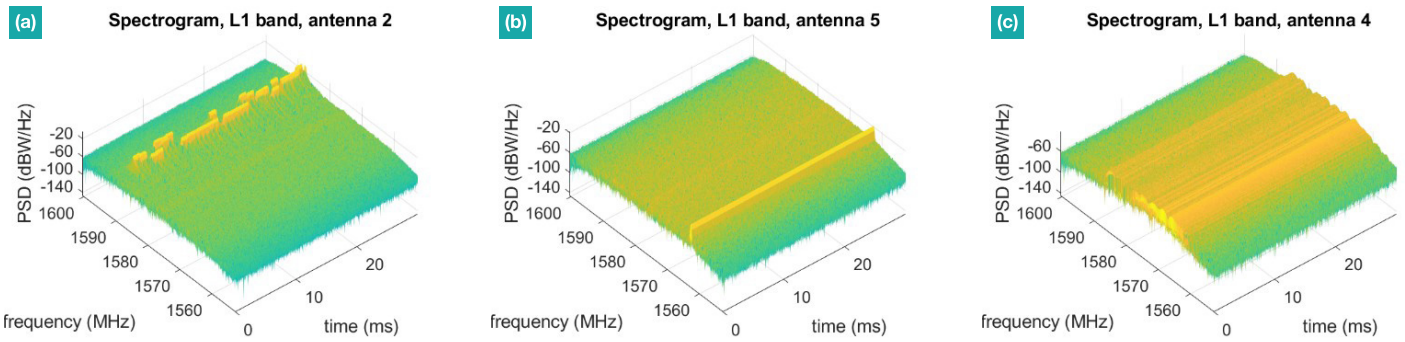


Fig. 9 Radio-frequency Interference Signal Types: narrowband multi-tone pulses (a), single-tone continuous-wave (b) and wideband chirp signal (c).

metrics that can indicate the presence of interference signals in the environment. Usually this approach might be misleading as the reduction of the signal quality might be due to suboptimal environmental conditions (e.g., hard weather conditions, physical coverage caused by tall buildings), or due to the absence of satellites in high-elevation. Because of these factors, the monitoring of the signal quality must be considered as an additional effort to help assessing the impact of interference events, or as supplementary method of interference detection.

One of these metrics is the Position, Velocity and Time (PVT) solution, which was evaluated in Tabatabaei Balaei et al. (2007) to assess the impact of interference, since receivers under interference heavy environments might not be able to accurately compute the PVT solution, or even to compute it at all. Another possibility is to monitor the drift in the PVT solutions: if the position and velocity change rate is suspicious (e.g., the navigation system is displaying a movement the receiver is not doing), or completely wrong.

Another widely used metric for monitoring is the C/N0, which represents the ratio between the power density of the signal of interest and the noise. This is a well-exploited metric to indicate the signal quality, and is often used even to decide if a tracked satellite should be or not considered for the PVT computation. As much as many factors may be sources of impairments that reduce the C/N0, it can still be used to monitor the presence of interference (Groves, 2005). Both of these metrics were adopted and used in the developed system prototypes, and are exemplified in Section 3.2.2.

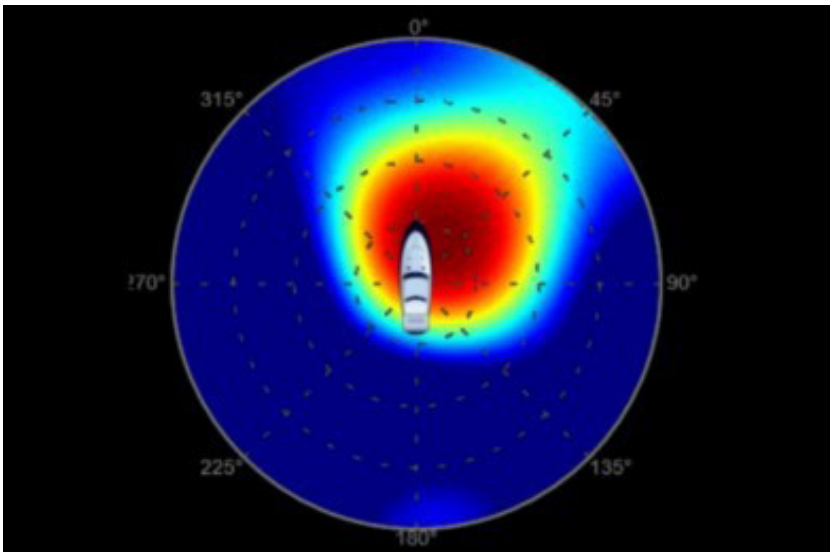


Fig. 10 Pre-whitening monitor displaying strong signal power in the environment from approximately 45° of rotation and 68° of elevation caused by test interference generated in laboratory.

3.4 Data processing

During the measurement campaigns data was processed automatically to detect interference signals and to display navigation information in real time. After the campaigns, the recorded data was further processed in laboratory to retrieve information on the interference nature: the signal waveform, the strength of the signals, and how it impacted the navigation capabilities of the receiver. Two sets of data were recorded: from the GALANT platform and from the u-blox receiver.

The GALANT raw data is recorded in binary files and is the output of the ADC in IF: the digitized samples of the real-signals of both L1/E1 and L5/E5a channels. It was processed in two steps: in pre and post-correlation domains. Correlation is the operation responsible for recovering the incoming signal from beneath the noise floor and for synchronizing it with the GNSS receiver. Signals modulated with the right satellite PRN code are enhanced while all the other are attenuated. A quick review on this process in the navigation receiver is described in Braasch & van Dierendonck (1999). With the raw data information like the signal waveform, the list of satellites whose signals were received and their respective C/N0 levels can be obtained, however position cannot be calculated.

The u-blox processing was performed by parsing its recorded data, which only possesses information already processed by the receiver, i.e. it does not provide raw data that can produce the same results of the pre-correlation stage of the GALANT raw data. Its use is for monitoring the navigation signal environment. Overall, u-blox is a very complete receiver that can provide many different sorts of information from parsing its data: list of tracked satellites, C/N0 levels, receiver heading orientation, interference status, gain of the AGC, and etc.

3.4.1 Pre-correlation processing

Pre-correlation data is predominantly thermal noise

https://doi.org/10.58440/ihr-30-2-a13

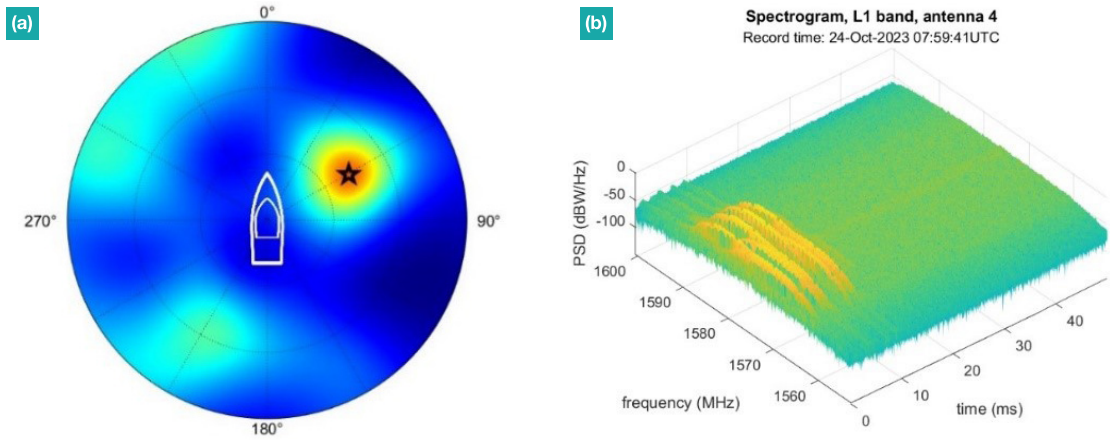


Fig. 11 Pre-correlation processing results of October 24, 2023, at 07:59:41 UTC: interference direction-of-arrival in the pre-whitening map (a), and its waveform in the spectrogram (b).

in nominal situations, and signal waveforms above noise level in situations of medium and strong interference. All the rest is below noise level, including GNSS signals. Some of the products of the pre-correlation processing are: the spectrograms (as in Fig. 9), power spectrum densities (PSDs, i.e. the profile of the spectrograms averaged in time), time plots of the digital samples, and signal DoA estimations (allowing for the rough localization of the interference sources). An example in Fig. 11 reproduces an event that raised the input power in more than 16 dB.

3.4.2 Post-correlation processing

As to the post-correlation data processing, satellite acquisition is performed providing valuable information on the navigation conditions under the influence of interference, to assess how it impacts the capabilities of a receiver to produce reliable PVT information. Some products of this processing are: the list of satellites that could be acquired, and the quality of their respective signals. The former can be compared to the actual constellation of visible satellites on the place and time of the interference event to assess how severe the impacts of the interference is. For this end the publicly available GPS and Galileo almanacs can be used (U.S. Department of Homeland Security, no date; European Union Agency of Space Programme, no date).

3.4.3 u-blox data processing

With the data recorded from the u-blox, navigation and satellites information could be retrieved to complement information from the GALANT platform, and to be displayed for real-time monitoring. Among the products of the u-blox data processing there are: the PVT solution, the list of acquired and tracked satellites in a sky-plot, and a bar-plot displaying the quality of the tracked signals with their respective C/N0 levels. On Fig. 12 the information and plots are reproduced as an example from the GUI (described in the next section), and was provided to the user in real-time for monitoring.

3.4.4 Real-time RFI monitoring using the GUI

The GUI assembled information from both the GALANT processing chain and the u-blox receiver to display in real-time for the operators. It was capable of recording screenshots whenever interference was detected, being a helpful guidance for the data analysis of the most relevant cases. One screenshot example (Fig. 13) – of a very strong interference event caused by a wideband signal in L1 band – illustrates the visual of the interface during an event so strong that prevented navigation capacity.

The impact on the satellites acquisition and tracking can be perceived on the C/N0 window of the GUI, with only four blue bars (corresponding to GPS signals in L1 band) out of the 11 appear and indicating very weak signal strengths, making it impossible to provide

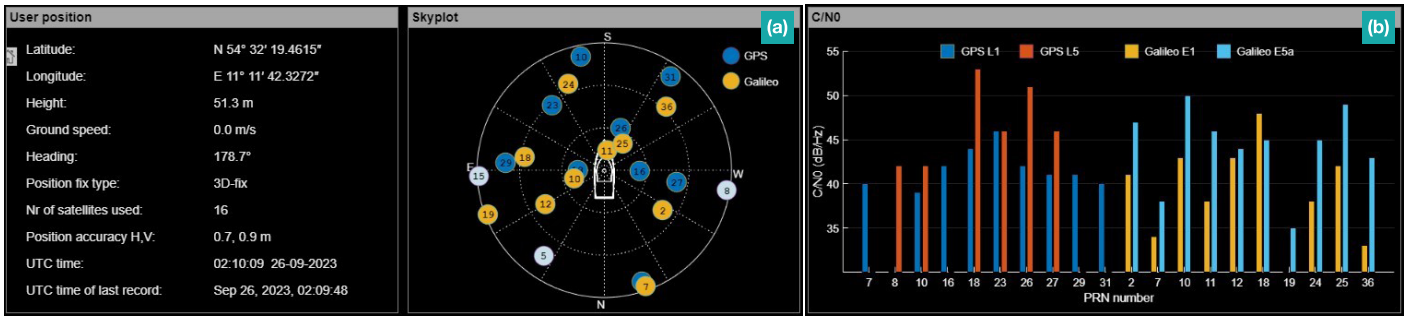


Fig. 12 Results of the u-blox processing from September 26, 2023, at 02:09:48 UTC. Information from the PVT solution (a, left), skyplot with GPS and Galileo satellites (a, right) and signal quality with the C/N0 of the respective tracked satellite signals (b).

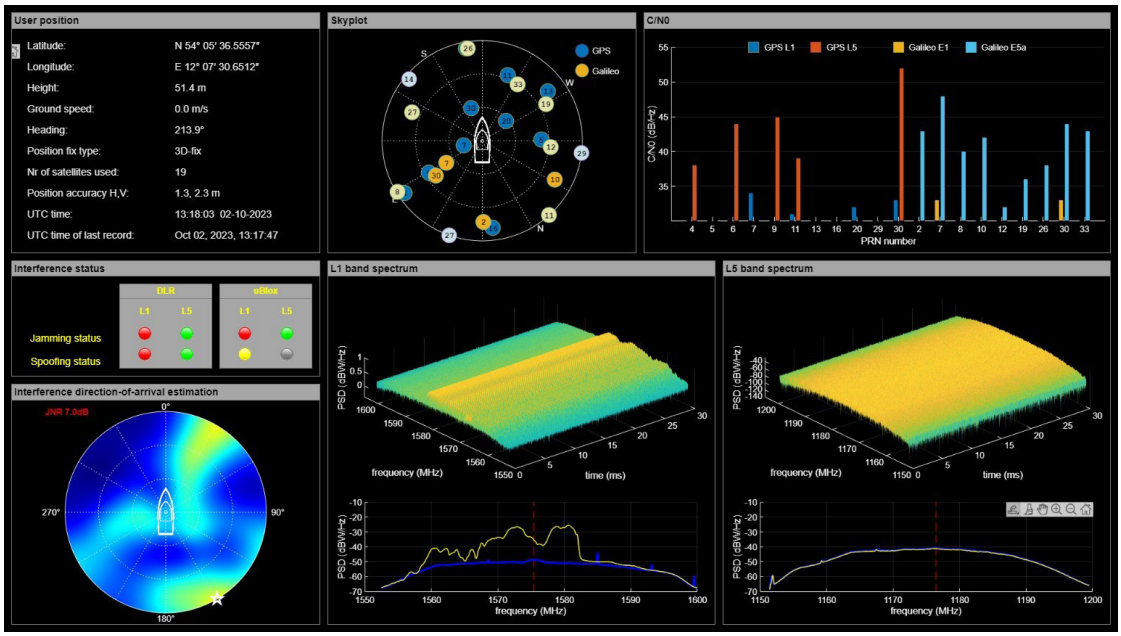


Fig. 13 GUI Snapshot of a very strong L1/E1 RFI event on October 2, 2023, at 13:17:47 UTC. All GPS and Galileo satellites were affected.

new PVT solutions. C/N0 levels between 40 and 55 dB-Hz are very good, and levels below 40 are prone to produce noisier PVT solutions the closer the C/N0 is to 30 dB-Hz, under which it becomes critical.

The interference type was flagged as jamming and spoofing by DLR's GALANT platform, and only as jamming by the u-blox receiver. The spoofing indication was probably due to the strong jamming power leaking through the correlators, thus propagating into the post-correlation domain. In this domain, the spatial technique described in 3.2 confuses this additional power as contributions from spoofing signals, causing the indication of spoofer.

The GUI could also deliver real-time DoA estimation of the RFI signal, allowing the interested operator to spot the source or at least the direction where it is coming from.

A second example of the GUI screenshot used for post-processing analysis is on Fig. 14, illustrating the detection of a strong L5 interference signal impinging on the receiver. The DoA estimation was not available for L5 band because it would require special calibration of the software for this band. From the spectrogram, the waveform and the center frequency of the signal indicate it to be an ARNS distance measurement equipment (DME) or its military counterpart tactical air-navigation (TACAN) signal (more details on section 4.2). Although often interfering with receivers positioned close to their stations, this type of signal usually does not cause considerable impacts on the navigation capabilities. In case of L5 interference, it is important to notice that some GPS satellites still do not

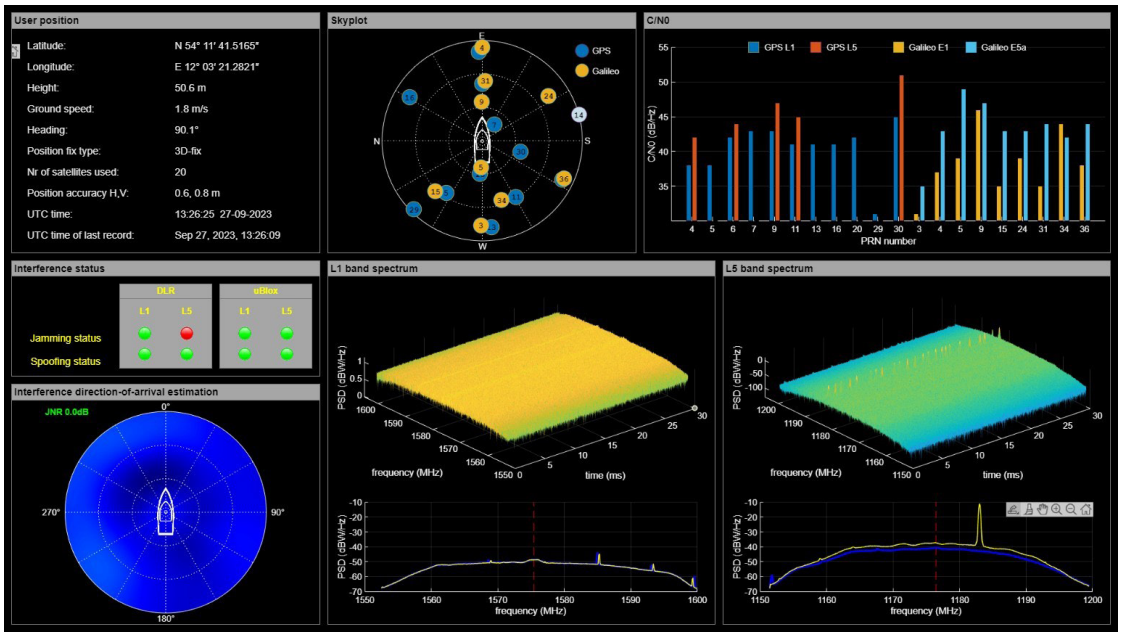


Fig. 14 GUI Snapshot of a strong L5/E5a RFI event on September 27, 2023, at 13:46:10 UTC.

https://doi.org/10.58440/ihr-30-2-a13

transmit L5 signal (QZSS, 2024). The lack of flagging by the u-blox receiver was due to the higher sensitivity of DLR's GALANT system compared to the u-blox, allowing only the former to detect it.

4 Radio-frequency interference events

Many relevant interference events have been assessed in the scope of the measurement campaigns post-processing analysis. In the campaigns deploying the GALANT demonstrator there were over 5000 detections in the L1 band as well in L5, but not all caused damaged to the receiver, so for this reason the focus of the analysis was on events that raised the nominal input power over 5 dB. Nonetheless this still represents a large number of events for this work, so only one analysis is reproduced here as an example of the procedure performed in the post-processing stage.

Moreover, in this section the overview of the geographical and time distributions of the interference events is presented. It is possible to identify the hot spots of interference occurrences using these plots (e.g. ports when the ship was moored). Thanks to the thorough analysis it was also possible to correlate the signal type and estimated direction-of-arrival with the probable source of the interference event.

4.1 Very strong interference event in GPS L1

On July 8, 2021 at 08:23:27 UTC, the GALANT platform detected a very strong interference signal that raised the nominal input power on 13.4 dB (see the second point above 5 dB in Fig. 8). According to the automatic identification system (AIS) data from the BSH ship, the latter was moored on the Fischereinhafen Eins port in Bremerhaven (Germany) the entire July 8, as depicted on Fig. 15.

Following the pre-correlation processing described in Section 3.2, the computations of the signal's spectrogram, PSD, and digital samples evolution in time (Fig. 16) indicate that the interference was caused by a wideband chirping signal, i.e. a signal whose frequency increases in time following some determined law by the signal generator. As to the wideband aspect of the signal, it is so classified due to its large spread around the carrier frequency of the GPS C/A



Fig. 15 Position of the BSH ship on July 8 2021 during the very strong interference event.

L1 signal, perceivable on the PSD (Fig. 16 bottom left). As it will be better seen later, wideband interference was the most efficient form of jamming in saturating the receivers and making it lose signal quality or even tracking of the satellites.

The most affected antenna by the interference signal was antenna element 4, and for this reason the analysis is performed on the signal recorded from this antenna channel. The duration of the even was short lasting approximately for 100 seconds, indicated by snapshots with detected interference (again via the statistical technique described in Section 3.1.1) before and after the snapshot. During the event the most affected antennas were elements 4, 5 and 3, identified by the plot of the instant power increase on Fig. 17.

Following the antenna channels power profile, the position of the ship, and the heading angle (the latter two information provided by the AIS data) the DoA of the interference signal can be estimated, and in this way the position of hot spots regarding interference sources could be tracked in multiple days of strong events. Whenever the ship was moored, the DoA would point towards the city, and whenever the ship was on the sea, it would point to the coasts.

Regarding the impacts of the interference event on

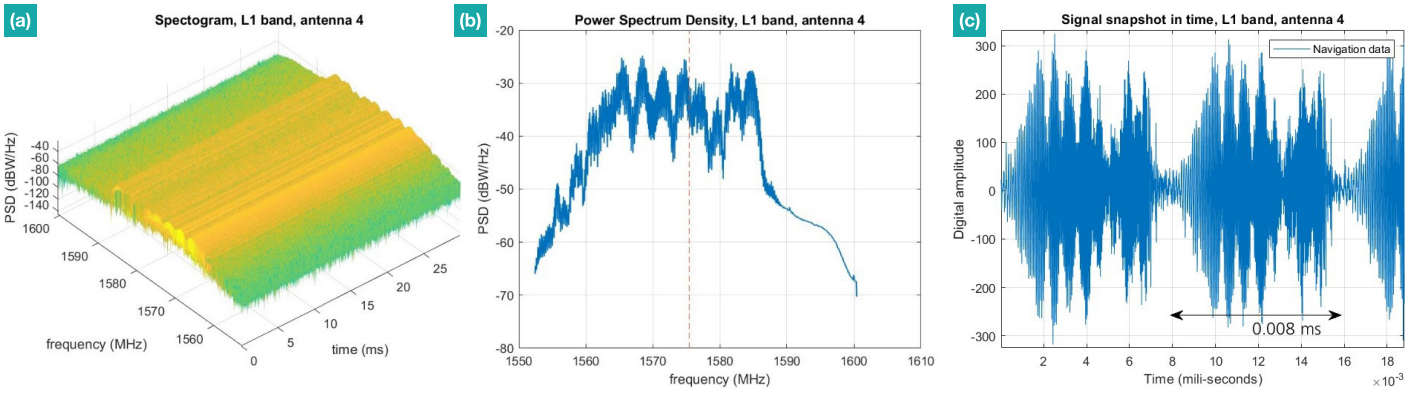


Fig. 16 Time-frequency spectral analysis of the very strong interference event on July 8, 2021. Spectrogram above noise-level (a), RFI spectrum superposing L1 C/A spectrum (b) and chirping characteristic and chirping period of the pulses (c).

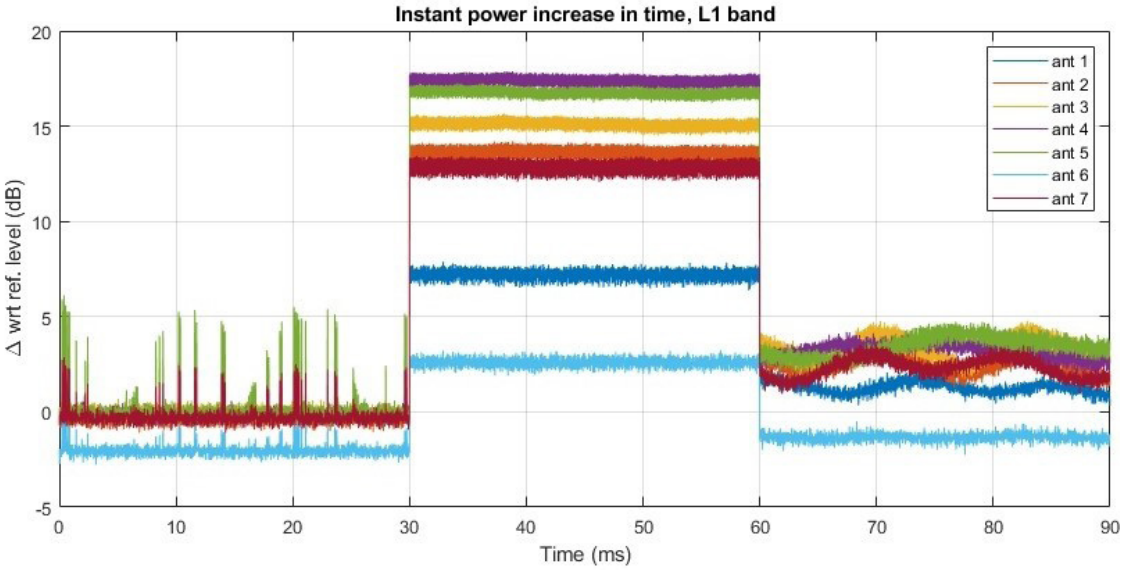


Fig. 17 Antenna channels power profile in consecutive snapshots due to very strong interference event in L1 band.

the receiver, the best way to assess it is by analyzing the satellites acquisition and the respective C/N0 of the signal. For this end, the post-correlation procedures (described in Section 3.2.2) was conducted with DLR software using the recorded data. In the case of this event, no satellite could be acquired, which demonstrates the aforementioned effectiveness of the wideband interference, making the receiver blind to all satellites in the visible constellation.

4.2 DME/TACAN interference in GPS L5

Differently to the case with GPS L1/Galileo E1, the GPS L5/Galileo E5a band is shared with ARNS systems. In the months of the measurement campaigns using the dual-frequency GALANT platform, the receiver recorded many instances of interference caused by the DME/TACAN system (Ostemeier, 2009). Since these are official systems, their structures are well known in the literature (Gao, 2007), and the methods to mitigate them as well.

On Fig. 18 the time-frequency signal waveforms are depicted from an actual case of interference. As it is the case with the effectiveness of wideband interference signals in L1, it is also true that the frequency sparse (and well located) structure of the DME/TACAN signal doesn't pose a big threat. Still, if not tackled, DME/TACAN interferences can become a nuisance to the GNSS receivers, being responsible for disturbances that can affect navigation capabilities.

The majority of the strongest interference events in L5 were caused by DME/TACAN signals, and as such, their source could be traced back to the DME/TACAN base stations located around the areas where the BSH ship navigated and the AIS at the respective time of the interference detection, with one example reproduced on Fig. 19 when the ship was constantly under the influence of a VOR (Very High Frequency Omnidirectional Range) -DME station in the Heligoland island. As mentioned before, these are official non-malicious systems whose intended purpose is solely to aid the navigation of airplanes when taking-off, approaching and landing.

4.3 Geographical overview of RFI events

In the pre-correlation processing, the power increase of the top array element with respect to the nominal levels (as described in Section 3.2.1) was profiled throughout the measurement campaigns. They provide the time distribution of the interference events throughout the months of the campaigns, which allows to investigate how active RFI sources in determined times of the year. On Fig. 20 are reproduced the power profiles with time in the GPS L1 band,

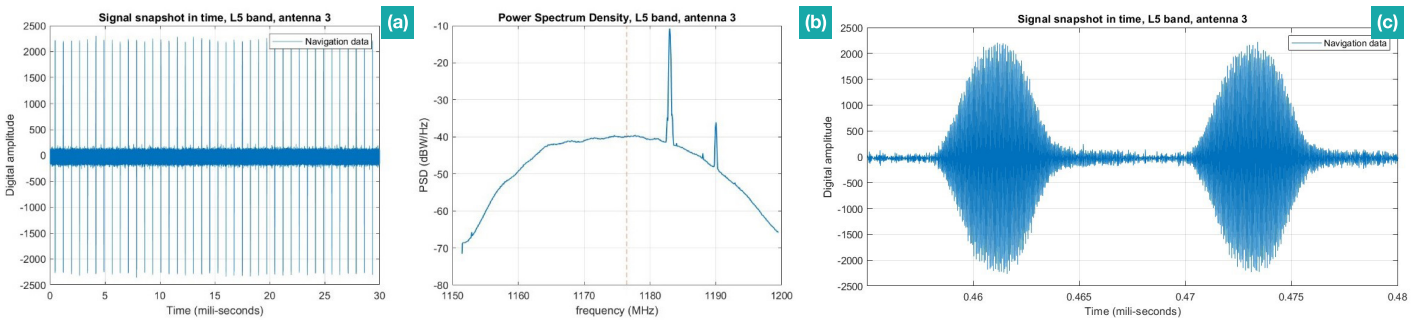


Fig. 18 Interference case in L5 band on June 16, 2021, at 13:18:45 UTC. TACAN signal in 30 ms snapshot (a), spectrum of TACAN signal (b) and DME mode-X pulse pair in TACAN signal (c).

https://doi.org/10.58440/ihr-30-2-a13

whereas on Fig. 21 are depicted the profiles in the GPS L5 band. The reason behind the gaps in the 2023 profiles in both L1 and L5 are due to a power shortage that turned off the monitoring system.

It is noticeable the wide power fluctuation of the interference events with time, indicative of the different type and sources of the interference signals. Very strong interference is rarer, but as the example analysis in Section 4.1 demonstrated, the risk is also related to the interference signal spectrum overlapping the navigation signal spectrum. In this way, even weaker interference events can still be dangerous.

Finally, using the RFI recordings and the AIS data of the ship, it was possible to also identify the geographical distributions of the most relevant RFI events in L1 and in L5 bands during the measurement campaigns, reproduced on Figs. 22 and 23 to provide geographical knowledge on the most affected areas in the Baltic and North Seas. On both maps each point does not necessarily represent a single event, but might refer to a cluster of several events in the same location.

The North Sea was not so much affected during the measurement campaigns as the Baltic Sea, in which the incidence of relevant interference events was most prominent in different areas: harbors, canals, and in waters, especially closer to the coasts. Although many interference cases have been observed far from the coast, the impact of these events on the receiver was not significant. In the special case of L5 there is, in addition to all of these hotspots, the geographical correlation of frequent relevant events and the proximity to DME/TACAN stations.

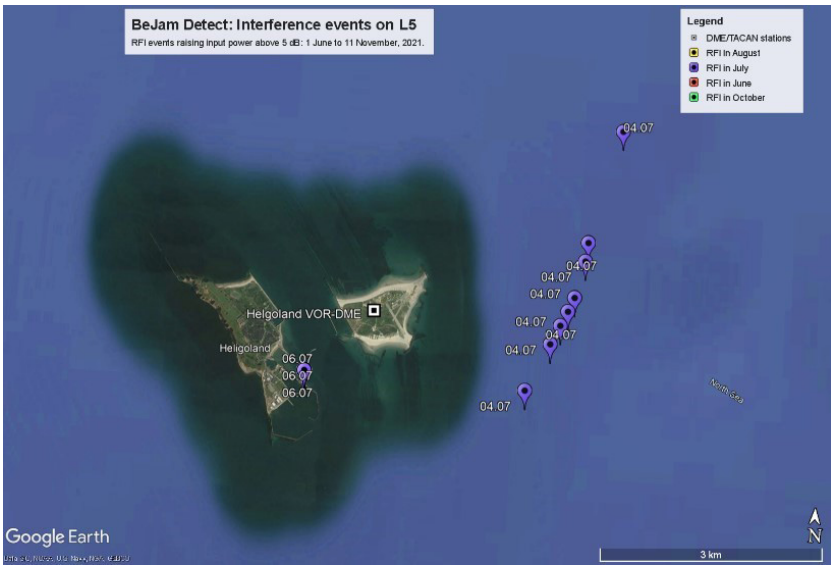


Fig. 19 Positions of the BSH ship next to VOR-DME station at moments of relevant interference events in L5 band.

5 Conclusions

The capacities of the GALANT platforms for monitoring RFI were presented: how they detected signals, recorded them, and displayed the real-time situation for live monitoring of the GNSS frequency bands and the occurrence of interference events. Among over 5000 detections in each band, many relevant events were identified and analyzed, demonstrating capacity to visibly disturb navigation systems, and sometimes even to cause denial-of-service. These concerning events could be traced back to specific areas of frequent occurrence: mostly close to the costs around the paths of the ships, in areas

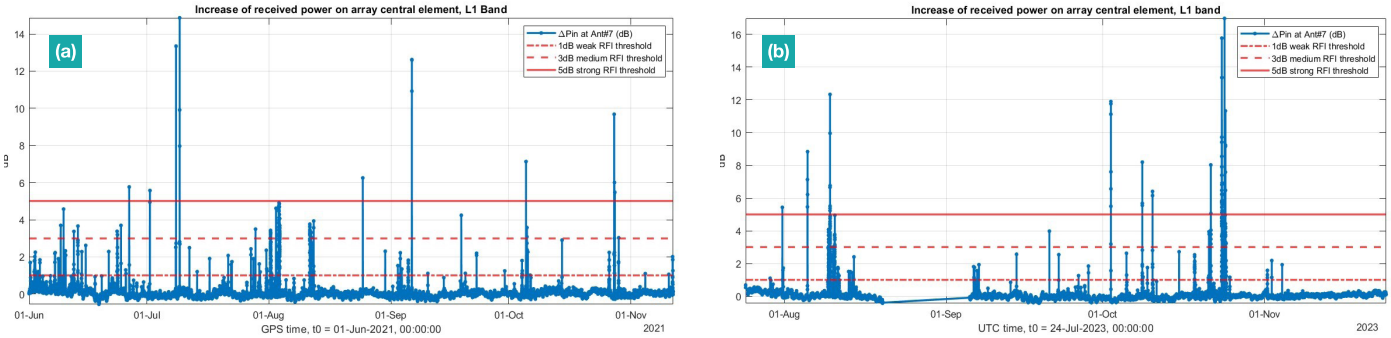


Fig. 20 Input Power Increase with respect to Nominal Levels in L1 Band: measurement campaign in 2021 (a) and measurement campaign in 2023 (b).

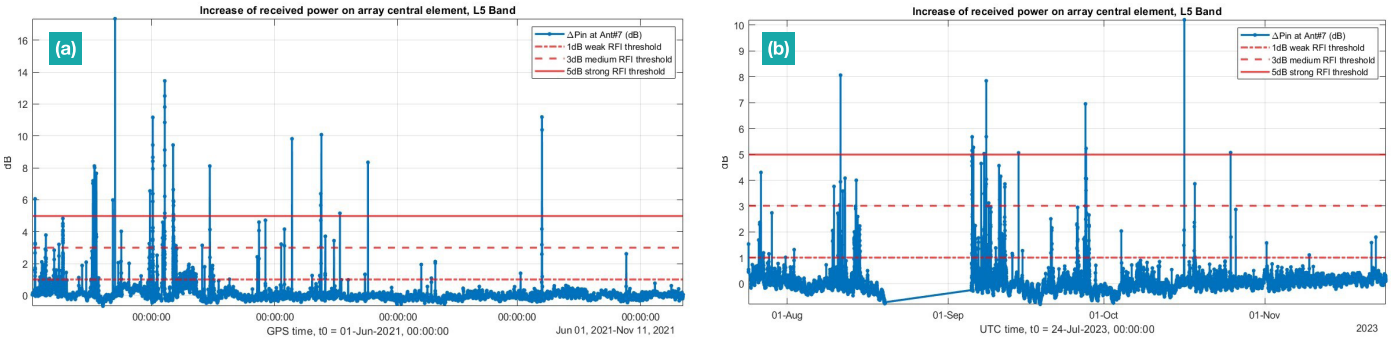


Fig. 21 Input Power Increase with respect to Nominal Levels in L5 Band: measurement campaign in 2021 (a) and measurement campaign in 2023 (b).



Fig. 22 Positions of most relevant interference events in L1 band.



Fig. 23 Positions of most relevant interference events in L5 band.

around harbors when the ships were moored, and in the vicinity of base stations of legitime and official systems that can nonetheless interfere with GNSS, such as DME/TACAN. In the open sea, the further the ships were to the surrounding coasts, the smaller was the frequency of RFI events, and also the weaker they were.

The power profile in time was very diverse but still featured considerable occurrences of strong events. Although not the only parameter to determine the capacity to damage receivers, the stronger the interference signal, the stronger is the disturbance. Also diverse were the signal types: continuous-wave, wideband signals similar to personal privacy devices (PPDs), pulsed signals with determined duty-cycle, out-of-band signals mostly caused by defects in non-malicious systems, and others. The majority of the events did not cause big impacts, however there have been some situations of complete loss of navigation capacity, and in many other times navigation was considerably disturbed, which could last uninterruptedly for more than 10 minutes as it happened several times, for more than one hour as in some occasions, or even during most of the day. The most dangerous signals were strong wideband chirps, because they naturally sweep the frequency band around the GNSS signal, making it easier for their spectrum to overlap. The scene is not static, varying in months and years, thus it needs to be monitored in order to track concerning evolutions of the situation, and the developed prototypes were proven to be suitable for this task.

Acknowledgements

The research results reported in the paper have been obtained in the project BeJamDetect funded by the German Federal Maritime and Hydrographic Agency (BSH). The interference measurement campaigns have been carried out by using ships of BSH and German Federal Maritime Police. This support is greatly acknowledged. The authors would also like to express their sincere gratitude to Friederike Fohlmeister of DLR for her valuable contributions enabling to set up the project and shape the structure of the research.

References

Akos, D. M. (2012). Who's Afraid of the Spoofer? GPS/GNSS Spoofing Detection via Automatic Gain Control (AGC). *NAVIGATION: Journal of the Institute of Navigation, 59*(4), pp. 281–290.

Antreich, F., Wendler, F., Iliopoulos, A., Appel, M., Sgammini, M., Caizzone, S., Konovaltsev, A., Troetschel, F., Marinho, M. and Cuntz, M. (2015). Robust Multi-Antenna GNSS Receiver for Maritime Applications. DLR *Kongress*, 2015/9.

Appel, M., Iliopoulos, A., Fohlmeister, F., Pérez Marcos, E., Cuntz, M., Konovaltsev, A. and Meurer, M. (2019). Experimental validation of GNSS repeater detection based on antenna arrays for maritime applications. *CEAS Space Journal*, *11*(1), pp. 7–19. https://doi.org/10.1007/s12567-018-0232-6

Bhatti, J. and Humphreys, T. E. (2017). Hostile Control of Ships via False GPS Signals: Demonstration and Detection. Navigation, *Journal of the Institute of Navigation, 64*, pp. 51–66.

Braasch, M. S. and Van Dierendonck, A. J. (1999). GPS Receiver Architectures and Measurements. *Proceedings of the IEEE,* January, pp. 48–64.

C4ADS (2019). Above us only Stars: Exposing GPS Spoofing in Russia and Syria. Technical Report of Center for Advanced Defense Studies. Washington, DC, USA.

Cuntz, M., Denks, H., Konovaltsev, A., Hornbostel, A., Dreher, A. and Meurer, M. (2008). GALANT-Architecture Design and First Results of A Novel Galileo Navigation Receiver Demonstrator With Array Antennas. *Proceedings of the 21st International Technical Meeting of the Satellite Division of The Institute of Navigation (ION GNSS 2008)*, pp. 1470–1477.

Dimc, F., Bažec, M., Borio, D., Gioia, C., Baldini, G. and Basso, M. (2017). An Experimental Evaluation of Low-Cost GNSS Jamming Sensors. *Navigation: Journal of The Institute of Navigation, 64*(1), pp. 93–109.

Dovis, F. (2015). *GNSS interference threats and countermeasures.* Artech House.

Duchet, D. and Berz, G. (2018). *GNSS RFI Mitigation: International Efforts to Protect Aviation*. EUROCONTROL. Miami, In Presentation at the 58th Civil GPS Service Interface Committee Meeting.

Dumville, M. (2018). *Initial Findings from the STRIKE3 GNSS Interference Monitoring Network*. https://www.gps.gov/

https://doi.org/10.58440/ihr-30-2-a13

governance/advisory/meetings/2018-05/dumville.pdf (accessed 10 July 2024).

European Union Agency of Space Programme (n.d). *European GNSS Service Centre*. https://www.gsc-europa.eu/gsc-products/almanac (accessed 03 July 2024).

Gao, G. X. (2007). DME/TACAN Interference and its Mitigation in L5/E5 Bands. *Proceedings of the 20th International Technical Meeting of the Satellite Division of the Institute of Navigation (ION GNSS 2007)*, pp. 1191–1200.

Gerrard, N., Rødningsby, A., Morrison, A., Sokolova, N. and Rost, C. (2021). GNSS RFI monitoring and classification on Norwegian highways–an authority perspective. *Proceedings of the 34th International Technical Meeting of the Satellite Division of The Institute of Navigation (ION GNSS+ 2021)*, pp. 864–878.

Grant, A., Williams, P., Ward, N. and Basker, S. (2009). GPS Jamming and the Impact on Maritime Navigation. T*he Journal of Navigation*, April, p. 15.

Groves, P. D. (2005). GPS Signal-to-Noise Measurement in Weak Signal and High-Interference Environments. *Navigation, 52*(2), pp. 83–94.

Günther, C. (2014). A survey on spoofing and counter-measures. *Navigation: Journal of the Institute of Navigation, 3*(61), pp. 159–177.

Heckler, M. V., Cuntz, M., Konovaltsev, A., Greda, L. A., Dreher, A. and Meurer, M. (2011). Development of robust safety-of-life navigation receivers. *IEEE Transactions on Microwave Theory and Techniques, 59*(4), pp. 998–1005.

IMO (2018). *E-Navigation Strategy Implementation Plan – Update 1*, MSC. 1/Circ. 1595, 25 May 2018. London, UK.

Jada, S., Bowman, J., Psiaki, M., Fan, C. and Joerger, M. (2022). Time-Frequency Analysis of GNSS Jamming Events Detected on US Highways. *Proceedings of the 35th International Technical Meeting of the Satellite Division of The Institute of Navigation (ION GNSS+ 2022)*, pp. 933–946.

Konovaltsev, A., Caizzone, S., Yinusa, K., Sgammini, M., Marcos, E. P., Appel, M., Cuntz, M., Elmarissi, W. and Meurer, M. (2017). Interference detection and characterization with an array based GNSS receiver using conformal antennas in maritime environments. *Proceedings of the 30th International Technical Meeting of The Satellite Division of the Institute of Navigation (ION GNSS+ 2017)*, pp. 2795–2811).

Konovaltsev, A., Kaelberer, U., Sgammini, M. and Meurer, M. (2009). GBAS RF interference detection threshold determination at Palermo airport. *Atti dell'Istituto Italiano di Navigazione, December*, pp. 45–55.

Liu Z., Lo S., Walter T. and Blanch J. (2023). *GNSS Interference: Getting to the Source*. Inside GNSS Media & Research LLC. https://insidegnss.com/gnss-interference-getting-to-the-source/ (accessed 11 September 2024).

Medina, D., Lass, C., Marcos, E. P., Ziebold, R., Closas, P. and García, J. (2019). On GNSS jamming threat from the maritime navigation perspective. *2019 22th International Conference on Information Fusion (FUSION)*, pp. 1–7. https://doi.org/10.23919/FUSION43075.2019.9011348

Morales-Ferre, R., Richter, P., Falletti, E., De La Fuente, A. and Lohan, E. S. (2019). A survey on coping with intentional interference in satellite navigation for manned and unmanned aircraft. *IEEE Communications Surveys & Tutorials, 22*(1), pp. 249–291.

Motella, B. and Lo Presti, L. (2014). Methods of goodness of fit for GNSS interference detection. *IEEE Transactions on Aerospace and Electronic Systems, 3*(50), pp. 1690–1700.

National Telecommunications and Information Administration (2016). *United States Frequency Allocation Chart.* https://ntia.gov/page/united-states-frequency-allocation-chart (accessed 13 April 2023).

Ostemeier, J. (2009). *Test of DME/TACAN Transponders: Application Note*, s.l.: Rohde and Schwarz.

Pérez-Marcos, E., Konovaltsev, A., Caizzone, S., Cuntz, M., Yinusa, K., Elmarissi, W. and Meurer, M. (2018). Interference and spoofing detection for GNSS maritime applications using direction of arrival and conformal antenna array. *Proceedings of the 31st International Technical Meeting of The Satellite Division of the Institute of Navigation* (ION GNSS+ 2018), pp. 2907–2922).

QZSS (2024). *List of Positioning Satellites*. https://qzss.go.jp/en/technical/satellites/index.html#GPS (accessed 6 September 2024).

Raghuvanshi, A., Bisnath, S. and Bond, J. (2024). Analyzing GNSS RFI Events in Canada. *Inside GNSS*, January 2024, pp. 34–41.

SkAI-Data-Services (2023). *Live GPS Spoofing Tracker Map*. https://spoofing.skai-data-services.com/ (accessed 10 July 2024).

Sokolova, N., Morrison, A. and Diez, A. (2022). Characterization of the GNSS RFI Threat to DFMC GBAS Signal Bands. *Sensors, 22*, p. 17.

Tabatabaei Balaei, A., Motella, B., Dempster, A. G. and Rizos, C. (2007). *Mutual effects of satellite signal quality and satellite geometry on positioning quality*. s.l., s.n.

Thombre, S., Bhuiyan, M. Z. H., Eliardsson, P. and Gabrielsson, B. (2017). GNSS Threat Monitoring and Reporting: Past, Present, and a Proposed Future. *The Journal of Navigation, 71*, p. 17.

U.S. Department of Homeland Security (n.d). *Navigation Center*. https://www.navcen.uscg.gov/gps-nanus-almanacs-opsadvisories-sof (accessed 03 July 2024).

Wiseman, J. (2022). *GPSJAM, Daily maps of GPS interference*. https://gpsjam.org/ (accessed 10 July 2024).

Authors' biographies



Thiago Azevedo de Vasconcelos

Thiago Azevedo de Vasconcelos obtained his bachelor's and master's degrees in Telecommunications Engineering in 2018 and 2020, respectively, from the Brazilian Federal University of Ceará, where he developed research in physically consistent array processing for mobile communication systems. In February 2022 he joined the Institute of Communications and Navigation of the German Aerospace Center (DLR), where he is working with signal processing algorithms of GNSS receivers. His current research interests are in GNSS interference detection and mitigation.



Lothar Kurz

Lothar Kurz studied Electrical Engineering and obtained his Diploma Degree in 2007 from RWTH Aachen University. Since then he was working as a scientist for the Chair of Electrical Engineering and Computer Systems (EECS) at RWTH Aachen University. In 2017 he joined the Institute of Communication and Navigation at the German Aerospace Center (DLR). His research interests are in GNSS signal processing and embedded receivers.



Andriy Konovaltsev

Andriy Konovaltsev received his engineer diploma and the Ph.D. degree in electrical engineering from Kharkov State Technical University of Radio Electronics, Ukraine in 1993 and 1996, respectively. He joined the Navigation Department of the Institute of Communications and Navigation of the German Aerospace Center (DLR) in 2001 where he is now a senior researcher and leads a team working on the signal processing techniques of GNSS receivers. His main research interest is in application of adaptive antenna arrays for improving performance of satellite navigation systems in challenging signal environments.



Tobias Ehlers

Tobias Ehlers studied Electrical Engineering at the University of Applied Sciences in Lübeck, Germany, graduated as Dipl.-Ing. in 2002. In 2003 he joined the Federal Maritime and Hydrographic Agency of Germany (BSH) and worked in the MARNET division as engineer for the development and maintenance of un-manned scientific measurement buoys in the Baltic and North Sea. Later on, he joined the Shipping Department and became a senior engineer in the BSH laboratory for positioning systems. His activities comprise type approval testing, standardization in IMO, IEC and CEN as well as research & development for the enhancement of navigation systems.

https://doi.org/10.58440/ihr-30-2-a13


Michael Meurer

Michael Meurer received the diploma in electrical engineering and the Ph.D. degree from the University of Kaiserslautern, Germany. After graduation, he joined the Research Group for Radio Communications at the Technical University of Kaiserslautern, Germany, as a senior key researcher, where he was involved in various international and national projects in the field of communications and navigation both as project coordinator and as technical contributor. From 2003 till 2013, Dr. Meurer was active as a senior lecturer and Associate Professor (PD) at the same university. Since 2006 Dr. Meurer is with the German Aerospace Centre (DLR), Institute of Communications and Navigation, where he is the director of the Department of Navigation and of the center of excellence for satellite navigation. In addition, since 2013 he is a professor of electrical engineering and director of the Chair of Navigation at the RWTH Aachen University. His current research interests include GNSS signals, GNSS receivers, interference and spoofing mitigation and navigation for safety-critical applications.

https://doi.org/10.58440/ihr-30-2-a13

PEER-REVIEWD ARTICLE

Macrophyte detection with bathymetric LiDAR – Applications of high-dimensional data analysis for submerged ecosystems

Authors

Jan Rhomberg-Kauert[1], Lucas Dammert[1], Michael Grömer[1,2], Martin Pfennigbauer[3] and Gottfried Mandlburger[1]

Abstract

Automatic detection and classification of point clouds is a research topic of wide interest, as manual annotation of individual points is time consuming and inefficient for large surveys. This also holds for the emerging field of submerged vegetation detection, surveyed by bathymetric LiDAR. In the point clouds generated, current best practices perform sub-optimally in extracting vegetation data. To date, only a modest number of methodologies have been proposed to overcome this problem and furthermore only briefly discuss their findings in an extensive evaluation with annotated data. In contrast to the domain of sonar, where the practice of feature selection and comparison to annotated data has been well established over the last decades. This study proposes a similar methodology based on high-dimensional data analysis and clustering that is commonly deployed in other fields of research. In addition to the method, two datasets are presented for a detailed comparison to manually annotated data, in which the method performed at a mean precision score of 0.70 to 0.86, for all manual annotations. This demonstrates that the method is able to detect aquatic vegetation based on its structural characteristics of the bathymetric LiDAR point cloud, yielding results that are comparable to those obtained through manual annotation. In conclusion, the method presents an alternative workflow to current best practices and improves automated vegetation detection through the application of high dimensional data analysis.

Keywords

LiDAR · vegetation detection · high-dimensional data · clustering · point cloud processing · bathymetry

Resumé

La détection et la classification automatiques des nuages de points est un sujet de recherche de grand intérêt, car l'annotation manuelle des points individuels est chronophage et inefficace pour les levés de grande envergure. Cela s'applique également au domaine émergent de la détection de la végétation submergée, étudiée par LiDAR bathymétrique. Dans les nuages de points générés, les meilleures pratiques actuelles ne sont pas optimales pour l'extraction des données sur la végétation. À ce jour, seul un petit nombre de méthodologies ont été proposées pour résoudre ce problème et leurs résultats ne sont que brièvement discutés dans le cadre d'une évaluation globale avec des données annotées. En revanche, dans le domaine du sonar, la pratique de la sélection des caractéristiques et de la comparaison avec des données annotées est bien établie depuis des décennies. Cette étude propose une méthodologie similaire, basée sur l'analyse et le regroupement de données de haute dimension, qui est couramment utilisée dans d'autres domaines de recherche. En plus de la méthode, deux ensembles de données sont présentés pour une comparaison détaillée avec des données annotées manuellement, où la méthode a obtenu un score de précision moyen de 0,70 à 0,86, pour toutes les annotations manuelles. Cela démontre que la méthode est capable de détecter la végétation aquatique sur la base des caractéristiques structurelles du nuage de points LiDAR bathymétrique, produisant des résultats comparables à ceux obtenus par annotation manuelle. En conclusion, la méthode propose un flux de travail alternatif aux meilleures pratiques actuelles et améliore la détection automatisée de la végétation grâce à l'application de l'analyse de données de haute dimension.

✉ Jan Rhomberg-Kauert · jan.rhomberg-kauert@geo.tuwien.ac.at

[1] TU Wien, Department of Geodesy and Geoinformation, Vienna, 1040, Austria

[2] VERBUND Hydro Power GmbH, Wien, 1150, Austria

[3] RIEGL Research Forschungsgesellschaft mbH, Horn, 3580, Austria

https://doi.org/10.58440/ihr-30-2-a16

Resumen

La detección y clasificación automáticas de nubes de puntos es un tema de investigación de gran interés, ya que la anotación manual de puntos individuales consume mucho tiempo y es ineficiente para grandes levantamientos. Esto también se aplica al campo emergente de la detección de vegetación sumergida, levantada mediante LiDAR batimétrico. En las nubes de puntos generadas, las mejores prácticas actuales no son óptimas para extraer datos sobre vegetación. Hasta la fecha, sólo se ha propuesto un número modesto de metodologías para superar este problema y además sus resultados solo se debaten brevemente en una amplia evaluación con datos anotados. En contraste con el ámbito del sonar, en el que la práctica de la selección de elementos y comparación con datos anotados lleva bien establecida desde hace décadas. Este estudio propone una metodología similar basada en el análisis y agrupación de datos de alta dimensión que se utiliza habitualmente en otros ámbitos de investigación. Además del método, se presentan dos conjuntos de datos para una comparación detallada con los datos anotados manualmente, en los que el método obtuvo una puntuación media de precisión de 0,70 a 0,86, para todas las anotaciones manuales. Esto demuestra que el método es capaz de detectar vegetación acuática basándose en las características estructurales de la nube de puntos LiDAR batimétrica, produciendo resultados comparables a los obtenidos mediante anotación manual. En conclusión, el método presenta un flujo de trabajo alternativo a las mejores prácticas actuales, y mejora la detección automatizada de vegetación mediante la aplicación de análisis de datos de alta dimensión.

1 Introduction

Aquatic vegetation plays a vital role in freshwater and marine ecosystems as the interaction between flora and fauna creates intricate systems susceptible to ecological changes. These systems correspond to interactions between different biological and physical processes, which shape the distribution of macrophytes population in the surveyed aquatic landscape (Lønborg et al., 2021; Coops et al., 2007; Carpenter and Lodge, 1986; Wood, 1963). Pronounced changes in submerged vegetation therefore lead to constant flux in species diversity and abundance, which becomes of importance for economic interests in water systems, as well as climate related analysis of ecosystem health (Yamasaki et al., 2021; Coops et al., 2007; Schmieder, 2004, 1995; Carpenter & Lodge, 1986). These changes can be observed through different remote sensing and in-situ measurements, where geometric differences in the vegetation can directly be monitored. Therefore, enhancing the analysis of remote sensing data through automation can greatly improve the understanding of climatic factors upon the ecosystem (Carpenter & Lodge, 1986; Lønborg et al., 2021).

Current state-of-the-art surveying is still in-situ measurements with extensive measuring campaigns exploring pre-selected areas (Lønborg et al., 2021). For those areas of interest, diver- or boat-based surveys are often deployed to collect biological samples, underwater images and annotate species distributions of the local vegetation in the selected transect or quadrant (Murphy et al., 2018; Zervas et al., 2018; Rowan & Kalacska, 2021; Lønborg et al., 2021). The data gathered during such field campaigns often constitute just a short temporal insight into a much larger and complex system and, due to the subjective interpretation by the diver, the observation is often difficult to reproduce. This limits the achievable accuracy apart from the high costs to deploy divers at a high frequency (Lønborg et al., 2021).

Another commonly used approach to analyze submerged vegetation on a larger scale is photogrammetry. For this, there are two commonly used systems: (i) satellite based remote sensing (Luo et al., 2016; Nelson et al., 2006; Mandlburger, 2022) and (ii) airborne imaging using high resolution, multi- and hyperspectral cameras. Techniques based on satellite images have the advantage of large aerial coverage and avoid the deployment of ground-borne teams across long surveys, resulting in cost and time efficient measurements compared to surveys of similar extent conducted by survey teams (Mumby et al., 1999). The down side of such measurements is the low spatial resolution, as most satellite images have a resolution of around 1 to 50 m (de Grandpr´e et al., 2022; Rowan & Kalacska, 2021). Considering that for most processes of interest, higher resolutions are crucial, this entails inaccuracies due to averaging the gathered data across large pixels (O'Neill & Costa, 2013; Ackleson & Klemas, 1987). The second option is using orthophotos and hyperspectral images, captured from either crewed or uncrewed aerial vehicles (Mandlburger, 2022). These images feature a much higher resolution, depending on the system used and the employed above-ground altitude of the airborne system. The compromise of high spatial resolution introduces a limitation of the spatial extent or prolongs the survey, as the altitude influences the field of view (Lønborg et al., 2021). The increased resolution, however, allows for detailed analysis of the vegetation distributions and provides indicative results on plant species, but provides limited insights on the structural component of the macrophytes population (Dierssen et al., 2021).

On-water remote techniques, such as boat-based hydroacoustic sensing methods (e.g. sonar), have been widely recognized in different areas of aquatic mapping (McCarthy, 1997; Sabol et al., 2002;

Aleksandra et al., 2015; Mandlburger, 2022). The application towards vegetation detection in particular has seen substantial improvement in terms of spatial resolution due to the application of multi-beam sonar (Aleksandra et al., 2015; Held & Schneider von Deimling, 2019). Systems pioneered by RoxAnn (single beam) and Questor Tangent Corporation (multi-beam), have introduced and improved the classification of seabed types. Both systems utilize a similar classification method, based on the recorded acoustic variables and relate to these measures such as roughness and hardness of the seabed (Schiagintweit, 1993; Serpetti et al. 2011). Such feature-based approaches can furthermore be applied to the automatic vegetation detection and can cover vast areas in acceptable time periods (Blondel, 2008).

The same applies to bathymetric LiDAR, where improvements in sensor technology and signal processing have overcome previous limitations (Mandlburger et al., 2023b). This has established LiDAR among the traditional approaches for mapping macrophyte populations in water ecosystems (Wagner et al., 2024; Calantropio et al., 2024; Mandlburger et al., 2023b). Furthermore, due to the rise of unmanned aerial vehicles (UAVs), the technology has become widely available enabling the implementation of those recent advances in practice (Espel et al., 2020). One of such advancements is the recent utilization of full waveform LiDAR (i.e., the availability of the complete temporal record of the returned echo pulse), which enables specifically tailored signal processing for bathymetric LiDAR, improving water surface detection and higher depth penetration (Schwarz et al., 2019). Overall, recent advancements have allowed users to not only capture detailed aquatic vegetation but furthermore create a basis for detailed data analysis, as a multitude of features can be extracted from the acquired point clouds (Mandlburger et al., 2023a). In this new type of data, one of the challenges is the classification of the acquired points into submerged terrain and vegetation, which can not sufficiently be achieved by established methods (Wagner et al., 2024). Consequently, research related to the development of new methods in the classification of macrophyte subtypes is of great importance.

For classification methods of both sonar and LiDAR that are based on recorded variables (features), for each measured point, feature selection plays a vital role. In general terms, a classifier transforms an input vector into an output of a single value, the classification (Domingos, 2012). Therefore, selection, transformations, and the overall dimension of the data influence the generated output (Bellman & Kalaba, 1959; Chen, 2009; Domingos 2012). Previous studies in both fields of LiDAR and sonar have addressed these challenges and introduced different approaches (Serpetti et al. 2011; Schi, 2021). In such recent results both general large feature space and manually selected feature approaches have been used to generate classifications of point clouds, where each approach has distinct advantages and challenges (Serpetti et al. 2011; Shi et al., 2021, Saputra & Radjawane, 2022). Single feature selection on one hand requires human supervision, while machine learning built on all features requires large amounts of data and training (Serpetti et al. 2011; García-Gutiérrez et al., 2015; Yang et al., 2020; Shi et al., 2021, Saputra & Radjawane, 2022).

Related scientific work has seen a large increase in the deployment of LiDAR across different fields related to geoscience over the last decade (Mandlburger et al., 2023b; Rowan & Kalacska, 2021; Lønborg et al., 2021). This is also the case for bathymetric applications, where LiDAR expanded from simple topographic modeling to capturing detailed structures of submerged aquatic vegetation (Wagner et al., 2024; Rowan & Kalacska, 2021; Mandlburger et al., 2020). While the use of infrared LiDAR is already a common tool in forestry and other terrestrial ecological research (Zhou et al., 2022; Michalowska & Rapiński, 2021; Koma et al., 2021), the use of LiDAR for aquatic ecosystems is still limited due to expensive initial costs, which applies to airborne data acquisition from both crewed and remotely piloted platforms. Furthermore, only recent advances in sensor technology, specifically the increase in spatial resolution (smaller laser footprints and higher scan rates) has enabled the detection of submerged objects beyond mere mapping of bathymetry (Mandlburger et al., 2023b; Lønborg et al., 2021). Therefore, many challenges such as vegetation classification in vegetated water bodies are still not entirely solved for bathymetric LiDAR. To overcome the challenges posed by bathymetric LiDAR, different methods have been presented over the last years ranging from unsupervised machine learning to LiDAR feature-based classification methods (Saputra & Radjawane, 2022; Amani & Mahdavi, 2021; Wagner et al., 2024). Each approach faces different challenges. While machine learning requires large annotated datasets, data driven approaches depend on the investigated area and the system used (Saputra & Radjawane, 2022; Wagner et al., 2024). Additional challenges arise in the evaluation of such methods as the lack of benchmark datasets does not allow for a general comparison to other methods and thus introduces obstacles in comparison of effectiveness (Calantropio et al., 2024). This further extends to the manual annotation in general, as manually labeled datasets are prone to differ if annotated by multiple experts (Calantropio et al., 2024; Zhu et al., 2019).

This study aims to improve the current state-of-the-art of vegetation detection via LiDAR bathymetry through the introduction of a new method for the classification of 3D point clouds. The method is based on working principles of single cell clustering, where groups of cells are classified and matched on the basis of genetic similarity, such as the genes extracted from the cells during RNA-sequencing

https://doi.org/10.58440/ihr-30-2-a16

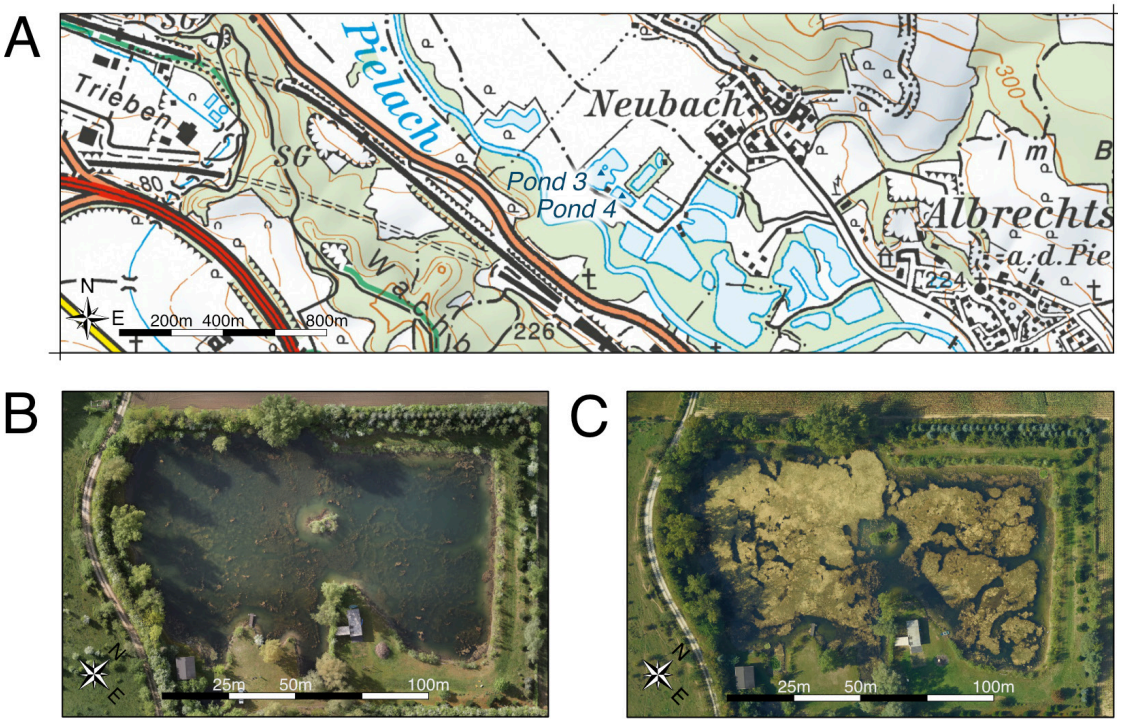


Fig. 1 Study area (a) Location of Pond 2 (48.2166 N, 15.3744 E) and 3a (48.2158 N, 15.3755 E) near Loosdorf (BEV, 2024). (b) Orthophoto of Pond 2 during early summer (May 2024). (c) Orthophoto of Pond 2 during autumn (October 2023).

(Luecken & Theis, 2019). Related methods in the field of sonar signal processing have used acoustic variables from multibeam backscatter in combination with Principal Component Analysis (PCA) to identify main characteristics and assign each data observation to a specific class (Schiagintweit, 1993; Preston, 2009; Serpetti et al., 2011; Held & Schneider von Deimling, 2019). Applied towards LiDAR data, this is equivalent to combine all measurements of the laser scanning setup into a high-dimensional dataset and group the points based on similarity of the recorded features through dimensional reduction and clustering. The difference in the proposed method and current state of the art classification is the usage of Uniform Manifold Approximation and Projection for Dimension Reduction (UMAP; Sainburg et al., 2021) instead of a standard PCA workflow. Through the application of UMAP in the dimensional reduction, points with close spatial proximity (in the 2D dimensionally reduced dataset) have a similarity of features in the initial high-dimensional dataset. This improves the extraction of points with similar features and thus enables vegetation classification based on geometric similarities.

The workflow described in this article extracts the submerged LiDAR point cloud using the surface-volume-bottom algorithm (SVB) by Schwarz et al. (2019). The extracted data can be seen as a high-dimensional dataset made up of features for each point and can be dimensionally reduced to a two-dimensional dataset with UMAP, which can be clustered by density-based clustering algorithms. The extracted clusters can then be grouped into vegetation and non-vegetation labels providing an automated classification of the point cloud. The aim of the study is to extend the bathymetric processing pipeline to match best practices in other areas of remote sensing applied to ecological monitoring such as forestry, where LiDAR has become a standard tool to survey large areas and track biological changes over time (Michalowska & Rapiński, 2021; Kumpumäki et al., 2015).

The article first introduces the dataset used for development and evaluation, together with the deployed pre-processing (Section 2). In Section 3, we describe the construction of the high-dimensional feature space and the clustering of the dimensionally reduced dataset. This includes an introduction into dimensional reduction techniques and the classification of the created macrophytes groupings. The results of the developed method are further compared to photogrammetric and manually annotated data (Section 4) and critically discussed in the light of state-of-the-art ecological research (Section 5).

2 Materials

2.1 Study area

The study area is located near Loosdorf in the region of Lower Austria (48.2010 N, 15.4004 E; WGS 84). The entire region comprises a near-natural section of the pre-alpine Pielach river and around a dozen freshwater ponds in the adjacent flood plain. A subset of the ponds, including Ponds 2 and 3a, contain submerged vegetation, which can clearly be seen in the orthophotos obtained throughout multiple surveys (Fig. 1). This vegetation is under constant flux across the seasons and therefore representative of the general research related to the monitoring of submerged ecosystems. Furthermore, the combination of two

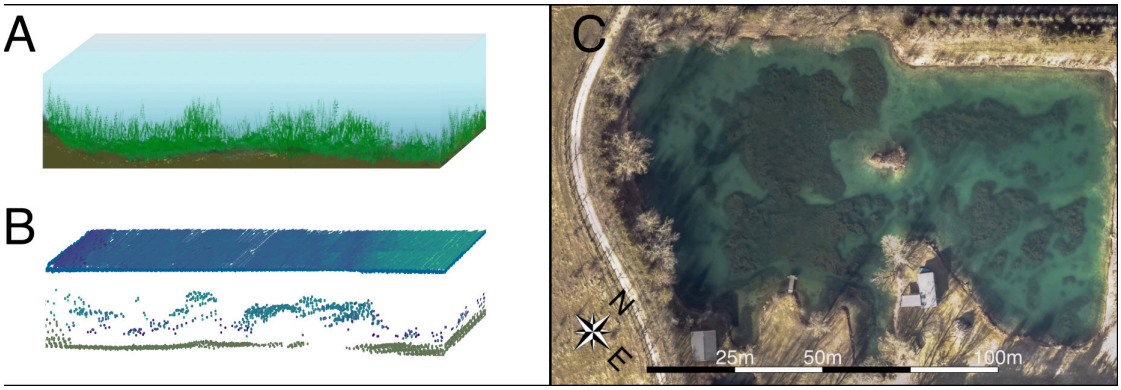


Fig. 2 (a) Illustration of an underwater transect with vegetation representative for the data used in the study. (b) Actual LiDAR point cloud corresponding to panel A. (c) Orthophoto of Pond 2 captured in February, 2022.

different datasets (aerial images and LiDAR) provides a comprehensive foundation for post-analysis of the aquatic ecosystem.

2.2 Datasets

To capture the diverse landscape of submerged vegetation, two systems were deployed to generate a comprehensive dataset. First, the data was surveyed using a topo-bathymetric LiDAR system, in this case a *RIEGL* VQ-840-G topo-bathymetric UAV laser scanner system. The sensor was mounted on a helicopter and flown at an average flying altitude of 187 m, during a single day measuring campaign on the 9th of February, 2022. The system uses a wavelength of 532 nm and medium sized footprints with an average footprint diameter between 0.82 m and 1.04 m (RIEGL, 2012, 2023). The data recorded by the LiDAR system was exported as a point cloud (Figs. 2a and 2b) in LAS format in a georeferenced coordinate system (ETRS89, UTM33; EPSG: 25833). Secondly, to capture reference data, standard photogrammetric methods were deployed to generate an orthophoto of the surveyed area (Fig. 2c). The orthophoto has a resolution of 5 cm per pixel based on images captured with a 12.4 MPix Manta G1236C camera mounted on the same helicopter setup as the LiDAR system. The orthophotos served as visual guidance for the annotation of the LiDAR point cloud, which has surface point densities of 34.4 points/m^2 and 27.4 points/m^2 for Pond 2 and 3a respectively.

The first pond (Pond 2) features a variety of vegetation with different vertical extent and varying density (Figs. 2b and 2c). The second pond (Pond 3a) is considerably smaller, with an irregular vegetation distribution and many smaller patches. The labels are generated using the PointCloudLabeler[1] add-on from OPALS version 2.6.0 (Pfeifer et al., 2014). This tool allows manual annotation of the point cloud in transects perpendicular to a digitized 2D axis (polyline). The transect is chosen so that the width covers the entire lake and the view-depth is set between 2 m to 5 m depending on operator preferences. The data were manually labeled by three experts. To avoid biases, the data were labeled twice by each expert, based on south-west and north-east oriented axis directions, respectively. In total, this resulted in six independently labeled data sets.

One of the challenges in the Pond 2 dataset is that the points are merged from two overlapping flight strips. The strip overlap area features higher point densities and varying distributions compared to the rest of the dataset. These differences are detectable throughout most of the features of the point cloud. To compensate for the artificial similarity of the features, we deploy point thinning in the overlap region. The thinning is based on an octree cutoff, reducing the number of points in the overlap to approximately match the rest of the point cloud. This leaves a final dataset comparable to the one of Pond 3a, which is only covered by a single flight strip. Together, both datasets are the input for the data processing (Section 3) and the final evaluation (Section 4).

2.3 Data preparation and water surface detection

The data acquired by the topo-bathymetric LiDAR system captures all the features of the landscape, at land and underwater. To focus on the aquatic landscape, preprocessing of the data becomes necessary to remove all points not related to the submerged domain. For this, we introduce an initial step in the analysis that extracts the underwater area (Fig. 3c) from the recorded point cloud (Fig. 3a) by detecting the water surface within the study site and selecting only the points beneath the calculated water level. For this, we employed the SVB algorithm by Schwarz et al. (2019). The algorithm uses exponential decomposition of bathymetric laser waveforms (Schwarz et al., 2017), which provides a reliable classification of laser pulses hitting the water surface as a side product (Fig. 3b). From the initial identification of water surface points, the general water surface height in the respective coordinate system of the point cloud can be estimated.

[1] https://github.com/TUW-GEO/opals PointCloudLabeler/ (accessed 17 August 2024).

https://doi.org/10.58440/ihr-30-2-a16

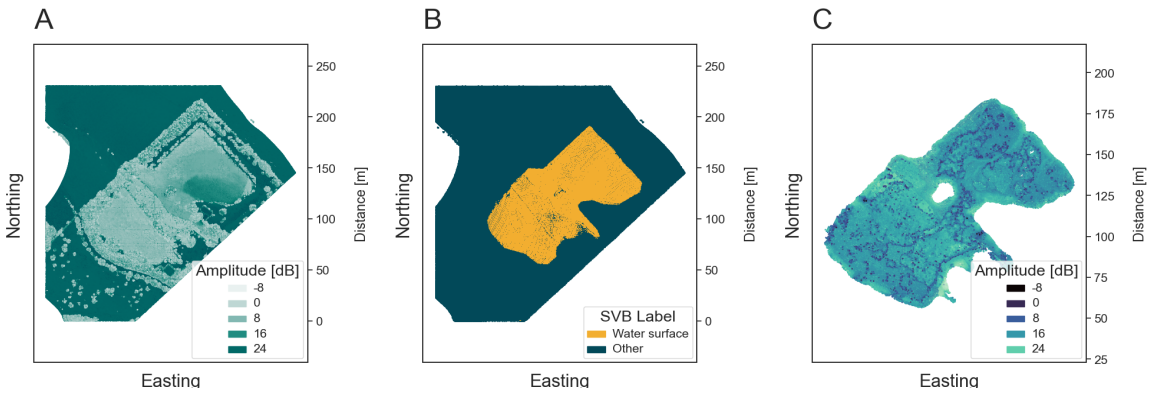


Fig. 3 Visualization of input dataset Pond 2. (a) displays the amplitude values of the initial scan, (b) the water surface classification from the SVB algorithm Schwarz et al. (2019), and (c) the pond data set after outlier removal.

To select all points below the lowest part of the water surface, a threshold height is chosen based on the z-coordinate of all points classified as water surface, which fall in the range of the 2nd–5th percentile of the height. This accounts for potential outliers below the water surface. All points below the calculated threshold are expected to belong to the submerged area of interest. Lastly, to remove the remaining outliers, a simple clustering approach is applied to the data. Here, density-based clustering was chosen to remove all points not directly linked to the pond. In particular, we used DBSCAN (Pedregosa et al., 2011; Schubert et al., 2017; Ester et al., 1996), with a minimum distance of 1 m between the points. After this filtering step, the data is ready for further analysis, as only submerged terrain and vegetation remain (Fig. 3).

3 Method

The vegetation classification algorithm is split into three major components, consisting of six steps including the preprocessing (Fig. 4): (i) Feature selection and normalization (Section 3.1–3.5), (ii) Dimensional reduction and clustering (Section 3.6–3.7) and (iii) Vegetation classification with additional label improvement (Section 3.8–3.9). The features obtained from the LiDAR point cloud can be represented as a high-dimensional dataset, which is reduced to a two-dimensional dataset with UMAP. This dimensionally reduced dataset is first clustered, which generates an output of groups which are mostly vegetation. Subsequently, the generated clusters are classified into two categories: vegetation and other, which is achieved through a clusterwise planarity score and further improved by graph theoretical methods, as the clusters do not capture all points belonging to the submerged vegetation.

3.1 LiDAR feature selection

The acquisition of LiDAR data yields a multitude of features for each recorded point, including the coordinates in the selected reference coordinate system, amplitude and reflectance (Pfennigbauer & Ullrich, 2010). Additionally, research-oriented processing of the LiDAR data also makes use of specialized software, such as OPALS (Pfeifer et al., 2014), to calculate normal vectors and eigenvalues. The output of the OPALS software generates values such as σ_0, λ_1, λ_2 and λ_3 (Table 2), generated based on the covariance matrix of the local neighborhood (10 neighbors) within the robust normal estimation (based on the three position vectors), where a robust plane fitting of the selected neighbors is used to calculate the corresponding normal vector (Jutzi & Gross, 2009; Pfeifer et al., 2014; Weinmann et al., 2015). In the same processing step an offset $\Delta n(p)$ for the fitted plane of the normal vector is calculated, introducing a local planarity measure (Pfeifer et al., 2014). In addition, we calculate the umbrella curvature and volume

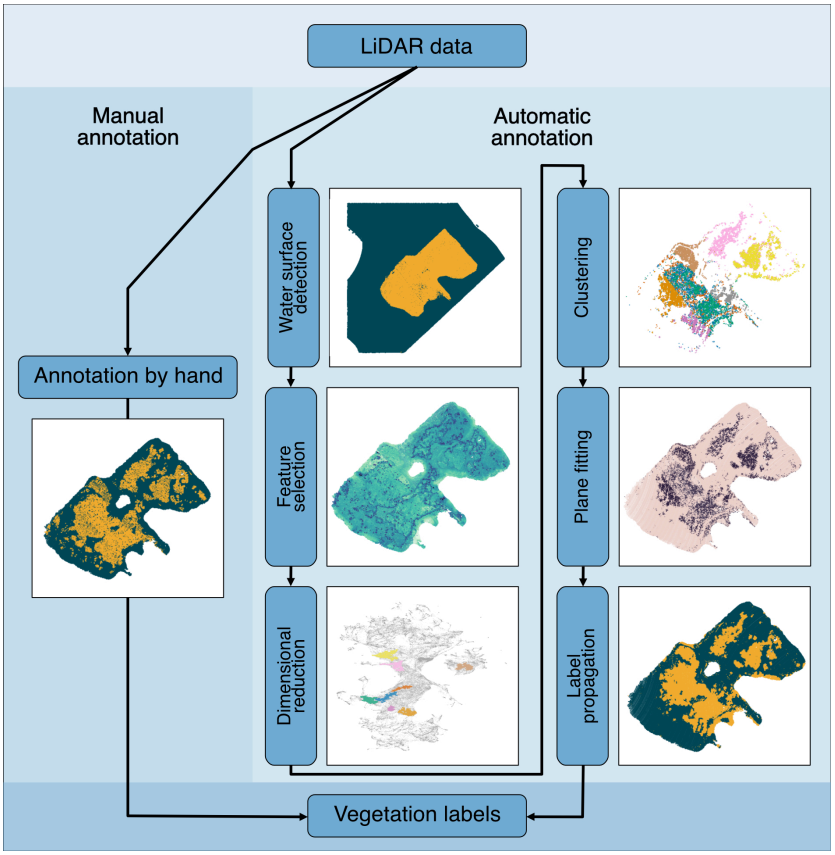


Fig. 4 Flow chart of the major steps outlined in the method section with the intermediate results produced by each step.

Table 1 Table displaying the different features of the LiDAR point cloud used for the high-dimensional data analysis. Each point $p \in \mathcal{P}$ of the point cloud is an array made of these descriptors and ordered as passed to the dimensional reduction.

Variable	Description	Reference	Unit
p_x	X-Coordinate		[m]
p_y	Y-Coordinate		[m]
p_z	Z-Coordinate		[m]
σ_0	σ_0 of normal estimation	(Pfeifer et al., 2014)	
λ_1	Eigenvalue 1 of normal estimation	(Pfeifer et al., 2014)	
λ_2	Eigenvalue 2 of normal estimation	(Pfeifer et al., 2014)	
λ_3	Eigenvalue 3 of normal estimation	(Pfeifer et al., 2014)	
Amplitude	Echo pulse amplitude	(RIEGL, 2012)	[dB]
Reflectance	Reflectance of the target	(RIEGL, 2012)	[dB]
V(p)	Volume	(Virtanen et al., 2020)	
κ(p)	Umbrella curvature	(Foorginejad & Khalili, 2014)	
Δn(p)	*Normal plane offset*	(Pfeifer et al., 2014)	
H(p)	Entropy	(Maity et al., 2010)	
λ_1/λ_3	Sphericity	(Thomas et al., 2018)	

of the local neighborhood of each point. For this, we first introduce a clear definition of the neighborhood (Section 3.2) and then calculate the umbrella curvature (Section 3.3) and volume (Section 3.4) for the selected points. Lastly, we calculate two more parameters based on the OPALS processing output: the sphericity and the entropy. Both calculated features provide insight into the object's structure beyond the single eigenvalue variables and therefore finalize the feature space (Jutzi & Gross, 2009; Thomas et al., 2018). The constructed array of features for each point (Table 1) contains substantial information about all points within the surveyed ecosystem and thus builds the basis for a higher-dimensional analysis. In conclusion, the more independent features describing the object can be extracted, the more stable the association becomes (Thomas et al., 2018).

3.2 Neighborhood and kNN-graph

Before we introduce the umbrella curvature (Section 3.3) and volume (Section 3.4), some preparatory steps are required, as these are measures of local neighborhoods within the point cloud. Let $\mathcal{P}$ be the set of position vectors from the observation (the set of *x-y-z* coordinates of the point cloud) for each observation $p \in \mathcal{P}$. We define the local neighborhood by selecting the 10 closest points for each point $p \in \mathcal{P}$ in 3D space, where the initial point $p \in \mathcal{P}$ is counted as the first point of the selected set. As a result, we can define the partially ordered set of all distances from $p \in \mathcal{P}$ as $\mathcal{D}(p)$ and apply this definition to characterize the local neighborhood $\mathcal{N}(p)$ of $p \in \mathcal{P}$ as:

In addition, the neighborhood definition allows us to create a network representation of the LiDAR point cloud. For this, we define the k-nearest neighbors graph (kNN-graph) of the point cloud on the basis of the neighborhood $\mathcal{N}(p)$ for all $p \in \mathcal{P}$. The created undirected unweighted graph consists of the subset of all unique edges and all points given by the neighborhood definition. Initially each point has 9 edges to its closest neighbors, but as two points in the local neighborhood are automatically each other's neighbors, the duplicated edges resulting in those connections are removed to obtain a simple graph. Furthermore, if the surveyed area is sufficiently connected, the graph also consists of a single connected component.

In accordance with current best practices in high-dimensional data analysis, the neighborhood parameter is again set to 10 (Luecken & Theis, 2019). However, this parameter can be adjusted depending on the dataset size, spatial resolution or other factors affecting the extent of the vegetation features that can be detected with the LiDAR system. The advantage of the generated graph representation is shown in Section 3.9. There, the kNN-graph is used to improve the final vegetation labels, and therefore the introduction of the neighborhood concept becomes a vital tool in the analysis of structural features within the point cloud dataset.

$$\mathcal{D}(p) = \left\{ \underbrace{\|p - p_{i_1}\|}_{d_1=0} \leq \underbrace{\|p - p_{i_2}\|}_{d_2} \leq \ldots \leq \underbrace{\|p - p_{i_n}\|}_{d_n} \;\middle|\; p_i \in \mathcal{P},\ n = |\mathcal{P}| \text{ and } n \in \mathbb{N} \right\} \quad (1)$$

$$\mathcal{N}(p) = \left\{ p_i \;\middle|\; \|p - p_i\| \leq d_{10} \text{ for } p_i \in \mathcal{P} \text{ and } d_{10} \in \mathcal{D}(p) \right\} \quad (2)$$

https://doi.org/10.58440/ihr-30-2-a16

3.3 Umbrella curvature

To measure the roughness in the point cloud, we deploy the measure of umbrella curvature in the local neighborhood of each point. The umbrella curvature for a point $p \in \mathcal{P}$ is defined as the sum of the curvatures between the current point p and its n closest neighbors, using the inner product and the normal vector n to the fitted plane at p (Foorginejad & Khalili, 2014).

$$\kappa(p, p_i) = \left| \left\langle \frac{p - p_i}{\|p - p_i\|}, \vec{n} \right\rangle \right| \tag{3}$$

Calculating this curvature for each point in the neighborhood, we get the umbrella curvature of p as

$$\kappa(p) = \sum_{i=1}^{10} \kappa(p, p_i) = \sum_{i=1}^{10} \left| \left\langle \frac{p - p_i}{\|p - p_i\|}, \vec{n} \right\rangle \right| \tag{4}$$

This measure can be compared to the amount an umbrella opens up with p as the umbrella's center (Foorginejad & Khalili, 2014). In the context of submerged vegetation, this measure indicates whether the neighborhood of a point is smooth or whether it has a varying vertical extent (Fig. 5).

3.4 Volume

To further expand the feature space related to structural features, we add a measure of volume for each local neighborhood. This measure is based on the volume of the convex hull of the points, which by definition is the smallest convex enclosement of the points selected (Moklyachuk, 2021).

Through the triangulation of the convex polytope, the volume V(p) can be numerically calculated, e.g., using SciPy (Virtanen et al., 2020). The convex hull is a measure for the general neighborhood size and also an estimate of the volumetric point density. Therefore, vegetation points should have larger volume as the points within the neighborhood exhibit varying vertical extent due to the fact that the laser pulses are reflected at different heights throughout the vegetation, while the terrain in the pond is generally smooth.

3.5 Entropy

Lastly, we also calculate the entropy $H(p)$ of the scattering object, which relates to the randomness of the scattering target (Maity et al., 2010; Jin & Cloude, 1994). Low entropy values indicate a single dominant scattering element and high values imply that the target has scattering components, where no single component dominates (Maity et al., 2010). The entropy H of the point p and the eigenvalues λ_1, λ_2 and λ_3 can be calculated through

$$H(p) = -\sum_{j=1}^{3} \left[\frac{\lambda_j}{\sum_{i=1}^{3} \lambda_i} \cdot \log \left(\frac{\lambda_j}{\sum_{i=1}^{3} \lambda_i} \right) \right] \tag{5}$$

The introduced parameter improves the understanding of the randomness of the scattered media and therefore further improves the understanding of the measured target (Fig. 5). A higher randomness corresponds to a higher diversity in the spatial distribution of the points, which is associated with vegetation canopy (Liu et al. 2022)

3.6 Data normalization

After feature selection, the next step in the analysis is to homogenize the value range of the individual features (z-score transformation), as they have different scales (Sainburg et al., 2021; Pedregosa et al., 2011). Taking all features F as one part of the dimensional input and the number of points in the point cloud as the second, a high-dimensional dataset with dimension of |F| can be constructed. This dataset cannot be visualized in conventional ways, as the data structure now has $|\mathcal{P}|$ points along |F| dimensions. In terms of data structure, the new

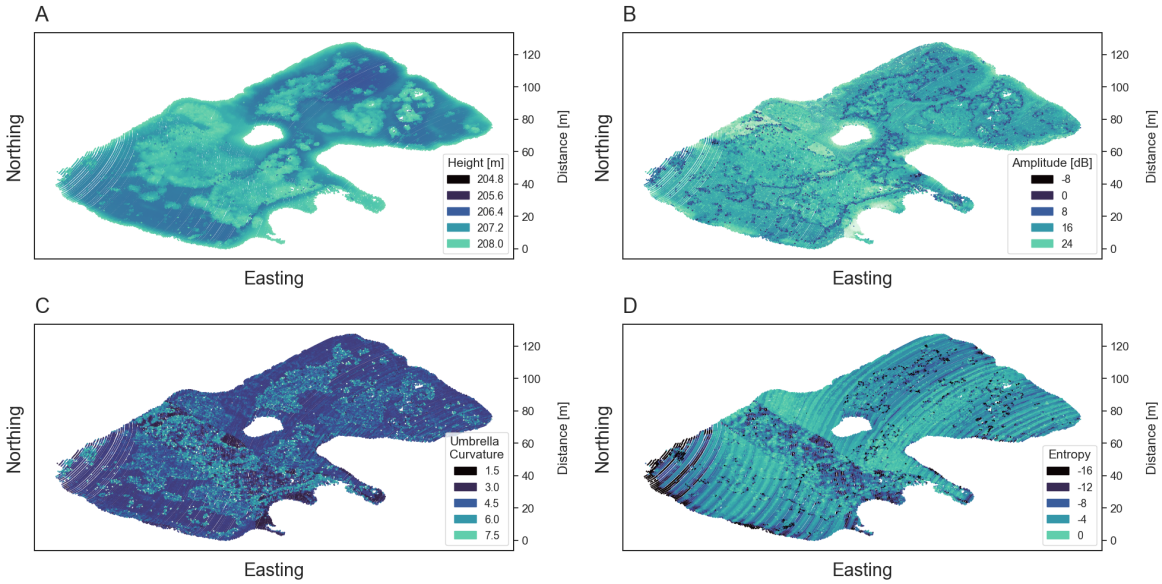


Fig. 5 Visualization of a selection of features introduced in Table 1 for Pond 2. (a) Vertical coordinate *Z*. (b) Recorded amplitude in dB. (c) Umbrella curvature for each point using a neighborhood of 10 points (Foorginejad & Khalili, 2014). (d) Entropy of each point (Jin & Cloude, 1994). In (d) the scan pattern of the LiDAR system and the overlapping regions of the scans becomes visible.

high-dimensional dataset corresponds to a matrix of the shape $|\mathcal{P}| \times |F|$. To finalize the data preparation for the dimensional reduction, a standard scaler has to be applied to all feature values (z-score normalization), otherwise the values would form different distributions based on their maximum or mean values rather than displaying similar patterns across all features. Let $\Phi \in F$ be a feature of the point cloud with feature values $v(\Phi)$, mean value μ_Φ and standard deviation σ_Φ, then the standard scaler is given by the following mapping.

$$v(\Phi) \mapsto \frac{v(\Phi) - \mu_\Phi}{\sigma_\Phi} \tag{6}$$

3.7 Dimensional reduction and clustering

All points of the point cloud are now in a form that allows to look for patterns regarding their features. But as these features are given in a high-dimensional space, they are affected by the "curse of high-dimensionality", meaning that commonly used unsupervised methods create unconventional results depending on the metrics used (Assent, 2012; Beyer et al., 1999). Therefore, we deploy a technique often used in single-cell clustering (Luecken & Theis, 2019), where we use dimensional reduction techniques to project the feature space to a regular two-dimensional space, using UMAP (Sainburg et al., 2021). This dimensional reduction method approximates the high-dimensional shape of the data and creates a two-dimensional image of the underlying manifold through mathematical processing (Sainburg et al., 2021). This is comparable to a workflow based on PCA, with the additional advantage of capturing the shape of the high-dimensional dataset and translating high-dimensional similarity of features to a two-dimensional spatial proximity, which can be detected using clustering methods (Kurita, 2019).

To separate the dimensional reduction into groups of interest, clustering is applied to the created dimensionally reduced dataset. To group the points into clusters of interest and remove outliers, a density-based clustering algorithm (DBSCAN) is applied to the dimensionally reduced dataset (Pedregosa et al., 2011; Schubert et al., 2017; Ester et al., 1996). DBSCAN strongly depends on the selection of the epsilon parameter, which defines the maximum distance between two samples to be considered in the neighborhood of one other (Pedregosa et al., 2011). This in turn influences the size and furthermore the number of clusters. For the vegetation classification, epsilon is fine-tuned within a range of 0.04 to 0.06, which corresponds to a sufficiently small neighborhood in the dimensionally reduced dataset. The epsilon parameter is selected within this range, to avoid over-clustering the data and simultaneously extract more than a single cluster. By applying DBSCAN, the different clusters of similar features can be extracted, which then form the basis for the following vegetation annotation. The extracted clusters are furthermore filtered in size by a general minimum cluster size of 500 points, as the vegetation should contain a large number of points and this helps to avoid excessive clustering of the data. The identified clusters can now be backtracked into the original LiDAR point cloud leaving multiple groupings of points with similar features, which are rooted in higher dimensional similarity rather than close spatial proximity. These clusters, extracted from the dimensionally reduced dataset, represent an initial extraction of the geometric similarities, displayed by the vegetation. Therefore, the groups detected by DBSCAN can be seen as the initial classification of submerged vegetation, with a subset of terrain that displays similar feature characteristics.

3.8 Vegetation classification via plane fitting

For each cluster that is not removed due to the minimum point filtering or DBSCAN outlier detection, a plane is based on the *x-y-z*-vector positions of the points and the distance to the plane is calculated for each point of the cluster, as this improves the vegetation within the clustering by removing planar clusters (terrain). Vegetation generally results in uneven surfaces with high vertical differences of the points due to multiple reflections in different height levels, recorded by the LiDAR system. In contrast, the underwater terrain of the surveyed ponds is generally smooth. Additionally, with the medium sized footprint of the deployed LiDAR system, small deviations in height are smoothed out. Therefore, the plane fitting creates two groups of clusters on a macro scale (compared Section 3.1), with either small or large pointwise deviations from the plane. To classify the vegetation, we introduce here a filtration of the plane fitting residual, where points with above mean residual are classified as vegetation and those below as terrain.

3.9 Label propagation

The vegetation detection method has so far introduced an initial classification based on UMAP, clustering and plane fitting. However, this classification is sparse, as the clustering fails to extract all vegetation points and therefore does not sufficiently capture the vegetation within the submerged ecosystem. We therefore improve the existing labels through label propagation, a tool commonly deployed in graph theory (Raghavan et al., 2007). For the label propagation, the neighborhood in the form of the kNN-graph introduced in the Section 3.2 is used. The labels from the initial classification are transferred to the vertices of the kNN-graph and the method then compares the labels of neighboring vertices, updating the vertex label based on a majority of labels within the current neighborhood (Csardi & Nepusz, 2006). By only adjusting the terrain labels and keeping all initial vegetation labels, the label propagation can extend the vegetation labels to vertices in the neighborhood that feature a high connectivity to vertices with the same label. Through this extension of the vegetation labels, the general under-performance of the UMAP extraction can be compensated and thus denser vegetation clusters can be annotated.

https://doi.org/10.58440/ihr-30-2-a16

3.10 Macrophyte canopy height estimation

Based on the aquatic vegetation extracted from the dataset, a map of the vegetation height can be created. This canopy height estimation uses the points classified as vegetation to estimate the height in relation to a digital terrain model (DTM) generated from the points classified as underwater terrain. To construct the DTM, we use the point cloud processing software CloudCompare (CloudCompare 2.12.4, 2024), which features a rasterization tool to generate DTMs. There the DTM is based on the shoalest z-values of the non-vegetation points for each grid cell, accounting for potential outliers in the water column. Furthermore, the z-values are computed based on a grid distance of 2.5 m. To derive the macrophyte canopy height above the interpolated ground, we can now subtract the height of each vegetation point from the closest DTM ground point and record all positive differences for the canopy height. The height estimation based on the averaged z-values, holds true for the surveyed ponds, as the vegetation within the pond predominantly consists of Charophyceae. This type of vegetation grows as a dense population and thus the majority of laser pulses are being reflected by the canopy. This generates a generally uniform point cloud, representing the uppermost layer of the vegetation as only few LiDAR echo pulses of the stem are recorded.

3.11 Area and volume estimation of the macrophyte population

The area of the ponds covered with submerged vegetation can be estimated by rasterizing both the water surface area and the submerged vegetation and comparing the created cells. This is done by first rasterizing the pond into 1m x 1m cells, both for the clustered vegetation $\mathcal{C}(P_V)$ and the pond's water surface $\mathcal{C}(P_W)$. For this, let $\mathcal{P}_V$ be the set of points classified as vegetation and $\mathcal{P}_W$ be the set of water surface points extracted with the SVB method (Schwarz et al., 2019). This approximation of the water surface could further be enhanced by manual annotation, but to improve on the automated detection, the provided surface model is solely based on the SVB algorithm. Therefore an underestimation of the water surface has to be taken into account, which typically only affects the closest . The cells are calculated by rounding the x- and y-coordinates of the vegetation and the water surface to the nearest integer and merging all cells with the same rounded coordinates. Dividing the vegetated area by the water surface area then provides an estimation of the vegetation coverage $A(\mathcal{P}_V)$ [%] of the pond.

$$A(\mathcal{P}_V) = \frac{|\mathcal{C}(\mathcal{P}_V) \cap \mathcal{C}(\mathcal{P}_W)|}{|\mathcal{C}(\mathcal{P}_W)|} \tag{7}$$

Furthermore, by multiplying the area of the vegetation cell $c_i \in \mathcal{C}(\mathcal{P}_V)$ with the average vegetation height of the cell $h_{mean}(c_i)$, a cell-wise vegetation volume can be calculated. by summing up all cell volumes, an overall estimation of the vegetation volume of the pond $\mathcal{V}(P_V)$ [m^3] can be derived, based on the canopy type and canopy height estimation (Section 3.10).

$$\mathcal{V}(P_V) = \sum_{c_i \in \mathcal{C}(\mathcal{P}_V)} c_i \cdot h_{\text{mean}}(c_i) \tag{8}$$

4 Results

To establish the context for the subsequent discussion, the results presented in this section display the labels produced by the classifier, a visual comparison using orthophotos and an overall quantitative evaluation. This provides an extensive insight into the labels produced by the classification, as well as a quantitative evaluation approach.

4.1 Vegetation classification

The results of the introduced vegetation classification can be seen in Fig. 6, where each major step of Section 3 is shown for Pond 2. After the preprocessing (Section 2.3) and the feature selection (Section 3.1–3.5), the vegetation classifier normalizes the data and extracts clusters of potential vegetation through dimensional reduction (Sections 3.6 and 3.7). The extracted clusters can be seen in Fig. 6a, where each cluster is larger than the minimum of 500 points and consists of points sharing a similarity of features. For each cluster, the plane fitting is applied (Section 3.8), distinctly separating the clusters into two groups of high and low plane fitting residuals (Fig. 6b). The high residual clusters are classified as vegetation and create an initial sparse classification (Fig. 6c), which is improved by the label propagation (Section 3.9). Leading to the final vegetation classification of the point cloud displayed in Fig. 6d.

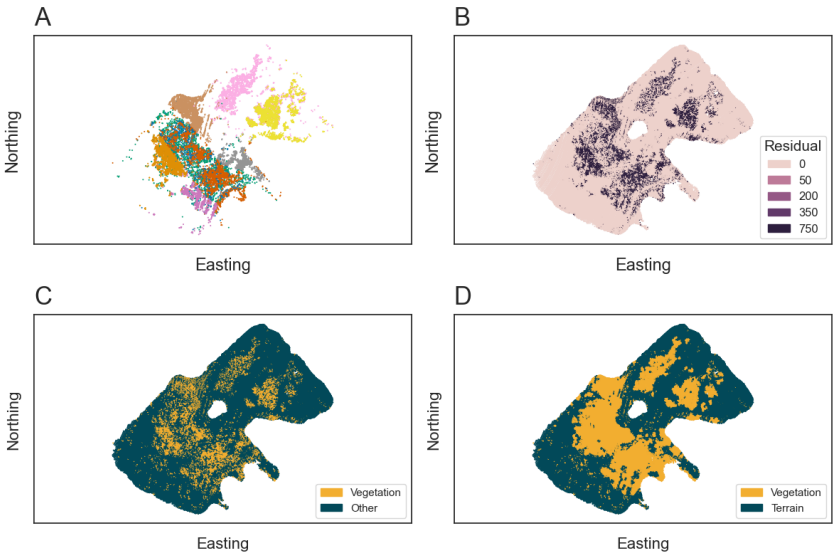


Fig. 6 (a) Clustering step after the dimensional reduction using UMAP (Sainburg et al., 2021). The points are colored by the clusters of Section 3.7 (b) Residual plot of the plane fitting from Section 3.8. Ground points have near zero deviation from the fitted plane, while the vegetation has a deviation higher than the mean. (c) Vegetation points as extracted after the plane fitting in orange and all other points in black. (d) The final vegetation labels after the label propagation of Section 3.9.

4.2 Visual comparison to photogrammetric data

The orthophotos allow for a visual comparison between the generated labels and the vegetation visible in the two ponds. In both cases, the classified LiDAR vegetation points can be compared with the vegetation visible in the ortho images (Fig. 7).

4.3 Comparison of manual annotations

For the manual annotation of the dataset, three experts in the field of bathymetry were selected. To evaluate labeling biases and put the results of Section 4.4 into a more comparative context, the individual manual annotations are cross-validated and furthermore compared to a randomly shuffled array of vegetation and terrain labels (Fig. 8). The results from Fig. 8 highlight the subjectivity of annotating point cloud data and the difference depending on the field of view from which the data is annotated. In addition, the distinction between true vegetation echoes and echoes from volume backscattering in the water column represents a general challenge for research in the extraction of underwater LiDAR echoes (Li et al., 2024). Therefore, the comparison underlines the minimum and maximum possible scores for the vegetation clustering.

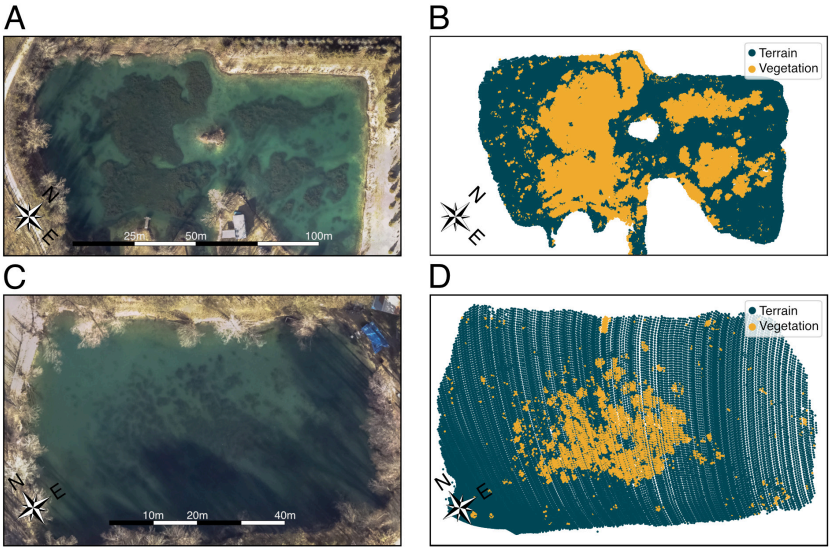


Fig. 7 Comparison of the orthophotos derived from the aerial images acquired within the measuring campaigns (pixel size: 5 cm) and the vegetation labels generated by the suggested vegetation detection method. (a) and (b) display the orthophotos and the labels for Pond 2. (c) and (d) display the corresponding data for Pond 3a, which also contains a small extent of vegetation.



Fig. 8 Comparison of all manually annotated labels and the random labels (truly random annotation) to one another, for the Pond 2 dataset. The number of each tick label corresponds to one of the experts annotating the data and the lengthwise- and across-nomenclature represent the direction of the annotation. Each value represents the mean score of the metrics introduced in Table 2, for the two labels compared. Additionally, each label is also compared to a random annotation for each point as a reference.

4.4 Accuracy assessment with annotated data

To evaluate the vegetation detection method on a quantitative basis, we compare the generated labels to manually annotated labels for the same pond. This is done for several metrics, displayed in Table 2. Each score compares the annotated vegetation labels to the labels of the classification algorithm and outputs a score between 0 and 1. The lowest possible score is 0, indicating a bad fit, and 1 indicates an ideal consensus between the two sets of labels (Pedregosa et al., 2011).

With the dataset introduced in Section 2.2 we can evaluate the labels generated by the described vegetation classification method. The quantitative results are reported in Fig. 9 displaying the confusion matrix of each manual annotation compared to the automatically generated labels. The matrices furthermore indicate the type I errors (false positives) and type II errors (false negatives) of the classification, which fall within a 10–30 % margin. Similarly, the true positives are approximately 80 % to 99 %. The results for Pond 3a display a true positive rate of close to 100 %, while for Pond 2 the scores reach a maximum of 87 %. Contrary, the true negatives are lower for Pond 2 compared to Pond 3a. This indicates that the method overestimated the vegetation in Pond 2, while in Pond 3a the vegetation was underestimated.

The applied metrics (RI, FMI, F1, Jaccard, Precision, Recall) are commonly used for assessing clustering methods, especially for two-class problems as in our case (Amigo et al., 2009; Fahad et al., 2014; Pedregosa et al., 2011). Most of the evaluation metric scores are in the range from 0.54 to 0.96 (Figs. 9a and 9c). For the majority of the scores (all except Jaccard), the scores are based on a comparison between true positives and true negatives and false positives and false negatives. Therefore, a score close to 1 reflects high true positives and true negatives, with furthermore low type I and II errors. The Jaccard index in contrast is based on set intersection, a score of 1 indicating that the labels share the exact same points. Comparing the different metrics therefore outlines how high the type I and II errors are for each pond and furthermore how identical the sets of labels are. In Pond 2, this mathematical basis of the metrics is reflected in a lower overall score due to the presence of higher errors. Contrary, Pond 3a, which exhibits more distinct vegetation, has an increased score.

We can conclude that the performance of the vegetation classification for Pond 2 and Pond 3a stands between 0.74 and 0.84 mean performance,

https://doi.org/10.58440/ihr-30-2-a16

Table 2 Table containing the different metrics used in the evaluation of new vegetation classification labels.

Acronym	Name	Scoring	Reference
F1	F1 score	[0, 1]	[(Pedregosa et al., 2011)
Recall	Recall	[0, 1]	[(Pedregosa et al., 2011)
RI	Rand Index	[0, 1]	(Pedregosa et al., 2011)
Jaccard	jaccard Index	[0, 1]	(Pedregosa et al., 2011)
Precision	Precision score	[0, 1]	(Pedregosa et al., 2011)
FMI	Fowlkes-Mallows Index	[0, 1]	(Pedregosa et al., 2011)

across all metrics. Pond 3a has an increased score due to higher true positives and true negatives, compared to Pond 2.

4.5 Vegetation parameters

The vegetation parameters obtained through the methodology, outlined in Section 3.10, can be expressed as a map of the canopy height (Figs. 10a and 10c) and distribution plots (Figs. 10d and 10b). For the calculated parameters of the Section 3.11 the results for the ponds are shown in Table 3.

The vegetation height map (Fig. 10) highlights the differences in vegetation growth for both ponds. The complex structures visible in Pond 2 show varying vertical extent. Patches of larger vertical extent are mostly concentrated in dense regions with small spatial extent and regions of low grown vegetation span across larger areas of the pond. Pond 3a, in turn, has a limited macrophyte population with a single patch of notable vegetation. These differences are furthermore reflected in the quantitative parameters of both ponds displayed in Table 3. Additionally, the differences in vertical extent can be seen in the two distributions displayed in Figs. 10b and 10d. There, Pond 2 displays a wide range of different heights with a higher degree of low vegetation (<0.5 m) compared to high vegetation (0.5–3 m), while Pond 3a displays a distribution of similar vertical extent.

5 Discussion

5.1 Challenges through scan strip overlap

One of the challenges in the dataset of Pond 2 is

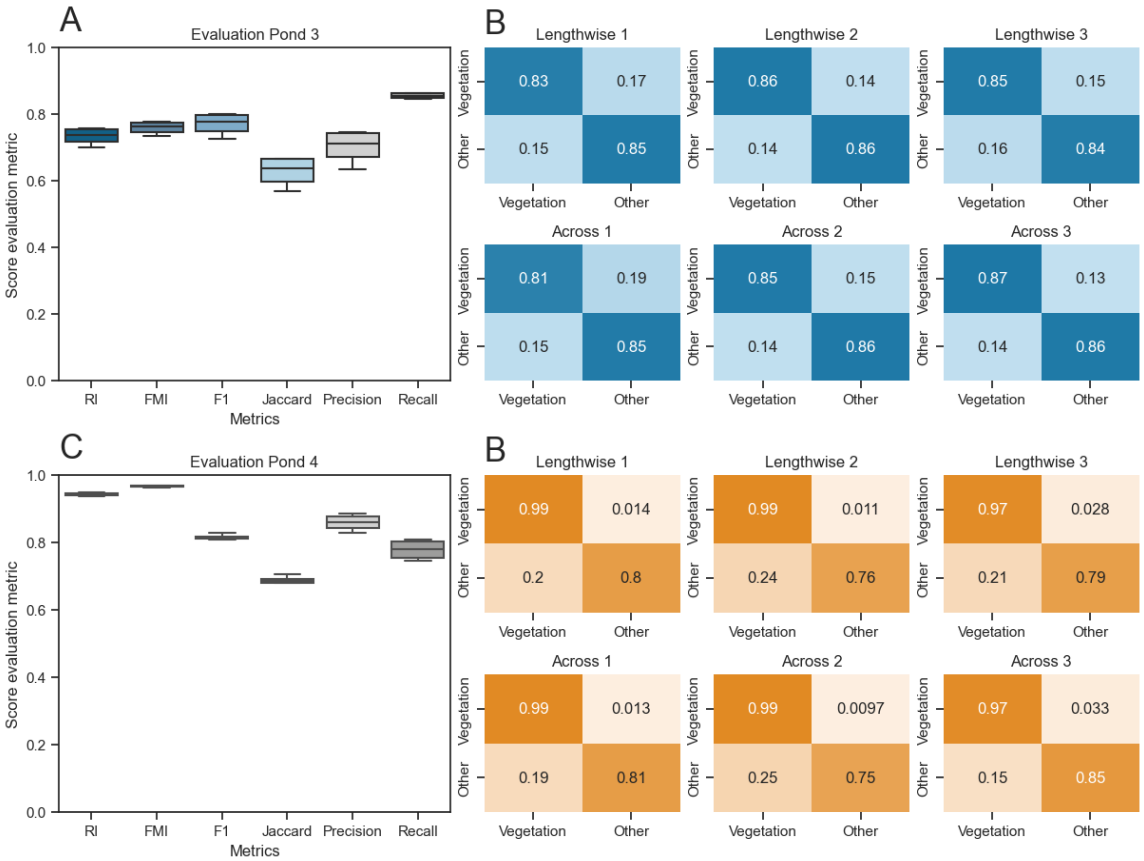


Fig. 9 (a, c) Boxplot of the evaluation scores for each comparison of the manually annotated data to the generated vegetation clustering. Each distribution contains the six different annotations from the three experts. The name and additional information about the metrics are displayed in Table 2. (b, d) Confusion matrices for each manual annotation used in the evaluation. The columns represent the individual experts and the rows the two employed axis directions used for labeling (first column: SW to NE / along, second column: SE to NW / across).2, for the two labels compared. Additionally, each label is also compared to a random annotation for each point as a reference.

Table 3 Vegetation parameters extracted for each of the two ponds.

Dataset	Water surface area	Vegetation covered area	Vegetation volume
Pond 2	9.904 m^2	42.9%	6.598 m^3
Pond 3a	3.546 m^2	21.6%	643 m^3

that the dataset contains points from two partially overlapping flight strips, requiring downsampling to achieve a homogeneous point density, which is a prerequisite for the introduced method. A disadvantage of the selected approach is that through the cutoff, the distribution of the point cloud changes and thus a partial bias towards the overlap remains. This change in point distribution is clearly visible in Fig. 5d and can also be detected in Fig. 6a. In Fig. 6a, the change in structure can be seen in the green and orange cluster. There, the clusters from the same outlines as seen in Fig. 5d highlight the similarity within the strip overlap and furthermore in the high-dimensional feature space.

The artificially increased similarity of the strip overlap could potentially be overcome by the selection of a fixed distance neighborhood instead of a k-nearest neighborhood and should improve deviations of the eigenvalue related measures, as the neighborhood selection is influenced by the point density. Therefore, the vegetation classification method underperforms in the case of Pond 2, which suggests using a more homogeneous thinning approach to avoid bias in the strip overlap.

Other factors to consider are the alignment of the point clouds. In case of Pond 2, the two point clouds were not perfectly aligned, leading to discrepancies in the point cloud features. Such offsets of the two flight strips could lead to misaligned terrain points, which could be interpreted by the method as low-grown vegetation. This could be improved through better georeferencing and should ideally minimize distribution-based errors (Pöppl et al., 2024). Overall, the observations from the dataset suggest the importance of ensuring the highest possible quality of alignment through pre-processing of the LiDAR data and to correct remaining feature offsets based on differences in densities to overcome potential offsets.

5.2 Parameter selection and supervision

A common challenge in high-dimensional data analysis, in addition to dimension reduction, is the extraction of features from the projected space (Luecken & Theis, 2019; Allaoui et al., 2020). In a two- or three-dimensional projection of the data, the distances do not relate to physical based metrics, which can induce problems in the parameter selection of clustering algorithms. Therefore, the selection of the correct clustering algorithm combined with a good parameter selection is essential for extracting good results from the dimensionally reduced datasets. For many of the commonly used clustering

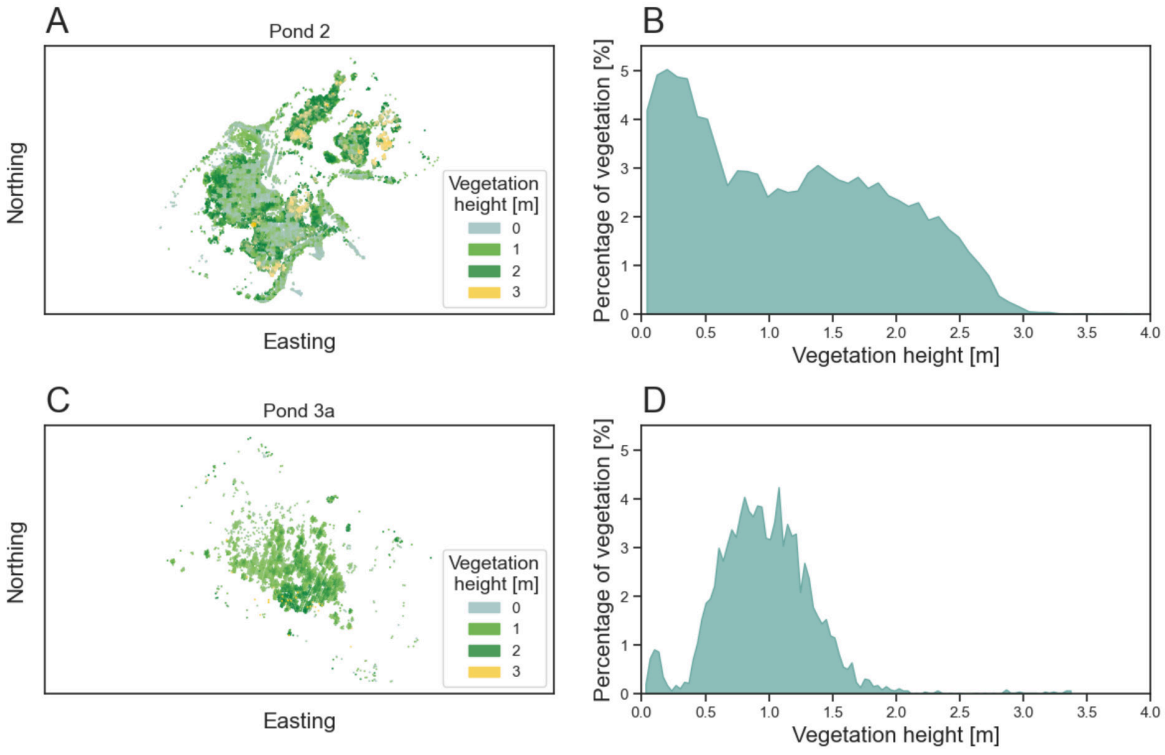


Fig. 10 (a, c) Plane view of the aquatic vegetation extracted from Pond 2 and Pond 3a datasets. Each point of the extracted vegetation is colored by the vegetation height in relation to the DTM. The second panel (b, d) shows the histogram of the extracted vegetation heights for each point of the two ponds, given as percentage compared to all points of the submerged vegetation.

https://doi.org/10.58440/ihr-30-2-a16

methods for two-dimensional projection of the data, a supervision or revisiting of the clustering step is required. This often results in fine-tuning distance parameters or clustering centroids (Luecken & Theis, 2019). Other algorithms use graph-based methods or multi-resolution clustering to reduce human supervision and time spent on parameter fine-tuning (Luecken & Theis, 2019; Levine et al., 2015; Wolf et al., 2019; Zappia & Oshlack, 2018). These methods show promising results in other fields, but require more complex workflows or, in the case of graph-based methods, data with more dimensions than the LiDAR dataset provides (MacQueen et al., 1967; Levine et al., 2015; Wolf et al., 2019).

Therefore, we use a simpler approach in this paper based on commonly used density-based clustering (DBSCAN), which further provides an integrated outlier detection (Pedregosa et al., 2011; Schubert et al., 2017; Ester et al., 1996). The downside of this method is the necessity of a resolution parameter for the dimensionally reduced space. DBSCAN uses a Euclidean distance measure to extract the clusters, which, if run with standard parameters, might lead to an over- or under-clustering of the projection space. This parameter requires supervision and a general knowledge of the dispersion of vegetation in the lake to achieve maximum accuracy. A promising solution for the extraction of detailed clusters without over-clustering is the emerging multi-resolution consensus clustering approach (Goggin & Zunder, 2023). This would cluster at different resolutions and merge clusters based on similarity, making the parameter selection obsolete (Goggin & Zunder, 2023; Zappia & Oshlack, 2018).

5.3 Annotation in submerged datasets

A different source of uncertainty is the lack of objective and reliable ground truth data. The general approach of labeling data is by human annotation and comparison of the labels to the method's output. The challenge in manual annotation is that in regions of ambiguous groupings, the annotations are different due to subjective assessments, which is why the labels must not only be compared to the generated labels by the method, but also among each other (Zhu et al., 2019). This creates the opportunity to give an evaluation range for the labeled data. In general, the evaluation of point cloud data profits from cross-comparison, as the large volume of data and the general complexity of 3D point clouds lead to differences in manual labeling by human operators (Anand & Rajalakshmi, 2023; Ye et al., 2021). It is furthermore noted that aerial images could potentially further be used for scene reconstruction via Dense Image Matching (Mandlburger, 2019). Such a comparison is currently outside the scope of this study, as the resolution and quality of the images are sub-optimal. Nonetheless, future studies could use high resolution images to reconstruct the vegetation canopy and through the comparison of the data, could potentially improve the evaluation.

5.4 Ecological insights

The extraction of the surface area covered with submerged vegetation and the vegetation volume both are quantities of importance in the analysis of the aquatic ecosystem. These measurements are already common for forestry LiDAR data (Zhou et al., 2022) and are important to the monitoring of ecosystems. The area and volume of the vegetation are used to estimate the biomass in the surveyed area and monitor vital changes of the ecosystem (Michalowska & Rapiński, 2021; Kumpumäki et al., 2015). Due to the larger footprint (0.91 m diameter) of the LiDAR system used in the survey, the measures introduced in this survey are based on large cells (1 m^2) and thus do only represent rough estimates of the vegetation parameters. This could potentially be improved by using UAV-borne surveys or smaller beam divergences for classical data acquisition with crewed aircraft, as this would allow for a higher point density and a higher spatial resolution, making smaller cells possible. In conclusion, the area and volume estimation techniques introduced in this study do not require expensive in-situ measurements and are solely data driven. This improves bottlenecks in the analysis of vast regions of aquatic landscapes, but could benefit from higher spatial resolutions.

6 Conclusion

The introduced vegetation detection method benefits from recent advancements in high-dimensional data analysis and establishes an automated workflow for vegetation detection with minimal parameter selection. Through the extension of standard LiDAR features in addition with calculated structural descriptors, a high-dimensional dataset of the LiDAR point cloud can be obtained. This high-dimensional dataset can then be analyzed for similarities of features through dimensional reduction and clustering. Each detected cluster is further tested for planarity to extract the clusters representing vegetation, which (i) builds the basis for vegetation labeling of the point cloud with only minimal parameter tuning and (ii) furthermore allows for estimation of vegetation area and volume.

This enables ecological analysis of submerged ecosystems, which is beneficial in a broader context as obtaining fundamental insights into the working principles and changes of aquatic ecosystems have become a primary focus of climate monitoring. Overall, the introduction of bathymetric LiDAR shows promising results for the automated extraction of vegetation in LiDAR point cloud and enables future work to go beyond what is currently possible using only in-situ measurements.

https://doi.org/10.58440/ihr-30-2-a16

References

Ackleson, S. and Klemas, V. (1987). Remote sensing of submerged aquatic vegetation in lower Chesapeake Bay: A comparison of landsat MSS to TM imagery. *Remote Sensing of Environment, 22*(2), pp. 235–248.

Aleksandra, K., Fantina, M., Marco, S., Ferrarin, C. and Giacomo, M. G. (2015). Assessment of submerged aquatic vegetation abundance using multibeam sonar in very shallow and dynamic environment. The Lagoon of Venice (Italy) case study. In *2015 IEEE/OES Acoustics in Underwater Geosciences Symposium (RIO Acoustics)*, pp. 1–7. IEEE.

Allaoui, M., Kherfi, M. L. and Cheriet, A. (2020). Considerably Improving Clustering Algorithms Using UMAP Dimensionality Reduction Technique: *A Comparative Study, International conference on image and signal processing*, pp. 317–325. Springer International Publishing.

Amani, M. and Mahdavi, G. (2021). *ML and LiDAR to map aquatic vegetation*.

Amigo, E., Gonzalo, J., Artiles, J. and Verdejo, F. (2009). A comparison of extrinsic clustering evaluation metrics based on formal constraints. *Information retrieval, 12*, pp. 461–486.

Anand, B. and Rajalakshmi, P. (2023). Pipeline for automation of lidar data annotation. In *2023 IEEE Sensors Applications Symposium (SAS)*, pp. 1–6. IEEE.

Assent, I. (2012). Clustering high dimensional data. *WIREs Data Mining and Knowledge Discovery, 2*(4), pp. 340– 350.

Bellman, R. and Kalaba, R. (1959). A mathematical theory of adaptive control processes. *Proceedings of the National Academy of Sciences, 45*(8), pp. 1288-1290.

Beyer, K., Goldstein, J., Ramakrishnan, R. and Shaft, U. (1999). When is "nearest neighbor" meaningful? In *Database Theory—ICDT99: 7th International Conference Jerusalem, Israel, January 10–12, 1999 Proceedings 7*, pp. 217–235. Springer.

Blondel, P. (2008). *A review of acoustic techniques for habitat mapping. Hydroacoustics, 11*, pp. 29–38.

Calantropio, A., Menna, F., Skarlatos, D., Balletti, C., Mandlburger, G., Agrafiotis, P., Chiabrando, F., Lingua, A. M., Giaquinto, A. and Nocerino, E. (2024). Under and through water datasets for geospatial studies: the 2023 ISPRS scientific initiative "nautilus". *ISPRS Annals of the Photogrammetry, Remote Sensing and Spatial Information Sciences, 10*, pp. 33–40.

Carpenter, S. R. and Lodge, D. M. (1986). Effects of submersed macrophytes on ecosystem processes. *Aquatic Botany, 26*, pp. 341–370.

Chen, L. (2009). Curse of Dimensionality. In L. Liu and M. T. Özsu (Eds.), *Encyclopedia of Database Systems*. Springer, Boston, MA. https://doi.org/10.1007/978-0-387-39940-9_133

CloudCompare (2024). *3D point cloud and mesh processing software*. Open source project, GPL.

Coops, H., Kerkum, F. C. M., van den Berg, M. S. and van Splunder, I. (2007). Submerged macrophyte vegetation and the european water framework directive: assessment of status and trends in shallow, alkaline lakes in the netherlands. *Hydrobiologia, 584*(1), pp. 395–402.

Csardi, G. and Nepusz, T. (2006). The igraph software. *Complex syst, 1695*, pp. 1–9.

De Grandpre, A., Kinnard, C. and Bertolo, A. (2022). Open-source analysis of submerged aquatic vegetation cover in complex waters using high-resolution satellite remote sensing: An adaptable framework. *Remote Sensing, 14*(2), p. 267.

Dierssen, H. M., Ackleson, S. G., Joyce, K. E., Hestir, E. L., Castagna, A., Lavender, S. and McManus, M. A. (2021). Living up to the hype of hyperspectral aquatic remote sensing: Science, resources and outlook. *Frontiers in Environmental Science, 9*.

Domingos, P. (2012). A few useful things to know about machine learning. *Communications of the ACM, 55(10)*, pp. 78–87.

Espel, D., Courty, S., Auda, Y., Sheeren, D. and Elger, A. (2020). Submerged macrophyte assessment in rivers: An automatic mapping method using pleiades imagery. *Water Research, 186*, 116353.

Ester, M., Kriegel, H.-P., Sander, J., Xu, X., et al. (1996). A density-based algorithm for discovering clusters in large spatial databases with noise. *KDD, 96*, pp. 226–231.

Fahad, A., Alshatri, N., Tari, Z., Alamri, A., Khalil, I., Zomaya, A. Y., Foufou, S. and Bouras, A. (2014). A survey of clustering algorithms for big data: Taxonomy and empirical analysis. *IEEE transactions on emerging topics in computing, 2*(3), pp. 267–279.

Federal Office of Metrology and Surveying, BEV, (2024). Austrian map online. https://www.bev.gv.at/Services/Produkte/Austrian-Map/Austrian-Map-online.html (accessed 10 November 2024).

Foorginejad, A. and Khalili, K. (2014). Umbrella curvature: A new curvature estimation method for point clouds. *Procedia Technology, 12*, pp. 347–352.

García-Gutiérrez, J., Martínez-Álvarez, F., Troncoso, A. and Riquelme, J. C. (2015). A comparison of machine learning regression techniques for LiDAR-derived estimation of forest variables. *Neurocomputing, 167*, pp. 24–31.

Goggin, S. M. and Zunder, E. R. (2023). *A hyperparameter-randomized ensemble approach for robust clustering across diverse datasets*.

Held, P. and Schneider von Deimling, J. (2019). New feature classes for acoustic habitat mapping—a multibeam echosounder point cloud analysis for mapping submerged aquatic vegetation (sav). *Geosciences, 9*(5), p. 235.

Jin, Y.-Q. and Cloude, S. R. (1994). Numerical eigenanalysis of the coherency matrix for a layer of random nonspherical scatterers. *IEEE Transactions on Geoscience and Remote Sensing, 32*(6), pp. 1179–1185.

Jutzi, B. and Gross, H. (2009). Nearest neighbour classification on laser point clouds to gain object structures from buildings. *The International Archives of the Photogrammetry, Remote Sensing and Spatial Information Sciences, 38*(1), pp. 4–7.

Koma, Z., Zlinszky, A., Bekö, L., Burai, P., Seijmonsbergen, A. C. and Kissling, W. D. (2021). Quantifying 3d vegetation structure in wetlands using differently measured airborne laser scanning data. *Ecological Indicators, 127*, 107752.

Kumpumäki, T., Ruusuvuori, P., Kangasniemi, V. and Lipping, T. (2015). Data-driven approach to benthic cover type classification using bathymetric lidar waveform analysis. *Remote Sensing, 7*(10), pp. 13390–13409.

Kurita, T. (2019). Principal component analysis (PCA). *Computer vision: a reference guide*, pp. 1–4.

Levine, J., Simonds, E., Bendall, S., Davis, K., Amir, E.-a., Tadmor, M., Litvin, O., Fienberg, H., Jager, A., Zunder, E., Finck, R., Gedman, A., Radtke, I., Downing, J., Pe'er, D. and Nolan, G. (2015). Data-driven phenotypic dissection of AML reveals

https://doi.org/10.58440/ihr-30-2-a16

progenitor-like cells that correlate with prognosis. *Cell, 162*(1), pp. 184–197.

Li, N., Truong, M.-L., Schwarz, R., Pfennigbauer, M. and Ullrich, A. (2024). Deep learning assisted exponential waveform decomposition for bathymetric lidar. *The International Archives of the Photogrammetry, Remote Sensing and Spatial Information Sciences, XLVIII-2-2024*, pp. 195–202.

Liu, X., Ma, Q., Wu, X., Hu, T., Liu, Z., Liu, L., Guo Q. & Su, Y. (2022). A novel entropy-based method to quantify forest canopy structural complexity from multiplatform lidar point clouds. *Remote Sensing of Environment, 282*, 113280.

Lønborg, C., Thomasberger, A., Stæhr, P. A. U., Stockmarr, A., Sengupta, S., Rasmussen, M. L., Nielsen, L. T., Hansen, L. B. and Timmermann, K. (2021). Submerged aquatic vegetation: Overview of monitoring techniques used for the identification and determination of spatial distribution in European coastal waters. *Integrated Environmental Assessment and Management, 18*(4), pp. 892–908.

Luecken, M. D. and Theis, F. J. (2019). Current best practices in single-cell rna-seq analysis: a tutorial. *Molecular Systems Biology, 15*(6).

Luo, J., Li, X., Ma, R., Li, F., Duan, H., Hu, W., Qin, B. and Huang, W. (2016). Applying remote sensing techniques to monitoring seasonal and interannual changes of aquatic vegetation in taihu lake, china. *Ecological Indicators, 60,* pp. 503–513.

MacQueen, J. et al. (1967). Some methods for classification and analysis of multivariate observations. In *Proceedings of the fifth Berkeley symposium on mathematical statistics and probability, 1*, pp. 281–297. Oakland, CA, USA.

Maity, S., Patnaik, C., Parihar, J. S., Panigrahy, S. and Reddy, K. A. (2010). Study of physical phenomena of vegetation using polarimetric scattering indices and entropy. IEEE Journal of Selected Topics in *Applied Earth Observations and Remote Sensing, 4*(2), pp. 432–438.

Mandlburger, G. (2019). Through-water dense image matching for shallow water bathymetry. *Photogrammetric Engineering amp; Remote Sensing, 85*(6), pp. 445–455.

Mandlburger, G. (2022). A review of active and passive optical methods in hydrography. *The International Hydrographic Review, 28*, pp. 8–52. https://doi.org/10.58440/ihr-28-a15

Mandlburger, G., Kölle, M., Pöppl, F. and Cramer, M. (2023a). Evaluation of consumer-grade and survey- grade uav-lidar. *The International Archives of the Photogrammetry, Remote Sensing and Spatial Information Sciences, 48*, pp. 99–106.

Mandlburger, G., Pfennigbauer, M., Schwarz, R. and Pöppl, F. (2023b). A decade of progress in topo- bathymetric laser scanning exemplified by the Pielach river dataset. *ISPRS Annals of the Photogrammetry, Remote Sensing and Spatial Information Sciences, 10*, pp. 1123–1130.

Mandlburger, G., Pfennigbauer, M., Schwarz, R., Flöry, S. and Nussbaumer, L. (2020). Concept and performance evaluation of a novel UAV-borne topo-bathymetric LiDAR sensor. *Remote Sensing, 12*(6), p. 986.

McCarthy, E. (1997). *Acoustic characterization of submerged aquatic vegetation*.

Michałowska, M. and Rapiński, J. (2021). A review of tree species classification based on airborne lidar data and applied classifiers. *Remote Sensing, 13*(3), p. 353.

Moklyachuk, M. (2021). *Convex optimization: Introductory course*.

Mumby, P. J., Green, E. P., Edwards, A. J. and Clark, C. D. (1999). The cost-effectiveness of remote sensing for tropical coastal resources assessment and management. *Journal of Environmental Management, 55*(3), pp. 157-166.

Murphy, F., Schmieder, K., Baastrup-Spohr, L., Pedersen, O. and Sand-Jensen, K. (2018). Five decades of dramatic changes in submerged vegetation in lake constance. Aquatic Botany, 144, pp. 31–37.

Nelson, S. A., Cheruvelil, K. S. and Soranno, P. A. (2006). Satellite remote sensing of freshwater macrophytes and the influence of water clarity. *Aquatic Botany, 85*(4), pp. 289–298.

O'Neill, J. D. and Costa, M. (2013). Mapping eelgrass (zostera marina) in the gulf islands national park reserve of canada using high spatial resolution satellite and airborne imagery. *Remote Sensing of Environment, 133*, pp. 152–167.

Pedregosa, F., Varoquaux, G., Gramfort, A., Michel, V., Thirion, B., Grisel, O., Blondel, M., Prettenhofer, P., Weiss, R., Dubourg, V., Vanderplas, J., Passos, A., Cournapeau, D., Brucher, M., Perrot, M. and Duchesnay, E. (2011). Scikit-learn: Machine learning in Python. *Journal of Machine Learning Research, 12*, pp. 2825–2830.

Pfeifer, N., Mandlburger, G., Otepka, J. and Karel, W. (2014). OPALS – a framework for airborne laser scanning data analysis. *Computers, Environment and Urban Systems, 45*, pp. 125–136.

Pfennigbauer, M. and Ullrich, A. (2010). Improving quality of laser scanning data acquisition through calibrated amplitude and pulse deviation measurement. In M. D. Turner and G. W. Kamerman (Eds.), *SPIE Proceedings*. SPIE.

Pöppl, F., Ullrich, A., Mandlburger, G. and Pfeifer, N. (2024). A flexible trajectory estimation methodology for kinematic laser scanning. *ISPRS Journal of Photogrammetry and Remote Sensing, 215*, pp. 62–79.

Preston, J. (2009). Automated acoustic seabed classification of multibeam images of Stanton Banks. *Applied Acoustics, 70*(10), pp. 1277–1287.

Raghavan, U. N., Albert, R. and Kumara, S. (2007). *Near linear time algorithm to detect community structures in large-scale networks*.

RIEGL (2012). LAS extrabytes implementation in RIEGL software. *Whitepaper*, p. 12.

RIEGL (2023). *Datasheet RIEGL VQ-840-G*.

Rowan, G. S. L. and Kalacska, M. (2021). A review of remote sensing of submerged aquatic vegetation for non-specialists. *Remote Sensing, 13*(4), p. 623.

Sabol, B. M., Eddie Melton, R., Chamberlain, R., Doering, P. and Haunert, K. (2002). Evaluation of a digital echo sounder system for detection of submersed aquatic vegetation. *Estuaries, 25*(1), pp. 133–141.

Sainburg, T., McInnes, L. and Gentner, T. Q. (2021). Parametric UMAP Embeddings for Representation and Semisupervised Learning. *Neural Computation, 33(*11), pp. 2881–2907.

Saputra, L. R. and Radjawane, I. M. (2022). *Seabed coverage classification using lidar bathymetry*.

Schiagintweit, G. E. O. (1993, October). Real-time acoustic bottom classification for hydrography a field evaluation of RoxAnn. In *Proceedings of OCEANS'93*, pp. III-214. IEEE.

Schmieder, K. (1995). Submersed macrophytes of two habitats in lake constance (untersee) and their relations to chemical composition of surface and sediment interstitial water. *Acta Botanica Gallica, 142*(6), pp. 651–657.

Schmieder, K. (2004). European lake shores in danger—concepts for a sustainable development. *Limnologica, 34*(1–2), p. 3–14.

Schubert, E., Sander, J., Ester, M., Kriegel, H. P. and Xu, X. (2017). Dbscan revisited, revisited: Why and how you should (still) use DBSCAN. *ACM Transactions on Database Systems, 42*(3), pp. 1–21.

Schwarz, R., Mandlburger, G., Pfennigbauer, M. and Pfeifer, N. (2019). Design and evaluation of a full-wave surface and bottom-detection algorithm for lidar bathymetry of very shallow waters. *ISPRS Journal of Photogrammetry and Remote Sensing, 150*, pp. 1–10.

Schwarz, R., Pfeifer, N., Pfennigbauer, M. and Ullrich, A. (2017). Exponential decomposition with implicit deconvolution of lidar backscatter from the water column. PFG – *Journal of Photogrammetry, Remote Sensing and Geoinformation Science, 85*(3), pp. 159–167.

Serpetti, N., Heath, M., Armstrong, E. and Witte, U. (2011). Blending single beam RoxAnn and multi-beam swath QTC hydro-acoustic discrimination techniques for the Stonehaven area, Scotland, UK. *Journal of Sea Research, 65*(4), pp. 442–455.

Shi, S., Bi, S., Gong, W., Chen, B., Chen, B., Tang, X., Qu, F. and Song, S. (2021). Land cover classification with multispectral LiDAR based on multi-scale spatial and spectral feature selection. *Remote Sensing, 13(*20), p. 4118.

Thomas, H., Deschaud, J.-E., Marcotegui, B., Goulette, F. and Gall, Y. L. (2018). *Semantic classification of 3d point clouds with multiscale spherical neighborhoods*.

Virtanen, P., Gommers, R., Oliphant, T. E., Haberland, M., Reddy, T., Cournapeau, D., Burovski, E., Peterson, P., Weckesser, W., Bright, J., van der Walt, S. J., Brett, M., Wilson, J., Millman, K. J., Mayorov, N., Nelson, A. R. J., Jones, E., Kern, R., Larson, E., Carey, C. J., Polat, İ., Feng, Y., Moore, E. W., VanderPlas, J., Laxalde, D., Perktold, J., Cimrman, R., Henriksen, I., Quintero, E. A., Harris, C. R., Archibald, A. M., Ribeiro, A. H., Pedregosa, F., van Mulbregt, P. and SciPy 1.0 Contributors (2020). SciPy 1.0: Fundamental Algorithms for Scientific Computing in Python. *Nature Methods, 17*, pp. 261–272.

Wagner, N., Franke, G., Schmieder, K. and Mandlburger, G. (2024). Automatic Classification of Submerged Macrophytes at Lake Constance Using Laser Bathymetry Point Clouds. *Remote Sensing, 16*(13), 2257.

Weinmann, M., Jutzi, B., Hinz, S. and Mallet, C. (2015). Semantic point cloud interpretation based on optimal neighborhoods, relevant features and efficient classifiers. *ISPRS Journal of Photogrammetry and Remote Sensing, 105*, pp. 286–304.

Wolf, F. A., Hamey, F. K., Plass, M., Solana, J., Dahlin, J. S., Göttgens, B., Rajewsky, N., Simon, L. and Theis, F. J. (2019). Paga: graph abstraction reconciles clustering with trajectory inference through a topology preserving map of single cells. *Genome Biology, 20*(1).

Wood, R. (1963). Adapting scuba to aquatic plant ecology. *Ecology, 44*(2), pp. 416–419.

Yamasaki, T. N., Jiang, B., Janzen, J. G. and Nepf, H. M. (2021). Feedback between vegetation, flow, and deposition: A study of artificial vegetation patch development. *Journal of Hydrology, 598*, p. 126232.

Yang, H., Lee, K., Choo, Y. and Kim, K. (2020). Underwater acoustic research trends with machine learning: Passive SONAR applications. *Journal of Ocean Engineering and Technology, 34*(3), pp. 227–236.

Ye, S., Chen, D., Han, S. and Liao, J. (2021). Learning with noisy labels for robust point cloud segmentation. In *Proceedings of the IEEE/CVF international conference on computer vision*, pp. 6443–6452.

Zappia, L. and Oshlack, A. (2018). Clustering trees: a visualization for evaluating clusterings at multiple resolutions. *GigaScience, 7*(7).

Zervas, D., Tsiaoussi, V. and Tsiripidis, I. (2018). Helm: a macrophyte-based method for monitoring and assessment of greek lakes. *Environmental Monitoring and Assessment, 190*(6).

Zhou, L., Li, X., Zhang, B., Xuan, J., Gong, Y., Tan, C., Huang, H. and Du, H. (2022). Estimating 3d green volume and aboveground biomass of urban forest trees by uav-lidar. *Remote Sensing, 14*(20), p. 5211.

Zhu, X. X., Hu, J., Qiu, C., Shi, Y., Kang, J., Mou, L., Bagheri, H., Häberle, M., Hua, Y., Huang, R., Hughes, L., Li, H., Sun, Y., Zhang, G., Han, S., Schmitt, M. and Wang, Y. (2019). *So2sat lcz42: A benchmark dataset for global local climate zones classification*.

https://doi.org/10.58440/ihr-30-2-a16

Authors' biographies

Jan Rhomberg-Kauert is a PhD student at TU Wien, working as a research assistant in the Department of Geodesy and Geoinformation. With a broad background in mathematics, computational biology and computer science, Jan currently focuses on developing innovative methodologies to improve hydrographic data classification and LiDAR signal processing. His research aims to enhance the understanding of full waveform bathymetric LiDAR with a focus on aquatic vegetation. There he actively engages with various academic and industry partners, contributing to different projects related to hydrography, photogrammetry and airborne LiDAR.



Jan Rhomberg-Kauert

Lucas Dammert is working as a PhD student at TU Wien on the trajectory estimation of multisensor systems (primarily unmanned airborne systems) using robotic total stations in a joint position between the groups of photogrammetry and engineering geodesy. During his B.Sc. and M.Sc., he studied Geodesy and Geoinformation in Dresden and Hamburg with a specialization in hydrography. His research interests lie in the fields of hydrography, photogrammetry and engineering geodesy with a focus on kinematic multisensor systems.



Lucas Dammert

Michael Grömer studied technical physics at Graz University of Technology and is currently writing his industrial dissertation on underwater inspections at hydropower plants, supervised by Gottfried Mandlburger from Vienna University of Technology. His industrial partner is the Austrian hydropower plant operator Verbund. The dissertation focuses on underwater photogrammetry for surveying and monitoring purposes using ROVs for new types of inspections and to avoid dangerous diving operations.



Michael Grömer

Dr. Martin Pfennigbauer holds a PhD in electrical engineering from Vienna University of Technology. He has been with RIEGL Laser Measurement Systems since 2005 and presently assumes the position of Chief Research Officer. Martin Pfennigbauer manages RIEGL's research activities and projects funded by the European Union and Austrian national programs. His special interest is the design and development of lidar instruments for surveying applications, with a focus on rangefinder design, waveform processing and point cloud analysis, specifically in the context of lidar bathymetry.



Martin Pfennigbauer

Dr. Gottfried Mandlburger studied geodesy at TU Wien, where he also received his PhD in 2006 and habilitated in photogrammetry with a thesis on "Bathymetry from active and passive photogrammetry" in 2021. In April 2024 he was appointed University Professor for Optical Bathymetry at TU Wien. His main research areas are airborne topographic and bathymetric LiDAR from crewed and uncrewed platforms, multimedia photogrammetry, bathymetry from multispectral images, and scientific software development. Gottfried Mandlburger is chair of the DGPF working group LiDAR and Austrians scientific delegate in EuroSDR. He received best paper awards from ISPRS and ASPRS for recent publications on bathymetry from active and passive photogrammetry.



Gottfried Mandlburger

https://doi.org/10.58440/ihr-30-2-a16

PEER-REVIEWED ARTICLE

Aguja Canyon – New approach added to the structural and morphological model in the continental margin of the Colombian Caribbean

Authors

Yerinelys Santos Barrera[1], María Fernanda Calderón Grande[1], Eliana Gutiérrez Rincón[2] and Johanna P. Vargas Morales[1]

Abstract

On the submerged continental margin of the Colombian Caribbean, the Aguja submarine canyon stands out, a structure formed by denudation processes that crosses the continental shelf and transports sediments to the deep waters in the Colombia basin. Using new hydrographic data and bathymetric analyses, this study shows a physical characterization of the canyon, which stretches for more than 197 km with depths of 10 m to 3,783 m and a width of 1 km to 8 km. Four segments controlled by regional structural geology are identified, each with a distinct channel direction. Aguja Canyon shows instability in its walls and surroundings with landslides, faults and mud volcanism, evidencing considerable tectonic and sedimentary activity along the continental margin.

Keywords

Aguja Canyon · submarine · morphology · Caribbean · bathymetry · roughness

Resumé

Sur la marge continentale submergée des Caraïbes colombiennes se distingue le canyon sous-marin de La Aguja, une structure formée par des processus de dénudation qui traverse le plateau continental et transporte des sédiments vers les eaux profondes du bassin de la Colombie. A l'aide de nouvelles données hydrographiques et d'analyses bathymétriques, cette étude présente une caractérisation physique du canyon, qui s'étend sur plus de 197 km avec des profondeurs de 10 m à 3 783 m et une largeur de 1 km à 8 km. Quatre segments contrôlés par géologie structurale régionale sont identifiés, chacun avec une direction de chenal distincte. Le canyon de La Aguja présente une instabilité de ses parois et de ses environs, avec des glissements de terrain, des failles et un volcanisme de boue, ce qui témoigne d'une activité tectonique et sédimentaire considérable le long de la marge continentale.

Resumen

En el margen continental sumergido del Caribe colombiano destaca el cañón submarino La Aguja, una estructura formada por procesos de denudación que atraviesa la plataforma continental y transporta sedimentos a las aguas profundas de la cuenca de Colombia. Usando nuevos datos hidrográficos y análisis batimétricos, este estudio muestra una caracterización física del cañón, que se extiende más de 197 km con profundidades de 10 m a 3.783 m, y una anchura de 1 km a 8 km. Se identifican cuatro segmentos controlados por la geología estructural regional, cada uno con una dirección de canal distinta. El cañón La Aguja muestra inestabilidad en sus paredes y alrededores con deslizamientos, fallas y volcanes de lodo, evidenciando una considerable actividad tectónica y sedimentaria a lo largo del margen continental.

✉ Yerinelys Santos Barrera · ysantosb@dimar.mil.co

[1] Dirección General Marítima de Colombia, Centro de Investigaciones Oceanográficas e Hidrográficas del Caribe (DIMAR-CIOH), Cartagena, Colombia

[2] Universidad Industrial de Santander (UIS), Bucaramanga, Colombia

https://doi.org/10.58440/ihr-30-2-a11

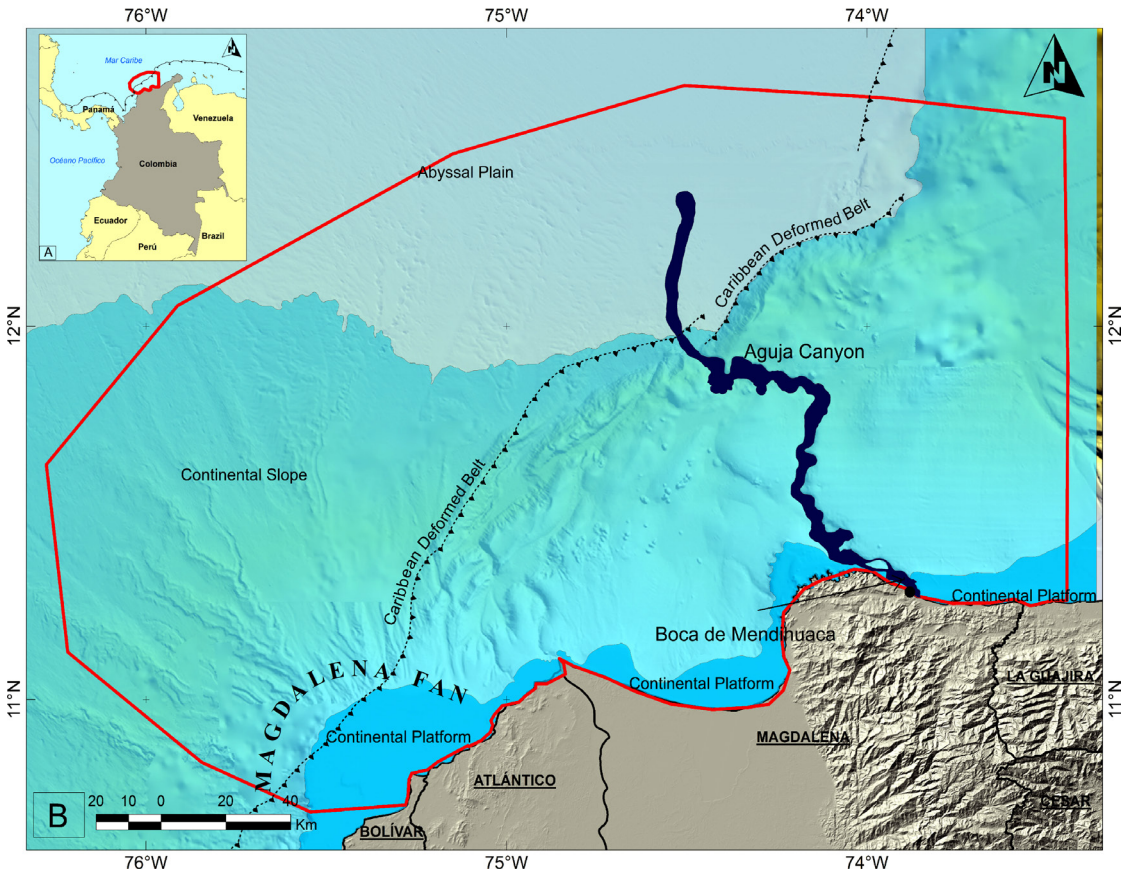


Fig. 1 Geographical location of the Aguja Canyon – department of Magdalena near the sector known as Boca de Mendihuaca. It crosses three parts of the continental margin: continental platform, continental slope and abyssal plain.

1 Introduction

A canyon identified north of the continental margin of the Colombian Caribbean is the Aguja Canyon, recognized from the vicinity of the coasts in submerged areas of the department of Magdalena, approximately 1.27 km from the point called Boca de Mendihuaca (Fig. 1). It extends between depths of 10 to 3,850 meters and covers a length of 197 kilometers based on the multibeam bathymetry conducted by the Caribbean Oceanographic and Hydrographic Research Center in 2020.Due to its morphological characteristics, this canyon can be classified, according to Goff (2001), as a large and mature canyon that breaks the edge of the shelf and zigzags downhill towards the abyssal plain, allowing access to the sediments of the continental shelf. However, current knowledge about the morphology and structural controls shaping this canyon remains limited, its configuration along the continental margin and its interaction with sediments from the continental shelf. While Aguja Canyon exhibits a meandering configuration with moderate to high sinuosity, the interactions between geological structures and hydrodynamic forces are not fully understood.

This paper addresses these knowledge gaps through a detailed analysis of the Aguja Canyon morphometry and structure, using multibeam bathymetry, 2D seismic data and Digital elevation model (DEM). Specifically, this research examines how the fault system Santa Marta-Bucaramanga (FBSM)- Oca (FOCA) (Cediel et al., 2003) and other local faults cut across this complex system influence the Aguja Canyons configuration, providing new insights into the structural and dynamic processes affecting the canyon's morphodynamics on both the shallow and deep seabed of the Colombian continental margin.

2 Physiographic characteristics of the area of the Aguja submarine canyon

Aguja Canyon (Fig. 1) spans the entire continental margin off the coast of the Colombian Caribbean, extending from the shallow coastal shelf at a depth of 10 meters down to the abyssal plain. It traverses three primary physiographic sections: the continental platform, slope, and deep-sea plain. Although it is not directly connected to nearby river systems, the canyon runs parallel to the Oca Fault (FOCA), suggesting tectonic influences on its morphology (Colmenares et al., 2007).

In the continental slope section (Fig. 2a), Aguja Canyon the canyon exhibits a meandering shape with structural features that redirect its course across four distinct directions, shifting from northwest to northeast (Arturo, R. F, 2009) This section is characterized by mass-wasting structures, including deposits and scarps, that shape the canyon walls and valley, indicating active sedimentary processes. (Rangel-Buitrago, 2010), as well as scarps aligned in a northeasterly direction in the elevations that are part of the accretion prism at the foot of the slope and in the

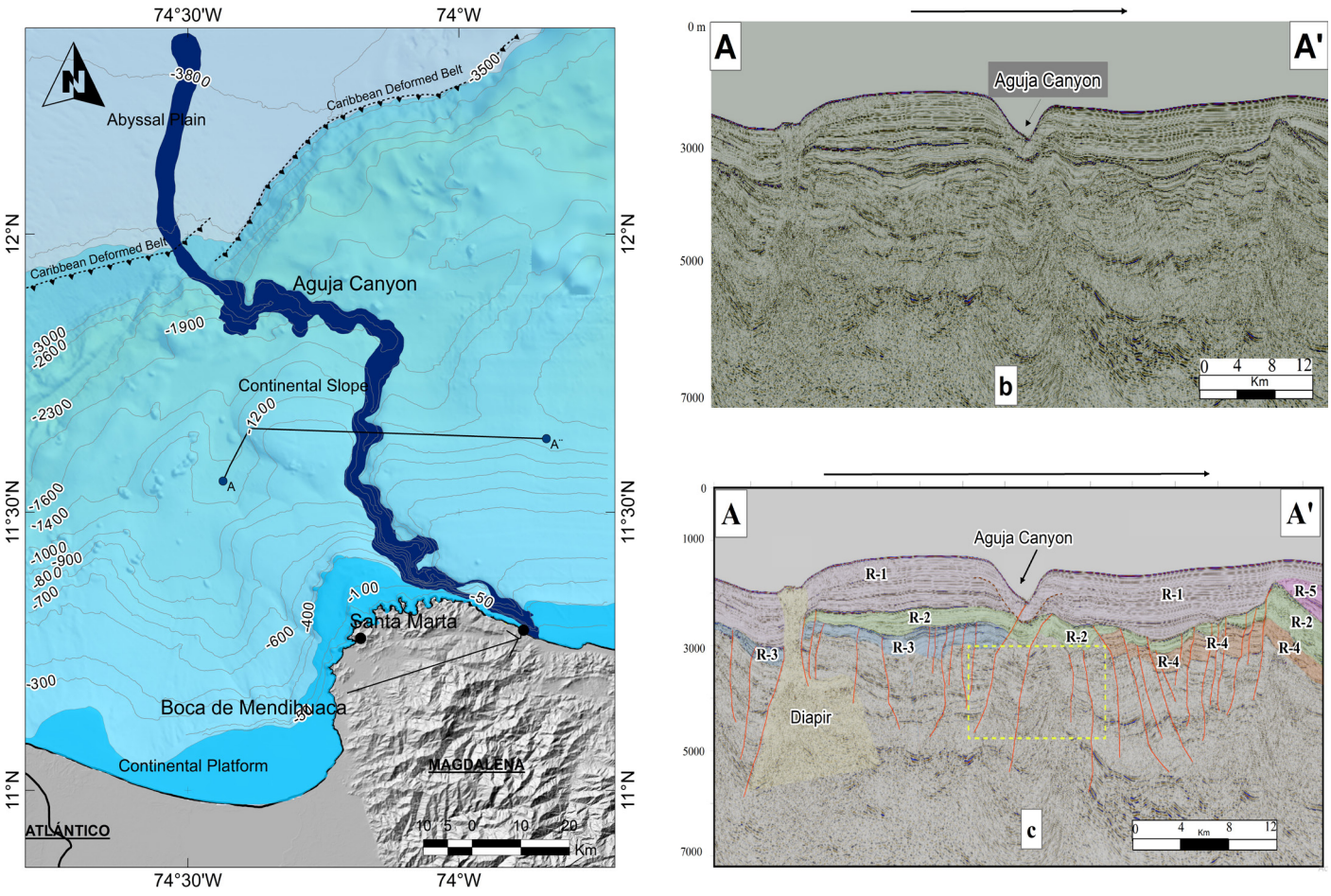


Fig. 2 (a) Location of seismic line A-A. The Aguja Canyon. (b) Original seismic line. (c) Interpretation of seismic line. The A-A' seismic line with W-E direction on the continental slope, reflects the discontinuities of the accretion prism in the area. The discontinuity on R-1, R-2, R-3, R-4 and R-5 seismic reflectors show normal and reverse fault jumps (red lines). The yellow box shows an area where the continuity of reflectors is not clearly identified.

walls of the main canyon, equally steep, with a predominance of mass removal phenomena

In the zone of influence of the Caribbean Deformed Belt lineament, the Aguja Canyon reaches its maximum depth at the abyssal plain, where it takes a northeasterly course (to the right) until it finally reaches a depth of 3,850 meters, visible through bathymetric and isobaths (Fig. 2a). Following the canyon from the shallowest part, in the coastal area, 10 meters deep, to the deepest part in the abyssal plain following the canyon valley, the Aguja Canyon it has a total extension of 197 km.

At its deepest point within the abyssal plain, the canyon reaches approximately 3,783 meters and follows a northeastward path influenced by the Caribbean Deformed Belt (CDB) lineament. Spanning a total length of 197 kilometers, the Aguja Canyon reflects complex interactions between tectonic and sedimentary processes

The AA' seismic line (Fig. 2b) exhibits significant discontinuities in its R-1, R-2, R-3, R-4, and R-5 reflectors, reflecting a sequence of normal and reverse faults covered by a sediment layer clearly visible in continuous reflectors (Fig. 2c).

The subduction of the Caribbean plate with the South American plate continues to be a topic of debate in the scientific community. Proposed models include subduction (Burke et al., 1984; Duncan & Hargraves, 1984; Ross & Scotesse, 1988), low-angle subduction (Taboada et al., 2000; Vargas & Mann, 2013; Galindo, 2016), obduction (Cediel et al., 2003), gravitational tectonics, and a combination of subduction and gravitational tectonics (Moreno et al., 2009). The current configuration of the continental margin crust is due to the east-northeast shift of the South American plate and the subduction of the Caribbean plate, which has generated a series of strike faults and displacements during the Cenozoic (Mantilla-Pimiento et al., 2009).

3 Methods

A 3D model of the Aguja Canyon section was generated using multibeam data obtained between 2010–2022. The bathymetric surface, in Csar format, was processed using the Caris Base Editor tool to create a base surface with a spatial resolution of 100 meters. This surface served as the foundation for generating additional elevation models (DEM).

The digital elevation model (DEM) was constructed from the bathymetric data (Fig. 3a). Using GIS tools, we then developed several other models: a digital slope model (Fig. 3b), a digital shadow model (Fig.

https://doi.org/10.58440/ihr-30-2-a11

3c), and a digital roughness model (Fig. 3d). The roughness model provides a topographic roughness index, which was used to determine key morphometric values for the canyon structure.

To analyze geological processes in the bathymetric model, we interpreted five 2D images of seismic track, covering approximately 542.9 kilometers in the study area (Fig. 2) These seismic lines, provided by the Petroleum Information Bank (EPIS), were crucial for identifying major fault structures, sediment deposition, and mass-wasting events (Fig. 2b). The seismic data interpretation followed standard seismic stratigraphy procedures, with a focus on horizon picking and fault mapping (Fig. 2c)

Through the depth model, digital maps of slope, roughness, shadow, aspect, and others were obtained, which, added to the morphometric information of the Aguja Canyon, as well as the 2D seismic data, revealed structural factors that control the canyon channel and the different directions it takes when crossing the continental margin.

4 Results

Structurally, the area of influence of the Aguja Canyon is affected by two major fault systems processes that occurs in the near continental section. These are the Bucaramanga-Santamarta Sinestral Strike Fault (FBSM) from almost north-northwest to south-south-east (Pindell, 1998; Lopez, 2005; Vence, 2008; Álvarez, 2015) and the dextral direction Oca Fault (FOCA) (Cediel et al., 2003; Lopez, 2005; Pindell et al., 1998; Vence et al., 2008). The latter, extends into the deep marine part of the Caribbean.

From the results of the interpretation carried out at approximately 542.9 km of 2D seismic lines around of the Aguja Canyon, as well as from the bathymetry, the roughness model, and the slope model, it was identified that the two fault systems (FOCA and FBSM) extend from the mainland to the seafloor, forming a set of main faults of the dextral and sinestral strike type, respectively, with normal satellite faults (Fig. 4a). This is evidenced in the structural control of the Aguja Canyon, as represented by the changes in the direction of the main channel along the continental slope. At a depth of 1,254.5 m the channel trends northeast; at 2,005.2 m, it shifts to a northwest direction and at 3,285.6 m it returns to a northeast direction. In addition, similar structural control is observed in the abyssal plain, close to the area influenced by the accretionary prism.

The set of faults found next to the Aguja Canyon is added to the group of reverse faults associated with the deformation processes of the Sinú Deformed Belt (CDS) in its northern section, in the vicinity of the Magdalena Fan. These faults have developed due

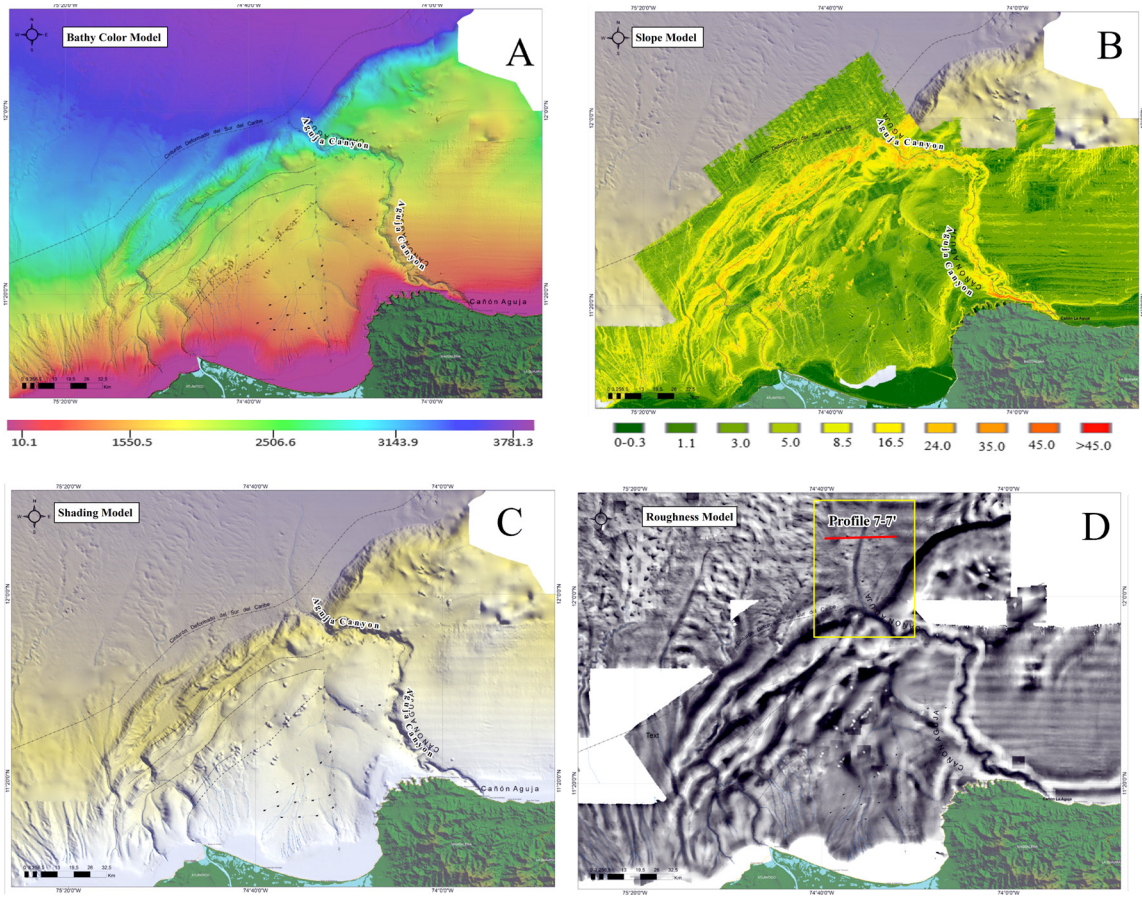


Fig. 3 (a) Depth model (meters). (b) Digital slope model (degrees). (c) Digital shadow model (d) Digital roughness model with profile 7-7' in red line; the red line marks the section of the canyon where it takes the shape of a channel as it sits over the abyssal plain. The segments correspond to fault lines, ridge channels and axes, or structural guidelines.

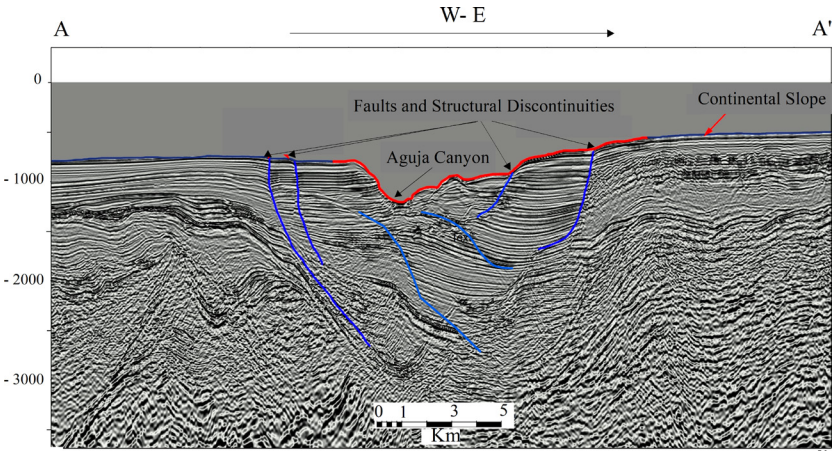


Fig. 4 Faulting and discontinuity of layers close to the section of Aguja Canyon. The 2D seismic profiles A-A' along with the interpretation of the reflectors show the faults, structural discontinuities.

to the dynamics and growth of the accretion prism, product of the interaction between the Caribbean plate and the South American plate, whose advance oscillates around 20 mm/year (Veloza et al., 2012).

The morphological conditions (Fig. 4) are consistent with zones whose characteristics are associated with faults, which often produce areas of instability and mass flow, or mass removal phenomena. To the southwest, there is a series of landslides whose origin is due to the structural folding of the layers, which are part of the accretionary prism and whose axis is oriented in a northeast-southwest direction, surrounded by valleys that form the deepest areas towards the Caribbean basin, represented by average elevation differences of 202.2 meters. These are located at the foot of the slope, becoming in areas of sediment accumulation from the different mass deposits transported from the platform and the slope (Cadena & Slatt, 2013).

In the bathymetry, the greatest deposition area of the Magdalena Submarine Fan was observed with complex mass transports (Galindo, 2016). The sediment load distributed in this section of the slope and observed in the 2D seismic, coincides with detrital and turbiditic deposits from the continental shelf, which generate an important slope deposit and landslides of large masses, which are also found forming part of the canyon walls.

5 Morphological and morphometric characteristics of the Aguja Canyon

The Aguja Canyon exhibits a varied morphological behavior along the continental margin, which allowed it to be divided into four sections because of this study, from the shelf to the abyssal plain in the north of the Colombian Caribbean. In addition, cross-sectional profiles showing the characteristics of the valley and its shape have been related (Fig. 5).

Aguja Canyon has a changing course, attributed to possible tectonic controls, which can be corroborated with the internal processes of the canyon valley in the different sections or stretches (Fig. 5). These controls are induced by regional structural processes in the area, mainly those related to activity in the fault system FOCA and the convergence deformation of the Caribbean and South American plates (Restrepo-Correa & Ojeda, 2020).

Within the depth model, the Aguja Canyon was divided into four sections (Fig. 5), which are distinguished by the direction of the main channel along the continental shelf until the abyssal plain. The different sections identified in this study area as follows:

Section A (upper): It is located at the top of the canyon or headwater, between the thin continental shelf of the area and the beginning of the continental slope, encompassing isobaths from 10 to 650 meters with direction of 64° north-west. In profile 1-1', points depths in the profile ends, vary between 14 and 126.7 meters. This section exhibits a sinuous morphology with moderate curves, highlighting a "U" shaped incision or valley inclined to the right, with an approximate depth of 367.3 meters and a width of 2.11 km. The 2-2' profile shows a variable morphology, with elevations and depressions within the valley and a marked difference in depth on both sides (profile ends) from 114 to 478.5 meters respectively, with a canyon width of 4.69 km and maximum depth 986.7 m.

Section B (middle): Located on the continental slope, it has a meandriform shape with an orientation of 14° north-east. In the 3-3' profile, depths vary from 867.0 to 767.8 meters in the profile ends. In this section, the canyon valley shows a very pronounced "V" shaped incision, with an approximate depth of 1,288.7 meters and a width of 3.65 km. At the lower end of this section, the 4-4' profile features depths ranging from 1,605.7 to 1,767.3 meters, where the shape of the valley changes to “U" shape with an open end to the left, reaching an approximate depth of 2055.1 meters and a width of 4.84 km.

Section C (medium-low): Located between the foot of the continental slope and the boundary with the abyssal basin, this section has an orientation of 86° north-west. In 5-5' profile, the depths vary from side to side of the canyon between 1857.7 and 2,271.2 meters. In this section the valley is 8.78 km wide and has an open "U" shape, with an approximate depth of 3072.8 meters.

In the abyssal plain area, section D, the canyon changes from a valley shape to a channel shape due to the slope and conditions of the basin, changing its course to 04° north-east. In 6- 6 profile with depths between 3,650.4 and 3,671.8 meters, the deepest section valley reaches approximately 3,698.6 meters. In the digital roughness model, you can see the depth of the canyon scar transformed into a channel and taking a deviation towards the northeast (Fig. 5)

Cross section profile 7-7' seen in Fig. 6, is the last profile of this study and is the representation of the deepest part of the canyon transformed into a channel that is noticeable in the bathymetry at a vertical exaggeration of 5X and in the roughness model.

The predominant slope (Fig. 3) throughout the

https://doi.org/10.58440/ihr-30-2-a11

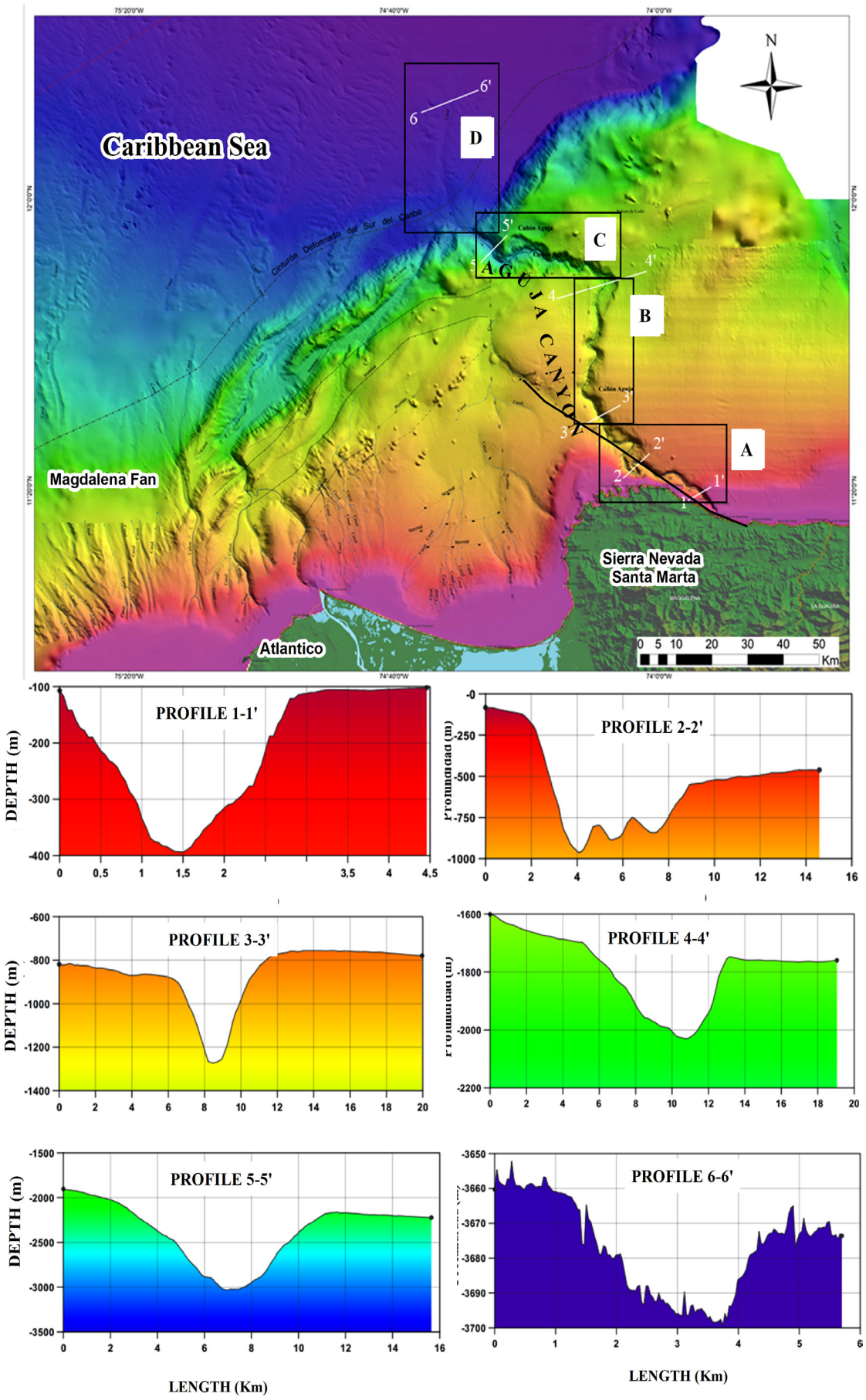


Fig. 5 Profiles transverse to the Aguja Canyon (VE.5X). The 1-1', 2-2', 3-3', 4-4', 5-5' and 6-6' cross-sectional profiles show the structural differences of the Aguja Canyon in the ocean floor. Sections A, B, C, and D shows the directional changes of the canyon along the continental shelf, continental slope, and abyssal plain (Colombia basin) due to structural processes.

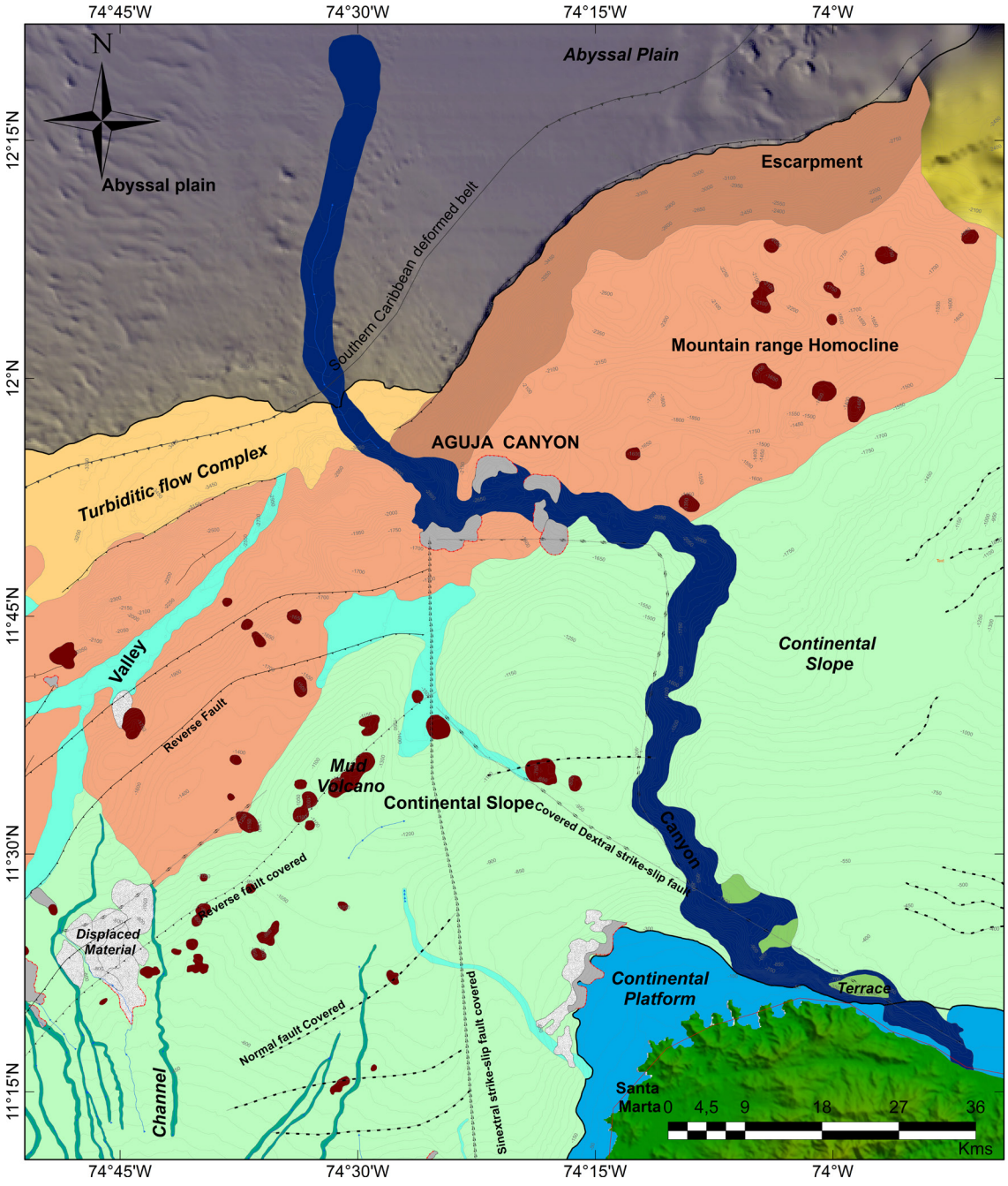


Fig. 6 Relief figures and faults around the Aguja Canyon and continental slope area: evidence of the variations in the direction of the main channel of the canyon. It crosses the continental margin and its final section in the Colombia basin forms a channel that is recognizable by bathymetry

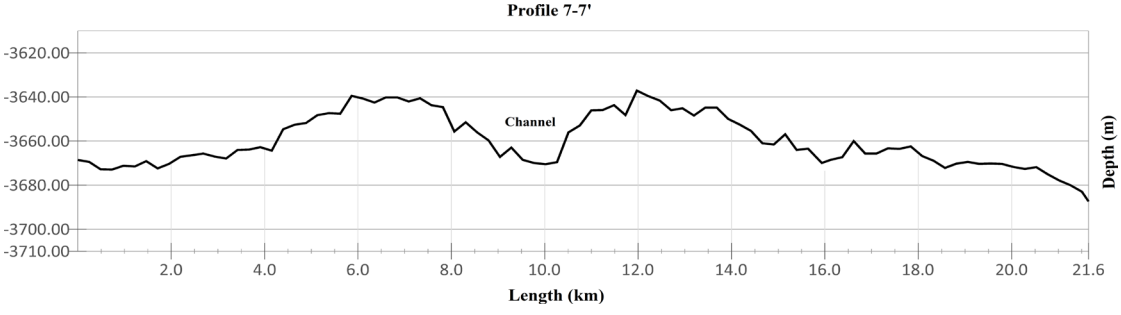


Fig. 7 A cross-sectional profile (7-7') of the Aguja Canyon in the abyssal plain area of the Colombia Basin at 74°31'37,093''W – 12°10'12,354''N, (EV 5.0). In the deepest and farthest part, the morphology of the Aguja Canyon change to a narrow 4 km channel.

https://doi.org/10.58440/ihr-30-2-a11

study area is relatively gentle, ranging from 0° to 8.5°, especially between the thin shelf boundary and the continental slope section. Moderate to high slopes are noted in the inner walls of the canyon (Fig. 5), as well as in the areas corresponding to the flanks of the elevations, which are presented as elongated homoclinal mountain ranges with northeast direction, located at the foot of the continental slope. These slopes vary between 16.5° and 45°, respectively.

The integration of data has made it possible to identify the morphology and structure of the study area. The continental shelf identified in the area is thin and it is affected by processes of flow transport and displacement material towards the continental slope. Adjacent to the continental shelf, in the continental slope, numerous mud diapirs (Isabel C. Restrepo Correa, Germán & Ojeda, 2020) and local fault systems are found; the slope is gentle and prolonged, which favors the development of thin flow channels that ends in the walls of homoclinal mountain ranges found at the foot of this continental slope, with an extension to the northeast, that is part of the Sinú accretion prism (Fig. 6).

The valley of the Aguja Canyon (Fig. 5a) presents identifiable terraces in the bathymetry, with erosive processes such as landslides and mass removal phenomena on the flanks, with the internal landslides being smaller compared to those in the areas adjacent to the canyon (Chaytor et al., 2009). A sinuous and meandriform behavior is observed mainly in the continental slope section, which changes markedly in the abyssal plain, where the bathymetric profile (Fig. 7) and the roughness model (Fig. 3d) show an important geomorphological change to a channel shape.

6 Discussion

Hay (2016) suggests that some submarine canyons may originate from rivers located in nearby continental areas, while others may be related to tectonic processes at active margins. On the other hand, Harris & Whiteway (2011) classified canyons into two main types. Type one: those that are connected to a continental river system. Type two: those that do not have a direct connection to a continental river system. According to this classification, type two canyons are more common in the continental slope compared to type ones. In the case of the Aguja Canyon, the bathymetric information does not allow a connection to be made with a nearby river or from any major fluvial system (Naranjo-Vesga et al. (2022), while its structural behavior allows it to be related as a canyon generated from tectonic processes that occurred on the continental slope.

The analysis of the structural and morphometric characteristics of the Aguja Canyon suggests important contributions in consideration of structural and connectivity factors, which are reflected in the results obtained for the study area. The Oca fault shows a downward strike displacement (Cediel et al., 2003; Lopez, 2005; Pindell et al., 1998; Vence et al., 2008), starting in the continental zone and continuing parallel to the continental shelf (Colmenares et al., 2017), plunging towards the Caribbean Sea in the head of the Aguja Canyon, where it takes a northwesterly course. Although this behavior does not allow a direct connection of the canyon with rivers or tributaries near the coastline, two rivers are identified in the vicinity: the Naranjo River and the Mendihuca River. Given the lack of precise evidence to establish a connection between these rivers and the canyon, the latter could be classified as type two according to Harris and Whiteway (2011). However, if there was a connection with any of the tributaries and structural displacements subsequently occurred, it could be considered as an abandoned or ancient canyon product of this structural process.

According to Harris et al. (2014), submarine canyons with strong geometric expressions are often associated with major faults, mainly of strike-slip. The Aguja Canyon is influenced by a significant number of strike-slip faults that control its course and behavior, primarily the FBSM and FOCA faults. These generate normal tensile satellite faults that affect the canyon's area of influence. This structural context is reflected in the morphological and morphometric features of Aguja Canyon, such as meanders, slope changes, course changes, and "V" and "U" valley shapes along its course.

On a regional scale, the displacements of the Aguja Canyon may be related to tectonic and connectivity processes in the continental zone, as well as to variations in course. These displacements could be the result of the relative displacement to the northeast of the Caribbean plate, the northern Andes plate, and the South American plate in the northern section of Colombia, according to the velocity vector model proposed by Wang et al. (2019). These tectonic processes are accompanied by a series of strike and reverse faults, such as the Bucaramanga-Santa Marta Fault System (SFBA) and the Oca Fault, whose displacements could also be influencing the behavior of the Aguja Canyon in its area near the continental shelf (Pousse Beltran et al., 2016).

7 Conclusion

The Aguja Canyon stands out as one of the prominent geographical features on the continental margin of the Colombian Caribbean after the Magdalena Submarine Fan in north direction, extending over 197 km with marked morphological expressions evident in the bathymetric surface. Its morphological characteristics suggest a structural context of compressive stress deformation, resulting from the activity and dynamics of displacement of regional and local faults in the area, as well as the subduction stress in the northern Colombian Caribbean.

Throughout its trajectory, the canyon exhibits changes in course, alternating between directions ranging from northwest to northeast, as well as variations in the profiles of the main channel, ranging from

"V" to "U" shapes. These behaviors can be attributed to the influence of strike fault systems and normal satellite faults generated by the inter-plate interaction affecting the zone, including the deep extension of the Oca fault margin, which impact the study area, along with the normal and reverse fault systems identified in this study and located around Aguja Canyon.

The geomorphological context reveals a zone of instability characterized by landslides, faults, volcanic mud activity, and channels, as well as a continental shelf with significant thinning due to the mass removal processes observed there. This dynamic points to considerable tectonic activity that has shaped the morphological character of the canyon and its variations along the continental margin.

The lack of a precise connection between the canyon and a nearby river on the mainland, as seen in bathymetry, suggests that the canyon may have been connected to one of the closest tributaries in the past, and its current disconnection could be attributed to tectonic shifts generated by the inter-plate dynamics area. This is supported by the presence of fault systems in the area, which also influence the changes on the canyon along the continental slope.

The differences in depth observed on both sides of the canyon, reflected in the profiles plotted in Fig. 5, could be related to tilting of subducted and other uplifted zones because of tectonic stresses controlled by regional and local processes, which may also be contributing to the changes in the path of the Aguja Canyon along the Colombian continental margin.

Acknowledgements

This publication is made with the support of the General Maritime Directorate, the Center for Oceanographic and Hydrographic Research of the Caribbean, Colombian Geological Survey and the Petroleum Information Bank, who provided the bathymetric and 2D seismic used to provide new information to the structural context of the Aguja Canyon.

References

Arturo, R. F. (2009). La morfología fluvial y su incidencia en la estabilidad de las obras viales. VIII *Congreso Internacional Obras de Infraestructura Vial, ICG, Lima*. https://www.imefen.uni.edu.pe/Temas_interes/ROCHA/Morfologia_fluvial_y_su_influencia.pdf (accessed 1 October 2022).

Burke, K., Cooper, C., Dewely, J., Mann, P. and Pindell, J. (1984). Caribbean Tectonics and Relative Plate Motions. In R. B. Bonini, R. B. Hargraves and R. Shagan (Eds.), The CARIBBEAN – South American *Plate boundary and Regional Tectonics* (pp. 31–63). Geological Society of America Memori, 162. https://doi.org/10.1130/MEM162-p31

Cadena, A. F. and Slatt, R. M. (2013). Seismic and sequence stratigraphic interpretation of the area of influence of the Magdalena submarine fan, offshore northern Colombia. *Interpretation, 1(*1), pp. 323–344. https://doi.org/10.1190/INT-2013-0028.1

Cediel F., R. Shaw y C. Cáceres. 2003. Tectonic assembly of the northern Andean Block. In C. Bartolini, R. T. Buffler and J. Blickwede (Eds.), *The Circum-Gulf of Mexico and the Caribbean: Hydrocarbon Habitats, Basin Formation and Plate Tectonics* (pp. 815–848). https://doi.org/10.1306/M79877C37

Chaytor, J. D., ten Brink, U. S., Solow, A. R. and Andrews, B. D. (2009). Size distribution of submarine landslides along the US Atlantic margin. *Marine Geology, 264*(1-2), pp. 16–27. https://doi.org/10.1016/j.margeo.2008.08.007

Colmenares, F., Mesa, A., Roncancio, J., Arciniegas, E., Pedraza, P., Cardona, A. and Vargas, A. (2007). Geología De La Planchas 11, 12, 13, 14, 18, 19, 20, 21, 25, 26, 27, 33 Y 34. In *Proyecto: Evolución Geohistórica de la Sierra Nevada de Santa Marta, Ministerio de Minas y Energía, Instituto Colombiano de Geología y Ministerio e Ingeominas*, pp. 71–134. https://recordcenter.sgc.gov.co/B12/23008010018162/documento/pdf/2105181621101000.pdf (accessed 13 November 2024).

Duncan R. A., and Hargraves R. B., (1984.) Plate tectonic evolution of the Caribbean region in the mantle reference frame. In W. E. Bonini, R. B. Hargraves and R. Shagam (Eds.), *The Caribbean-South American Plate Boundary and Regional Tectonics, 162* (pp. 81–93). https://doi.org/10.1130/MEM162-p81

Galindo, P. (2016). *Transtension and transpression in an oblique subduction setting: Evolution of the Bahia Basin, Colombian Caribbean margin* [Doctoral dissertation, Imperial College London]. https://doi.org/10.25560/31408

Goff, J. A. (2001). Quantitative classification of canyon systems on continental slopes and a possible relationship to slope curvature. *Geophysical Research Letters, 28*(23), 4359–4362. https://doi.org/10.1029/2001GL013300

Harris, P. T. and Whiteway, T. (2011). Global distribution of large submarine canyons: Geomorphic differences between active and passive continental margins. *Marine Geology, 285,* pp. 69–86. https://doi.org/10.1016/j.margeo.2011.05.008

Harris, P. T., Barrie, J. V., Conway, K. W. and Greene, H. G. (2014). Hanging canyons of Haida Gwaii, British Columbia, Canada: Fault-control on submarine canyon geomorphology along active continental margins. *Deep Sea Research Part II: Topical Studies in Oceanography, 104*, pp. 83–92. https://doi.org/10.1016/j.dsr2.2013.06.017

Hay, W. W. (2016). Submarine Canyons. In J. Harff, M. Meschede, S. Petersen, J. Thiede (Eds.), *Encyclopedia of Marine Geosciences* (pp. 807–808). Encyclopedia of Earth Sciences Series, Springer, Dordrecht. https://doi.org/10.1007/978-94-007-6238-1_150

Mantilla-Pimiento, A. M., Jentzsch, G., Kley, J. and Alfonso-Pava, C. (2009). Configuration of the Colombian Caribbean Margin: Constraints from 2D seismic reflection data and potential fields interpretation. *Subduction zone geodynamics, Springer, Berlin, Heidelberg,* pp. 247–272. https://doi.org/10.1007/978-3-540-87974-9_13

Naranjo-Vesga, J., Paniagua-Arroyave, J. F., Ortiz-Karpf, A., Jobe, Z., Wood, L., Galindo, P. and Mateus-Tarazona, D. (2022). Controls on submarine canyon morphology along a convergent tectonic margin. *The Southern Caribbean of Colombia. Marine and Petroleum Geology, 137,* 105493. https://doi.org/10.1016/j.marpetgeo.2021.105493

Pindell, J., George, R., Jr. Kennan, L., Higgs, R. and Cristancho, J. (1998). *The Colombian Hydrocarbon Habitat: Integrated Sedimentology, Geochemestry, Paleogeographic Evolution*. Geodynamics, Petroleum Geology, and Basin Analysis, Appendix 1, Text part 2 of 2: Plate Kinematics of plates affecting the evolution of Colombia, and Appendix 2, Text part 2 of 2: Synopsis of the evolution of the Caribbean Region. Tectonic Analysis, Inc. in research collaboration with Ecopetrol.

Pousse Beltran, L., Pathier, E., Jouanne, F., Vassallo, R., Reinoza, C., Audemard, F., ... and Volat, M. (2016). Spatial and temporal variations in creep rate along the El Pilar fault at the Caribbean-South American plate boundary (Venezuela). *Journal of Geophysical Research*: Solid Earth, 121(11), 8276–8296.

Rangel-Buitrago, N., Idárraga-García, J., and INVEMAR. (2010). Geología general, morfología submarina y facies sedimentarias en el margen continental y los fondos oceánicos del mar Caribe colombiano. In INVEMAR (Eds.), *Biodiversidad del Margen Continental del Caribe colombiano* (pp. 29–51). https://www.researchgate.net/publication/261154499_Geologia_general_morfologia_submarina_y_facies_sedimentarias_en_el_margen_continental_y_los_fondos_oceanicos_del_mar_Caribe_Colombiano (accessed 13 November 2024).

Restrepo-Correa, I. C. and Ojeda, G. Y. (2010). Geologic controls on the morphology of La Aguja submarine canyon. *Journal of South American Earth Sciences, 29*(4), pp. 861–870 https://doi.org/10.1016/j.jsames.2010.07.001

Ross, M. I., and Scotese, C. R. (1988). A hierarchical tectonic model of the Gulf of Mexico and Caribbean region. *Tectonophysics, 155*(1-4), pp. 139–168. https://doi.org/10.1016/0040-1951(88)90263-6

Taboada, A., Rivera, L., Fuenzalida, A., Cisternas, A., Philip, H., Bijwaard, H., Olaya, J. and Rivera, C. (2000). Geodynamics of the Northern Andes: subductions and intra-continental deformation (Colombia). *Tectonics, 19(5)*, pp. 787–813. https://doi.org/10.1029/2000TC900004

Veloza, G., Styron, R., Taylor, M. and Mora, A. (2012). Open-source archive of active faults for northwest South America. *Gsa Today, 22*(10), pp. 4–10. https://doi.org/10.1130/GSAT-G156A.1

Vence, E. M. (2008). *Subsurface basement, structure, stratigraphy, and timing of regional tectonic events affecting the Guajira margin of northern Colombia* [Master of Science Thesis, Universidad of Houston, Texas]. https://doi.org/10.1190/int-2020-0016.1

Wang, G., Liu, H., Mattioli, G. S., Miller, M. M., Feaux, K. and Braun, J. (2019). CARIB18: A stable geodetic reference frame for geological hazard monitoring in the Caribbean region. *Remote Sensing, 11*(6), p. 680. https://www.mdpi.com/2072-4292/11/6/680

Authors' biographies

Yerinelys Santos Barrera is a geological Engineer from the Pedagogical and Technological University of Colombia in 2008. She completed a specialization in Geomatics in 2011. Since 2012, she has been part of the Oceanographic and Hydrographic Research Center of the Caribbean (CIOH) and the National Hydrographic Service (SHN), where she serves as a lead researcher in marine geology, focusing on the geomorphological characterization of the seabed in the Caribbean and Pacific. Her main research activities include the analysis and interpretation of hydroacoustic data, as well as geophysical variables such as seismic, gravimetry, and magnetometry, aimed at understanding the structural deformation processes of the seafloor.



Yerinelys Santos Barrera

María Fernanda Calderón Grande graduated as a geologist from the Industrial University of Santander, began her career contributing to various projects for the Colombian Petroleum Institute (ICP). Following this experience, she completed further studies in Geographic Information Systems (GIS), expanding her expertise in spatial-temporal analysis, cartography, database management, spatial statistics, organic petrography, sedimentology, stratigraphy, and geochemistry. Since 2021, she has been a member of the Marine Geology research group at the Caribbean Oceanographic and Hydrographic Research Center, where she contributed to a deep-water multibeam hydrographic survey off the coast of La Guajira and a sub-bottom profiler survey for the National Hydrocarbons Agency. Currently, she applies her experience to the development of geomorphological mapping of the Colombian seafloor.



María Fernanda Calderón



Eliana Gutiérrez Rincón

Eliana Gutiérrez Rincón obtained her Master's degree in Geophysics from the Industrial University of Santander (Colombia). She specializes in marine geophysics, focusing on submarine geomorphology and underwater geo-hazards. Her professional career began at the Agustín Codazzi Geographic Institute, where she was involved in the geomorphological interpretation of Colombia's territory using remote sensing imagery. She then worked at the Colombian Petroleum Institute, interpreting subsurface geobodies based on geophysical data. Subsequently, she contributed to scientific marine research at the Caribbean Oceanographic and Hydrographic Research Center (CIOH), part of the Colombian Directorate General of Maritime Affairs (DIMAR). Her research includes the study of underwater geo-hazards and submarine geomorphology, with a focus on applying geophysical methods to understand and mitigate geological risks in coastal and offshore environments.



Johanna P. Vargas Morales

Johanna P. Vargas Morales graduated as a geologist from the Industrial University of Santander in 2014, she has experience in coordinating projects in applied geophysics for exploration and cartographic development. Since 2023, she has been part of the marine geology research team at the Caribbean Oceanographic and Hydrographic Research Center and the Hydrographic Service of Colombia, where she focuses on analyzing seabed geophysical data to create structural feature maps and geomorphological units of Colombian maritime territory.

https://doi.org/10.58440/ihr-30-2-a11

NOTE / TECHNICAL REPORT

Sedimentation analysis at the mouth of the Dique Channel to the Cartagena Bay through hydrographic surveys

Author

Harold Rojas Macías[1], Octavio Martinez Martinez[1] and Marjohnny Monterroza Pantoja[1]

Abstract

This article demonstrates the problem currently facing Cartagena Bay due to excessive sedimentation at the mouth of the Dique Channel, based on the analysis carried out by the Hydrographers of the National Hydrographic Service taking advantage of the management of the different seabed research technologies available to the Caribbean Oceanographic and Hydrographic Research Center (CIOH). Between December 2022 and January 2023, a hydrographic survey was carried out at the mouth of the Dique Channel, carrying out a multitemporal analysis with the hydrographic data from 2012 and 2020 stored in the hydrographic database, allowing a clear identification of the volume of the sedimentation rate in this important area of Cartagena Bay. The article shows the need for high monitoring of the study area by the National Maritime Authority, also because the port of Cartagena is one of the most important in Colombia.

Keywords

hydrography · sedimentation · echosounders · erosion · single beam

1 Introduction

The Dique Channel is an artificial bifurcation of the Magdalena River that enables its navigation towards Cartagena Bay. It was constructed during the Spanish colonial period in the 16th century. Presently, the outlet of the Dique Channel into Cartagena Bay is a distinctive area due to the transit of cargo vessels. This, combined with the high sedimentation generated by the river's flow, turns this area into a critical location for navigation. The Dique Channel represents a fluvial contribution with transport of fine terrigenous sediments (0–31 µm) (Lonin et al, 2004). According to Tosic, Restrepo, Lonin, Izquierdo and Martins (2018), historical records indicate an average flow rate of 398 m^3s^{-1} before 2000 and an increase to 508 m^3s^{-1} during the period 2000–2010. Also, sediment load displayed an increase of 48 % when comparing the mean load of 16,153 t/day during the 1984–2000-year period with the observed inter-annual mean of 23,906 t/day for the 2005–2010-year period. These results are in close agreement with the observed trends during the period between 1980 and 2010 in sediment loads of the main tributaries of the Magdalena River and also with the steep increase in deforestation during the last three decades.

The Colombian Maritime Authority, through the Caribbean Center for Oceanographic and Hydrographic Research, conducted hydrographic surveys at the mouth of the Dique Channel in January 2023. The objective was to characterize the seafloor and carry out various multi-temporal analyses, considering other hydrographic surveys conducted in the same area but in different years (2012 and 2020). This was done to understand the dynamics and influence of the Dique Channel on Cartagena Bay. This effort aims to provide scientific information to support decision-making for the benefit of maritime activities in the region, ensuring comprehensive maritime safety.

✉ Octavio Martinez Martinez · omartinez@dimar.mil.co

[1] Center for Oceanographic and Hydrographic Research of the Caribbean (CIOH), Colombia

https://doi.org/10.58440/ihr-30-2-n13

It contributes to the country's development and the protection of natural resources and the environment, serving as fundamental pillars within the guidelines of the Colombian national government[1].

2 Study area

Cartagena Bay located in the northwestern part of South America, within the Colombian Caribbean, between 10°16'N–10°26'N and 75°36'W–75°30'W (Fig. 1). The mouth of the Dique Channel is located to the southeast of Cartagena Bay. This discharges sediments directly into the bay, creating a sediment lobe (SL) consisting of a sedimentary deposit of fluvial origin, which due to its muddy and shallow condition makes it difficult to carry out a bathymetric survey. (Villanueva-Garcia et al., 2022)

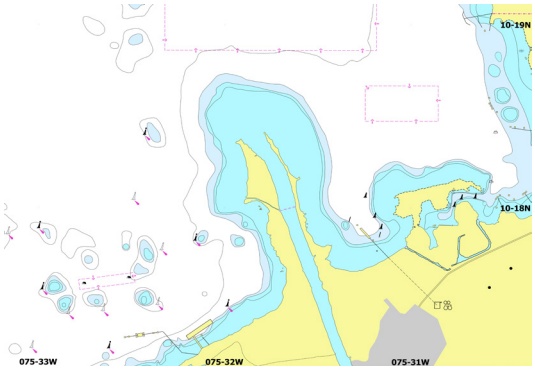


Fig. 1 Study area: The mouth of the Dique Channel (ENC CO500261, coordinate system WGS84 / UTM zone 18N).

3 Data collection

The last hydrographic survey was conducted in order 1b according IHO specification S-44 Edition 6.1.0. This data was compared with the data from 2012 and 2017 using the software Hypack.

The 2023 survey was conducted onboard the Soundermax hydrographic boat (Fig. 2), using a single beam system with echosounder Teledyne Odom Echotrac, DGPS Trimble R7 and SVP AML Base X2. The devices were used for collecting bathymetric information, for ensure optimal functioning of each peripheral component of the system.



Fig. 2 The Soundermax hydrographic boat.

The hydrographic survey using the singlebeam system at the mouth of the Dique Channel was carried out on the days of December 13th, 14th, and 16th, 2022, and on January 19th, 2023. The initial planning was conducted using Hypack software version 2022, with the most update electronic chart of the study area as the foundation. The main consideration was to determine the outbound route of the Dique Channel to a depth of 20 m, which is considered a safe water area for navigation, taking into account the types of vessels transiting the area.

Upon entering the study area, two safety lines were

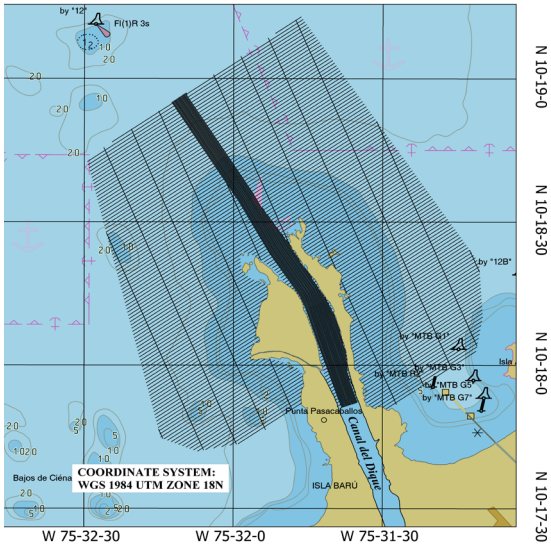


Fig. 3 Planned survey lines.

conducted to determine areas of shallower depth, revealing significant variations in the bottom morphology due to the high sedimentation caused by the river. This prompted a reevaluation of the initial study area to fulfill the primary objective of identifying safe waters in Cartagena Bay. To achieve this, longitudinal lines were planned every 5 m and transverse lines every 150 m at the mouth of the Dique Channel, aiming to determine the navigable area and average depth. Outside the canal, perpendicular lines to the coast were planned with a 20-meter spacing for run lines and 200 m for check lines. In accordance with the IHO Standards for Hydrographic Surveys S-44, 6th Edition, the survey is classified as Order 1b because a uniformly distributed bathymetric coverage of 5 % of the survey area is available. This means that some features may not be detected, but the distance between the areas of bathymetric coverage will limit the size of those undetected features. (IHO, 2020).

During the survey, the Teledyne Odom Echotrac CVM single beam echosounder was employed to measure depth. This echosounder features a dual-frequency transducer (38 kHz and 200 kHz), which was installed at the stern of the vessel to acquire data through the acoustic window method, using the high frequency of 200 kHz for shallow waters to avoid the penetration of the sound wave into the seabed due to

[1] https://www.eluniversal.com.co/especial/puertos/2020/10/26/la-bahia-de-cartagena-es-la-protagonista-de-la-actividad-economica-local/ (accessed 27 October 2024).

the type of muddy sediment found in the study area. For positioning, the GNSS receiver Trimble R7 with Fugro Marinestar satellite differential signal was used. The AML Base X2 profiler was employed to determine the speed of sound in the water, while water level corrections were made using data from the vertical tide network of the Colombian Maritime Authority, with the data referenced to Mean Lower Low Spring (MLWS).

The software used for data collection, processing, and analysis was Hypack version 2021. Through its Hypack Survey module, this software enabled the configuration of data reception from each peripheral to obtain location information on the nautical chart and monitor the echosounder coverage.

4 Coverage area

A total area of 2 km^2 was successfully covered using the single beam system over the course of 4 days of hydrographic survey, in accordance with the initial plan. A minimum depth of 0.8 m and a maximum depth of 25 m were determined.

During this study, a depth of 1.2 m was verified and plotted on ENC CO500261, near buoy No. 18 of the navigable channel of Cartagena Bay, located in front of the mouth of the Dique Channel. When carrying out hydrographic search lines on the shallows, it was determined that this depth did not correspond to current conditions, since depths of 7 m were previously recorded in the area (Fig. 4).

This information is of great importance for the update the ENC CO500261 "Cartagena Bay".

5 Analysis of the information

The analysis of the information was conducted using the data collected in the year 2023 (Fig. 7), which were compared with the most recent studies of the same area. This information is stored in the hydrographic database of the Caribbean Center for Oceanographic and Hydrographic Research and corresponds to surveys conducted in the years 2012 and 2020 (Figs. 5 and 6).

The data from 2012 correspond to those used at that time for the update of ENC CO500261 "Cartagena Bay", these were acquired with 200 kHz single-beam systems and the data from 2020 correspond to a monitoring carried out by the Caribbean Oceanographic and Hydrographic Research Center where a 200 kHz single-beam system was also used.

To perform the comparison of the change in the seabed configuration in the area, comparisons were conducted between the surfaces of hydrographic surveys from the same sector (Figs. 8 and 9).

In Fig. 8, the areas of higher sedimentation in the sector over an 8-year period (2012–2020) are observed. The blue colors represent areas where depths have not undergone significant changes, while the red colors correspond to zones that have experienced greater changes due to sedimentation. Similarly, in Fig. 9, differences over a 3-year period (2020–2023) are depicted. By maintaining the same color scale, stable areas and sediment-affected zones can be clearly identified.

Longitudinal and transverse profiles were also conducted throughout the entire study area to perform depth comparison analyses among the different surveys (Figs. 10 and 13). This approach was undertaken to validate the significant changes in the seafloor geomorphology caused by sediment deposition resulting from the Dique Channel 's influence on the Bay of Cartagena over time.

In Figs. 11 and 12, the comparison of profiles between the surveys conducted in the years 2012 and 2020 can be observed. The red line represents the year 2012, while the blue line represents the survey conducted in the year 2020. Similarly, in Figs. 14 and 15, the respective profile comparisons between the hydrographic surveys of the years 2020 and 2023 are evident.

6 Analysis of the coastline

Using the Google Earth tool, the digitization of the coastlines at the mouth of the Dique Channel for the years 1970, 2011, 2020, and 2022 was carried out. These data were exported in *.kmz format and converted to *.shp using ESRI's Geographic Information System software (ArcGIS), as shown in Fig. 16.

Using the multiyear shorelines, an analysis of the evolution of the coastal edge was performed, revealing that the shoreline has moved longitudinally 916.69 m towards the Bay of Cartagena between 1970 (green line) and 2022 (black line), evidencing the high sedimentation in this 52-year period. See Fig. 17 for reference.

7 Results

Between the hydrographic surveys of the years 2012 and 2020, it was observed that the 4-meter depth contour in the Bay of Cartagena shifted 420 m towards the 324° mark. Depths that were previously 21 m deep now measure 4 m. Similarly, between the surveys of the years 2020 and 2023, the 4-meter contour moved 200 m towards the inner part of the Bay of Cartagena at the 327° mark, leaving it only 800 m away from the navigable channel.

The depths found in the navigable river channel, once the multi-temporal comparisons were completed, remain between 2 m and 3 m deep.

The volume calculation was conducted between the two surveys of the years 2012 and 2020, revealing that during this period, the study area experienced sedimentation of 6,389,937.3 m^3 over an area of 2,186,107 m^2, and erosion of 329,525.2 m^3 over an area of 539,722.2 m^2.

Similarly, the volume calculation was conducted between the two surveys of the years 2020 and 2023, revealing that the study area has undergone sedimentation of 1,795,944.5 m^3 over an area of 1,420,878.7 m^2, and erosion of 116,163.9 m^3 over an area of 532,491.7 m^2.

https://doi.org/10.58440/ihr-30-2-n13

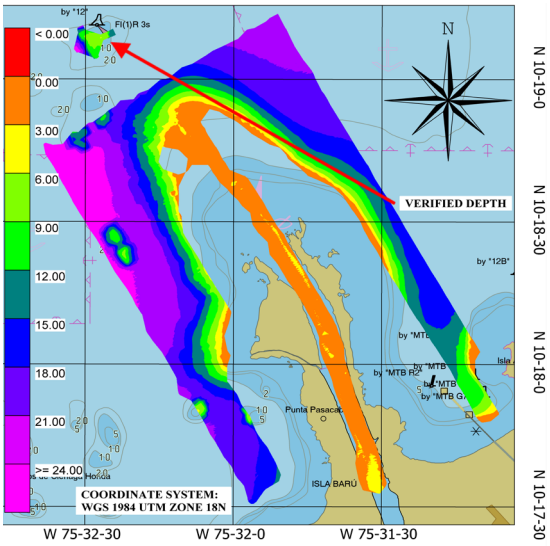


Fig. 4 Coverage area of 2023 survey and depth verification.

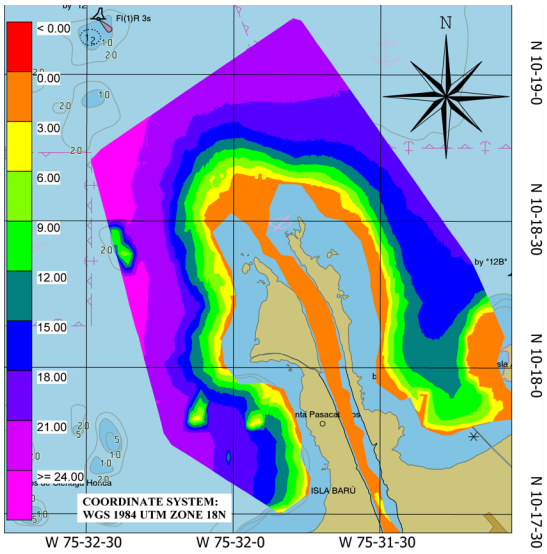


Fig. 5 Hydrographic survey of 2012.

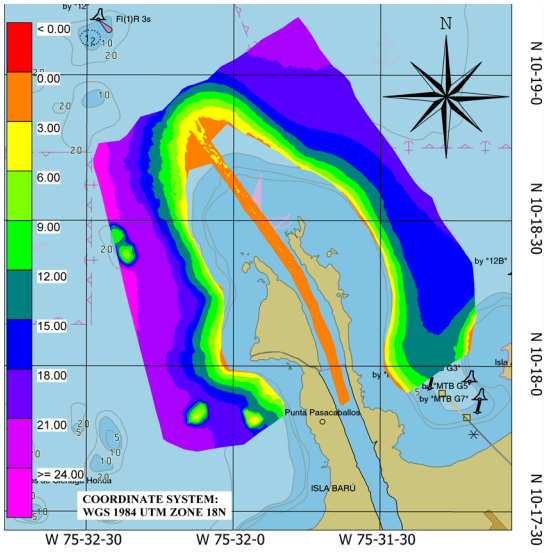


Fig. 6 Hydrographic survey of 2020.

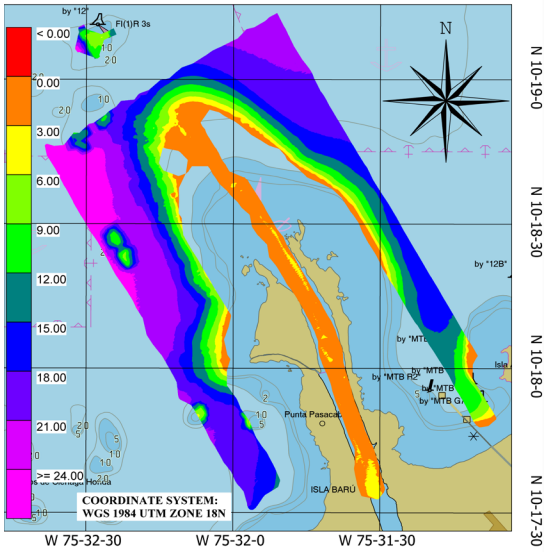


Fig. 7 Hydrographic survey of 2023.

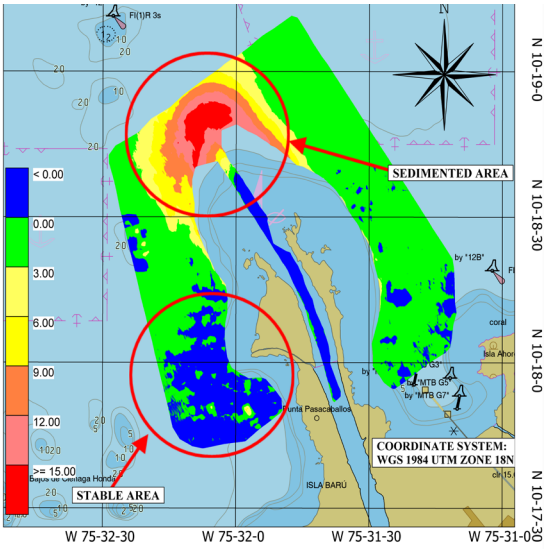


Fig. 8 Difference in depths between surveys from 2012–2020.

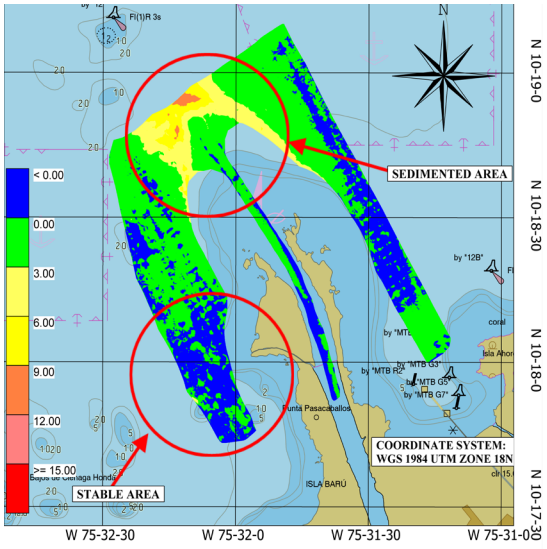


Fig. 9 Difference in depths between surveys from 2020–2023.

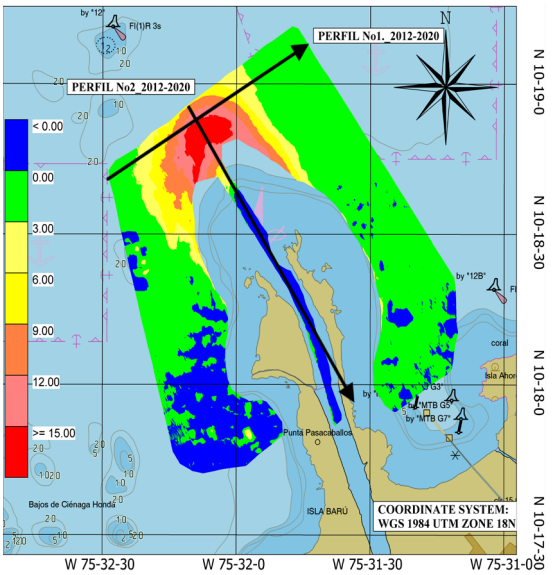


Fig. 10 Verification profiles between surveys 2012–2020.

8 Conclusions

The multitemporal analysis carried out with the three hydrographic surveys during the years 2012, 2020, and 2023 at the mouth of the Dique Channel, allows us to identify a high sedimentation rate in the Bay of Cartagena (approximately 744,171.073 m^3 annually), due to the influence of the Dique Channel. Over the years, considerable changes in the morphology of the seabed will occur, along with an annual erosion averaging around 40,517.2 m^3. See Table 1 for details.

The contour velocity at a depth of 4 m advances significantly (from 52.5 m/year to 66.6 m/year). For more details, See Table 2.

The area of erosion recorded is relatively smaller compared to the sedimentation area (18 times less). These areas are located outside the Dique Channel, which does not contribute to safe navigation.

The coastline at the mouth of the Dique Channel has longitudinally shifted 916.69 m towards the Bay of Cartagena over a span of 52 years. See Fig. 17 for reference.

The displacement of the coastline is due to the sediments brought by the Dique Channel, causing erosion at its mouth in the same direction.

The sedimentation in the studied area poses a danger to navigation and challenges the management of the coastal zone.

9 Recommendations

Considering that the Dique Channel is a fork of the Magdalena River that flows into the Bay of Cartagena, therefore the flow is one of the most influential factors in the transport of sediments in the sector and taking into account that during the year there are different meteorological periods such as dry or wet seasons influenced sometimes by the El Niño or La Niña phenomena, where the flow of this river artery increases or decreases and directly proportional its contribution of sediment to the bay, it is necessary to carry out hydrographic surveys more frequently in this sector, in order to provide sedimentation and erosion values in shorter intervals, which would help the authorities to establish contingency measures to reduce the probability of accidents that mainly affect human life at sea, environmental conservation and the economic development of the country.

The advancement of the shallower depths towards the navigable channel of the Bay of Cartagena could be managed by continuous dredging, both in the Dique Channel and at its mouth.

Currently we do not have documented the number of dredging cycles performed in this sector, however it should be taken into account that performing

Table 1 Dique Channel Mouth statistics in Cartagena Bay.

Sedimentation			
Years between surveys	Sedimentation in m^3	Area in m^2	Annual rate
8	6.389.937,3	2.186.107	798.742,163
3	1.795.944,5	1.420.878,7	598.648,167
11	8.185.881,8		744.171,073
Erosion			
Years between surveys	Erosion in m^3	Area in m^2	Annual rate
8	329.525,2	539.722,2	41.190,65
3	116.163,9	532.491,7	38.721,3
11	445.689,1		40.517,1909

Table 2 4-meter contour displacement towards navigable channel.

Distance	Years	Velocity in m/year
420	8	52,5
200	3	66,7

https://doi.org/10.58440/ihr-30-2-n13

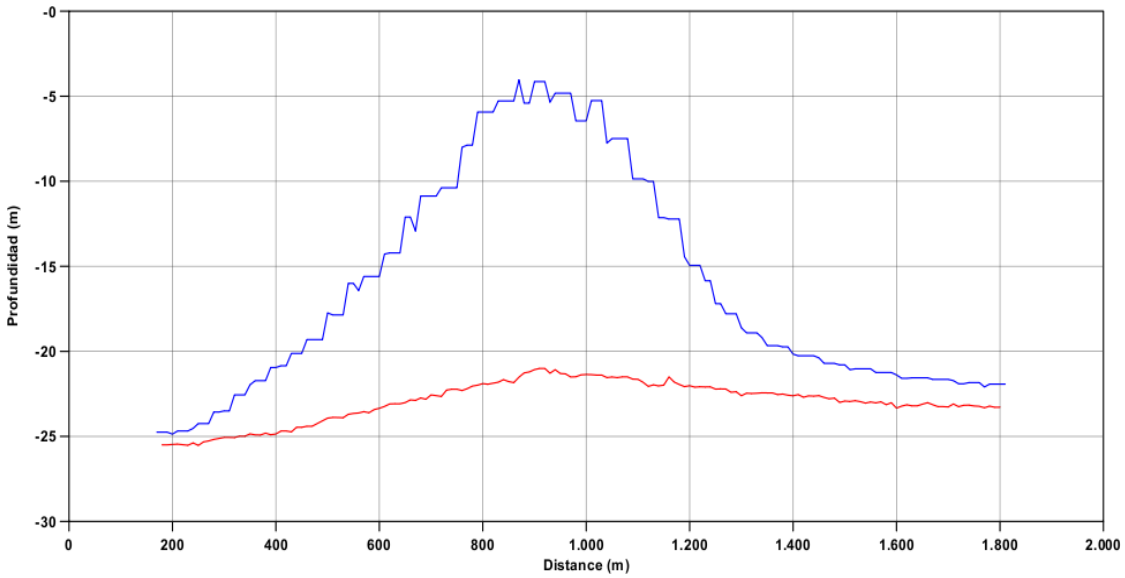


Fig. 11 Profile No. 1 between surveys 2012 (red) – 2020 (blue).

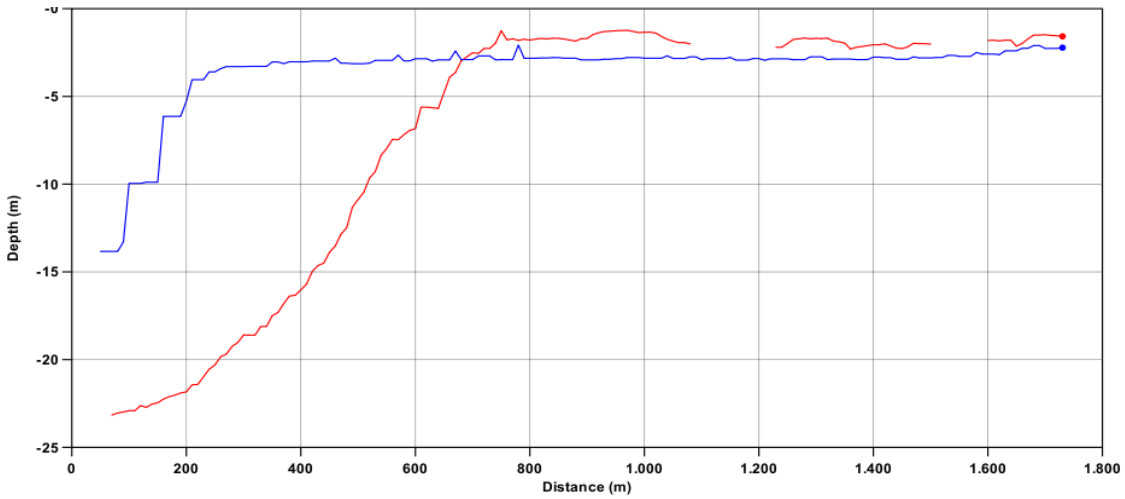


Fig. 12 Profile No. 2 between surveys 2012–2020.

operations that involve removing the seabed could increase toxicity and contamination due to the presence of metals such as Co, Cr, Cu, Ni, V and Zn, which show significant concentrations in the sediments of the Bay of Cartagena, attributed to the industrial zone of Mamonal and the Dique channel (Espinosa-Díaz et al., 2021)

Considering that in the study area there is a high traffic of tugboats with barges, it is recommended to install more navigation aids that clearly delimit the navigable channel for this type of vessel and in this way avoid maritime accidents due to grounding in the sector, in the same way take into account that it is a dynamic channel due to sedimentation, for this reason it is necessary to have updated bathymetry for the repositioning of floating navigation aids when required.

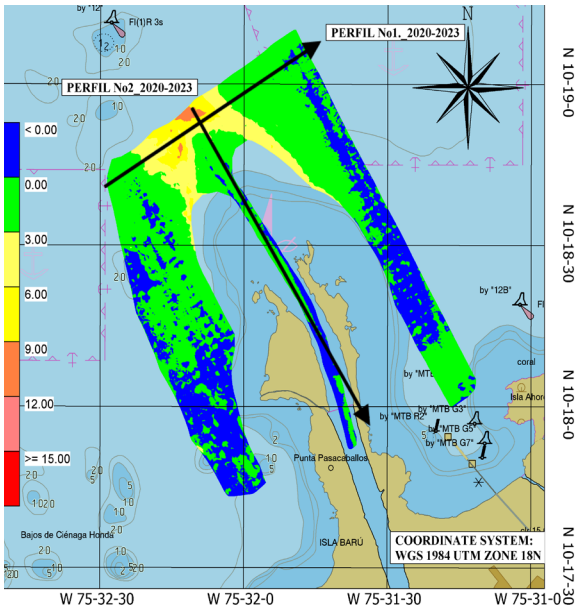


Fig. 13 Verification profiles between surveys 2020–2023.

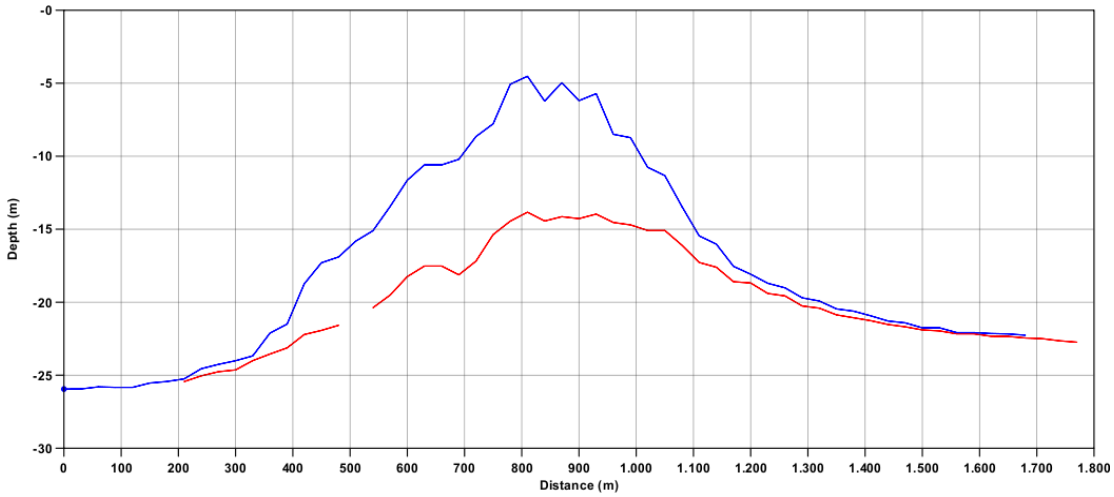


Fig. 14 Profile No. 1 between surveys 2020–2023.

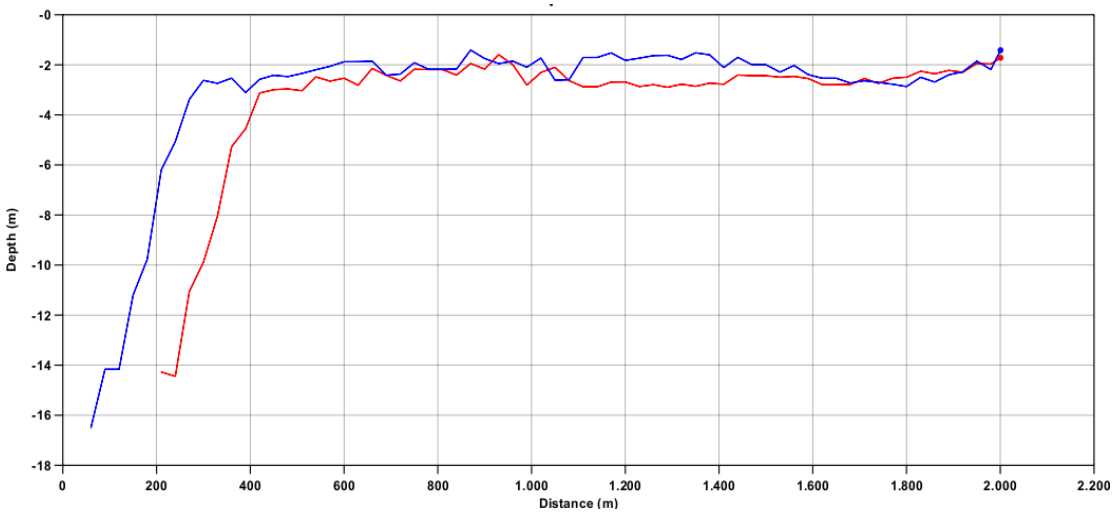


Fig. 15 Profile No. 2 between surveys 2020–2023.

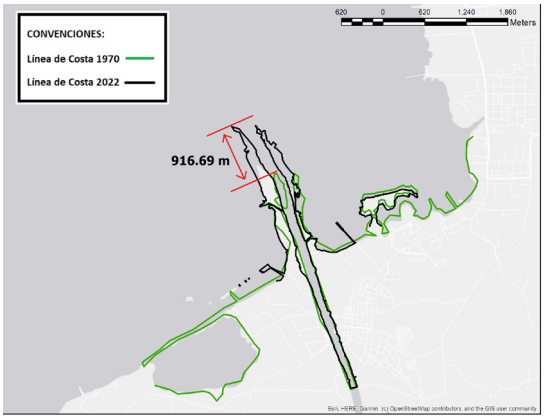


Fig. 17 Coastline comparison between the years 1970 and 2022.

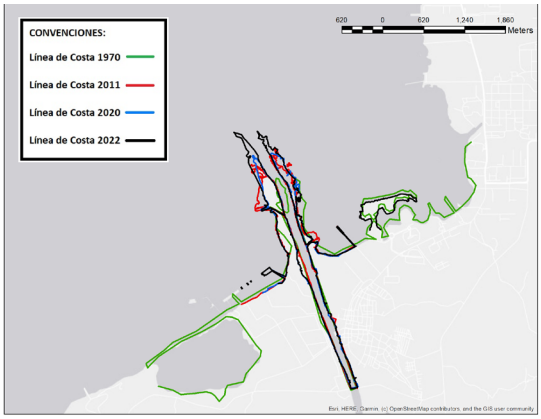


Fig. 16 Coastlines in the Dique Channel.

References

Espinosa-Díaz, L. F., Sanchez-Cabeza, J. A., Sericano, J. L., Parra, J. P., Ibarra-Gutierrez, K. P., Garay-Tinoco, J. A., Betancourt-Portela, J. M., Alonso-Hernandez, C., Ruiz-Fernandez, A. C., Quejido-Cabezas, A. and Diaz-Asencio, M. (2021). Registro sedimentario del impacto de las acciones de manejo sobre la contaminación de la bahía de Cartagena, Colombia. *Marine pollution Bulletin, 172*. https://doi.org/10.1016/j.marpolbul.2021.112807

IHO (2020). *Standards for Hydrographic Surveys* (6th ed.). IHO Special Publication S-44, International Hydrographic Organization, Monaco.

https://doi.org/10.58440/ihr-30-2-n13

Ordoñez, J. I., Cubillos Peña, C. E. and Forero, G. (2007). Balance hídrico y sedimentológico del Dique Channel y sus efectos sobre la sedimentación de la Bahía de Cartagena. *Third regional symposium in hydraulics on rivers*, 18 pp. http://irh-fce.unse.edu.ar/Rios2007/index_archivos/C/6.pdf (accessed 17 February 2024).

Lonin, S., Parra, C., Andrade, C. and Thomas, Y. F. (2004). Patrones de la pluma turbia del Dique Channel en la Bahía de Cartagena. *Bol. Cient. CIOH, 22,* pp. 77–89. https://ojs.dimar.mil.co/index.oho/CIOH/article/view/130/87 (accessed 27 October 2024).

Tosic, M., Restrepo, J. D., Lonin, S., Izquierdo, A. and Martins, F. (2018). Water and sediment quality in Cartagena Bay, Colombia: Seasonal variability and potential impacts of pollution. *Estuarine, Coastal and Shelf Science, 216*, pp. 187–203. https://repository.eafit.edu.co/server/api/core/bitstreams/c1be59bf-7538-4f72-8f33-5ee393e2fa5d/content (accessed 27 October 2024).

Villanueva-García, E. P., Parra-León, N., Parodi Jaramillo, J. and Restrepo López, J. C. (2022). Caracterización sedimentológica y morfológica de la bahía de Cartagena (2000–2020). *Bol. Cient CIOH, 41*(1), pp. 33–47. https:// doi.org/10.26640/22159045.2022.587

NOTE / TECHNICAL REPORT

Investigation of tempo-spatial variability of the Black Sea hydrodynamics by means of neural networks

Author
Emre Gülher[1]

Abstract

The tempo-spatial variability of the Black Sea surface circulation was investigated using satellite data from the Archiving, Validation, and Interpretation of Satellite Oceanographic data (AVISO) project. Self-Organizing Maps (SOMs) were utilized, a neural network-based method known for its unsupervised learning capabilities, to analyze and categorize the circulation patterns, for the very first time. To assess the clustering precision achieved by the SOM algorithms the Davies-Bouldin Index (DBI) was employed as an internal validation metric. Through this comprehensive analysis, six distinct spatial patterns were identified, each exhibiting unique temporal variabilities and occurrence rates. Pattern 1: Characterized by the Sevastopol Cyclonic and Batumi Dipole Eddies, occurring 21 % of the time; Pattern 2: Defined by the Cyclonic RIM Current and Anticyclonic Batumi Eddy, with a 16 % occurrence rate; Pattern 3: Consisting of Anticyclonic Sevastopol and Batumi Eddies, occurring 17 % of the time; Pattern 4: Featuring the Cyclonic RIM Current and Cyclonic Batumi Eddy, also with a 21 % occurrence rate; Pattern 5: Marked by the Anticyclonic RIM Current and Batumi Dipole Eddies, with a 15 % occurrence rate; Pattern 6: Characterized by the Anticyclonic RIM Current and Multi Eddies, occurring 10 % of the time. To further validate the identified patterns, their relevance for predicting the hydrodynamics of the Black Sea was examined. This was achieved by exploring potential correlations between these patterns and major climatological indices, such as the North Atlantic Oscillation (NAO), the East Atlantic/West Russian (EAWR) oscillation, and the El Niño-Southern Oscillation (ENSO). These indices are known to influence large-scale atmospheric and oceanographic conditions, and understanding their relationship with the identified patterns can enhance predictive models of Black Sea dynamics. The findings from this study provide valuable insights into the complex circulation patterns of the Black Sea and their temporal behaviors. The use of advanced neural network techniques such as SOMs, combined with rigorous validation methods like the DBI, underscores the robustness of the analysis. Moreover, the established connections with climatological indices offer a promising avenue for improving long-term forecasts and understanding the broader climatic impacts on the Black Sea's surface circulation.

Keywords
self-organizing maps · neural network · Black Sea · oceanographic circulation

✉ Emre Gülher · gulher18@itu.edu.tr

[1] Istanbul Technical University, Ayazağa, Istanbul

https://doi.org/10.58440/ihr-30-2-n12

1 Introduction

Recent military, political, and economic developments in the Black Sea region (Fig. 1) underscore the urgent need for a deeper understanding of the basin's nature and mechanisms. The tempo-spatial variation of the Black Sea is of critical importance, particularly for operational purposes in navigation, security, and resource management (MacFarlane, 2024; Kılıçer & Kök, 2024).

This research primarily focuses on obtaining a comprehensive dataset concerning the geostrophic velocity anomalies of the Black Sea. The objective is to analyze the tempo-spatial variations and identify recurrent patterns in the surface currents by applying sophisticated clustering algorithms.

Self-Organizing Maps (SOMs) were specifically chosen for this study due to their high accuracy and effective performance in pattern recognition. Despite their proven efficacy, SOMs are not used in the Black Sea region, presenting a novel application in this context.

The integration of advanced clustering algorithms with satellite data provides a robust framework for understanding the complex circulation patterns of the Black Sea. This approach not only contributes to the scientific knowledge of the region but also has practical implications for addressing the emerging challenges posed by recent geopolitical and economic developments (Amarouche & Akpinar, 2023).

Despite the steady advancement in data availability through both in-situ observations and remote-sensing techniques, there remains a significant gap in the efficient and consistent processing and usage of this data. It's estimated that only around 1% of the immense amount of satellite imagery collected is ever seen or analyzed by humans. This is largely due to the sheer volume of data produced by thousands of satellites constantly capturing images of Earth. As a result, artificial intelligence and machine learning technologies are increasingly relied upon to process and analyze this data, allowing for the identification of key patterns without requiring human review for every image (Frazier & Hemingway, 2021; Petrou, 2024).

The potential wealth of information contained within these unprocessed images is immense. Remote-sensing data can offer unparalleled insights into various oceanographic, atmospheric, and terrestrial processes. However, the current bottleneck in data processing limits the ability to fully harness these insights for scientific and operational purposes. Advanced processing tools and algorithms, such as SOMs and other machine learning techniques, are increasingly essential to bridge this gap. These tools can automate the analysis of large datasets, identify significant patterns, and extract relevant features with high precision and efficiency.

In the context of the Black Sea study, the use of SOMs exemplifies the application of advanced neural network methods to overcome the challenges of data processing. By leveraging such techniques, researchers can maximize the utility of remote-sensing data, ensuring that a higher percentage of collected images are analyzed and utilized effectively. This approach not only enhances the understanding of the Black Sea's tempo-spatial variability but also sets a precedent for similar studies in other regions.

Ultimately, addressing the inefficiencies in data processing will enable more comprehensive and accurate environmental monitoring and forecasting. By improving the tools and methods available for data analysis, we can better manage and interpret the vast amounts of information collected, leading to more informed decision-making and a deeper understanding of the natural world.

The SOM is introduced as a viable solution to bridge the ever-widening gap between available data and processed data. SOM, also known as the Kohonen map, is an unsupervised neural network method grounded in competitive learning principles (Kohonen, 1988). One of the most significant features of SOM is its ability to preserve the neighborhood relationships of high-dimensional input data while projecting it onto a lower-dimensional, preferably two-dimensional, space. This capability makes SOM a topology-preserving technique.

2 Study area

The Black Sea's circulation is characterized by its dominant feature, the basin-wide cyclonic circulation known as the Rim Current, spanning 40–80 km in width. This distinctive circulation pattern is primarily driven by the mean cyclonic wind pattern prevailing in the region, coupled with the substantial input of buoyancy (Oguz et al., 1995). Notably, model simulations have underscored the crucial role of bathymetric data in sustaining the Rim Current; without incorporating bathymetry, the Rim Current diminishes significantly (Oguz et al., 1995).

Furthermore, model simulations have revealed that variations in wind stress, particularly weakening during spring and summer, lead to a reduction in the intensity of the mean current (Stanev, 1990; Grégoire et al., 2008). This decrease in intensity triggers intensified meandering of the Rim Current, particularly along the Turkish and Caucasian coastlines, giving rise to the formation of large meanders spanning 100–200 km. These meanders not only alter the flow patterns but also play a significant role in the redistribution of water masses and associated properties.

Satellite data analysis and hydrographic observations have provided further insights into the Black Sea's circulation dynamics. Both data sources have confirmed the existence of recurrent, near-shore, anti-cyclonic eddies situated between the Rim Current and the coastline, alongside several cyclonic gyres within the central basin area (Oguz et al., 1992; Oguz et al., 1993; Oguz et al., 1994). These eddies and gyres contribute significantly to the local mixing and transport processes, influencing the distribution of heat, salt, and nutrients within the Black Sea.

The Black Sea's circulation exhibits a rich tapestry

of dynamical features, from the basin-wide Rim Current to the formation of meanders, eddies, and gyres along its coastline and central regions. These circulation patterns not only shape the physical environment of the Black Sea but also influence its biological productivity, ecosystem dynamics, and connectivity with adjacent water bodies (Fig. 2).

Understanding the complex interplay between these circulation features is essential for deciphering the Black Sea's dynamics and its broader implications for regional and global oceanographic processes. By integrating observational data, model simulations, and remote-sensing techniques, researchers can gain a comprehensive understanding of the underlying mechanisms driving the Black Sea's circulation and its response to external forcing factors.

Among these near-shore and anti-cyclonic eddies, two persistent eddies are noticeable: the Batumi Eddy and the Sevastopol Eddy. The interior part of the Rim Current, on the other hand, is composed of detached cyclonic gyres. These detached cyclonic gyres consist of either one gyre located in the eastern part of the sea and the other located in the western part of the sea, or a single extended cell dominates the basin. The scales of the central gyres and eddies vary from tens to hundreds of kilometers. Inter-annual variability of the Black Sea circulation is significantly affected by river discharges, local dynamics, and wind forcing's seasonal variability (Stanev et al., 1995). Mesoscale, seasonal, and inter-annual variability was best described by the observations made by satellite altimeters (Stanev et al., 2000).



Fig. 1 Geographical location of the Black Sea.

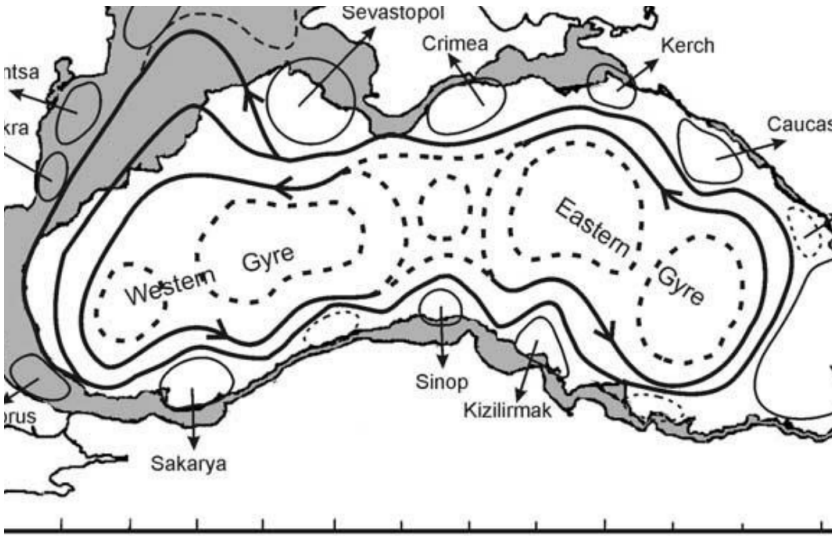


Fig. 2 The schematic pattern of the Black Sea (Korotaev et al., 2003).

3 Data

The AVISO project plays a pivotal role in advancing our understanding of ocean dynamics through the systematic collection, validation, and interpretation of satellite-derived oceanographic data[1] (Ducet et al., 2000). Initiated with the aim of harnessing the wealth of information provided by satellite observations, AVISO serves as a comprehensive repository for oceanographic data, facilitating global-scale studies on ocean circulation, sea level variations, and related phenomena.

By collating data from a network of satellite missions equipped with altimeters and other remote-sensing instruments, AVISO provides researchers with a rich source of high-quality data spanning diverse spatio-temporal scales. The project employs rigorous validation procedures to ensure the accuracy and reliability of the collected data, enabling scientists to analyze and interpret oceanographic processes with confidence.

Moreover, AVISO offers valuable tools and resources for data visualization, analysis, and model validation, fostering collaboration and knowledge exchange among the global oceanographic community. Through its user-friendly interface and comprehensive data archives, AVISO facilitates interdisciplinary research efforts aimed at addressing key scientific questions related to climate variability, ocean circulation, and marine ecosystems.

The geostrophic velocity data from 1992 to 2012 were obtained from AVISO to provide data on the surface currents. Different time frames were selected and examined throughout the initial analyses. A ten-year-long data set was found to be sufficient when extracting the patterns of the long-term temporal and spatial variation due to the fact that any data sets covering a period longer than 10 years do not affect the results. Therefore, this research focuses on data sets from 1999 to 2009.

4 Methodology

In this study, the extensive dataset provided by the AVISO project is leveraged to investigate the tempo-spatial variability of the Black Sea surface circulation. By combining satellite-derived data with advanced analytical techniques, such as SOMs, it's

[1] Istanbul Technical University, Ayazaga, Istanbul

https://doi.org/10.58440/ihr-30-2-n12

aimed to uncover recurrent patterns and dynamics within the Black Sea, shedding light on its complex oceanographic processes and their interactions with larger-scale climatic phenomena.

The methodology involves the detailed examination of satellite-derived data from the Archiving, Validation, and Interpretation of Satellite Oceanographic data (AVISO) project. By applying SOMs, classification, and interpretation of the variability in surface circulation is aimed to help providing valuable insights into the dynamical processes governing the region. The study then seeks to correlate these identified patterns with large-scale teleconnection indices, such as the North Atlantic Oscillation (NAO), the East Atlantic/West Russian (EAWR) oscillation, and the El Niño-Southern Oscillation (ENSO). Understanding these correlations is vital, as these indices significantly influence atmospheric and oceanographic conditions on a global scale.

4.1 'Learning' in neural networks

Before we explore the learning capability of SOM, it's crucial to establish a clear understanding of the concept of learning in neural networks. Learning can be conceptualized in two distinct ways: biologically and mechanically. Biologically, learning refers to the process through which an organism undergoes experiences that result in alterations to its state and enhance its performance in similar situations thereafter. In contrast, mechanical learning involves a computational approach aimed at achieving new intelligence and organizing this intelligence to acquire new abilities (Noyes, 1992). Considering these definitions, it becomes evident that for a neural network to be deemed useful, it must possess the ability to learn. The training process of neural networks facilitates learning, enabling the network to acquire knowledge and adapt its behavior for practical applications (Mishra, 2024).

Another approach to categorizing the learning process involves considering the level of control over the data. In this context, two primary forms of learning emerge: supervised learning and unsupervised learning.

In supervised learning, the network is provided with accurately labeled data, and the objective is to train the network to produce corresponding outputs for given inputs. Both input and output vectors benefit from supervised learning. Once the output vectors are generated, they are compared with the expected outputs to assess the network's performance and identify any discrepancies.

Reinforcement learning represents a specialized form of supervised learning wherein the network receives feedback solely on the accuracy of its outputs. This feedback mechanism is often implemented through back-propagation algorithms (Mishra, 2024).

In unsupervised learning, the availability of accurate answers beforehand is either limited or absent altogether. Unlike supervised learning, where accurate answers guide the training process, input vectors are handled independently in unsupervised learning. Output vectors play no role in the learning process. Instead, the network operates as a self-governing entity, tasked with autonomously extracting patterns from the input data without any external interaction, particularly human intervention. This autonomous feature is particularly valuable when dealing with large and complex datasets, where manual computation is impractical or infeasible due to time constraints or computational complexity.

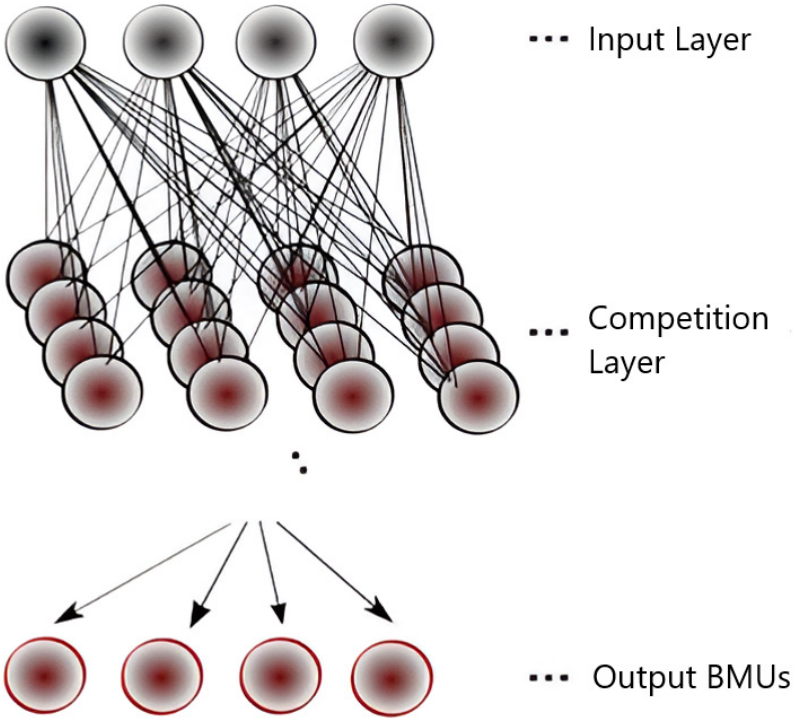


Fig. 3 Illustration of the structure of a SOM (Maung, 2012).

Unsupervised learning serves as the foundation for methodologies such as self-organizing maps (Guthikonda, 2005), wherein the network autonomously organizes and represents the input data in a structured manner, revealing inherent patterns and relationships without the need for explicit supervision.

4.2 SOM

SOMs are first introduced by Tuevo Kohonen (Kohonen, 1988) and derive their name from their inherent ability to organize themselves autonomously, without the need for external supervision. SOMs employ competitive learning, enabling them to learn independently.

The term "maps" in SOMs refers to their method of handling input datasets, wherein they endeavor to map the weights of the data. Nodes within the SOM network strive to mimic the characteristics of the input datasets they receive initially. This responsive behavior of the nodes forms the cornerstone of the entire learning process.

Central to the functioning of SOMs is the principle of preserving the essential characteristics of the input datasets. This principle distinguishes SOMs from other methods and underscores their significance. By retaining the topological relationships among the input data and mapping these relationships onto an

Table 1 Main six steps of the algorithm of the SOM.

1st step	Each node's weight is initialized with a random number between 0 and 1.
2nd step	A random vector is selected from the training data set and introduced to the network.
3rd step	Each node in the network is inspected in order to find out which one resembles the input vector more accurately in terms of weights. BMU is the name given to the winning node. The Euclidean distance formula, which measures the similarity between two data sets, is used to do this selection. The BMU is found by the calculation of the distance between the weights of node and the input vector.
4th step	The radius of the neighborhood of the BMU is calculated. This radius is initialized as the network's radius and decays with each time-step until reaching the BMU itself.
5th step	All the nodes that fall in the radius of the BMU are adjusted to make them as similar as possible to the input vector. The weight of the closest node to the BMU is changed the most, and the degree of this change diminishes as the range between the BMU, and the nodes increases.
6th step	The second step is repeated for N iterations.

SOM network, SOMs offer a valuable means of representing complex datasets (Guthikonda, 2005)

SOMs exhibit a relatively simple structure, with several noteworthy aspects. Fig. 3 illustrates a 4 × 4 SOM network, serving as the competition layer. Each input node establishes connections with every map node, resulting in a considerable number of connections even in small networks, such as the one depicted in Fig. 3 (e.g., 4 × 4 × 4 equals 64 connections). In contrast, there are no direct connections between map nodes within the network. The organization of nodes forms a two-dimensional grid, facilitating visualization of outputs and aiding in the implementation of the SOM algorithm. Each node in the network is assigned a unique coordinate (*i,j*), simplifying node referencing and range determination. However, it's important to note that map nodes are unaware of the values held by their neighbors, as they solely interact with input nodes. Consequently, each node must rely on information from input vectors to update its weights.

The weight vectors of both the map nodes and the input vectors should match to enable the algorithm to perform properly (Mishra, 2004).

As an unsupervised learning algorithm, SOM has learning and prediction phases. During the learning phase, map is built; network organizes using a competitive process with a training set. During the prediction phase, new vectors are quickly given a location on the converged map, easily classifying, or categorizing the new data. The algorithm of the self-organizing map can be described as six main steps, which are presented in Table 1 in detail (Kohonen, 2013).

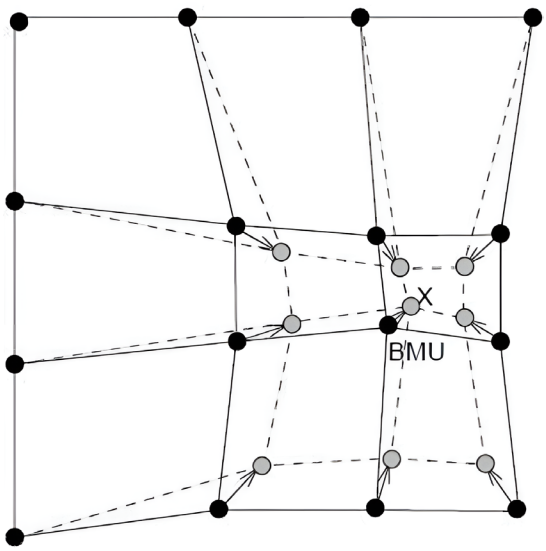


Fig. 4 An illustration of the process of updating BMU along with its neighbors towards the "x", which in this case is the input sample (Vesanto et al., 2000).

The degree of influence that the node's distance from the Best Matching Unit (BMU) has on the node's learning is shown by the influence rate. Initially, influence rate is set to 1 for all the neighboring nodes of the BMU and zero for the ones that are away from the BMU. At the end, due to weights' random distribution and numerous iterations, SOM is able to settle down to a map of stable zones (Fig. 4), where nodes that do not fall into the neighborhood radius are entirely ignored (Kohonen, 2013).

The fact that the network is composed of nodes that are on a two-dimensional grid makes the calculation possible. The amount learned by the nodes on the edge of the neighborhood radius is a fractional value that is smaller than 1.0.

4.3 Davies-Bouldin index

Davies-Bouldin index (DBI) is exerted to the data sets along with the SOM, to determine the number of patterns that best represents a data set. DBI was introduced by Davies et al. (1979) and is a measure that is used for assessing clustering algorithms.

$$DBI = \frac{1}{N}\sum_{i=1,i\neq j}^{N} \max\left[\frac{\sigma_i + \sigma_j}{d(c_i, c_j)}\right] \quad (1)$$

DBI operates as an internal scheme, and the authentication of how precise the clustering has been accomplished is made using characteristics of the data set (Davies et al., 1979). In Eq. 1, *N* is the number of clusters, σ_i is the average distance of all patterns in cluster *i* to their cluster centers (c_i, σ_j) is the average distance of all patterns in cluster *j* to their cluster centers c_j, and $d(c_i,c_j)$ is the distance between cluster centers c_i and c_j. Small values of DBI correspond to clusters that are compact, and whose centers are far away from each other. Consequently, the number of clusters that minimizes DBI is taken as the optimal number of clusters.

https://doi.org/10.58440/ihr-30-2-n12

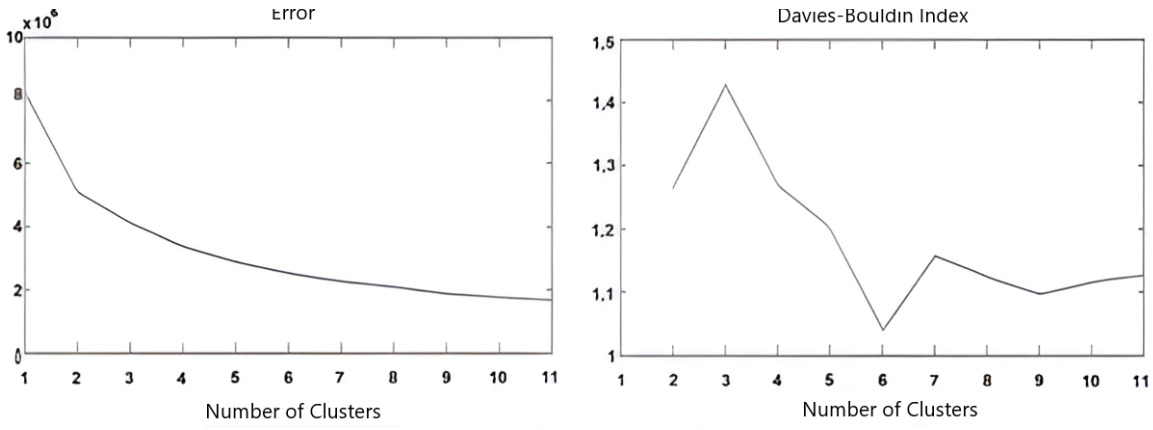


Fig. 5 The DBI results concerning the proper number of clustering of surface geostrophic velocity data (which justifies the six different patterns provided by the SOM).

5 Results and discussion

To study the temporal and spatial variation of the surface geostrophic velocities, the Black Sea basin is subject to iterative SOM analysis. The DBI demonstrates the best option with regards to the selection of total number of clusters to represent the whole data set. The smaller the DBI, the better and more practical the data representation is. Therefore, considering the DBI, the SOM analysis for the surface currents is based on six clusters (Fig. 5).

5.1 Six (spatial) patterns

Pattern 1 (Sevastopol Cyclonic and Batumi Dipole Eddies): The first pattern represents more than 20 % of the whole data set. In this pattern, the Batumi dipole eddies are detected at the southeastern corner of the basin. The eddy on the right is strong, cyclonic, and it spins at ~8 cm/s, whereas the other eddy is weak and anti-cyclonic. At the northwestern corner of the basin, the cyclonic Sevastopol eddy which spins at ~5 cm/s is evident. The general circulation is comprised of two main gyres. The western main gyre is anti-cyclonic and weak. The eastern main gyre, on the other hand, is cyclonic and strong. The northerly boundary current forms in the west. No eddy formation is observed in the open parts of the basin (Fig. 6).

Pattern 2 (Cyclonic RIM Current and Anti-cyclonic Batumi Eddy): More than 16 % of the data set is represented by the second pattern. The main feature of this pattern is the strong, anti-cyclonic Batumi eddy spinning at ~8 cm/s. Apart from the Batumi eddy, no other eddy structure, including the major Sevastopol eddy, is observed. The general circulation is formed by the strong and cyclonic RIM current flowing at ~5 cm/s. The basin's open parts are relatively calm compared to the coastal regions. Therefore, this particular pattern is mostly dominated by the RIM current (Fig. 7).

Pattern 3 (Anti-cyclonic Sevastopol and Batumi Eddies): The third pattern represents almost 16 % of the whole data set. The major eddies of the basin are the Batumi and Sevastopol eddies which spin at ~7–8 cm/s. Both of these major eddies are strong and anti-cyclonic. The RIM current does not appear which means that the general circulation is formed by the western and eastern main gyres. The weak Caucasus eddy exists in the northeastern corner, while the strong northerly boundary current is present in the west (Fig. 8).

Pattern 4 (Cyclonic RIM Current and Batumi Eddy): The fourth pattern comprises more than 20 % of the whole representation of the data set. In this pattern, the Black Sea basin is almost entirely dominated by the strong cyclonic RIM current which flows at ~10 cm/s. The open parts of the sea stay relatively calm, and the very weak cyclonic Batumi eddy is detected but it is nearly absorbed by the RIM current (Fig. 9).

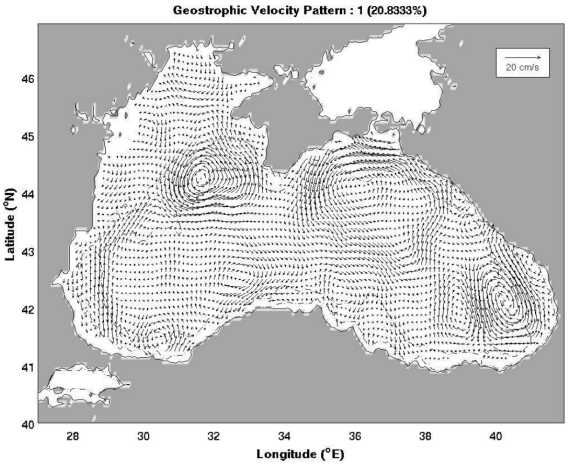


Fig. 6 The first pattern and its percentage.

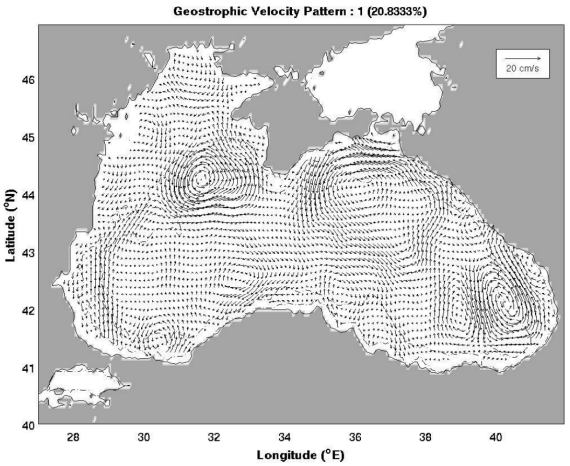


Fig. 7 The second pattern and its percentage.

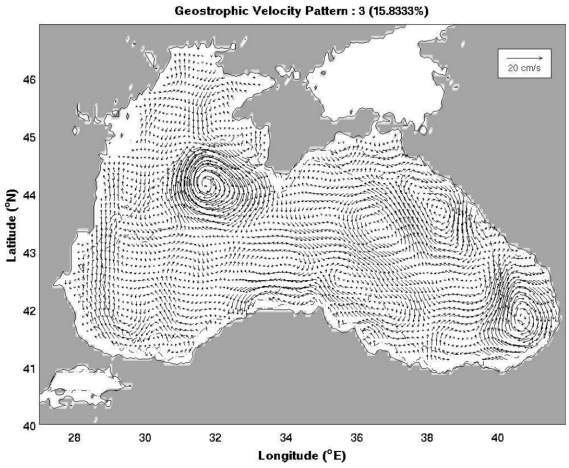


Fig. 8 The third pattern and its percentage.

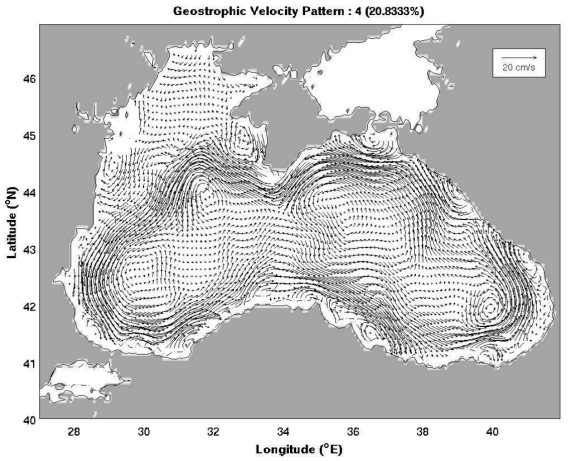


Fig. 9 The fourth pattern and its percentage.

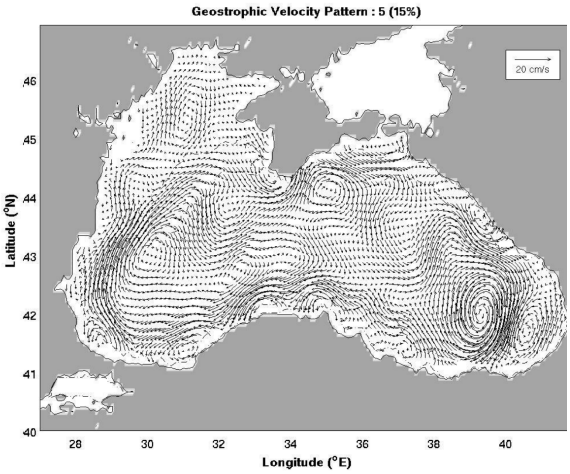


Fig. 10 The fifth pattern and its percentage.

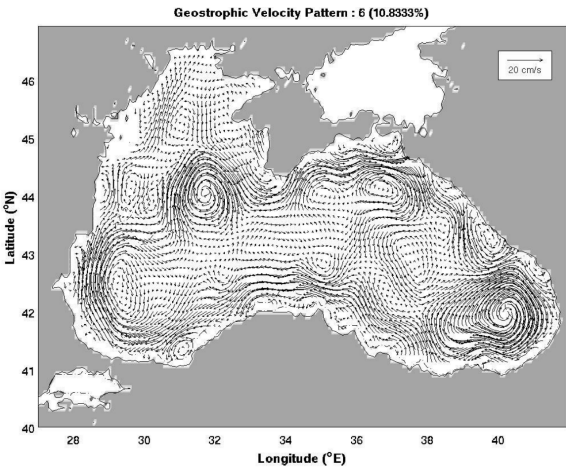


Fig. 11 The sixth pattern and its percentage.

Pattern 5 (Anti-cyclonic RIM Current and Batumi Dipole Eddies): The fifth pattern represents 15 % of the whole data set and it demonstrates a basin-wide, chaotic environment. At the southeastern corner the Batumi dipole eddies take place and the stronger eddy spins at ~7 cm/s. The weak, anti-cyclonic Crimea eddy is observed in the north, whereas the Sevastopol eddy disappears. The general circulation is formed by the strong, anti-cyclonic RIM current which flows at ~6–7 cm/s (Fig. 10).

Pattern 6 (Anti-cyclonic RIM Current and Multi Eddies): More than 10 % of the total representation for the data set is covered by the sixth pattern. The southeastern corner of the basin is entirely dominated by the strong, anti-cyclonic Batumi eddy spinning at ~8 cm/s. At the north of the Batumi eddy, the cyclonic Suchumi eddy is detected. The weak, anti-cyclonic Kerch eddy is observed in the north. At the northwestern corner the strong anti-cyclonic Sevastopol eddy forms, which spins at ~6 cm/s. The general circulation is comprised of the strong, anti-cyclonic RIM current (Fig. 11).

5.2 Temporal variation

To better illustrate the monthly and seasonal variability of the surface currents, the rate of occurrence of the six patterns was computed and the results are shown in Fig. 12. Pattern 1 is one of the two patterns that dominates winter-like and fall-like months. Its maximum contribution is in January with ~45 % and it disappears completely in June. Even though there is less than 35 % chance it will appear, it is the pattern most likely to be observed in December. Pattern 2 is more likely to be observed during springtime. Its maximum contribution is detected in April with more than 50 % and it has the highest percentage among the six patterns in this particular month. In summer and fall it tends to stay at around 20 %, it declines in winter-like months, and it completely disappears in June. Pattern 3 tends to appear towards the end of spring and the beginning of summer. It reaches its maximum in May and becomes the pattern most likely to appear during that time of the year. It oscillates during fall-like months and never shows up in January and February. The first three months of the year are dominated by Pattern 4. It tends to appear strongly during cold periods, whereas during warm periods, it exhibits a weak contribution. Pattern 4 disappears in May and doesn't appear again until September. Although Pattern 5 shows maximum percentages in fall-like months and dominates in October, it has no significant seasonality and occurs occasionally throughout the year. Pattern 6 completely disappears from November to April, appearing only five months during the year. It dominates the period from June to September and reaches its maximum in July. With more than 40 % contribution, it becomes the pattern most likely to be detected in July.

The time series of the six patterns of the surface currents from 2000 through 2009, with year 2004

https://doi.org/10.58440/ihr-30-2-n12

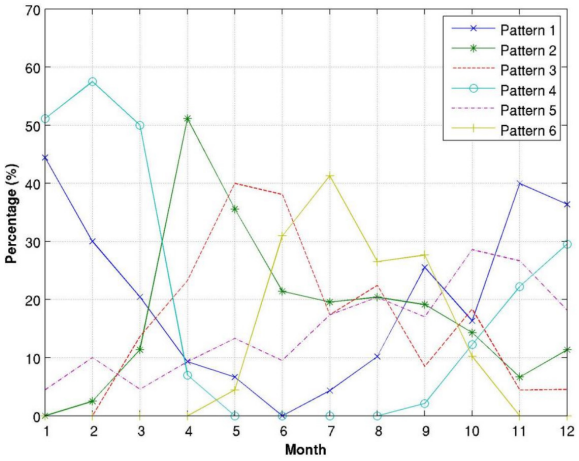


Fig. 12 The monthly percentage of the six patterns of the surface currents.

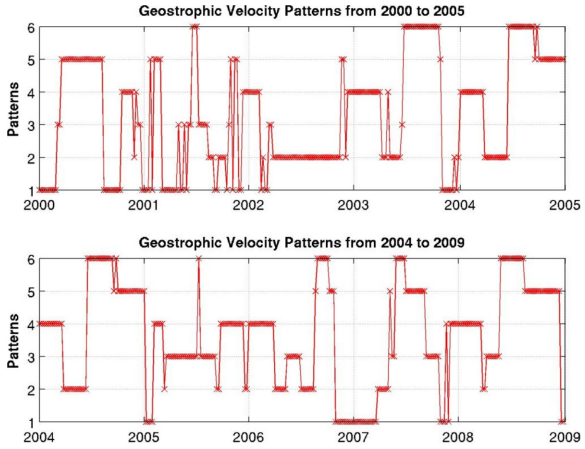


Fig. 13 The inter-annual variability of the six patterns of the surface currents.

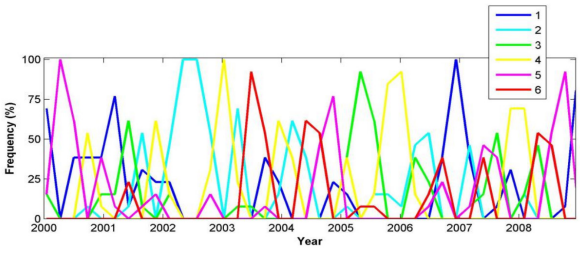


Fig. 14 The frequency of inter-annual variability of the six patterns.

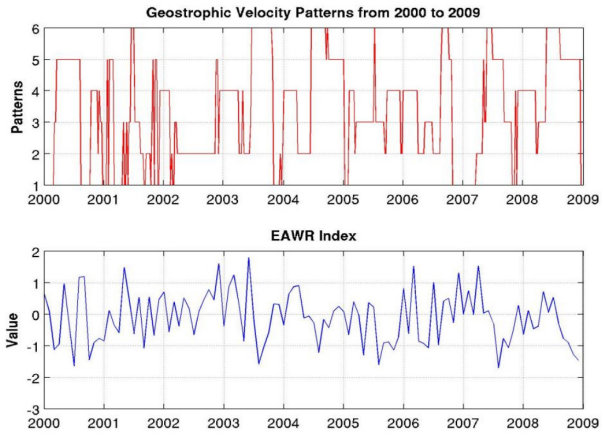


Fig. 15 Comparison of the inter-annual variability of the six patterns regarding the surface currents with the EAWR index

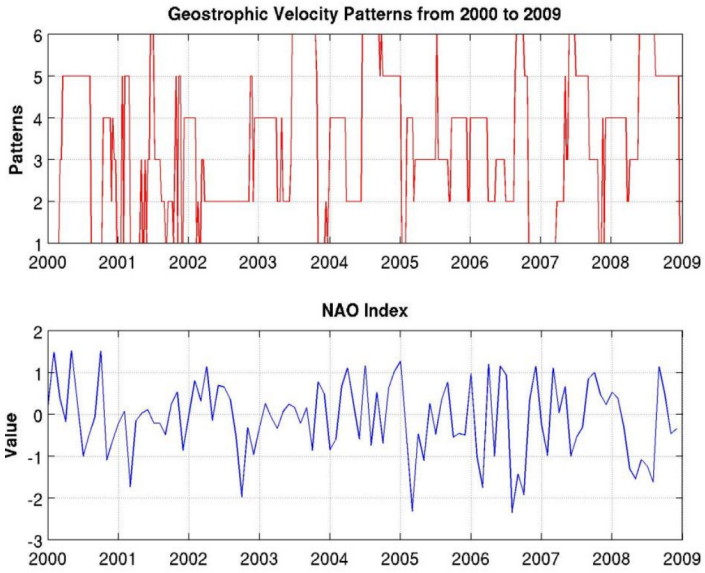


Fig. 16 Comparison of the inter-annual variability of the six patterns regarding the surface currents with the NAO index.

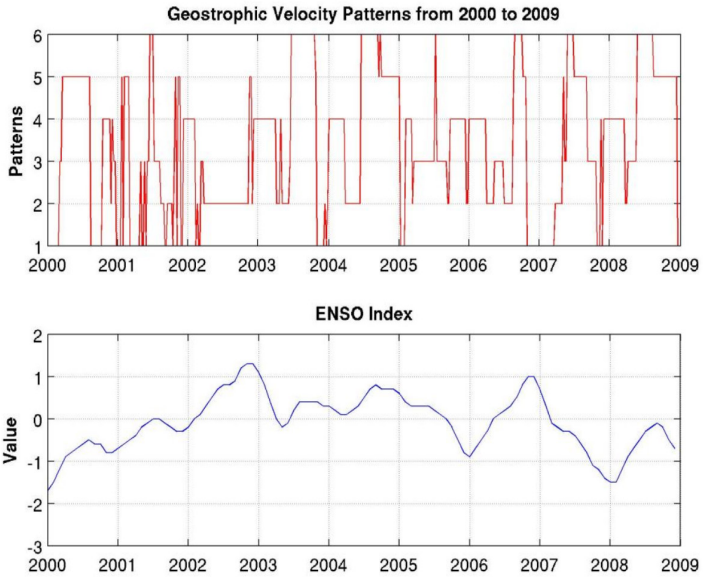


Fig. 17 Comparison of the inter-annual variability of the six patterns regarding the surface currents with the ENSO index.

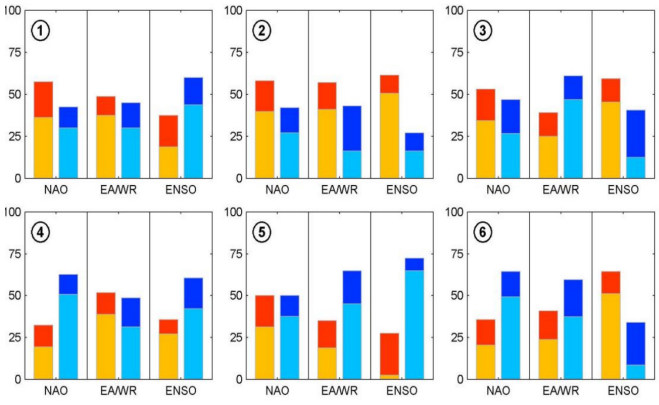


Fig. 18 Distribution of each pattern of the surface currents between positive (red) and negative (blue) phases of the teleconnection indices. The darker shades represent the strong phases for which the index's absolute value is greater than corresponding standard deviation

Table 2 The percentages of the six patterns regarding the surface currents with the large-scale teleconnection indices superimposed.

	Geostrophic velocity					
	(+) NAO	(-) NAO	(+) EAWR	(-) EAWR	(+) ENSO	(-) ENSO
Pattern 1	20%	13%	20%	14%	11%	20%
Pattern 2	25%	15%	25%	16%	30%	11%
Pattern 3	14%	16%	11%	18%	14.5%	14.5%
Pattern 4	15%	24%	22%	16%	20%	23%
Pattern 5	17%	17%	12%	22%	7%	23.5%
Pattern 6	9%	15%	10%	14%	17.5%	8%

shown in Fig. 13 and the evolution of the duration and the frequency of the same patterns is shown in Fig. 14 in order to illustrate the inter-annual variability.

Furthermore, Figs. 15, 16, and 17 demonstrate the contemporaneous EAWR, NAO, and ENSO indices respectively, along with the times series of the surface currents. In addition to those figures, Table 2 is provided to allow a deeper understanding of the relationship between the surface currents and the large-scale teleconnection indices. The potential influence of large-scale teleconnection indices on the recurrent patterns of the surface currents (shown in Figs. 5–10) are evaluated by estimating for each recurrent pattern the value of the climate indices (i.e. EAWR, NAO, ENSO), acquired for different months mapped towards this pattern. This process enables determining whether a recurrent pattern is associated to either positive or negative value of a particular index significantly, and therefore a prospective connection between the surface currents over the Black Sea and large-scale teleconnection indices. Fig. 18 shows for each recurrent pattern of the surface current, the distribution of positive and negative phases of the three teleconnection indices. According to this figure, the EAWR index and the ENSO index are negative significantly during months mapped towards Pattern 5, which indicates that the occurrence of Pattern 5 (Anti-cyclonic RIM Current and Batumi Dipole Eddies) is promoted by the absence of these indices. On the other hand, ENSO index is significantly positive during months mapped towards Pattern 2 (Cyclonic RIM Current and Anti-cyclonic Batumi Eddy) and therefore influences the surface current structure.

6 Conclusion

Surface geostrophic velocity data from 1999 to 2009 were obtained from AVISO as the base dataset on the surface currents. Six patterns as to these velocities were found after conducting the SOM analyes. The inter-annual variability of the surface currents was also obtained.

The rate of occurrence of the six patterns was computed. Pattern 1 is one of the two patterns that dominates winter-like and fall-like months. Its maximum contribution is in January with ~45 % and it disappears completely in June. Pattern 2 is more likely to be observed during springtime. Its maximum contribution is detected in April with more than 50 %. It declines in winter-like months, and it completely disappears in June. Pattern 3 tends to appear towards the end of spring period and the beginning of the summer period. It reaches its maximum in May and becomes the pattern most likely to appear during that time of the year.

The first three months of the year are dominated by Pattern 4. It tends to appear strongly during cold periods, whereas during warm periods it exhibits a weak contribution. Pattern 4 disappears in May and does not appear again until September. Even though Pattern 5 shows maximum percentages in fall-like months and dominates in October, it has no significant seasonality and occurs occasionally throughout the year. Pattern 6 completely disappears from November to April and appears only five months during the year. It dominates the period from June to September and reaches its maximum in July. With more than 40 % contribution, it becomes the pattern most likely to be detected in July. The EAWR index and the ENSO index are detected significantly negative during months mapped towards Pattern 5, which indicates that the occurrence of Pattern 5 is promoted by the absence of these indices. On the other hand, ENSO index is detected significantly positive during months mapped towards Pattern 2 (Pattern 2 has the highest possibility to form among the six patterns at 25 %) and therefore influence the surface current structure. As the last example of the significant indications, Pattern 6 has the smallest possibility of occurring at only 8 % when the ENSO index is negative.

The topology-preserving nature of SOM ensures that similar patterns in the input data are mapped to neighboring regions on the output map. This characteristic offers a substantial advantage in pattern recognition and feature extraction from complex datasets. By clustering similar data points together, SOM facilitates the identification of underlying structures and trends within the data, which might otherwise be obscured in high-dimensional spaces.

In practical applications, such as the analysis of Black Sea surface circulation that is carried out in this research, SOM can efficiently handle large and

https://doi.org/10.58440/ihr-30-2-n12

complex datasets derived from satellite observations. It enables researchers to discern meaningful patterns and variations in the data, which are crucial for understanding the tempo-spatial dynamics of the region. The ability to visually represent these patterns in a two-dimensional map simplifies the interpretation and communication of results, making SOM an invaluable tool for both data analysis and decision-making processes.

Moreover, the application of SOM in this context highlights its potential to enhance the processing and utilization of remote-sensing data. By reducing the dimensionality of the data while preserving its intrinsic relationships, SOM allows for more efficient data processing and more accurate identification of key features. This not only maximizes the utility of the available data but also paves the way for more informed and effective environmental monitoring and management strategies. The integration of SOM into the data processing workflow addresses the critical challenge of managing large volumes of high-dimensional data. Its topology-preserving properties and ability to cluster similar patterns make it a powerful tool for extracting valuable insights from complex datasets, thereby bridging the gap between data availability and data utilization.

The research findings are expected to enhance predictive models and operational strategies for the Black Sea. By identifying the tempo-spatial patterns and their driving mechanisms, we can better anticipate changes in the basin's dynamics. This, in turn, will support various operational activities, from maritime navigation to environmental monitoring and disaster response. The innovative application of SOMs in this region highlights the potential for advanced neural network techniques to offer new perspectives and more accurate analyses of oceanographic data.

Acknowledgements

I would like to offer my sincere gratitude to distinguished Professor Peter C. Chu, for his encouragement, scientific guidance, and instructions throughout the course of the research. This study would not have been this educational and exciting without his wealth of knowledge and motivation. I also want to express my heartfelt appreciation to Doctor Ming-Jer Huang for his support and sharing his expertise unconditionally.

References

Amarouche, K. and Akpınar, A. (2023). *Long-term spectral wave climate in the Black Sea based on directional wave spectra*. 21 February 2023, PREPRINT (Version 1) available at Research Square https://doi.org/10.21203/rs.3.rs-2596229/v1

Davies, D. L. and Bouldin, D. W. (1979). A Cluster separation measure. *IEEE Transactions on Pattern Analysis and Machine Intelligence, 2*, pp. 224–227. https://doi.org/10.1109/TPAMI.1979.4766909

Ducet, N., Le Traon, P. Y., Reverdin, G. (2000). Global high-resolution mapping of ocean circulation from TOPEX/Poseidon and ERS-1 and -2. *J. Geophys. Res., 105*(C8), 19477–19498.

Frazier, A. E. and Hemingway, B. L. (2021). A Technical Review of Planet Smallsat Data: Practical Considerations for Processing and Using PlanetScope Imagery. *Remote Sens., 13*, 3930.

Grégoire, M., Raick, C. and Soetaert, K. (2008). Numerical modeling of the central Black Sea ecosystem functioning during the eutrophication phase. *Progress in Oceanography, 76*(3), pp. 286–333. https://doi.org/10.1016/j.pocean.2008.01.002.2004

Guthikonda, S. M. (2005). *Kohonen Self-Organizing Maps*. Wittenberg University.

Kılıçer, A. and Kök, O. (2024). Is the Black Sea Already a NATO Sea? *Atlântica, 5.* https://doi.org/10.58867/DBYO3056

Kohonen, T. (1988). *Self-Organization and Associative Memory*. Springer-Verlag, ISBN 0-387-18314-0.

Kohonen. T. (2013). Essentials of the self-organizing map. *Neural Networks, 37*, pp. 52–65.

Korotaev, G., Oguz, T., Nikiforov, A. and Koblinskyet C. (2003). Seasonal, interannual, and mesoscale variability of the Black Sea upper layer circulation derived from altimeter data. *Journal of Geophysical Research: Oceans, 108*(C4).

MacFarlane, S. N. (2024). NATO and Black Sea Security. In K. Kakachia, S. Malerius and S. Meister (Eds.), *Security Dynamics in the Black Sea Region. Contributions to International Relations.* Springer, Cham. https://doi.org/10.1007/978-3-031-62957-0_5

Maung, P. P. (2012). *Augmented Reality using a Neural Network.* Ripon College

Mishra, V. (2024). Neural networks and deep learning: theoretical insights and frameworks. https://doi.org/10.61909/AMKEDTB022409

Noyes, J. L. (1992). *Artificial Intelligence with Common Lisp: Fundamentals of Symbolic and Numeric Processing*. D. C. Heath, Lexington, MA.

Oguz, T. V., Aubrey, D. G., Latun, V. S., Demirov, E., Koveshnikov, L., Sur, H. I., Diaconu, V. S., Besiktepe, S., Duman, M., Limeburner, R. and Eremeev, V. (1994). Mesoscale circulation and thermohaline structure of the Black Sea observed during HydroBlack '91. *Deep-Sea Research I, 41*, pp. 603–628.

Oguz, T. V., Latun, V. S., Latif, M. A., Vladimirov, V. V., Sur, H. I., Markov, A. A., Ozsoy, E., Kotovshchikov, V. V., Eremeev, V. V. and Unluata, U. (1993). Circulation in the surface and intermediate layer of the Black Sea. *Deep-Sea Research I, 40*, pp. 1597–1612.

Oguz, T., La Violette, P.E. and Unluata, U. (1992). The upper layer circulation of the Black Sea: its variability as inferred from hydrographic and satellite observations. *Journal of Geophysical Research, 97*(C8), 12569–12584.

Oguz, T., Malanotte-Rizzoli, P. and Aubrey, D. (1995). Winds and thermohaline circulation of the Black Sea driven by yearly mean climatology forcing. *Journal of Geophysical Research, 100*(C4), pp. 6845–6863.

Petrou, M. (2004). Special issue – Pattern Recognition for Remote Sensing (PRRS 2002) Preface. *Pattern Recognition Letters, 25*, 1459, ISSN: 0167-8655.

Stanev, E. V. (1990). On the mechanisms of the Black Sea circulation. *Earth-Science Reviews, 28*(4), pp. 285–319. https://doi.org/10.1016/0012-8252(90)90052-W.1990

Stanev, E. V., Le Traon, P. Y. and Peneva, E. L. (2000). Sea level variations and their dependency on meteorological and hydrological forcing: analysis of altimeter and surface data for the Black Sea. *Journal of Geophysical Research, 105 (C7)*, 17203–17216.

Stanev, E. V., Roussenov, V. M., Rachev, N. H. and Staneva, J. V. (1995). Sea response to atmospheric variability, Model study for the Black Sea. J*ournal of Marine Systems, 6*, pp. 241–267.

Vesanto, J., Himberg, J., Alhoniemi, E. and Parhankangas, J. (2000). *SOM toolbox for Matlab 5*. Helsinki, Finland: Helsinki University of Technology.

https://doi.org/10.58440/ihr-30-2-n12

NOTE / TECHNICAL REPORT

The establishment of the Hydrographic and Oceanographic Service of the Chilean Navy (SHOA) – A succinct chronological account of its 150 years

Author
Hugo Gorziglia[1]



Fig. 1 Actual headquarters of the Chilean Navy Hydrographic and Oceanographic Service (SHOA).

1 Introduction

On May 1, the Hydrographic and Oceanographic Service of the Chilean Navy (SHOA; Fig. 1), formerly the Hydrographic Institute of the Navy (IHA), celebrated 150 years since its foundation. To illustrate to the reader the significance that Hydrography has had in the history of Chile, it is necessary to highlight the steps taken from its discovery until the eighteenth century; and then go on to recount the transcendent events that have occurred up to the present day. This work would not be complete without the inclusion of the challenging prospect that will have to be faced in the immediate future.

2 Origin of hydrography in Chile

Chile was discovered from the sea. In fact, on November 1, 1520, Ferdinand Magellan, an eminent Portuguese navigator in the service and under the protection of Charles 1 – King of Spain and Emperor of Germany as Charles V – sailed, in command of the caravels Victoria, Concepción and Trinidad, the navigable passage between the North Sea and the South Sea, calling it "Strait of All Saints", which today bears its name, Strait of Magellan.

In addition to Magellan's expedition, there are many others that contributed to the hydrographic and geographical knowledge of the extensive and rugged coastline of Chile. In 1615 the Dutchman Jacobo Le



Fig. 2 Spaniard José de Moraleda y Montero during the period 1787–1796 was the greatest hydrographic-scientific contributor.

✉ Hugo Gorziglia · hgorziglia.hydro@gmail.com
[1] Hydrographic and Oceanographic Service of the Chilean Navy (SHOA), Chile

https://doi.org/10.58440/ihr-30-2-n07

Maire, in search of a less dangerous passage than the Strait of Magellan to reach the Moluccas, discovered, further south, the strait that bears his name and, later, the great passage that joins the two largest oceans on earth, the Atlantic with the Pacific, today the Drake Passage. Also, other navigators and scientists ventured these coasts, making new contributions to their knowledge, among others, Bartolomé García de Nodal and Gonzalo Nodal (1619) and Jacobo L'Hermite (1624).

The scientific spirit and intellectual thrust of the eighteenth century also reached the expeditions. Among them, we can mention: Commodore John Byron (1764), James Cook (1768 and 1774), José de Moraleda y Montero (1787 and 1796; Fig. 2) and Alejandro Malaspina (1789 and 1794). Undoubtedly, until the end of the eighteenth century, the work carried out by the Spaniard Moraleda y Montero was the greatest hydrographic-scientific contributions, especially in the area of Chiloé and the Chonos archipelago.

3 The transcendent nineteenth century

Four episodes occurred during the nineteenth century, which have become true milestones in the history of national hydrography.

The expeditions of the Englishman Phillip Parker King between 1826 and 1830 and the continuation of these by Robert Fitz Roy between 1831 and 1836, the latter accompanied by the legendary Charles Darwin. The information generated was the first on which the documentation on the coasts and sea of Chile began to be structured.

The beginning of national marine scientific activity (1834–1874): In December 1834, the war brig Aquiles (Fig. 3), which under the command of Frigate Captain Don Roberto Simpson surveyed the cove and mouth of Rio Bueno in the province of Valdivia; an event considered the birth and beginning of the national marine scientific activity, while Admiral Simpson, who later became Commander in Chief of the Navy, is recognized as the first Chilean hydrographer.

For 40 years, hydrographic and oceanographic activities on the extensive Chilean coastline and island gradually increased. This effort was joined by foreign explorers, navigators and scientists, among them: Jules Cesar Dumont D'Urville (1837) and James Clark Ross (1842). This is the end of the foreign contribution that, with its feverish scientific, intellectual, commercial and military spirit, gives way to a consolidated and thriving Chile.

The Establishment of the National Navy's Hydrographic Office: On May 1, 1874, the Government issued the Supreme Decree that created the "Hydrographic Office of the National Navy". Commander Francisco Vidal Gormaz (Fig. 4) was appointed as its first Director, as a recognition for his efforts that made its creation possible, and in line with his extensive dedication and relevant qualities as a distinguished hydrographer, geographer, astronomer and prolific writer.

The Hydrographic Office was the first national cartographic body, the first created in Latin America and the 12th in the world.

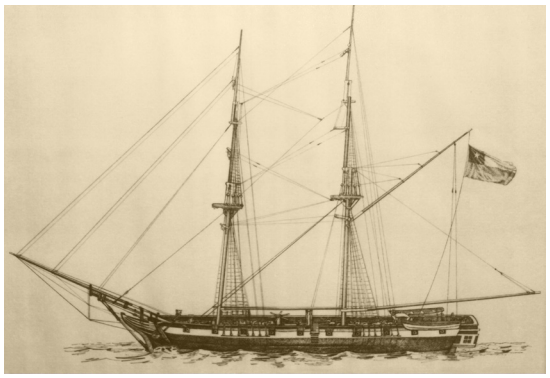


Fig. 3 The war brig Aquiles, which under the command of Roberto Simpson in December 1834 surveyed the cove and mouth of Rio Bueno, event considered the birth and beginning of the national marine scientific activity.



Fig. 4 Commander Francisco Vidal Gormaz who was appointed as the first Director, of the recently established "Hydrographic Office of the National Navy" on 1 May 1874).



Fig. 5 Rapa Nui (Easter Island) chart, ordered to be drawn up by Lt. Cdr. Policarpo Toro, commander of the cruiser Angamos, in September 1888.

https://doi.org/10.58440/ihr-30-2-n07

The Hydrographic survey of Easter Island (Rapa Nui): The nineteenth century, in terms of hydrographic events of transcendence, closed with the preparation of the Easter Island chart (Fig. 5), ordered to be drawn up by Lieutenant Commander Don Policarpo Toro, commander of the cruiser Angamos, in September 1888, with which he reaffirmed the incorporation of said possession into the Republic of Chile, attaching it as an illustrative document to the act that he signed together with the Chiefs of said island, testifying to its full, complete and unreserved cession.

4 The twentieth century and the development of hydrographic capabilities

During this period, the structure for carrying out hydrographic and oceanographic activity was strengthened with the different legal provisions that set the responsibilities of the then Hydrographic Institute of the Navy (IHA). This allows us to better face the continuous, intense and sustained study of our extensive coast and its vast oceanic territory.

Milestones within the first half of the century are the creation in 1914 of the School of Navigation and Hydrography for officers that to this day has graduated 273 officers specializing in these disciplines, including officers from other countries; the participation in 1921 of the foundation of the International Hydrographic Bureau (IHB), in the Principality of Monaco, together with 17 other foreign hydrographic services and the beginning in 1941 of the systematic and uninterrupted observation of tides, publishing from 1947, the corresponding Tide Tables of the Coast of Chile.

In accordance with Chile's proposal, in 1957 the IHB Directing Committee worked on the text of a draft declaration or agreement by which the Member States would recognize the legal personality of the Bureau. But also of great relevance was the celebration of the International Geophysical Year (1957/1958), with the SHOA assuming the representation of Chile in the area of physical oceanography, with singular success in terms of participation. In 1959, Chile joined the Seismic Sea-Wave Warning System in the Pacific, putting its own national system into service on July 30, 1964; both instances were made official by Supreme Decree No. 26 of January 1966.

In 1960, the first oceanographic operation of great importance called MARCHILE began, an initiative of joint efforts between the IHA, universities, government entities and the Technical Assistance Program, which constituted a great contribution to the national oceanographic community, incipient at that time. During the eighteen cruises carried out until 1984, in transects that covered areas between Arica and Chiloé, the oceanic island and the Drake Passage, physical and chemical parameters of seawater, bathythermography, bathymetry, plankton collection, bentology, geological samples and meteorology were measured.

On 3 May 1967, the final text of the IHB Convention (and annexed Regulations) was deposited with the Government of Monaco and opened for signature by Member States. On that day, 17 countries signed it, including Chile.

In 1968, Law No. 16,771 was enacted, which establishes the functions of the IHA and its character as an official, technical and permanent service of the State, in everything related to Hydrography, Nautical Cartography, preparation and publication of navigation charts of national waters, Oceanography, among others. It is defined as a functionally decentralized service and its financing sources were identified and established. The National Oceanographic Data Center is also created; today the National Center for Hydrographic and Oceanographic Data (CENDHOC).

In 1969 and based on the aforementioned law, the IHA's Organic Regulations were proposed and approved, explaining its mission and functions and at the same time, establishing within its responsibilities to constitute itself as the official, technical and permanent service of the State before the International Hydrographic Organization (IHO); before the Intergovernmental Oceanographic Commission (IOC), founded in 1960; to the Scientific Committee on Oceanic Research (SCOR)) and to the International Association of Physical Sciences of the Ocean (IAPSO), and other similar organizations, both foreign and international, such as representation before the "International Bureau of Time" (Fig. 6). It is also



Fig. 6 Main international organizations to which SHOA was nominated its national representative, 1969.



Fig. 7 Inaugural meeting of the National Oceanographic Committee (CONA), 1971.

https://doi.org/10.58440/ihr-30-2-n07

provided that the IHA will become the official representative of Chile to the International Pacific Tsunami Warning System, with responsibility for taking charge within the country of the general coordination of this system, operating the National Tsunami Warning System and controlling, on behalf of the State, marine scientific and technological research carried out by foreign vessels in national waters.

In 1971, the National Oceanographic Committee (CONA) was created, with headquarters at the IHA (Fig. 7). The Committee has the responsibility of advising the Director of the IHA – who chairs it – in his role of coordination and control of marine scientific and technological research in jurisdictional waters.

Between 1975 and 1980, the IHA, with the support of the AGS "Yelcho", collaborated with the international oceanographic research project in the Southern Ocean, called "International Southern Ocean Studies (ISOS)", covering the Southeast Pacific, Drake Passage and the Scotia Sea. The initiative was sponsored by the Office of the International Decade for Ocean Exploration (IDOE), an entity dependent on the National Science Foundation (NSF) of the United States and its objective in general terms was to expand the description and variability of the oceanographic characteristics of the Southern Ocean and the circulation of the Antarctic circumpolar current. This intense study gave rise to a large number of publications that substantially improved the knowledge of a marine area whose characteristics and variability exert an important influence on climate and planetary health.

In 1979 the IHA began the systematic study of waves, thanks to the acquisition of a Waverider directional buoy, which marked a milestone by being the first instrument acquired in Chile for the direct measurement of waves, allowing the determination of safety patterns to be applied in navigation, naval construction, determination of coastal erosion and in numerous other civil and naval applications.

In 1980, the then Hydrographic Institute of the Navy (IHA) became a member of the Executive Committee of the International Association of Maritime Signalling Authorities and taught the first course for Specialist Officers in Maritime Signalling, and also the first course for Oceanography for Officers.

In 1984, the three-year pilot project called "Tsunami Hazard Reduction through the Use of Systems Technology (THRUST)" was initiated under the agreement signed between the IHA and the National Oceanic and Atmospheric Administration (NOAA) of the United States, which was implemented in the National Tsunami Warning System.

In 1985, Chile, through the IHA, began its participation in the Tropical Ocean and Atmosphere Observation Program (TOGA), through a collaboration agreement signed with the National Oceanic and Atmospheric Administration (NOAA) of the United States.

In 1986, the first sample of dispersed/dissolved hydrocarbons was taken in the bay of Valparaíso and the mouth of the Aconcagua River as part of the Environmental Pollution Program. Currently, the Chemical Oceanography Laboratory of the SHOA issues an average of 43 technical reports per year, which help to establish the corresponding responsibilities and legal actions.

It should be noted that during the XIII International Hydrographic Conference (1987), Chile was nominated "Coordinator of the International Cartographic Scheme", for area C2.

In 1989 and within the framework of participation in the "International Decade for the Reduction of the Effects of Natural Disasters", convened by the UN, the SHOA, with the collaboration of other national agencies, materialized the EDUTSU project that culminated in the preparation and delivery in 1994 of textbooks for pre-basic, basic and secondary education on earthquakes and tsunamis, which were later translated into several languages.

In order to reflect more accurately the remarkable development achieved during the last 50 years by oceanographic science in the country and to better represent the mission and functions of the IHA, in 1990 the name of "Hydrographic and Oceanographic Service of the Navy" (SHOA) was established.


"Acta de Constitución"

Fig. 8 Establishment of the "Regional Hydrographic Commission of the Southeast Pacific", whose charter was signed in Valparaíso, Chile, on June 19, 1991.

In 1991 two events took place that need to be highlight. In the first place, the SHOA obtains from the International Advisory Board on Standards of Competence for Hydrographers and Nautical Cartographers, the international homologation in category "A" of the Hydrographic Engineering course with academic recognition in the specialties of nautical cartography and coastal surveys, being empowered to provide such a course. Also, at the initiative of the SHOA, the Directors of the Hydrographic Services of Colombia, Ecuador and Peru are invited to establish the South-East Pacific Regional Hydrographic Commission (SEPRHC, whose charter was signed in Valparaíso, Chile, on June 19, 1991 (Fig. 8).

During this decade, several other relevant events took place, including:

- The "Autochart" system entered in operation – an automated cartography system – which allowed the processes of compilation, drawing, production and maintenance of nautical cartography to be optimised and accelerated. (1992).
- In 1992, the AGOR 60 "Vidal Gormaz" was incorporated into the Navy, a unit whose role was to carry out oceanographic research, in the physical, chemical, geological and biological areas as it was equipped with adequate instruments and equipment. It was in operation until August 2010. One of its transcendental activities was the participation in the international WOCE (World Ocean Circulation Experiment) program, through cruises (SR-1 and PR-14) that collected oceanographic data that allowed the development and validation of models to predict climate change at a global level. The last campaign carried out was SR-1, which covered the area between Cape Horn and the South Shetland Islands in 1998.
- Chile hosted the first meeting of the IHO Permanent Working Group on Cooperation in Antarctica (now the Antarctic Hydrographic Commission) held at the SHOA, Valparaíso in 1993 (Fig. 9).
- In 1994, the SHOA published an "Oceanographic Atlas for Education", thus taking another step forward in what has traditionally been the concern of this Service: to contribute to education and awareness of the sea and its development possibilities.
- In 1995 and derived from the interest in increasing the knowledge of the ocean and its ecosystems, the National Oceanographic Committee (CONA) worked on a research program with the aim of studying in a multidisciplinary way the oceanographic, meteorological, marine biodiversity and underwater morphology aspects in remote geographical areas, in view of which the SHOA required extraordinary funding to start the so-called CIMAR Cruises (Marine Research Cruises in Remote Areas, Fig. 10). The first of them was carried out between October 18 and November 11 of that year, in the area between Puerto Montt and Laguna San Rafael. To date, 28 cruises with the broad participation of the entire marine scientific community of Marine Sciences at the national level, which were carried out on board the AGOR 60 "Vidal Gormaz" until 2011 and from 2012 to date on the AGS 61 "Cape Horn".



Fig. 9 The first meeting of the IHO Permanent Working Group on Cooperation in Antarctica (now the Antarctic Hydrographic Commission) was hosted by Chile at the SHOA, Valparaíso in 1993.

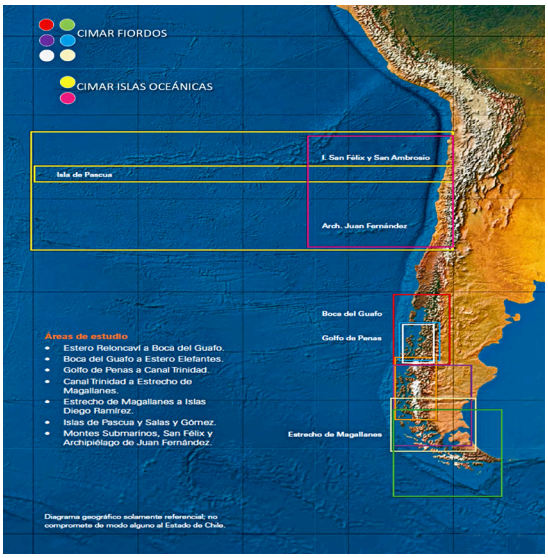


Fig. 10 Different ocean areas covered by CIMAR projects.

- In 1995, also following the scientific line, the SISMOMAR project was presented, which aimed to obtain the magnitude and location of all the sensitive seismic events that affect the national territory, in a period of no more than 20 minutes after they occurred, with the purpose of discriminating in the shortest possible time, those coastal seismic events capable of generating a tsunami. This initiative began in 1996 through the implementation of the TREMORS system (Tsunami Risk Evaluation trough seismic moment from a Real-time System), whose seismic sensors and transmission device were installed on the summit of Cerro El Roble in the commune of Olmué, which was operational until 2014.
- During 1996, work was done on the development of the computational modeling methodology for the implementation of the Project "Tsunami Flood Letters (CITSU)", which aimed to simulate floods in the main coastal cities of the country, in an initial period of five years, which was implemented from 1997, the year in which the CITSU of Arica, Iquique and Antofagasta were published.
- Chile was a member of the Working Group on Strategic Planning established in 1997 to consider and approve a new IHO Strategic Plan and its as-

https://doi.org/10.58440/ihr-30-2-n07

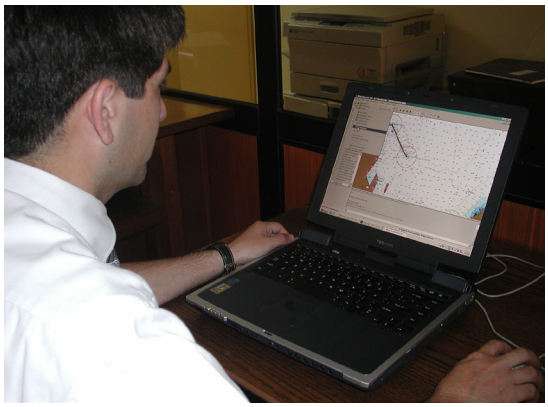


Fig. 11 A cartographer reviewing and validating an ENC.

sociated Work Programme.

- Within the framework of the International Year of the Ocean, in 1998, the first Regional Oceanographic Cruise was held, which consisted of joint and simultaneous campaigns of the member countries of the Permanent Commission of the South Pacific (CPPS), with Chile represented by SHOA and IFOP. Likewise, another milestone in the context of this global initiative was the execution of the Valparaíso-Easter Island Oceanographic Cruise of the "Integrated Oceanopolitical Program (POI)", with the aim of increasing the knowledge of the areas covered and the economic development of the country.
- Since 1998, the State of Chile, represented by the SHOA, has held the position of Associate Director of the International Tsunami Information Center (ITIC), an entity created in 1965 and staffed by personnel from the United States and our country.
- In 1999 the SHOA produced the last nautical chart using manual procedures for separating colours in plastic and the process began entirely with digital methods and the use of the WGS-84 datum. The first electronic nautical chart (ENC) is published (Fig. 11).

It should be noted that before the beginning of the 21st century, the SHOA had an important global technological development and the details of some of them are presented below:

Automation of the nautical chart correction process: Based on low-cost elements – digitizer and plotter under the control of a microcomputer and graphic design program – an important level of automation was achieved for the correction of nautical charts, affected by the notice to mariners issued from their printing, before being provided to users.

Improvement of the National Tsunami Warning System: The system called "TREMORS", of French technology, was incorporated, whose main characteristic was to drastically reduce the warning times in the event of a tsunami, as well as to allow the epicenter of the phenomenon and its magnitude to be determined with great precision.

Professional training: The Navy formalized the creation of the hydrography specialism for officers and enlisted personnel, in order for them to work in the areas of hydrography and oceanography.

Modernization of aero-photogrammetric equipment: This initiative was based on the need to streamline the digital production of topographic information, arriving in a format suitable for acceptance by the processes of computer-aided cartography and that required by electronic cartography.

Capacity development to produce electronic charts: The SHOA, considering that the IHO was in the final stage of developing technical specifications for the production of Electronic Cartography, began the development of its own capacity for the production of official ENCs, significantly optimizing the safety conditions for navigation on the routes and access to the main ports. For validation, distribution, and commercialization instances, SHOA partnered with IC-ENC.

Improvement of the National Tidal Network: During 1999 and in response to the permanent concern and a sustained desire for the technology used, the SHOA carried out the replacement of the METERCRAFT tide gauges with automatic data collector platforms and satellite transmission. Along the same lines and in order to improve the technical capabilities of the SHOA, the Department of Oceanography acquired two of the first acoustic profilers (Acoustic Doppler Current Profiler) used in Chile, to make measurements of current speed and direction throughout the water column, thus replacing the work of mechanical currentmeters.

The SHOA thus culminates the twentieth century with a technological level that would allow it to face the challenges of the twenty-first century. Chile and its extensive participation in the main themes of IHO and IOC, contributed with strong ideas based on the experience that, as a developing Service, it was experiencing in the transition from analogue to digital. On the other hand, the benefit obtained by knowing in detail and in advance the experiences achieved by more developed countries allowed informed decisions to be made to incorporate the necessary technological advance safely and at a reasonable cost.

5 Evolution of the SHOA from 2000 to date

This part of the document briefly details the evolution of the SHOA from 2000 to date. It includes technological development and participation in the international arena.

On May 1, 2000, the SHOA made available to the national and international maritime community its first Electronic Nautical Charts (ENC) of the main shipping routes.

In 2001 the SHOA incorporated multibeam technology and the nautical charts produced include the multibeam soundings. The first meeting of the recently established Working Group on the Hydrography Manual (MoHWG) is also held, on which occasion the Table of Contents and the

program for its development were defined. Chile was nominated its President.

The Sixteenth IHO Conference (2002) was very important for Chile, due to its participation in the revision studies of the IHO Convention and also due to the fact that the Conference elected a new Steering Committee composed of the VA Maratos (Greece); CA Barbor (USA) and CN Gorziglia (Chile). With this, Chile became the first IHO Member State to provide a Spanish-speaking Director and the fourth from South America to reach the IHO Directorate.

During the second half of 2002, the First Geophysical Research Cruise was carried out on board the AGOR 60 "Vidal Gormaz", an initiative organized by the Pontificia Universidad Católica de Valparaíso (PUCV), the University of Chile and the SHOA and which, in later stages, had the collaboration of other entities such as SERNAGEOMIN, SIPETROL and ENAP, as well as foreign universities from Germany. Canada, Denmark, Norway and the United States. The specific objective of this project was to develop a scientific and technological framework for the exploration of methane from gas hydrates. its main result being the knowledge of the distribution and volumes of hydrates and underlying free gas of the most promising areas to be exploited.

On the occasion of the centenary of the "General Bathymetric Chart of the Oceans" (GEBCO) project in 2003, a joint project of IHO and the Intergovernmental Oceanographic Commission (IOC) of UNESCO, all those who had contributed to GEBCO were recognized, including our country, Chile. Another important event that linked Chile to IHO in 2003 was the establishment of the Capacity Building Committee (CBSC) and subsequently the implementation of the Capacity Building Fund, initiatives promoted by the recently elected Director of IHO from Chile.

During the XVII General Assembly of IODE (Committee on International Oceanographic Data and Information Exchange) held at UNESCO Paris headquarters in 2003, the representative of Chile was elected as Vice-President of IODE for the period 2003–2005 and later re-elected for an additional term (2005–2007).

The most important contribution that Chile made to IHO in 2004 was the work carried out within the Working Group on Strategic Planning, which drafted proposals to amend the IHO Convention and other related documents that would be examined in 2005, on the occasion of the 3rd Extraordinary Hydrographic Conference that would be convened for that purpose.

Within the framework of the SHOA's Five-Year Plan 2001–2005, in 2003 the first DART (Deep-ocean Assessment and Reporting of Tsunami) system was acquired, which was transported by the R/V ship "Roger Revelle" and installed off the coast of Pisagua by the team of the Woods Hole Oceanographic Institution (WHOI) of the United States with the participation of SHOA specialists. Other wind, temperature, current, and wave sensors were also installed in order to obtain high-quality information in real time and thus support academic and institutional research. The installation of an AANDERAA satellite tide gauge in Covadonga, Antarctica and the deployment off the coast of Valparaíso, of 02 APEX (Autonomous Profiler Expert) buoys are part of this effort.

SHOA was a member of the Working Group that prepared and revised the content of the 1st edition of the IHO Hydrography Manual (2005). Once the English version was finished, several Spanish-speaking countries took on the task of bringing it into Spanish and once this was accomplished, it was



Fig. 12 Directing Committee for the period 2007–2012: VA Maratos (Greece, center), CN Gorziglia (Chile, right) and CN Ward (Australia, left).


BUREAU VERITAS
Certification

Certificación
Otorgada a

SERVICIO HIDROGRÁFICO Y OCEANOGRÁFICO DE LA ARMADA.
Errázuriz 232, Playa Ancha - Valparaíso
CHILE

Bureau Veritas Certification, certifica que el Sistema de Gestión de la organización mencionada ha sido evaluado y se muestra acorde con los requerimientos de las normas detalladas a continuación.

NORMA

ISO 9001:2000
NCh 9001. Of 2001

ALCANCE DEL SISTEMA

PLANIFICACIÓN, CAPTURA DE DATOS, PROCESAMIENTO, ELABORACIÓN, IMPRESIÓN, VENTA, ACTUALIZACIÓN Y DISTRIBUCIÓN DE CARTAS Y PUBLICACIONES NÁUTICAS.

Fecha de aprobación original: Enero 11, 2008

Sujeto a una continua y satisfactoria operación del Sistema de Gestión de la organización, el certificado es válido hasta: Enero 11, 2011

Para verificar la validez de este certificado llamar al teléfono (0056)(2)4859000. Futuras aclaraciones en cuanto al alcance de este certificado y la aplicabilidad del Sistema de Gestión se puede obtener consultando a la organización.

Certificado Número: 3388 *Fecha:* Enero 31, 2008

Roberto Cordero Piazze
Gerente General

INN - CHILE SISTEMA NACIONAL DE ACREDITACION SC 006

Fig. 13 Evidence of SHOA's ISO certification.

https://doi.org/10.58440/ihr-30-2-n07

up to the SHOA to edit the publication, which was printed and distributed by the SHOA to the international Spanish-speaking hydrographic community.

In the years 2005–2009, SHOA was actively involved in the International Tsunami Warning System Group (ICG/ITSU) and the Joint WMO/IOC Technical Commission for Oceanography and Marine Meteorology (JCOMM).

In 2006, the first DART II system was anchored in Chile and South America, which represented an important effort for mitigation against tsunamigenic events in contribution to the coastal communities of our country as well as the Pacific basin and to the International Tsunami Warning System, through real-time transmission with the Iridium satellite system.

In 2007, the National Committee of SCOR (CNSCOR) was created, under the coordination of CONA, with the aim of promoting and regulating activities related to SCOR International in our country, whose representation has fallen to the SHOA since 1968.

The XVII International Hydrographic Conference (2007) elected a new Directing Committee for the period 2007–2012, which was made up of VA Maratos (Greece) and CN Gorziglia (Chile) who were re-elected and CN Ward (Australia). With this re-election, Chile maintains a relevant position within the IHO (Fig. 12).

Following the growing international trend, Chile decided to go for ISO certification with respect to cartographic processes (Fig. 13). This effort was a great challenge for the SHOA, which concluded with this certification in 2008.

In May 2008, the SHOA hosted the International Course called "ComMIT/MOST Workshop (Community Modelling Tsunami Interface/Method of Splitting Tsunami)", which was aimed at professionals from the Tsunami Warning Centers of the countries that make up the then called Regional Tsunami Warning Group of the Southeast Pacific Ocean, made up of Chile, Colombia, Ecuador and Peru. The instruction was in charge of NOAA's Pacific Marine Environmental Laboratory (PMEL).

Chile's permanent and active contribution to the objectives of IHO was recognized by the cordial invitation extended to it to participate as a guest at the III Conference of the Southwest Atlantic Hydrographic Commission, held in Uruguay in 2009. On the occasion, Chile shared with its peers the experiences obtained in the implementation of the new Print on Demand procedures. We also participated in the 1st meeting of the recently structured IHO Working Group on Water and Tidal Levels (TWLWG) and in the VII meeting of the Sub-Committee on Capacity Building where the existing demands in Chile and those of the other three CHRPSE countries, on their behalf, were presented.

The earthquake and tsunami that occurred in the country in February 2010, made it necessary to readjust Chile's participation in the international tribune of the IHO, limiting participation only to the meetings of the two Regional Hydrographic Commissions that make up Chile; the HCA and the SEPRHC.

Based on capitalizing on the experiences obtained in this event, the SHOA developed, among other activities, the preparation of the "Five-Year Sustainability Plan for the Continuity of Development 2011–2015"; which included, among others, the development of the hydrographic campaigns of the "Extended Continental Shelf" Project; renewing the National Nautical Cartography and strengthening the National Tsunami Warning System (SNAM).

In his role as President of the Regional Hydrographic Commission of the Southeast Pacific, Chile hosted the 10th Meeting of the Commission held in April 2011 in Valparaíso. The participants (Colombia, Ecuador and Peru), led by Chile, analyzed and decided on the capacity demands and updated the 2013–2017 regional capacity building program.

In recognition of the experience gained and the continuous progress made in the National Tsunami Warning System (NAS), SHOA was elected Vice-Chair of the Intergovernmental Coordination Group of the Pacific Tsunami Warning and Mitigation System for the period 2011–2013, a position he held for a second term when he was re-elected at the next biannual meeting in 2013.

In 2012, Chile attended the XVIII IHO Conference, on which occasion the national representative Captain Patricio CARRASCO was elected Vice-President of the Conference, a distinction granted to Chile for its active participation in the IHO rostrum. It is the result of teamwork guided by a clear objective of serving the safety of navigation and contributing to national, regional and global development. The Conference elected a new Steering Committee and in September the term in which Chile held the position of Director of IHO, 2002–2007 and 2007–2012, came to an end.

In 2012, the first version of the Diploma course called "Tsunami on the Pacific Coast of South America: Scientific Bases, Threat and Vulnerability" was given, organized by the Pontificia Universidad Católica de Valparaíso (PUCV) and the United Nations Educational, Scientific and Cultural Organization (UNESCO) and with the collaboration of SHOA and the SATREPS Program (Science and Technology Research Partnership for Sustainable Development). This training program has been carried out in various modalities to this day for the benefit of countries such as Chile, Colombia, Ecuador, Peru and some other nations in the region and the Caribbean.

In 2013, the appointment of the Director of SHOA as one of the five representatives of the IHO to the Steering Committee of the GEBCO Project (General Bathymetric Charts of the Oceans) stands out, adding this designation to the one made to participate in SCUFN. This recognizes the degree of commitment that Chile has had in GEBCO and with the knowledge of the bathymetric characteristics of the oceans.

One of the great milestones that marked the year 2013 was the delivery of the new research vessel AGS 61 "Cabo de Hornos" to the Chilean Navy (Fig. 14). The inaugural cruise was the CIMAR 19 Fjords, which took place between July 1 and 20 of that year. The Navy has established that the CONA will be the entity that receives, assesses and coordinates the research requirements of the national and international scientific community, and must always take into consideration the requests for research that are linked to the National Oceanographic Plan and the CIMAR Five-Year Plan.

The year 2014 ended with Chile as the host of the 6th HSSC Meeting (November) that took place in Viña del Mar. On the occasion, an exhaustive review was made of the degree of compliance with the IHO Work Program, an opportunity in which the experience of Chile was shared in order to develop realistic plans in accordance with the human and financial resources available.

At the end of September 2015, with the participation of SHOA professionals and technicians from the National Oceanic and Atmospheric Administration (NOAA) of the United States, the funding of two prototypes of the 4G DART System provided by NOAA was carried out within the framework of a Memorandum of Understanding signed between SHOA and this entity. This technology provides an essential source of data so that alert centers, and especially the SNAM, can detect, predict and warn of these events.

One of the most relevant milestones this year was the inauguration of the new facilities of the Operations Room of the National Tsunami Warning System (SNAM; Fig. 15). This Warning Center has been recognized as a benchmark for the region and one of the most important in the world. Its design allows a panoramic view of the events that are unfolding, which is in direct support of those in charge of decision-making, thus optimizing the quality of information and response times.

The last IHO event of 2015 in which Chile actively participated was the 7th meeting of the Subcommittee on the World Marine Advisory Service, which was held in Monaco in August. NAVAREA coordinators, including Chile, benefited from the information provided by the IMO Secretariat on the modernization of the Global Maritime Distress and Safety System (GMDSS) and on the GMDSS Master Plan. In the process of establishing the drafting of standard messages in the event of tsunamis, Chile had a significant participation.

In 2016, the "Integrated Tsunami Prediction and Warning System (SIPAT)" was officially launched, as part of the SNAM Decision Support System. This tool consists of a database of pre-modeled events using high-performance computational modeling that allows the prediction of tsunamis on the Chilean coast and thus sectorize tsunami threat levels.

The oceanographic vessel AGS 61 "Cabo de Hornos" carried out the CIMAR 22 "Oceanic Islands" Cruise, the first of this type of campaigns whose scientific research contemplated the protected area of the Nazca-Desventuradas Marine Park, which exceeds three hundred thousand square kilometers of ocean surface, making it the largest in the Southeast Pacific. The objective of the cruise was to study the bio-oceanographic and meteorological characteristics between the American continent and the islands of San Felix, San Ambrosio and the archipelago of Juan Fernandez.

Finally, one of the most relevant contributions of the SHOA in recent years and which is directly linked to its Mission of providing safety to navigation, was the preparation and edition of the first version of the SHOA Publication No. 3015 "Tidal Current Tables of the Coast of Chile" year 2017, which contemplated the inclusion of fifteen locations and a spatial coverage from the Chaco Channel to the Beagle Channel. To date, this product includes 21 sectors with daily current forecasts.

Although the Cat "A" Hydrography Course taught by Chile, through the SHOA, had its adequate international recognition, recent modifications adopted by the International Council on the Standards of Competence of Hydrographers and Nautical Cartographers, demanded the SHOA to work on a new presentation that had the support of the Naval Polytechnic Academy and external advisors of the



Fig. 14 The new Chilean Navy research vessel AGS 61 "Cabo de Hornos".



Fig. 15 The operation room of the National Tsunami Warning System (SNAM).

https://doi.org/10.58440/ihr-30-2-n07

University of Playa Ancha. achieving the recognition of the program for a period of six years. This took place in New Zealand, in March 2017. Given the success of the presentation, SHOA was asked to prepare an article for the International Hydrographic Review sharing the experience gained in the preparation of the Programme. This has been the level of cooperation with which Chile has worked within the IHO, for the benefit of its Member States.

In April 2018, the 19th meeting of the Authorities of the Asia-Pacific Maritime Safety Agencies was held in Chile. On the occasion, IHO asked the Director of SHOA, in his capacity as Hydrographer of Chile, to represent the organization to highlight the role that hydrography plays for the economic development of maritime states.

In August 2018, the International Tsunami Training Program (ITP 2018) was carried out at SHOA facilities, which since it was implemented in the seventies had been carried out only in Hawaii, United States, this being the first time it was taught in another country. The choice of Chile to develop this training was a reflection of the trust placed in it by the International Tsunami Information Centre (ITIC) and the Intergovernmental Oceanographic Commission (IOC) of UNESCO, as well as the recognition of the level achieved by the country as an example of an Integrated Tsunami Warning and Mitigation System thanks to the experience acquired in these events by the SNAM.

During this same year (2018), the capacity of the Service was substantially increased through the acquisition of a new instrument, the SeaExplorer underwater glider (Glider), which corresponds to an autonomous detection platform designed to collect physical, chemical, biological and/or acoustic data profiles, depending on the sensors installed.

In 2019 and for the first time, Chile participates as a member of the Working Group on the Maintenance of Electronic Nautical Chart Standards. It also participated in the 16th Meeting of the Hydrographic Commission on Antarctic, an opportunity in which, in addition to discussing the progress made by the Commission, a Seminar was organized and dictated, at the proposal of Chile, for the Members of the Antarctic Treaty Consultative Meeting on the importance of Hydrography. This Seminar had the active participation as a speaker, the Director of the SHOA.

At the beginning of 2020, the second backup unit of the National Tsunami Alarm System, called SNAM Alternativo II, was inaugurated, located on the grounds of the Naval Polytechnic Academy in the city of Viña del Mar. This structure, like the one put into operation in 2015 adjacent to the main Operations Room, has all the necessary equipment to execute the necessary actions by the team on duty when facing an emergency.

In 2020 all meetings of the Committees, Working Groups and even the scheduled 2nd IHO Assembly had to be rescheduled in response to the global Covid19 pandemic. Notwithstanding this, an important issue



Fig. 16 Cat "A" Certificate of Recognition and some national and international students.

resolved was the decision to establish the Working Group on Hydrographic Surveys (HSWG), a proposal that was originally submitted by Chile in 2014.

One of the themes highlighted by IHO was to highlight the need to incorporate women in hydrography. On this subject, Chile notes that women have worked as cartographic draftsmen; oceanographers, data processors; digitizers; and lately hydrographs, without any limitation or restriction. Chile's experience was shared through an article in the International Hydrographic Review.

The work of the Service and the Navy in many aspects had to adapt to the health crisis caused by the pandemic, in view of which several activities and commitments had to be carried out remotely, such as the first training for Tsunami Field Observers, carried out by SHOA specialists via videoconference.

As the First Centenary of IHO is commemorated in 2021, Chile confirms the importance for the development of national maritime interests of maintaining since its inception in 1921, an active and forceful participation in the activities of the Organization, always seeking to contribute to the fulfillment of its objectives. Also this year was the 50th anniversary of the National Oceanographic Committee (CONA), an organization that coordinates marine scientific activity in our country and that honored this new anniversary with the publication of the National Oceanographic Plan for the period 2021–2030 as a response to the United Nations 2030 Agenda, also assuming the role of national focal point for the Decade of Ocean Science for Sustainable Development (Fig. 17).

Since the mission of the SHOA is to provide safety to navigation through the official nautical cartography of the State of Chile, it is important to note that this final product is the result of a series of hydro-carto-oceanographic processes, which capture and generate a large amount of data and information. In this context, in 2021 the IDE-SHOA Office (Spatial Data Infrastructure) was established, with the aim of creating and maintaining a single and centralized management system that through a geospatial graphic interface will allow the administration, search and expeditious access to



Fig. 17 National Oceanographic Plan 2021–2030.

the information generated as a result of the work and processes of the Service's work.

Following the experiences gained from the tsunami of January 15, 2022 generated by the eruption of the Hunga Tonga-Hunga Ha'pai volcano and within the framework of the activities of the Southeast Pacific Tsunami Warning Working Group (GT-ATPS) while Chile held the Chair, SHOA organized the workshop called "Shared access to sea level data: Tool for an effective regional response to tsunami emergencies", aimed at representatives of the Tsunami Warning Centers of Colombia, Ecuador, Peru and Chile.

The year 2023 began with one of the most powerful El Niño events in recent years, it is for this reason that through the CONA the Universidad Católica del Norte (UCN) and the Universidad de Concepción (UdeC) were invited to carry out the First "CIMAR Glider" Cruise together with the SHOA. This initiative contemplated the simultaneous use of the autonomous vehicles that each institution has, in transects off the coasts of Coquimbo, Taltal and Iquique, in order to collect oceanographic information relevant to the monitoring of this warm phase of the ENSO climate phenomenon.

In this same line of research and support for the scientific community, the Plenary Assembly approved the formation of two new Working Groups of the National Oceanographic Committee: Ocean Culture (GT-COCEAN) and Integrated Management of Coastal Areas (GT-GIAC). The first of them arose as a need to take action with respect to what is set forth in the National Ocean Policy enacted in 2018, which in its chapter dedicated to the Sectoral Area "Scientific Development", establishes as a main axis of action for the development of science and technology that of "Marine Education of Society"; while the second aims to promote knowledge, models and methodologies that promote sustainable development in the face of adaptation to climate change and coastal resilience.

During the 32nd Assembly of the Intergovernmental Oceanographic Commission (IOC) of UNESCO, held in June 2023, Chile was elected for the first time as a member of the Steering Committee of the Global Ocean Observing System (GOOS) as a Regional Expert by Electoral Group III of which our country is a member, for the period 2023–2025.

6 Current participation of the SHOA in the international tribune

It is impossible for SHOA to be represented in all committees, working groups, task teams and others, established by the IHO and the IOC either to deal with technical or administrative issues.

Chile is constantly analyzing the advisability of integrating existing and new groups that are formed, which is subject to this being in line with the objectives of the SHOA and in accordance with the human and economic capacity to sustain the commitment to integrate such groups.

All in all, it is estimated that Chile, through the SHOA, is a member of the main decision-making groups and at all times willing to contribute to the mission of the IHO, as it has been doing since the establishment of the Organization on June 21, 1921, and of the IOC since its establishment in 1960.

The SHOA currently participates actively in the International Hydrographic Organization (IHO) having responsibilities in the following instances:

- Assembly
- Council
- Finance Committee (FC)
- Hydrographic Services and Standards Committee (HSSC)
  - » ENC Standards Maintenance Working Group (ENCWG)
  - » Tide, Water Levels and Currents Working Group (TWCWG)
  - » Working Group on Hydrographic Surveys (HSWG)
  - » Working Group on the S-100 (S-100 WG)
- Inter-Regional Coordination Committee (IRCC)
  - » Southeast Pacific Regional Hydrographic Commission (CHRPSE)
  - » Hydrographic Commission on Antarctica (HCA)
  - » Sub Committee of the Global Navigation Safety System
  - » Sub-Committee on Capacity Building
  - » FIG-IHO-ICA International Committee on Standards of Competence for Hydrographers and Nautical Cartographers (IBSC)
  - » Coordinator of the international cartographic scheme area C2

For its part, it also has extensive participation in the Intergovernmental Oceanographic Commission (IOC), within which it is a member of the Executive Council and directly or through the National Oceanographic Committee, it is mainly represented in the following global programmes:

https://doi.org/10.58440/ihr-30-2-n07

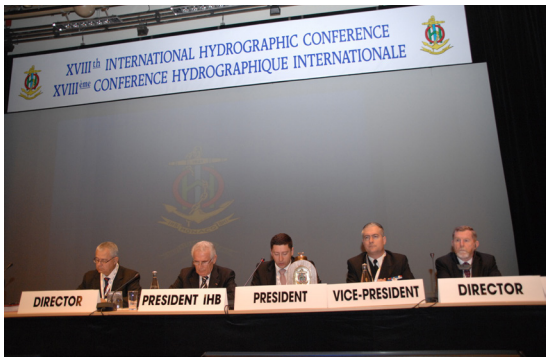


Fig. 18 Chilean contribution to the XIII International Hydrographic Conference (2012). Rear Admiral Patricio Carrasco (Vice President) and Captain Hugo Gorziglia (Director IHB).



Fig. 19 SHOA's Director Rear Admiral Arturo Oxley at the Executive Council of the IOC (second from left), 2024.

- GOOS Steering Committee (Group III)
- Associate Director of the International Tsunami Information Centre (ITIC)
- Research and monitoring of marine pollution.
- International Oceanographic Data and Information Exchange (IODE)
- Global Sea Level Observation System (GLOSS)
- Advisory Council of Experts on the Law of the Sea (ABE-LOS)
- Joint Committee on Marine Oceanography and Meteorology (JCOMM)
- IOC International Panel on Harmful Algal Blooms (IP-HAB)
- The Seabed 2030 Project
- Ocean literacy

Also in regional programs, under the auspices of the Permanent Commission of the South Pacific (CPPS), among which we can highlight:

- Scientific Committee of the Program of the Regional Study of the "El Niño" Phenomenon in the Southeast Pacific (ERFEN).
- Committee of the Global Ocean Observing System Alliance for the Southeast Pacific (GRASP)
- Southeast Pacific Tsunami Warning Working Group (GT-ATPS)

Finally, we can highlight that the SHOA is also related to other international organizations, among which we can mention:

- Pan American Institute of Geography and History (PAIGH)
- International Federation of Geometers (FIG)
- Permanent Commission for the South Pacific (CPPS)
- Scientific Committee on Antarctic Research (SCAR)

7 SHOA's challenges

At any time, whatever the technologies and procedures, SHOA must be a service of excellence. The challenges are many, but we could mention:

1. Keep the National Nautical Cartographic Coverage updated, completing all charts in DATUM WGS-84 reference, to allow the coverage of the Electronic Nautical Chart to be completed.
2. Successfully face the next "up-grade" or update to the new standard for Electronic Cartography, called S-101 and which replaces the current S-57.
3. Complete the publication of the new Tsunami flood charts, with new modelling and complete coverage of populated coastal areas.
4. To satisfy the demands of the State and the private sector that contribute to national development.
5. Ensure the availability of the technological capacity to meet the objectives and meet the requirements in emergency situations.
6. Maintain and increase the availability of human resources that are trained, committed and proud to serve Chile and the Navy from the deck of the SHOA.



Fig. 20 SHOA personnel at a special call to highlight the 150th anniversary.

NOTE / TECHNICAL REPORT

Overview of the IHO–Nippon Foundation GEOMAC project and its evolution over 15 years

Authors

Masanao Sumiyoshi[1], Kazufumi Matsumoto[1,2], Leonel Manteigas[1] and Lucy Fieldhouse[3]

Abstract

The IHO-Nippon Foundation Cooperation Project, through the IHO Capacity Building Programme, has been providing opportunities for Category "B" nautical cartographer training at the UKHO for 15 years. Since the start of the Japan Capacity Building Project (JCBP) in 2008, which sought to develop and promote human capacity building of technical personnel in nautical cartography, through the Cartography, Hydrography and Related Training (CHART) and Geospatial Marine Analysis and Cartography (GEOMAC) projects by the partnerships of the Organizations shown in Fig. 1, the number of alumni from these projects is now approaching 100 from over 50 countries. This paper reviews the 15-year evolution of these projects and their achievements in supporting IHO Member States, as well as the current training course content.

Fig. 1 The partnerships of the JCBP, the CHART and the GEOMAC projects.

✉ Masanao Sumiyoshi · masanao.sumiyoshi@iho.int

[1] International Hydrographic Organization, 98000 Monaco, Principality of Monaco

[2] Hydrographic and Oceanographic Department, Japan Coast Guard, Tokyo 100-8932, Japan

[3] United Kingdom Hydrographic Office, Taunton, Somerset TA1 2DN, United Kingdom

https://doi.org/10.58440/ihr-30-2-n11

1 Introduction

The history of the IHO-Nippon Foundation Geospatial Marine Analysis and Cartography (GEOMAC) project began in 2008 with the Japan Capacity Building Project (JCBP), which provided training courses to develop nautical cartographers. At that time, with the global push to publish Electronic Nautical Charts (ENCs), training technicians to produce and maintain up-to-date nautical charts was an international challenge. Therefore, the International Hydrographic Organization Secretariat (IHO Secretariat; then called the International Hydrographic Bureau: IHB) and the Japan Hydrographic Association (JHA), together with the United Kingdom Hydrographic Office (UKHO) and the Japan Hydrographic and Oceanographic Department (JHOD), launched the JCBP to train nautical cartographers of developing countries in a course internationally recognized as meeting the Standards of a Category "B", particularly in Asia and the adjacent regions. The JCBP received financial support from the Nippon Foundation, a non-profit organisation established in Japan in 1962.

The IHO-Nippon Foundation Cartography, Hydrography and Related Training (CHART) project was launched in 2014 as a successor of the JCBP. The project, that continued to provide an international recognized course with the Category "B" for nautical cartographers, mainly from developing countries, was implemented by the IHO together with the UKHO and the JHOD, with the financial support of the Nippon Foundation.

In recent years, the number of IHO Member States has increased from 80 countries in 2009 to 100 countries in 2024, and the global demand for training nautical cartographers is even stronger. In addition, IHO Member States are also expected to respond to the digital age, including the processing and management of large volumes of bathymetric data, the creation of next-generation S-100 products, and uncrewed vessels.

To address these challenges in terms of navigational charts, the IHO-Nippon Foundation GEOMAC project was launched in 2020 as a successor to the CHART project by the IHO together with the UKHO and the JHOD, with the financial support of the Nippon Foundation. The GEOMAC project is currently providing the 16th training course in 2024.

In this paper, Section 2 reviews the evolution of the project management basically from 2008 to 2023. Section 3 describes the current training course of the GEOMAC project, Section 4 introduces the Alumni Seminars, and Section 5 discusses the achievements. Section 6 provides a summary and future perspectives.

2 Change in the project management

2.1 Management system

To implement the JCBP, the IHB signed a Memorandum of Understanding (MoU) with the JHA (acting on behalf of the JHOD) in October 2008, valid until 2013. As stated in the IHO CL 77/2008 (IHO, 2008), the Nippon Foundation supported the project financially, the IHB implemented and managed the project in consultation with the JHA, and the UKHO was selected as the training provider for the nautical cartographer courses internationally recognized with the Category "B".

In December 2013, a new MoU was established between the IHO and the Nippon Foundation, as stated in the IHO CL 10/2014 (IHO, 2014). The purpose of the MoU was to provide the overarching framework for the continuation of discussion and consultation between the two parties in relation to enhancing human relations, capacity building, and awareness of the need to survey and map the world's seas, oceans and coastal waters and other matters of mutual interest.

In accordance with the purpose of the MoU, a three-year capacity building project, the IHO-Nippon Foundation CHART project, was proposed by the IHB to the Nippon Foundation and started in 2014 following approval. The management framework of the CHART project gave IHB responsibility for the implementation and management of the project, which had previously been the undertaken by the JHA. However, the financial and delivery system was continued, with the Nippon Foundation providing financial support and the UKHO providing the training course.

This management system has been continued in the IHO-Nippon Foundation GEOMAC project, launched in 2020, where the Nippon Foundation provides financial support for the project, the IHO Secretariat implements and manages the project, and the UKHO provides the training of the “Geospatial Marine Analysis and Cartography” course for nautical cartographers, which is recognised as Category “B” by the FIG-IHO-ICA International Board of Standards of Competence for Hydrographic Surveyors and Nautical Cartographers (IBSC).

2.2 Budget

The annual budget for the implementation of training courses from the CHART project in 2014 to the GEOMAC project in 2023 is shown in Fig. 2. This budget includes the course fee, travel expenses and per diem for the students. The budget was initially around 200 000 €/year, but now exceeds 300 000 €/year



Fig. 2 The annual expenses of the implementation from the CHART project in 2014 to the GEOMAC project in 2023.

https://doi.org/10.58440/ihr-30-2-n11

due to the longer training periods mainly associated with the introduction of new modules for more advanced training in the GEOMAC project.

The budget from the Nippon Foundation is one of the most generous and significant contributions to the Capacity Building Fund to support the IHO Capacity Building Programme, as reported in the Finance Report of the 21st Capacity Building Sub-Committee Meeting (IHO, 2023a).

2.3 Objectives and expected outcomes

The project focuses on two key objectives currently facing the world of hydrography:

1. To drastically reduce the existing gap between countries in terms of their capacity to comply with their obligations and responsibilities as sovereign states, as mandated by international instruments such as the SOLAS and UNCLOS conventions.
2. To prepare hydrographers and nautical cartographers for the ever-increasing technological developments, ensuring the maximum societal gain in the blue economy and social achievements in a sustainable way, while preserving the safety of navigation.

In order to continue to meet these objectives, the current GEOMAC project expects students who complete the training course to be able to:

1. Be involved as a nautical cartographer in their organizations and improve the capacity, the quality and usefulness of electronic and paper nautical charts and hydrographic services of their countries.
2. Take a leading role in guiding the organization to adapt to the ongoing and future digital innovations such as IHO S-100 framework, Maritime Spatial Data Infrastructures (MSDI), Digital Twins and uncrewed vessels.
3. Share the knowledge gained with their colleagues in their Hydrographic Offices and contribute to the strengthening of cooperation between alumni; and
4. Engage in and support international cooperation projects, including but not limited to the Nippon Foundation-GEBCO Seabed 2030 project, and play a leading role in their respective regions.

2.4 Application

Following the yearly IHO Circular Letter calling for nominations, each IHO Member State has been able to nominate one suitable candidate for the training course at the UKHO.

In accordance with the IHO Capacity Building Strategy (IHO, 2021), this training course is open only to candidates from IHO Member States who are employed by a hydrographic office, a port authority or a related national agency of the nominating country. Also, the national authority nominating candidates should confirm that appropriate opportunities will be in place for the individual to apply the knowledge on their return for the maximum benefit and that they meet the prerequisite criteria for attending the Category "B" course.

2.5 Selection

The selection process in the recent years has started with a Coordination meeting between the IHO Secretariat, UKHO and JHOD. At this meeting, the selection criteria and the annual plan for the implementation of the training course are discussed.

For example, for the GEOMAC training course in 2023, as stated in the IHO CL 09/2023 (IHO, 2023b), nominated candidates must meet the following criteria:

- A very good standard of English, both written and spoken, with reasonable technical English.
- A high standard in mathematics and geography.
- A background in cartography, hydrographic surveying, geospatial sciences or related areas.
- Individual commitment for international cooperative activities such as Seabed 2030.

A Selection Panel meeting between the IHO Secretariat, UKHO and JHOD carefully reviews all applications, and the IHO Secretariat and the Nippon Foundation make the final selection of the candidates for the training course. An IHO Circular Letter then issued to announce the successful nomination of candidates and individual notification letters are also sent to each candidate's organisation.

2.6 Timeline by project period

2.6.1 JCBP (2008–2013)

The main events in the JCBP from 2008 to 2013 are summarised in Table 1.

This project was originally scheduled to end in March 2013, but due to huge demands for the training and generous support from the Nippon Foundation, it was continued for another year.

2.6.2 CHART project (2014–2016)

The main events in the CHART project from 2014 to 2016 are summarised in Table 2.

2.6.3 CHART project (2017–2019)

The main events in the CHART project from 2017 to 2019 are summarised in Table 3.

2.6.4 GEOMAC project (2020–2022)

The main events in the GEOMAC project from 2020 to 2022 are summarised in Table 4.

With the spread of the COVID-19 pandemic, the 12th training course was provisionally scheduled from 1 September to 18 December 2020. However, given the lack of improvement in the pandemic situation and the paramount importance of ensuring the safety of all people involved in the training course, the IHO Secretariat, in close contact with the Nippon Foundation and the UKHO, decided to postpone the first time in July 2020, the second time in February

https://doi.org/10.58440/ihr-30-2-n11

Table 1 List of major events in the JCBP from 2008 to 2013.

Event	Date	Venue	Remark
1st Coordination meeting	11 February 2009	IHB	
Announcement of application	13 February 2009	-	IHO CL 10/2009
2nd Coordination meeting	22 April 2009	IHB	49 applications from 41 countries
Announcement of candidates	24 April 2009	-	IHO CL 27/2009
1st training course	7 September – 18 December 2009	UKHO	6 students
3rd Coordination meeting	3–4 February 2010	JHOD	
Announcement of application	8 February 2010	-	IHO CL 15/2010
4th Coordination meeting	16 April 2010	IHB	39 applications from 37 countries
Announcement of candidates	27 April 2010	-	IHO CL 30/2010
2nd training course	6 September – 17 December 2010	UKHO	6 students
5th Coordination meeting	9 February 2011	IHB	
Announcement of application	10 February 2011	-	IHO CL 14/2011
6th Coordination meeting	19 April 2011	IHB	21 applications from 19 countries
Announcement of candidates	26 April 2011	-	IHO CL 29/2011
3rd training course	5 September – 16 December 2011	UKHO	6 students
7th Coordination meeting	6–7 February 2012	UKHO	
Announcement of application	8 February 2012	-	IHO CL 16/2012
8th Coordination meeting	19 April 2012	IHB	30 applications from 27 countries
Announcement of candidates	7 May 2012	-	IHO CL 46/2012
4th training course	3 September – 14 December 2012	UKHO	6 students
9th Coordination meeting	31 January – 1 February 2013	JHOD	
Announcement of application	7 February 2013	-	IHO CL 10/2013
10th Coordination meeting	18 April 2013	UKHO	33 applications from 27 countries
Announcement of candidates	30 April 2013	-	IHO CL 30/2013
5th training course	2 September – 13 December 2013	UKHO	6 students

Table 2 List of major events in the CHART project from 2014 to 2016.

Event	Date	Venue	Remark
Coordination meeting	15–16 January 2014	JHOD	
Announcement of application	5 February 2014	-	IHO CL 12/2014
Selection Panel meeting	23–24 April 2014	IHB	20 applications from 19 countries
Announcement of candidates	2 May 2014	-	IHO CL 36/2014
6th training course	1 September – 12 December 2014	UKHO	7 students
Coordination meeting	15 January 2015	UKHO	
Announcement of application	28 January 2015	-	IHO CL 10/2015
Selection Panel meeting	16–17 April 2015	IHB	28 applications from 27 countries
Announcement of candidates	4 May 2015	-	IHO CL 35/2015
7th training course	7 September – 18 December 2015	UKHO	7 students
Coordination meeting	14 January 2016	UKHO	
Announcement of application	20 January 2016	-	IHO CL 04/2016
Selection Panel meeting	19 April 2016	IHB	32 applications from 29 countries
Announcement of candidates	27 April 2016	-	IHO CL 20/2016
8th training course	5 September – 16 December 2016	UKHO	7 students

Table 3 List of major events in the CHART project from 2017 to 2019.

Event	Date	Venue	Remark
Coordination meeting	12 January 2017	UKHO	
Announcement of application	13 January 2017	-	IHO CL 04/2017
Selection Panel meeting	30 March 2017	IHO Sec.	33 applications from 29 countries
Announcement of candidates	13 April 2017	-	IHO CL 31/2017
9th training course	4 September – 15 December 2017	UKHO	7 students
Coordination meeting	11 January 2018	UKHO	
Announcement of application	17 January 2018	-	IHO CL 04/2018
Selection Panel meeting	4 April 2018	IHO Sec.	28 applications from 27 countries
Announcement of candidates	12 April 2018	-	IHO CL 27/2018
10th training course	3 September – 14 December 2018	UKHO	7 students
Coordination meeting	10 January 2019	UKHO	
Announcement of application	15 January 2019	-	IHO CL 04/2019
Selection Panel meeting	11 April 2019	IHO Sec.	31 applications from 31 countries
Announcement of candidates	24 April 2019	-	IHO CL 22/2019
11th training course	2 September – 13 December 2019	UKHO	7 students

Table 4 List of major events in the GEOMAC project from 2020 to 2022.

Event	Date	Venue	Remark
Coordination meeting	9 January 2020	UKHO	
Announcement of application	7 February 2020	-	IHO CL 09/2020
Selection Panel meeting	7 May 2020	VTC	24 applications from 24 countries
Announcement of candidates	28 May 2020	-	IHO CL 20/2020
12th training course	7 February – 27 May 2022	UKHO	7 students
Coordination meeting	4 February 2022	VTC	
Announcement of application	14 February 2022	-	IHO CL 08/2022
Selection Panel meeting	26 April 2022	VTC	45 applications from 31 countries
Announcement of candidates	18 May 2022	-	IHO CL 19/2022
13th and 14th training courses	1 August – 16 December 2022	UKHO	13 students

Table 5 List of major events in the GEOMAC project from 2023 to 2024 (ongoing).

Event	Date	Venue	Remark
Coordination meeting	11 January 2023	VTC	
Announcement of application	27 February 2023	-	IHO CL 09/2023
Selection Panel meeting	30 March 2023	VTC	18 applications from 17 countries
Announcement of candidates	12 April 2023	-	IHO CL 16/2023
15th training course	24 July – 15 December 2023	UKHO	7 students
Coordination meeting	10 January 2024	VTC	
Announcement of application	16 January 2024	-	IHO CL 03/2024
Selection Panel meeting	11 March 2024	VTC	28 applications from 28 countries
Announcement of candidates	20 March 2024	-	IHO CL 17/2024
16th training course	15 July – 13 December 2024	UKHO	7 students, planned

https://doi.org/10.58440/ihr-30-2-n11

2021 (IHO CL 08/2021) and the third time in August 2021 (IHO CL 31/2021). After overcoming these difficulties, the 12th course was successfully held from 7 February to 27 May 2022.

At the same time, preparations were made for the next training courses. Due to the delay of the 12th training course, impacting the scheduling of the 13th training course, it was agreed to hold both the 13th and 14th course at the same time. The 13th and 14th training courses were held from 1 August to 16 December 2022.

2.6.5 GEOMAC project (2023–2025, in progress)

The main events in the GEOMAC project from 2023 to 2024 (ongoing) are summarised in Table 5. This project will be continued until 2025.

3 Training course

3.1 Evolution of course content

The evolution of the content of the training courses from the JCBP to the GEOMAC project is shown in Fig. 3. Each training course consists of several modules and meets the IHO S-8B Standards of Competence for Category "B" Nautical Cartographers. In addition, the training course has been enhanced to take into account the issues that nautical cartographers currently face/will face with the rapid innovations of modern technology.

3.2 Current course content

The current training course consists of seven modules ("Distance Learning Module", "Foundation Module", "Geospatial Fundamentals Module", "Compilation Module", "Product Construction Module", "Data Assessment and Product Maintenance Module" and "Final Project"), which are recognised as a Category "B" accredited course, and two modules ("Cooperation Module" and "Digital Twin & S-100 Implementation Module"), which are focus on the wider use of data and the future realm of nautical cartography beyond Category "B" course.

The Category "B" course content and Digital Twin and S-100 Implementation Module are delivered by the UKHO training team (as shown in Fig. 4), supplemented by presentations given by UKHO specialist speakers and visits to relevant UKHO work areas. The Cooperation Module is provided by OceanWise and Map the Gaps.

In addition, as shown in Fig. 5, field trips are undertaken to enrich the class-based training for the students to understand nautical chart use, data collection, national and port responsibilities.

During the course the IHO Secretariat staff visit the UKHO, as shown in Fig. 6, to give presentations to the students on the roles and responsibilities of the IHO and to reinforce their understanding the importance of international cooperation.

Students are formally assessed throughout the course through tests and assignments undertaken at the end of each module and must meet or exceed the standard. Ongoing feedback is given to students to help them develop and prepare for the formal assessments. An overall assessment is made of each student and feedback is given at the end of the course. A certificate stating successful completion of the Category "B" course is awarded to all those who complete the training course satisfactorily.

The training course is fully evaluated by the students both during and at the end of the course. All students are requested to provide feedback to their training team on their learning progress and any issues they may have, giving them direct input into their own learning and helping to resolve any issues. They are also requested to complete a final evaluation to review the whole training programme.

Alongside the training course, the training team organise weekend excursions to sites of local interest, and a number of social events allowing students to socialise in an informal atmosphere and contribute to a stronger network.

JCBP	CHART project			GEOMAC project	
2009 - 2013	*2014 - 2016*	*2017*	*2018 - 2019*	*2020 - 2022*	*2023 - (in progress)*
Module 1 - Marine Cartography	Pre-learning/course Module (off-site)			Distance learning Module (off-site)	
Module 2 - Hydrographic Data Processing	Foundation Module			Foundation Module	
Module 3 - Electronic Navigational Charts	/	/	S-57 Foundation Module	S-57 Foundation Module	Geospatial Fundamentals Module
	Compilation Module			Compilation Module	
	Product Construction Module			Product Construction Module	
	Data Assessment Module			Data Assessment Module	
	Maintenance Module		/	Final Project	
	/	Final Project		Cooperation Module	
				/	Digital Twin Module

Fig. 3 The evolution of the content of the training courses from the JCBP to the GEOMAC project.

4 Alumni seminar

The IHO-Nippon Foundation Alumni Seminars are held to strengthen the alumni network, promote co-operation among alumni, enhance global friendship and receive feedback from alumni on the impact of the respective courses to them, to their organizations and their countries.

The first alumni seminar (then called workshop) was held in Bangkok, Thailand from 2 to 4 November 2016, and the second in Singapore from 29 to 31 October 2019.

Most recently, the third alumni seminar was held in London, UK from 25 to 27 October 2023 (Fig. 7). This alumni seminar was attended by 48 alumni from 32 countries, 16 invited guest speakers and others, such as the Executive Director of the Nippon Foundation, the UK National Hydrographer, the IHO Director, the FIG President, IBSC Members and the Director of the Nippon Foundation-GEBCO Seabed 2030. The guest speakers presented on a wide range of topics including the vital role of nautical cartographers, the challenges within the maritime



Fig. 4 Classroom teaching at the UKHO.



Fig. 5 Field trips.



Fig. 6 Group photo with students, UKHO staff and IHO staff during the visit of IHO staff to UKHO in 2023.



Fig. 7 Participants of the IHO-Nippon Foundation Alumni Seminar in 2023.

https://doi.org/10.58440/ihr-30-2-n11

environment and digitalisation.

During the seminar, the alumni participants had a group work to strengthen the alumni networking. The alumni were divided into several groups with different countries of origin and different training years, and each group discussed ocean-related topics such as the use of chart data, the S-100 world, and the AI-era, concluding with a short presentation.

Throughout the seminar, alumni learned about the latest technological developments in their related field and actively shared their experiences, recent achievements and best practices.

Based on some of the input received in the alumni seminar in 2019, a LinkedIn group page for the alumni was launched in 2019. By the end of 2023, more than 50 alumni had joined this group. The group page is expected to be a platform to share specific and practical information and to communicate with each other beyond the alumni year.

5 Achievement

The most significant achievement of the JCBP/CHART/GEOMAC project is the worldwide active network of the IHO-Nippon Foundation alumni, one of the largest communities of nautical cartographers. The number of alumni has been steadily increasing and at the end of 2023 there were 99 alumni from 51 countries, as shown in Fig. 8. The alumni list and distribution are available on the website at https://iho.int/en/alumni-list-and-distribution/.

Many alumni have actively participated in many IHO related meetings representing their organisations and nations. At the regional level, some alumni have participated in meetings of Regional Hydrographic Commissions (RHCs) as leading cartographers in their offices. At the international level, some alumni have been involved in working with the Regional ENC Coordinating Centres (RENCs) as well as in the IHO technical meetings.

The statistics based on the IHO Publication C-55 "Status of Hydrographic Surveying and Nautical Charting Worldwide" show that alumni countries have made better progress than non-alumni countries in terms of the world nautical charting coverage. In the technical document CBSC17-08.4B of the 17th meeting of the IHO Capacity Building Sub-Committee (IHO, 2019), the average increase in the total sum of charting coverage from 2014 to 2019 is 41 points for alumni countries and 17 points for non-alumni countries. In the recent statistics, the average increase in the total sum of charting coverage from 2019 to 2023 is 20 points for alumni countries and 5 points for non-alumni countries.

6 Conclusion

Since the start of the JCBP in 2008, through the CHART and GEOMAC projects, the number of alumni of these projects is approaching 100 in over 50 countries. They are active in a wide range of national, regional and international stages, and their efforts are contributing to the quality and acceleration the nautical charting coverage worldwide.

The project has continuously improved its training content, budget and management system to ensure that it adapted to cover the evolution on the skills required by nautical cartographers of all eras, as well as the rapidly developing advanced technologies of recent years. These efforts have made the GEOMAC project one of the greatest success stories of the IHO Capacity Building Programme.

This GEOMAC project is open to the IHO Member States and the IHO Secretariat expects their positive applications and participation. Up-to-date information on the GEOMAC project can be found in

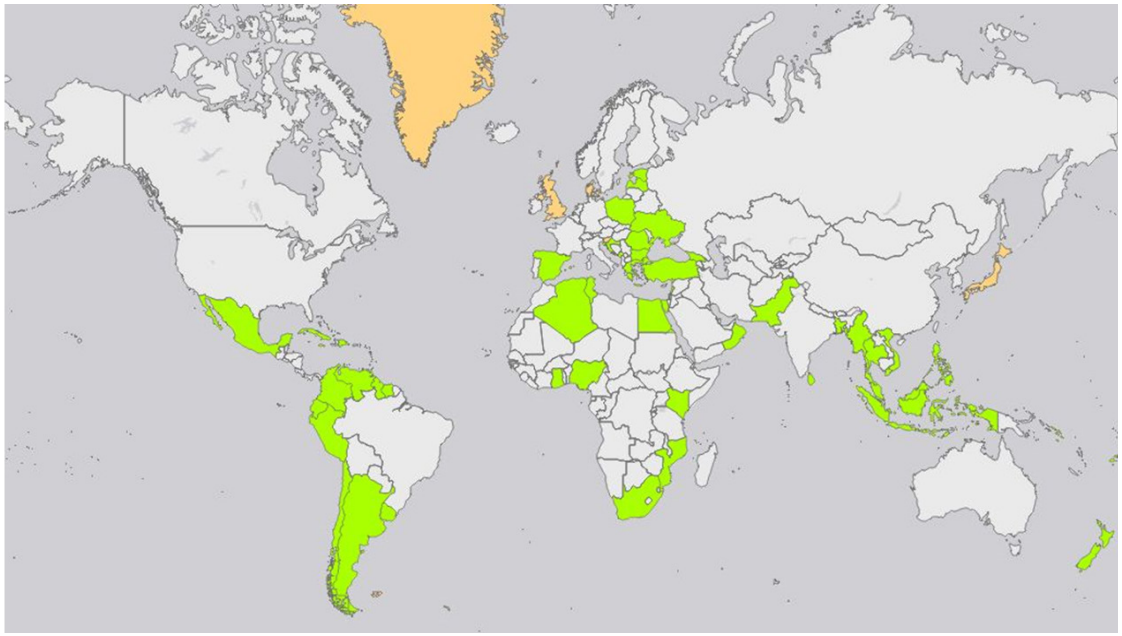


Fig. 8 Alumni distribution at the end of 2023. Light green shows the IHO-Nippon Foundation alumni and yellow shows the extended alumni who attended the same training course through different programmes.

the IHO Circular Letters and on the IHO website at https://iho.int/en/iho-nf-geomac-project/.

Acknowledgements

The authors would like to express their great appreciation to the Nippon Foundation, which has provided significant financial support for the project and has worked together to improve the project through many constructive exchanges of views on the revisions of the course based on the prospects for the next era. Special thanks are extended to Mr Unno, Executive Director of the Nippon Foundation, for his various forms of support, including his participation in the alumni seminars.

The authors would like to thank the UKHO for providing the training courses for the project. Special thanks are due to the current UKHO training team, support staff and to Mr Bryant, who has been involved in this training for many years.

The authors would like to thank the IHO responsible for the management of this project. Special thanks are due to Mr Nakabayashi, Mr Yamao, Dr Kaneda and Mr Nagasaka, the Japanese secondments at the IHO.

Finally, the authors would like to thank the JHOD and JHA for their support of the project since its inception.

References

IHO (2008). *Japan capacity building project and secondment of personnel*. IHO Circular Letter 77/2008, International Hydrographic Organization, Monaco. https://legacy.iho.int/mtg_docs/circular_letters/english/2008/Cl77e.pdf (accessed 16 October 2024).

IHO (2014). *Signing of the Memorandum of Understanding between the International Hydrographic Organization and the Nippon Foundation*. IHO Circular Letter 10/2014, International Hydrographic Organization, Monaco. https://legacy.iho.int/mtg_docs/circular_letters/english/2014/Cl10e.pdf (accessed 16 October 2024).

IHO (2019). *A quantitative analysis of a capacity building activity, the IHO-Nippon Foundation CHART project*. CBSC17-08.4B, 17th Meeting of the IHO Capacity Building Sub-Committee IHO-CBSC17, Genoa, Italy, 29–31 May 2019. https://legacy.iho.int/mtg_docs/com_wg/CBC/CBSC17/CBSC17-08.4B_2019_EN_CHART_project_analysis_v1.pdf (accessed 16 October 2024).

IHO (2021). *IHO Capacity Building Strategy*. International Hydrographic Organization, Monaco. https://iho.int/uploads/user/Inter-Regional%20Coordination/CBSC/MISC/Capacity_Building_Strategy_2021_ver05.pdf (accessed 16 October 2024).

IHO (2023a). *Finance Report*. CBSC21-09.2, 21st IHO Capacity Building Sub-Committee Meeting, Tokyo, Japan 7–9 June 2023. https://iho.int/uploads/user/Inter-Regional%20Coordination/CBSC/CBSC21/CBSC21-09.2_EN_CB_Finance_Report_v1.pdf (accessed 16 October 2024).

IHO (2023b). *Call for Applications to the IHO - Nippon Foundation, Geospatial Marine Analysis and Cartography (GEOMAC) Project, UKHO Taunton UK.* IHO Circular Letter 09/2023, International Hydrographic Organization, Monaco. https://iho.int/uploads/user/circular_letters/eng_2023/CL09_2023_EN_v1.pdf (accessed 16 October 2024).

https://doi.org/10.58440/ihr-30-2-n11

NOTE / TECHNICAL REPORT

Importance of environmental and hydrospatial monitoring systems – The UK Hydrographic Office Marine Environmental Monitoring Stations Framework

Author

Becky Conway[1]

Abstract

An ever-increasing need for reliable, real-time marine environmental and hydrospatial data has lead to development of a Marine Environmental Monitoring Stations framework by the UK Hydrographic Office. This framework, executed in partnership with OceanWise, involves the installation, operation, and maintenance of monitoring stations across various global locations, whilst emphasizing the importance of local stakeholders engagement. The framework aims to enhance navigational safety, provide critical data for climate change research, and support various government initiatives. OceanWise's cloud-based data platform enables real-time data visualization as well as access to historical records to support this. This approach not only supports scientific research and maritime safety but also fosters local capacity building and long-term sustainability in data management.

Keywords

environmental monitoring · data sharing · capacity building · informed decision making

1 Introduction

There has always been a need for environmental monitoring across many industries but particularly within the marine environment and the hydrospatial domain, however this need, and importance is growing ever stronger with increasing demand and pressure on global supply chains. Some of the key factors driving its importance are included here with particular attention drawn to digitalisation and data reliability (Fig. 1).

As we move into a digital world with more and more systems and processes becoming digital and even automated through the emergence of Artificial Intellignece (AI) and Machine Laerning (ML), there is a greater need to make data easily Findable, Accessible, Interoperable and Reusable (FAIR). This data must be timely, accurate and reliable for informed decisions to be made whilst ensuring user confidence. Having accurate environmental hydrospatial data available and accessible for a range of users is a key principle behind the UK Hydrographic Office's (UKHO) Marine Environmental Monitoring Stations (MEMS) framework.

2 The requirement

The UKHO identified the installation and operation of MEMS as an important component of several UK Government programmes. Maritime users can benefit from MEMS through improving navigational safety and enhanced knowledge of the marine environment in the hydrospatial domain as well as assisting with scientific research in understanding the implications of climate change.

In 2022, OceanWise were contracted by the UKHO under a 3-year framework agreement to install, operate and maintain a number of monitoring sites in various locations around the world. The framework includes provision of equipment, data management and a display platform. As well as undertaking local training and mentoring through community engagement.

Observational data collected at the sites is provided to local communities and global initiatives such as the Global Sea Level Observation System (GLOSS) and the Intergovernmental Oceanographic

✉ Becky Conway · becky.conway@oceanwise.eu

[1] OceanWise Ltd., Alton, Hampshire, United Kingdom

https://doi.org/10.58440/ihr-30-2-n05



Fig. 1 The importance of environmental monitoring within the marine industry.

Commission's (IOC) Sea Level Station Monitoring Facility, whilst also assisting in refining tidal modelling and predictions. Additionally, all data collected is automatically analysed, processed and archived in a centralized and dedicated online server. Data is made available for the purposes of maritime and navigational safety, planning and situational awareness including assisting with ongoing programmes to update charts and associated navigational publications, and for Tsunami warnings as required.

3 The solution

To date, OceanWise have attended sites in a number of overseas locations including, Turks and Caicos, the Cayman Islands, Anguilla and Guyana. At each location, site surveys are carried out to establish the current state of existing sensors and infrastructure, alongside undertaking remedial work to re-instate existing sensors as well as installation of new and improved technology to measure environmental and hydrospatial parameters and telemetry systems for the transfer and sharing of data (Fig. 2).

Sites such as those on Anguilla and Montserrat required new full MEMS installations which involves a standard suite of sensors which include met stations, tide gauges and telemetry equipment, tailored to meet the specific requirements of the user and the given locality. Where required, our team of engineers undertake Global Navigation Satellite Systems (GNSS) surveys to establish geodetic benchmarks for tide gauge levelling and establishing a local datum (Fig. 3).

In addition to onshore MEMS installations, OceanWise have also deployed a GNSS tide buoy and profiler on behalf of the UKHO to collect tidal height and stream data offshore of Guyana. The purpose and requirement of this data is to as accurately as possible assess both tidal characteristics and spheroidal separation for the area. The buoy will be collect data for a minimum of 30 days, following which the data will be processed by the UKHO's Tide Department to establish Chart Datum for the area. Once this part of the project is completed the buoy with be reconfigured with additional sensors such as a met station and redeployed on a long-term basis as a metocean data buoy with data being stored and displayed within the UKHO's Port-Log.

A main part of the framework agreement is the provision of an online data platform to host, visualise, store, and facilitate the sharing of environmental and hydrospatial data. OceanWise's Port-Log provides the ideal platform to facilitate this (Fig. 4).

Port-Log is used by a range of customers across the globe and is a quick and easy management and publishing platform for environmental and hydrospatial data. Being a cloud-based data platform, it gives



Fig. 2 Marine Environmental Monitoring Station at Sapodilla Bay, Turks and Caicos Islands. Remedial works was undertaken on the existing Sutron tide gauge, with installation of OceanWise's ip.buffer smart telemetry system, a meterological sensor and GNSS leveling.

https://doi.org/10.58440/ihr-30-2-n05



Fig. 3 GNSS leveling at Sapodilla Bay, Turks and Caicos Islands to establish geodetic benchmarks for tide gauge levelling and establishing a local datum.

the ability to store data securely and publish it in near real-time via the web as well as maintaining long-term historical records and archive for future reference if and as required. Within Port-Log the user has the ability to view sites in a map view for geographic distribution as well as tabular data feeds from each site as seen here on the right. This latest page shows a list of the most recently received data from all sites and sensors on the network as well as incorporating tidal predictions where available to calculate surge or cut values.

To ensure this table is always showing the most up to date and as reliable data as possible there are several indicators and Quality Control and Assurance factors built into the system to warn of a decrease in data validity. The indicators operate using a simple colour coded warning system which helps to give the user confidence (or not) in the data and to treat it accordingly. Alerts are also displayed and the user can click through to view the received error message to assist with fault finding and resolution.

The dissemination of data to all users who require it is at the forefront of how Port-Log operates and therefore the platform can be viewed through a web-browser on any device. There is also the ability to integrate within third-party systems such as dredge management software or Portable Pilot Units (PPU). Of course, it is not only the real-time data that is important, historical data and long-term records and archival are also significant and the good management of these datasets is vital for decision making and coastal resilience.

All data collected can be accessed for each site, along with associated statistics and graphs such as time series all of which are customizable to the records you are interested in. There is also the ability to download the data in numerous formats for ongoing analysis in other software environments.

4 Outreach and training

Education and awareness ensure communities and local users understand the purpose of the environmental and hydrospatial monitoring equipment and potential impacts of it not being operational.

Throughout the processes of installing equipment and carrying out required maintenance and improvements to existing infrastructure, our team of engineers have provided onsite training to local organisations and users in the setup of the equipment as well as the importance of regular maintenance to ensure accurate and reliable data continues to be received. Good maintenance of equipment also assists in prolonging the longevity of the sensors and extending

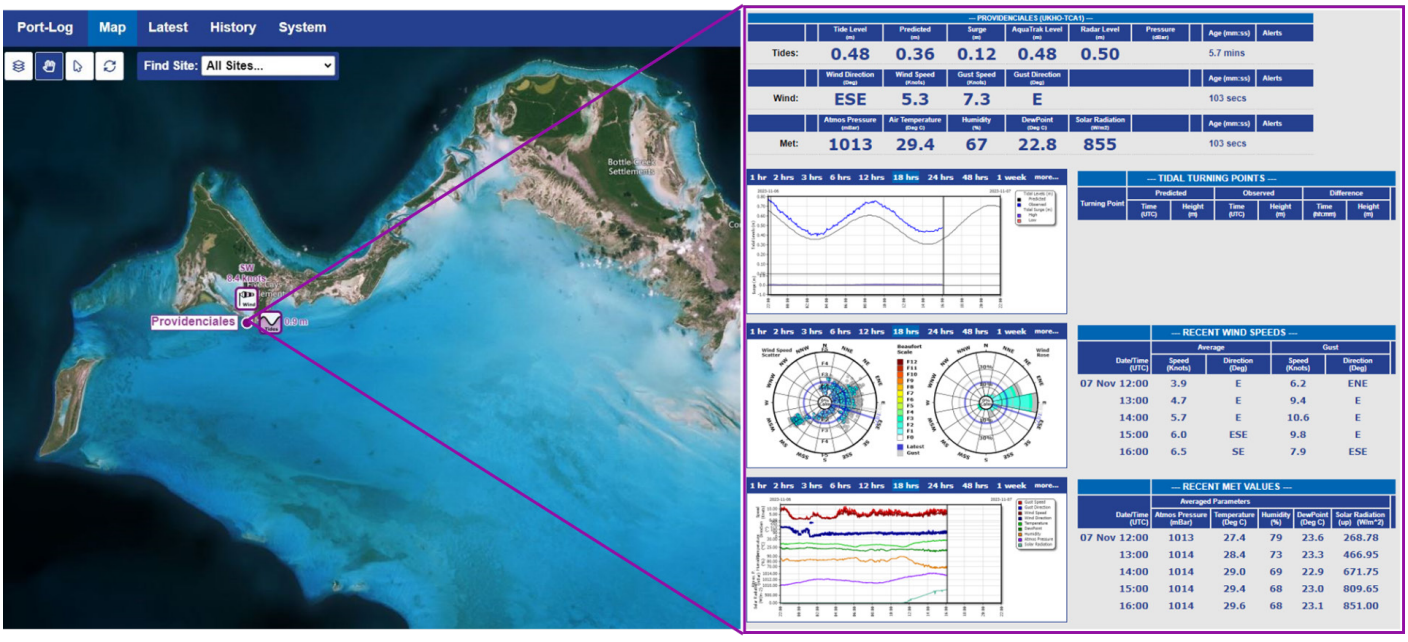


Fig. 4 Example of data visualization within OceanWise's Port-Log online data platform, showing real-time and historical records for tide and meterological parameters.

https://doi.org/10.58440/ihr-30-2-n05



Fig. 5 Onsite training for Montserrat Port Authority provided by OceanWise in the functionality of the MEMS and the importance of proactive maintenance to ensure continuity in reliable data.

the asset lifespan. Of great importance when trying optimize and stretch out limited budgets!

An example of this is the training provided to Montserrat Port Authority to ensure the users get the most out of the system and its data (Fig. 5). This training also led to discussions and changes to their Hurricane Preparation Plan which OceanWise assisted with by marking cables with green and red tags to help with the removal of the met mast in preparation for a storm event – (red cables should be removed, green should remain in place).

5 Conclusion

In conclusion, the UKHO's MEMS framework delivered by OceanWise, represents a beneficial approach to marine environmental data management and accessibility. By deploying modern and reliable monitoring equipment worldwide, the framework delivers accurate, real-time data that can be used to the safety of navigation, climate research, and coastal resilience. For the UKHO, this initiative has delivered data to support hydrographic survey efforts required to update nautical charts and publications in the locations where they have been installed. The UKHO has provided this data to local and regional stakeholders to enable improved marine situational awareness and better inform decision-making. The Port-Log online data platform also facilitates seamless data integration and sharing, which benefits local communities by improving their access to marine environmental data.

The model presented in this paper could offer a useful example for other Hydrographic Offices and Hydrospatial Organisations globally, demonstrating how to effectively combine technology, community engagement, and data management to support local blue economies and strengthen global maritime safety and environmental monitoring efforts.

References

Hains, D., Schiller, L., Ponce, R., Bergmann, M., Cawthra, H. C., Cove, K., Echeverry, P., Gaunavou, L., Kim, S.-P., Lavagnino, A. C., Maschke, J., Mihailov, M. E., Obura, V., Oei, P., Pang, P. Y., Njanaseelan, G. P., Sharma, S. L. (2022). Hydrospatial – update and progress in the definition of this term. *The International Hydrographic Review, 28*, pp. 221–225. https://doi.org/10.58440/ihr-28-n14

NOTE / TECHNICAL REPORT

Mapping the plastic – Helping communities address the global plastic waste crisis

Authors

Simon Ironside[1], Gordana Jakovljevic[1] and Naa Dedei Tagoe[1]

1 Introduction

Is the threat from plastic really apocalyptic? Surely it doesn't compare to climate change or a world-wide pandemic. The answer, unfortunately is yes, and it does (Campbell, 2022).

Plastic is everywhere! It affects the daily lives of almost everyone on the planet, in all corners of the globe, and is overwhelming us. The effects of plastic pollution on the Earth's oceans are well documented, potentially catastrophic and increasing exponentially year on year. The effects on our waterways and coastal environments are equally devastating.

The International Federation of Surveyors (FIG) has formed the Mapping the Plastic Working Group (WG 4.3) as the international surveying and spatial sciences community's response to this huge global problem, focussing on the plastic waste transported in waterways and along coastlines, dealing with the problem before it reaches the ocean.

WG 4.3 has successfully developed a method to detect, extract and classify floating and land-based plastic from Unmanned Aerial Vehicles (UAV) captured imagery using deep learning algorithms. Research has determined the optimum relationship between spatial resolution and detectable plastic size, enabling detection of plastic pieces as small as 0.01m^2 to meet internationally recognized litter assessment frameworks.

This represents a significant breakthrough, offering a cost-effective technological solution to countries/regions suffering from plastic pollution to better understand the extent of their problem but, due to competing demands on relatively scarce resources, have been unable to do so. Accurate knowledge of the problem is a necessary pre-requisite to finding its solution, a concept surveyors, spatial professionals and engineers are well accustomed to.

The WG 4.3 plastic mapping solution is currently being used in Ghana, where several communities are severely impacted by the effects of plastic pollution. As part of a programme of remediation work along the country's coast line, UAV captured imagery is used to classify the type and extent of the plastic and other waste at pre-determined locations. The baseline pollution loading is assessed from the initial UAV surveys and subsequent monitoring surveys determine the success (or not) of the remediation works. The scientific rigour of the capture and data processing has gained the confidence of all participants, fostering a concerted effort for change.

2 The problem

The statistics are confronting. Almost every piece of plastic ever made is still on our planet in one form or another, and 75 % of it is now waste, with most of it discarded into landfills or dumped into marine environments (Fava, 2022). The United Nations Environment Programme estimates that only nine percent of the nine billion tonnes of plastic produced globally has been recycled, and each year more than eight million tonnes of plastic end up in our oceans, which equates to around 15 tonnes of plastic entering our oceans every minute (UNEP, 2024). Eighty percent of all litter in our oceans is now made of plastic. Without action, the World Wide Fund for Nature (WWF) estimates that by 2050 there will be more plastic in the sea than fish by weight (WWF, 2022).

Plastic is difficult to recycle, slow to decay, expensive and polluting to burn, and it breaks down into microplastics, particles smaller than 4.75 mm in diameter, that enter the food chain and cause harm to animals and potentially humans (McVeigh, 2022). The ubiquitous images of fish and sea-birds choking on, or trapped by, plastic are only the tip of the iceberg. Microplastics are present in the clothes we wear, the water we drink and throughout the food chain. There are an estimated 14 million tonnes of them are residing on the sea floor (Barrett et al., 2020).

✉ Simon Ironside · sironside@xtra.co.nz

[1] International Federation of Surveyors (FIG), Working Group 4.3, Mapping the Plastic

https://doi.org/10.58440/ihr-30-2-n10

Rivers are a recognised contributor to the ocean plastic problem. Plastic litter is predominantly concentrated on banks, coastal beaches and in the upper limits of surface water bodies during the transportation process. Researchers estimate that ten major river systems carry more than 80 % of the plastic waste that ends up in the Earth's oceans, with eight of them located in Asia (Schmidt et al., 2017; Fig. 2).

3 It must stop! Formation of WG 4.3

Plastic pollution is an intolerable situation that needs immediate and far-reaching action. Eric Solheim, former head of UN Environment, speaking at the launch of the #CleanSeas campaign in 2017, argued that it was past time to tackle the plastic problem that blights our oceans. 'We've stood by too long as the problem has gotten worse,' he said, 'it must stop'.

The International Federation of Surveyors (FIG) and the international surveying and spatial sciences professions agree. Representing the interests of surveyors in over 120 countries, FIG has formed Working Group 4.3, Mapping the Plastic (WG 4.3) to help combat the global plastic waste crisis. It is a combined initiative of FIG Young Surveyors Network and Commission 4 (Hydrography).

Given the GIS, remote sensing, hydrographic surveying, project management and overall measurement science skillsets within the group, the WG 4.3 focus has been on the plastic waste transported in waterways, dealing with the problem before it reaches the ocean. Accurate, repeatable and cost-effective plastic waste data at specific 'hot spot' locations assists local communities, regulators and policy makers to inform remediation and land use control decisions.

4 A plastic mapping solution

Currently, much of the plastic waste data has been obtained from large scale empirical estimates or from detailed plastic litter surveys, which are confined to relatively small areas.

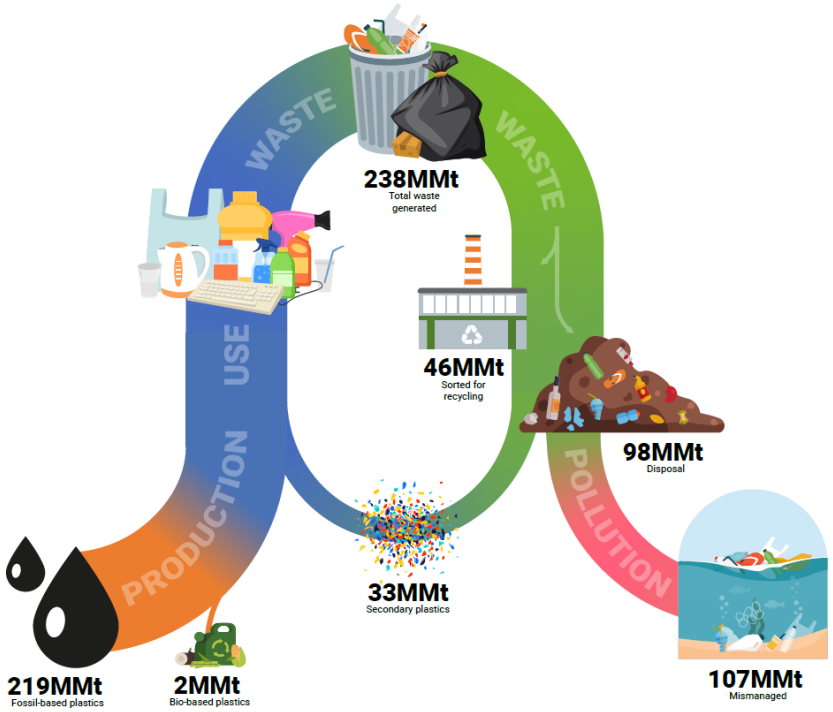


Fig. 1 Short-lived plastic flows in 2020 (UNEP, 2023): The figure illustrates the problem, based on a snap shot of 2020 data, in million metric tonnes (MMt).

The global estimations of plastic debris entering oceans annually, although numerous, are typically based on local or regional scale surveys, and vary from 250,000 tons (Eriksen et al., 2014) to 4.8–12.7 million tons of plastic (Jambeck et al., 2015). Therefore, the amount of plastic in the global oceans remains poorly understood with a knowledge gap in terms of the temporal and spatial distribution of plastics, degradation, and beach processes.

Several efforts have been made to establish a standardized monitoring methodology, such as Oslo and Paris Conventions (OSPAR; OSPAR, commission 2020), Commonwealth Scientific and Industrial Research Organization (CSIRO; Hardesty

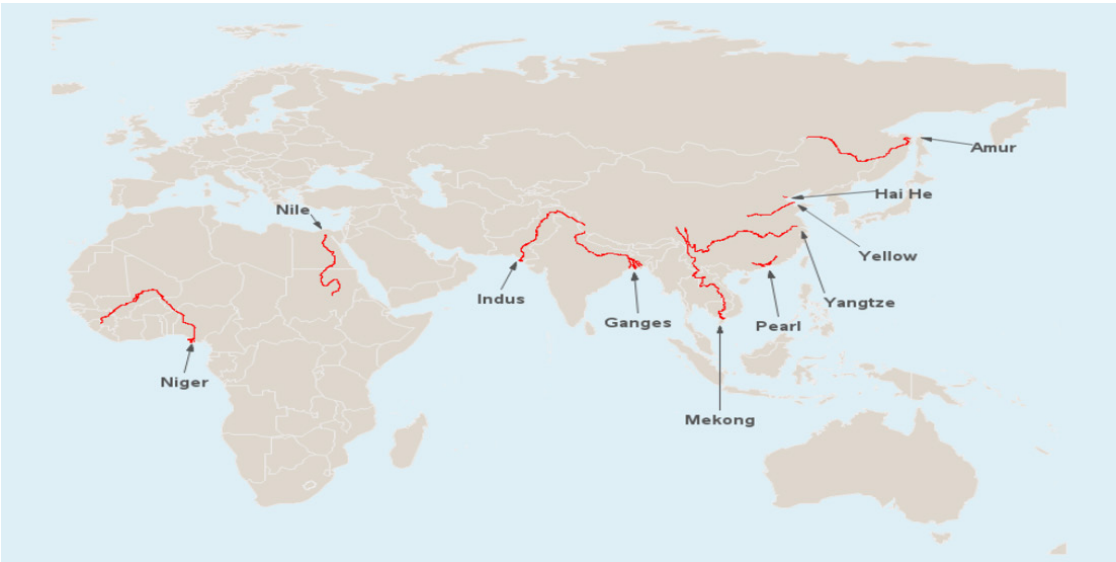


Fig. 2 80 % of plastic polluting the world's oceans comes from these ten rivers (Schmidt et al., 2017).

et al., 2016), National Oceanic and Atmospheric Administration (NOAA; Opfer et al., 2012), and United Nations Environment Programme / Intergovernmental Oceanographic Commission (UNEP/IOC; Cheshire et al., 2020). Those methodologies are based on traditional beach monitoring by visual counting of plastic pieces along transects.

The accuracy of the beach survey results is dependent upon the skill of the observer and the differences in these protocols make the integration and comparison of beach litter survey data difficult. They are also time and labour intensive and do not measure the amount of plastic being conveyed within a river system, only those items discarded during transportation.

However, new research using remote sensing data from satellites and airborne platforms has shown that this can be a reliable source of information over large geographic areas. Assessment of the spatial extent and variability of plastic is possible due to the unique spectral signature of polymers in the near-infrared part of the electromagnetic spectrum. Research by WG 4.3 members at the University of Banja Luka in Bosnia and Herzegovina and the University of Novi Sad in Serbia has, therefore, concentrated on distinguishing plastics from surrounding litter/debris classes using remote sensing techniques. Initial research focussed on the analysis of satellite imagery. An object-pixel based algorithm for mapping plastic distribution in (fresh) surface water using red, green, blue and multi spectral images from high resolution WorldView2 satellite images was developed with the paper published and presented at the FIG Working Week held in Hanoi, Vietnam in May 2019 (Jakovljevic et al., 2019). This research was subsequently refined to focus on higher accuracy plastic detection over smaller geographic areas (Fig. 3) using UAV captured imagery to successfully develop a surveying and mapping solution to accurately detect, extract and classify floating and land-based plastic as small as 0.01 metres (Jakovljevic et al., 2020).

The solution captures floating and land based plastic waste data relatively easily at 'hot spot' locations using unmanned aerial vehicle (UAV) imagery with the data processed using deep learning algorithms. The extent of each survey is limited only by the operational parameters of the UAV and the only field personnel required are a suitably qualified pilot and spotters. The orthophotos are processed remotely but can be processed locally depending on the availability of the processing infrastructure.

The results inform remediation and ongoing monitoring campaigns. The initial baseline is established from the first survey and the effectiveness of the



Fig. 3 Workflow used in this study.

https://doi.org/10.58440/ihr-30-2-n10

remediation response evaluated against the subsequent monitoring surveys.

5 How it works

The solution uses deep learning algorithms to extract floating and land-based plastic from high-resolution UAV images. Customizable flight routes at low-level altitudes in combination with new algorithms, such as the Structure from Motion (SfM) algorithm, for photogrammetric processing provide a cost-effective solution for the acquisition of geospatial data with high spatial and temporal resolution. UAVs provide the appropriate spatial and temporal resolution to produce suitable data for mapping plastic, however, to date, the methods developed are largely based on visual interpretation and manual labeling of plastic pieces, which is time-consuming and labour-intensive.

The WG 4.3 solution instead uses U-Net architecture (the ResUNet50 algorithm) with an encoder-decoder structure, to undertake image classification, including automatic classification, object detection and semantic segmentation. The encoder generates feature maps with high-level semantic but low resolution and the decoder upsamples the low-resolution encoder feature maps, retrieving the location information and obtaining fine-scaled segmentation results (Jakovljevic et al., 2020).

5.1 Pre-processing

Orthophotos are generated from the captured aerial imagery of each UAV survey. The pixel classes are delineated and labelled and then merged using multi resolution segmentation algorithms to create non-overlapping polygons.

As this research is the first attempt to map floating plastic data from UAV imagery, previous ground truthed data is not available and the delineation, classification and labelling is done manually. It is expected that the pre-processing time will reduce as the polymer 'libraries' grow, and this process becomes increasingly automated.

5.2 Classification

An end-to-end semantic segmentation model is used for floating and land based plastic classification based on the U-Net deep learning architecture (Fig. 3). The model consists of an encoder and a decoder. The encoder extracts and abstracts the image pixel information and the decoder extracts the plastic from the orthophotos.

5.3 Testing

Testing and refinement of the plastic mapping solution has involved the processing of UAV imagery from two sites in Bosnia and Herzegovina (Fig. 6). One, at the confluence of the Crna Rijeka and Drina Rivers, was chosen because it is inundated with plastic and other waste, and the other, at Lake Balkana, is a pristine deep-water lake. They were chosen to test the algorithm's ability to differentiate floating and submerged plastic from the surrounding water body and to test its ability to differentiate floating and land-based plastic from other litter (Fig. 5).

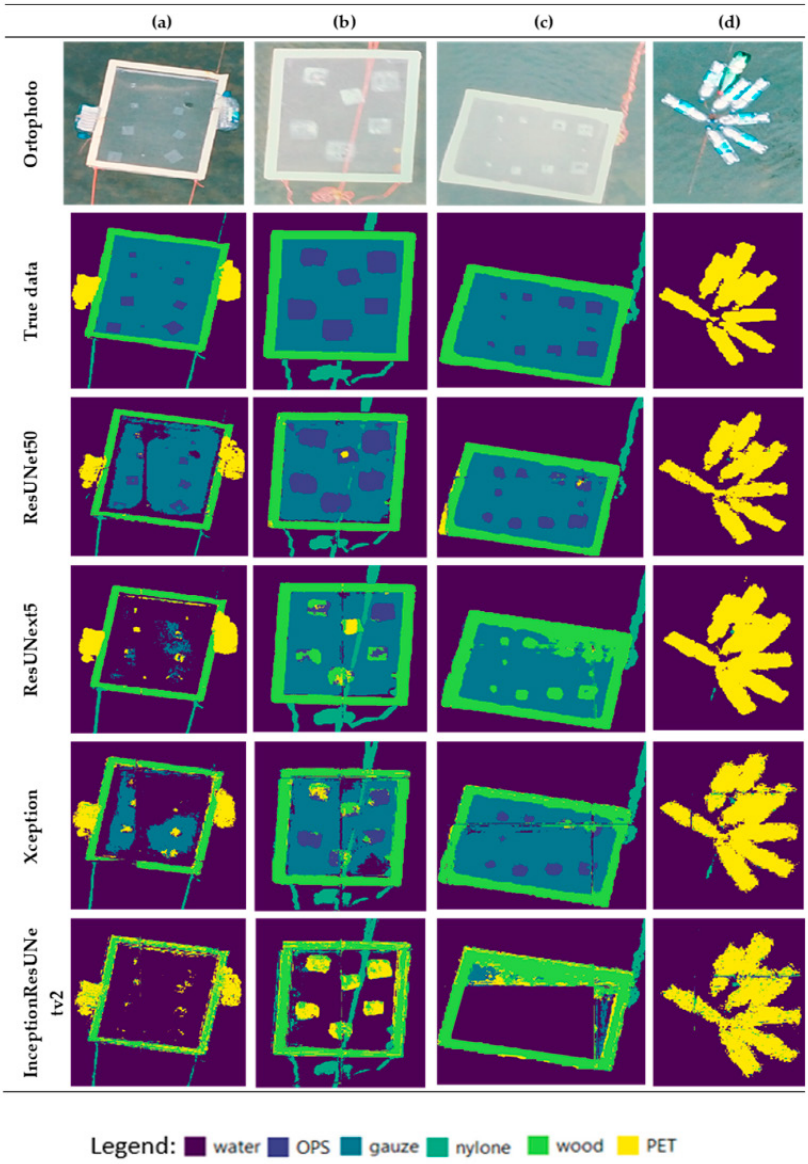


Fig. 4 Ground truth data and results of the classification using the four tested models for detecting different plastic materials, located underwater (a) and overwater (b–d).

The algorithm detected plastic accurately in shallow water, which is a challenging environment for mapping plastic because the presence of the river bed increases water reflectance. Unexpectedly, the algorithm accurately extracted the plastic pieces that were omitted from the training data, showing good generalization abilities. The model also demonstrated its ability to detect plastic not just in water but also on land.

6 Plastic not seen: Mapping solution in Ghana

An example of this plastic mapping solution in action is in Ghana, where plastic pollution is severely impacting communities. The government has committed to addressing the problem and has implemented a National Plastic Action Partnership between

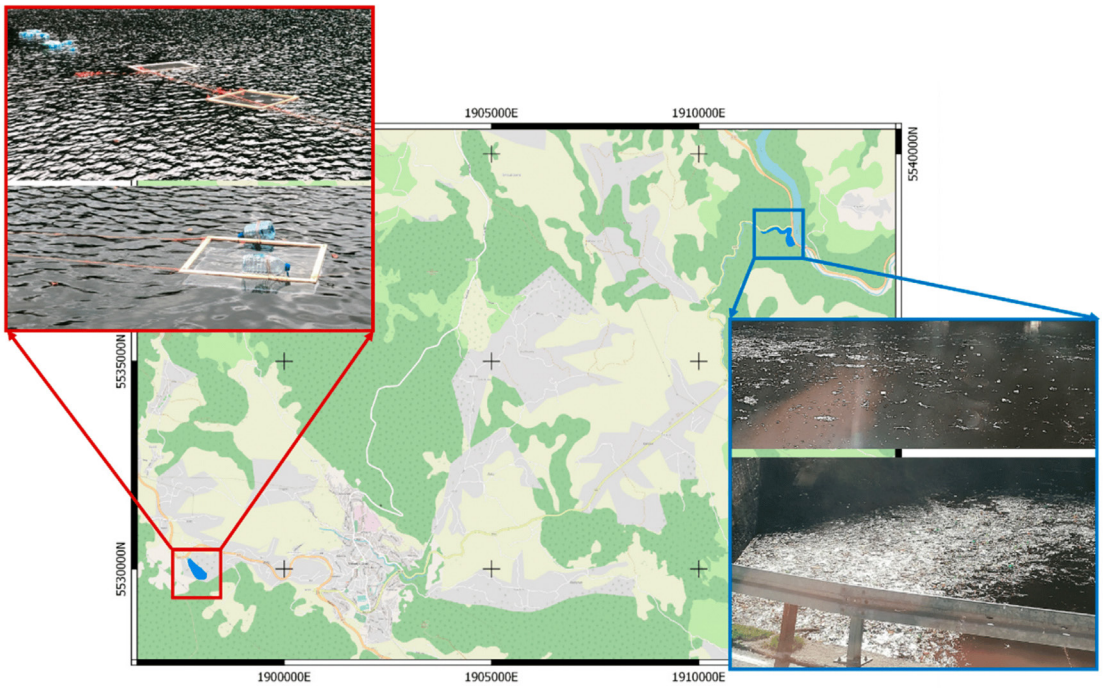


Fig. 5 Study areas: Lake Balkana (left) and Crna Rijeka River (right).

the government, experts, civil society, community organizations, and the private sector. The Ministry of Environment, Science, Technology & Innovation (MESTI) plays a key role in its implementation.

6.1 The current situation

Ghana's coastline is, unfortunately, impacted with plastic and other litter, in some places quite severely (Figs. 7 and 8).

There is infrastructure available to recycle selected plastic waste, and, currently, informal recyclers scour the beaches and other locations for items of value, such as plastic bottles (Fig. 9). Payment is on a per-weight basis; however, the waste that has no value is left behind (Fig. 10).

6.2 Plastic not Seen

Based on the evaluation of preliminary UAV surveys undertaken at Korle Gonno Beach in Accra by students from the University of Mines and Technology, Takoradi under the supervision of Dr Naa Dedei Tagoe and processed by WG 4.3, MESTI is implementing the 'Plastic Not Seen' initiative.

Korle Gonno Beach is one of many coastal locations throughout the country where informal settlements of indigent people eke out a subsistence living, part of which is recycling plastic waste (Fig. 11). The 'Plastic Not Seen' initiative is an expansion of the current informal recycling process, whereby local people are assigned a portion of coastline adjacent to their settlement and paid to clean it and keep it clean.

The work programme is currently being finalised. Initial UAV surveys at each location will establish the baseline waste levels with subsequent monitoring surveys undertaken to determine the level of compliance with the agreed clean up plan. The baseline

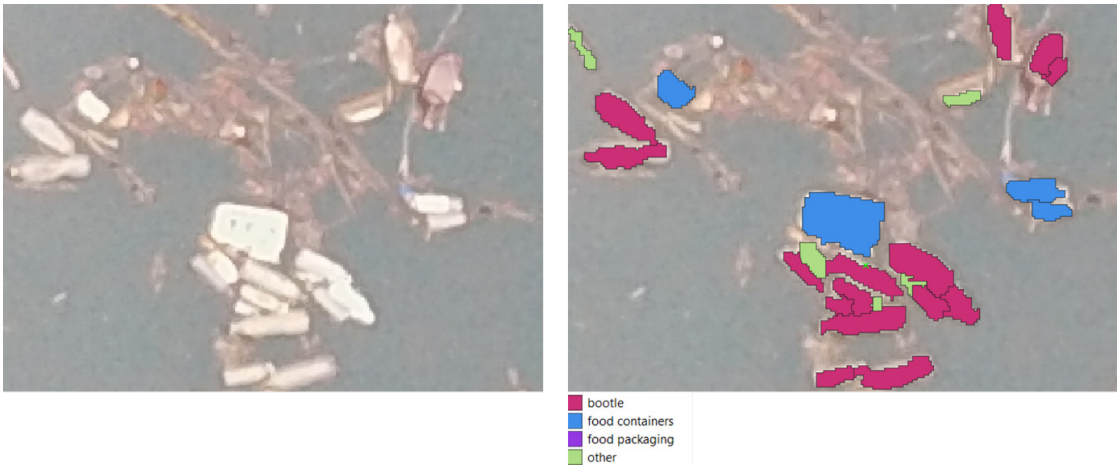


Fig. 6 The algorithm has successfully extracted and classified different plastic litter types (left) from the orthophoto (right). From the Crna Rijeka River study area.

https://doi.org/10.58440/ihr-30-2-n10



Fig. 7 Korle Gonno Beach, Accra, Ghana on 8 May 2024. Photo credit: Naa Dedei Tagoe.



Fig. 8 Beach Clean-up, Jamestown Beach, Accra. Photo credit: The Guardian online edition 24 September 2024 – Where does the UK's fast fashion end up? I found out on a beach clean in Ghana.



Fig. 9 Informal recycling, Korle Gonno Beach, May 2024. Photo credit Torben Lund Christensen, Danish Association of Surveyors.



Fig. 10 Payment is by weight with the price varying between 1 to 3 Ghanaian Cedi (as of May 2024) depending on the type of plastic. Photo credit Torben Lund Christensen, Danish Association of Surveyors.

and monitoring surveys will be undertaken locally with the captured imagery processed remotely, at least initially, by WG 4.3 (Fig. 12).

This approach has been chosen largely because the imagery and processed results accurately depict the situation at each location at any given time and there is no basis for misunderstanding or dispute about the amount of plastic seen or not seen by any of the parties involved.

Although not directly addressing the root causes of coastal pollution, it is an innovative and sophisticated step towards plastic waste eradication at a community level using this technology.

7 Policy enablement through accurate mapping and ongoing monitoring

This mapping solution is relatively inexpensive, requiring only a survey-specific UAV and a qualified pilot to capture the required data. The algorithms can be modified to identify other features, and the data can be processed remotely or locally depending on the available infrastructure. It can be used to inform policy changes in other areas.

7.1 Ocean governance and policy

Floating plastic and other litter are predominantly concentrated on the surface or within the upper limits of a water body. The deep learning algorithms have been trained to extract plastic and other litter from the surrounding water (salt or fresh) by differentiating the spectral signatures of the plastic and the water body. This methodology can be used to map plastic waste in marine environments, including the so-called ocean gyre 'garbage patches,' with UAVs deployed from a support vessel and the survey results processed onboard or remotely.

7.2 Coastal conservation and restoration

The WG 4.3 solution can also be used in coastal environments as the algorithm can detect plastic waste and other litter deposited on beaches and riverbanks. It is ideal for beach litter surveys (plastics and other debris), with the algorithms able to detect and classify plastic as small as 1.0 cm^2 to meet international litter assessment standards. The orthophotos from subsequent UAV surveys can be used to monitor the effects of restoration works over time. If required, the algorithm can be trained to differentiate and classify specific features as required. The only limitations are those that would impede UAV data capture, such as overhanging trees.

7.3 Equity and economic justice, particularly for small island states

UAV captured imagery and the processed data enables the communities in small island developing states (SIDS) to better understand the extent of the problems they face. It can also inform cases for



Fig. 11 Informal coastal settlements will play a major role, and be a principal beneficiary of the 'Plastic not Seen' initiative. Photo credit Torben Lund Christensen, Danish Association of Surveyors.



Fig. 12 UAV demonstration at Korle Gonno Beach, courtesy of the Ghana Lands Commission, May 2024. Photo credit Torben Lund Christensen, Danish Association of Surveyors.

equity and economic justice in international forums, and ongoing monitoring ensures adherence to international agreements.

7.4 Waste management

Accurate knowledge of the quantum of plastic waste and other litter in waterways and coastal areas assists in the formulation of action to eradicate their discharge into them. The captured imagery defines the baseline and informs policy and regulation. On-going monitoring provides accurate and quantifiable information against which adherence can be determined.

7.5 Climate change

UAV captured imagery is an effective way of monitoring land use patterns over time, and the algorithm can be adapted to interrogate specific items of interest. The data informs policy and regulator decision-making and provides affected communities, including indigenous communities and those living in SIDS, accurate information on critical climate change indicators such as sea-level rise or deforestation.

8 Conclusion

Although initially developed to map floating plastic in rivers and waterways to stop it adding to the huge amount of waste already in our oceans and so begin to ease their degradation, this mapping solution has also proven effective in mapping land-based plastic, thus broadening its scope. This cost-effective, sophisticated and accurate data capture and AI-based processing methodology provides the spatial information needed for effective land use control decisions and a monitoring tool to ensure the required outcomes are being achieved.

References

Barrett, J., Chase, Z., Zhang, J., Holl, M. M. B., Willis, K., Williams, A., Hardesty, B. D. and Wilcox, C. (2020). Microplastic Pollution in Deep-Sea Sediments From the Great Australian Bight. *Front. Mar. Sci.*, 7:576170. https://doi.org/10.3389/fmars.2020.576170

Campbell, Gordon (2022). *On The Global War Against Plastics*. Scoop Media, New Zealand. https://www.scoop.co.nz/stories/HL2201/S00013/on-the-global-war-against-plastics.htm (accessed 15. October 2024).

Cheshire, A. C., Adler, E., Barbière, J., Cohen, Y., Evans, S., Jarayabhand, S., Jeftic, L., Jung, R. T., Kinsey, S., Kusui, E. T., et al. (2009). *UNEP/IOC Guidelines on Survey and Monitoring of Marine Litter.* UNEP Regional Seas Reports and Studies 2009, No. 186; IOC Technical Series No. 83: xii + 120 pp. https://www.nrc.govt.nz/media/10448/unepioclittermonitoringguidelines.pdf, (accessed on 25 April 2020).

Eriksen, M., Lebreton, L. C. M., Carson, H. S., Thiel, M., Moore, C. J., Borerro, J. C., Galgani, F., Ryan, P. G. and Reisser, J. (2014). Plastic pollution in the world's oceans: More than 5 trillion plastic pieces weighing over 250,000 tons afloat at sea. *PLoS ONE, 9*(12), 9, e111913, https://doi.org/10.1371/journal.pone.0111913

Fava, M. (2022). *Ocean plastic pollution an overview: data and statistics*. Intergovernmental Oceanographic Commission of UNESCO. https://oceanliteracy.unesco.org/plastic-pollution-ocean/ (accessed 9 August 2024).

Hardesty, B. D., Lawson, T. J., van der Velde, T., Lansdell, M. and Wilcox, C. (2016). Estimating quantities and sources of marine debris at a continental scale. *Front. Ecol. Environ., 15*, pp. 18–25, https://doi.org/10.1002/fee.1447

Jakovljevic, G., Govedarica, M. and Alvarez Taboada, F. (2019). Remote Sensing Data in Mapping Plastic at Surface Water Bodies. *Proceedings of the FIG Working Week 2019 Geospatial Information for A Smarter Life and Environmental Resilience,* Hanoi, Vietnam, 22–26 April 2019.

Jakovljevic, G., Govedarica, M. and Alvarez-Taboada, F. (2020). A Deep Learning Model for Automatic Plastic Mapping Using Unmanned Aerial Vehicle (UAV) Data. *Remote Sens., 12*, 1515. https://doi.org/10.3390/rs12091515

Jambeck, J. R., Geyer, R., Wilcox, C., Siegler, T. R., Perryman, M., Andrady, A., Narayan, R. and Law, K. L. (2015). Plastic waste inputs from land into the ocean. *Science, 347*(6223), pp. 768–771.

https://doi.org/10.58440/ihr-30-2-n10

McVeigh, K. (2022). *Plastic summit could be most important green deal since Paris accords, says UN.* The Guardian, Guardian News & Media Limited. https://www.theguardian.com/environment/2022/feb/25/plastic-summit-could-be-most-important-green-deal-since-paris-accords-says-un (accessed 9 August 2024).

Opfer, S., Arthur, C. and Lippiatt, S. (2012). *NOAA Marine Debris Shoreline Survey Field Guide*. National Oceanic and Atmospheric Administration, USA. https://marinedebris.noaa.gov/sites/default/files/ShorelineFieldGuide2012.pdf (accessed on 25 April 2020).

OSPAR commission (2010). *Guideline for Monitoring Marine Litter on the Beaches in the OSPAR Monitoring Area* (1st ed.). OSPAR Commission, London, UK. ISBN 90 3631 973 9. https://www.ospar.org/documents?v=7260 (accessed on 22 April 2020).

Schmidt, C., Krauth, T. and Wagner, S. (2017). Export of Plastic Debris by Rivers into the Sea. *Environ Sci Technol., 51*(21), 12246–12253. https://doi.org/10.1021/acs.est.7b02368

UNEP (2023). Turning off the Tap: How the world can end plastic pollution and create a circular economy. United Nations Environment Programme, Nairobi. ISBN: 978-92-807-4024-0.

UNEP (2024). *Plastic Pollution*. UN Environment Programme. https://www.unep.org/plastic-pollution/ (accessed 9 August 2024).

WWF (2022). *Ocean plastic pollution to quadruple by 2050, pushing more areas to exceed ecologically dangerous threshold of microplastic concentration.* World Wide Fund for Nature (WWF). https://oceanliteracy.unesco.org/plastic-pollution-ocean/ (accessed 9 August 2024).

NOTE / TECHNICAL REPORT

Utilizing crowd-sourced bathymetry for post disaster analysis – A case study

Authors

Shaul Solomon[1], Uri Yoselevich[1] and Ariel Tunik[1]

Abstract

This paper discusses two main use cases where DockTech's Crowd-Sourced Bathymetry (CSB) was utilized to aid the port of Rio Grande (Brazil) during severe flooding. (1) Daily Data Collection and Analysis: DockTech implemented a system to collect daily bathymetric information from tugboats operating in the port. By comparing this data to established reference points, the port was able to estimate daily changes in the underwater environment, enabling timely and informed decision-making. (2) Emergency Monitoring Operations: In the absence of accessible traditional surveys, the port commissioned two tugboats, equipped with CSB equipment, to conduct survey operations in the entrance channel. The data collected through these efforts allowed the port to make informed adjustments to draft restrictions by an extra 30 cm, ensuring safe passage for vessels despite the challenging conditions. Key findings from these efforts include the identification of channel edges with deposition, the detection of shallow regions in the entrance channel, and the facilitation of lifting draft restrictions from 11.9 m to 12.2 m. These outcomes demonstrate the practical applications and advantages of CSB-based technologies in responding to natural disasters, providing critical support to port operations under challenging conditions.

1 Terminology

In this paper, the term Crowd-Sourced Bathymetry (CSB) is used consistently. According to the official definition provided in the B-12 document, CSB refers to "the collection and sharing of depth measurements from vessels, using standard navigation instruments, while engaged in routine maritime operations" (IHO, 2022a). Notably, this definition excludes scenarios where vessels are specifically commissioned for surveying purposes, as these do not constitute "routine maritime operations". The authors deliberately use the term "CSB-equipped vessels" to bridge the gap between the broader potential of CSB technology and the particular necessity demanded here from a commissioned operation.

2 Introduction

In recent years, there has been a growing recognition of the significance and potential of CSB within the maritime community (Hains et al., 2024; Jencks & Jimenez Baron, 2024). While traditional hydrographic surveys remain the gold standard for acquiring detailed and precise bathymetric data, CSB has emerged as a valuable complementary resource (Masetti et al., 2020; Grinker et al., 2022; Klemm, 2023). Its ability to provide real-time, high-frequency data from various sources presents numerous theoretical use cases. However, as a burgeoning technology, practical applications of CSB are still relatively scarce.

In May 2024, southern Brazil experienced the worst flooding in over 80 years, prompting the declaration of a six-month state of emergency. The port of Rio Grande, a critical hub in the region, faced unprecedented challenges in maintaining navigational safety and operational continuity amidst rapidly changing conditions. DockTech, in collaboration with the tugboat company WilsonSons and the Practicagem Pilots, actively engaged with the port of Rio Grande to mitigate the impacts of this catastrophic event through the use of CSB.

This paper explores two primary use cases where DockTech's CSB initiatives provided crucial support to the port of Rio Grande during the flooding crisis. Through these case studies, we illustrate the practical applications and advantages of CSB-equipped

✉ Shaul Solomon · shauls@docktech.net

[1] DockTech Ltd., Tel Aviv-Jaffa, Israel

https://doi.org/10.58440/ihr-30-2-n06

vessels in responding to natural disasters and highlight the innovative approaches employed by DockTech. This paper aims to contribute to the ongoing discourse on the integration of CSB into broader hydrographic practices, demonstrating its value as a dynamic and responsive tool in times of crisis.

3 Data collection and methodology

3.1 Daily data collection and analysis

DockTech employs proprietary technology to convert raw data into Real-Time Surface (RTS) data, which includes integrating offsets/tide, filtering Echosounder/GPS noise, and utilizes spatio-temporal modeling. To establish a baseline, data from April 2024 was used to create a reference RTS, representing the last depth map before the flooding. Additionally, an RTS map was generated for each vessel equipped with the CSB data logger, to account for any potential errors from incorrect offset values.

Throughout May 2024, we compared (Figs. 1–3) the daily depth data from each vessel against the reference RTS. This comparison allowed us to identify consistent trends of change, which we plotted on a single map to highlight areas of deposition and erosion. While noise is an inherent challenge, observing similar trends across different vessels over time provides strong indicators for the port to monitor these changes closely.

3.2 Emergency monitoring operations

Although DockTech provided continuous monitoring of the main channel, the pilot vessels reported signs of siltation in the entrance channel, particularly during maneuvers with heavy ships. Adverse weather conditions prevented traditional hydrographic surveys, leading the port to commission DockTech and WilsonSons to conduct an emergency survey.

On June 6th and 7th, two tugboats from the fleet were deployed to map the entrance channel (Fig. 4). These vessels operated for approximately 1.5 hours each day, sailing in a criss-cross overlapping pattern (Fig. 5) at speeds below 10–12 knots. Tidal data was collected from the nearest tide station to the entrance channel, Molhe Sul. Tidal station data was vital because the observed water level raised more than a meter at the entrance of the port, compared to astronomical predictions.

4 Data analysis

4.1 Daily data collection and analysis

Every day the depth data (once filtered and enriched with tide and vertical offsets) from the past 24 hours are compared with the reference data (similar to Figs. 1 and 3). Depth difference is calculated and smoothed. Continuous observations of similar depth difference are clustered together. While a single cluster of difference might be a product of noise, as we compare the clusters generated across time and across vessels, larger trends become noticeable and confidence increases.

Below are two screenshots illustrating the trend polygons: erosion-only polygons (Fig. 6) and deposition-only polygons (Fig. 7). As shown, most of the main channel exhibits deposition. Erosion polygons, however, are limited to two areas: where the tugboats are berthed and along the eastern edge of the channel.

When we shared this information with the port authorities, they confirmed that these patterns of erosion and deposition were consistent with those observed in previous years, albeit on a smaller scale. This confirmation provides confidence that operations in the main channel can continue as usual, with a recommendation to avoid the eastern parts of the channel when possible.

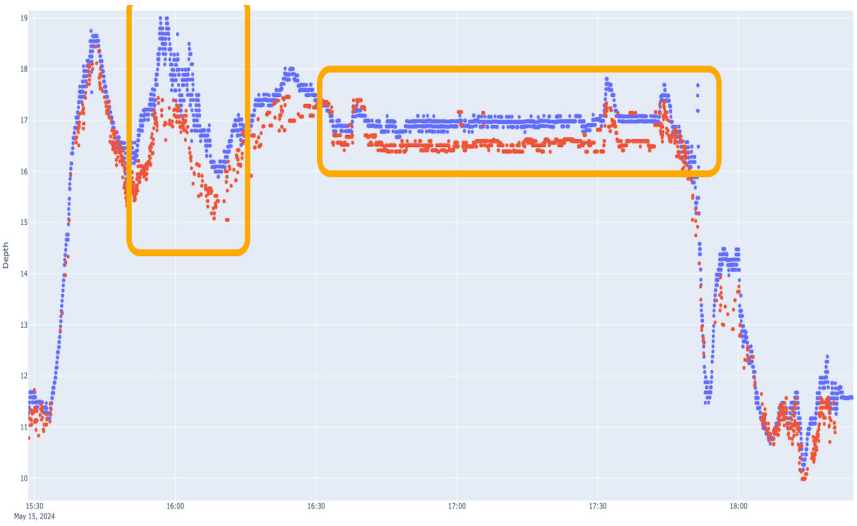


Fig. 1 *X*-axis timestamp (May 15 2024, between around 15:30 and 18:00), *Y*-axis Depth (meters, referenced to the chart datum). The blue scatter plot represents the depth logged from a CSB-Equipped Vessel from May 15, 2024. The red scatter plot represents the depth logged for that given cell from the reference bathymetric layer. The orange boxes represent two clear periods of time, where even when the seafloor changed, the difference between the local depth and the reference depth stayed relatively consistent.



Fig. 2 Satellite view of the port of Rio Grande (Brazil). The line represents the graphical location of the port during the scatterplot in Fig. 1. The observations colored in yellow are those within the orange boxes of Fig. 1

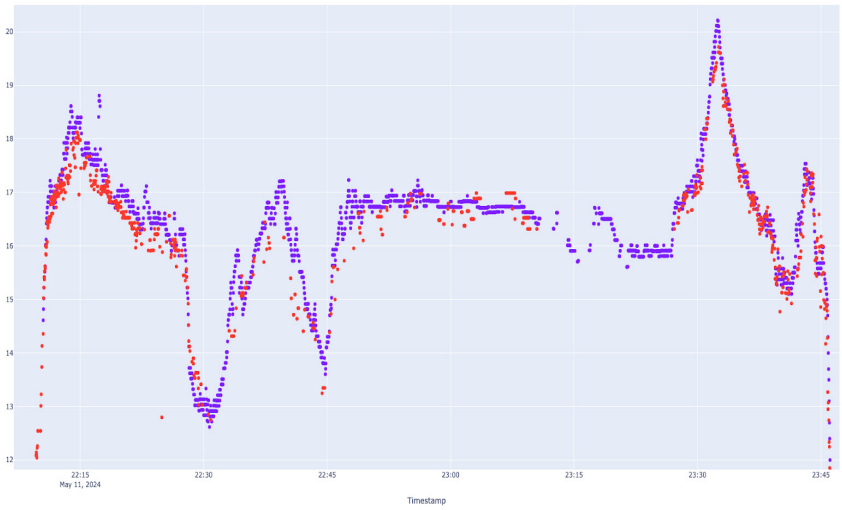


Fig. 3 *X*-axis timestamp (May 11 2024, between around 22:10 and 23:47), *Y*-axis Depth (meters, referenced to the chart datum). The blue scatter plot represents the depth logged from a CSB-Equipped Vessel from May 11, 2024. The red scatter plot represents the depth logged for that given cell from the reference bathymetric layer. As opposed to Fig. 1, there are no clear periods of consistent difference between the two layers.

4.2 Emergency monitoring operations

The pipeline (Fig. 8) running the code operates end-to-end without direct human involvement. Consequently, within a half-hour of the on-demand dredging operation, the results were available on DockTech's app, Aquascope AI.

An immediate use case for the mapping was to identify the best possible entrance for a large shipping container with a draft deeper than the restrictions allowed. Using the general map (Figs. 9 and 10) we identified the shallower regions of the entrance channel. The pilot used this information in their decision-making process, successfully navigating the container vessel to the desired terminal.

Two weeks later, the port conducted a traditional hydrographic survey using single-beam echo-sounder equipment. We compared our depth map to theirs, and while the ranges between the two layers are off by about a meter ([7.38, 21.39] for the survey, and [8.74, 22.88] for our layer), we can visually identify that the relative changes in the port are persistent (Fig. 11).

For each of the two layers, we binned the depth into the four quartiles ([[0, 0.25), [0.25,0.5), [0.5,0.75), [0.75,1.0]] and for each bin assigned a color (Table 1).

Despite some small pockets of noise in the PDR operation, the overall trends are clearly captured.

5 Data quality

5.1 Preface

When discussing the quality of the data, it is essential to establish a few key points.

Distinction of terms – The distinction between terms like precision, accuracy, and uncertainty has been well-documented (Heiskanen & Moritz, 1967; IHO, 2022a). Here, we will reference these distinctions without delving into detailed explanations. It is important to note that while there are many potential steps needed for correction/calibration (IHO, 2005), for simplicity we focus exclusively on the final output data.

Accuracy – To validate accuracy, we require some form of external validation (e.g., traditional surveys).

Precision – To validate precision/consistency, we can rely on the internal consistency of the data itself, both per vessel and across vessels. We compare measurements in the same location from various times and vessels.

If we have high accuracy (with low variance) we have confidence in our estimations as to accurately predicting the seafloor. If we have high precision, even with low accuracy, we can't trust a particular reading, but we can rely on changes to reflect trends.

5.2 Daily data collection and analysis

As we aim to capture daily change trends in a region with high uncertainty, we lack an external validation mechanism to evaluate the accuracy of our model. However, to estimate precision and consistency, we can examine the trend polygons generated (Figs. 6 and 7). By comparing overlapping polygons (demo example Fig. 12) and evaluating the depth differences, we derive the plot below (Fig. 13). These polygons were assessed over six days (May 16 to May 21).

Although capturing overlapping polygons precisely is challenging, the samples we have (n=46) show that the polygons are generally quite similar, with consistent trends even in cases with higher standard deviations.

5.3 Emergency monitoring operations

Because the vessels overlapped in their operations, we can calculate the *precision* of the model by evaluating the consistency (standard deviation) of the cells over time.

In most of our vessels we have observed a sampling frequency of two seconds for the depth data. In our particular use case, one of the two vessels has a

Table 1 Color legend for Fig. 11. While the range of values differ between the Survey Layer and the PDR Operation, the maps look very similar.

Color	Survey Layer – Range	PDR Operation – Range
Red	7.38, 12.14	8.74, 13.20
Orange	12.14, 13.41	13.20, 14.37
Light Green	13.41, 13.98	14.37, 14.70
Dark Green	13.98, 21.39	14.70, 22.88

https://doi.org/10.58440/ihr-30-2-n06

sampling frequency of one second. As our cells are approximately 5 m × 5 m (geohash precision 9; Fox et al., 2013), we often have two subsequent readings per cell (when vessels go slower than 4.86 knots). To better understand precision, we created a boxplot per vessel, with the *X*-axis representing the time interval between measurements. The plots below (Figs. 14 and 15) show that while there are outliers (noise) causing internal variance per cell to exceed 50 cm, 95 % of the standard deviation is within 25 cm, and 98 % is within 35 cm.

Upon direct examination of the data, we did not observe traditional noise (e.g., shallow readings from fish or air bubbles), but we did identify an interesting phenomenon (Figs.16 and 17):

1. Depth observations in relation to neighboring points indicate noise.
2. Despite the vessel's movement, the depth remained constant for half a minute before abruptly changing by over four meters.

Due to the port's immediate need for results, we did not filter out any of the noise. As the primary goal was to track general trends, any minor noise could be empirically identified and ignored.

When comparing our RTS data to the survey data collected (Fig. 9), we plot the error histogram (Fig. 18). Since the hydrographic survey occurred two weeks later, we cannot simply treat the survey as "ground truth". Due to constant sediment transport, bathymetric surveys are, by definition, only accurate at the time of collection. Normally, this is not an issue, as sediment transport does not change drastically. However, in our case, since the situation occurs at the end of a flooding event, additional debris deposition is expected. Nevertheless, we can still assess the overall quality of our data.

Overall, we see a mean error of around 40 cm, with a standard deviation of around 42 cm.

- Overall the residual error looks gaussian, which allows us to more easily define Confidence Intervals and Accuracy of the data.
- It is unclear what the mean error comes from. A shift from the mean error has often come from using inaccurate water level/tidal data or static offsets (echosounder to water level offset). In this scenario, *in-situ* tidal measurements were used and offsets were validated with blueprints. One speculation is the dynamic draft that is not yet being counted for, however as there are potentially other sources of error (e.g. speed of sound), further investigation is needed.
- Even with the mean error, as the spread is not too significant (± 2m fits within S-44's Special Order; IHO, 2022b), the internal consistency of the port allows us to ensure that we can capture regions with general trends decently.
- We can also observe clear outliers, with depth difference values near ± 4 m. This would demand extra precautions if used to assist navigational maneuvering, but for the sake of trend detection, they are inconsequential.

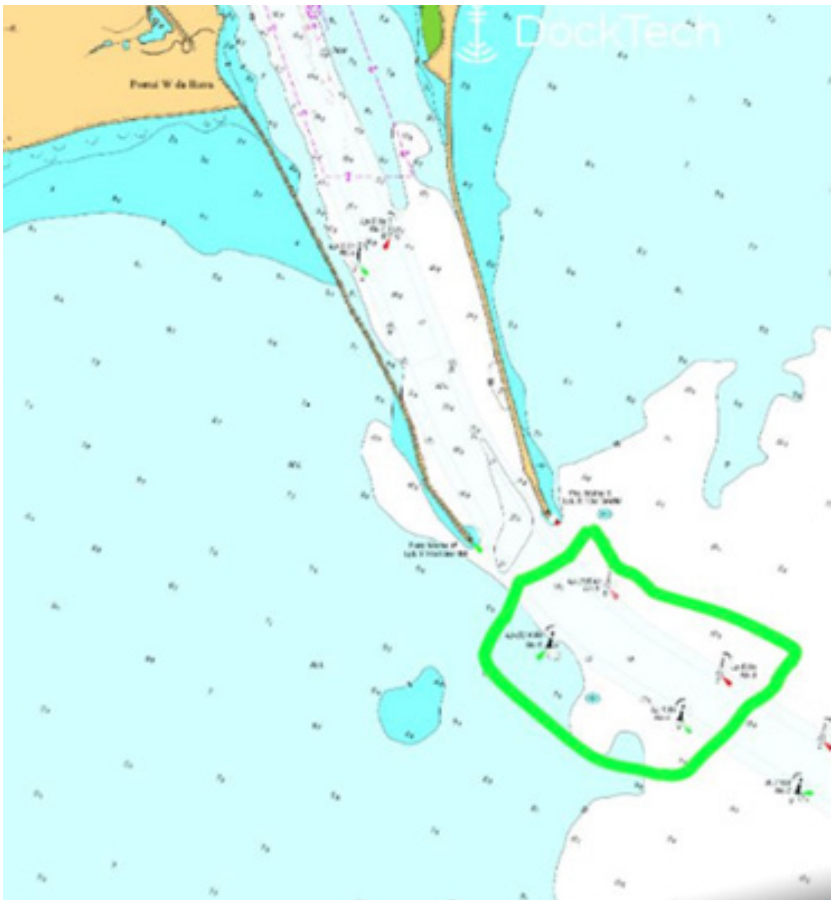


Fig. 4 ENC Chart (Cartas da costa brasileira 2101) of the Region of Interest within the Port of Rio Grande (Brazil). Green box highlights the entrance channel. Tugboats typically don't travel there for routine operations, which required the need for a commissioned operation.

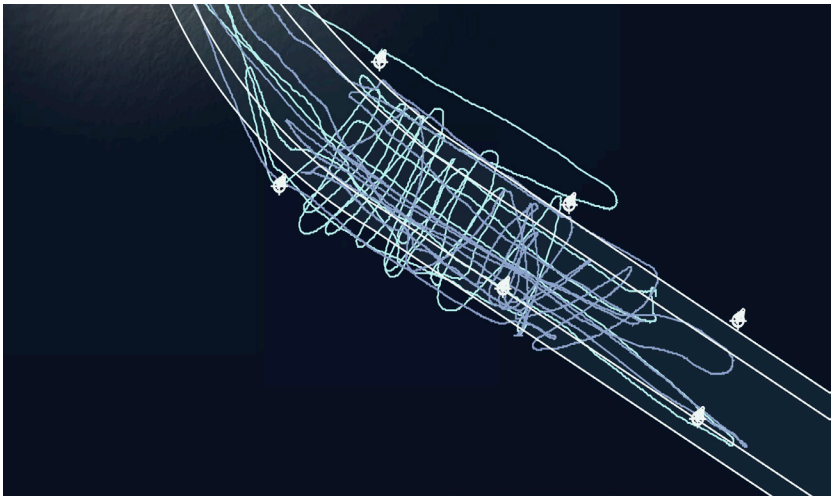


Fig. 5 Satellite view of the Region of Interest (highlighted in Fig. 4). The white line traces the extent of the port. The two shades of blue represent the exact path that the two vessels took

Conclusion

As the port of Rio Grande in Brazil experienced a once-in-a-century flooding event, existing hydrographic surveys became unreliable, necessitating the implementation of a CSB-centric solution to detect

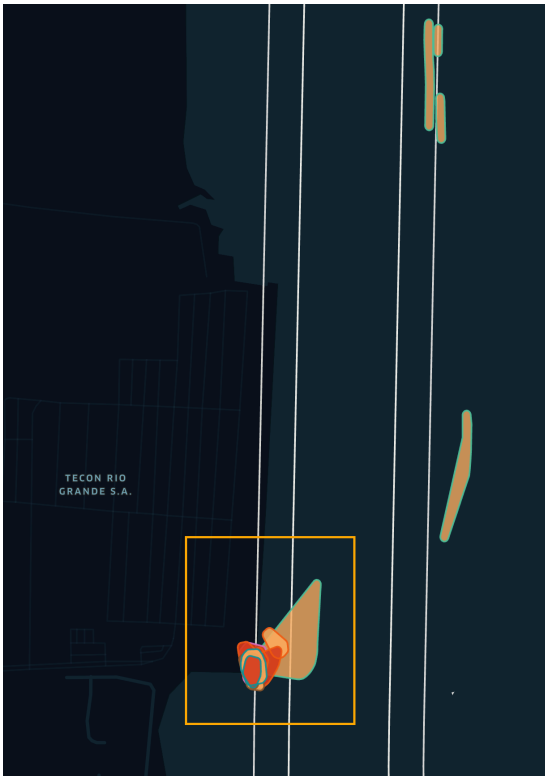


Fig. 7 Deposition polygons. Similar polygons to Fig. 6 but only those with deposition. The orange box is where the vessels berth. Reddish hue for deposition greater than 1 m, and orange for deposition smaller than 1 m.

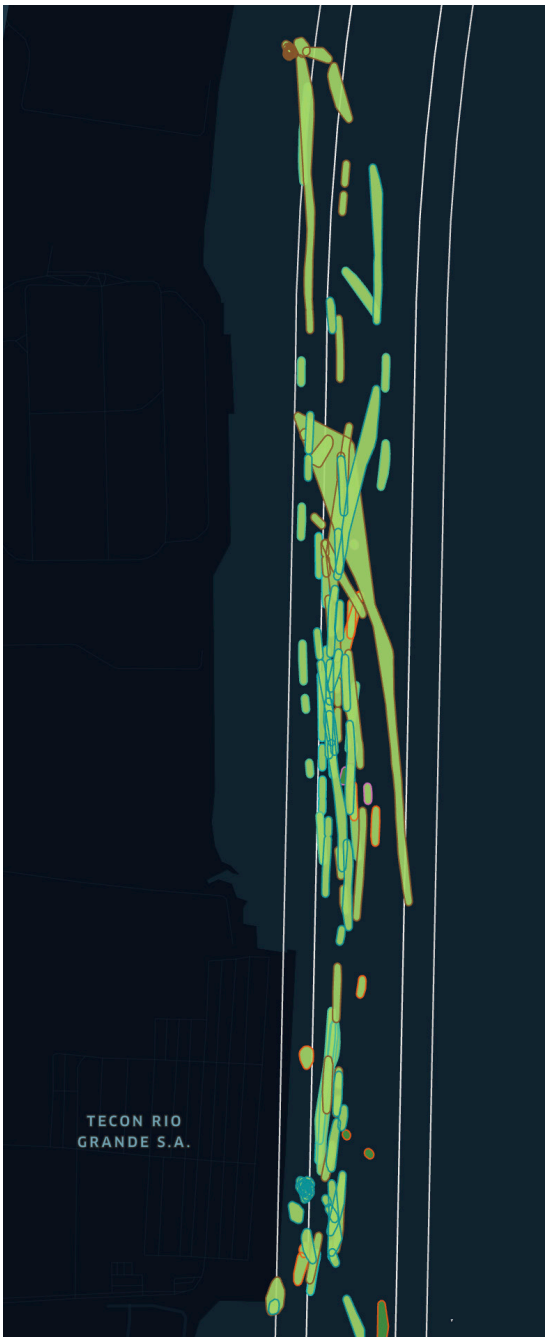


Fig. 6 Erosion polygons. Each polygon represents a shared difference to the reference bathymetric layer. Dark green for erosion greater than 1 m, and light green for erosion lower than 1 m.

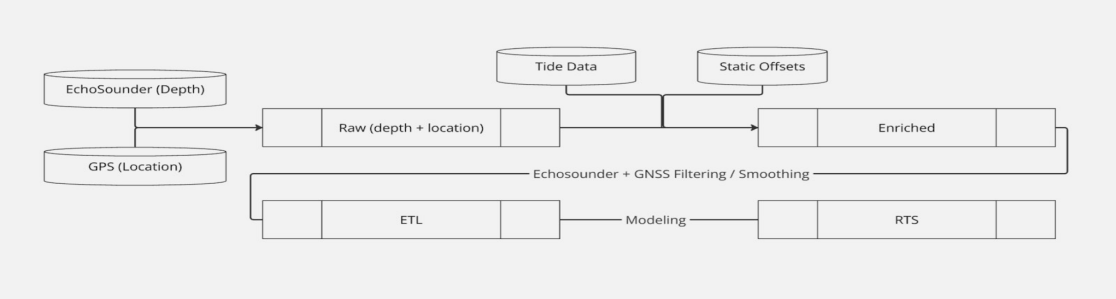


Fig. 8 Basic diagram of the pipeline converting raw bathymetric data into RTS (Real-Time Surface) Data. Classically, this pipeline is run daily for the past 30 days, however it can also run for any given period of time.

https://doi.org/10.58440/ihr-30-2-n06

trends and identify areas to avoid.

It is important to emphasize that CSB is intended to complement, not replace, traditional bathymetric surveys. The two use cases presented demonstrate how this approach can effectively identify trends in seafloor changes and provide clear guidance on navigation risks. While the second case may not fully align with the B-12 definition of CSB, the insights generated are theoretically achievable in a comprehensive CSB framework.

The application within the port of Rio Grande was crucial in allowing the port to safely reduce draft restrictions. This case study underscores the potential of CSB-equipped vessels as a dynamic and responsive tool in crisis management, offering valuable support during natural disasters.

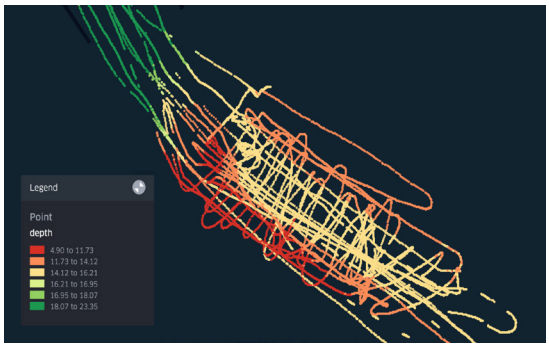


Fig. 9 Depth map of entrance channel (same as Fig. 4).

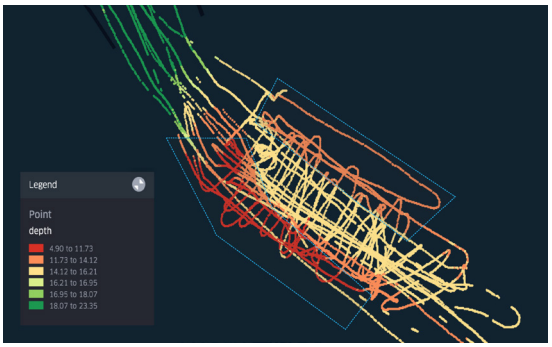


Fig. 10 Same depth map (Figs. 4 and 9) as before with stay-away regions in highlighted blue polygons.

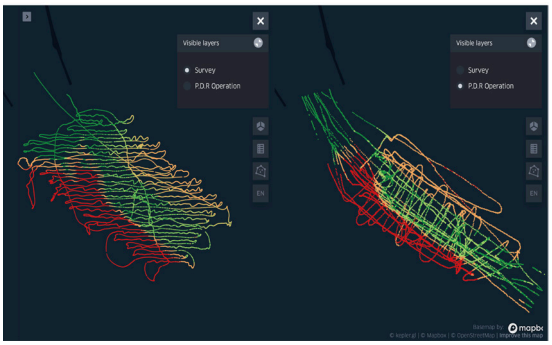


Fig. 11 Comparative map of the survey vs. on-demand "post-disaster recovery" operation (Table 1).



Fig. 12 Demo example of two polygons (green and red polygons on the left), and their corresponding union and intersection areas (light green and orange on the right, respectively). Polygons were considered "overlapped" if intersection_area / union_area · 100 > 20.

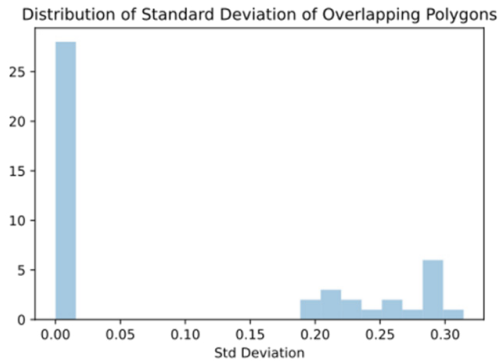


Fig. 13 Histogram of the standard deviation (m) of the diff for overlapping polygons.

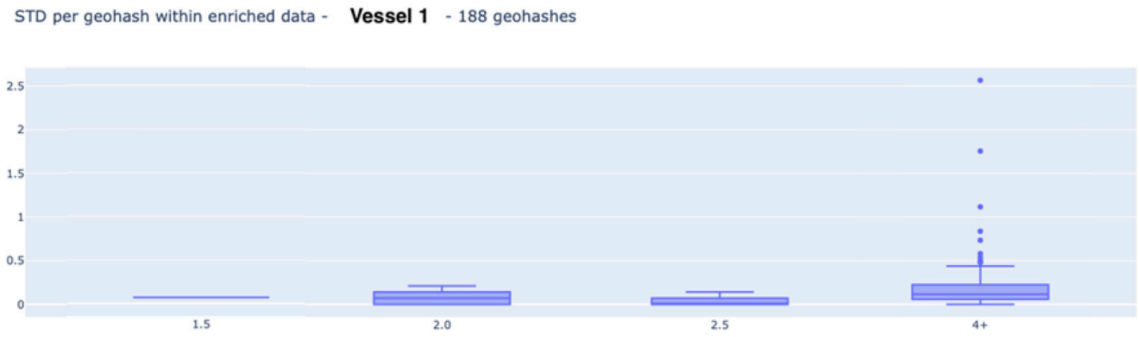


Fig. 14 Standard deviation for Vessel 1, where *X*-axis is the amount of time between observations (seconds). Outliers initially made the plot unreadable, so all values greater than 4 were binned into "4+".

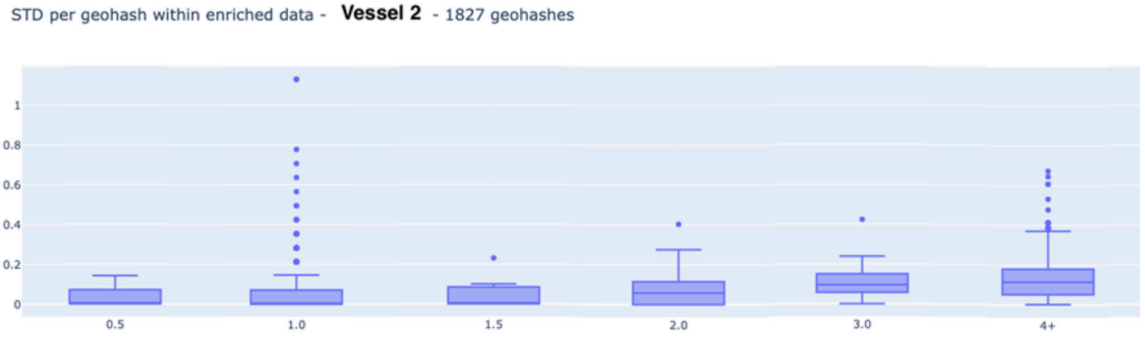


Fig. 15 Standard deviation for Vessel 2 where *X*-axis is the amount of time between observations (seconds). Outliers initially made the plot unreadable, so all values greater than 4 were binned into "4+".

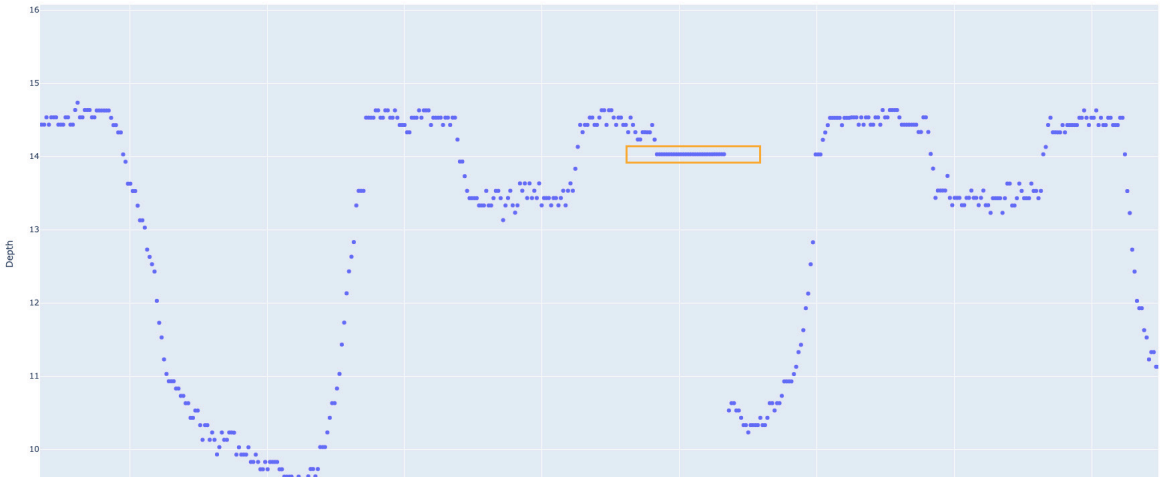


Fig. 16 Scatterplot of depth data from tugboat on June 6 2024 (between approximately 19:45 and 20:05). *X*-axis is timestamp and the *Y*-axis is depth (m). The highlighted orange box is noisy data.

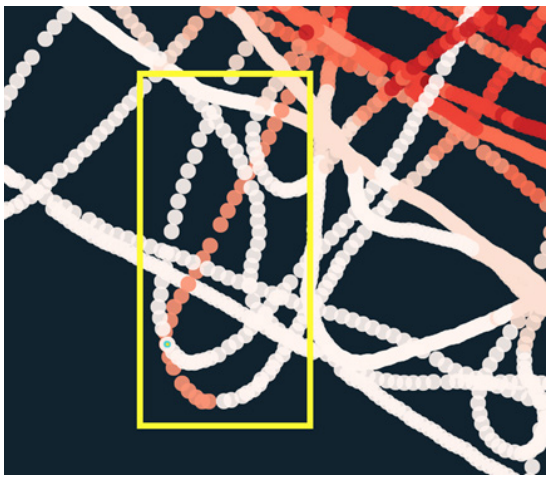


Fig. 17 Orange box in Fig. 15, shown in geospatial reference to other observations (red observations within yellow box). Color of observations reflect depth binned in a gradient between white (approx. 7 m) and deep red (approx. 22 m).

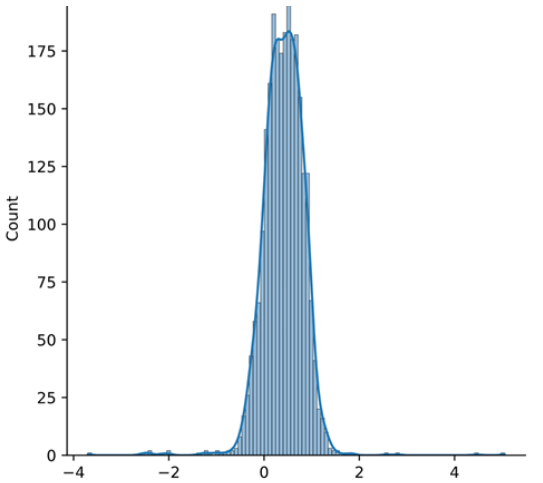


Fig. 18 Histogram of difference (meters) between RTS and survey data.

https://doi.org/10.58440/ihr-30-2-n06

References

Fox, A., Eichelberger, C., Hughes, J. and Lyon, S. (2013). Spatio-temporal indexing in non-relational distributed databases. *2013 IEEE International Conference on Big Data*, Silicon Valley, CA, USA, 2013, pp. 291–299. https://doi.org/10.1109/BigData.2013.6691586.

Grinker, B., Solomon, S. and Hassin, A. (2022). Evaluation of a crowd sourced bathymetric approach. *The International Hydrographic Review, 28*, pp. 158–171. https://doi.org/10.58440/ihr-28-a08

Hains, D., Keating, S. G., Rathnayake, C., Obura, V., Sharma, S. and Hall, S. (2024). Citizen Hydrospatial Sciences – To csB or not to csB, that is the question! *The International Hydrographic Review, 30*(1), pp. 162–170. https://doi.org/10.58440/ihr-30-1-n02

Heiskanen, W. A. and Moritz, H. (1967). *Physical Geodesy*. W. H. Freeman and Company, San Francisco.

IHO (2005). *Manual on Hydrography* (1st ed.). IHO Publication C-13, International Hydrographic Organization, Monaco. https://iho.int/uploads/user/pubs/cb/c-13/english/C-13_Chapter_1_and_contents.pdf (accessed 3 October 2024).

IHO (2022a). *Guidance to crowdsourced bathymetry* (3rd ed.). IHO Publication B-12, International Hydrographic Organization, Monaco. https://iho.int/uploads/user/pubs/bathy/B_12_CSB-Guidance_Document-Edition_3.0.0_Final.pdf (accessed 3 October 2024).

IHO (2022b). *Standards for Hydrographic Surveys* (6th ed.). IHO Special Publication S-44, International Hydrographic Organization, Monaco. https://iho.int/uploads/user/pubs/standards/s-44/S-44_Edition_6.1.0.pdf (accessed 3 October 2024).

Jencks, J. and Jimenez Baron, B. (2024). CSB as part of the modern hydrographic toolbox. *The International Hydrographic Review, 30*(1), pp. 150–160. https://doi.org/10.58440/ihr-30-1-n03

Klemm, A. R. (2023). *Introduction to Crowdsourced Bathymetry: The Power of Community.* Medium. https://medium.com/@anthony.klemm/introduction-to-crowd-sourced-bathymetry-the-power-of-community-ad941ac20469 (accessed 3 October 2024).

Masetti, G., Rondeau, M., Jimenez Baron, B., Wills, P., Petersen, Y. M. and Salmia, J. (2020). *Trusted Crowd-Sourced Bathymetry – From the Trusted Crowd to the Chart.* A whitepaper jointly prepared by Danish Geodata Agency and Canadian Hydrographic Service. https://eng.gst.dk/media/9079/trusted-crowd-sourced-bathymetry-from-the-trusted-crowd-to-the-chart20200621.pdf (accessed 3 October 2024).References

NOTE / TECHNICAL REPORT

Marine accidents ascribe to man or machine?

Author
BK Ramprasad[1]

Abstract
The International shipping industry is responsible for the carriage of around 90 % of the world trade (ICS, 2024). The efficient Marine Safety Information Services (MSIS) have been made available to the mariner besides national / international regulations using the upgraded navigational tools like ENCs and virtual e-navigation. A roadmap to switch over to the S-100 data model and generating new S-101 ENCs has already been prepared by the IHO. Irrespective of technological developments, marine accidents are increasing worldwide every year and the reports (MAIB, 2017) reveals that lack of trained manpower on bridge, lack of familiarization to the digital equipment and its use was the root cause of many of these marine casualties. The sub working group members of the NCWG have prepared a document on the Future of the Paper Nautical Chart (FOTPNC) in view of maximal use of ECDIS and ENCs onboard ships. The present study after analysing the aforesaid investigation reports reveals that the increase of marine accidents may be attributed to both man and machine.

1 Introduction
Let us have a look at the existing national and international regulations in force for the safety of navigation at sea. The International Maritime Organization (IMO) is the United Nations specialized agency with responsibility for the safety and security of shipping and the prevention of marine and atmospheric pollution by ships. The 1974 International Convention for the Safety of Life at Sea (SOLAS), together with subsequent amendments, has been adopted by the Member States of the IMO. Chapter V of SOLAS specifies the requirements for the navigational services to be used on board ships entitled to fly the flag of a party to the SOLAS Convention. The SOLAS Convention includes a requirement for all ships to carry up-to-date nautical charts and publications for the intended voyage. Progressively from 2012, the chart carriage requirement for certain classes of vessels is to be satisfied by electronic means using an Electronic Chart Display and Information System (ECDIS; IHO, 2018a).

IMO Member States are obliged to adopt IMO rules and regulations, such as those in SOLAS, into their national legislation. However, only when the Convention have been incorporated into national legislation do they take effect for the individual ships registered by that State. This process of incorporation into national legislation may vary from a few months to several years (IHO, 2018b).

The State in which a ship is registered and hence which flag it is flying is known as the Flag State. It is the national maritime administration representing the Flag State that controls the ship's adherence to the SOLAS carriage requirements (Flag State control).

The national maritime administration is also responsible for Port State control. Ships arriving at a port may be subject to Port State control by local officials (Port State Control Officers, PSCO). Port State control is based on Flag State regulations and international agreements. Port States cooperate within regions to apply consistent standards; for example, European nations and Canada cooperate under the umbrella of

✉ BK Ramprasad · bkrp1972@gmail.com
[1] National Hydrographic Office, Dehradun, Uttarakhand, India

https://doi.org/10.58440/ihr-30-2-n09

the Paris Memorandum of Understanding[1]. Article 94 of the United Nation's Convention on Law of the Sea (UNCLOS) defines responsibility on the flag state to carryout inquiry into marine casualty. Also, under SOLAS regulation I/21, Load Lines Convention article 23 and MARPOL articles 8 and 12, each Administration undertakes to conduct an investigation into any casualty occurring to ships under its flag. The Indian Maritime Administration conducts investigations and inquiries into marine casualties in accordance with Part XII of the Indian Merchant Shipping Act, 1958 (as amended; INDIA CODE, 2024). These inquiry reports are made available on the Directorate General of Shipping website[2] aiming at preventing future accidents and generating awareness in mariners. In addition to IMO regulations, Marine Safety Act 1998 of India states its following objects:

a) To ensure the safe operation of vessels in ports and other waterways,
b) To promote the responsible operation of vessels in those waters so as to protect the safety and amenity of other users of those waters and the amenity of occupiers of adjoining land,
c) To provide an effective framework for the enforcement of marine legislation,
d) To provide for the investigation of marine accidents and for appropriate action following any such investigation,
e) To consolidate marine safety legislation.

According to SOLAS-V, charts issued *by or on the authority of a Government, authorized Hydrographic Office or other relevant government institutions* are official and may be used to fulfil carriage requirements (provided they are kept up to date). All other nautical charts are by definition not official and are often referred to as unofficial or private charts. These charts are not accepted as the basis for navigation under the SOLAS Convention. There are two kinds of official digital nautical charts commonly available: Electronic Navigational Charts (ENC) or Raster Navigational Charts (RNC), where ENC are not available.

Besides the above regulations, Nautical Chart Working Group is a subsidiary of the HSSC (Hydrographic Services and Standards Committee) which provides expert and authoritative advice and guidance to relevant IHO bodies and non-IHO entities on the concept of nautical cartography including revision of IHO's publications viz., S-4 Regulations for International (INT) Charts and Chart Specifications of the IHO, S-11 Guidance for the Preparation and Maintenance of International (INT) Chart and ENC Schemes and Catalogue of International (INT) charts, INT 1 (Symbols and Abbreviations used on Paper Charts), INT2 (Borders, Graduation, Grids and Linear Scales) and INT3 (Use of Symbols and Abbreviations). The aim of the international chart concept is to facilitate the provision of minimum sets of charts suitable for the navigational requirements of international (foreign-going) shipping adopting common world wide specifications. Such internationally-adopted charts will also enable those IHO Member States who provide, or wish to provide, charts outside their own national waters, to print by facsimile reproduction with only superficial modifications, selected modern charts under the terms of a bilateral arrangement between the Member States (IHO, 2018b). The purpose of INT charts and the INT chart product specifications will lose its identity as some of the Member Hydrographic Offices are heading towards paper less bridge. For example, Netherlands regulations allow paperless navigation and paper allowed as back up (IHO, 2020). Digital navigational aids may be of good accuracy but the lack of trained personnel at bridge lead to increase in number of accidents in comparison with the good old analogue navigational tools. The statistics below pertaining to marine accidents is a clear evidence of the above statement.

2 Review of statistics – marine accidents

According to the European Maritime Safety Agency (EMSA)'s accident investigation reports on marine casualty, across the period 2011–2015 (EMSA, 2016), numerous fatalities occurred on board passenger ships. During 2015 itself, 115 reported fatalities, 976 persons injured, 36 ships lost and 125 investigations launched (EMSA, 2016). Over the period 2011–2015, half of the casualties were of a navigational nature (Fig. 1). Human erroneous action represented 62 % of accidental events and 71 % of accidental events were linked to shipboard operations as a contributing factor (European Marine Casualty Information Platform-EMCIP, 2016; Fig. 1). The total number of reported marine casualties and incidents over the period from 2014 to 2022 was 23,814, with a yearly average of 2,646 casualties and incidents. The total number of reported marine casualties and incidents in 2022 alone was 2,510 (EMSA, 2023).

In 2015 more than 1,700 cargo ships were involved in marine casualties and incidents that resulted in 64 fatalities, an abnormally high number due to the loss of the general cargo ship El Faro with 33 victims. In 2017, 1232 accidents (casualties and incidents) to UK vessels or in UK coastal waters were reported to the Marine Accident Investigation Branch (MAIB). These involved 1352 vessels. 42 of these accidents involved only non-commercial vessels, 499 were occupational accidents that did not involve any actual or potential casualty to a vessel. There were 708 accidents involving 779 commercial vessels that involved

[1] https://www.parismou.org/ (accessed 26 October 2024).

[2] https://dgshipping.gov.in (accessed 26 October 2024).

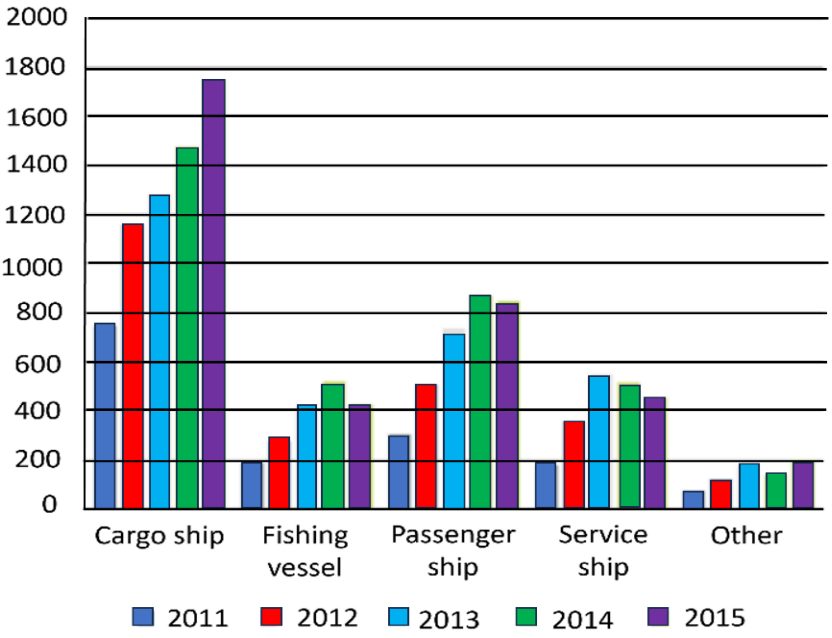
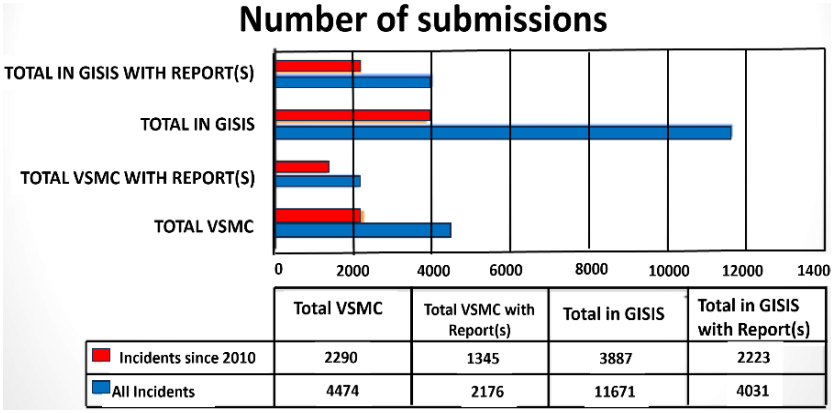


Fig. 1 Distribution of ships involved by main category 2011–2015 (Source: European Maritime Safety Agency Report 2016).



	Total VSMC	Total VSMC with Report(s)	Total in GISIS	Total in GISIS with Report(s)
Incidents since 2010	2290	1345	3887	2223
All Incidents	4474	2176	11671	4031

Fig. 2 Number of incidents reported since 2010 (Source: https://www.imo.org/).

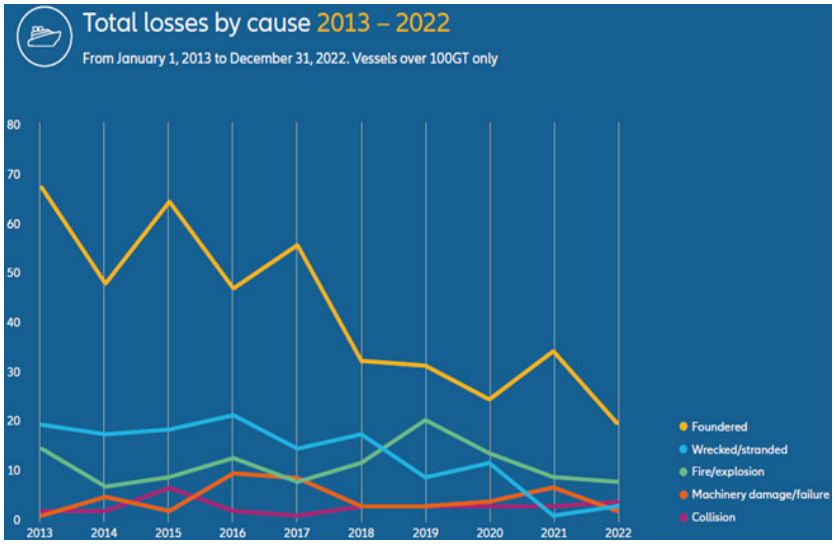


Fig. 3 Safety and shipping review-2023 by Allianz Global Corporate & Specialty (Source: Lloyd's List Intelligence Casualty Statistics Data Analysis & Graphic: Allianz Global Corporate & Specialty).

actual or potential casualties to vessels (MAIB, 2017).

The number of submissions in the Global Integrated Shipping Information System (GISIS) Maritime Casualties and Incidents (MCI) and reporting rate from 2010 to 2019 are shown below in Fig. 2.

According to Lloyd's List Intelligence reports, incidents totalled 700 in the third quarter of 2022, the highest number of incidents since 2008. Machinery damage or failure, and collisions were the most common causes of casualty, accounting for 62 % and 12 % of all incidents during the year 2022. Incidents of this nature have been steadily increasing over the past decade (Fig. 3). During the first quarter of this year, accidents caused by machinery damage accounted for 57 % of all casualties, up from 40 % in the same period of 2015 (Fig. 4). Machinery damage or failures happen worldwide and impact all vessel types.

3 Analysis of accident investigation reports

According to paragraph 209 of the Casualty Investigation Code (CIC), "a marine casualty means an event, or a sequence of events, that has resulted in any of the death or serious injury to a person, loss of a person from ship, presumed loss or abandonment of a ship, material damage to ship, involvement of a ship in collision, material damage to marine infrastructure external to a ship, severe damage to the environment etc. However, a marine casualty does not include a deliberate act or omission with the intention to cause harm to the safety of a ship, an individual or the environment"[3].

The following investigation reports pertaining to grounding of ships Kea Traders, Nova Cura, Muros and CMA CGM Vaco de Gama supports the above findings (Fig. 5).

Report by Marine Safety Investigation Unit (MSIU) on grounding of container ship *Kea Trader*: At 00551 on 12 July 2017, the Maltese registered container ship *Kea Trader* ran ground and stranded in position 22° 02.28' S 168° 38.25' E (*Recif Durand*) in the Pacific Ocean. At the time, the vessel was on a passage from Papeete, Tahiti, to Noumea, New Caledonia. *Kea Trader* was using electronic chart display and information system (ECDIS) as the primary means of navigation and there were no paper charts on board. The officer of the watch (OOW) was monitoring a route displayed on the ECDIS. The zone of confidence (ZOC) of the electronic navigation chart (ENC) was 'D' and displayed a caution symbol and textual message "*[t]his chart cannot be accurately referred to WGS 84 datum; see caution message*".

The following findings in the Marine Safety Investigation Report No.14/2018 by the MSIU is a clear evidence of untrained staff and malfunctioning

[3] https://www.imo.org/ (accessed 26 October 2024).

https://doi.org/10.58440/ihr-30-2-n09

of the equipment at the bridge (MSIU, 2018):

(i) The revised route resulted in the track virtually passing over the isolated danger;
(iii) An over-scale indication and vertical lines on the ECDIS indicating positional discrepancy of charted objects and loss of navigational information was missed by the OOW;
(iv) No warnings or reference to the isolated danger was documented;
(v) The ECDIS route check function had not been enabled;
(vi) The master's confidence in the second mate's competency in the use of ECDIS, and application of planning procedures led him to believe that the route was safe and no independent route check was carried out;
(vii) The detection vector had a width of 0.1 nm and 1.9 nm ahead and the detection sector was set at 45° over the same distance, effectively giving the OOW just about six minutes to respond to the safety alarm;
(viii) Since the safety settings during the navigational watch hand over were neither checked nor logged in the deck logbook, none of the watchkeepers was aware of the actual safety settings on the ECDIS;
(ix) The audible alarm was set to zero and remained switched off during the vessel's passage to Noumea;
(x) The displayed symbol had not been interrogated;
(xi) The 'caution area' message repeatedly displayed in the subsequent navigational watches was largely overlooked by the bridge team;
(xii) The OOW earnestly believed that the vessel's position displayed within the XTL was safe and required no action other than of adjusting the heading to regain the track;
(xiii) No evidence of the safety alarm - crossing safety contour, approaching underwater rock / obstruction / wreck or dangerous symbol – was found triggered on the ECDIS to alert or indicate to the OOW or lookout of imminent danger of grounding;
(xiv) The fact that the isolated danger symbol on the chart and the caution area message in the alarm panel remained displayed during successive navigational watches, may have suggested that there were no immediate and/or perceivable effects on the vessel or the voyage per se;
(xv) The benefits of technology became a burden, hindering the skillful use of equipment and only mitigated by the de-activation of the safety barrier system.

Report by Dutch Safety Board (DSB) on grounding of Dutch ship *Nova Cura*: On 20 April 2016, the Dutch freighter Nova Cura was en-route from Eregli on the Black Sea (Turkey) to Aliaga (Turkey). The ship was loaded with 4,400 tonnes of steel products. At 09:551 hours the Nova Cura ran aground in Mytilini Strait (to the north of Lesbos) at operating speed. As a result, all of the double-bottom tanks were breached and filled with water, as was the engine room and the bow thruster room. The ship was a total loss. The digital chart in the ECDIS (Electronic Chart Display and Information System, indicated that the sea should be 112 metres deep at the ship's position. However, the ship appeared to have run aground in shallow water at Lamnas Reef. This accident is classified as a very serious accident as referred to in the Casualty. On the day of the grounding, 20 April 2016, the Nova Cura was en-route from Eregli (Turkey) to Aliaga (Turkey) carrying 4,400 tonnes of steel products. This gave the ship a draft of 5.80 meters. (Source: Investigation Code of the International Maritime Organization (IMO) and EU Directive 2009/18/EC).

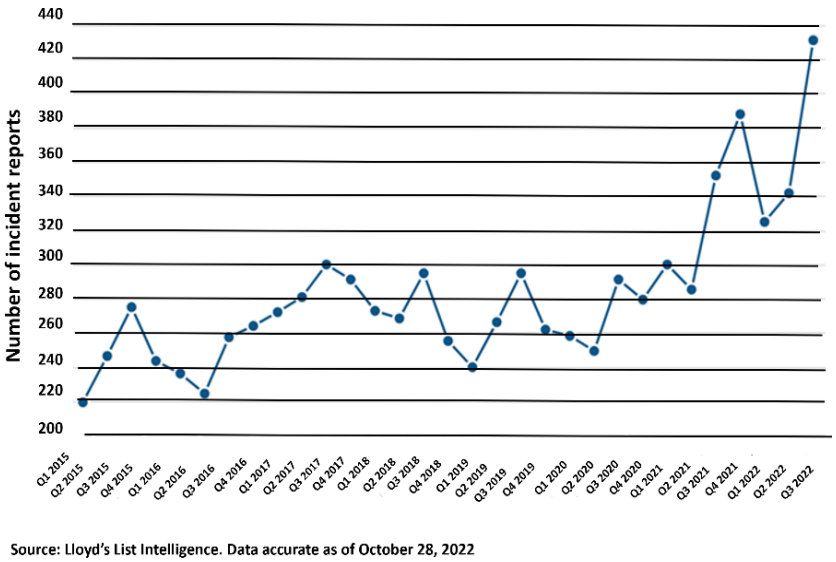


Fig. 4 Number of incidents reported since 2010 (Source: https://www.imo.org/).

United Kingdom Marine Accident Investigation Branch (MAIB): On 2 December 2015 the 2,998 gross ton Spanish bulk carrier Muros (Fig. 2), carrying a cargo of bulk fertilizer, was en-route from Teesport (United Kingdom) to Rochefort (France). The vessel's original Passage Plan had the vessel transiting through North Hinder Junction. During the watch handover from the Master to the Second Officer (2/O), occurring from 2350 (2 December 2016) to 0010 (3 December 2016), the Master ordered the 2/O to amend the Passage Plan to transit via the Sunk Traffic Separation Scheme (Fig. 1). The vessel went aground on a falling tide on Haisborough Sand off the east coast of the United Kingdom in the early morning hours of 3 December 2016, about 2 hours after the watch handover. The vessel remained aground for 6 days before being refloated. Rudder damage required the vessel be towed to Rotterdam for repairs (Source: The MAIB Report No. 22/2017 was released on 19 October 2017). The possible cause of the grounding was an unsafe Passage Plan resulting from changing the vessel transit from via North Hinder Junction to via Sunk Traffic Separation Scheme.

Grounding of Ultra-large container vessel *CMA CGM Vasco de Gama*: In the early hours of the morning on 22 August 2016, the 399.2m ultra-large container

vessel *CMA CGM Vasco de Gama*, grounded on the western side of the Thorn Channel whilst approaching the Port of Southampton. *CMA CGM Vasco de Gama* was the largest ship on the UK ship registry and had two Southampton pilots embarked. One of the pilots had control of the vessel's navigation at the time of the grounding. Fortunately, *CMA CGM Vasco de Gama* was undamaged by the grounding and was able to be refloated, with tug assistance, on the rising tide. The grounding occurred because the vessel was too far north of the intended track when the turn into the Thorn Channel was commenced. This reduced the sea room available for the maneuver and, given the environmental conditions, *CMA CGM Vasco de Gama* was unable to sustain the rate of turn required to remain in the dredged channel.

The execution of the vessel's turnaround Bramble Bank and into the Thorn Channel by the lead pilot was not in accordance with the port's guidance for large inbound vessels. *CMA CGM Vasco de Gama*'s bridge team, assistant pilot and the Vessel Traffic Services, could not usefully monitor the lead pilot's actions, or the vessel's progress through the Precautionary Area. This was because a detailed pilotage plan had not been produced; the lead pilot's intended maneuver around Bramble Bank was not explained; the bridge team roles and responsibilities were unclear; and the electronic navigation aids on board were not fully utilized.

The investigation identified that the vessel's bridge team and the port pilots had the experience, knowledge and resources available to effectively plan and execute the pilotage. However, the standards of navigation displayed during the pilotage fell short of the standards expected by CMA Ships and Associated British Ports. It was apparent that complacency and a degree of over confidence on the part of the master and port pilots contributed to this accident. However, it was also apparent from recent similar incidents and the findings of previous MAIB reports that many of the practices evident in this case were not specific to this single pilotage act, or to *CMA CGM Vasco de Gama*.

Actions have been taken by CMA Ships and Associated British Ports to address some of the issues identified in this report and to improve navigational safety. The findings of this report will be used by the MAIB as part of a safety study that will investigate the use of modern electronic navigation aids on board merchant vessels, and the impact they have had on navigation practices. Recommendations aimed at reducing the likelihood of future groundings and improving levels of navigation, bridge resource management, and use of electronic navigation aids have been made to CMA Ships and Associated British Ports.

Grounding of *Muros*: At 0248 (UTC+1) on 3 December 2016, the bulk carrier *Muros* ran aground on Haisborough Sand on the east coast of the United Kingdom. Attempts to maneuver clear of the shallows were unsuccessful but the vessel was re-floated 6 days later with tug assistance (Fig. 5). There were no injuries and no pollution, but damage to *Muros*'s rudder necessitated the vessel being towed to Rotterdam, Netherlands, for repair.

The MAIB investigation identified the following shortfalls:

a) The vessel was following a planned track across Haisborough Sand. The passage plan in the ECDIS had been revised by the second officer less than 3 hours before the grounding and it had not been seen or approved by the master.
b) A visual check of the track in the ECDIS using a small-scale chart did not identify it to be unsafe, and warnings of the dangers over Haisborough Sand that were automatically generated by the system's 'check route' function were ignored.
c) The second officer monitored the vessel's position using the ECDIS but did not take any action when the vessel crossed the 10m safety contour into shallow water.
d) The effectiveness of the second officer's performance was impacted upon by the time of day and a very low level of arousal and she might have fallen asleep periodically.
e) The disablement of the ECDIS alarms removed the system's barriers that could have alerted the second officer to the danger in time for successful avoiding action to be taken.

The MAIB has recently investigated several grounding incidents in which the way the vessels' ECDIS was configured and utilized was contributory. There is increasing evidence to suggest that first generation ECDIS systems were designed primarily to comply with the performance standards required by the IMO, as these systems became a mandatory requirement on ships, with insufficient attention being given to the needs of the end user. As a consequence, ECDIS systems are often not intuitive to use and lack the functionality needed to accommodate accurate passage planning in confined waters. This situation has led to seafarers using ECDIS in ways which are at variance with the instructions and guidance provided by the manufacturers and/or expected by regulators (MAIB, Report on the investigation of the grounding of Muros Haisborough Sand North Sea 3 December 2016).

The MAIB is conducting a safety study, in collaboration with the Danish Maritime Accident Investigation Board, designed to more fully understand why operators are not using ECDIS as envisaged by regulators and the system manufacturers. The overarching objective is to provide comprehensive data that can be used to improve the functionality of future ECDIS systems by encouraging the greater use of operator experience and human centred design principles (MAIB Report no. 22/2017 of October 2017).

The recent accident which was happened on 26 March 2024, where a cargo ship named Dali was slammed into the 'Francis Scott Key Bridge' at

https://doi.org/10.58440/ihr-30-2-n09

Baltimore, Maryland State, United States of America. The central part of the bridge is completely collapsed. The preliminary reports from the news agencies says that there was a power issues with the ship prior to collision and the crew made a mayday message to the authorities. Six construction workers who were working on the bridge are missing and presumed to be dead according to the news agency reports (BBC, 2024). The ship owner declared that entire 23-member crew onboard are safe. Since the bridge which was constructed in 1977, is a main life line for the trade in this area, the entire business came to a halt. The collapse of the bridge had an impact on the supply chain and worsely affected the ship movement into entry and exit of the Baltimore harbour. Detailed accident investigation report is awaited. Fig. 6 shows the allision of Dali against the bridge.

4 Conclusion

In the name of technological advancements in the field of navigational equipment, we are deviating from the main objective i.e., safety of life at sea. The rapid technological growth in the marine sector causes delay in familiarization of existing resources. For example, the use of S-57 ENCs started in the early 2000 and the manufacturers had produced the S-57 compliant ECDIS. When the mariner not fully familiar and user friendly with the existing functions of ECDIS, IHO has switched over to S-100 (IHO Universal Hydrographic Data Model) series of products with the respective specifications including ECDIS display standards S-52. Now it is the time for the ECDIS manufactures to produce machines that are compliant with the S-1xx series of products for example S-101 (ENC), S-102 (Bathymetric Surface), S-104 (Water Level Information), S111 (Surface currents), S-129 (Under Keel Clearance Management) etc., under phase-I of S-100 implementation road map of IHO (S-100 Implementation Strategy) with relevant software upgradations including WECDIS to read AMLs. In the bargain the men at bridge neither fully conversant with the existing tools nor getting familiar with the upgraded software/hardware tools which may lead to a wrong judgment yet times.

Let us analyse the marine investigation report on grounding of bulk carrier American Mariner. On January 7, 2023, about 0734 local time, the bulk carrier American Mariner had begun transiting outbound in the Vidal Shoals Channel, near Sault Ste. Marie, Ontario, en route to Superior, Wisconsin, when the vessel grounded and sustained damage to three ballast water tanks (see Fig. 7). No pollution or injuries were reported. Damage to the vessel was $600,000 (MIR-24-16 by the NTSB). The National Transportation Safety Board (NTSB) determines that the probable cause of the grounding of the bulk carrier American Mariner was the master manoeuvring the vessel away from the dock and into the channel while alone on the bridge, which required him to multitask (navigation, steering, and lookout duties) and resulted in the vessel overshooting the turn into the channel and running



Fig. 5 Ill-fated ships ran aground.



Fig. 6 Ill-fated cargo ship *Dali* which slammed into Francis Scott Key Bridge at Baltimore (Source: BBC News, www.bbc.com/news accessed on 26 March 2024).



Fig. 7 Damage to the port water ballast tanks of bulk carrier *American Merine* due to grounding (Source: US Coast Guard).

aground on the shoals on the opposite side of the channel. American Mariner was outfitted with a RosePoint electronic chart system (ECS). The ECS was not configured to display the footprint of the vessel, according to the master, and safety depths were not programmed into the ECS. Which shows the un-familiarisation of bridge crew with the safety functions of the ECS system.

The NTSB report also opined that while manoeuvring in confined waters, it is difficult for a single bridge crewmember to effectively drive, lookout, and monitor and use available bridge equipment. The composition of a bridge team may vary based on the complexity of the manoeuvre or operation being carried out. Typically, manoeuvres like docking or undocking, transiting in or out of port, or operating in areas of high traffic density require additional personnel to handle navigation-related duties. Owners, operators, and vessel masters are responsible for ensuring that bridge teams are staffed with a sufficient number of certified/credentialed mariners who are familiar with all bridge navigation equipment and able to independently take immediate action. Additionally, the effective use of all available resources by a bridge team, including visual scanning, radars, electronic charts, and an automatic identification system (AIS), increases collective situational awareness and contributes to a safe navigation watch (NTSB, 2016).

Therefore, at most care must be taken to avoid human negligence while exercising safety measures onboard. Language should not be a barrier while imparting safety information. Technological changes must improve the safety of life at sea rather increasing risk factor. The crew must be trained in using digital navigational tools and ability to comprehend the resources their alarms on an ECDIS to overcome the risk. Awareness towards latest IHO standards and specifications pertaining to ENC/ECDIS is essential. Mariner must keep an updated ENC set from an authorized hydrographic office, onboard for the planned voyage.

In the recent allision of the cargo ship Dali which slammed the Francis Scott Key bridge at Baltimore port, the ship was identified a faulty pressure gauge for fuel heating by the authorities and the same was fixed before the ship leaving from the port at Singapore. Just before the allision, the Dali experience a blackout losing power and its steering control system. Such blackouts are rare but hazardous on ships. The preliminary reports say that the impure fuel used might be one of the reasons for power failure. The ship was undergoing routine engine check-up just before the allision. Human negligence and dilution of standards may be the cause of this particular accident. However, a detailed accident investigation report is awaited in this case.

The above statistics are the clear evidence of increasing marine accidents in the past two decades as we have been claiming the era of artificial intelligence. In the name of safety, too much research had been taken place towards developing new software and hardware that can replace the use of hard copies of charts and other navigational publications onboard. The increase in number of marine accidents is the clear indication that the main objective viz., "safety of life at sea" has not been achieved with the technological upgradation. Moreover, the change of face at bridge onboard a ship is industry driven irrespective of the adoption and familiarization of technology by the personnel onboard. In other words, the mariner could not keep up pace with technological advancements which are leap frogging and mariner is at a snail's pace. The charm of being at sea is at the risk of life versus economic benefits. Lack of knowledge in marine cartography, improper procedures followed by the untrained manpower with least exposure to ECDIS display and its alarms and warning while navigating through unfamiliar waters will increase the probability of risk to the ships.

The following are recommended to reduce the risk of marine incidents and to overcome the shortfalls while using digital navigational tools onboard:

- Regular, periodic training to be conducted for onboard use of navigational equipment including ECDIS functions to the bridge crew is mandatory.
- ECDIS system and procedures which safeguards intended to prevent groundings must be strictly followed.In case of amended Passage Plan if any must be thoroughly checked on an appropriate scale to avoid the mismatch.
- Visual checks while planning the passage must be on desired scale rather using "standard" chart view.
- Audible alarms must be enabled and no safety alarms to be disregarded or over ruled.
- The upgraded versions of the ECDIS machines and the software which are compliant to IHO standards and specifications are recommended.
- Familiarization of on-board navigational equipment including ECDIS to the bridge team is very essential.
- Detailed reporting on bridge activity including change of passage if any by the navigating officer on duty to the second officer while handing over the charge is very important.
- Master must check or approve the amended Passage Plan prior to execution.
- Comfortable duty hours, good health and mental status of the navigating team at bridge must be given high priority to overcome the inefficiency due to fatigue.
- No compromise on standards to be maintained onboard whether it is equipment, fuel and procedures to follow.
- Safety should be given at most priority.

https://doi.org/10.58440/ihr-30-2-n09

References

Fox, BBC (2024). *Baltimore bridge collapse: Six presumed dead after ship collides with bridge.* British Broadcasting Corporation (BBC). https://www.bbc.com/news/world-us-canada-68663318 (accessed 26 October 2024).

EMSA (2016). *Marine Casualties and Incidents. Summary Overview 2011–2015.* European Maritime Safety Agency. https://www.emsa.europa.eu/component/flexicontent/download/4685/3011/23.html (accessed 26 October 2024).

EMSA (2023). *Annual Overview of Marine Casualties and Incidents 2023*. European Maritime Safety Agency. https://emsa.europa.eu/component/flexicontent/download/7639/2713/23.html (accessed 26 October 2024).

ICS (2024). *International Chamber of Shipping*. https://www.ics-shipping.org (accessed 26 October 2024).

IHO (2018a). *Facts about Electronic Charts and Carriage Requirements* (1st ed.). IHO Special Publication S-66, International Hydrographic Organization, Monaco. https://iho.int/iho_pubs/standard/S-66/S-66%20Edition%201.1.0_Final_Clean.pdf (accessed 26 October 2024).

IHO (2018b). Resolutions of the International Hydrographic Organization (2nd ed.). IHO Publication M-3, International Hydrographic Organization, Monaco. https://iho.int/iho_pubs/misc/M3-E-AUGUST18.pdf (accessed 26 October 2024).

IHO (2020). *The Future of the Paper Nautical Chart* – Final Report. Nautical Cartography Working Group (NCWG), International Hydrographic Organization, Monaco. https://iho.int/uploads/user/Services%20and%20Standards/HSSC/HSSC12/2020-08-28%20Future%20of%20the%20Paper%20Nautical%20Chart%20Final%20Report%20FINAL.pdf (accessed 26 October 2024).

INDIA CODE (2024). *INDIA CODE. Digital Repository of Laws – A system of laws for communication*. https://www.indiacode.nic.in (accessed 26 October 2024).

MAIB (2017). *Report on the Investigation of Grounding of Muros*. Report no. 22/2017, Oct 2017, Marine Accident Investigation Branch. https://www.transportes.gob.es/recursos_mfom/maib-invreport_22_2017.pdf (accessed 26 October 2024).

MSIU (2018). *Safety Investigation into the grounding of the Maltese registered container ship Kea Trader.* Report No. 14/2018, Marine Safety Investigation Unit.

NTSB (2016). *Grounding of the Bulk Carrier American Mariner.* Marine Investigation Report MIR-24-16, National Transportation Safety Board, USA. https://www.ntsb.gov/investigations/AccidentReports/Reports/MIR2416.pdf (accessed 26 October 2024).

Acknowledgement to peer-reviewers

The International Hydrographic Review (IHR) would like to express its gratitude to the following individuals for their invaluable contribution to the peer review process, having reviewed one or more scientific manuscripts during the period spanning 2022 to 2024.

Alberto Pedrassani Costa Neves
Elias Adedirans
Panagiotis Agrafiotis
Mohammad Ashphaqs
Mohammad Ashphaqs
Andrey Babeyko
Senthil Balaganesh
Evgenia Bazhenova
Fiona Bloor
Andreas Boesch
Elizabeth de Bol
Mirko Bothe
Brian Calder
Ian Church
Carlos Zapata Cortés
Olagoke Daramola
Neil Cunningham Dobson
Paraskevi Drakopoulou
Tanja Dufek
Hassan El-Halawany
Artu Ellmann
Lina Eyouni
Luca Fallati
Ruth Farre
Saeed Farzaneh
Peter Feldens
Italo Oliveira Ferreira
Rosa Virginia Garone
Mohamed Ali Ghannami
Hendrik Göhmann
Kyle Goodrich
Peter Grabbert
Knut Hartmann
Anja Heßelbarth
Matthias Hinz
Josh Humberston
Jennifer Jencks
Shuaidong Jia
Belen Jimenez
Christopher Jones
Mareike Kampmeier
Johannes Karstensen
Christos Kastrisios
Dafrosa Kataraihya
William Kelly
Hannu Koivula
Rita Lammeren
Jean Laporte
Søren Reime Larsen
Volkmar Leimer
Bertrand Lobo
Holly Lopez-Woytak
Jacek Lubczonek
Mona Lütjens
Brandon Maingot
Kimberly Mason
James Massey
Ivana Golub Medvešek
Fabio Menna
Irène Mopin
Tanja Morgenstern
Christian Mulsow
Tamer Nada
Majid Nazeer
Cindy Niemeyer
Frank Niemeyer
Jean-Guy Nistad
Maaria Nordman
Yusaku Ohta
Emmanouil Oikonomou
Felix Ott
Christopher Parrish
Alyssa Pietraszek
Purbo Poerbandono
Julia Powell

https://doi.org/10.58440/ihr-30-2-i03

H. M. Indika Prasanna
Jonathan Pritchard
Alexander Proelß
Pete Ramsay
Katja Richter
Swen Roemer
Ole Roggenbuck
Mathieu Rondeau
Christian Rost
Eslam Ali Saleh
Thierry Schmitt
Jens Schröder-Fürstenberg
Joachim Schwabe
Scott Simmons
Patricia Slabon
Daouda Sylla
Nasar T
Kelvin Kang Wee Tang
Trevor Taylor
Arkadiusz Tomczak
Kareem Tonbol
Kayacan Ünal
Matthias Vahl
Lambert Wanninger
Christoph Werner
Ellen Werner
Bibin Wilson
Paul Wintersteller
Daniel Wright
David Wyatt

https://doi.org/10.58440/ihr-30-2-i03

BOOK REVIEW

Legal and regulatory aspects of telecommunication submarine cables

By Andrés Fígoli Pacheco, independently published (30 July 2024), 158 p., ISBN-13 979-8332883187.

Authors

Aldo Monaca[1] and Gioia Alessia Chiara Grazia Indelicato[1]

In the growing world of telecommunication infrastructure, submarine cables serve as the foundation of global connectivity, carrying nearly 99 % of transoceanic data traffic. Despite their critical role, the regulatory landscape governing these cables remains complex and, at times, fragmented. Andrés Fígoli *Pacheco's Legal and Regulatory Aspects of Telecommunication Submarine Cables* stands out as a key book that clarifies these complex aspects. The book addresses the essential legal and regulatory challenges facing this critical infrastructure and offers practical solutions to enhance its security, resilience, and functionality.

Andrés Fígoli brings a wealth of experience to this topic. As the director of Fígoli Consulting, he provides specialized legal and regulatory advice on all aspects of subsea cable work. Mr. Fígoli's academic background includes a law degree from the University of the Republic in Uruguay, earned in 2002, and a Master of Laws (LLM) from Northwestern University. His nearly 21 years of experience in submarine cable projects at a major wholesale telecommunications company, coupled with his role as Director and Member of the Executive Committee of the International Cable Protection Committee (2015–2023), lend him a deep and practical understanding of the subject matter.

Written with the intent of guiding cable operators, policymakers, legal professionals, and scholars, the book offers a comprehensive and accessible overview of the regulatory challenges and considerations surrounding submarine cables. Fígoli's book serves as a practical guide, not merely a theoretical work, to help readers navigate the complex legal landscape of submarine cable operations. The author has gathered a collection of articles, many of which appeared in *Submarine Telecoms Forum Magazine*, and complemented these with in-depth examinations of court cases and specific rules from different jurisdictions. The book is structured into categories and sub-chapters, each focusing on distinct legal aspects such as ownership, installation, operation, and maintenance of submarine cables. This layout allows readers to easily find their specific areas of interest, making it both a reference guide and a holistic introduction to the field.

Fígoli's book deals with several critical themes surrounding the legal and regulatory landscape of submarine cables, beginning with the urgent need to enhance the security and resilience of these infrastructures. He argues that the current international protection framework, rooted in an 1884 convention designed for telegraphy, is no longer fit for purpose. This outdated regulatory foundation, combined with the lack of coordinated international efforts, leaves submarine cables vulnerable to negligent damage, such as that caused by fishing or anchoring activities. Fígoli calls for countries to take immediate action to update their regulations to better protect these underwater assets. He suggests that governments, telecom regulators, and local navies should collaborate as part of a digital sovereignty strategy to safeguard these critical components of global connectivity. To further this cause, he proposes the development of a new international treaty, guided by the UN, to criminalize harmful activities targeting submarine cables – drawing parallels to existing international regulations in aviation and cyberspace.

The book also touches upon the intersection of geopolitics and business in the deployment of

✉ Aldo Monaca · a.monaca@oceanscables.com

[1] Oceans & Cables Ltd., Birkirkara BKR 9037, Malta

https://doi.org/10.58440/ihr-30-2-b02

new submarine cables. Fígoli notes that some government strategies focus more on geopolitical objectives, such as establishing a country as a communications hub, rather than prioritizing the practical protection of cables from everyday threats. He emphasizes that countries aiming for digital sovereignty must diversify their suppliers of cable-laying and maintenance services to avoid over-reliance on any single provider, which could lead to vulnerabilities. While geopolitical concerns are important, Fígoli stresses that they should not overshadow the need for robust measures to address more traditional threats to cables, such as fishing activities and anchor dragging—still the leading causes of cable damage globally. He argues that these two perspectives, geopolitical strategy and practical risk management, are not mutually exclusive and must be balanced to ensure the security of submarine cables.

A major theme in the book is the growing dominance of Over-the-Top (OTT) players in the global bandwidth market. Fígoli discusses how these companies have come to control the major routes of global data traffic, raising concerns about oligopolistic tendencies. He points out that the current environment makes it challenging for new submarine infrastructure projects to proceed without OTT involvement, as their financial power and scale can easily overshadow the efforts of traditional telecom operators. The book critically examines the implications of this trend for competition and national digital sovereignty. Fígoli calls for more vigilant oversight from telecom and antitrust regulators to ensure a fair and competitive market, especially when it comes to forming submarine cable consortiums and negotiating long-term capacity lease agreements or Indefeasible Right to Use (IRU) agreements.

The complexity of contracts and regulations in the submarine cable sector is another area of focus. Fígoli highlights how legal, engineering, and sales teams within cable companies often struggle with the intricacies of drafting and negotiating agreements, such as cable landing agreements and the various provisions required by financial stakeholders. He describes how these challenges are exacerbated by the increasing interdependence of legal work, technical specifications, and commercial considerations. The book offers tools and strategies to help industry professionals navigate these complexities, reduce litigation risks, and achieve more balanced and secure agreements. It also addresses the evolving nature of litigation in this field, noting the rise of more sophisticated fraudulent schemes are emerging, involving actors like opportunistic landowners, local backhaul providers, or even fishermen who might exploit legal and regulatory gaps.

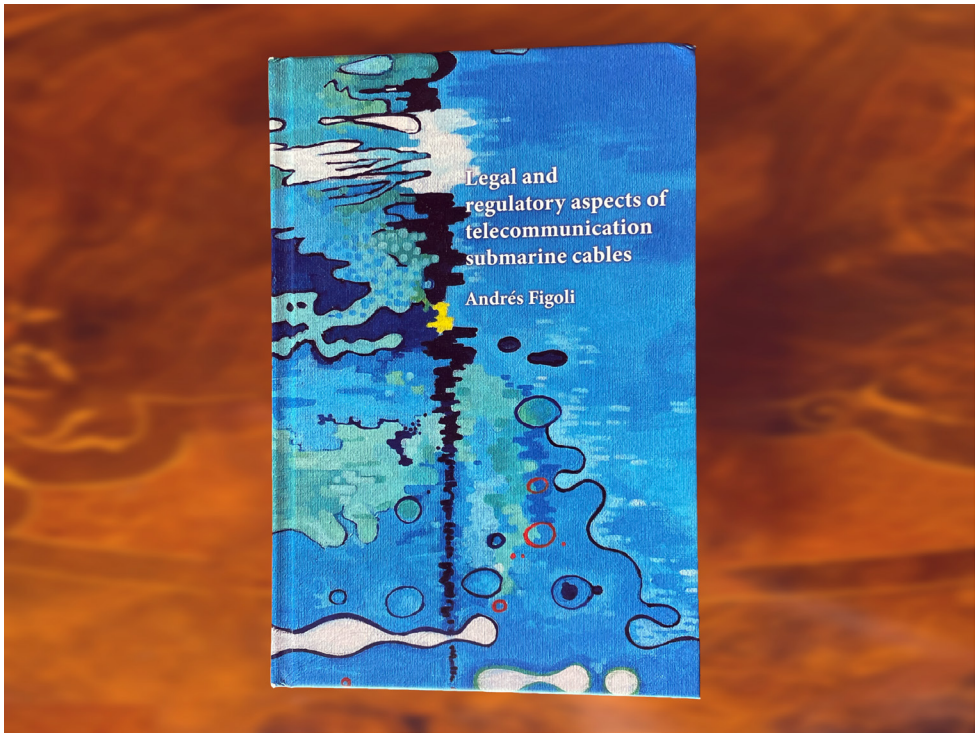
Fígoli looks ahead and talks about how the global submarine cable market might grow. He believes that new companies can still join as long as antitrust and telecom regulators keep the system safe from unfair business practices. He also advocates for the submarine cable industry to take part in maritime planning initiatives to ensure the coordinated and sustainable use of the seabed alongside other activities such as mining or fishing. He raises the idea of SMART cables, which integrate traditional telecom functions with marine scientific research. These cables offer additional benefits, such as early tsunami detection and enhanced cable protection measures. Fígoli views SMART cables as a paradigm shift for the industry but also emphasizes that they require a new regulatory framework to maximize their potential benefits while ensuring legal clarity and environmental sustainability.

A recurring theme throughout the book is the need to harmonize legal frameworks across regions to ensure the integrity of submarine cable networks. Fígoli argues that the fragmented legal systems currently governing these cables pose a significant risk to their stability and calls for a coordinated global effort to protect these critical infrastructures. He introduces three tests to assess the level of digital sovereignty in any given country, encouraging stakeholders to engage in open discussions aimed at improving policies and strategies. Additionally, the book explores Maritime Spatial Planning (MSP) as a tool for managing ocean activities in a sustainable way, balancing the need to protect submarine cables passing through Exclusive Economic Zones (EEZs) with respect for national rights and environmental concerns.

Overall, Fígoli's book raises critical awareness about the environmental, legal, and competitive challenges facing the submarine cable industry. He critiques the practice of greenwashing, where superficial environmental measures are adopted without genuine impact, and calls for more transparent and meaningful sustainability practices. The book also provides practical recommendations for improving the legal frameworks governing submarine cables, from enhancing IRU agreements and Cable Supply Agreements (CSAs) to tackling antitrust concerns. It serves

as both a call to action for stakeholders in the industry to engage in meaningful dialogue and a strategic guide for navigating the complexities of this critical infrastructure.

As the reliance on global digital connectivity continues to increase, the importance of the legal frameworks governing submarine cables cannot be overstated. Fígoli's book provides a timely reminder of the necessity for robust, harmonised regulations that safeguard these vital infrastructures while facilitating innovation and international collaboration.



Cover of the book “Legal and regulatory aspects of telecommunication submarine cables” by Andrés Fígoli Pacheco.

https://doi.org/10.58440/ihr-30-2-b02

OBITUARY

In Memoriam: Jean-Nicolas Pasquay (1932–2024)

Author
Gilles Bessero[1]

Born in Strasbourg in 1932 in a family of manufacturers, Jean-Nicolas Pasquay joined the prestigious Ecole Polytechnique in Paris in 1954 and opted for the Corps of Naval Hydrographic Engineers upon graduating, attracted by a career that combined a maritime and a scientific dimension.

His first survey experiences during his hydrographic training were along the coast of Morocco and Algeria in 1957–1958. As soon as 1961, he was entrusted to lead the special amphibious survey unit set up in 1950 to survey landing sites and was then operating on the south-west coast of France. In 1964–1965, he directed a survey campaign in the Western Indian Ocean with the survey vessel *La Pérouse* that focused on Madagascar and Mayotte. Back in France, he was responsible for another survey unit devoted to wreck searches from 1967 to 1969. During this assignment, he participated with the survey vessel *La Recherche* in the search for the French submarine *Minerve* that was lost in the western Mediterranean Sea in January 1968. He drew from this operation a paper on its radio positioning aspects that was presented to an international conference organized by the European Institutes of Navigation in Rome, Italy in 1970. The "wet" component of Jean-Nicolas Pasquay's career ended with the command of the Atlantic Hydrographic Mission based in Brest, France from 1972 to 1974. With up to four survey vessels under his authority, including the newly refurbished survey vessels *L'Espérance* and *L'Estafette*, he completed the survey of the western approaches to Brest. Then he undertook the survey of the eastern part of the Channel. Close cooperation was developed with the United Kingdom Hydrographic Office for a joint survey effort in the Channel, including agreeing on a dividing line of responsibility and setting up a shared radio-positioning system covering the whole area.

After a term as Head of the Oceanography Department of SHOM Main Establishment in Brest (EPSHOM) from 1974 to 1976, Jean-Nicolas Pasquay was assigned to SHOM Head Office in Paris. Up until 1981, he was responsible for planning and monitoring the activities of SHOM units. He then oversaw prospective studies and requirement assessments and coordinated external relations, a rapidly expanding domain at the time. He contributed to the development of bilateral relations, in particular with the Hydrographic Offices of the Netherlands, Portugal and the United Kingdom. He assisted the French National Hydrographer at the 12th International Hydrographic Conference in 1982 and in the working group on election of Directors and functions of the International Hydrographic Bureau that was established by the Conference and reported to the Member States in 1985. He was the French point of contact for the understanding between Belgium, France, Netherlands and the United Kingdom on national responsibilities for hydrographic surveying in the southern North Sea and Dover Strait that was agreed in 1983. He contributed to the establishment of the Eastern Atlantic Hydrographic Commission that held

✉ Gilles Bessero · gilles.bessero@orange.fr
[1] Member of the French Maritime Academy (Académie de marine); formerly Director of the International Hydrographic Organization and French National Hydrographer

https://doi.org/10.58440/ihr-30-2-o01

its first Conference in Paris in 1986 and participated in the activities of two other regional hydrographic commissions: the North Sea Hydrographic Commission and the Mediterranean and Black Seas Hydrographic Commission.

From 1987 to 1990, Jean-Nicolas Pasquay was the Director of EPSHOM in Brest. His mandate was marked by the generalization of digital surveying and charting methods and tools, and the early studies related to electronic charts.

Appointed National Hydrographer in 1990, Jean-Nicolas Pasquay paid particular attention to the implementation of the extended national responsibilities allocated to SHOM in military oceanography. He was head of the French delegation to the 14th International Hydrographic Conference in 1992. He chaired both the Mediterranean and Black Seas Hydrographic Commission (1990–1991) and the North Sea Hydrographic Commission (1993–1994) and initiated the participation of France to the South-West Pacific Hydrographic Commission and the Meso American - Caribbean Sea Hydrographic Commission. During his last year in office, in 1994, he oversaw the contribution of SHOM to the celebrations of the 50th anniversary of the Normandy D-Day, with the publication of a commemorative nautical chart of the area, and several articles on the meteorological and oceanographic aspects of the operation.

Throughout his career and after his retirement, he was mindful of the importance of nautical charts and publications in support of navigational safety. In 1986, he published in this review an article on "Safety of Modern Shipping and Requirements in Hydrographic Surveying and Nautical Charting". In 1992, he authored the handbook "Hydrography, nautical documents, their imperfections and proper use" still included in today's SHOM collection of nautical publications. His conclusion "Navigation will never be a black box case" remains as relevant as ever. From 1985 to 2018, he contributed more than twenty articles on related issues in the Journal of the French Institute of Navigation together with a dozen commentaries of articles published in Seaways, the Journal of the Nautical Institute.

Pedagogue in his own way, for the benefit of the students who benefited from his geodesy class in the late 1960s–early 1970s, his subordinates in his successive assignments, his contacts in developing countries urged to consider building their hydrographic capacities, or the readers of his articles, Jean-Nicolas Pasquay combined a benevolent rigour with a subtle sense of humour that earned him the esteem of the international hydrographic community.



Ingénieur général Jean-Nicolas Pasquay (second from the right) aboard the survey ship *D'Entrecasteaux* in 1992.

https://doi.org/10.58440/ihr-30-2-o01


IHO
International
Hydrographic
Organization